# EFFICIENT FREE-SPACE OPTICAL PUMPING OF A DEFORMED MICROCAVITY LASER

**Juhee Yang [a], Sang-Bum Lee [b], Songky Moon [a], Soo-Young Lee[a], Jeong-Bo Shim [c], Sang Wook Kim [d], Jai-Hyung Lee [a],and Kyungwon An [a]**

[a)] School of Physics and Astronomy, Seoul National University, Seoul 151-742, Korea
[b)] Korea Research Institute of Standards and Science, Daejeon 305-340, Korea
[c)] Max Plank Institute for the Physics of Complex Systems, NÄothnitzer Str. 38, Dresden, Germany
[d)]Department of Physics Education and Department of Physics, Pusan National University, Busan 609-735, Korea
*E-mail:kwan@phya.snu.ac.kr*

**Abstract:** Tenfold enhancement in the pumping efficiencyhas been observed at a properly chosen pumpingangle and a position in chaos-assissted nonresonant optical pumping in a deformed microcavity laser.The pumping efficiencydistribution resembles the output emission intensity distribution for the samemicrocavity, consistent with the concept of the time-reversal ray tracing.

## 1. Introduction

Optical pumping is widely used for microcavities which can confine light in a small mode olume with high quality factors. Especially, in a deformed microcavity, free-space pumping is possible without special arrangements such as a prism[1] or tapered fiber[2]. Since the incident pumping angle is not preserved inside the cavity due to cavity asymmetry, a ray can be refracted into the cavity and circulate many times undergoing total internal re°ections.

Recently, we have demonstrated an efficient nonresonant optical pumping based on chaotic ray dynamics inan asymmetric resonant cavity (ARC) [3], where the light initially undergoing total internal re°ections is eventually emitted out via refractive escape since the incident angle at each re°ection is not preserved. Conversely, if a ray is injected in the reverse direction, it will undergo total internal re°ections in a time-reversed way for many round trips, e®ectively pumping the modes distributed near the cavity boundary. With a °*ood* pumping geometry, *i.e.*, the pump beam covering the entire side width of the cavity a three-fold enhancement was achieved in the pumping efciency compared to that of a circular microcavity for a properly chosen pumping angle. Since an initially circulating ray emerges only at particular emission points on the boundary of an ARC with a well-defined emission angle, the pumping efficiencyshould be strongly dependent not only on pumping angle but also on pumping position[4]. In the present work, we have investigated the pumping efficiencyas a function of the pumping angle and the pumping position with a tightly focused pump beam. We have achieved an order of magnitude enhancement in the pumping efficiencyfor the pumping position and the pumping angle that are consistent with the output emission point and output emission angle of the given ARC, clearly supporting the validity of the present concept of time reversal ray tracing.

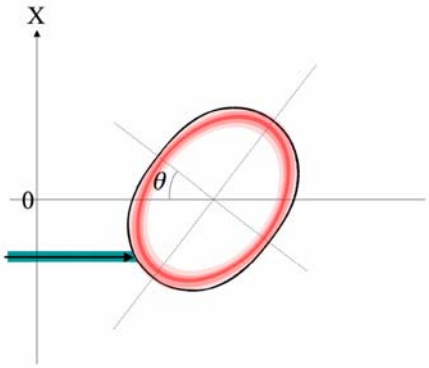


**Fig. 1**. Schematic of pumping configuration. A focused pump beam is incident on the cavity at an angle $\theta$ displaced from the center 0 by $X$.

## 2. Experiment

Our experiment is performed on a two-dimensional ARCmade of a liquid jet of ethanol. The technical details of our liquid-jet microcavity are described elsewhere [5]. The boundary of the ARC is specified in the polar coordinates by the equation $\rho(\emptyset) = a(1 + \eta_2 cos2\phi + \eta_4 cos4\phi)$ where $\eta_2$=19% and $\eta_4$=1.5% are deformation parameters for quadrupole and octapole respectively and $a$=15 μm is a mean radius of the ARC. These parameters have beenmeasured by using the surface mapping technique based on small-angle forward light diffraction [6].

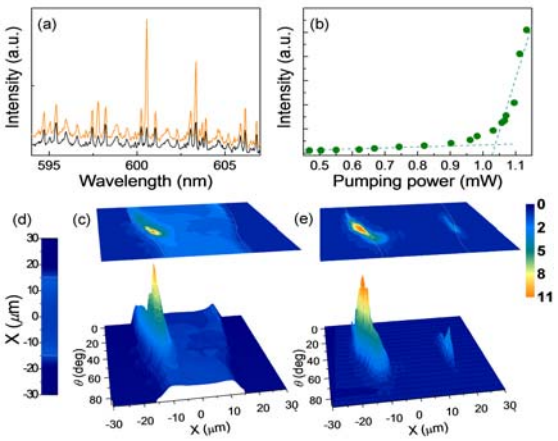


Fig. 2. (a) Cavity-modified fluorescence and lasing spectra of our ARC with a pump power of .74mW and 1.05mW at $\theta$ = 500° and $X$ = -13:5$\mu m$. (b) Observed lasing threshold curve for same $\theta$ and $X$ as (a). (c) Experimentally observed pumping efficiency as a function of the pumping angle $\theta$ and the pumping position $X$ for our ARC. A solid line indicate the projected edge of the ARC. (d) Observed pumping efficiency in a circular cavity of a similar size. (e) Observed output intensity distribution with the imaging technique described in the text.

The cavity medium is doped with Rhodamine B dye at a concentration of $10^{-4}$ mol/l so as to provide a lasing gain for low-loss cavity modes when optically pumped. The cavity apparatus is mounted in the center of a computer controlled rotational stage so that the pumping angle θ, measured with respect to the minor axis of ARC (see Fig. 1), can be changed at will. The optical pumping is done with a frequency-doubled Nd:Vanadate laser (wavelength λ=532 nm) focused down to a beam waist of 0.8 μm on the cavity column from the side. The polarization of the pump laser is parallel to the cavity column. The pump beam is translated by a displacement $X$ from the position of the center of ARC projected into the direction of the pump beam as shown in Fig. 1 in a step size ~ 0.6 μm driven by a stepper motor.

### *2.1 Pumping efficiency distribution*

Fig. 2(a) shows the cavity-moded fluorescence(CMF) and lasing spectra emitted from our ARC for a fixed pumping angle. In that spectrum, there exist several groups of cavity modes with well defined free spectral ranges. As the pumping power increases, a single mode undergoes a laser oscillation. The observed lasing mode is a cavity mode of radial mode order $l$ = 1 with $Q$ of $5x10^{-5}$. The $Q$ value was obtained from both the laser threshold analysis and the cavity-modified fluorescence analysis [7,8]. By recording the peak height of this lasing mode as the pumping power is varied, a lasing threshold curve can be obtained like Fig. 2(b). We first measure the threshold pump power while scanning the pumping position $X$ on the microcavity surface for a given pumping angle $\theta$ and repeated the measurements for various pumping angles. We finally plot the inverse of the threshold pump power, proportional to the pumping efficiency[3], so that a complete map of pumping efficiency as a function of $\theta$ and $X$ or the pumping efficiency distribution $f_p(\theta;X)$ is obtained as shown in Fig.2(c). The solid gray lines indicate the projected edges of the ARC as $\theta$ is varied. A maximum pumping efficiencyis observed when $\theta$ ~ 50° and $X$ ~ 13μm. The efficiency is eleven times higher than a reference value observed at $\theta$ = 0° and $X$=0. The pumping efficiency for a circular microcavity with a radius of 15$\mu m$ is also shown in Fig. 2(d) for comparison. Obviously, the pumping efficiency in this case has no $\theta$ dependence due to rotational symmetry and it only shows a minor enhancement at the edge. Its value at $X$=0 is about the same as that of the reference single-pass pumping at $\theta$ = 0± and $X$=0 for the DMC.

The distribution in Fig. 2(d) was obtained experimentally for $\theta = 0^o$. Since the lasing modes of the circular cavity have much higher $Q$ values than those of the ARC, the magnitude of the distribution in Fig. 2(d) has been normalized according to the ray tracing simulations results which will be described in section 3. We calculate an effective path length with same absorption coefficient in each case of circular cavity and ARC for $\theta = 00$. Then, its value at $X$=0 of circular cavity is 1.2 times higher than that of the reference efficiency of the ARC at $\theta = 0^o$ and $X$=0. With this factor the relative pumping efficiency between circular cavity and ARC has been corrected.

### *2.2 Emission intensity distribution*

The observed $f_p(\theta;X)$ should be closely related to the output intensity distribution $f_o(\theta;X)$ of the given ARC due to the time-reversed relation in ray dynamics. In order to check this relation experimentally, we have also measured the lasing output intensity distribution of the same ARC when uniformly pumped. The output was imaged on a charge-coupled-device (CCD) camera with a small numerical aperture of 0.13 for resolving both emission point ($X$) and emission angle ($\theta$). The results are summarized in Fig. 2(e). A similar imaging technique was employed in Ref. [9]. It is reassuring that the observed $f_o(\theta;X)$ in Fig. 2(e) resembles the observed $f_p(\theta;X)$ in Fig. 2(c) except that the $f_o(\theta;X)$ does not show the almost constant background seen in $f_p(\theta;X)$. The reason is that the background efficiencyin $f_p(\theta;X)$ corresponds to basically single pass pumping which can still weakly pump the $l$=1 lasing mode via a small overlap with the intracavity mode distribution whereas the output emission of the same lasing mode occurs only at unique emission positions and emission angles as in Fig. 2(e). In addition, the small discrepancy in the peak positions of the two distributions in Figs. 2(c) and (e) might be due to the wave nature of the cavity mode and interference e®ect in the buildup of the pump field inside the cavity, both of which cannot be accounted for in the ray picture which the present pumping scheme is based upon.

## 3. Ray tracing Simulation

Nonetheless, major features of our experimental results can be reproduced in ray tracing simulations, which we will describe below. For this, it is convenient to consider a Poincare surface of section (PSOS) [10], which is a phasespace trajectory map of a ray undergoing infinite number of reflections, obtained by recording its polar angle ϕ(position) and incident angle $\hat{A}$ (momentum) upon every reflection off the boundary. A PSOS for our ARC is shown in Fig. 3(a) and (b) as a underlying picture.

### *3.1 Pumping efficiencysimulation*

In order to estimate the pumping efficiency, we performed a ray simulation, where we treat the incident pump as a set of a large number(~ 70000) of equally distributed below the line of critical angle (LCA), which is defined as sin $\chi_c = 1/m$ with $m$ = 1:361 the refractive index of the cavity medium marked by a red dotted line in Fig.3(a) and (b). We then calculate an eflective path length which each ray has travelled inside the cavity before refractive escape by taking into account the transmission coefficient into the cavity, the reflection coefficient upon each subsequent reflection and the absorption coefficient of the cavity medium. In addition, we had considered a spatial overlapping with a lasing mode by only summing path length of rays which circulate near the cavity bound ary ($r > 0{:}95a$). The details of a similar ray model can be found in Ref. [3]. In this model, the intracavity pump intensity is proportional to the eflective path length foreach ray. The result is shown in Fig. 3(a) as a color-coded distribution projected onto the PSOS below the LCA. It shows that the pumping is highly directional (specified by $\chi$) from particular locations (specified by $\phi$)on the cavity boundary.

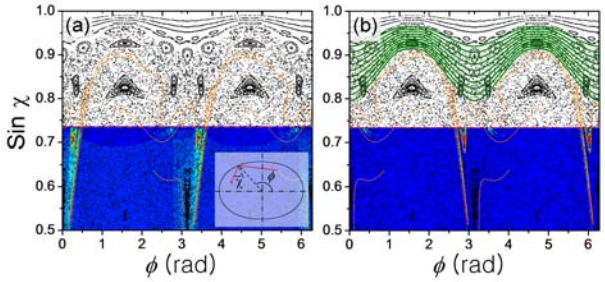


**Fig. 3.** Ray tracing simulation for (a) pumping mechanism and (b) output mechanism. Path lengths for (a) and accumulated intensity for (b) of rays, circulating counterclockwise is projected onto the Poincare surface of section of our COM. Red dotted line represents the line of critical angle.

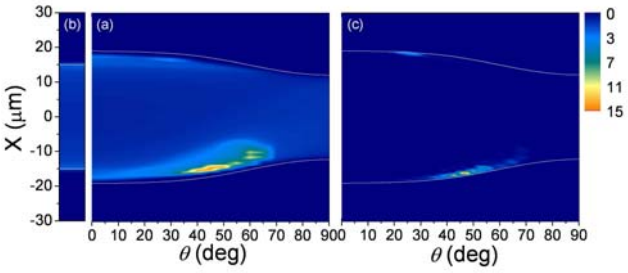


**Fig. 4**. (a) Pump intensity distribution reconstructed from Fig. 3 (a) as a function of pumping angle $\mu$ and pumping position $X$ for the same ARC as in the experiment. (b) Pump intensity distribution for a circular cavity. (c) Output intensity distribution reconstructed from Fig. 3 (b) with combination of clockwise and counterclockwise rays.

### *3.2 Output intensity simulation*

One can also simulate the output intensity distribution by considering refractive escape of the rays initially undergoing total internal re°ections near the cavity boundary [11]. In this case, we consider a large number (~ 20000) of rays initially prepared in an upper region of phase space along adiabatic KAM curves representing whispering gallery trajectories, $\sin\chi(\phi) = [1 - (1-S^2)k(\phi)^{2/3}]^{1/2}$ where $S$ parameterizes the adiabatic curve and $k(\phi)$ is the curvature of the COM boundary, like green line in Fig. 3(b). As we follow these rays, they will undergo many reflections and then cross the LCA mostly at some fixed locations. The intensity distribution of refracted rays is then obtained by summing up all rays which have crossed LCA with the $\phi$ and $\chi$ ($< \chi_c$) weighted by Fresnel refractive coefficient s at that phase-space point ($\phi$; sin $\chi$). The result is shown in Fig. 3(b) as a color-coded distribution.

It has been shown in many recent works that the output distribution in open chaotic cavity is predominantly determined by the phase-space structure called unstable manifolds [10] of ray motion [8], which are drawn in Fig.3(b) as orange lines. We can easily check that the output intensity distribution is formed along the unstable manifolds structure. Interestingly, the pumping efficiencydistribution also nicely follows a similar structure drawn in Fig. 3(a) as orange lines, which are the so-called stable manifolds. They are corresponding to a time-reversal structure of unstable manifold. This result clearly shows the time reversal symmetry between the pumping and the emission processes. In addition, by using the concept of turnstile transport which constitutes major chaotic ray transport in a chaotic microcavity, more details of the output and input mechanism can be understood [12].

The calculated pumping and output distribution in phase space can then be transformed to the distributions in the same coordinate as those in the experiment. The results are shown in Fig. 4(a) and(c), where we plot a normalized intracavity pump intensity as a function of $\theta$ and $X$. It is plotted with combination of clockwise (-sin $\chi$) and counterclockwise (+ sin $\chi$) rays. In addition, it was smoothed out to a same resolution of experiment, i.e. $5^o$ in θ and 0:7 $\mu m$ in $X$ coordinate. A strong enhancement is reproduced at $\theta = 40^o \sim 50^o$ with a displacement $X$~-15μ$m$. Compared to the reference single-pass pumping at $\theta = 0^o$ and $X$=0, the enhancement is about a factor of 15. The location of the peak and its magnitude are very close to the values experimentally observed in Fig. 2. Again for comparison, the normalized pump intensity calculated for a circular microcavity with a radius of 15μ$m$ is also shown in Fig. 4(b).

Both $f_p(\theta;X)$ and $f_o(\theta;X)$ show asymmetry along $X$ for a given $\theta$, particularly for $\theta \sim 50^o$. The asymmetry is due to the different ray trajectories depending on circulation directions. At the strong emission position ($\theta \sim 50^o; X \approx -15\lambda$m), rays can refract out more easily as they approach

from the lower to the higher curvature boundary than from the higher to the lower curvature boundary for the counter-clockwise-circulating rays. Conversely, for the clockwise-circulating rays the pumping efficiencyis more favorable for $X < 0$ than $X > 0$. The discrepancies in details between the observed and the calculated distributions might be due to several factors including the wave nature that has been completely neglected in the ray simulations. In addition, the real pump beam focused on the cavity necessarily has a finite divergence angle whereas in the ray model the pump beam is treated as a bundle of parallel rays. This divergence may have decreased the pumping efficiencyand somewhat smoothed the overall distribution.

## 4. Conclusion

We have studied the optical pumping efficiency with a focused pump beam in a deformed microcavity laser. We have achieved a tenfold enhancement in the pumping efficiency at a properly chosen pumping angle and a position, compared to the usual single-pass pumping in our nonresonant optical pumping scheme. The observed pumping efficiency distribution resembles the output emission intensity distribution of the same cavity, confirming the concept of the time reversal ray tracing. Our results may well find applications in highefficient microlasers with a directional output.

## References

1. V. Sandoghdar, F. Treussart, J. Hare, V. Lefe`vre-Seguin,J.-M. Raimond, and S. Haroche, Phys. Rev. A 54, R1777 (1996).
2. S. M. Spillane, T. J. Kippenberg, and K. J. Vahala, Nature (London) 415, 621 (2002).
3. S.-B. Lee, J.-B. Shim, J. Yang, S. Moon, S.-W. Kim, H.W. Lee, J.-H. Lee, and K. An, Appl. Phys. Lett. 90, 041106(2007).
4. J. Yang, S.-B. Lee, J.-B. Shim, S. Moon, S.-Y. Lee, S.-W.Kim, J.-H. Lee, and K. An, Appl. Phys. Lett. 93, 061101(2008).
5. J. Yang, S. Moon, S.-B. Lee, S.-W. Kim, J.-B. Shim, H.-W.Lee, J.-H. Lee, and K. An, Rev. Sci. Instrum. 77, 083103(2006).
6. S. Moon, J. Yang, S.-B. Lee, J.-B. Shim, S.-W. Kim, J.-H.Lee, and K. An, Optics Express 16, 11007 (2008)
7. S. B . Lee, J. H. Lee, J. S. Chang, H. J. Moon, S. W. Kim,K. An, Phys. Rev. Lett. 88, 033903 (2002).
8. S.-B. Lee, J.-B. Shim, J. Yang, S. Moon, S.-W. Kim, H.-W.Lee, J.-H. Lee, and K. An, Phys. Rev. A. 75, 011802 (2007).
9. N. B. Rex, H. E. Tureci, H. G. L. Schwefel, R. K. Chang,and A. D. Stone Phys. Rev. Lett. 88, 094102 (2002).
10. L. E. Reichl, *The Transition to Chaos in Conservative Classical Systems: Quantum Manifestations* (Springer-Verlag, New York, 1992).
11. J. U. NÄockel and A. D. Stone, Nature 385, 45 (1997).
12. J.-B. Shim, S.-B. Lee, S. W. Kim, S.-Y. Lee, J. Yang, S.Moon, J.-H. Lee, and K. An, Phys. Rev. Lett. 100, 174102(2008).

# FEMTOSECOND SUPERCONTINUA GENERATED IN Sub-cm PHOTONIC CRYSTAL FIBERS: APPLICATION TO BROADBAND ULTRAFAST SPECTROSCOPY

**N. Lecong [a], J. Léonard [a], O. Crégut [a], and S. Haacke [a], P. Leproux [b], P. Viale [b], V. Couderc [b]**

[a] Institut de Physique et Chimie des Matériaux de Strasbourg; UMR 7504 ULP-CNRS;
23, rue du Loess ; BP 43 ; F-67034 STRASBOURG CEDEX 2 ; FRANCE
[b] XLIM – Photonics group; UMR CNRS n°6172
123, avenue Albert Thomas; F-87060 LIMOGES CEDEX ; France
*E-mail :lecong@ipcms.u-strasbg.fr*

**Abstract:** Femtosecond single-pulse supercontinua extending spectrally from the near-UV to the Infrared are produced in sub-cm photonic crystal fibers. We show the experimental condition to obtain such pulses and demonstrate the use of these pulses in ultrafast broadband spectroscopy.

## 1. Introduction

Supercontinua (SC) generated in photonic crystal fibers (PCF) have emerged in the past years as attractive light sources for optical coherence tomography [1], non-linear microscopy [2,3] and ultrafast spectroscopy [4,5]. For the latter application, a supercontinuum is required to be not only a broadband spectrum but also a femtosecond single-pulse. We have generated the femtosecond supercontinua in 8 mm-long birefringent PCF [6] with moderate energies of a few nJ derived from Ti:Sa oscillators and used it in the pump-probe experiment examining the ultrafast internal conversion in malachite green [7].

We report here on new findings, obtained by imaging the input surface of the fiber under excitation and by studying the spectro-temporal properties of the SC as a function of fiber length. We demonstrate that the broadest spectra are generated by injection in the glass interstitials in the cladding and not in the fiber core. Spectral "holes" have to be avoided, which set stringent condition on the choice of the fiber length. In addition, a single-mode PCF is recommended to obtain a single pulse.

## 2. Photonic crystal fiber

The PCF in this work was produced at the XLIM laboratory (Limoges, France) by using the standard stack-and-draw method. There are two types of fibers: the ones with a symmetric core (Fig. 1a) and an asymmetric core (Fig. 1b). The asymmetric core induces strong birefringence, thus the light output in this core has a linear polarisation. The cladding is composed by a periodic micro structure made of air holes and silica. Its refractive index is the effective index of air-silica matrix structure. Guiding takes place in the core, but is also possible in the cladding interstitials. Light propagation undergoes the material dispersion and guiding dispersion. The latter is an important effect in the PCF. It depends on the architecture of the micro structure of cladding and core. Thus, we can tune the dispersion property by different designs [8]. The guiding dispersion is not the same with different propagation modes and, in the birefringent PCF, it also depends on the polarisation direction entering into the PCF. The PCF with symmetric core has one zero-dispersion wavelength (ZDW) at 814 nm, while the birefringent PCF has four ZDW's at 866, 827, 764 and 757 nm respectively for four different modes $LP_{01y}$, $LP_{01x}$, $LP_{11y}$ and $LP_{11x}$.

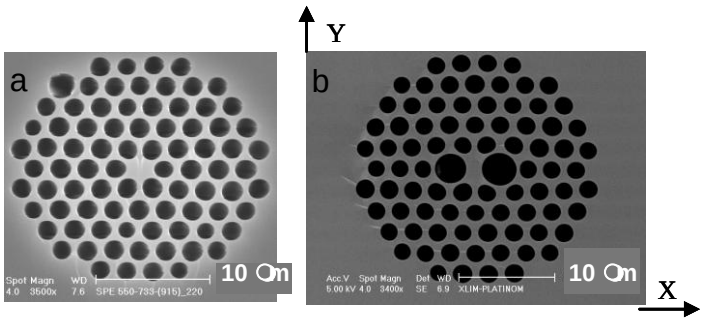


**Fig.1.** Cross-section of the PCF. (a) PCF with symmetric core.
(b) Birefringent PCF with asymmetric core.

Femtosecond SC generation in the PCF only requires laser pulses of a few nJ for injection. Thanks to the micro structure, the light is confined in a small diameter of silica, the abnormal dispersion favors the soliton propagation, and a high excitation density is created and kept during the propagation. Those enhance the non linear phenomena like: self phase modulation, cross phase modulation, four wave mixing, Raman stimulation, soliton propagation…which are responsible for the SC generation. When the fiber is short enough, soliton fission is prevented, and the SC output is a single pulse.

## 3. Supercontinuum generation and characterization

The experimental setup for SC generation and characterization is presented in Fig.2. Our laser source is a Ti:$Al_2O_3$ oscillator (KML's TS laser kit), pumped by a 5W cw VERDI laser (532 nm). A multipass cavity [9] has been inserted, in order to reduce the repetition rate down to 27 MHz, thus increasing the pulse energy up to 15 nJ. The central wavelength can be tuned between 780 - 860 nm and the pulse duration can be as short as 30 fs. A fraction of the laser power is split off and injected into a short piece of a PCF by a microscope objective with a 0.5 numerical aperture. A simple microscopy system is installed before the PCP to visualize the position of the laser injection on its front face. The SC output is sent into a Jobin-Yvon H25 spectrometer, equipped with a CCD camera (Roper Scientific, Spec10), to detect its spectral properties. The main part of the laser power is frequency doubled in 1 mm BBO crystal, producing 3-nJ pump pulses around 420 nm and used as the gating pump pulse. The SC temporal property is investigated by time-gated non-degenerated two-photon absorption (2PA) (a

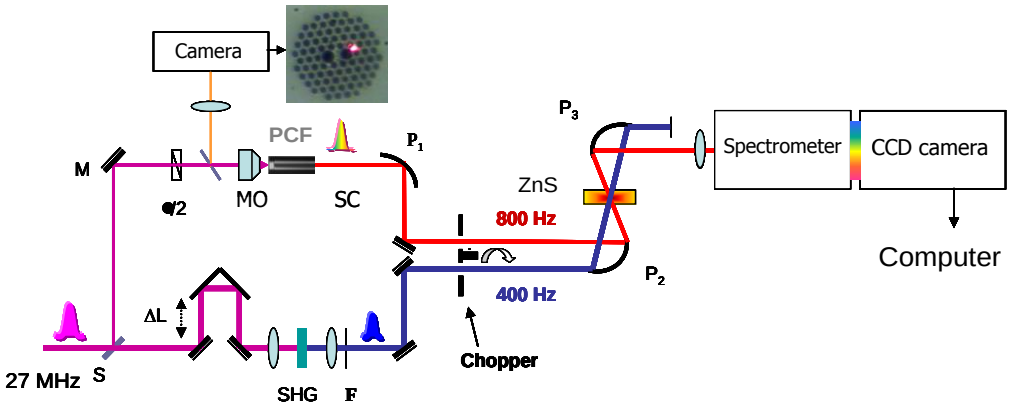


**Fig.2.** Experimental setup. Femtosecond SC and gating pulses are focused into the 40 Mm ZnS plate. Non-degenerate 2PA signal (420 nm gating pulse+ SC) in ZnS is measured vs the variable delay.S : Beam splitter ; M : Mirror ; $P_1 \rightarrow P_3$ : Parabolic mirror; MO : Microscope Objective ; PCF : Photonic crystal fiber ; SHG : Second Harmonic Generation, BBO crystal type I ;ΔL : Variable delay ; F : Color filter BG39.

photon of gate + a photon of SC). For this characterization, both the SC and gating beams are focused and overlapped in a 40 Mm thick ZnS plate by a dispersionless reflective parabolic mirror, with a 25-mm effective focal length. The maximum excitation density is 1,3 mJ/cm$^2$. A chopper modulates both beams, the frequency of the SC being twice as high as the one of the gating pulse. In fast acquisition mode, the camera can record up to 800 spectra per second with low noise level. Using the chopper and a variable delay we can thus record the spectrally- and time-resolved two photons absorption of the SC beam, with a maximum sampling rate of 400 Hz.

## 4. Result and discussion

The below data (fig.3) have been obtained with a 7.2 mm piece of birefringent PCF. The SC generated in the interstice, by 50-fs laser pulses at 840 nm with 1nJ energy, extends from 460 nm to more than 1100 nm (limited by detection) (fig.3a). The spectro-temporal distribution detected by 2PA signal in 40 μm ZnS (fig.3b) shows that the SC is a single pulse. Its duration is not larger than 400 fs over the whole wavelength window. The duration is increased by group velocity dispersion (chirp) in the fiber. This SC is suitable for application in ultrafast broadband spectroscopy. We have also identified the spectro-temporal behavior of the SC generated in the core and in the interstices for different fiber lengths, up to 22 mm. We have found that the chirp increases linearly as a function of the fiber length, as expected. Temporal soliton break-up is not observed (<22mm). For the SC generated in the core, two modes of $LP_{01}$ and $LP_{11}$ can propagate simultaneously and a double-pulse is observed in the resulting SC (not show).

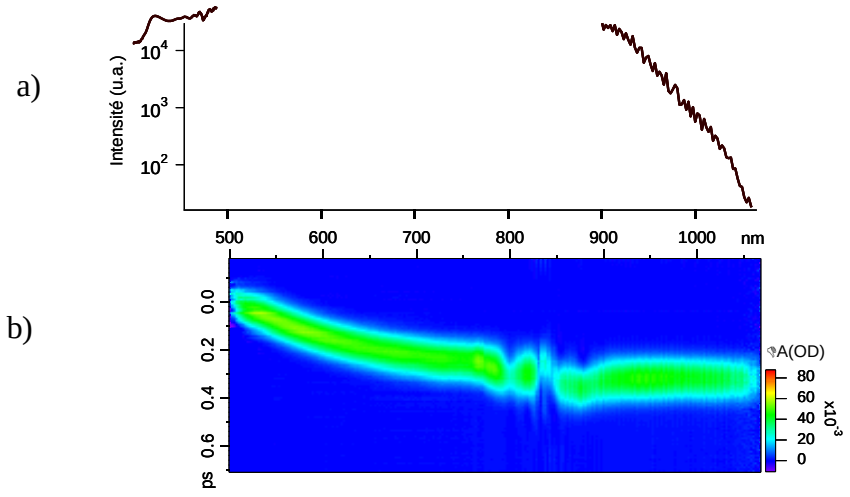


**Fig.3.** (a) Spectra obtained by coupling incident laser pulse: 50 fs,1 nJ, 840 nm, into the interstice of the cladding of a piece 7.2 mm of birefringent PCF. (b) Non-degenerated 2PA (420 nm gate + SC) in 40 μm ZnS plate with a color scale coding for differential absorption of the SC.

By studying the SC properties generated in one of the interstices and in the core (fig.4), we have found that the SC generated in the interstice extends more in the blue than the SC generated in the core. The larger spectral coverage is most probably due to the smaller diameter of the cladding structures, which afford for a shorter zero dispersion wavelength.

We have observed that the spectral width of the SC increases for the longer fiber pieces. However, for a length larger than 10 mm, the spectral extension into the blue is unchanged because the excitation peak intensity is reduced by increased chirp. In addition, the spectrum exhibits more peaks, leading to “spectral break-up” (fig.4b, length fiber 13.8 mm).

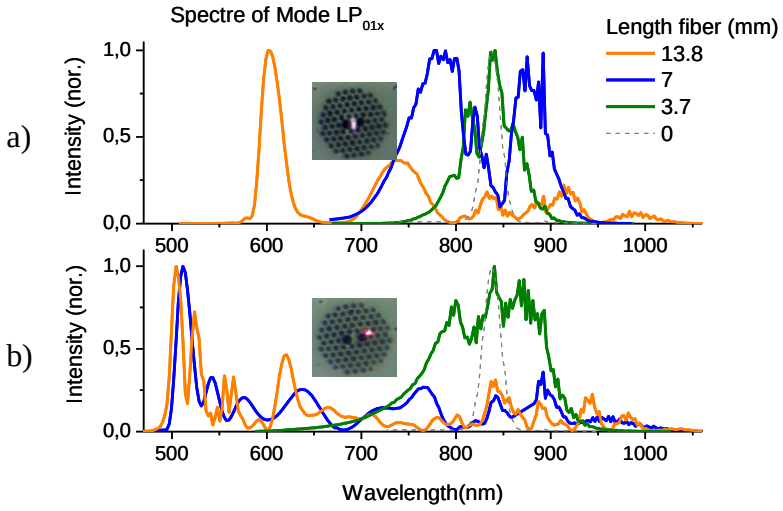


**Fig.4.** SC spectrum as a function of fiber length. The parameters of laser input are fixed at 840 nm, 50 fs, 1 nJ. (a) SC generated in the core of the birefringent PCF. (b) SC generated in interstice of the birefringent PCF.

## 5. Conclusion

Sub-cm PCF's can be used to generate single pulse femtosecond supercontinua. The present work shows that spectral modulation in the SC can be minimized in fibers shorter than 10 mm. For the application to transient absorption spectroscopy, a single mode PCF is recommended, a fiber length of 7 mm is a good trade-off to achieve the broadest spectra with minimum chirp and limited "spectral break-up".

## References

1. I. Hartl, X. D. Li, C. Chudoba, R. K. Ghanta, T. H. Ko, and J. G. Fujimoto, J. K. Ranka and R. S. Windeler, "Ultrahigh-resolution optical coherence tomography using continuum generation in an air–silica microstructure optical fiber", Opt. Lett. **26**, 608 (2001).
2. H. N. Paulsen, K. M. Hilligsøe, J. Thøgersen, S. R. Keiding, J. J. Larsen, "Coherent anti-Stokes Raman scattering microscopy with a photonic crystal fiber based light source", Opt. Lett. **28**, 1123 (2003).
3. L. Fu, A. Jain, H. Xie, C. Cranfield, and M. Gu, «Nonlinear optical endoscopy based on a doubleclad photonic crystal fiber and a MEMS mirror », Opt.Exp. **14**, 1027 (2006).
4. V. Nagarajan, E. Johnson, P. Schellenberg, W. Parson, R. Windeler, « A compact versatile femtosecond spectrometer », Rev. Sci. Instrum. **73**, 4145 (2002).
5. S. O. Konorov, D. A. Akimov, E. E. Serebryannikov, A. A. Ivanov, M. V. Alfimov, A. M. Zheltikov, « Cross-correlation frequency-resolved optical gating coherent anti-Stokes Raman scattering with frequency-converting photonic-crystal fibers », Phys. Rev. E **70**, 057601 (2004).
6. C. Lesvigne, V. Couderc, A. Tonello, P. Leproux, A. Barthélémy, S. Lacroix, F. Druon, P. Blandin, M. Hanna, and P. Georges. Optics letters. Vol. 32, No .15, 2173. (2007).
7. J. Léonard, N.Lecong, J.P Likforman, O. Crégut, S. Haacke, P.Viale, P. Leproux, V.Couderc . Optics express. Vol. 15, No. 24, 1624 (2007).
8. W.H. Reeves, J.C. Knight, and P.St.J. Russell. Optics express, Vol.10, N°14, (2002).
9. S. H. Cho, B. E. Bouma, E. P. Ippen, and J. G. Fujimoto, « Low-repetition-rate high-peak-power Kerr-lens mode-locked Ti:Al2O3 laser with a multiple-pass cavity » , Opt. Lett. 24, 417 (1999).

# BEHAVIOR OF DIAL REMOTE SENSED ETHYLENE AND OZONE IN PRESENCE OF NITROGEN OXIDES

**T.Gasmi**

Faculty of Science & Engineering. Saint Louis University-Madrid campus.
Avenida del valle, 34. Madrid 28003, Spain
Tel: +34 91 5545858; Fax: +34 91 5546202
*E-mail: gasmit@madrid.slu.edu*

**Abstract:**Correlation between ozone concentration and ethylene evolutions in the urban atmosphere in presence of nitrogen oxides is both demonstrated and is supported by a photochemical smog model. The results ascertain that ethylene has a role to play in the generation of tropospheric ozone.
**OCIS codes:** (280.1120) Air pollution monitoring; (280.1910) DIAL, differential absorption lidar

## 1. Introduction

We present experimental results to underline the dynamics of ethylene and ozone in presence of urban nitrogen oxides. Then, we demonstrate the effective role played by ethylene, as a representative of volatile organic compounds, in the formation of urban ozone. The campaign proceeds with earlier investigations of ozone dynamics [2-4] in response to the human activity.

## 2. Results and discussion

The area monitored by the Lidar is a residential area located north-west of Madrid (40° 27' N, 3° 44' W, 680m above sea level). The main source of pollution is attributed to vehicle exhaust and to a very low extent to wind transport of ethylene from the southern industrial region. Measurements were made on several days between approximately 10:00 and 19:30, and the standard deviation varied between 1% and 7%. The standard deviation of 7% is an equivalent measurement uncertainty of almost 2-ppb when averaging 200 pulse pairs.

Ethylene and ozone behaviours show a high degree of coincidence Fig.1. Both gases start to increase, reach a peak and then decay to a plateau, which lasts 3 hours. The net difference (i.e.

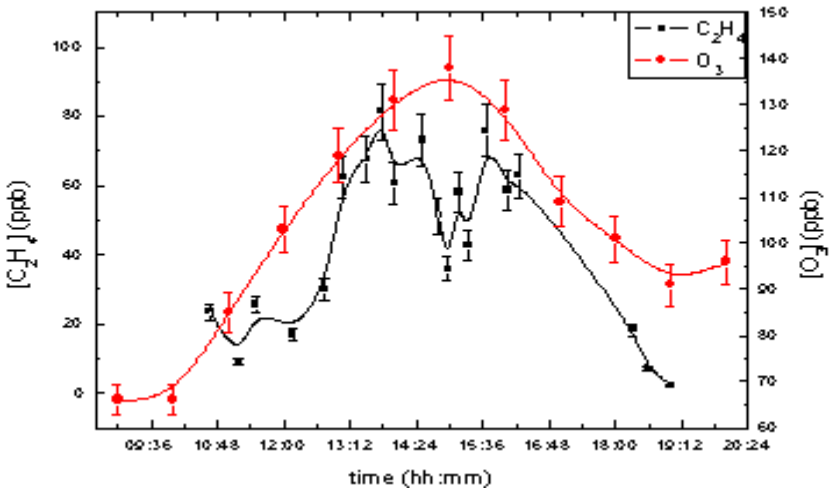


**Figure 1**: Ethylene and ozone behaviors show a high degree of coincidence

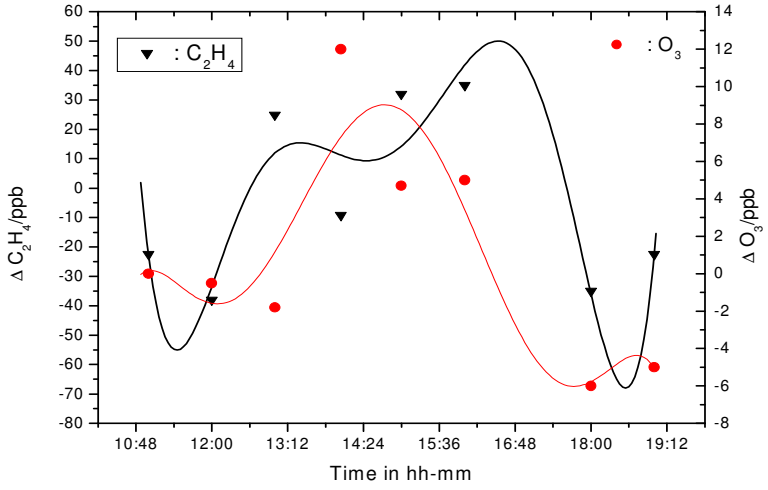


**Figure 2:** The net difference in ethylene concentration ($\Delta C_2H_4$) versus that of ozone ($\Delta O_3$)

12th minus 13th of May) in ethylene concentration ($\Delta C_2H_4$) versus that of ozone ($\Delta O_3$) for the two days in question is depicted in figure 2. ($\Delta O_3$) mimics to a good extent the behaviour of ($\Delta C_2H_4$) and hence reveal a good correlation between ethylene and ozone. One could also note a time shift of more than an hour between the peaks of the two curves that is attributed to the ozone build up time. However it is well established that in the lower troposphere, especially in urban areas, chemical reactions of biogenic and anthropogenic VOC (Volatile Organic Compounds) and anthropogenic $NO_X$ emissions dominate over those of methane and its degradation products. Thus, it is widely accepted that tropospheric ozone results from the interaction of pollutant oxides of nitrogen and non-methane hydrocarbons with solar radiation via the following photochemical mechanism:

$$RH + OH + O_2 \rightarrow RO_2 + H_2O$$
$$RO_2 + NO + O_2 \rightarrow NO_2 + HO_2 + CARB$$
$$HO_2 + NO \rightarrow NO_2 + OH$$
$$2(NO_2 + h\nu + O_2 \rightarrow O_3 + NO)$$
$$net \quad RH + HO_2 + h\nu \rightarrow 2O_3 + CARB$$

CARB represents carbonyl compounds than can further break down to produce additional $O_3$. A key non-methane compound is the ethylene whose atmospheric chemistry is well studied. Essentially the basic role of this alkene is the efficient conversion of NO to $NO_2$ and subsequently, the increase of tropospheric ozone. The overall result of the hydroxyl radical attack on ethene is known to be.

$$C_2H_4 + OH + NO \rightarrow NO_2 + 1.44HCHO + 0.28HOCH_2CHO + HO_2$$

Therefore according to this basic photochemical smog model one should expect a direct correlation between the $C_2H_4$ evolution and that of $O_3$ under similar meteorological conditions for the urban atmosphere and UVB radiation that prevailed during the days of the campaign. All these observation constitute additional evidence to the many models [5-11] that state that ethylene, being a hydrocarbon, has a role to play in the generation of tropospheric ozone.

## 3. Conclusion

Correlation between ozone concentration and ethylene, as volatile organic compounds representative, was demonstrated. Our observations are additionally supported by a basic

photochemical smog model that indeed suggests a direct correlation between the $C_2H_4$ evolution and that of $O_3$ under similar conditions for the urban atmosphere under investigation.

**References**


1. Gasmi T., González Ureña A., 2002: $CO_2$-TEA, Mid-Infrared, Laser-Based Dial System: Featuring Ozone Dynamics during a "vehicle-free Day", Instr. Sci. & Technol, **30**, 4, pp:427-438.
2. Gasmi. T., H. Zeaiter, Ropero G. and González Ureña A., 2000: Plasma-based nitrogen tail pulse shutter for $CO_2$-TEA lidar dial systems, Appl. Phys. B, **B71**, pp. 169-175.
3. Gasmi, T., Ropero G. and González Ureña A., 2000: Excess traffic effects on Madrid urban atmospheric pollution: featuring ozone dynamics by infrared DIAL technique in DOAS mode of operation, J. Opt. A: Pure Appl. Opt. **2** , pp. 565-568
4. Gasmi T., González Ureña A., 2002: $CO_2$-TEA, Mid-Infrared, Laser-Based Dial System: Featuring Ozone Dynamics during a "vehicle-free Day", Instr. Sci. & Technol, **30**, 4, pp:427-438.
5. Finlayson-Pitts, B. J., et al.; 1997: Tropospheric air pollution: Ozone, airborne toxics, polycyclic aromatic hydrocarbons, and particles, Science, **276**, pp. 1045-1052.
6. R. R. Dickerson et al, 1997: "The Impact of Aerosols on Solar Ultraviolet Radiation and Photochemical Smog", *Science* **278,** pp. 827-830
7. Seinfield J. H., Pandis S. 1981."*Atmospheric Chemistry and Physics*", Wiley, N. Y. Chap.5, pp. 268-271
8. Lloyd, A.C., Atkinson, R., Lurmann, F.W. and Nitta, B.; 1983: "Modeling Potential Ozone Impacts from Natural Hydrocarbons. I. Development and Testing of a Chemical Mechanism for the $NO_x$-Air Photo-oxidations of Isoprene and **a**-pinene under Ambient Conditions." Atmos. Environ. **17**: pp. 1931-1950.
9. Derwent, R G, Jenkin M E and Saunders S M; 1998:"Photochemical ozone creation potentials for organic compounds in northwest Europe calculated with a master chemical mechanism", Atmospheric Environment Vol **32,** 14/15, pp. 2429-2441.
10. Zolghari A., Monsion M., Henry D., Marchionini C. and Petrique SC; 2004: "Development of an operational model-based warning system for tropospheric ozone concentration in Bordeaux, France". Environ. Modelling and Software, **19**, Nº 4, pp. 369-382alez,
11. Gonzalez, C., Gasmi, T.and Gonzalez Ureña, A. ; 2005. "Dial Remote Sensed Ethylene and Ozone-Ethylene Correlation in Presence of Urban NOx" Journal of Atmospheric Chemistry, Vol. 50, No. 2. pp. 159-169.

# A LIDAR SYSTEM FOR STUDY OF AEROSOL IN THE ATMOSPHERE.

**Dinh Van Trung and Nguyen Thanh Binh, Nguyen Van Thuong, Vu Tran Thanh Thuy, Bui Van Hai, Vu Thi Bich, Nguyen Dai Hung**

Institute of Physics,
Vietnamese Academy of Science and Technology
10 DaoTan, BaDinh, Hanoi, Vietnam
*E-mail: dvtrung@iop.vast.ac.vn, tbnguyen@iop.vast.ac.vn*

**Abstract:** LIDAR or light detection and ranging is a very powerful technique to probe the physical condition and chemical composition of the atmosphere. In this paper we briefly review the principle of this technique and describe our effort to design and develop a LIDAR system at the Institute of Physics to study aerosol in the atmosphere. With this system we have obtained some initial and encouraging measurements of backscattering signal from the lower atmosphere and clouds.

## 1. Introduction

Determining the spatial and temporal aerosol distribution in the atmosphere provides important information for atmospheric science research. Aerosol particles play a role in climate change both directly, by affecting the energy balance of the Earth, and indirectly by affecting cloud properties. In addition, both natural and man-made aerosols impact the air quality, especially in the urban environment, with human health implications. Aerosol distribution in the atmosphere is very non-uniform, with most of the aerosols occurring in the first few kilometers of the atmosphere. In situ aerosol measurements might be carried out with airborne or balloon-borne instruments and provide direct and specific information on aerosols. However, such techniques are expensive and unsuitable for measuring fast temporal evolution of the aerosol properties.

Laser remote sensing or LIDAR (Light Detection And Ranging) is a very important and widely used technique to study the physical conditions and chemical properties of the atmosphere (Measures 1992). LIDAR technique has been used to probe the structure of the higher atmosphere, the upper troposphere (Chen et al. 2004) and stratosphere (Nee et al. 1998). The LIDAR technique has found extensive use in the study of particulate matter in the atmosphere. Specifically, the LIDAR signal allows the retrieval of atmospheric aerosol distribution with high spatial (a few meters) and temporal (~minute) resolution (Larcheveque et al. 2002, Frejafon et al. 1998). In this paper we describe the design, development and initial operation of a LIDAR system in our laboratory. Our goal is to build a complete and operational LIDAR to study aerosols in the atmosphere and its link to air pollution in Vietnam.

## 2. Principle of LIDAR technique

When a laser beam is sent into the atmosphere, the laser light is scattered strongly by the aerosol particles present along the propagation path, and by the ubiquitous molecules and atoms in the air. LIDAR systems frequently use an optical telescope in coaxial or co-linear configuration with respect to the laser emitter to collect the backscattered signal. The signal is then focus onto a fast light detector through a spectral filter adapted to the laser wavelength. Because a laser pulse is used, the backscattered signal can be recorded as a function of time and thus provides the required spatial resolution of the measurement. The basic LIDAR equation is (Georgoussis et al. 2006)

$$P(z) = P_o \frac{c\tau}{2} \frac{1}{z^2} \beta(z) A_{tel} O(z) \exp[-2 \int_0^z \alpha(z) dz]$$

where P(z) is the detected backscattered signal from the atmospheric layer at distance z, $P_o$ is the laser output power, $\tau$ is the laser pulse duration, c is the speed of light, $\beta(z)$ is the volume backscatter coefficient, $\alpha(z)$ is the atmospheric extinction including absorption and scattering at the laser wavelength, $A_{tel}$ is the collecting area of the telescope, O(z) is the overlap function between the laser beam and the field of view of the telescope.

According to the above LIDAR equation, the backscattered signal carries the information on aerosol and molecular concentration as a function of distance or height in the atmosphere. The aerosol concentration is encoded in two parameters, namely the backscatter coefficient $\beta$ and the extinction $\alpha$. These two parameters depend on the shape, size and composition of the aerosol particles. Because there is only one set of measurements and there are two sets of parameters to find, in order to invert the above equation to derive the aerosol concentration, the usual method is to assume a priori value for the ratio $\alpha/\beta$, which is called the LIDAR ratio.

## 3. LIDAR design description

The schematic of our LIDAR system is shown in Figure 1. Our LIDAR consists of three main components: a laser transmitter, a receiving telescope and a detection system. The laser transmitter is based on the second harmonic of a high power Nd:YAG pulse laser from Quantel. The laser produces pulses of 100 mJoule in energy and a pulse-width of 7 ns at 532 nm. The laser operates at a repetition rate of 20 Hz. A beam expander is used to reduce the divergence of the laser beam before launching the beam into the atmosphere. To collect the backscattered light we use a Cassegrain reflecting telescope Meade LX200 of 20 cm in diameter and aperture ratio of F/10. A field stop is placed at the focal point of the telescope to limit the field of view to about 1 mrad. The collected backscattered light is then collimated with the collimation optics and pass through a narrow band interference filter (FWHM = 3nm) at 532 nm to in order to reject the background light and improve the S/N ratio;

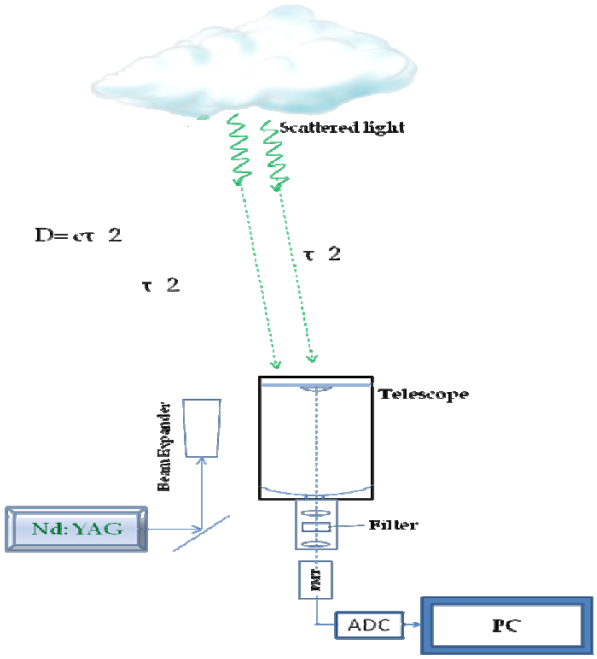


**Figure 1.** Principle of LIDAR measurement and schematic of our LIDAR system to study aerosol in the atmosphere.

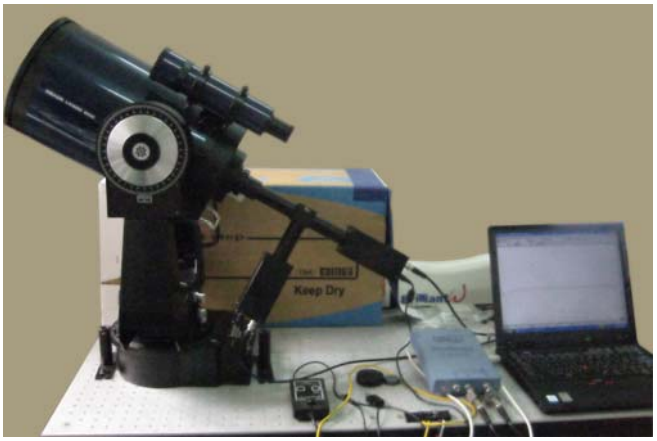


**Figure 2.** Close-up view of our LIDAR system.

Our detection system uses a Hamamatsu photomultiplier tube R7400U to perform the light detection. We take precaution to baffle and shield the detector box in order to minimize the stray light coming from the laser. The signal from the photomultiplier tube can be optionally amplified by a broadband amplifier, which is made in-house. The digitization of the LIDAR signal is then done using a fast (200 MHz bandwidth) 8-bit oscilloscope from Picoscope. The data are subsequently transferred to a computer for off-line analysis.

A close-up view of our LIDAR including the laser transmitter, the receiving telescope, the detection box and the laptop computer for control and data acquisition is shown in Figure 3. The alignment of the laser beam and the receiving telescope is achieved using the usual procedure of maximizing the return signal at a fixed distance of about 1 km.

## 4. Initial measurements of LIDAR signal

Using this LIDAR system we have made some initial measurements of the backscattered signal from the atmosphere. The raw data taken for each laser pulse are smoothed to reduce noise and baseline subtracted. We then average the data to further enhance the signal. The time delay $t$ between the start of the laser pulse and the signal sample point is converted to spatial distance $z$ using the usual relation $z = ct/2$, where c is the speed of light. In Figure 3 we show the typical LIDAR signal in presence of a cloud layer at 3 km along the line of sight. We could recognize

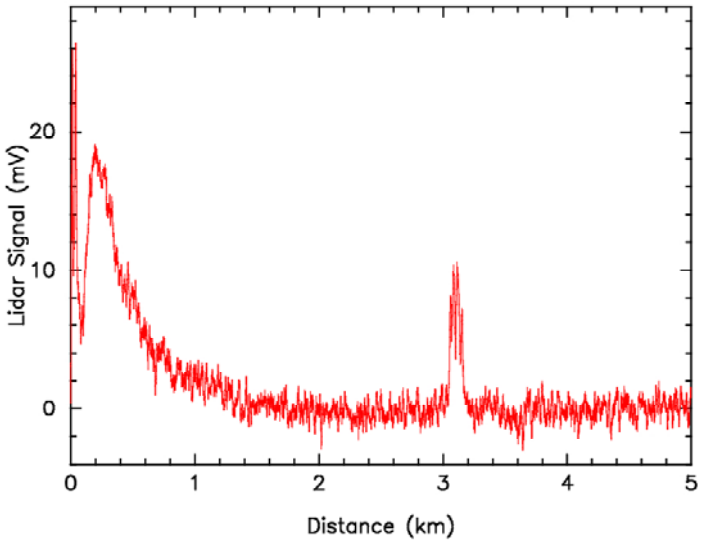


**Figure 3.** LIDAR signal obtained in the presence of a cloud layer at distance of about 3 km along the line of sight.

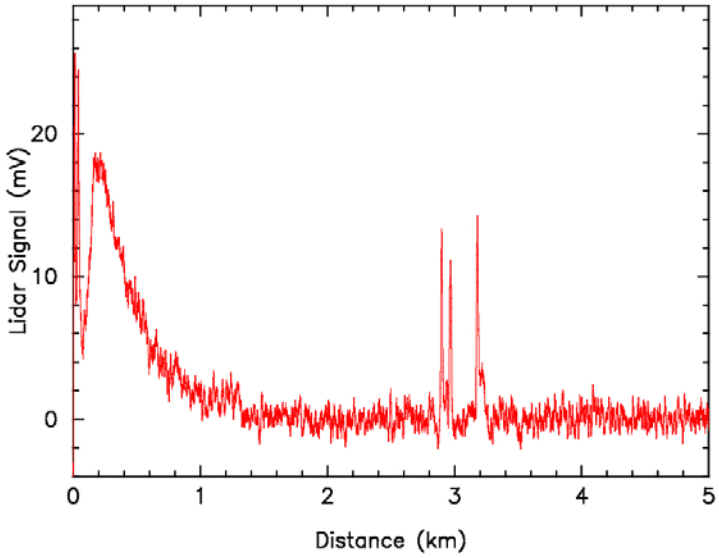


**Figure 4.** LIDAR signal obtained a few minutes after the data shown in Figure 2. The thick cloud layer has now separated into three thin layers represented by the sharp peaks in the signal intensity around a distance of 3 km.

distance. A cloud layer located at distance of 3 km produces a very strong backscattered the usual LIDAR signal peaking strongly at about 300 m when the laser beam fully enters into the field of view of the receiving telescope. The signal then decreases almost monotonically with signal resulting in an easily identified and narrow peak in the detected signal. We find that the LIDAR signal from the cloud layer is fast changing on timescale of seconds to minutes. In Figure 4 we show an example of the LIDAR signal acquired a few minutes later. The cloud layer seen previously has separated into three thin layers represented by the sharp peaks in the signal intensity.

## 5. Future development

Our LIDAR system is currently under active development toward completion in 2009. The data analysis pipeline is being setup so that the acquired data can be automatically baseline subtracted, averaged and smoothed. The processed data will then be used in the data inversion program to extract the backscattering coefficient of atmospheric aerosols. The full operation of our LIDAR system is planned for the end of 2009.

***Acknowledgement***

*We thank the Vietnamese Academy of Science and Technology for the generous grant to our aerosol LIDAR project that has made possible the developments presented here. We are also grateful for the support of the Institute of Physis, where the LIDAR is developed. We thank the kind help from Dr. Wen-Nai Chen of Center for Research on Environmental Changes, Academia Sinica, Taiwan for sharing his experience on building and operating LIDAR.*

## References

1. G. Larcheveque, I. Boalin, R. Nessler et al.Development of a muliwavelength aerosol and water vapor lidar at the Jungfraujoch Alpine station in Switzerland, 2002, Applied Optics vol. 41, p. 2781-2790

2. W.N. Chen, C.C. Tsao, J.B. Nee Rayleigh lidar temperature measurements in the upper troposphere and lower stratosphere, 2004, Journal of Atmospheric & Solar-Terrestrial Physics vol. 66, p. 39- 49
3. J.B. Nee, C.N. Len, W.N. Chen, C.I. Lin, Lidar observations of the cirrus clouds in the tropopause at Chung-Li, 1998, Journal of the Atmospheric Sciences vol. 55, p. 2249-2257
4. R. Measures, Laser remote sensing: fundamentals and applications, 1992, Krieger publishing company
5. E. Frejafon, J. Kasparian, P. Rambaldi, et al., Three-dimensional analysis of urban aerosols by use of a combined lidar, scanning electron microscopy, and x-ray microanalysis, 1998, Applied Optics vol. 37, p.2231-2237
6. G. Georgoussi, G. Chourdakis, E. Landulfo, et al., Monitoring of air pollution and atmospheric parameters using a mobile backscatter lidar system, 2006, Optica Pura Y Applicada vol. 39, 3rd workshop LIDAR measurements in Latin America

# OPTICAL AND ELECTRICAL PROPERTIES OF ZnO AND RELATED HETERO-STRUCTURES

**T. Makino[a], A. Tsukazaki [b], A. Ohtomo[b], M. Kawasaki1[b,c,d], and Y. Segawa [c]**

[a)] WPI-Advanced Institute for Materials Research, Tohoku University, Sendai 980-8577, Japan
[b)] Institute for Materials Research, Tohoku University, Sendai 980-8577, Japan;
[c)] Cross-Correlated Materials Research Group (CMRG), Advanced Science Institute (ASI), RIKEN, Wako 351-0198, Japan
[d)] Japan Science and Technology Agency (CREST), 4-1-8 Honcho, Kawaguchi 332-0012, Japan

**Abstract.** We investigated the optical properties of epitaxial *n*-type ZnO films and ZnO/Mg0.22Zn0.78O quantum wells grown on lattice-matched ScAlMgO4 substrates. As the Ga doping concentration (*n*-type films) increased up to 6×1020 cm−3, the absorption edge showed a blueshift, consistent with the Burstein-Moss effect. A near-bandedge photoluminescence (PL) could be observed even at room temperature, the intensity of which increased as the doping concentration was increased. It indicates that nonradiative transitions dominate at a low doping density. Both a Stokes shift and broadening in the PL band are monotonically increasing functions of donor concentration, which was explained in terms of potential fluctuations caused by the random distribution of impurities. The quantum well samples were also studied to evaluate the well-width dependence (1 to 10 nm) of exciton transition energies. Under weak excitation, the photoluminescence shows a quantum-confined Stark effect for the wide wells, while with an increase in excitation intensity, blueshift of the luminescence was observed, suggesting photo-excitation screening of fields. The well width dependence of the experimental transition energies are compared with reported calculations. The internal electric field is comparable with 650 kV/cm.

**PACS.** 68.55.Ln Thin film defects and impurities including doping, implantation, distribution, concentration –78.66.Hf Optical properties of II-VI semiconductors (thin films) – 78.55.Et Photoluminescence in II-VI semiconductors– 71.55.Gs Impurity and defect levels in II-VI semiconductors

## 1. Introduction

Optical properties of ZnO are currently subject of tremendous investigations, in response to the industrial demand for shortwavelength optoelectronics devices [1, 2]. Production of highquality doped ZnO films is indispensable for the device application. Room-temperature (RT) near-bandedge (NBE) luminescence has not been observed in donor-doped ZnO except for lightly-doped ones despite the long research history of this material as a transparent conductive window [3–6]. Indeed when ZnO:Al films were grown on lattice matched substrates, detectable NBE PL could be observed only at 5 K. In this publication, we report observation of the RT NBE luminescence from ZnO:Ga epitaxial layers. The radiative efficiency, threshold energy and the linewidth of the near-band-gap optical transition are investigated. In addition, introduction of magnesium into ZnO plays a key role in band-gap engineering [7, 8]. In ZnO/Mg*x*Zn1−*x*O QWs grown along the *c*-axis, its optical properties are affected by both spontaneous and piezoelectric polarization effects. Bretagnon and his coworkers pointed out the importance to lengthen a barrier layer thickness (*LB*) to precisely evaluate the built-in electric field and determine its magnitude to be 900 kV/cm for the single quantum wells (SQWs) [9]. In this work, we also report optical properties of ZnO quantum wells and a screening effect of the built-in electric field with photocarriers studied by estimating the excitation intensity dependence of the photoluminescence.

## 2. Experimental Procedures

Ga-doped ZnO andSQW samples were grown by laser molecularbeam epitaxy on ScAlMgO4 substrates. The Ga doping was varied to achieve doping densities in the range of 8 × 1018 to 6×1020 cm−3 [10]. The photoluminescence measurements were performed using an He-Cd laser (325 nm). Our SQW samples were grown by laser MBE on high-temperature annealed MgZnO templates (being 100 nm in thickness). The top
barrier layer is composed of 50-nm-thick Mg*x*Zn1−*x*O (*x*=0.22). It can be, thus, regarded as a ZnO well sandwiched by Mg*x*Zn1−*x*O barriers [11].

## 3. Results and Discussion

### *3.1 Room-temperature luminescence in n-type ZnO:Ga*

Figure 1(a) shows room-temperature near-bandedge photoluminescence spectra (left-hand side) in *n*-type Ga-doped ZnO samples with different doping densities. The corresponding absorption spectra (right-hand side) are also shown, and they indicate a clear blue-shift (at most _ 430 meV) related to the well-known Burstein-Moss effect [12, 13]. All of the luminescence spectra displayed intense near-bandedge transitions. In order to identify the physical nature of this near-bandedge

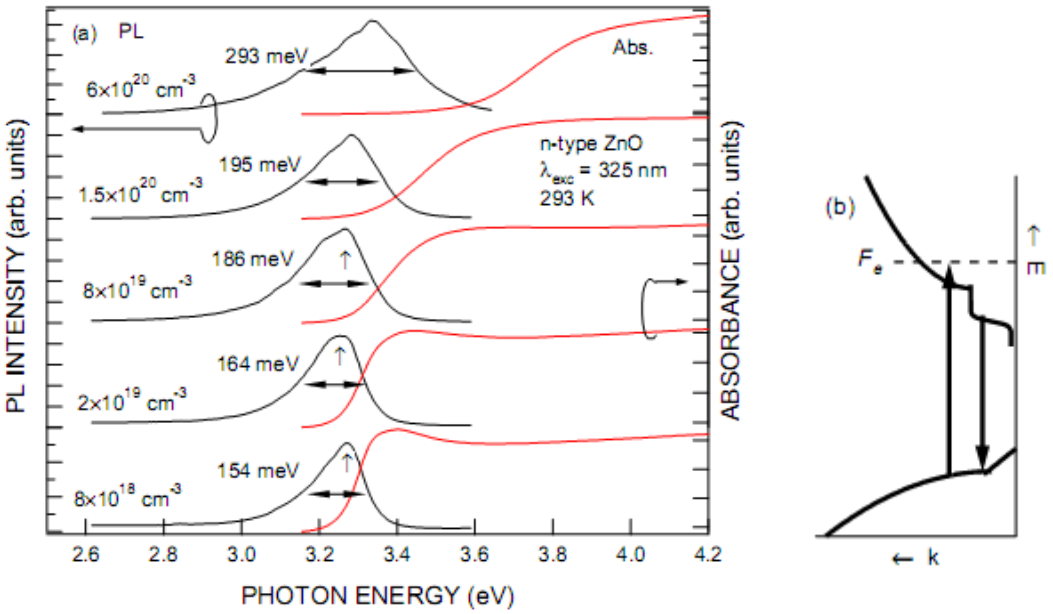


**Fig. 1.** (a) Room-temperature PL spectra (left) of *n*-type ZnO doped at different Ga concentrations. Also shown are the corresponding absorption spectra (right). (b) An energy diagram of doped ZnO illustrating the corresponding optical transition thresholds.

transition, comparison with absorbance data was made. In *n*-doped ZnO, as shown in Fig. 1(b), an absorptive optical transition occurs from the valence band to the Fermi level or conduction band, while an emissive transition occurs from an impuritydonor band to the valence band. This is the reason for the occurrence of a Stokes shift, i.e., the luminescence peak is redshifted from the absorption threshold. The dominant luminescence transition is therefore thought to be due to such a donorto-free-hole recombination. Since the Stokes shifts exceed a sum of the donor and acceptor ionization energies in samples at the highest doping levels (1.5×1020 to 6×1020 cm−3), they are assigned to recombination of donor-acceptor pairs [1, 14].

The intensity of the near-bandedge transition increased markedly as the doping concentration increases. Figure 2 shows integrated intensity as a function of doping concentration. The integrated intensity increases by a factor of 17 as the doping density is increased from 8×1018 to 1.5×1020 cm−3 and then finally decreases at the highest level (6×1020 cm−3). The relatively low intensity at low doping concentrations is attributed to nonradiative transitions. The lifetime of the nonradiative channel is determined by the nonequilibrium minority

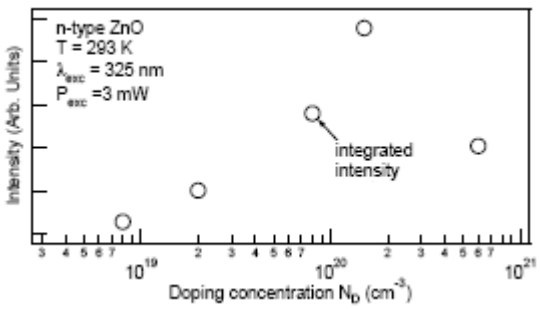


**Fig. 2.** Emission intensity of the NBE transition of *n*-type ZnO as a function of the doping concentration

carrie (hole) concentration and the concentration of traps participating in the recombination. In *n*-type semiconductors, the trap recombination rate is proportional to *NT p*, whereas the radiative recombination rate is proportional to *np* = *NDp*. The ratio of radiative to nonradiative recombination rates is *ND/NT* [15]. If *NT* is independent of the doping concentration, radiative transitions increase with increase in doping concentration. Thus, higher efficiency is expected as *ND* increases. This increase in efficiency was indeed observed experimentally. The monotonic increase in luminescence efficiency with an increase in doping concentration also shows that luminescence killers (deep levels) do not increase with increase in doping concentration, which is indicative of high quality of the epitaxial films. In

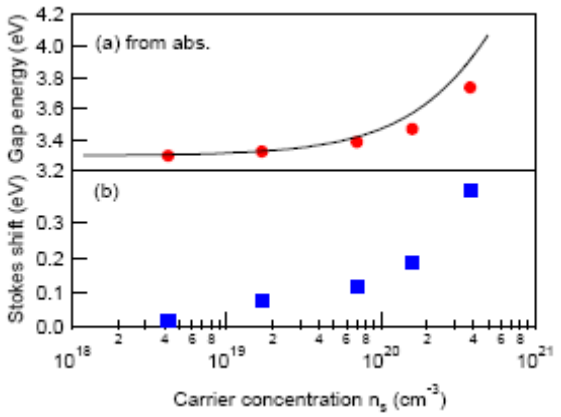


**Fig. 3.** (a): Band gap *vs.* electron density for ZnO:Ga films (solid circles) and a computed result (solid curves). A solid curve refers to the theory cited from Ref. [3]. Also shown by open squares are the Stokes shifts (b).

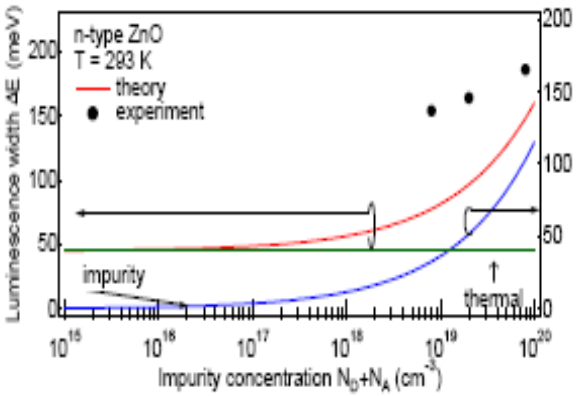


**Fig. 4.** Experimental linewidth of the near-bandedge transition of *n*type ZnO as a function of the doping concentration. Also shown are the theoretical thermal broadening and broadening due to random impurity concentration fluctuations.

the case of ZnO epitaxy, it has been difficult to achieve such a situation, i.e., impurity doping has so far induced a sizable increase in the trap center concentration [4, 16, 6]. On the other hand, the luminescence efficiency decreases at the highest doping concentrations. This decrease is probably attributed to compensating native defects [17]. The RT NBE PL could not be observed in ZnO:Al films grown on the lattice-matched substrate.

We determine the energy position of the absorption edge by taking the zero crossing of the second derivative spectrum of the absorption coefficient. Solid marks in Fig. 3(a) show experimental data as a function of electron density *ns* that was measured by the Hall-bar method. The experimental results are compared with the "full" theory of Sernelius *et al* [3]. This has been developed for polar semiconductors, taking the band gap renormalization, Burstein-Moss effect and polaron effect into account. A solid curve show a result which computes an energy difference between the valence band and the Fermi level. All of the quantities required to

calculate this curve were taken equal as those used in Ref. [3]. The experimental data for ZnO:Ga are seen to agree well with the solid curve.

Inspection of the spectra respectively reveals that the Stokes shift energy increases from 22.4 to 396 meV and the linewidth of the transition increases from 154 to 293 meV as the doping concentration increases from 8×1018 to 6×1020 cm−3. Open squares in Fig. 3(b) show the Stokes shift that is difference between the PL peak and the absorption threshold. Both the enhancement are explained in terms of potential fluctuations caused by the random distribution of doping impurities [15]. It is thought that the localization of photocreated carrier due to the fluctuation determines the Stokes shift. The localization depth grows with an increase in the randomness. In a reminder of the letter, a quantitative comparison will be made only for the latter case. Randomly distributed dopants lead to unavoidable fluctuations of the doping concentration on a microscopic scale. These microscopic concentration fluctuations result in potential fluctuations. By taking the standard deviation of the potential fluctuation, the broadening of the near-bandedge transition was calculated [15], the result of which is used in this work. The full width at half-maximum (FWHM) is then given by;

$$\Delta E_{\mathrm{FWHM}} = \frac{2e^2}{3\pi\varepsilon}\sqrt{(N_D+N_A)\frac{\pi r_s}{3}}\exp(-3/4)\times 2\sqrt{2\ln 2}, \quad (1)$$

where ∑ is the dielectric constant, *ND* (*NA*) stands for the concentration of donors (acceptors), and *rs* is either the Debye or Thomas-Fermi screening radius. The factor 2√2ln2 accounts for the difference between the standard deviation and theFWHM of a Gaussian distribution. The other symbols used in Eq. (1) have the usual meaning. A comparison of experimental linewidth and theoretical data is shown in Fig. 4. Since band filling is not taken into account in the model presented here, this model is applicable only for *ND* < *nM*, where *nM* is the the Mott critical density
(_ 7×1019 cm−3 in ZnO) above which the Fermi level enters into the conduction band. The data for the two highest doping levels were therefore omitted. The FWHM given by Eq. (1) and the thermal broadening given by 1.8*kT* are shown in Fig. 4. In addition, the total broadening by the two uncorrelated broadening mechanisms is shown. With an increase in concentration from 8×1018 to 8×1019 cm−3, the FWHM became larger, which is a similar tendency to that of the theoretical impurity broadening, as expected. The measured broadening is, however, quantitatively in poor agreement with the theory, i.e., significantly larger than the calculated broadening. Although the reason for this discrepancy is not clear, it is probably from the contribution of the phonon replicas superimposing on a zero-phonon luminescence band. In the case of *n*-GaN:Si, there were weak shoulders in the Stokes sides of the main luminescence peaks [15]. In ZnO:Ga, on the other hand, the intensity of a one-phonon replica could be comparable to that of a zero-phonon peak, which leads to larger FWHMs. A further systematical study is necessary to elucidate that.

### *3.2 Internal electric field effects for the luminescence in ZnO quantum wells*

Figure 5(a) shows near-band edge photoluminescence (PL) spectra in ZnO/Mg0.22Zn0.78O SQWs for eleven different well thicknesses (2.7 nm ≤ *Lw* ≤ 8.3 nm). The excitation intensity is ~160 kW/cm2. For wide well-widths (*Lw* ≥ 3.9 nm), the QW spectra exhibit PL peaks below the exciton resonance in bulk ZnO in energy (3.37 eV, a vertical dashed line in figure).

Stronger excitation yielded in different PL features, as shown in Fig. 5(b). The strong excitation condition was performed by the frequency-tripled pulsed beam from a Q-switch yttrium aluminum garnet laser (3.49 eV, ~1.6 kW/cm2) was used. Now, the PL peak energies are higher than or nearly equal to the resonance energy of the bulk (a vertical dashed line). Secondly, the width of the peak became sharper under such stronger excitation.

Figure 6 shows the emission energy (triangles and squares) as a function of *Lw* with *Lw* = 1 – 10 nm under weaker excitation. The PL energies obtained for the two specimens are in a reasonable

agreement with each other. As expected, the emission from ZnO QWs exhibits strong dependence on *Lw*. Due to the quantum confinement effect, the blue-shift of the emission was observed when *Lw* is decreased. When *Lw* ≥ 3.9 nm, strong red-shift observed under weak excitation is a typical phenomenon of the existence of a quantum-confined Stark effect (QCSE), as illustrated in the inset of Fig. 6 [18]. The electric field pushes the electrons and holes in the well layer to the opposite direction, and hence leads to the fundamental transition below the exciton gap of the material. Our data exhibited linear relationship between the PL energies and the well thickness, as shown by a dashed line. The linearity is valid as long as the exciton binding energy is independent of the well thickness as later discussed in detail. The slope of the dashed line leads to an internal electric field of ~560 kV/cm

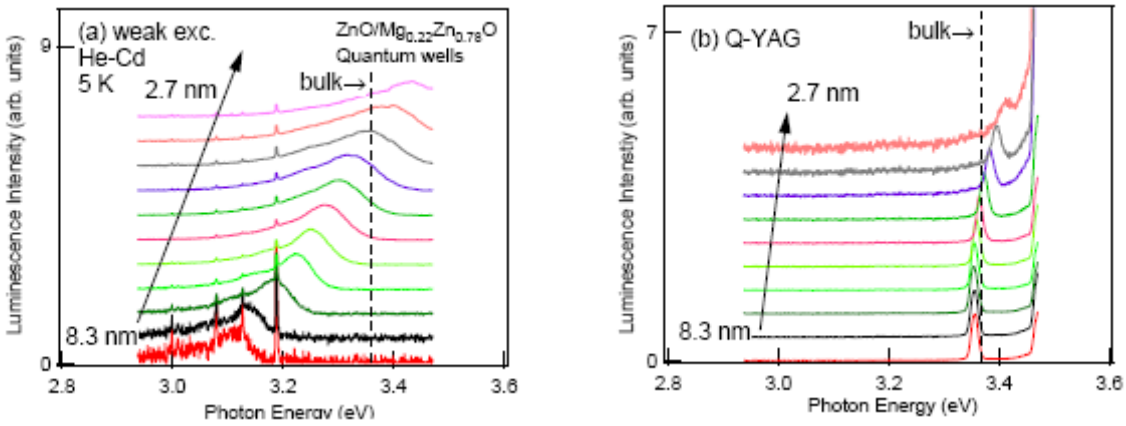


**Fig. 5.** PL spectra in ZnO/(Mg,Zn)O QWs at 10 K. The well widths (*Lw*) were varied from 2.7 to 8.3 nm. Two sets of experimental spectra are shown under weak (a) and strong (b) excitation conditions. Vertical dashed lines indicate the energy of free-exciton in bulk ZnO.

The experimental data under stronger excitation (~1.6 kW/cm2) were also plotted against *Lw* (open circles, *Lw* = 2.7 – 8.8 nm). It is obvious that the emission energies became close to the calculation result of the excitonic transition energies (blue solid line) neglecting an electric field (*F* =0 kV/cm) theoretically deduced by Bretagnon *et al.* [9]. It can be understood as a result of the screening of the internal electric field caused by the excitation-induced carriers. The energy difference between experiments (open circles) and calculation (solid line), for *Lw* = 6.6 nm, is about 40 meV. This energy difference could corresponds to a localization energy of the QW excitons. The localization of excitons occurs due to fluctuations of the well width and/or barrier heights [19].

Here, we try to evaluate the built-in electric field of our samples. Bretagnon and coworkers calculated the exciton transition energies as a function of Mg composition (*x*) of the barrier layers including the effects of internal electric field [9]. The quenching of the excitonic binding energies (*Eex b* ) due to the presence of the field is also taken into account in the calculation. For sufficiently wide wells, where the quantum-confinement effects are negligible, it can be regarded as an impact of electric field (*F*) on the transition energies. Our experimental re-sults are again plotted in Fig. 7 with the results of calculation above-mentioned [9] for *F* =300, 650 and 900 kV/cm. As is understood from the comparison in Fig. 7, the experimental data are in a reasonably good agreement with the calculated results for the field of 650 kV/cm. The value is slightly greater than that obtained in Fig. 6 (≈560 kV/cm), neglecting the effect of the field-induced instability of excitons. It is reasonable because the *Eex b* tends to be a decreasing function of *Lw* under $F \neq 0$.

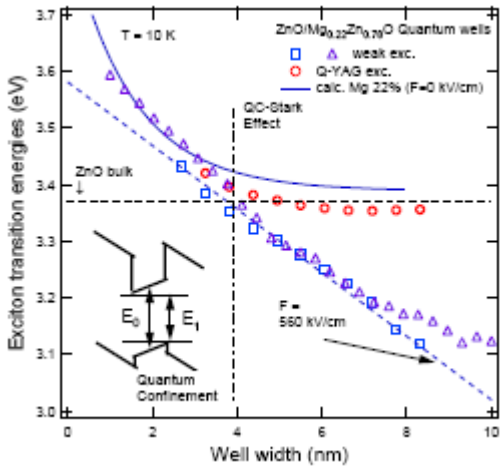


**Fig. 6.** Well width dependences of PL energies in the QWs (open circles, triangles and squares). Also shown by a solid line is calculated energies of excitons neglecting the electric field. Dashed line corresponds to behavior of the energy shift with the presence of the built-in electric field of 560 kV/cm.

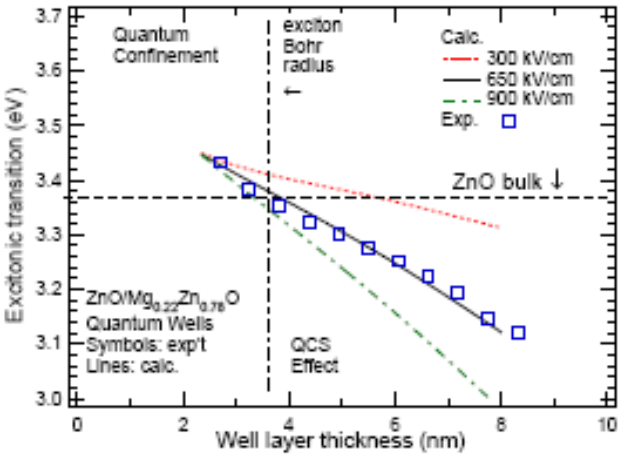


**Fig. 7.** Calculated energies of excitons taking effects of the electric field (dashed, solid, and dash-dotted lines), cited from Ref. [9]. Also shown is the well width dependence of experimental PL energies under weaker excitation (open circles).

Bretagnon and coworkers determined the electric field inherent to a ZnO/Mg0.22Zn0.78O single quantum wells (SQW) to be 900 kV/cm, which is slightly greater in magnitude than our value. The magnesium composition of our SQWs is similar to that evaluated in Ref. [9], whereas the barrier layer thickness (*LB* = 50 nm) is different from that of the latter QWs (*LB* = 200 nm). The difference in the evaluated electric field can be explained in terms of what-is-called a "*LB*-dependent geometrical effect". The field in the well is approximately proportional to *LB*/(*Lw*+*LB*). This may be a possible reason of the difference in the electric field.

We discuss the QCSE quenching at the high-excitation power [20, 21]. As the excitation power increases, the PL transition moved to the higher energy side especially for enough wide wells. A self-consistent theoretical approach predicted the screening effect of the built-in polarization [20, 22] by photoexcited carriers. The photocreated charged carriers accumulated on the two edges of the well layer compensate the built-in electric field, thus leading to a blueshift of the emission. The photoinduced energy shift is dependent on the *Lw*. For narrow wells, energy difference is smaller than those at greater *Lw*s. This tendency on *Lw* is considered to be consistent with the photoinduced
removal of the QCS effect.

## 4. Summary

Observation of the room-temperature NBE luminescence in ZnO:Ga grown by laser-MBE is reported for Ga doping concentrations ranging from 8×1018 to 6×1020 cm−3. A comparison of luminescence and absorption results shows that the NBE luminescence is assigned to donor-to-free-hole recombination for relatively low dopant concentrations and to donor-acceptor pairs for higher concentrations. The intensity increases monotonically with an increase in doping concentration except for the highest one, indicating the presence of luminescence killers in moderately doped ZnO.

The relevancy of recombination centers is reduced at high doping concentrations. Doping yielded a band-gap widening to as large as ~0.4 eV. The sizable amounts of Stokes shift and PL broadening were explained in terms of the localization effect of photocreated carriers. The study of photoluminescence energies of excitons as a function of well width (*Lw*) was also presented for ZnO/Mg0.22Zn0.88O single quantum wells. From the comparison between weakly and

strongly photoexcited conditions, a quantum confined Stark effect is revealed. We deduced an internal electric field strength as large as ~650 kV/cm, which is slightly smaller than the previously reported value for the almost same Mg composition [9]. It is explained in terms of the geometrical factor. The photocarrier screening effect of internal electric field on the luminescence energy has been also evidenced by the luminescence blueshift with an increase in excitation intensity.

## References


1. D. C. Look, D. C. Reynolds, C. W. Litton, R. L. Jones, D. B.Eason, and G. Cantwell, Appl. Phys. Lett. **81**, 1830 (2002).
2. A. Tsukazaki, A. Ohtomo, T. Onuma, M. Ohtani, T. Makino, M.Sumiya, K. Ohtani, S. F. Chichibu, S. Fuke, Y. Segawa, H. Ohno, H. Koinuma, and M. Kawasaki, Nat. Mater. **4**, 42 (2005).
3. B. E. Sernelius, K. F. Berggren, Z. C. Jin, I. Hamberg, and C. G.Granqvist, Phys. Rev. B **37**, 10244 (1988).
4. H. J. Ko, Y. F. Chen, S. K. Hong, H. Wenisch, T. Yao, and D. C.Look, Appl. Phys. Lett. **77**, 3761 (2000).
5. M. Lorenz, E. M. Kaidashev, H. Vonwenckstern, V. Riede, C.Bundesmann, D. Spemmann, G. Benndorf, H. Hochmuth, and A.Rahm, Solid State Electron. **47**, 2205 (2003).
6. T. Makino, K. Tamura, C. H. Chia, Y. Segawa, M. Kawasaki, A.Ohtomo, and H. Koinuma, Phys. Rev. B **65**, 121201(R) (2002).
7. T. Makino, Y. Segawa, M. Kawasaki, A. Ohtomo, R. Shiroki, K.Tamura, T. Yasuda, and H. Koinuma, Appl. Phys. Lett. **78**, 1237 (2001).
8. T. Makino, Y. Segawa,M. Kawasaki, and H. Koinuma, Semicond.Sci. & Technol. **20**, S78 (2005).
9. T. Bretagnon, P. Lefebvre, T. Guillet, T. Taliercio, B. Gil, and C.Morhain, Appl. Phys. Lett. **90**, 201912 (2007).
10. T. Makino, C. H. Chia, N. T. Tuan, Y. Segawa, M. Kawasaki, A.Ohtomo, K. Tamura, and H. Koinuma, Appl. Phys. Lett. **76**, 3549 (2000).
11. H. Koinuma and I. Takeuchi, Nat. Materials **3**, 429 (2004).
12. E. Burstein, Phys. Rev. **93**, 632 (1954).
13. T. S. Moss, *Optical Properties of Semiconductors* (Academic Press, New York, 1961).
14. K. Tamura, T. Makino, A. Tsukazaki, M. Sumiya, S. Fuke, T.Furumochi, M. Lippmaa, C. H. Chia, Y. Segawa, H. Koinuma, and M. Kawasaki, Solid State Commun. **127**, 265 (2003).
15. E. F. Schubert, I. D. Goepfert,W. Grieshaber, and J. M. Redwing, Appl. Phys. Lett. **71**, 921 (1997).
16. T. Makino, C. H. Chia, Y. Segawa, A. Ohtomo, K. Tamura, M.Kawasaki, and H. Koinuma, Phys. Status Solidi (B) **299**, 853 (2002).
17. L. Carderon, Y. Lu, H. Shen, J. Pamulapati, M. L. W. Yang, and P. D. Wright, Appl. Phys. Lett. **60**, 1597 (1992).
18. T. Makino, A. Ohtomo, C. H. Chia, Y. Segawa, H. Koinuma, and M. Kawasaki, Physica E **21**, 671 (2004).
19. T. Makino, N. T. Tuan, H. D. Sun, C. H. Chia, Y. Segawa, M.Kawasaki, A. Ohtomo, K. Tamura, and H. Koinuma, Appl. Phys.Lett. **77**, 975 (2000).
20. F. Bernardini and V. Fiorentini, Phys. Rev. B **57**, R9427 (1998).
21. T. V. Shubina, A. A. Toropov, O. G. Lublinskaya, P. S. Kop'ev, S. V. Ivanov, A. El-Shaer, M.Al-Suleiman, A. Bakin, A. Waag, A. Voinilovich, E. V. Lutsenko, G. P. Yablonskii, J. P.Bergman, G. Pozina, and B. Monemar, Appl. Phys. Lett. **91**, 201104 (2007).
22. S. F. Chichibu, T. Sota, K. Wada, S. P. DenBaars, and S. Nakamura, MRS Int. J. Nitride. Semicond. Res. **4S1**, G2.7 (1999).

# DOT-TO-WELL TRANSITIONS IN InAs/InGaAs DOTS-IN-A-WELL PROBED VIA PHOTOCURRENT AND ELECTROLUMINESCENCE SPECTROSCOPY

**M. Defensor, V. Magusara, E. Estacio, C. Mateo**
**A. Somintac, A. Salvador**

Condensed Matter Physics Laboratory, National Institute of Physics,
University of the Philippines Diliman,
Quezon City 1101, Philippines
*E-mail: mdefensor@gmail.com*

**Abstract:** Hole states of InAs/InGaAs dots-in-a-well (DWELL) are probed indirectly by observing inter-QuantumWell-QuantumDot (inter-QW-QD) transitions through photocurrent (PC) and low temperature electroluminescence (LT-EL) spectroscopy. We find multiple sharp peaks have spacing in the range of 10-20meV in between the expected QD and QW signals. Our results show that these features are due to transitions between the QW electron ground state energy level and the confined hole states of the QDs. The QD hole level energy spacing are found to be within range of the hole level spacing derived through 8-band ***k·p*** theoretical methods. The transitions also fall within the range of values experimentally deduced from photoluminescence excitation (PLE) experiments. The data extracted from these transitions provide experimental values for the QD hole confinement energies which can potentially aid in verification of theoretical models in QD structures.

PACS: 73.21.La, 78.67.Hc, 73.63.Kv

## 1. Introduction

The research on InAs QDs in InGaAs QWs (dots in a well or DWELLs) has recently attracted much attention. Such structures have been widely used to emit light at the 1.3μm optical window.[1,2] DWELLs have also been shown promise in applications for detection of light in the infrared region. This is brought about by intraband–quantum well–quantum dot (intraband-QW-QD) transitions. Devices using this principle are called QD infrared photodetectors (QDIPs).[3]

For InAs QDs grown on GaAs the growth occurs via the Stranski-Krastanow growth mode.[4,5] In this mode the strain between the GaAs matrix and the InAs over-layer is controls the shape as well as the size of the grown QDs. It is important to note that although the bandgap of InAs is only 0.35eV the band gap of the dot is in the range of 1.1eV.[4]

This large difference is mainly due to the large compressive strain in the dots. The large lattice mismatch between InAs and GaAs makes it necessary to consider not only coupling between heavy hole, light hole and split-off bands, but also the conduction band states. This has led to the use of eight-band *k·p* method and other full band structure models to determine the electronic states[5-7]

The typical InAs QD grown on GaAs has a ground state transition of around 1.1eV which in wavelength corresponds to 1.13μm. In order for QDs to be useful for fiber optic communication, the emission wavelength must be increased to 1.3μm or 1.55μm. The easiest approach to this problem is to increase the growth time of the QDs so that larger dots may form. However, due to the large strain on the dot, thick layers of InAs tend to be defective. Another method used is by depositing an $In_xGa_{1-x}As$ layer above the QDs to decrease the strain, thus, allowing larger islands to form. The most common method however is to grow the InAs QDs in an $In_xGa_{1-x}As$ well with an Indium content of $x<0.2$.[1-3,8] This method has been shown successful in producing high quality QDs having ground state emissions at 1.3μm.[1]

The non-uniformity in the QD size distribution, which is a consequence of the self-assembled growth, affects the optical properties of dense QD distributions. The size distribution varies by as much as 5%. This effectively negates the sharpness of the individual QD energy levels making

the resulting QD signal broad. The production of highly uniform QD while maintaining high density has been one of the most important areas of research in semiconductor quantum structures. However, even with the most uniform QDs it is very difficult to observe the quantum confinement levels at room temperature conditions.

Many researchers have also studied the carrier capture phenomenon and energy levels of these structures via optical techniques such as photoluminescence (PL), PL excitation (PLE), and photocurrent (PC) spectroscopy,8–10 and via electrical techniques such as capacitance voltage and deep-level transient spectroscopy.[11–13] Modeling of InAs QDs via eight-band $k \cdot p$ also recently available.[6,7,14] However, few have extended the models to DWELLs largely because of the difficulty in determining the shape of individual dots.[4]

One theoretical phenomenon in DWELLs that has not been observed experimentally is the interband-QW-QD transitions, or transitions between QWelectron↔QDhole and QDelectron↔QWhole states. Although intraband transition or QW to QD electron/hole transitions have been observed using photocurrent spectroscopy QW-QD electron-hole recombinations have not been observed. Observation of interband transitions could provide better understanding of the confined states in DWELL structures.

In this work, experimental evidence of the observation of interband-QW-QD emission and detection is presented. We observed multiple closely spaced signals in between the QW and QD signals in both electroluminescence (EL) and PC spectra. Considering the spacings and the behavior of the EL at varying temperatures and current, we conclude that these are transitions between the QW electron ground state and the QD hole states (QWelectron↔QDhole).

## 2 Experimental Setup

The sample used in this work is grown using a RIBER 32P molecular beam epitaxy (MBE). The schematic of the heterostructure is shown in Fig. 1a and the transmission electron microscope (TEM) cross sectional image of the structure is shown in Fig. 1b.

The QD layer investigated is grown on an $n^+$-GaAs (100) substrate. A Be/AlGaAs-GaAs-Si/AlGaAs P-I-N structure was grown and a single layer of QD was grown inside a graded InGaAs QW. The growth of InAs QDs inside InGaAs QWs has been known to reduce the strain and allow the growth of larger dots. QW and QD growth was done at 530°C. The dots were grown at the center of a graded InGaAs QW. The QW was designed such that the Indium content is larger at the center where the dots are located. The dots are grown via a two step growth process, where ~1.9 monolayers (MLs) of InAs was grown initially, followed by a 10 s growth interrupt under flowing $As_4$ after which regrowth was continued for another ~1.9 MLs. The estimated average mole fraction of the QW is x~0.15 with each InGaAs layer (below and above the dots) measuring approximately 60Å. TEM studies of the sample show that the QDs have an average base diameter of 20 nm.

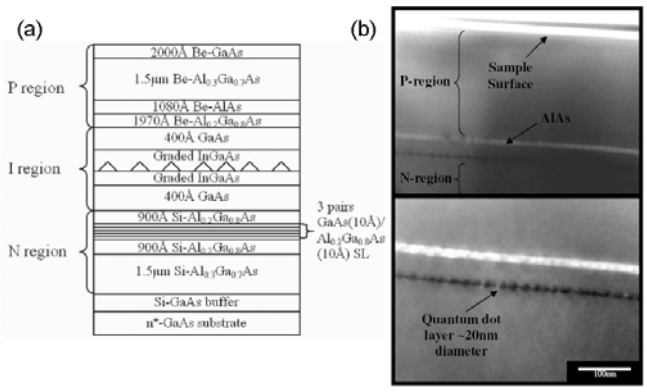


**Fig.1** Schematic diagram of MBE grown Sample (a), and the cross-sectional TEM images of the sample (b). A single layer of InAs QDs was placed in a standard P-I-N heterostructure. The Focused ion beam sample preparation was done at Intel Philippines.

The samples are cleaved into ~1.5mm x 1.5mm pieces and indium was used for both the P and N contacts. The contacts were alloyed for approximately 5mins in a 350$^{o}$C hotplate. The samples are clipped on a bias assembly and the prepared samples have an average turn-on voltage of ~1.2V. The room-temperature EL setup is shown in figure 2. Edge EL spectra are obtained via a 600μm core IR fiber-optic cable positioned approximately 5mm from (and perpendicular to) the sample edge. The emitted light is then fed to a fiber coupled Horiba Jobin Yvon HR460 monochromator with a Hamamatsu low noise InGaAs photodiode. Current input is supplied by an Agilent pulse generator operating at 1 kHz repetition rate and 5% duty cycle.

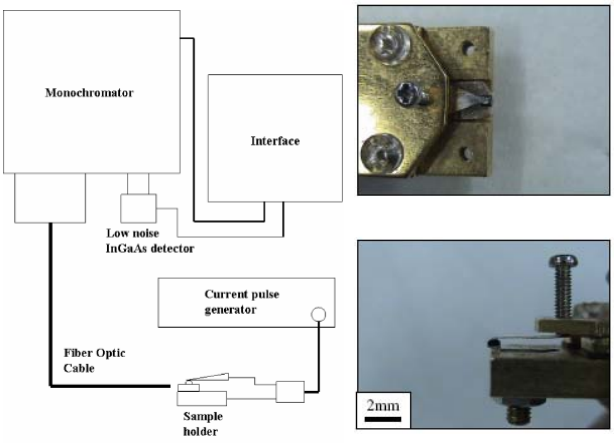


**Fig.2**. Experimental Setup used for room temperature EL experiment. The current was supplied by an Agilent Pulse generator operating at 1 kHz and 5% duty cycle. The monochromator used was a fiber coupled HR460 with an InGaAs PIN detector. Images of the Sample holder are shown on the right.

Low temperature (77K) EL is obtained by attaching the sample on a small piece of glass cut from a microscope slide coated with a layer of indium. The indium coating was applied by melting indium on top of the slide in a 350$^{0}$C hotplate and spreading the melted indium with a sharp blade. The patterning of the indium is then performed by mechanically etching parts of the indium. The sample which has been prepared using the same method for room temp EL is then bonded to the patterned slide by alloying the sample on top of the slide at 350$^{0}$C. A gold wire is then connected to the indium contact on top of the sample and the other end is bonded on an indium pad. Insulated nickel wires are then connected to the indium pads. To provide mechanical stability, the whole sample except the emission edge was coated by Apeizon Wax melted at 150$^{0}$C. The Sample is then mounted using apiezonN grease inside an LN2 cooled APD Heli-Tran cryostat and the nickel wires are connected to electrical feedthroughs which provide electrical access from outside the cryostat.

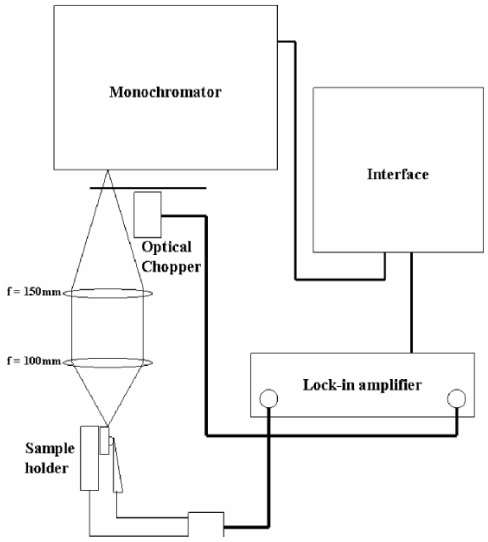


**Fig.3**. Experimental setup used in PC spectral acquisition. A 100W tungsten halogen lamp was used as a broadband light source dispersed by a computer controlled SPEX 500m monochromator.

PC experiments are done using optically chopped light from a 100W tungsten halogen source dispersed by a SPEX 500m monochromator which is focused on the edge of the sample. The sample is the same one used for room temperature EL. The PC is recorded via standard lock-in techniques. The experimental setup for the PC measurements is shown in figure 4.

## 3. Experimental Results

Room temperature EL and PC spectroscopy was done on the sample. The result of the spectral acquisition is shown in Fig. 4a. We identify three distinct signal distributions at 0.85-1.0eV (dots-in-a-well), 1.1-1.3eV (Features attributed to QW-QD transitions), and an InGaAs QW signal at 1.3eV. We note that the intensity of QD transitions are very weak compared to that of the

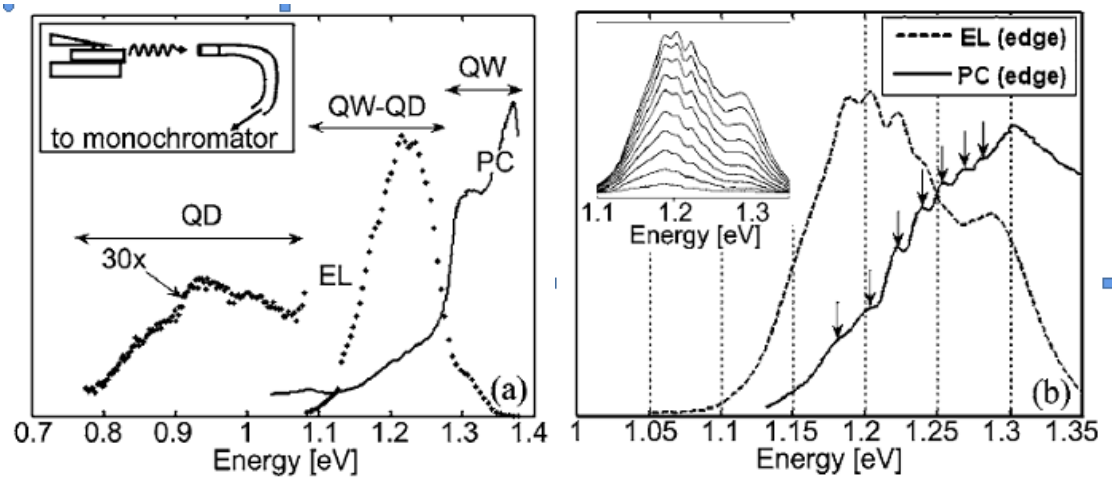


**Fig. 4.** Superimposed EL spectra at 150 mA pulsed operation and PC spectra of sample at 300 K. Full scale scans (a) exhibit three distinct peak distributions (inset shows collection geometry). Close up scan (b) of the 1–1.35 eV region on a different piece shows the presence of multiple sharp features in both PC and EL. Inset shows the enhancement of the features as the current is increased.

QW as well as the QW-QD transitions. The intensity of the observed transitions in the 1.1-1.3eV region suggests that most of the carriers are captured midway between the QW and QD energy levels.

To fully understand the features found in the 1.1eV to 1.3eV regions of the spectra, the measurement was repeated for several other pieces of the sample until a clearer scan was obtained. The most notable scan obtained from the sample is shown in Fig. 4b. It can be seen from the figure that the EL spectra is actually composed of several closely spaced peaks whose energy is about 150 to 100meVs below the QW feature found at 1.3eV. PC spectroscopy reflects the density of states of the system; therefore features observed in PC reflect confinement states. Due to the presence of the features in both PC and EL spectra it is unlikely that the features are phonon related.

To eliminate the possibility that the signals are due to interference effects, the current excitation of the sample was sequentially increased. Several peaks were observed, as shown in the inset of Fig. 4b in the 1.1–1.3 eV region. Note that as the current was increased the positions of the peaks did not shift and the line shape of the EL spectra changed significantly from an initially broad distribution to a collection of sharp closely spaced peaks. This change in the line shape confirms that the sharp features are not caused by interference. This behavior also suggests that the increase in emission intensity is responsible for the enhancement of the features which can be explained by the collection geometry used in our setup. The edge EL collection could have allowed the light emitted from the center, which then propagated through the active region of the sample, to optically pump the QDs near the edge.

The room temperature data suggests that the features found in the PC and EL spectra are brought about by electron-hole recombination. Interference effects can safely be excluded as suggested by the current dependent line shape. Also, the spacing between features are too small even for monolayer step multimodal QD size distributions.[14] In addition, the trend of the peak spacing does not follow the trend expected for multimodal QDs; the spacing between high energy peaks should be larger. These observations imply that the only possible transitions that could account for these features are QW electron ground state to QD hole states and QW hole ground state to QD electron states transitions.

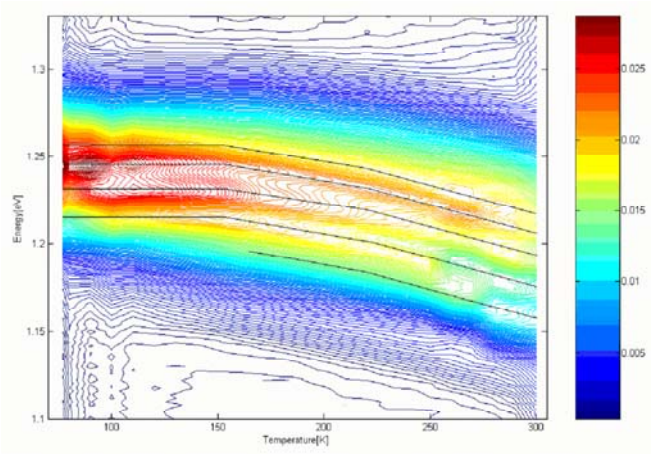


**Fig.5.** Contour plot of the temperature dependent EL spectrum showing the nearly identical shift of the features designated by the solid lines tracing the peaks. The EL spectra were acquired at 77K, and 80K to 300K at steps of 10K.

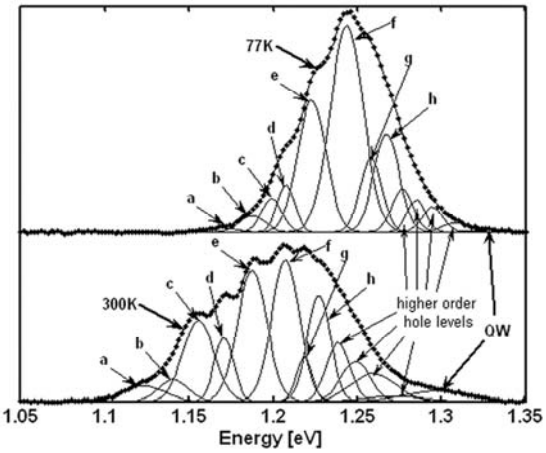


**Fig.6.** Superimposed Plot of 77K and 300K EL spectra fitted using multiple gaussian distributions to determine the temperature induced energy shift of the QW-QD transitions.

In order to determine if the transitions are due to a combination or brought about by only one of the two possible transitions EL experiments are performed at temperatures 77K to 300K. Fig. 5 shows a contour plot of the EL taken from 77K to 300K. As we can easily see from the figure the peaks shift collectively, and no peak crossing can be observed. This behavior indicates that the features are either caused by QW electron ground state to QD hole states transitions or QD electron states to QW hole ground states only; it cannot be caused by both. This is because these two possible transitions involve different band energy combinations that do not shift at the same rate. If the features were caused by a superposition of two types of transitions, then we would expect to see crossing of peaks or at least obvious differences in temperature induced shift of the peaks.

We also see an increase in the relative intensity of the lower energy features as the temperature is increased. The 77K and 300K EL spectra are superimposed with each other for clarity in Fig. 6. Gaussian fitting was employed to determine the peak positions.

The number of peaks was initially chosen for the 300K scan by marking (manually assigning a guess energy position) the well resolved peaks **c**, **d**, **e**, **f**, and **g** and using a computer program to generate the gaussians for the non-well-resolved peaks. After the 300K spectrum was fitted the number of peaks was recorded and the FWHM of each peak was kept constant. The 300K gaussian fits were then used as the guess peaks for the 290K scan, the 290K scan for the 280K scan, and so on until the 77K scan. We note that the peaks were monitored from 300K to 77K and no interchanging of peaks was observed. This is also easily seen in the EL contour plot. The approximated average shift of the peaks due to the QD transitions is ~75meV. This finding is consistent with the experimentally observed shift of the QD peaks in DWELLs found by several other authors.[15-18] Low temperature EL reveals that the multiple peaks that are associated with the QW-QD transitions exhibits a slightly faster shift (38-45meV) with respect to the quantum well signal marked by "QW" (30meV) in Fig. 6. The data supports the assumption that the observed features are due to inter-QW-QD transitions as the shift of the features are slower than the QD shift but faster than the QW shift.

The relatively small peak spacings suggest that the signals are due to transitions between excited hole states of the QD and the electron ground state of the QW. The spacing of the adjacent peaks therefore represents the various confined hole states in the QD. Using this observation we hypothesize that the mechanism that allows the inter-QW-QD emission is related to the spacing between the discrete levels of the QDs.

Since the electron levels have a larger inter-level spacing the carrier capture into the QD electron levels is slower than the capture to the hole levels. This mechanism concurrently allows the QW electron ground state level and the QD hole levels to be filled with carriers. This also accounts for the redistribution of the intensity from the higher energy peaks to the lower energy peaks with increasing temperature (seen in Fig. 6). Due to the slower phonon relaxation rate at lower temperatures it becomes harder to populate the deeper hole levels which lead to the decrease in intensity of the lower energy peaks. This phenomenon has been experimentally suggested by pump-probe experiments.[19]

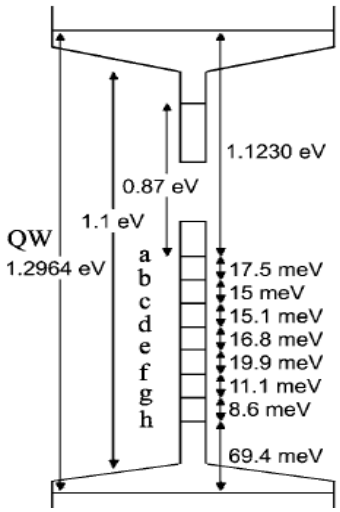


**Fig. 7** Schematic diagram of the electronic structure of the DWELL sample (not drawn to scale); the observed features are attributed to hole energy states. The spacings are found to be within 10–20 meV.

The theoretical electronic state model derived from 300K experimental data of the dot-in-a-well is shown in Fig. 7. The spacing between adjacent peaks (10-20meV) fall within the range of inter hole level spacing calculated via eight-band **k·p** and observed via PLE.[6,7] The only difference is in the number of transitions observed in this work, which is more than what was theoretically expected and observed via PLE. This is expected since only the transition near the QD ground state is easily observed via PLE. In contrast, for PC the higher energy states are more prominent, and for EL the most populated states (those that are easily accessible via carrier relaxation) will have more intense emission. The behavior of the EL spectra implies that phonon bottleneck limits the relaxation rate which leads to a decrease in the emission intensity of lower energy features.

In most cases the higher states are deliberately not calculated in **k·p** simulations because they are not of interest to researchers who compare the model to PLE data. This is because PLE is less sensitive to states very far from the ground state. A more extensive comparison with this type of model is yet to be performed.

## 4. Summary and Conclusion

We find multiple sharp peaks having spacing in the range of 10-20meV in between the expected QD and the QW signals. Current dependent EL spectroscopy shows that these features are enhanced, therefore, proving that the said features are not interference effects. The photocurrent spectra also confirm that such features are due to states of the QD system and invalidate the possibility that the signal are due to phonon related effects. The spacings and the observed temperature dependent shift of the EL suggests that the features are brought about by transitions between the QW electron ground state and the QD hole states. The relatively low capture rate into the QD electron levels due to the large inter-level spacing in the QDs was the key to the observation of such features. The data extracted from these transitions provides experimental values for the QD hole confinement energies which can potentially aid in verification of theoretical models in QD structures.

***Acknowledgements**: The authors would like to acknowledge INTEL Philippines for the FIB preparation of the sample. This work is supported in part by grants from DOST-PCASTRD and University of the Philippines OVCRD.*

## References


1. K. Nishi, H. Saito, S. Sugou, and J.S. Lee, Appl. Phys. Lett. **74**, 1111, (1999).
2. D.L. Huffaker, G. Park, Z. Zou, O.B. Shchekin, and D.G. Deppe, Appl. Phys. Lett. **73**, 2564, (1998).
3. S. Raghavan, D. Forman, P. Hill, N.R. Weisse-Bernstein, G. von Winckel, P. Rotella, S. Krishna, S.W. Kennerly, and J.W. Little, J. Appl. Phys. **96**, 1036, (2004), and references therein.
4. J. Singh, Electronic and Optoelectronic Properties of Semiconductor Structures, *(Cambridge University Press. 2003)*
5. D. Bimberg, M. Grundmann, and N. Ledentsov, Quantum Dot Heterostructures *(Wiley, Chichester, 1999)*
6. O. Stier, M. Grundmann, and D. Bimberg, Phys. Rev. B **59**, 5688, (1999).
7. R. Heitz, O. Stier, I. Mukhametzhanov, A. Madukhar, and D. Bimberg, Phys. Rev. B. **62**, 11017, (2000).
8. H. Nam, J.D. Song, W.J. Choi, J.I. Lee H. Yang, H.S. Kwack, and Y.H. Cho, J. of the Korean Phys. Soc. **47**, 1002, (2005).
9. H. Nam, J.D. Song, W.J. Choi, J.I. Lee H. Yang, H.S. Kwack, and Y.H. Cho, J. of the Korean Phys. Soc. **47**, 1002, (2005).
10. F. Fossard, A. Helman, G. Fishman, F.H. Julien, J. Brault, M. Gendry, E. Peronne, A. Alexandrou, S.E. Schacham, G. Bahir, and E. Finkman, Phys. Rev. B **69**, 155333, (2004).
11. P.N. Brounkov, A. Polimeni, S.T. Stoddart, M. Henini, L. Eaves, P.C. Main, A.R. Kovsh, Yu. G. Musikhin, and S.G. Konnikov, Appl. Phys. Lett. **73**, 1092, (1998).
12. R.J. Luyken, A. Lorke, A.O. Govorov, J.P. Kotthaus, G. Medeiros-Ribeiro, and P.M. Petroff, Appl. Phys. Lett. **74**, 2486, (1999).
13. C.M. A. Kapteyn, F. Heinrichsdorff, O. Stier, R. Heitz, M. Grundmann, N.D. Zakharov, D. Bimberg, and P. Werner, Phys. Rev. B **60**, 265, (1999).
14. R. Heitz, F. Guffarth, K. Potschke, A. Schliwa, D. Bimberg, N.D. Zakharov and P. Werner, Phys. Rev. B **71**, 045325, (2005).
15. M. Bayer and A. Forchel, Phys. Rev. B. **65**, 041308(R), (2002).
16. Y.M. Park, Y.J. Park, K.M. Kim, J.C. Shin, J.D. Song, J.I. Lee, and K.H. Yoo, Phys. Rev. B. **70**, 035322, (2004).
17. A. Fiore, P. Borri, W. Langbein, J.M. Hvam, U. Osterle, R. Houdré, R.P. Stanley, and M. Ilegems, App, Phys. Lett. **76,** 3430, (2000).
18. L. Kong, Z. Wu, Z.C. Feng, and I.T. Ferguson, J. Appl. Phys. **101**, 126101, (2007).
19. J. Feldmann, S.T. Cundiff, M.Arzberger, G.Böhm, and G. Abstreiter, J. Appl. Phys. **89**, 1180, (2001).

# TEMPERATURE AND ENVIRONMENT EFFECTS ON PHOTOLUMINESCENCE OF CdSe/ZnS QUANTUM DOTS

**Vu Duc Chinh[a], Pham Thuy Linh[a], Dinh Hung Cuong[a], Nguyen Xuan Nghia[a], Le Ba Hai[a], Pham Thu Nga[a], Vu Thi Bich[b], Khong Cat Cuong[a,c], Nguyen Van Hung[c], C. Barthou[d], C. Vion[d], P. Bennalloul[d], A. Maitre[d]**

[a)] Institute of Materials Science, Vietnamese Academy of Science & Technology, Hanoi, Vietnam
[b)] Institute of Physics, Vietnamese Academy of Science & Technology
[c)] Faculty of Physics, Hanoi National University of Education
[d)] Institut des Nanosciences de Paris, UMR-CNRS 7588, Université Pierre et Marie Curie, Paris, France
*E-mail address: phtnga@ims.vast.ac.vn*

**Abstract:** Quantum dots (QDs) with their unique physical properties made them an attractive tool for a wide range of applications in life science and in material science. The fabrication method of QDs in colloidal solution via chemical synthesis has been shown to be a promising route to QDs realization. However, for different applications, QDs are embedded in different matrices. In order to have a better understanding on how the properties of the QDs are influenced by different environments, we investigated the photoluminescence (PL) of core-shell CdSe/ZnS QDs. In this work, we report on the effect of the thickness of ZnS shell on enhanced intensity, peak position, spectral full width at half maximum (FWHM), decay time of the emission of CdSe/ZnS QDs in the temperature range from 4 K to 300 K. Compared to the QDs in the original colloidal solutions in toluene, the observed shift of the photoluminescence of the QDs in nano- powder form and polymer matrix will be interpreted.
***Keywords:*** *Colloidal nanocrystals; CdSe/ZnS quantum dots, Photoluminescence, PL decay time.*

## 1. Introduction

The intrinsic optical properties of semiconductor quantum dots (QDs) have received much attention in the past few years partly in order to optimize and explore these materials for applications including diodes, lasers, photovoltaic cells [1-3], fluorescent biological labeling [4] and quantum computing [5]. There is a great improvement in the quantum yield (QY) obtained by optimizing inorganic surface passivation techniques [6]. Photoluminescence (PL) properties of QDs depend on their size, but because of their large surface-to-volume ratios, the QD surface structure or the surrounding environment also have important influence to their PL. Even in core/shell QDs, PL properties are very sensitive to the local and immediate environment surrounding them [7–9]. In going from CdSe to ZnS, the bulk band gap at 300 K gradually increases from 1.756 eV of CdSe (hexagonal wurtzite-WZ) and 1.66 eV (cubic zinc blende- ZB) to 3.741 eV of ZnS (ZB) and 3.722 eV (WZ), respectively. On the other hand, the lattice parameter gradually increases from 6.077 Å (ZB) or 4.3 Å (WZ) of CdSe to 5.406 Å (ZB) or 3.82 Å (WZ) of ZnS. The band gap difference in core/shell structure affects the both hole and electron wave function at the core/shell interfaces, whereas the lattice parameter mismatches influences the defect formation at the interface. The interactions between nanoparticles and surrounding environments play essential roles in their optical responses. PL blinking of nanoparticles is a unique optical phenomenon revealed by single-nanoparticle spectroscopy [9]. This PL blinking behavior of single QDs is very sensitive to the immediate environments surrounding QDs, such as ambient gases, dispersed matrices, and substrate materials. In this work, we present new results of the investigation on the PL properties at 5 K temperature and an anomalous PL behavior with the temperature of CdSe/ZnS core/shell QDs that were prepared in large amount in our laboratory. For the aim of different potential applications and to find the optimal thickness of the ZnS shell to conserve the intrinsic properties of the CdSe QDs, we

observe the behavior of these QDs in different environments such in powder form, in toluene solvent, poly-methylmethacrylate (PMMA), poly-N-vinylcarbazole (PVK), paraffin, epoxy resist and in water soluble form.

We will present the study of the spectroscopic properties of the samples with the ZnS different thickness at the temperatures 5 K and room temperature together with their PL. In this study, the inhomogeneous PL line broadening from QDs ensemble is assumed from the fact that in QDs ensemble, each individual nanocrystal has slightly different properties induced by fluctuation in size, shape, and symmetry. This leads to a variation of energy levels resulting in an inhomogeneous line-width. The affect of the environment and temperature (4 K – 300 K) on PL spectra of CdSe/ZnS QDs will be presented and discussed in comparison with those reported in [10].

## 2. Experiment

The CdSe cores (2.3 – 6.2 nm in diameter) were prepared following the method described by Bawendi and co-workers, Peng et al. and developed in our laboratory [11] by growing the nanocrystals in the organometallic solution. We have grown the ZnS shell by using the approach described by Talapin et al. in Ref. [12]. The diameter of the core increases with growing temperature of the nanocrystal preparation. The thickness of the ZnS shell varies from 0.38 nm to 2.3 nm which corresponding to the 1 monolayer (ML) to 6 ML. The X-ray diffraction (XRD) was done without any size selection on diffractometer D5005 (Siemens). The PL measurements were performed by the photonic excitation at 400 nm which was obtained with a dye laser (Laser Photonics LN102, Coumarine 420) pumped by a pulsed nitrogen laser (Laser Photonics LN 1000, 0.14 mJ energy per pulse, pulse width 0.6 ns). The visible emitted light from the sample, collected by an optical fiber on the same side as the excitation, was analyzed with a Jobin-Yvon Spectrometer HR460 and a multichannel CCD detector (2000 pixel). The low temperature experiments were carried out in a Janis Supertran-VP dewar with a variable temperature controlled between 4 to 300 K. Some samples were excited by 488 nm line from $Ar^+$ laser.

## 3. Results and discussion

Fig. 1 presents the PL spectra of the different samples of the CdSe cores to show the possible emissions from 520 nm to 640 nm of CdSe samples prepared in our laboratory. For example: No.10 and No.10a CdSe QDs samples were fabricated at 290$^o$C for 5 minutes, No.88 and 88a samples were fabricated at 290$^o$C (1h), No.97 at 200$^o$C (15 min.), No. 9 at 280$^o$C (5 min.), No. 11-1 at 205$^o$C (18 sec.). We confirm that the most important preparation parameters influenced to the QDs size are temperature and time. Fig. 2 presents the shift and broadening of the PL spectra of the same sample CdSe/ZnS 2.5 ML which was dispersed in toluene solvent and in solid powder form. A displacement of the maximum fluorescence band of 6 – 10 nm to shorter wavelengths and a narrower of 8 nm of the FWHM were observed for the QDs in toluene solvent. It means that the contribution of the surface states is important in powder form CdSe/ZnS QDs. Figs. 3 and 4 show the PL spectra of CdSe/ZnS with different thicknesses of the ZnS shell from 0.6 nm (1.6 ML) to 2.3 nm (6 ML) at 300 K (fig.3) and 5 K (fig.4) in normalized intensity. We used the powder form samples, which were recovered from colloidal solution by adding excess methanol and then eliminating and evaporating the solvent. The sample No.11.1 is the CdSe core, the remaining samples were CdSe/ZnS with ZnS different thicknesses (No.11.2-1ML, 11.3-1.6ML, 11.4-2.5ML, 11.5-4ML, 11.6-6ML). At 300K, for the CdSe core, we observe two bands: the sharp excitonic band emission at 530 nm, corresponding to 2.34 eV, and the broad emission at longer wavelength 700 nm (1.77 eV). The broad emission at 700 nm arising from the recombination of trapped charge carriers at the surface states and be attributed to “deep trap emission”. This is a localized electronic state which captures charge carriers. The trap levels

exist only in relatively small regions of space around the trap potential. This trap is considered to be originated from the dangling surface atoms or surface defects on CdSe nanocrystals. The overcoating of CdSe nanocrystal surface by ZnS shell seems to remove the dangling atoms from the core/shell interface by coordinative saturating the surface atoms, but introducing structural defects at the interface due to the lattice mismatch. In Fig. 3, a very weak band of the deep trap emission was observed at 300K from CdSe/ZnS 1ML to 6ML.

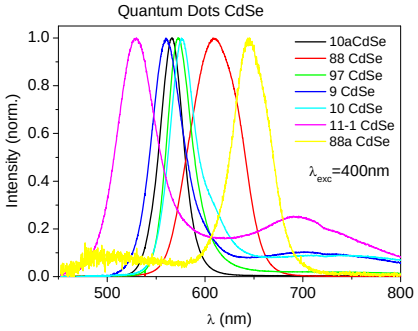


**Fig.1.**Normalized intensity PL spectra of 7 samples of CdSe core dispersed in toluene (10a, 88 and 97) and in powder form (9, 10, 11-1 and 88a), under 400 nm excitation.

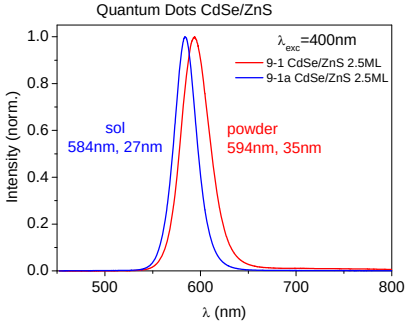


**Fig. 2**. Normalized intensity PL spectra of the CdSe/ZnS 2.5 ML in toluene and powder form, $\lambda_{exc.}$ = 400 nm.

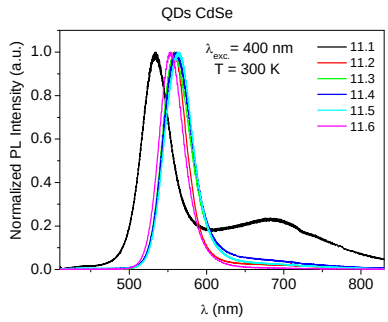


**Fig.3.** Normalized PL spectra of the series of CdSe (the black line 11.1) and CdSe/ZnS samples with the different thicknesses of the ZnS shell from 1.6 ML to 6 ML in nano-size powder form at 300K (excitation at 400 nm).

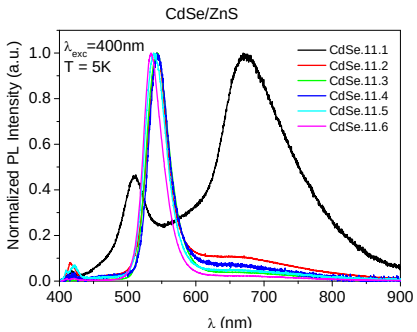


**Fig.4.** Normalized PL spectra of the same series of CdSe (the black line 11.1) and CdSe/ZnS samples of the Fig.1, in nano-size powder form at 5K (excitation at 400 nm).

The ZnS shell structure appears to be better in removing the deep traps although it has a greater lattice mismatch with core materials. The ZnS shell addition reduces and even eliminates the emission attributed to the surface states, but displaces the maximum of the emission band to the red by the modification of the confinement of the exciton. The ZnS 1ML shifts the excitonic emission to the red by 30 nm (for the diameter of the core 2.3 nm). An increasing of the shell thickness has a little influence on the shift of the emission band. Furthermore, the thickness of shell of 1 ML and combined with the more fine synthesis method will bring a narrowing of the band of 10 nm and the PL intensity can be augmented to hundred times. At 5 K (Fig.4), an abnormal PL intensity relates to surface states was observed: the relative intensity of the excitonic emission decreases, while the deep-trap emission increases and even their intensity is more strength than intrinsic emission (for the case of the CdSe core). As reported in [13], we can see that at low temperature, the main decay mechanism is defect trapping meanwhile phonon assisted decay playing a major role in the higher temperature (above 50 K that we will present below). The peak was shifted about 18 nm to the shorter wavelengths in comparison with those at 300K (Fig.5). At 5K the FWHM varies between 33 and 39 nm and can be compared with the value of 35 to 44 nm at 300K. But the emission intensity at 700 nm is higher than intrinsic emission intensity at 530 nm for the case of CdSe core and the emission at 700 nm were appeared even for another samples CdSe/ZnS at 5K (Fig. 4). This observation hasn't been

reported and analyzed yet in details before, so we will discuss in the following part. It was the QD samples with the small diameter (size = 2.3 nm) and we performed the PL measurement in powder form, so that the role of the surface states is important and the main decay mechanism is defect trapping at 5 K. This observation confirms the dominant role of the defect states at low temperature as reported in [13].

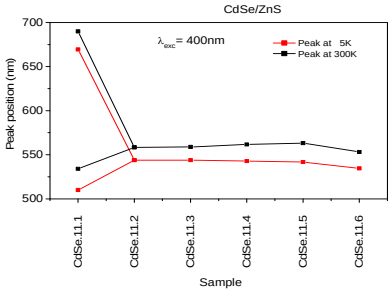


**Fig.5.** Excitonic emission peaks shifting at 5K (red line) and 300K (black line) of the CdSe (11.1) and CdSe/ZnS (1ML to 6ML corresponding to 11.2 to 11.6) nanocrystal samples.

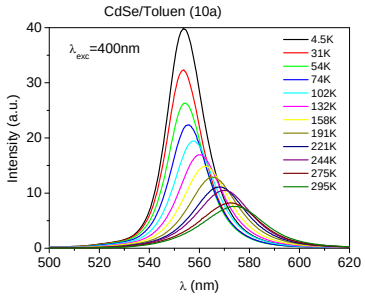


**Fig. 6**. Fluorescence spectra of the sample CdSe QD cores at different temperatures from 4.5 K to 295K (excitation at 400 nm).

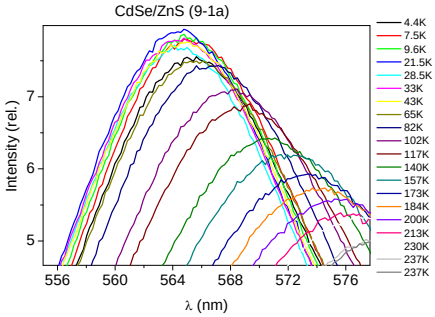


**Fig. 7.** PL peak maximum shifts at different temperatures from 4.4 K to 280K of the sample CdSe/ZnS 2.5 ML QDs (excitation at 400 nm).

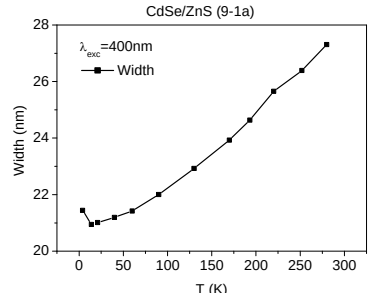


**Fig.8.** FWHM of the emission band of the CdSe/ZnS 2.5 ML QDs as a function of temperature.

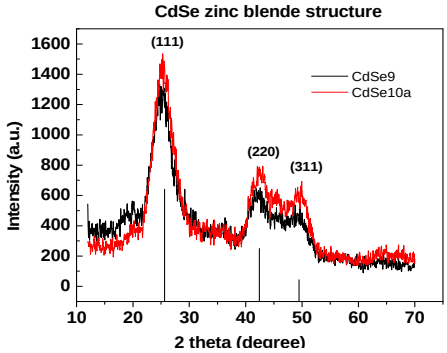


**Fig.9.** X-Rays diffraction patterns of the CdSe powder (No.9 and No.10a) show the pure cubic ZB crystal phase of the QDs samples.

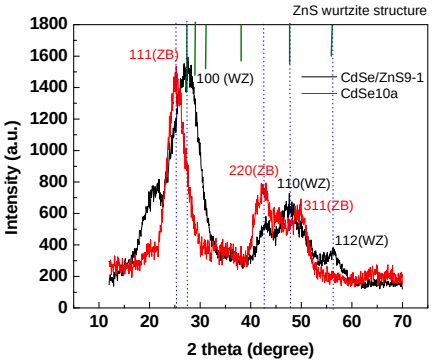


**Fig.10.** XRD patterns of the CdSe/ZnS 2.5 ML powder (No.9-1) and No.10a (CdSe core) shows the mixture ZB-WZ crystal phase of the core/shell sample.

Figs. 6 and 7 show the PL spectra, at different temperatures (4 - 295 K), of two samples of CdSe core QDs (size is 6.1 nm) and of CdSe/ZnS 2.5 ML QDs (size is 5 nm). QD samples were at first in toluene then were dispersed in PMMA (2 wt. %). Temperature dependent PL measurements provide information related to electron-phonon interactions. In the PL spectrum at 4.5 K (Fig.6), a strong green intrinsic emission peak from CdSe QDs is dominantly observed around 550 nm (2.25 eV), the FWHM is the narrowest **(19 nm).** *As the sample temperature is increased, the PL intensity decreases regularly, the emission energy red-shifts and the spectra become broader.* The temperature dependence is due to the intrinsic properties of the CdSe lattice. We would like

to emphasize that the QDs in No.10a has the pure ZB crystal lattice (Fig. 9). With increasing temperatures, the intensity of QDs decreases due to the non-radiative recombination process. At 4.5 K, the PL intensity augmented up to 5 times in comparison with PL intensity at 300 K. Our observation is essentially qualitative agreement with the results reported in [10-13]. In CdSe/ZnS 2.5 ML similar tendency was observed. A shift of 15 nm of the peak position from 4.4 K to 237 K is observed (fig. 7). At 4.4 K, the intrinsic PL intensity is the strongest, the PL intensity decrease only about 1.5 times than that at 280 K. The FWHM is 21.5 nm and augments to 27.2 nm at 280 K. Fig. 8 shows the FWHM of the emission bands of the sample as a function of temperature. At the lowest temperatures, the bandwidth reflects the inhomogeneous distribution resulting from small variations in size, shape, or local environment of the quantum dots. We think the increase in the FWHM with temperature is related to the exciton – phonon coupling in CdSe dots. The integrated intensity of the PL peak as a function of temperature can be used to obtain the main exciton decay mechanism. The QDs in No. 9-1a in its original has pure ZB lattice structure (Fig. 9). In order to achieve a high quantum yield of CdSe QDs, we used Cd/Se ions proportion of 1.38/2 leading to an excess amount of Se in dangling bonds before over-coating with ZnS shell. Further growth of the ZnS shell, the XRD peaks become broader and the peak position shifts to higher diffraction angles, toward the position of the bulk ZnS WZ lines (Fig.10), as those reported in [14]. In this sample, it is possible to have a very thin layer of Se at interface. However the WZ –ZB mixture structure was observed, we think this Se layer may play an important role in the PL of the QDs core/shell structure. As seen in fig. 10, we can not distinguish clearly two crystalline phases, may be CdSe/ZnS 2.5 ML crystallized in the WZ lattice structure of the ZnS lattice. Therefore the observed PL behavior of the sample has a small change in intensity compared to those in pure CdSe QDs (fig. 6).

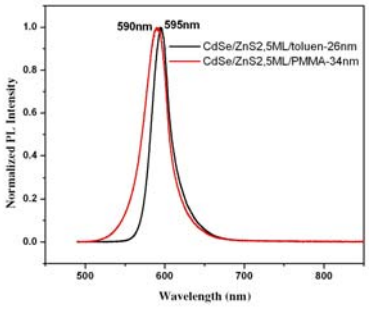


**Fig.11.** Normalized intensity PL spectra of the CdSe/ZnS QDs in toluene solvent and PMMA, $\lambda_{exc.}$ = 488 nm.

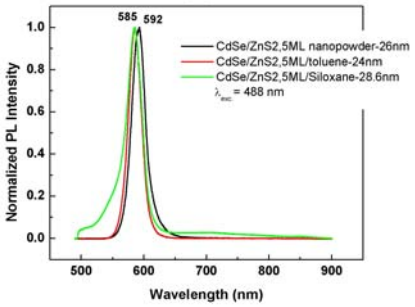


**Fig.12.** Normalized intensity PL spectra of the CdSe/ZnS QDs in solid powder, toluene solvent and water solution, $\lambda_{exc.}$ = 488 nm.

In the case of core/shell QDs, potential barriers between CdSe core and ZnS barrier layer are induced by strain, thermal expansion coefficients and lattice mismatch. We think that this potential barrier prevents carrier diffusion from ZnS barrier layer into CdSe QDs. The shift of the position of the maximum peak to the longer wavelength (from 568 nm to 586 nm) with increasing temperatures is observed. From the study on the PL of the different capping CdSe/ZnS QDs in different environments, such as QDs in the normal atmosphere (in powder form), TOPO-HDA, acid oleic, paraffin, PMMA, PVK (not show here), siloxane-water soluble environment and toluene, we remark that the effect of capping and environment on the peak shift and the bandwidth appears as a different in the relative emission intensity of the ensemble of dots (Figs. 11,12). Fig. 11 shows the normalized PL spectra of CdSe/ZnS QDs in toluene and PMMA. In comparison with the emission in toluene, the PL peak of QDs in PMMA shifts 5 nm to shorter wavelength, we may observe clearly an broadening of blue side of emission band (FWHM of 34 nm), meanwhile PL band of QDs in toluene is narrower (FWHM = 26 nm). The blue-shift could be attributed to the oxidation of the QDs' surface make the QDs effective radius smaller and give emission at shorter wavelengths. The blue shift and increasing of FWHM of QDs in PMMA was also reported in [15]. Similarly, in the case of QDs in PVK matrix, the PL peak shifts 7 nm to

longer wavelength. However, in the case of CdSe/ZnS QDs in epoxy and paraffin (spectrum not shown here), we observed a shift 5 nm to shorter wavelengths, emission band seems to be narrower. It means the paraffin and epoxy matrix can strongly confine QDs in these environments. For the QDs capping with siloxane groups, PL emission is broader than in toluene. A broadening at blue side of emission and a broad emission at longer wavelength 700 nm were observed. This emission can be attributed to active sulphurs (-S-) group acting as anchor points for conjugation and covalent siloxane bonds (Si-O-Si). For more detail, it needs further investigation.

## 4. Conclusions

We have prepared with success a large variety of CdSe/ZnS quantum dots with various sizes, shells, and environments. The PL study at different temperatures shows the complex mechanism of PL QDs depending on those parameters and the role of intrinsic and surface states on the emission process in our CdSe/ZnS QDs samples. We attributed this thermal recovery of the fluorescence to defect states appeared at the core/shell interface by the lattice parameter mismatches of the CdSe and ZnS shell. We showed that the role of intrinsic and surface states on the emission process in our CdSe/ZnS QDs samples. In particular, we showed that the emission band is more intense at 4K.

***Acknowledgments:*** *Research supported, in part, by the bilateral VAST–CNRS France Scientific Research project 2007-2008 and by the VAST Research project 2007-2008 and the National Natural Science Program. We thank to Prof. Nguyen Van Hieu and Prof. Nguyen Dai Hung (IoP) for their helps in this research.*

## References

1. G. D. Scholes and G. Rumbles, Nat. Mater. **5**, 683 (2006).
2. G. Morello, M. Anni, P.D. Cozzoli, L. Manna, R. Cingolani, M. De Giorgi, Superlattices and Microstructures **43,** 528–531(2008).
3. E.C. Scher, L. Manna, A.P. Alivisatos, Philos. Trans. R. Soc. Lond. A 361, 241(2003).
4. W.C.W. Chan, D.J. Maxwell, X. Gao, R.E. Bailey, M. Han, S. Nie, Curr. Opin. Biotech. **13,** 40 (2002).
5. D. Loss and D. P. DiVincenzo, Phys. Rev. B **57**, 120 (1998).
6. L. Qu, X. Peng, J. Am. Chem. Soc.**124,** 2049 (2002).
7. K.T. Shimizu, W.K. Woo, B.R. Fisher, H.J. Eisler, M.G. Bawendi, Phys. Rev. Lett. **89,** 117401 (2002).
8. A. Issac, C. von Borczyskowski, F. Cichos, Phys. Rev. B **71,** 161302 (2005).
9. M. Nirmal, B.O. Dabbousi, M.G. Bawendi, J.J. Macklin, J.K. Trautman, T.D. Harris, L.E. Brus, Nature **383**, 802 (1996).
10. A. Al Salman, A. Tortschanoff, M. B. Mohamed, D. Tonti, F. van Mourik, and M. Chergui, Applied Physics Letters **90,** 093104 (2007).
11. Pham Thu Nga, Nguyen Van Chuc, Vu Duc Chinh, Nguyen Xuan Nghia, Phan Tien Dung, Dao Nguyen Thuan, Pham Thai Cuong, Chu Viet Ha, Vu Hong Hanh, Vu Thi Kim Lien, C. Barthou, P. Benalloul, M. Romanelli, A. Maître; IEEE SENSORS 2006, Daegu, Korea, October 22-25 (2006).
12. D.V. Talapin, A.L. Rogach, A. Kornowski, M. Haase, H. Weller, Nano Lett. **1,** 207 (2001).
13. G. W. Walker, V. C. Sundar, C. M. Rudzinski, A. W. Wun, M. G. Bawendi, and D. G. Nocera, Appl. Phys. Lett. **83**, 3555 (2003).
14. A.V. Baranov, Yu.P. Rakovich, J.F. Donegan, T.S. Perova, R.A. Moore, D.V. Talapin, A.L. Rogach, Y. Masumoto and I. Nabiev; Physical Review B **68,** 165306 (2003).
15. Lin Pang, Kevin Tetz, Yaoming Shen, Chyong-Hua Chen, and Yeshaiahu Fainman, J. Vac. Sci. Technol. B 23(6), 2413-2418,Nov/Dec (2005).

# COOPERATIVE ENHANCEMENT OF CHANNELING OF EMISSION FROM ATOMS INTO A NANOFIBER

**Fam Le Kien and K. Hakuta**

Department of Applied Physics and Chemistry, University of Electro-Communications, Chofu, Tokyo 182-8585, Japan

**Abstract:** We show the possibility of directional guided superradiance from a linear array of distant atoms separated by one or several wavelengths in a line parallel to the axis of a nanofiber. We find that the rate and efficiency of channeling of emission from the atoms into the fiber are cooperatively enhanced by the guided modes.

## 1. Introduction

Coupling of light to subwavelength structures and its control pose one of the greatest challenges of recent research [1–3]. In the case of dielectric waveguides, it has been shown that a significant fraction of emission from a single atom can be channeled into a nanofiber [2, 3]. The cooperation of two distant atoms via a nanofiber has been discussed [4]. It has been shown that, at large distances between the atoms, a substantial energy exchange can survive due to the guided modes [4]. In this paper, we show the possibility of a directional guided superradiant emission process that can enhance the rate and efficiency of channeling of emission from a linear array of distant atoms into a nanofiber.

Before we proceed, we note that superradiance is a problem of fundamental interest [5]. Despite a great deal of research [6], certain aspects of the problem are still not well understood. Recently, the angular distribution of emission from a spatially extended array of atoms in free space has been treated by the quantum trajectory method [7]. The dynamic mode selection has been studied [8]. Superradiant conversion of atomic spin gratings into single photons in an optical cavity has been demonstrated [9].

## 2. Model

Consider N identical two-level atoms interacting with the quantum electromagnetic field in the vicinity of a nanofiber (see Fig. 1). The fiber has a cylindrical silica core of radius a and refractive index n1 = 1.45 and an infinite vacuum clad of refractive index n2 = 1. We assume that the atomic transition frequency !0 is well below the cutoff frequency of the fiber, so the single-mode condition is satisfied for this frequency. In view of the very low losses of silica in the wavelength range of interest, we neglect material absorption. The atoms are located at points (rj, ‘j , zj), where j = 1, 2, . . . ,N labels the atoms and (r, ‘, z) is the cylindrical coordinates with z being the axis of the fiber. We assume that the field is initially in the vacuum state. The field can be decomposed into the contributions from the guided and radiation modes, whose quantum expressions are given in Ref. [2].

Assume that the characteristic atomic lifetime is large as compared to the optical period 2_/!0 and to the light propagation time between two different atoms. The master equation for the reduced density operator _ of the atomicsystem in the electric-dipole, rotating-wave, and Born-Markov approximations has been previously derived [4, 6, 7]. In the interaction picture, it reads

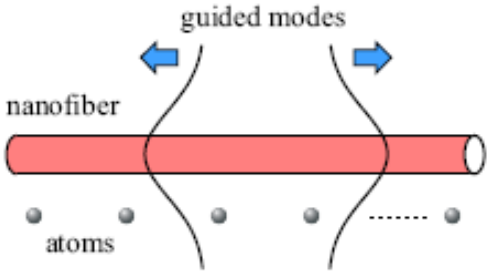


**Fig. 1**: Linear array of atoms in the vicinity of a nanofiber.

$$\dot{\rho} = \frac{1}{2}\sum_{i,j=1}^{N} \gamma_{ij}(2\sigma_j \rho \sigma_i^\dagger - \sigma_i^\dagger \sigma_j \rho - \rho \sigma_i^\dagger \sigma_j). \quad (1)$$

Here $\sigma_j$ and $\sigma_j^\dagger$ are the pseudospin operators that describe the downward and upward transitions of the atoms.

The coefficients $\gamma_{ij} = \gamma_{ij}^{(\mathrm{gyd})} + \gamma_{ij}^{(\mathrm{rad})}$, with $i, j = 1, 2, \ldots, N$, characterize the collective spontaneous emission process,

Where $\gamma_{ij}^{(\mathrm{gyd})}$ and $\gamma_{ij}^{(\mathrm{rad})}$ are the contributions from the guided and radiation modes, respectively [4].

### 3. Intensity of emission into guided modes

We introduce the total emission intensity $I \equiv \sum_{\mathrm{all}} \hbar\omega_\alpha \langle \dot{n}_\alpha \rangle$, the intensity of emission into the guided modes $I_{\mathrm{gyd}} \equiv \sum_{\mathrm{gyd}} \hbar\omega_\alpha \langle \dot{n}_\alpha \rangle$, and the intensity of emission into the radiation modes $I_{\mathrm{rad}} \equiv \sum_{\mathrm{rad}} \hbar\omega_\alpha \langle \dot{n}_\alpha \rangle$. Here the notation $\sum_{\mathrm{all}}, \sum_{\mathrm{gyd}}, \mathrm{and} \sum_{\mathrm{rad}}$ mean the summations over all the modes, the guided modes, and the radiation modes, respectively, and $\omega_\alpha$ and $\langle n_\alpha \rangle$ are the frequency and mean number, respectively, of photons in a field mode $\alpha$. We find $I = \hbar\omega_0 \sum_{ij} \gamma_{ij} \langle \sigma_i^\dagger \sigma_j \rangle = I_{\mathrm{gyd}} + I_{\mathrm{rad}}$, I , where

$I_{\mathrm{gyd}} = \hbar\omega_0 \sum_{ij} \gamma_{ij}^{(\mathrm{gyd})} \langle \sigma_i^\dagger \sigma_j \rangle$ and $I_{\mathrm{rad}} = \hbar\omega_0 \sum_{ij} \gamma_{ij}^{(\mathrm{rad})} \langle \sigma_i^\dagger \sigma_j \rangle$. We note that $I = -\hbar\omega_0 \dot{P}$, where $P = \sum_i \langle \sigma_i^\dagger \sigma_j \rangle$ is the total population of the excited levels of the atoms. The total energy emitted from the atoms is $U = \int_0^\infty I(t)\, dt = U_{\mathrm{gyd}} + U_{\mathrm{rad}}$, where $U_{\mathrm{gyd}} = \int_0^\infty I_{\mathrm{gyd}}(t)\, dt$ and $U_{\mathrm{rad}} = \int_0^\infty I_{\mathrm{rad}}(t)\, dt$ are the energies emitted into the guided and radiation modes, respectively. The fractions of energy emitted into the guided and radiation modes are given by $f_{\mathrm{gyd}} = U_{\mathrm{gyd}}/U$ and $f_{\mathrm{rad}} = U_{\mathrm{rad}}/U = 1 - f_{\mathrm{gyd}}$, respectively.

The decay coefficients $\gamma_{ij}^{(\mathrm{gyd})}$ and $\gamma_{ij}^{(\mathrm{rad})}$ have been calculated in Ref. [4]. The diagonal decay coefficients $\gamma_{jj}$ describe the spontaneous decay of individual atoms. The off-diagonal decay coefficients $\gamma_{jj'}$, with the convention $j \neq j'$, characterize the energy transfer between two atoms. According to Ref. [4], the contribution $\gamma_{jj'}^{(\mathrm{gyd})}$ of the guided modes to the transfer rate is periodic in the z direction with the period $\lambda_F = 2\pi/\beta_0$, where $\beta_0$ is the longitudinal propagation constant of the guided modes at the atomic frequency $\omega_0$. Meanwhile, the contribution $\gamma_{jj'}^{(\mathrm{rad})}$ of the radiation modes reduces to zero with increasing interatomic distance $|z_j - z_{j'}|$. Therefore, in the limit of large $|z_j - z_{j'}|$, the energy transfer coefficient $\gamma_{jj'}$ is mainly determined by the contribution $\gamma_{jj'}^{(\mathrm{gyd})}$ of the guided modes and is almost periodic with the spatial period $\lambda_F$.

We now assume that the atoms are aligned along a line parallel to the fiber axis, with relatively large atomic separations being equal to integer multiples of the longitudinal wavelength $\lambda_F$. In other words, we assume that $r_j = \mathrm{const} \equiv r_0$, $\varphi_j = \mathrm{const} \equiv \varphi_0$, and $z_{j+1} - z_j = q_j \lambda_F$, with qj being nonzero, positive integer numbers. In addition, we assume that the dipoles of the atoms are oriented in the same direction. Under these conditions, the guided energy transfer coefficients $\gamma_{jj'}^{(\mathrm{gyd})}$ achieve their maximum value with respect to the axial direction, $\gamma_{jj'}^{(\mathrm{gyd})} = \gamma_{jj}^{(\mathrm{gyd})} = \gamma_{j'j'}^{(\mathrm{gyd})}$.

Meanwhile, due to the large separations between the atoms, the radiative (unguided) energy transfer coefficients $\gamma_{jj'}^{(\mathrm{rad})}$ are small. In this case, we have

$\gamma_{jj} = \gamma_{jj}^{(\mathrm{gyd})} + \gamma_{jj}^{(\mathrm{rad})} = \gamma = \gamma_{\mathrm{gyd}} + \gamma_{\mathrm{rad}}$ and $\gamma_{jj'} \cong$ . Here $\gamma_{\mathrm{gyd}}$ and $\gamma_{\mathrm{rad}}$ are the rates of decay into the guided and radiation modes, respectively. They do not depend on the axial coordinate z of the atoms, but increase with decreasing atom–surface distance r – a. We note that the parameter $\eta = \gamma_{\mathrm{gyd}}/\gamma_{\mathrm{rad}}$ characterizes the cooperativity of a single atom with the guided modes as well as the fiber-assisted cooperativity between distant atoms.

We calculate the decay rates $\gamma_{\mathrm{gyd}}$, $\gamma_{\mathrm{rad}}$, and $\gamma = \gamma_{\mathrm{gyd}} + \gamma_{\mathrm{rad}}$ and the cooperativity parameter $\eta = \gamma_{\mathrm{gyd}}/\gamma_{\mathrm{rad}}$ . In general, these characteristics depend on the radius of the fiber, the orientation of the dipole, and the position of the atom [2, 4]. We display in Fig. 2 the numerical results for the case of a radially oriented dipole with the transition wavelength $\lambda_0 = 852$ nm. We choose the transition wavelength of 852 nm for our calculations because it is the wavelength of the cesium D2-line transition, which was used in the experiments on atoms near a nanofiber [3]. We take the radial orientation for the atomic dipole because, according to the results of Refs. [4] for a two-level atom, such an orientation leads to the strongest enhancement of the decay rates $\gamma_{\mathrm{gyd}}$, $\gamma_{\mathrm{rad}}$, and $\gamma$. The left panel of Fig. 2 shows that the decay rate into the guided modes $\gamma_{\mathrm{gyd}}$ and the cooperativity parameter $\eta$ achieve their largest values when the fiber radius a is about 200 nm. This is in agreement with the results of Ref. [2] for a realistic cesium atom. The right panel of Fig. 2 shows that the decay rates $\gamma_{\mathrm{gyd}}$, $\gamma_{\mathrm{rad}}$, and $\gamma$ and the cooperativity parameter $\eta$ increase with decreasing atom–surface distance r – a. The rate of decay into the guided modes gyd and the cooperativity parameter $\eta$ can be significant when the atom is close enough to the fiber surface. For example, when the atom–surface distance is r – a = 100 nm, we obtain $\gamma_{\mathrm{gyd}} = 0.26\gamma_0$, $\gamma_{\mathrm{rad}} = 1.06\gamma_0$, and $\gamma = 1.32\gamma_0$ leading to $\eta = 0.25$. Here $\eta = 0.25$. is the atomic natural linewidth, whose magnitude is about 5.3 MHz in the case of the cesium D2 line. The significant values $\gamma_{\mathrm{gyd}} = 0.26\gamma_0$ and $\eta = 0.25$ show that the atom can efficiently radiate into the guided modes and can effectively cooperate with the other atoms in the array over long distances. The rate of decay into the guided modes $\gamma_{\mathrm{gyd}}$ and the cooperativity parameter $\eta$ can achieve more substantial values when the atom is closer to the fiber surface. However, when the atom is very near to the surface, the effect of the surface-induced potential must be taken into account. We emphasize that the energy transfer coefficient $\gamma_{jj'} = \gamma_{\mathrm{gyd}}$, obtained here for distant atoms, is due to the guided modes and is substantially larger than that for distant atoms in free space [7].

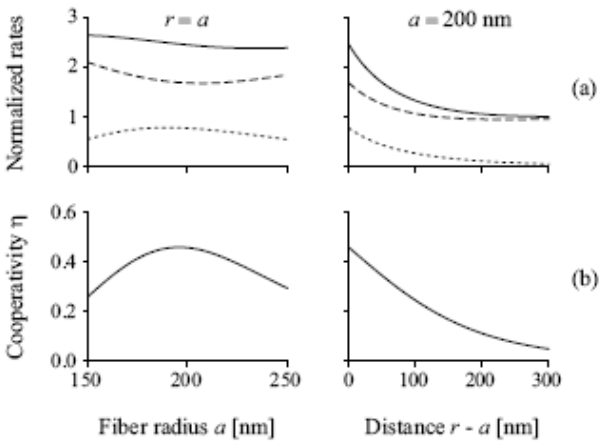


**Fig. 2**: Atomic decay and cooperativity parameters as functions of the fiber radius a (left panel) and the atom–surface distance r − a (right panel).
Part (a): The total decay rate $\gamma$ (solid lines) and the contributions $\gamma_{\mathrm{rad}}$ (dashed lines) and $\gamma_{\mathrm{gyd}}$ (dotted lines) from the radiation and guided modes, respectively. The rates are normalized to the atomic natural linewidth $\gamma_0$.
Part (b): The cooperativity parameter $\eta = \gamma_{\mathrm{gyd}}/\gamma_{\mathrm{rad}}$. The transition wavelength $\lambda_0 = 852$ nm and the radial dipole orientation are used.

We note that the creation of regular strings of atoms in a standing wave optical dipole trap has been demonstrated [10]. Superradiance of linear arrays of atoms in free space has also been studied [7]. Therefore, the model of a linear array of atoms is worth consideration.

For the linear array of atoms described above, we find that the intensity of emission into the radiation modes is $I_{\mathrm{rad}} = \hbar\omega_0\gamma_{\mathrm{rad}}P$ and, hence, the intensity of emission into the guided modes is

$$I_{\mathrm{gyd}} = -\hbar\omega_0\left(\frac{dP}{dt} + \gamma_{\mathrm{rad}}P\right) \quad (2)$$

Meanwhile, the total excited-state population P is governed by the equation

$$\frac{dP}{dt} = -\gamma P - \gamma_{\rm gyd} \sum_{j \neq j'} \langle \sigma_j^\dagger \sigma_{j'} \rangle. \quad (3)$$

Below we examine two cases of initial atomic states, the case of an entangled state and the case of a product state.

### *A. Symmetric one-excitationstate*

First we consider the case where the atomic system is initially prepared in the symmetric one-excitation state $|1\rangle = N^{-1/2} \sum_j |1_j\rangle$. Here $|1_j\rangle = |e_j\rangle \otimes \prod_{j' \neq j} |g_{j'}\rangle$ is the product state in which only atom j is excited, with $|e_j\rangle$ and $|g_j\rangle$ being the excited and ground states, respectively, of atom j. We introduce the notation $|0\rangle = \prod_j |g_j\rangle$ for the state in which all the atoms are in their ground states. We find that the system of N two-level atoms prepared in the entangled state $|1\rangle$ like a single effective two-level system whose upper and lower levels are the states $|1\rangle$ and $|0\rangle$ respectively. We obtain from Eq. (1) the solution $\rho_{11} = e^{-\Gamma t}$, $\rho_{00} = 1 - e^{-\Gamma t}$, and $\rho_{10} = \rho_{01} = 0$, with the collective decay rate

$$\Gamma = \gamma_{\rm rad} + N\gamma_{\rm gyd} \quad (4)$$

This rate is enhanced [5] by the cooperativity of the atoms via the guided modes. The above solution yields the total excited-state population $P = e^{-\Gamma t}$ and the intensity of emission into the guided modes

$$I_{\rm gyd} = \hbar\omega_0 N \gamma_{\rm gyd} e^{-\Gamma t}. \quad (5)$$

Hence the energy emitted into the guided modes is $U_{\rm gyd} = \hbar\omega_0 N\gamma_{\rm gyd}/\Gamma$. Meanwhile, the total emitted energy is $U = \hbar\omega_0$. Consequently, the fraction of energy emitted into the guided modes is

$$f_{\rm gyd} = \frac{N\gamma_{\rm gyd}}{\gamma_{\rm rad} + N\gamma_{\rm gyd}}. \quad (6)$$

It is clear that $f_{\rm gyd}$ increases with increasing atom number N and that $f_{\rm gyd} \to 1$ in the $N \to \infty$. Thus the efficiency of channeling of emission from the atoms into the fiber is cooperatively enhanced. We use Eq. (6) to calculate $f_{\rm gyd}$ as a function of N and display the results in Fig. 3. For N = 100 and $r - a = 100$ nm, we obtain $f_{\rm gyd} \geq 0.92$ (see the endpoints of the curves). In particular, for N = 100 and r – a = 100 nm, the factor $f_{\rm gyd}$ reaches the value 0.96 (see the endpoint of the dashed curve). Such a high efficiency indicates that the single photon emitted from the atoms is almost entirely directed into the guided modes. A very similar result has been obtained for the superradiance of atoms in an optical cavity [9]. Indeed, in terms of the cooperativity parameter $\eta = \gamma_{\rm gyd}/\gamma_{\rm rad}$, the channeling efficiency fgyd given by Eq. (6) coincides with the success probability $\mathcal{P} = N\eta/(1 + N\eta)$ for conversion in the cavity case [9]. Such a coincidence is due to the fact that the nanofiber mode and the cavity mode have many common features. We note that, at the distance of 100 nm from the surface of the 200-nm-radius fiber, the

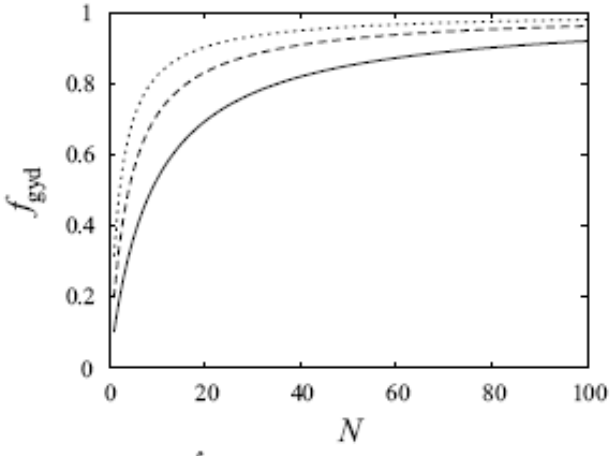


**Fig. 3**: Fraction $f_{\rm gyd}$ of energy emitted from atoms initially prepared in the symmetric one-excitation state into the guided modes as a function of the atom number N. The atom–surface distance is r − a = 200 nm (solid line), 100 nm (dashed line), and 0 (dotted line). The fiber radius a = 200 nm and the atomic wavelength $\lambda_0 = 852$ nm are used. The atomic dipoles are radially oriented.

cooperativity parameter is $\eta = 0.25$ (see Fig. 2). This value is substantially larger than the value $\eta = 6.9 \times 10^{-3}$ for a moderate-finesse cavity [9].

We emphasize that, if the initial one-excitation state is not a symmetric, entangled state but simply an asymmetric, product state with a single excited atom and N −1 unexcited atoms, then we have $f_{\rm gyd} = \gamma_{\rm gyd}/(\gamma_{\rm rad} + N\gamma_{\rm gyd})$. This factor reduces with increasing N. This is a signature of subradiance in the system.

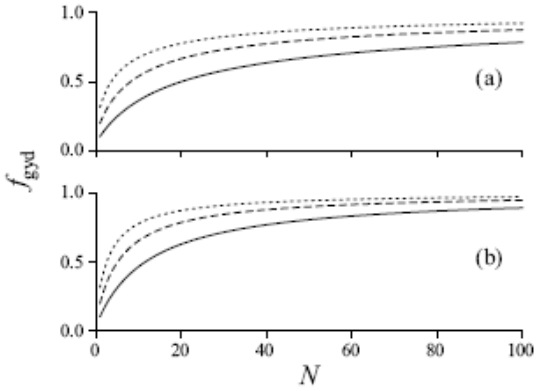


**Fig. 4**: Fraction $f_{\rm gyd}$ of energy emitted from atoms initially prepared in a product state into the guided modes as a function of the atom number N. The angle $\theta$ for the initial product state is (a) $\theta = 0$ (full excitation) and (b) $\theta = \pi/2$ (one-half excitation). The atom–surface distance is r − a = 200 nm (solid line), 100 nm (dashed line), and 0 (dotted line). The parameters used are as in Fig. 3.

### *B. Coherent product state*

We now consider the case where all the atoms are initially prepared in the same coherent superposition state, that is, the initial state of the atoms is the product state $|\Psi\rangle = \prod_j (\cos\frac{\theta}{2}|e_j\rangle + e^{i\phi}\sin\frac{\theta}{2}|g_j\rangle)$. Such a state can be prepared by using a plane-wave optical pulse to excite the atoms.

In order to get insight into the case of large N, we make an approximation for the last term in Eq. (3). For the initial product state $|\Psi\rangle$, we have $\langle\sigma_j^\dagger\sigma_{j'}\rangle = P(N-P)/N^2$ for every pair $j \neq j'$. We assume that this relation is valid for the whole emission process. Such an assumption is reasonable under the condition $N \gg N - P_0 \gg 1$ [6]. With this assumption, Eq. (3) yields

$$\frac{dP}{dt} = -P[\gamma + (1 - N^{-1})\gamma_{\rm gyd}(N - P)]. \tag{7}$$

The solution to the above equation, subject to the initial condition P(0) = P0, is $P = N(\kappa+1)/[\kappa + e^{\Gamma(t+t_a)}]$, where $\kappa = (N-1)\gamma_{\rm gyd}/\gamma$ and $t_a = \tau\ln[(\kappa+1)(N/P_0) - \kappa]$, with $\tau = \Gamma^{-1}$. The intensity of emission into the guided modes is

$$I_{\rm gyd} = \hbar\omega_0 N\frac{\kappa+1}{\kappa + e^{\Gamma(t+t_a)}} \times \left[\gamma(\kappa+1)\frac{e^{\Gamma(t+t_a)}}{\kappa + e^{\Gamma(t+t_a)}} - \gamma_{\rm rad}\right]. \tag{8}$$

If $t_a < t_p$, where $t_p = \tau\ln\{(1-N^{-1})[2+(N-2)(\gamma_{\rm gyd}/\gamma)]\}$, then the intensity Igyd(t) has a local peak with the height $I_{\rm gyd}^{\rm max} = \hbar\omega_0\gamma_{\rm gyd}N^3/[4(N-1)]$ at the time $t = t^{\rm max} \equiv t_p - t_a$. Otherwise, the function $I_{\rm gyd}(t)$ monotonically decreases from its initial value $I_{\rm gyd}(0) = \hbar\omega_0 P_0\gamma_{\rm gyd}[1 + (N-1)(1-P_0/N)]$.

It follows from Eq. (8) that the energy emitted into the guided modes is

$$U_{\rm gyd} = \hbar\omega_0 P_0\left\{1 - \frac{N\gamma_{\rm rad}}{P_0\gamma}\frac{1}{\kappa}\ln\frac{\kappa+1}{1+(1-P_0/N)\kappa}\right\}. \tag{9}$$

Meanwhile, the total emitted energy is $U = \hbar\omega_0 P_0$. Hence the fraction of energy emitted into the guided modes is

$$f_{\rm gyd} = 1 - \frac{N}{P_0}\frac{\gamma_{\rm rad}}{\gamma}\frac{1}{\kappa}\ln\frac{\kappa+1}{1+(1-P_0/N)\kappa}. \tag{10}$$

For $P_0$ = N, we have

$$f_{\mathrm{gyd}} = 1 - \frac{\gamma_{\mathrm{rad}}}{\gamma}\frac{\ln(\kappa+1)}{\kappa} \qquad (11)$$

Equation (11) together with the expression $\kappa = (N-1)\gamma_{\mathrm{gyd}}/\gamma$ indicate that fgyd increases with increasing N and that $f_{\mathrm{gyd}} \to 1$ in the limit $N \to \infty$ (see Fig. 4). We use Eq. (10) to calculate $f_{\mathrm{gyd}}$ as a function of N and display the results in Fig. 4. Comparison between Figs. 4(a) and 4(b) shows that the effect of the coherently excited initial population per atom $P_0/N$ on the channeling efficiency factor $f_{\mathrm{gyd}}$ is weak.

Since the propagation effects are neglected in our model, the above results are valid only if a photon can traverse the sample in a time shorter than the characteristic time scale of the collective decay. Therefore, the length L of the atomic string in our model is limited by the condition $L \ll L_0$, where $L_0 = c/\Gamma$ is the cooperativity length. When we take N = 100 and $\gamma_0 = 5.3$ MHz, and use the parameters $\gamma_{\mathrm{gyd}} = 0.26\gamma_0$ and $\gamma_{\mathrm{rad}} = 1.06\gamma_0$, obtained in Fig. 2 for the atom–surface distance r – a = 100 nm, we find $L_0 = 33$ cm. For $L \gtrsim L_0$, the collective effects can still survive but
the propagation effects must be included.

## 4. Conclusions

In conclusion, we have shown the possibility of directional guided superradiance from a linear array of distant atoms that are separated by one or several wavelengths in a line parallel to the axis of a nanofiber. The rate of emission is enhanced by the cooperativity of the atoms via the guided modes. The efficiency of channeling of emission into the guided modes increases with increasing atom number and approaches unity in the limit of large numbers of atoms.

## References

1. A. Maier et al., Nat. Mater 2, 229 (2003); T. W. Ebbesen et al., Nature (London) 391, 667 (1998); A. Wallraff et al., Nature (London) 431, 162 (2004); D. E. Chang, A. S. Sorensen, P. R. Hemmer, and M. D. Lukin, Phys. Rev. Lett. 97, 053002 (2006).
2. Fam Le Kien, S. Dutta Gupta, V. I. Balykin, and K. Hakuta, Phys. Rev. A 72, 032509 (2005).
3. K. P. Nayak et al., Opt. Express 15, 5431 (2007); K. P. Nayak and K. Hakuta, New J. Phys. 10, 053003 (2008).
4. Fam Le Kien, S. Dutta Gupta, K. P. Nayak, and K. Hakuta, Phys. Rev. A 72, 063815 (2005).
5. R. H. Dicke, Phys. Rev. 93, 99 (1954).
6. M. Gross and S. Haroche, Phys. Rep. 93, 301 (1982).
7. H. J. Carmichael and K. Kim, Opt. Commun. 179, 417 (2000); J. P. Clemens, L. Horvath, B. C. Sanders, and H. J.Carmichael, Phys. Rev. A 68, 023809 (2003); J. Opt. B:Quantum Semiclassical Opt. 6, S736 (2004).
8. C. K. Law and S. K. Y. Lee, Phys. Rev. A 75, 033813 (2007).
9. A. T. Black, J. K. Thompson, and V. Vuletic, Phys. Rev. Lett. 95, 133601 (2005).
10. Y. Miroshnychenko et al., Nature (London) 442, 151 (2006); Y. Miroshnychenko et al., New J. Phys. 8, 191 (2006).

# LARGE-SIZED ZINC OXIDE SINGLE CRYSTAL GROWN BY THE HYDROTHERMAL METHOD AS FAST SCINTILLATOR FOR FUTURE EXTREME ULTRAVIOLET LITHOGRPHY

**Nobuhiko Sarukura[a], Tomoharu Nakazato[a], Yusuke Furukawa[a], Momoko Tanaka[b], Masaharu Nishikino[b], Hiroshi Yamatani[b], Tetsuya Kawachi[b], Keisuke Nagashima[b], Toyoaki Kimura[b], Hidetoshi Murakami[a], Shigeki Saito[a], Hiroaki Nishimura[a], Kunioki Mima[a], Yuji Kagamitani[c], Dirk Ehrentraut[c], Tsuguo Fukuda[(c)]**

[a)] Osaka University, 2-6, Yamadaoka, Suita, Osaka 565-0871, Japan
[b)] Japan Atomic Energy Agency,8-1,Umemidai, Kizugawa, Kyoto 619-0215, Japan
[(c)]Tohoku University, 2-1-1 Katahira, Aoba-ku, Sendai 980-8577, Japan
*E-mail: sarukura-n @ile.osaka-u.ac.jp*

Applications in next-generation lithography has stirred interest for optical technology research in the extreme ultraviolet (EUV) region. As such, efficient EUV light sources have been demonstrated quite recently [1,2]. In conjunction with these advances, efforts have also been made for the development of functional optical components in this short wavelength regime. In particular, efficient and fast imaging scintillator devices with sufficient size is a key component in EUV lithography. As a scintillator material, hydrothermal method grown zinc oxide (ZnO) is a prominent candidate. ZnO has been intensively studied in the past decade and its growth characteristics have been greatly improved in the aspect of crystalline quality and size of up to 3-inch-diameter [3]. In this paper, the EUV optical properties of a hydrothermal method grown ZnO was studied using a nickel-like silver laser operating at 13.9 nm as the excitation light source. This laser possesses large pulse energy of up to about micro-joules level and a sufficiently short pulse duration down to several picoseconds [4]. The optical properties of ZnO as a scintillator in the EUV region was evaluated in the context of response time and fluorescence wavelength and their temperature dependence.

In the experiment, an EUV laser operating at 13.9 nm was employed as the excitation source. The lasing scheme is the 4p-4d transition of the nickel-like silver ion pumped with the transient collisional excitation [4]. The two gain medium plasmas of the EUV laser were generated by irradiating flat silver targets with double laser pulses, whose durations are 200 ps and 3 ps for prepulse and main pulse, respectively, at a wavelength of 1053 nm [5]. The pulse energy of the EUV laser emission was 0.5 <μJ with a pulse width of 7 ps; which is sufficiently short for this experiment. The single crystal ZnO was grown by hydrothermal method combined with a platinum inner container [3]. The High-purity ZnO single crystal having a large size of 50 x 50 x 15 $mm^3$ was sliced with a (0001) surface orientation. The excitation laser was focused on the sample using a Mo/Si multilayer spherical EUV mirror suitable for 13.9 nm while a <0.2μm thick Zr foil, placed before the EUV mirror filtered out continuous emission from the plasma. The fluorescence spectrum and the fluorescence decay of the ZnO sample were measured using a 25 cm-focal length spectrograph coupled to a streak camera system. The scintillation properties of the ZnO crystal were also evaluated using the 110 ps pulse width, 351 nm third harmonic of the 1053 nm chirped pumping source of the EUV laser. In the latter case, the ZnO was excited at a photon energy slightly above the bandgap.

The streak camera image for the EUV excited ZnO emission is shown in Fig. 1(a). Although a single frame was enough to obtain an image, there frames were integrated in this figure in order to reduce the noise levels. The time profile at the spectral peak is shown in Fig. 2(a). It can be fitted by a double exponential decay function with time constants of 0.9 ns and 2.7 ns. These two decay constants have been measured previously for UV excited ZnO single crystals. The fast decay is attributed to the lifetime of the free exciton and the slower decay is assigned to trapped carriers in ZnO. The corresponding streak camera image and the time profile for UV excitation (351 nm) are shown in Fig. 1(b), 2(b), respectively. In both excitation conditions, a prominent fluorescence peak of the ZnO excitonic transition was observed at around 380 nm. Similarly, two decay lifetimes were observed in both cases and the time profiles were very similar despite the huge difference in the excitation photon energy. It may be inferred that the fluorescence lifetime is sufficiently short and is suitable for nanosecond-scale characterization of the laser plasma EUV source. Moreover, a large-sized and homogeneous crystal such hydrothermal grown ZnO is potentially attractive for EUV imaging applications, including lithography.

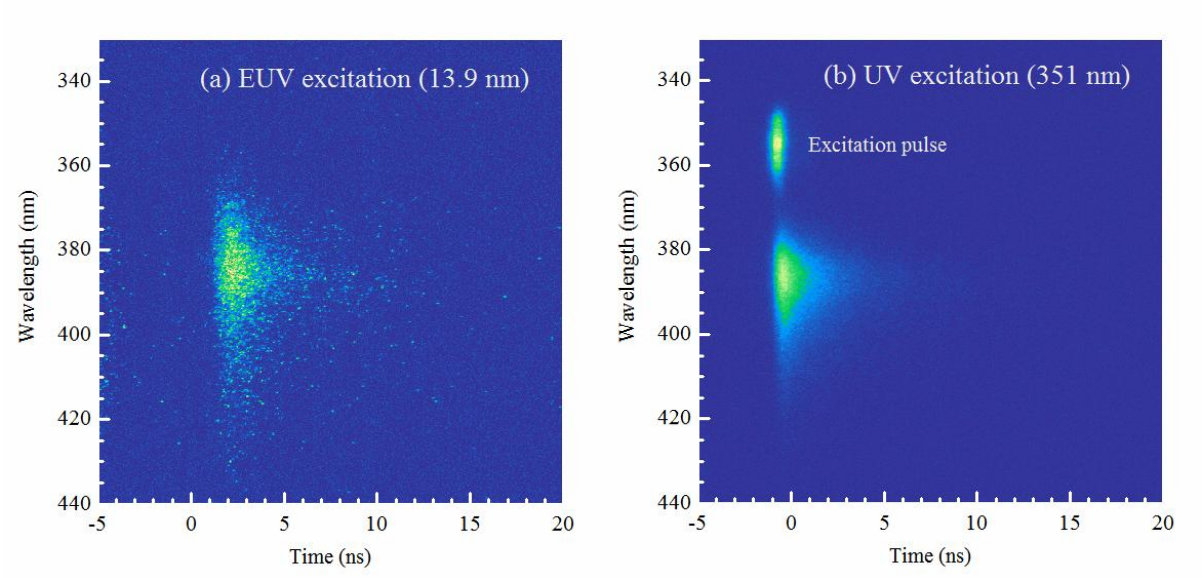


**Fig. 1**: Streak camera images of the fluorescence from ZnO excited by a) EUV laser pulses (13.9 nm) and b) UV laser pulses (351 nm).

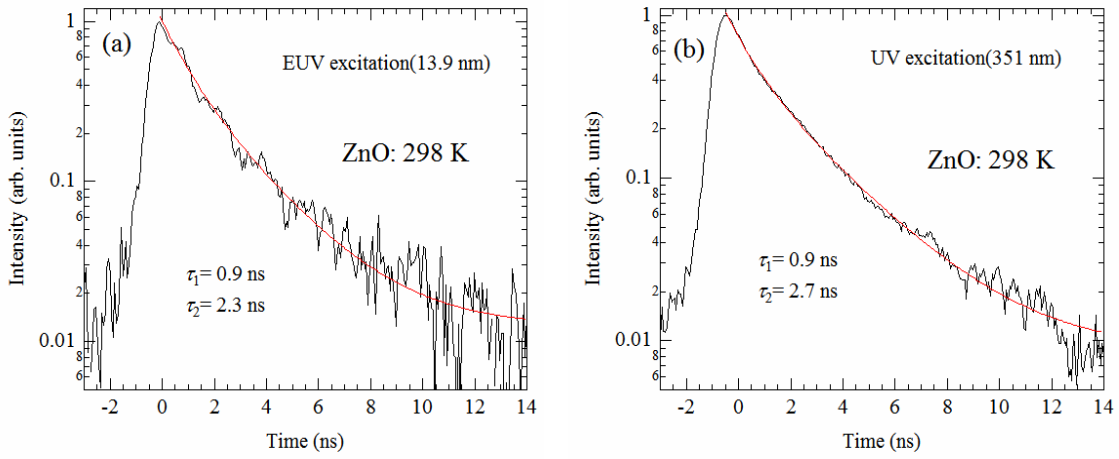


**Fig. 2:** Temporal profiles of the fluorescence rom ZnO, which are excited by a) EUV laser pulses (13.9 nm) and b) UV laser pulses (351 nm). Both profiles can be fitted by a double exponential decay function.

***Acknowledgments***

*This work was performed in part by the auspice of MEXT project on mono-energetic quantum beam science with PetaWatt lasers. The results were achieved under the Facilities Utilization system of Japan Atomic Energy Agency.*

**References**

1. Y. Shimada, N. Nishimura, M. Nakai, K. Hashimoto, M. Yamaura, Y. Tao, K. Shigemori, T. Kawamura, A. Sunahara, T. Nishikawa, A. Sasaki, K. Nagai, T. Norimatsu, S. Fujioka, S. Uchida, N. Miyanaga, Y. Izawa, and C. Yamanaka, "Characterization of extreme ultraviolet emission from laser-produced spherical tin plasma generated with multiple laser beams," *Appl. Phys. Lett.* **86**, 51501 (2005).
2. S. Fujioka, H. Nishimura, K. Nishihara, A. Sasaki, A. Sunahara, T. Okuno, N. Ueda, T. Ando, Y. Tao, Y. Shimada, K. Hashimoto, M. Yamaura, K. Shigemori, M. Nakai, K. Nagai, T. Norimatsu, T. Nishikawa, N. Miyanaga, Y. Izawa, and K. Mima, *Phys. Rev. Lett.* **95**, 235004 (2005).
3. E. Ohshima, H. Ogino, I. Niikura, K. Maeda, M. Sato, M. Ito, and T. Fukuda, "Growth of the 2-in-size bulk ZnO single cryatals by the hydrothermal method," *J. Cryst. Growth* **260**, 166 (2004).
4. T. Kawachi, M. Kado, M. Tanaka, A. Sasaki, N. Hasegawa, A. V. Kilpio, S. Namba, K. Nagashima, P. Lu, K. Takahashi, H. Tang, R. Tai, M. Kishimoto, M. Koike, H. Daido, and Y. Kato, "Gain saturation of nickel-like silver and tin x-ray lasers by use of a tabletop pumping laser system," *Phys. Rev. A* **66**, 33815 (2002).
5. M. Tanaka, M. Nishikino, T. Kawachi, N. Hasegawa, M. Kado, M. Kishimoto, K. Nagashima, and Y. Kato, "X-ray laser beam with diffraction-limited divergence generated with two gain media," *Opt. Lett*. **28**, 1680 (2003).

# A STUDY OF AVALANCHE PHOTODIODES AS SINGLE PHOTON DETECTORS

**Siew-Li Tan and Duu-Sheng Ong**

Faculty of Engineering, Multimedia University,
Persiaran Multimedia, 63000 Cyberjaya, Selangor.
*E-mail: dsong@mmu.edu.my*

**Abstract**: Single Photon Avalanche Diodes (SPAD) have emerged as very promising devices for single photon detection owing to advantages such as low bias voltage, low power, low cost, small size and robustness, which are essential for integration into arrays and into CMOS technology. Avalanche Photodiodes (APD) may be converted to SPADs simply by operating in the above-breakdown regime, however, certain combinations of performance attributes that work best for APDs may be detrimental for SPADs. In this work, a simple and fast numerical model which incorporates random ionization path length (RPL) following a hard-threshold dead space is used to assess the performance of APD for Geigermode operation, specifically for single photon detection. It is known that reducing the multiplication width increases the breakdown probability relative to the breakdown voltages, as the effect of dead space becomes more dominant in thinner devices. Furthermore, reducing the multiplication width of SPAD results in smaller breakdown time and jitter despite increased in dead space. The present simulations show that SPAD with thin multiplication region produces the most uniform mean breakdown time consistent with the experimental findings (J. Mod. Optics, Vol.54 (No. 2), 141-149 2007). The 2D-RPL model simulations show that lateral diffusion increases the breakdown time and jitter at a given overbias when avalanches are initiated near the lateral edge of the active region. Nevertheless, the mean breakdown time and jitter reduce significantly as a function of breakdown probability due to lateral spreading and diffusion of carriers out of multiplication region. Hence, it is possible to improve the breakdown probability, breakdown time and jitter in SPADs by decreasing the multiplication layer hickness and area at the cost of higher dark counts associated with operating at higher fields

***Keywords**: Single Photon, Avalanche Breakdown, Jitter, Detector*

## 1. Introduction

Single photon detectors are essentially p-n junctions reverse biased well above the breakdown voltage (*i.e.* Geiger mode) so that a single photon can be absorbed to trigger a self-sustaining avalanche multiplication leading to a large current pulse that can be detected and quenched by external circuits. Avalanche photodiodes (APDs), which normally operate in linear mode below the breakdown voltage, can detect single photons when operating in Geiger mode. Such detectors are known as single photon avalanche diodes (SPADs). An understanding of the differences between APDs and SPADs in terms of performance is important in a study of APDs as single photon detectors. A good review of the working principle of SPADs and the differences between APDs and SPADs can be found in Ref.[1].

Geiger-mode operation means that the detection efficiency of a SPAD not only depends on the detector's quantum efficiency but also on its breakdown probability, which is irrelevant for an APD operating below breakdown. By definition, breakdown probability is the probability that a photo-generated charge carrier (electron or hole) triggers an avalanche breakdown in the multiplication region of a SPAD. Since the false counts detected by a SPAD in the absence of light (*i.e.* dark counts) increase with bias voltage, it is desirable that the breakdown probability increases rapidly with bias above the breakdown voltage. To minimise dark counts, SPADs are biased above the breakdown voltage during the gate-on time to detect photons and then quenched by lowering the bias to below the breakdown voltage during the gate-off or 'dead time'. Shorter gate-on time reduces the likelihood of detecting a false count, whereas longer dead time and higher operating temperature reduce afterpulsing, which is dark count triggered by the release of

trapped charge carriers generated from a previous avalanche. However, the drawbacks associated with increasing the dead time and operating temperature, which will limit the photon detection rate and increase the number of thermally generated dark carriers, must be overcome so as not to compromise the overall detector performance. Apart from a low dark count rate, the performance of SPADs can also be improved by reducing the temporal variation between photon absorption and detection of an avalanche current, which is known as the timing jitter and is measured as the standard deviation of the time required for each avalanche current to reach a detectable threshold level, or as the full width at half maximum (FWHM) of the timing response (counts versus time) of the detector.

In the multiplication region of an APD or SPAD, high electric field is applied to promote the excitation of electrons from the valence band to the conduction band by the scattering of energetic carriers. This process is known as impact ionisation and at sufficiently high electric field, results in a self-sustaining avalanche multiplication process by which each of the resulting free carriers continues to generate new electronhole pairs. The probability that a charge carrier impact ionises was assumed to be solely a function of the local electric field within the multiplication region by early studies of the avalanche multiplication process and noise characteristics in APDs [2-4]. Later studies [5,6] incorporated the dead space, which is the minimum distance that newly generated carriers must travel before gaining sufficient energy to impact ionise [7]. Both theoretical and experimental studies [5, 6, 8] have shown that dead space reduces the excess noise in thin APDs where the avalanche region is short.

In one of the first theoretical studies on the avalanche multiplication process in SPADs [9], diffusion-assisted avalanche spreading was shown to be responsible for the avalanche current rise time, and the effect of dead space was neglected. As a result of the lateral spreading of avalanche carriers, the avalanche current was predicted to rise faster if the avalanche is trigged closer to the centre of the device area [10, 11]. Other impact ionisation models which included the effect of dead space [12, 13] have predicted that higher breakdown probability at a given overbias (*i.e.* relative excess bias voltage) could be achieved by increasing the multiplication region thickness. This prediction implies that the increased dead space in SPADs with thin multiplication regions has either a negligible or detrimental effect on the breakdown probabilities, contrary to the prediction by Ng *et al.* [14] that breakdown probability increases more rapidly with overbias as dead space increases for all values of the enabled ionisation coefficient ratio, $k_*=\beta_*/\alpha_*$. In a recent experimental study by [15], SPADs with thin multiplication regions showed the most uniform detection delay and the smallest timing jitter across the detector active area, implying that the contribution of diffusion-assisted avalanche spreading is negligible.

Using a simple numerical model based on random ionisation path length (RPL) after a hard-threshold dead space, we have investigated the breakdown probability and jitter in SPADs and concluded that increasing the multiplication region thickness may not necessarily increase the breakdown probability at a given overbias, due to the dominant effect of dead space in thin multiplication regions at realistic ionisation threshold energies for GaAs [16]. We also showed that reducing the multiplication thickness leads to smaller jitter and breakdown time despite the increased dead space, due to compensation by the large feedback ionisation ($k_*$) at the high fields required for 3 multiplication in thin multiplication regions [16]. Here, we extend the previous work by developing a bi-dimensional (2D) RPL model and using it to investigate the effects of lateral diffusion on the breakdown probability and timing performance of SPADs.

## 2. Random Path Length Models

In this work, the avalanche multiplication process of a Geiger-mode APD or SPAD is simulated in the *i*-region of a GaAs $p^+$-*i*-$n^+$ diode structure, which is a (*x*, *y*) plane where *x* is parallel to the electric field and *y* is in a direction lateral to the field. Fig.1 shows the 2D carrier distribution profile obtained from a full-band Monte Carlo (FBMC) model [17], which is typically Gaussian distributed.

The spread of the distribution of carriers in the *y* direction is shown in Fig.2 to increase linearly with time, which means that the final *y* position of a carrier at time *t* after a lateral spreading process can be simplified as a summation of the initial position $y_0$ and *N* individual lateral diffusion path lengths represented by normally distributed random numbers. The 2D RPL model incorporates a PDF that describes the random lateral diffusion path lengths of the carriers, which are
normally distributed with mean and standard deviation as fitting parameters to the FBMC carrier distribution results, using the Box-Muller method [18] for generating random numbers with a Gaussian (normal) distribution.

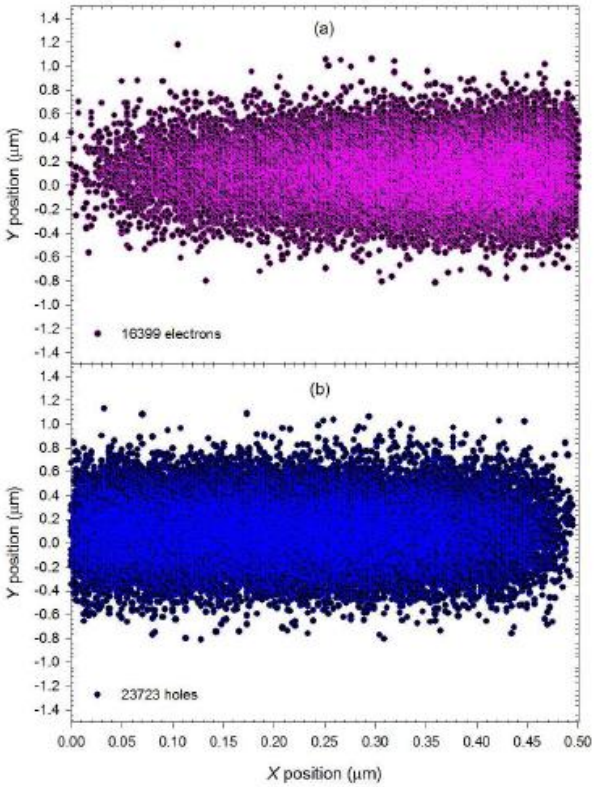


**Fig.1.** Bi-dimensional carrier distribution of (a) electrons and (b) holes at time 44.1 ps obtained from FBMC simulation of avalanche current generated by an injected electron at (x = 0, y = 0) in a 0.50 μm *i*region at 506.4 kV/cm.

By fitting the distribution of *y* positions of electrons and holes generated by the RPL model to the FBMC carrier distribution data for different *i*-region thicknesses, bias voltages and simulation time, the best-fit parameters for the PDF of random lateral diffusion path lengths correspond to a mean of $\mu = 0\mu m$ and a standard deviation of $\sigma = 0.0350$ μm. These parameters are used by the Gaussian random deviate generator of
the 2D RPL model to simulate the lateral trajectories of the carriers. We tested the accuracy of the fitting parameters by comparing the PDFs of the *y* positions of electrons and holes simulated by the 2D RPL model for different *i*-region thicknesses and total number of carriers against the FBMC results. The 2D RPL results fitted reasonably well to the FBMC results for both electrons and holes and different *i*-region thicknesses. Fig.3 shows an example of the fitting results.

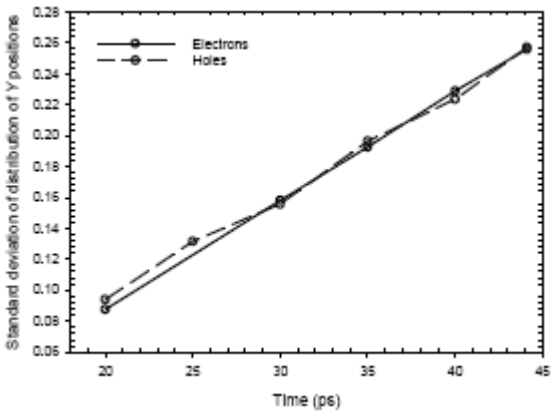


**Fig.2.** Time evolution of the spread of the distribution of carriers in the *y* direction generated by FBMC simulation of electron-initiated avalanche current in a 0.50 μm *i*-region at 506.4 kV/cm.

## 3. Simulation Results

Fig.4 shows the mean multiplication values simulated using the simple 1D RPL model at a range of electric fields and different carrier injection positions for a 0.25 μm *i*-region. As expected, the mean multiplication in each case increases exponentially with electric field, approaching infinity at high fields. Before the onset of avalanche breakdown, pure electron and pure hole initiated multiplication have higher mean multiplication values compared with multiplication initiated by an electron-hole pair due to mixed injection.

In a given range of overbias ratio in Fig. 5, the breakdown probability transition is sharper for pure electron and pure hole injection compared with mixed injection, and decreases as mixed carrier injection occurs further away from $x = 0$. Pure electron or hole injection, which occurs at the edge of the *i*-region, ensures that the offspring carriers have a higher chance of triggering avalanche breakdown because they have a longer distance to travel before exiting the avalanche region.

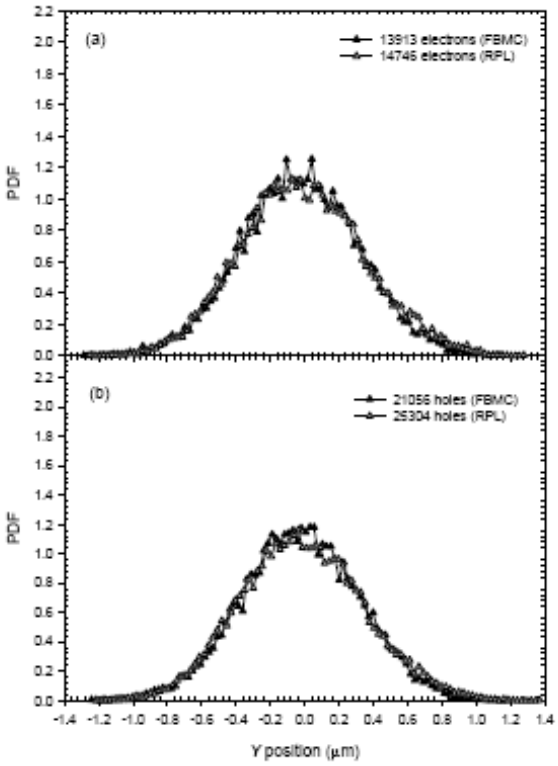


**Fig.3.** PDF of the positions of (a) electrons and (b) holes in the *y* direction generated by FBMC and RPLsimulation of electron-initiated avalanche current in a 1.0 μm *i*-region at 410.28 kV/cm.

The corresponding mean breakdown time and jitter for the 0.25 μm *i*-region were also calculated as a function of the overbias ratio for different carrier injection positions, as shown in Fig.6. The effect of carrier injection position on the mean breakdown time and jitter is negligible at low overbias values and becomes slightly

more visible as the overbias increases, with pure electron injection at $x = 0$ consistently showing the lowest mean breakdown time and jitter. The mean breakdown time and its jitter are plotted in Fig.7 as a function of the breakdown probability with different carrier injection positions. For a given breakdown probability, the mean breakdown time and jitter are smaller for mixed injection

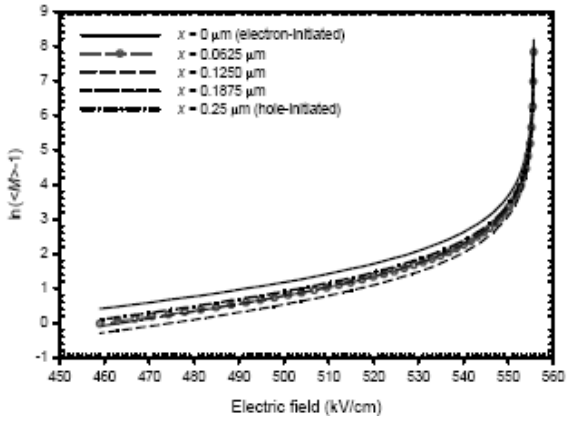


**Fig.4**: $\ln(< M > -1)$ as a function of electric field for 0.25 μm *i*-region at different initial carrier injection positions.

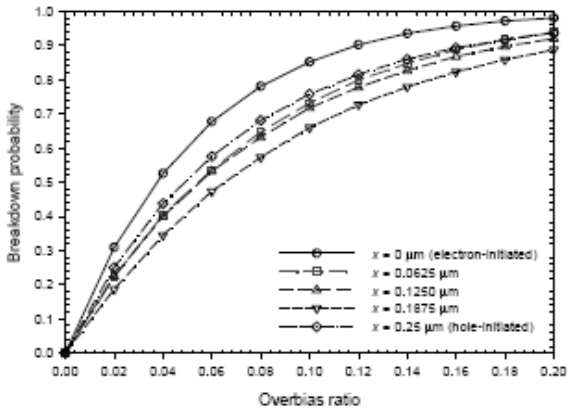


**Fig.5**: Breakdown probability as a function of overbias ratio for 0.25 μm *i*-region at different initial carrier injection positions.

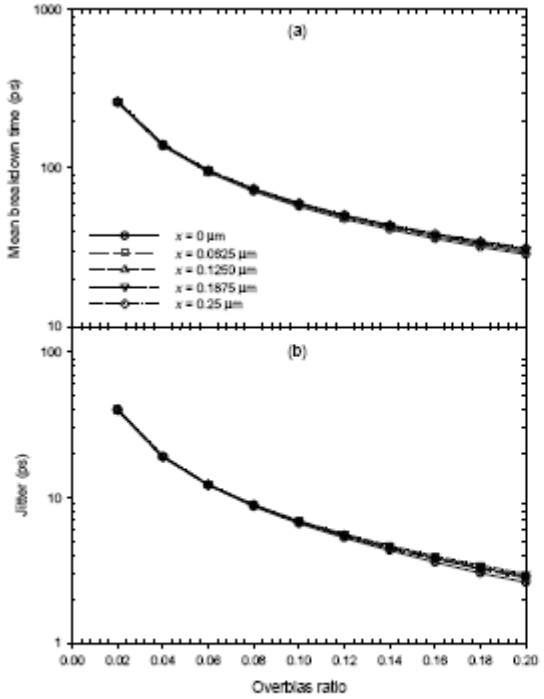


Fig.6: (a) Mean breakdown time and (b) jitter versus overbias ratio for 0.25 μm *i*-region at different initial carrier injection positions.

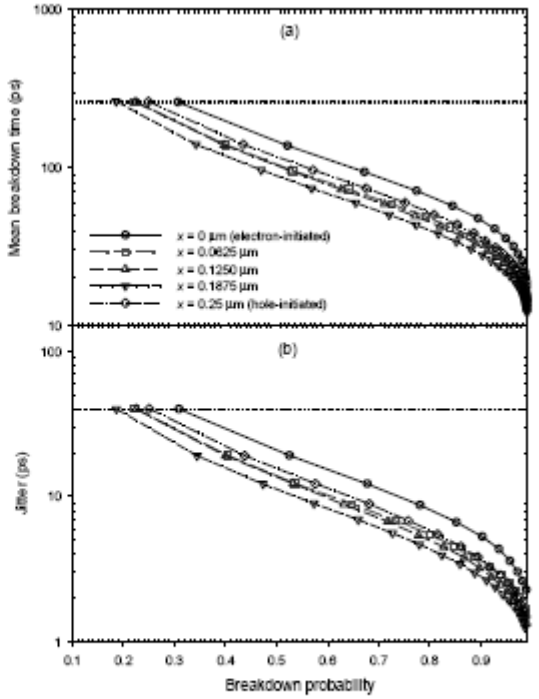


Fig.7: (a) Mean breakdown time and (b) jitter versus breakdown probability for 0.25 μm *i*-region at different initial carrier injection positions.

that occurs away from $x = 0$, and are larger for pure electron and pure hole injection. Each incremental data point on the curves in the figure represents a $\Delta V$ increase in the bias voltage, and all the curves have similar bias increments, though corresponding to different breakdown probabilities. For example, the dotted line drawn across the first set of symbols of the curves in Fig.7 represents a $\Delta V$ overbias from the breakdown voltage; similarly, the next set of symbols across the curves represents the next $\Delta V$ increase in overbias. Although different carrier injection positions result in different breakdown probabilities at a given overbias, the mean breakdown time is almost the same for the different cases of carrier injection for breakdown probabilities lower than 0.8; similar observation is true for jitter. For breakdown probabilities above 0.8, the effect of carrier injection position on both mean breakdown time and jitter at a given overbias is noticeable, though fairly weak. Apparently, the simulation results show that avalanche breakdown initiated by carrier injection at $x = 0.1875\mu$m or $0.75w$ (where $w$ is the i-region thickness), produces the smallest mean breakdown time and jitter as a function of breakdown probabilityFig.8 presents the breakdown probability results as a function of the overbias ratio for different 2D carrier injection positions, simulated using the 2D RPL model. Pure electron and pure hole injections produce faster breakdown probability transition against overbias ratio than mixed injection. The breakdown probability transition is insensitive to the carrier injection positions that are closer to the lateral centre ( $y = 0$ ) of the *i*region. Carrier injection near the lateral edge of the *i*-region significantly reduces the breakdown probability transition against

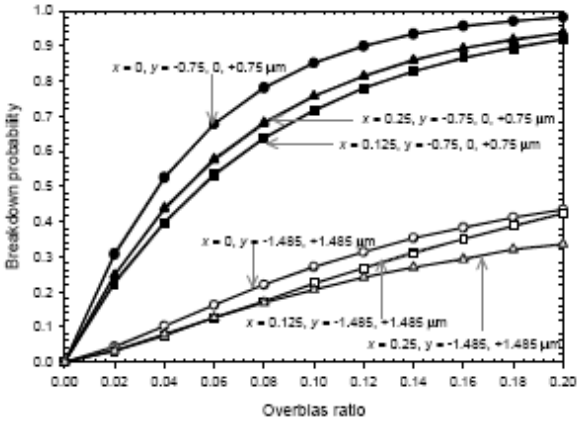


**Fig.8**: Breakdown probability as a function of overbias ratio for 3μ*m*×0.25μ*m i*-region at different 2D initial carrier injection positions.

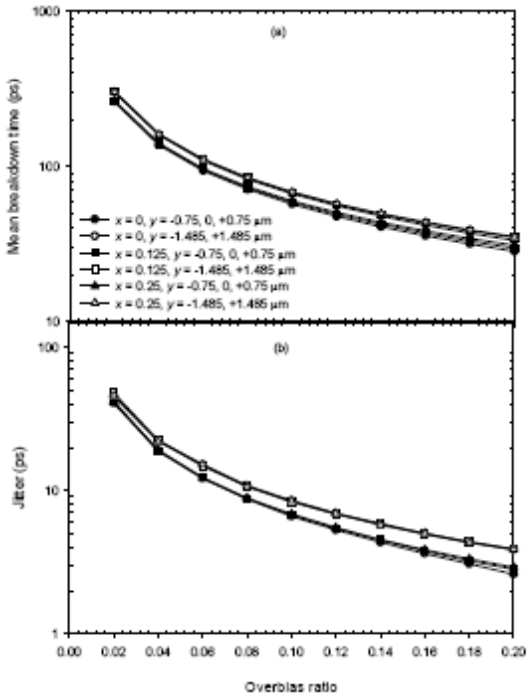


Fig.9: (a) Mean breakdown time and (b) jitter versus overbias ratio for $3\mu m \times 0.25\mu m$ *i*-region at different 2D initial carrier injection positions.

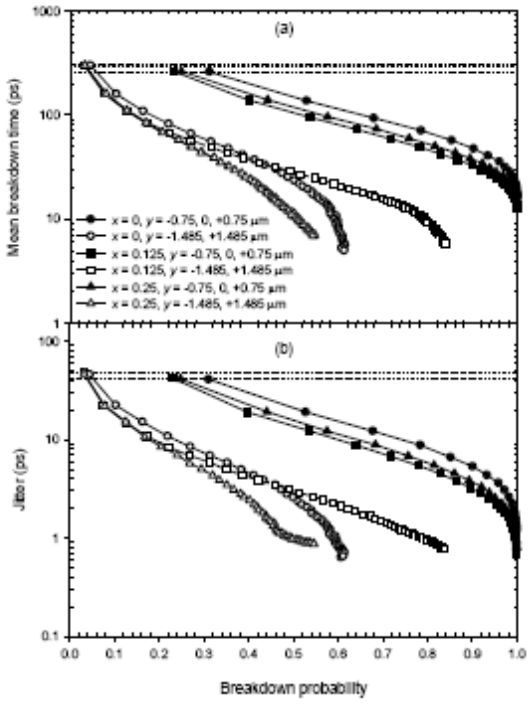


Fig.10: (a) Mean breakdown time and (b) jitter versus breakdown probability for $3\mu m \times 0.25\mu m$ *i*-region at different 2D initial carrier injection positions.

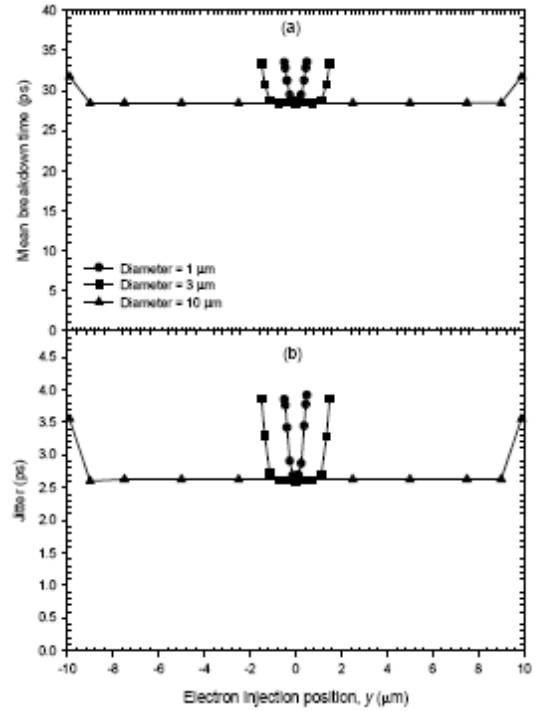


Fig.11: (a) Mean breakdown time and (b) jitter of 0.25μm devices biased at 666.84kV/cm with dfferent diameters as a function of electron injection positions in the *y* direction ($x = 0$).

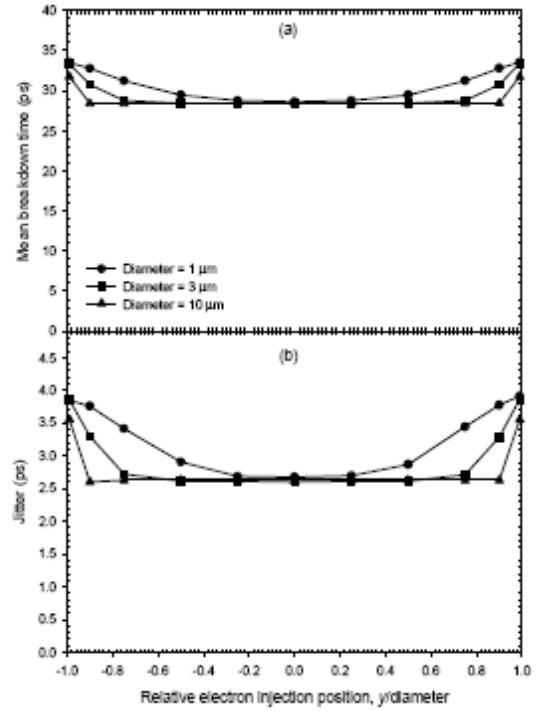


Fig.12: (a) Mean breakdown time and (b) jitter of 0.25μm devices biased at 666.84kV/cm with different diameters as a function of relative electron injection positions in the *y* direction.

overbias ratio. This is true because carriers injected near the lateral edge and their offspring carriers are more likely to diffuse out of the *i*-region, thus causing slower avalanche build-up.

In Fig.9, the mean breakdown time and jitter are plotted as a function of the overbias ratio for 3μ*m*×0.25μ*m* *i*-region at different 2D carrier injection positions. At the same overbias, the mean

breakdown time and jitter are larger when carriers are injected near the lateral edge. In addition to the effect of carrier injection position, carrier injection near the lateral edge causes diffusion out of the *i*-region, and hence slower avalanche build-up. The mean breakdown time and jitter are plotted in Fig.10 as a function of the breakdown probability. For a given breakdown probability and carrier injection that occurs closer to the lateral centre ( $y = 0$ ) of the *i*-region, pure electron and pure hole injections produce larger mean breakdown time and jitter than mixed injection. The results deviate strongly when carriers are injected near the lateral edge of the *i*-region. In this case, the mean breakdown time and jitter reduce significantly with breakdown probability.

Figures 11 and 12 compare the uniformity of the jitter and mean breakdown time across different diameters of a device with 0.25 μm *i*-region. The device with the largest diameter gives the most uniform jitter and breakdown time with respect to the lateral injection positions. This suggests that reducing the active area of the device may degrade the timing resolution as the avalanche build-up is limited by the lateral diffusion of carriers out of the avalanche region.

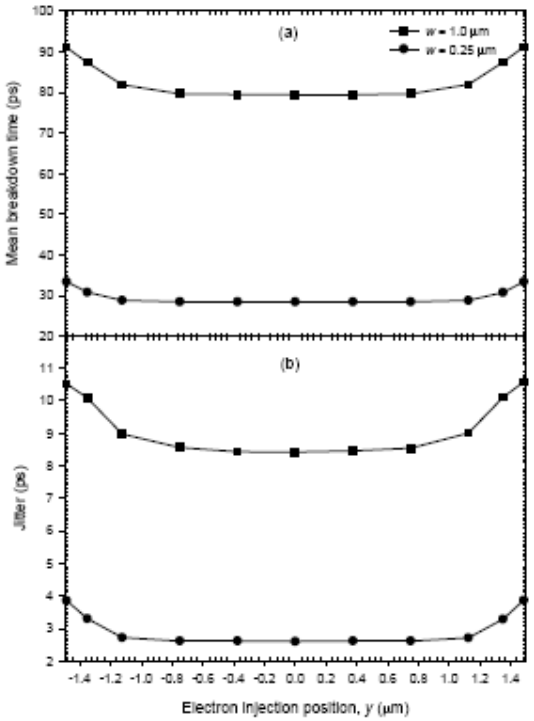


**Fig.13**: (a) Mean breakdown time and (b) jitter of 3μ*m*×0.25μ*m* and 3μ*m*×1.0μ*m* *i*-regions biased at 666.84 kV/cm and 410.28 kV/cm respectively (20% above breakdown) as a function of electron injection positions in the *y* direction ($x = 0$).

Fig.13 shows that the thin *i*-region produces the most uniform mean breakdown time (also known as detection delay) and the smallest jitter across the diameter ( $y = -1.5$ μm to $y = +1.5$ μm) of device's active area. This means that the 2D RPL simulation results are consistent with the recent experimental findings by Prochazka *et al.*[16]. The uniformity of the breakdown time and jitter across the device's active area is determined by the effects of dead space and $k^*$ at a given bias electric field.

## 4. Conclusions

The effects of carrier injection position and lateral diffusion on the avalanche build-up characteristics of SPADs have been analysed using the 1D and 2D RPL models. In the 1D case, pure electron or hole injection into the edge ( $x = 0$) of the avalanche region triggers faster breakdown probability transition as a function of overbias, because it allows more ionisation events to occur before the primary and offspring carriers escape the avalanche region. In the 2D case, carrier injection toward the lateral edge of the active region significantly slows down the breakdown probability transition as a function of overbias as a result of lateral diffusion. Lateral diffusion increases the breakdown time and jitter when carriers are injected near the lateral edge of the active region. At different carrier injection positions across the diameter of a device's active area, the jitter and mean breakdown time are smaller and more uniform as the *i*-region thickness is reduced. The 2D RPL model also predicted that lateral diffusion increases the non-uniformity in the jitter and mean breakdown time at different carrier injection positions, as the size (*i.e.* diameter) of a device's active area decreases.

**References**


1. Zappa, F., Tisa, S., Tosi, A., Cova, S. (2007). Principles and features of single-photon avalanche diode arrays. Sensors and Actuators A: Physical, Vol. 140(No. 1), 103-112.
2. McIntyre, R. J. (1966). Multiplication noise in uniform avalanche diodes. IEEE Trans. Electron Devices, Vol. 13(No. 1), 164-168.
3. Kaneda, T., Takanashi, H., Matsumoto, H., and Yamaoka, T. (1976). Avalanche buildup time of silicon reach-through photodiodes. J. Appl. Phys., Vol. 47(No. 11), 4960-4963.
4. Teich, M. C., Matsuo, K., Saleh, B. E. A. (1986). Time and frequency response of the conventional avalanche photodiode. IEEE Trans. Electron Devices, Vol. 33(No. 10), 1511-1517.
5. Marsland, J. S. (1990). On the effect of ionization dead spaces on avalanche multiplication and noise for uniform electric fields. J. Appl. Phys., Vol. 67(No. 4), 1929-1933.
6. Hayat, M. M., Saleh, B. E. A., and Teich, M. C. (1992). Effect of dead space on gain and noise of double-carrier-multiplication avalanche photodiodes. IEEE Trans. Electron Devices, Vol. 39(No. 3), 546-552.
7. Okuto, Y. and Crowell, C. R. (1974). Ionization coefficients in semiconductors: A nonlocalized property. Phys. Rev. B, Vol. 10(No. 10), 4284-4296.
8. Li, K. F., Ong, D. S., David, J. P. R., Rees, G. J., Tozer, R. C., Robson, P. N., Grey, R. (1998). Avalanche multiplication noise characteristics in thin GaAs p+-i-n+ diodes. IEEE Trans. Electron Devices, Vol. 45(No. 10), 2102-2107.
9. Spinelli, A. and Lacaita, A. L. (1997). Physics and numerical simulation of single photon avalanche diodes. IEEE Trans. Electron Devices, Vol. 44(No. 11), 1931-1943.
10. Lacaita, A. and Mastrapasqua, M. (1990). Strong dependence of time resolution on detector diameter in single photon avalanche diodes. Electronics Letters, Vol. 26(No. 24), 2053-2054.
11. Lacaita, A., Ghioni, M., Zappa, F., Ripamonti, G., and Cova, S. (1993). Recent advances in the detection of optical photons with silicon photodiodes. Nucl. Instrum. Methods A, Vol. 326, 290-294.
12. Wang, S., Ma, F., Li, X., Karve, G., Zheng, X., and Campbell, J. C. (2003). Analysis of breakdown probabilities in avalanche photodiodes using a history-dependent analytical model. Appl. Phys. Lett., Vol. 82(No. 12), 1971-1973.
13. Ramirez, D. A., Hayat, M. M., Karve, G., Campbell, J. C., Torres, S. N., Saleh, B. E. A., and Teich, M. C. (2006). Detection efficiencies and generalized breakdown probabilities for nanosecond-gated near infrared single-photon avalanche photodiodes. IEEE J. Quantum Electron., Vol. 42(No. 2), 137-145.
14. Ng, J. S., Tan, C. H., David, J. P. R., and Rees, G. J. (2003). Theoretical study of breakdown probabilities in single photon avalanche diodes. Proc. 16th Annual Meeting IEEE Lasers and Lectro-Optics Society 2, 773-774.
15. Prochazka, I., Kral, L., Hamal, K., and Sopko, B. (2007). Photon counting timing uniformity – unique feature of the silicon avalanche photodiodes K14. J. Mod. Optics, Vol.54(No. 2), 141-149.
16. S.L. Tan, D.S. Ong, and H. K. Yow, (2007). Theoretical Analysis of Breakdown Probabilities and Jitter in Single Photon Avalanche Diodes, Journal of Applied Physics, vol.102, 044506,
17. Ong, D. S., Li, K. F., Plimmer, S. A., Rees, G. J., David, J. P. R., and Robson, P. N. (2000). Full band Monte Carlo modeling of impact ionization, avalanche multiplication, and noise in submicron GaAs p+-i-n+ diodes. J. Appl. Phys., Vol. 87(No. 11), 7885-7891.
18. Box, G. E. P. and Muller, M. E. (1958). A note on the generation of random normal deviates. Ann. Math. Statistics, Vol. 29(No. 2), 610-611.

# A SIMULATION-BASED DESIGN OF A CCD IMAGE SENSOR FOR A 100-Mfps VIDEO CAMERA

**C. Vo Le [a], H.D. Nguyen [a], V.T.S. Dao [a], K. Takehara [a], T.G. Etoh [a], T. Akino [b], K. Nishi [c], K. Kitamura [d], T. Arai [d], H. Maruyama [d]**

[a)] Graduate School of Science and Engineering, Kinki University, 3-4-1 Kowakae, Higashi-Osaka, Osaka, 577-8502 Japan
[b)] School of Biology-oriented Science and Engineering, Kinki University 930 Nishi-Mitani, Kinokawa City, Wakayama, 649-6494 Japan
[c)] Kinki University Technical College 2800 Arima-cho, Kumano, Mie, 519-4395 Japan
[d)] Science and Technology Research Laboratories, NHK

**Abstract:** This paper presents a part of a feasibility study on development of a video camera of 100 Mega frames per second (Mfps). The image sensor utilizes a special CCD structure, ISIS, and backside illumination technology. One of the major limiting factors to the ultra-high frame rate, traveling time of signal electrons in a pixel, is analyzed by simulations. We developed a special wafer with double epitaxial layers of n and p types with very thin and smoothly changing concentration, and applied a curved design method to the design of the collection gate. The combinatorial use of these two technologies dramatically decreases the traveling time to less than 10 ns, i.e., 100 Mfps is possible in terms of the electron traveling time.

***Keywords:*** *CCD, ISIS, High Speed*

## 1. Introduction

In 2001, the authors developed an ultra-high-speed video camera which can capture images up to 1 Mfps[1)]. To achieve the extremely high speed, a special CCD imager structure invented by Etoh and Mutoh was introduced. The structure has been known as ISIS, the In-situ Storage Image Sensor. Since 2004, we have been developing a new image sensor for image capturing at the frame rate as high as 10 Mfps with sub-ten-photon sensitivity by combining the ISIS structure, CCM, Charge Carrier Multiplication, and the backside illumination technology. The ISIS structure is fabricated on the front surface of the device for the ultra-high frame rate. The CCM is mounted between the readout HCCD and the readout amplifier, which amplifies very low signals, even less than readout noise level, to a level detectable by the readout amplifier. Backside illumination increases the fill factor to 100% and the quantum efficiency to more than 80%.

Furthermore, backside illumination significantly increases the maximum frame rate, since wide and multi-layer metal wiring can be introduced to the CCD design on the front side without care for decrease of the fill factor at the backside. The driving circuitry even can be directly attached to the front side.

Through simulation studies, it is expected that the theoretical maximum frame rate of the Backside-illuminated ISIS (BI-ISIS) can be reached higher than 100 Mfps. In this paper, we focus on proving the theoretical maximum frame rate higher than 100 Mfps with simulation results.

Potential limiting factors to achieve the extremely high frame rate are listed as follows:
(1) Transfer speed of signal electrons generated in the collection gate to the first CCD memory element
(2) Transfer speed of signal electrons in the memory CCD
(3) Drain rate of holes in the hole accumulation layer at the backside
(4) Speed of hole movement in the CCD circuitry on the front side
(5) Amplitude attenuation of the driving voltage waveforms mainly due to RC delays
(6) Heat generation associated with the driving voltage attenuation
(7) Cross-talk and noise-generation due to electro-magnetic waves generated by very high frequency and large voltage swing of the CCD driving circuitry

(8) Electro-magnetic force to reduce the driving voltage amplitudes
(9) Stability of the clock generator

In this paper, technologies to manage with the factors (1) will be discussed with simulation results.

## 2. Structure and dimensions of the BI-ISIS

### *2.1 Surface plane structure*

Figure 1(a) depicts the surface structure of the BI-ISIS in the X-Y plane. A 43.2 x 43.2 micron$^2$ pixel of the BI-ISIS consists of the collection gate and the in-situ linear CCD memory. The VCCDs are introduced to read out the signal electron packages after image capturing, which are connected by the connection elements to the in-situ storage CCDs. Around the photo-receptive area, a HCCD for readout and the CCM for amplification with noise reduction are also added.

The collection gates capture electrons generated in the backside area creating a signal electron packet, which is a content transferred to and stored in in-situ CCD storage channels as seen in Fig. 1(b).

The in-situ CCD storage has 120 storage elements, stretching downward from the collection gate. At each step, new contents of a new picture are shifted from the collection gates to the first element of the in-situ CCD channels, and all the contents of in-situ CCD elements are shifted one step down to the next elements. Since the number of storage elements is limited to 120, when an in-situ CCD channel is full, the content in the last element of the storage channel is drained through a drain, which is not drawn.

A readout VCCD stretches beside each column of the collection gates and is connected to the in-situ CCDs through the connection elements. When the sensor stops capturing images, contents stored in the in-situ CCD elements are moved to the readout VCCDs through the connection elements, and to the HCCD. The HCCD transfers the contents to the CCM and finally to the amplifier.

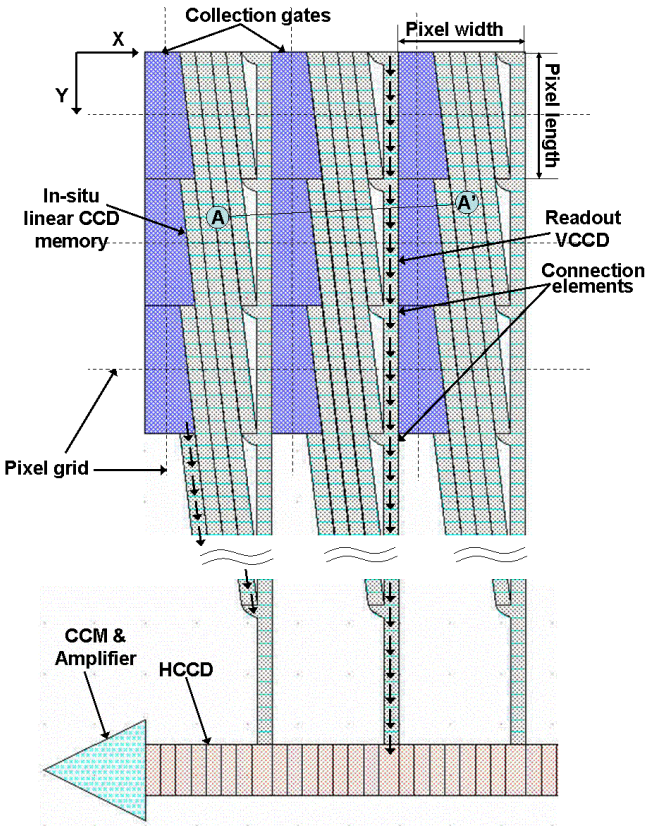


**Figure 1(a).** Surface plane structure of the BI-ISIS

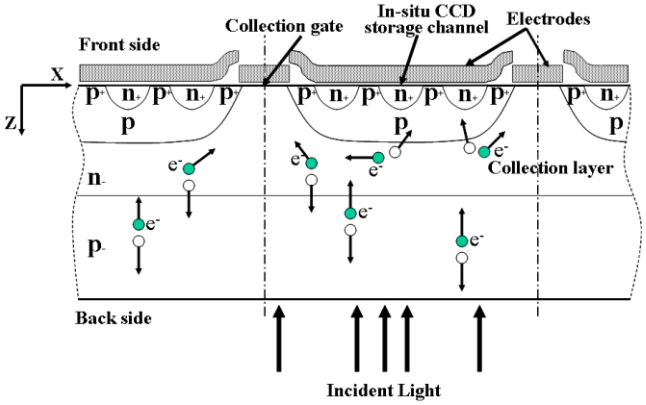


**Figure 1 (b).** Cross section of the BI-ISIS

### *2.2 Cross-section structure*

Figure 1(b) shows the cross section (A-A') in Fig. 1(a). The structure of the BI-ISIS is far more complex than that of the conventional backside illuminated CCD image sensors, because of the in-situ memory for each pixel.

To avoid direct intrusion of incident light, especially with a long wave length, to the in-situ storage, the sensor is to be thick enough. On the other hand, to attain fast transfer of electrons generated near the backside to the collection gate, the sensor should be fully depleted and, thus, thin. For these reasons, the thickness of the chip was decided to be 24 microns.

As depicted in Fig. 1(b), when incident light comes to the backside, electron-hole pairs are generated. The electrons are transported to the collection gates through the collection layer and then to the in-situ storage CCD; the holes to the backside or to the p-well to be drained from the sensor respectively.

To create the complex cross-section structure, a special wafer with double n-and-p-epi layers with smoothly-changing doping concentration was developed.

## 3. Maximum Frame Rate vs. Electron Traveling Time within a Pixel

### *3.1 Traveling time within a pixel*

The pixel size of the BI-ISIS is much larger than that of usual CCD sensors due to the In-situ linear CCD memory inside every BI-ISIS pixel. For example, the pixel size of the ISIS-V12 is 43.2 x 43.2 $\mu$ m$^2$, while that of standard CCD sensors is about 1.8-20 $\mu$ m. In addition, the thickness of the BI-ISIS was decided to 24 $\mu$ m as stated above.

Because of the thickness and the wider pixel size of the BI-ISIS, photo-electrons move through a very long distance from the edge of a pixel near the backside to a collection gate which is inserted in the center of the front side of the pixel. The traveling time of the electrons through the path have to be fast enough attain 100 Mfps.

On the other hand, as the collection gate is designed in long size, traveling time of signal electrons through the area to the first CCD memory element is a decisive factor to achieve 100 Mfps.

The total traveling time of the electrons through the path and the collection gate must be less than or equal to 1 ns to attain 100 Mfps.

### *3.2 Traveling time from backside to the collection gate inserted in the front side*

Figure 2 shows an example simulation result of the electric field in the X-Z section of the BI-ISIS. After being generated, signal electrons affected by the built-in electric field by smoothly-changing impurity concentration drift to the collection gate immediately. The traveling time for an electron from the furthest point of the pixel (X= 43.2 $\mu$ m, Y= 43.2 $\mu$ m, Z=24.0 $\mu$ m) to the collection gate is evaluated through simulations by SPECTRA developed by Mutoh.

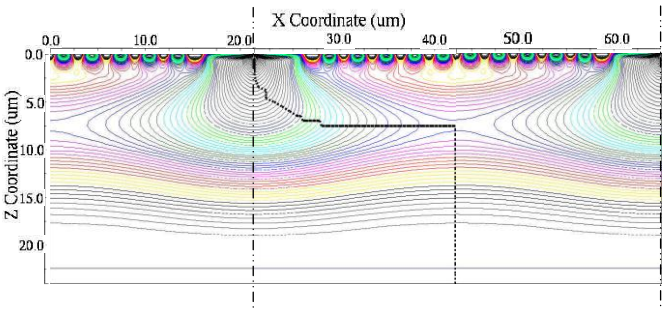


**Fig. 2**.Simulated electric field of X-Z section of the BI-ISIS

The doping profile has been optimized to minimize the traveling time through repeating simulations. The final result is shown in Fig. 2, which has achieved only 5.61 ns.

### *3.3 Traveling time in the collection gate*

The model of the collection gate for the simulation study is as follows:
(1) The size is 33x10 $\mu$ m$^2$,
(2) Potential gradient is created by two or three-step implant of N-type impurity and
(3) The potential difference along the path of an electron is 1V and 10.5V.

The model is made to evaluate the effectiveness of the curved design in comparison with the Kosonocky's one.

To decrease the traveling time, Kosonocky et al[2)] employed a three-step implant of the n-type impurity with each potiential step of 0.5 V, i.e., the total potential difference is 1.0 V. The maximum length of each of the three steps is about 11 $\mu$ m, making the total path 33 $\mu$ m.

Kosonocky et al. found that the traveling time is less than 1 $\mu$ s which guarantees the frame rate more than 1 Mfps. As shown in Fig. 3(a) and Table 1, it was confirmed by a simulation that the time is 0.98 $\mu$ s (< 1 $\mu$ s).

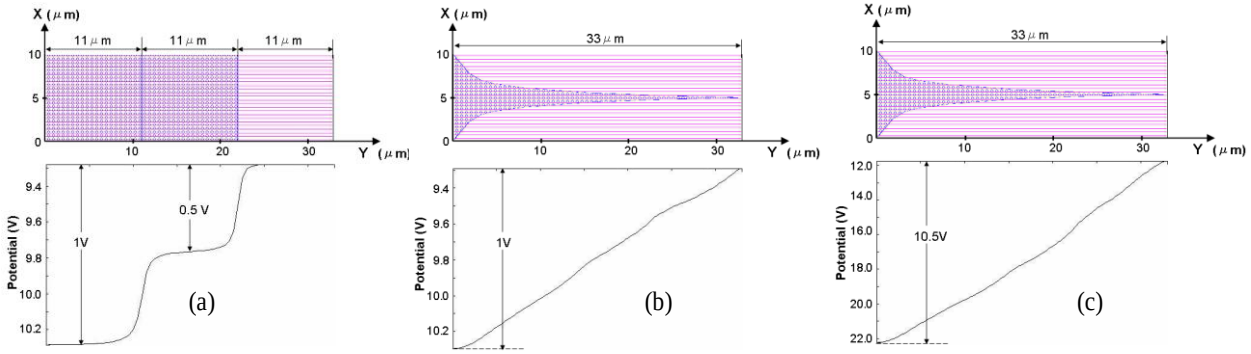


**Fig. 3.** Comparison of potential profiles
(a) Three-step doping and the three step potential (1 volt potential difference)
(b) Two-step curved doping shape and the linear potential (1 volt potential difference)
(c) Two-step curved doping shape and the linear potential (10.5 volts potential difference)

In our design, two-step implant is used for the CCD channel design. To reduce the total steps of the implantation, we apply the two-step implantation to the collection gate with the same concentration as applied to the channel.

**Table 1.** Comparison of electrons travelling time and potential profiles

| Type of doping concentration | Voltage difference (V) | Transport time of electrons (ns) | Potential profile |
|---|---|---|---|
| Three step regtangular | 1 | 980 | Three levels |
| Curved two steps | 1 | 9.13 | Linearity |
| | 10.5 | 0.89 | Linearity |

Theoretically, the traveling time of electrons in the collection gate will be minimized if the minimum electric gradient is maximized, which results in a linear potential profile. Curved design with the two constant doping layers has applied proving its efficiency.

Using the same model described above, as in Fig. 3(b) and Table 1, the traveling time of the curved design reduces considerably to 9.13 ns which is about 100 times smaller than that of the three-steep implant method but still large to achieve 100 Mfps.

In our design, the concentration of the second n implant is much higher than that of Kosonocky et al. Therefore, the potential difference becomes 10.5 V. Simulation results indicate that the potential along Y direction of the collection gate increases almost linearly and the traveling time declines considerably to 0.89 ns, as shown in Fig 3(c) and Table 1.

### *3.4 Maximum frame rate for electron transfer in a pixel*

The theoretical maximum frame rate limited by the electron traveling time in a pixel is evaluated by the inverse of the sum of the traveling time in the collection layer and in the collection gate, i.e., 6.5 ns (= 5.61+0.89), and thus, more than 100 Mfps.

## 5. Other factors

In this section, we will briefly discuss other limiting factors listed at the first part of this paper.

Transfer time of signal electrons in the memory CCD (2) is much shorter than that from the collection gate to the first memory element. Therefore, this is not the primary limiting factor.

Drain rate of holes in the hole accumulation layer at the backside (3) can be increased by covering the backside with ITO or by placing a metal mesh for hole drainage on the backside with some sacrifice of quantum efficiency. While application of these technologies increases dark current, it decreases inversely proportionate to the frame rate for the ISIS. For ultra-high-speed imaging with cooled sensors, it is expected that the dark current per pixel decreases to negligible level.

Speed of hole movement in the CCD circuitry on the front side (4) is relating to evaluation of capacitance, and, thus, to RC delay. It is expected that slower movement of holes in the CCD area decreases the capacitance. However, further analysis is necessary.

Amplitude attenuation of the driving voltage waveforms (5) has been fully analyzed with a simple and accurate evaluation method developed by the authors[3)]. The result is promising.

Heat generation (6) has not been analyzed. HCCD of standard CCD image sensors, however, continuously operates at more than 25 MHz, and, yet, shows no harmful effect. In addition, as ultra-high-frame imaging usually takes very short time, no serious effect of heat generation is expected even in image capturing at four-time faster frame rate, 100 Mfps.

Electro-magnetic effect may be another serious problem, (7) and (8). The authors has proposed an operation scheme of ISIS to suppress electro-magnetic noise, i.e., "digitalnoiseless ultra-high-speed imaging"[4)]. CCD channels can be driven with voltages with precise sinusoidal waveforms with the same frequency. During image capturing operation, the ISIS with linear CCD storage continues only transfer of image signals with automatic drainage without readout[1)]. When image capturing operation stops after occurrence of the target event, the image signals stored in the CCD storage are slowly readout. Readout is operated by means of various pulsed signals generated in digital circuitry. Therefore, the ISIS can be operated only by sinusoidal driving voltages during image capturing, releasing only electro-magnetic waves with single wave length and no random components from pulses, of which EMI is much easy to control.

Frequency of digital circuits keeps rising to provide faster CPUs, which requires clock generators stable for much higher frequency. Thus, we can expect supply of a reasonable clock generator for an image sensor of 100 Mfps, which solves the problem (9).

Consequently, it is most possible that the primary factor to limit the highest frame rate is the first factor (1), the transfer speed of signal electrons in a pixel, which is discussed in this paper.

## 6. Concluding Remarks

This paper presents a part of a feasibility study on development of a video camera of 100 Mfps. One of the major limiting factors to the ultra-high frame rate, traveling time of signal electrons generated in a pixel, is analyzed by simulations.

The conclusions are as follows:

(1) Traveling time of an electron generated near the backside to the collection gate on the front side is effectively decreased by employment of a special wafer with double epitaxial layers of n and p types with very thin and smoothly changing concentration.

(2) Traveling time of an electron from the collection gate to the first element of the CCD storage is minimized by applying a curved design method to the design of the collection gate.
(3) The combinatorial use of these two new technologies dramatically decreases the sum of the traveling time to less than 10 ns, and, therefore, 100 Mfps is possible in terms of the electron traveling time.
(4) Effects of other factors possibly limiting the maximum frame rate are also briefly examined. As far as the preliminary examination, the traveling time of electrons in a pixel is the primary factor to decide the theoretical maximum frame rate.

Further research is necessary for more precise evaluation.

**References**

1. T. G. Etoh et al., A CCD image sensor of 1 Mframes/s for continuous image capturing of 103 frames, Digest of Technical Papers, ISSCC'02, pp.46-47, 2002.
2. W. K. Kosonocky et al., 360x360-element very-high frame-rate burst-image sensor, Digest of Technical Papers, ISSCC'96, pp. 182-183, 1996.
3. V. T. S. Dao et al., Estimation of driving voltage attenuation of an ultra-high-speed image sensor by dimensional analysis, Proc. Int. Workshop on Photonics and Applications, to be issued, 2008.
4. T. G. Etoh, A digitalnoiseless ultra-high-speed video camera, patent pending in the Japanese patent office, 2008.

# BIREFRINGENCE AND PHONON-MODE ABSORPTION OF A ß-BaB2O4 (BBO) CRYSTAL IN THE TERAHERTZ REGION

**Elmer Estacio[a], Shigeki Saito[a], Tomoharu Nakazato[a], Minh Hong Pham[b], Marilou Cadatal[b], Hiroshi Mizuseki[c], Yoshiyuki Kawazoe[c] and Nobuhiko Sarukura[a]**

[a)] Institute of Laser Engineering, Osaka University, Yamadaoka, Suita, Osaka 565-0871, Japan
[b)] The Graduate University for Advanced Studies Shonan Village, Hayama 240-0193, Japan
[c)] Institute for Materials Research, Tohoku University, Sendai 980-8577, Japan
*E-mail: estacio-es@ile.osaka-u.ac.jp*

As a nonlinear optical material, beta barium borate ($\beta$-$BaB_2O_4$ or BBO) has played an important role in harmonic generation. It has proven very effective in terms of frequency doubling and for the design of highly tunable optical parametric oscillators[1]. Research in BBO, however, has been delegated to its optical nonlinear properties in the visible and ultraviolet region. Although its transmission extends beyond 3500 nm, its optical properties for even longer wavelengths have not been given much attention [2]. Here we report on the optical properties of BBO in the 0.1 to 1.1 terahertz (THz) region. It was found that this material is significantly transparent for submillimeter waves and it was also demonstrated that this material exhibits birefringence in the THz range. These results may help in understanding phase matching conditions to realize BBO-based THz frequency doublers and even future THz optical parametric amplifiers.

We used a type I 10mm x 10 mm x 1 mm (thick) BBO crystal (Type I, $\theta=90^0$, $\Phi= 90^0$, Crylight Photonics, Inc.) for the study. The THz radiation was from a femtosecond laser irradiated bulk InAs surface, delivering transient pulses centered at ~0.8 THz ranging from 0.1 THz to ~1.5 THz. The predominantly p-polarized THz radiation was collimated and focused using paraboloidal mirrors and the azimuthal dependence of the THz transmission of the BBO detected using a liquid-He cooled Silicon bolometer detector. Additionally, the transmission spectra's angular dependence (for every $5^0$ steps over $360^0$) was measured using a far infrared fourier transform spectrometer fitted with the same bolometer. All transmittance spectra were deconvolved with the reference, which is an aperture whose diameter is equal to the BBO crystal holder aperture.

The azimuthal angle dependence of the broadband THz transmittance is shown in Fig. 1(a). The y-axis is the % transmittance calculated from the voltage reading of the lock-in amplifier-measured bolometer reading and divided by the reference signal. The two-fold

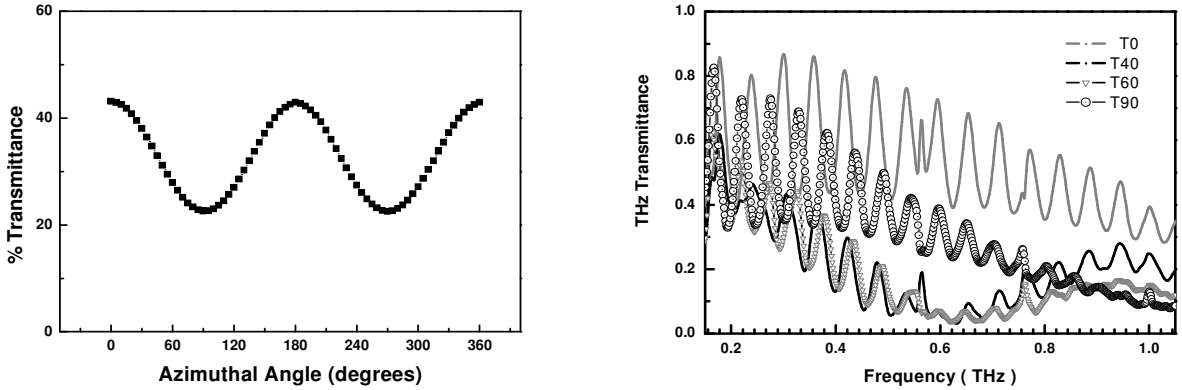


**Fig. 1.** (a) Azimuthal angle dependence of the broadband % THz transmittance showing birefringence. (b) Terahertz transmitance spectra for selected azimuthal angle orientations. A strong absorption band at 0.65 THz for the $40^0$ to $60^0$ orientations is attributed to low frequency phonon modes of the $[B_3O_6]^{3-}$ rings. The BBO crystal exhibits 60% transmittance at 0.35 THz.

dependence of its transmission properties for a 360-degree rotation implies THz birefringence. The data also confirms that the crystal c-axis of the BBO is parallel to the $0^0$ sample orientation in the experiment.

Figure 1(b) shows the plot of the THz transmittance spectra for selected azimuthal angle orientations. At the $0^0$ orientation, the BBO crystal exhibited a transmittance of 0.6 at 0.35 THz. This makes BBO a suitable nonlinear medium for femtosecond laser-irradiated InAs THz emitters. In addition, at the angular orientation range, $40^0$ to $60^0$ with respect to the C-axis, an absorption band at about 0.65 THz (or ~21.45 cm-$^1$) was observed. First-principles calculations of the crystalline vibrations of a BBO crystal unit cell in the THz region were performed using periodic density functional theory methods to account for this observation. It was found that this is attributed to low frequency phonon modes of the $[B_3O_6]^{3-}$ rings[3]. Figure 2(a) depicts the vibrational modes of the $[B_3O_6]^{3-}$ rings. The dipole derivatives (in atomic units) of the two strongest phonon modes at ~27 cm$^{-1}$ are shown in the inset of Fig. 2(b). The y-z plane projection of these modes' calculated dipole moments modes are shown in Fig. 2(b), where the x-axis (a-axis, normal to the paper surface) coincides with the THz radiation propagation direction. The angles of the dipole derivative projections with respect to the vertical c-axis are $46.1^0$ and $61.9^0$ for the 26.97 cm$^{-1}$ and 26.98 cm$^{-1}$ mode, respectively. This suggests that maximum absorption at the 0.65 THz band must coincide with orientations equal to these angles and in their equivalent directions.

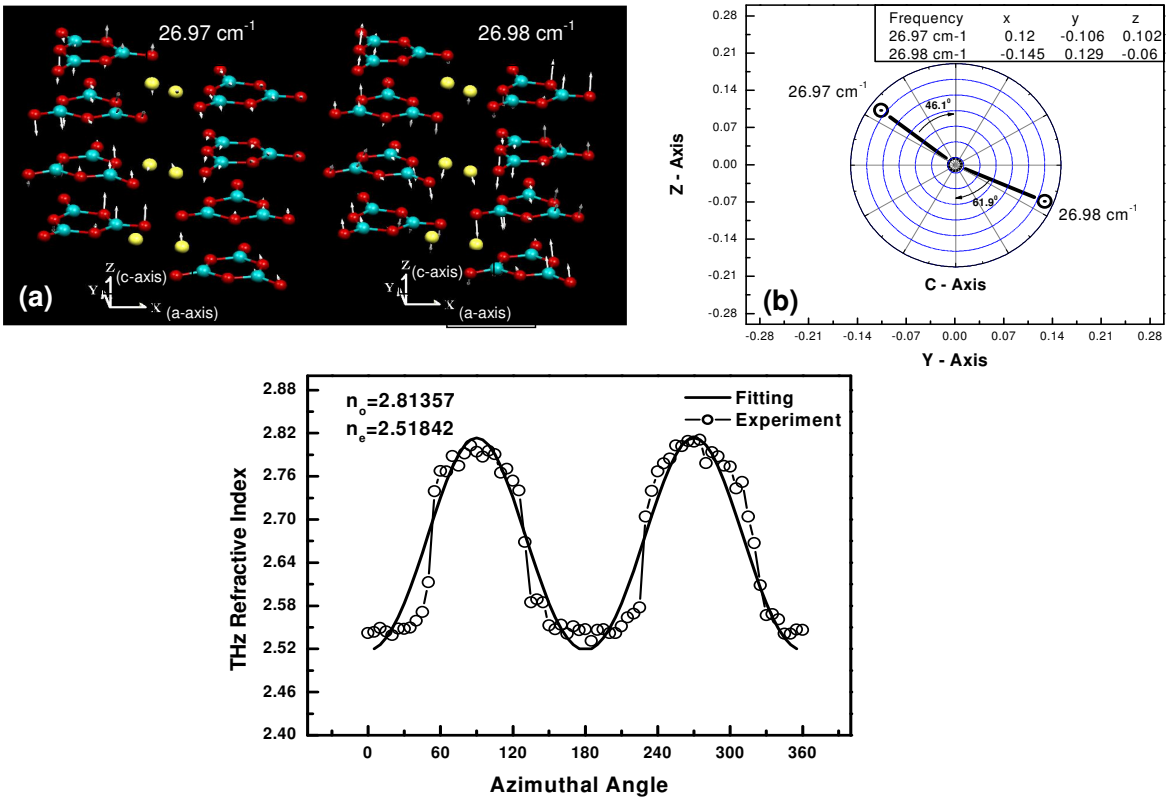


**Fig. 2.** (a) Depiction of the $[B_3O_6]^{3-}$ rings' calculated phonon modes at ~27 cm$^{-1}$. (b) The projection of the calculated dipole moments to the y-z plane. The angle with respect to the c-axis of the dipole derivative projections coincide with orientation where the absorption at 0.65 THz band was observed. (c) The angular dependence of the calculated refractive index values are shown in the open circle trace while the continuous line trace is a least squares fit.

The frequency spacing of the Fabry-Perot fringes that were shown in Fig. 1(b) was used to calculate the THz refractive index of the sample for different angle orientations. Figure 2(c) shows the results where open circle symbols are the values based on the spectra while the continuous line trace is a least squares fit from theory[4]. A reasonable agreement was achieved

with $n_o$ and $n_e$ fitting values of 2.81357 and 2.51842, respectively. This clearly shows a high refractive index contrast $\Delta n$ value of ~0.296. These results suggest that BBO crystals may prove useful as a nonlinear optical material in the THz region.

## References

1. D.N. Nikogosyan, "Beta Barium Borate (BBO) A Review of its Properties and Applications" APA 52, 359-368 (1991).
2. W. R. Bosenberg, L. K. Cheng, and C. L. Tang, "Ultraviolet optical parametric oscillation in $\beta$-$BaB_2O_4$" APL 54, 13-15 (1989).
3. P. Ney, M.D. Fontana, A. Maillard, and K. Polgar, "Assignment of the Raman lines in single crystal barium metaborate ($\beta$-$BaB_2O_4$) JPCM 10, 673-681 (1998)
4. A. Yariv, *Introduction to Optical Electronics*, (Holt, Rinehart, and Winston, 1976), Chap. 8.

# ESTIMATION OF DRIVING VOLTAGE ATTENUATION OF AN ULTRA-HIGH-SPEED IMAGE SENSOR BY DIMENSIONAL ANALYSIS

**V. T. S. Dao [a], C. Vo Le [a], H. D. Nguyen [a], T. G. Etoh [a], K. Takehara [a], T. Akino [b], K. Nishi [c]**

[a)] Graduate School of Science and Engineering, Kinki University, 3-4-1 Kowakae, Higashi-Osaka, Osaka, 577-8502 Japan
[b)] School of Biology-oriented Science and Engineering, Kinki University, 930 Nishi-Mitani, Kinokawa City, Wakayama, 649-6494 Japan
[c)] Kinki University Technical College, 2800 Arima-cho, Kumano, Mie, 519-4935 Japan

**Abstract:** In 2001, the authors developed an ultra-high-speed video camera system that records more than 100 consecutive images at the frame rate of 1 mega frames per second. Currently, researches have been continued to much higher frame rate and sensitivity. One of the most critical factor in achieving higher frame rate 100 mega frames per second image sensor is attenuation of voltage pulses which drive the CCD. In this paper, we propose an efficient method to estimate driving voltage attenuation through RC networks representation of the ultra-high-speed image sensor. The ubiquitous Elmore delay metric is utilized as the first-order approximation. To further improve the accuracy of Elmore model, we apply dimensional analysis to SPICE simulation data. The proposed method was applied to a number of RC networks and estimation error of the resultant expression is less than 2%. The framework of this analysis can be extended to address delay or attenuation issues of other VLSI structures.

***Keywords:*** *Signal Attenuation, RC network, Elmore model, Dimensional Analysis, Ultra-High-Speed Image Sensor.*

## 1. Background on Current Work

### *1.1. Multi-level structure of the ISIS*

High speed imaging has tremendous applications for various fields such as scientific, industrial and military applications. With the creation of an ultra-high-speed CCD sensor, Etoh et al. [1]-[2] has created a de facto standard in high speed video camera systems. The image sensor is called the ISIS, the In Situ Image Sensor. Each pixel is equipped with more than 100 slanted memory elements which enables more than 100 images to be captured. Ongoing research has been carried out ever since to develop new sensor with working frame rate as high as 100Mfps with sub-ten photon counting capability [3]-[5].

One of the most critical technical barrier is the loss of voltage waveforms necessary to drive the CCD due to propagation delay on the sensor chip. The authors proposes an efficient method to estimate the attenuation of input waveforms through RC networks representation of CCD structure as shown in Fig 1b.

Fig. 1(b) shows a fundamental RC chain circuit with series resistance $r_S$, parallel resistance $r_P$ and capacitor c. The fundamental model can be replaced with some allowance of accuracy by the electrically-equivalent simplest model with equivalent resistance $R_{eq}$ and capacitor $C_{eq}$ as shown in Fig. 1(a). CCD structure is usually represented with a multi-level model of the fundamental structure as shown in Fig. 1(c) and similar equivalence steps are repeated depending on the number of metal layers of the IC. The final equivalent resistance and capacitance are used to balance the RC delay of the CCD.

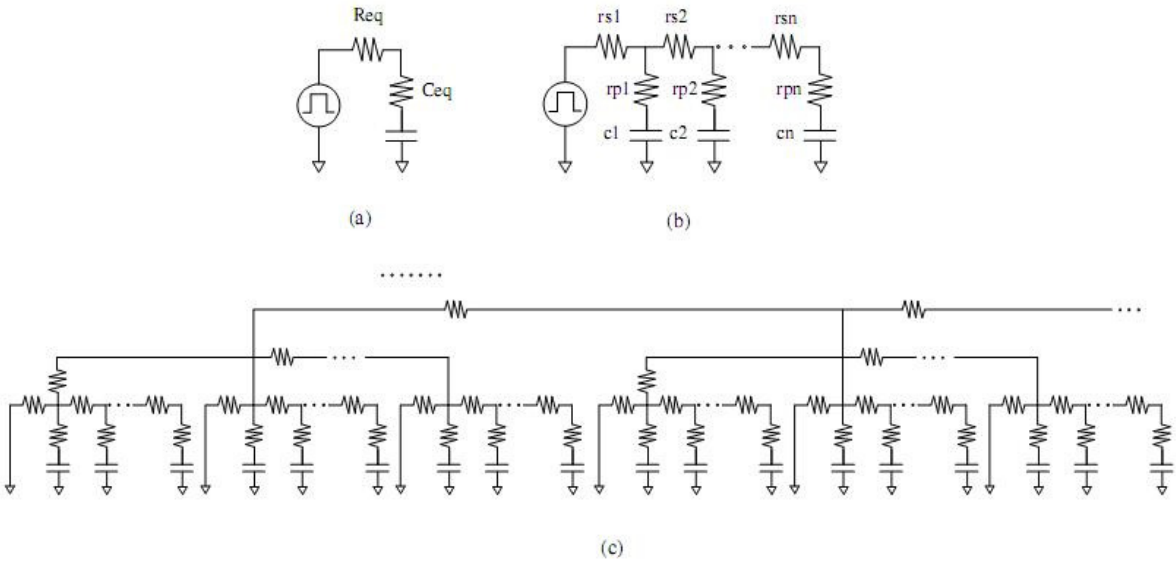


**Fig 1**. Circuit structures (a) Equivalent RC circuit (b) Fundamental RC circuit (c) Multi-level RC circuit.

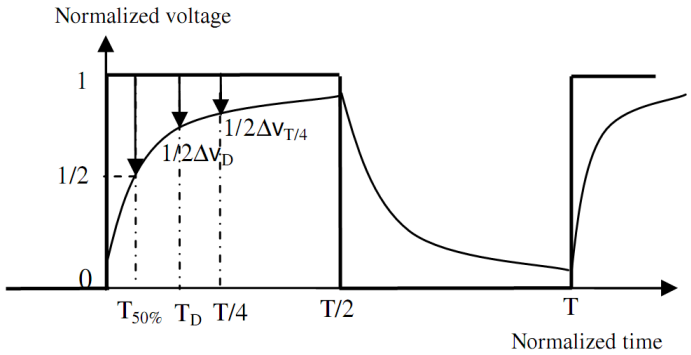


**Fig 2**. Input–output waveform pair; $½\Delta V_D$, $½\Delta V_{T/4}$: half signal loss calculated at $T_D$ and at quarter cycle (T/4).

Interconnect model derived in this paper is based on the following assumptions:
(1) Uniformly distributed RC networks in Fig. 1(b) with constant $r_S$, $r_P$ and c;
(2) Square input waveform - duty cycle is 50%, which is normally used in high speed CCD transfer;
(3) Performance evaluation is based on amplitude response of the furthest-end node.

### *1.2. Dimensional analysis*

We have seven factors involved in evaluating amplitude loss through a fundamental RC chain shown as in Fig. 1(b) and Fig. 2 as: parallel resistance $r_P$, series resistance $r_S$, capacitance c, pulse period T, maximum input voltage $V_0$, amplitude loss at quarter cycle $\Delta V_{T/4}$, number of sub-circuit segments n. To reduce the number of governing factors of the system and derive a generalized expression for the RC delay, base parameters are selected as: n, $r_S$, $r_P$, c and T.

Then, the following three dimensionless parameters are introduced as in Table 1.

Dimensional analysis results in the new system relation $\Phi\left(\overline{\Delta V}_{T/4}, A, B\right) = 0$ (4)

We focus on finding the explicit function, which is more useful: $\overline{\Delta V}_{T/4} = \Phi_1\left(A, B\right)$ (5)

The functional relationship in (5) can be estimated through an equivalent circuit with the resistance $R_{eq}$ and the capacitance $C_{eq}$, where: $C_{eq} = C_E = nc$.

The expression of $R_{eq}$ is assumed as follows:

$$R_{eq} = \alpha\left(R_P + \beta R_S\right) \quad (6)$$

**Table 1**: New dimensionless parameters

| New dimensionless parameters | Formulae |
|---|---|
| Dimensionless amplitude loss at quarter cycle | $\overline{\Delta V}_{T/4} = \Delta V_{T/4}/V_0$ (1) |
| Ratio of equivalent parallel resistance and series resistance | $A = \frac{R_p}{R_S} = \frac{r_P/n}{n+1/2\, r_S} = \frac{2}{n(n+1)}\frac{r_P}{r_S}$ (2) |
| Ratio of the Elmore delay and pulse period (where f is the working frequency) | $B = T_D/T = T_D f = R_E C_E f$ (3) |

Then, our problem is reduced to obtain an expression of α and β in terms of dimensionless parameters A and B. They were determined experimentally by using a practical procedure described in the next section.

Theoretically, B can vary from 0 to ∞. However, if B is too small, attenuation becomes almost negligible, and if B is too large, signal becomes completely attenuated; both cases are of no interest for practical applications. Therefore, the range of B is fixed between 0.055 and 0.18 which corresponds to the one-side attenuation $1/2\,\overline{\Delta V}_{T/4}$ of 1% and 25% of input voltage amplitude of a single RC circuit shown in Fig. 1(a).

## 2. Semi-Empirical Interconnect Model (SEIM)

### *2.1. Two extreme cases (A = ∞ or A = 0)*

For A = ∞ ($r_S = 0$), we have an exact solution: $R_{eq} = R_p = r_p/n$, $C_{eq} = nc$. Therefore, $\alpha = 1$.

For A = 0 ($r_P = 0$), hence, $r_P = 0$, and from (6), we have: $R_{eq} = \alpha\beta R_S$. We can expect that the value of $\alpha$ distributes around unity, which is the exact solution for $A = \infty$. It is convenient for the following analysis if $\alpha$ can be fixed at a constant. Therefore, $\alpha$ is assumed to be one. Then, we searched for an expression of $\beta$ with respect to B.

The coefficients were found by applying a curve fitting technique to fit SPICE data with a wide range of number of circuit segments (n) from 10 to 20,000 at different value of B.

The resultant expression is as follows:

$$\beta = 0.86B + 0.8 \text{ with } 0.055 \le B \le 0.18 \quad (7)$$

Fig. 3 shows an excellent linear fitting result between SEIM and Spice data with less than 0.7% for A = 0 and $\alpha = 1$.

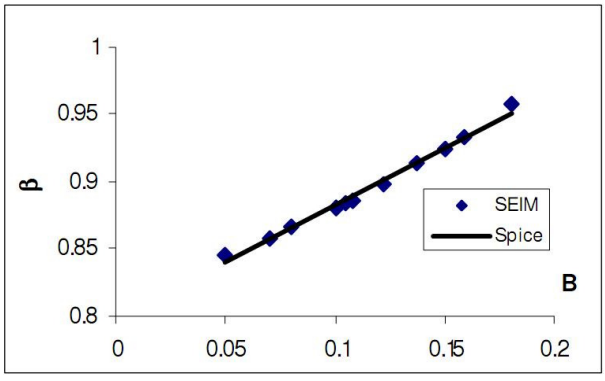


**Fig 3**. $\beta$ fitting result when A = 0.

### *2.2. General cases (A ≠ 0 and A ≠ ∞)*

The two simple cases examined above are used as "boundary conditions" to find the functional relationship for the whole range of A. For cases of A which distributes from 0 to ∞, we assume that expression of $\beta$ with respect to B remains unchanged, and $\alpha$ changes with respect to A.

We employed the following expression to approximate the change of $\alpha$ with respect to A for $0 < A < \infty$:

$$\alpha(A) = 1 + aA^b e^{-cA}, \text{a = a(B); b = b(B); c = c(B)} \quad (8)$$

The coefficients a, b and c in (9) were found by using a minimization technique to fit SPICE data with a wide range of circuit at different combinations of (n, rS, rP, c and f) for different cases of B as shown in Fig. 4. Finally, we have a simple functional form of SEIM as follows:

$$\begin{aligned} &R_{SEIM} = \alpha(R_P + \beta R_S); C_{SEIM} = nc \\ &\text{where: } \beta(B) = 0.86B + 0.8;\ \alpha(A) = 1 + aA^b e^{-cA};\ 0.055 \le B \le 0.18 \\ &\quad a(B) = 0.67B; b(B) = -3B + 0.8; c(B) = 7.42B - 0.3 \end{aligned} \quad (9)$$

Since $\alpha$ changes around unity as shown in Fig. 4, we can further simplify the expression of $\alpha$ by using the average values of $\alpha$ for each case of B. The Simplified - Semi Empirical Interconnect Model (S-SEIM) is as follows:

$$\begin{aligned} &R_{S-SEIM} = \alpha(R_P + \beta R_S); C_{S-SEIM} = nc \\ &\text{where: } \beta(B) = 0.86B + 0.8; \alpha(B) = 0.34B^2 + 0.0047B + 1; \\ &\quad 0.055 \le B \le 0.18 \end{aligned} \quad (10)$$

Estimation errors of amplitude response of S-SEIM, SEIM, Elmore[6] and Celik[13] model are shown in Table 2. SEIM and S-SEIM give much better results compared with other models.

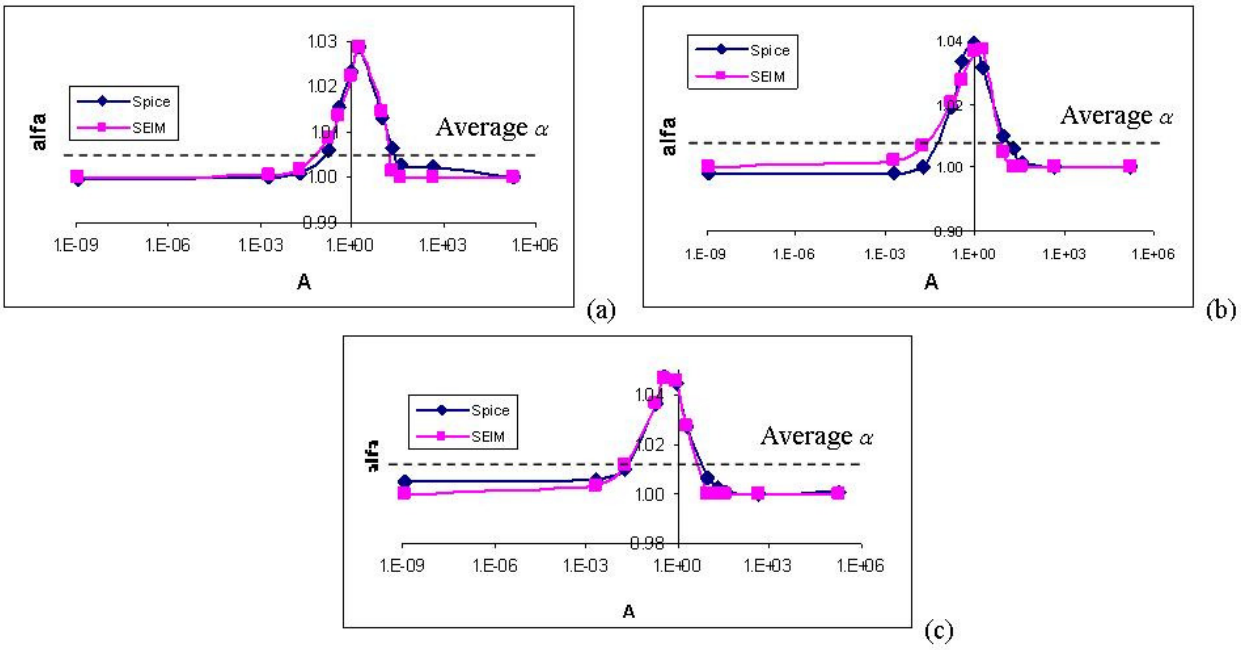


**Fig 4**. $\alpha$ fitting result when B = 0.055; 0.11 and 0.165.

**Table 2**: Comparison between estimation errors of amplitude response by different models

| N | B | Elmore | Celik | SEIM | S-SEIM |
|---|---|---|---|---|---|
| 5880 | 0.117 | -6.6% | -17.0% | -0.5% | -0.6% |
| 1280 | 0.150 | -7.6% | -49.5% | -0.9% | -1.2% |
| 720 | 0.056 | -1.3% | -5.5% | 0.0% | 0.0% |
| 360 | 0.133 | -7.9% | -26.9% | -0.7% | -1.2% |
| 144 | 0.076 | -1.6% | -5.6% | 0.2% | 0.8% |
| 90 | 0.100 | -2.9% | -9.6% | 0.4% | 1.2% |

## 3. Conclusion

Explicit closed-form expressions to estimate driving voltage attenuation of RC networks of an ultra-high-speed image sensor have been developed. Dimensional analysis is applied to circuit simulator data to seek a simple expression that significantly improve the accuracy of Elmore model. Different fundamental RC chains have been considered and simulated demonstrating the accuracy of the proposed model with respect to Elmore model and Celik model.

The paper also shows that combination of dimensional analysis and analytical approach is a powerful research tool to reach a practical expression, yet, keeping the fundamental importance of the investigating problem.

Finally, it is worth noting that the proposed approach could be extended to address delay or attenuation of other VLSI structure with different input conditions rather than square input waveform with no input rise time.

## References

3. T. G. Etoh, D. Poggermann, A. Ruckelshausen, A. J. P. Theuwissen, G. Kreider, H. O. Folkerts, H. Mutoh, Y. Kondo, H. Maruno, K. Takubo, H. Soya, K. Takehara, T. Okinaka, Y. Takano, T. Reisinger, and C. Lohman, "A CCD image sensor of 1Mframes/s for continuous image capturing of 103 frames", *Digest of Technical Papers, International Solid-State Circuits Conf.*, San Francisco, CA, (2002), 46-47.
4. T. G. Etoh, D. Poggermann, G. Kreider, H. Mutoh, A. J. P. Theuwissen, A. Ruckelshausen, Y. Kondo, H. Maruno, K. Takubo, H. Soya, K. Takehara, T. Okinaka, and Y. Takano, "An image sensor which captures 100 consecutive frames at 1,000,000 frame/s", *IEEE Trans. Electron Dev.*, 50(1), (2003), 144-151.
5. C. Vo Le, N. Otsuka, T. Akino, K. Nishi, K. Takehara, and T. G. Etoh, "Towards 100 Mfps: an innovative ultra-high-speed video camera", *ITE Technical Report*, 31(3), (2007), 1-4.
6. T. G. Etoh, C. Vo Le, Y. Hashishin, N. Otsuka, K. Takehara, H. Ohtake, T. Hayashida, and H. Maruyama, "Evolution of ultra-high-speed CCD imagers", *Plasma and Fusion Research,* 2, (2007), S1021.
5. P. Karimov, C. Vo Le, K. Takehara, S. Yokoi, and T. G. Etoh, "Photo-triggering system for an ultra high speed video microscopy", *Review of scientific instruments 78*, (2007), 113702.
6. W.C. Elmore, "The transient response of damped linear networks with particular regard to wide-band amplifiers," *J. Appl. Phys.*, 19(1), (1948), 55–63.
7. S. Y. Kim and S. S. Wong, "Closed-form RC and RLC delay models considering input rise time," *IEEE Trans. Circuits Syst.-I, Regular Papers*, 54(9), (2007), 2001-2010.
8. Y. I. Ismail and C. Amin, "Computation of Signal Threshold Crossing Times Directly from Higher Order Moments", *IEEE Trans. Comput-Aided Des. Integr. Circuits Syst.,* 23(8), (2004), 1264-1276.
9. M. Celik and L. T. Pillegi., "Metrics and bound for phase delay and signal attenuation in RC(L) clock trees," *IEEE Trans. Comput-Aided Des. Integr. Circuits Syst.*, 18(3), 1999, 293–300.

# EVALUATION OF AN IMAGE SENSOR WITH SUB-TEN-PHOTON SENSITIVITY AND ULTRA-HIGH FRAME RATE

**H. D. Nguyen[a], C. Vo-Le[a], V. T. S. Dao[a], M. Tanaka[a], K. Takehara[a], T. G. Etoh[a], Y. Kondo[b], H. Maruno[b], H. Tominaga[b], H. Soya[b], H. van Kuijk[c], J. Bosiers[c], W. Klaassens[c], G. Ingram[c], V. P. Singh[c], and M. Lesser[d]**

[a)] Graduate School of Science and Engineering, Kinki University, Higashi-Osaka,Osaka, 577-8502 Japan, [b)] Shimadzu Corporation, [c)] DALSA, [d)] University of Arizona
*E-mail: hdnguyen@civileng.kindai.ac.jp*

**Abstract:** The authors are developing a video camera with ultra-high sensitivity and ultra-high frame rate. To achieve the ultra-high sensitivity, the CCD image sensor employs the following three technologies; backside illumination, cooling and CCM, charge carrier multiplication. A test image sensor has been manufactured and evaluated. At room temperature without cooling, the video camera has about ten-time higher sensitivity than the previous one, which was supported by a conventional frontside illumination technology. Furthermore, the video camera can capture images under extremely weak illumination by using CCM at -40 degree C. This paper describes the evaluation camera and shows preliminary evaluation results with special emphasis on the sensitivity and performance of the CCM.

***Key Words:*** *High-speed Video Camera, High-sensitivity, ISIS, Backside Illumination, CCM*

## 1. Introduction

We are developing a video camera which operates at 10 Mega frames per second (Mfps) with sub-ten-photon sensitivity [1]-[2]. A test image sensor has been designed, fabricated and evaluated. While it operates at 250 kfps with full dynamic range and at 1 Mfps with some loss of dynamic range, it shows extraordinary high sensitivity. This paper describes the preliminary evaluation of the test sensor.

The ultra-high frame rate is supported by employment of the in-situ storage image sensor (ISIS) with slanted linear CCD storage, which was invented by Etoh and Mutoh. In 2001, a video camera mounting the ISIS-V2, the version two, achieved 1Mfps [3]-[4]. While the ISIS-V2 archieved the ultra-high frame rate, since it is a frontside illuminated image sensor, the fill factor and the quantum efficiency are lower than backside illuminated image sensors. A new test sensor, ISIS-V12, was designed with backside illumination technology, based on the design of the ISIS-V2 for the frontside design.

Backside illumination supports not only very high sensitivity with 100% fill factor and very high quantum efficiency, but also substantially increases the maximum frame rate with almost free design of the metal wiring on the front surface with no care for reduction of the fill factor. Since the frame rate can be easily increased by improvement of the design of the metal wiring, first of all, we set our major target in designing the current test sensor to achievement of the ultra-high sensitivity. On the other hand, for risk aversion to any mistake in the design change, change in the metal wiring design from that of the ISIS-V2 was minimized. Therefore, while the frame rate of ISIS-V12 is almost the same as the ISIS-V2, the sensitivity was dramatically improved.

The ultra-high sensitivity is supported by two conventional technologies, backside illumination and cooling, together with an innovative CCD technology, CCM, charge carrier multiplication. The CCM was invented by Hynecek [5] and now widely applied to fluorescence imaging in cell biology which requires very high sensitivity.

In the following sections, we will briefly describe the evaluation camera, and, then, present preliminary evaluation results with special emphasis on the sensitivity and performance of the CCM.

## 2. Evaluation camera

### *2.1. Camera structure*

Fig. 1 shows the evaluation camera of ISIS-V12. It is composed of the camera head, which is a vacuum container with one printed circuit board, PCB, inside, and other four PCBs at the backside of the camera head. Two of them are placed on a top of an empty box and the other two are attached at both sides of the box. They generate driving voltage patterns of the CCD, accept the output signals from the image sensor, and amplify and send them to a computer. A cooling rod is placed in the box and the head of the rod is attached to the backside of the package of the sensor. The PCBs are electrically connected to a computer to control the whole system in image capturing phase and reproduce images after the readout phase.

The standard operating temperature is –40 degree C. Although the vacuum chamber can be cooled down to –100 degree C, most of ICs on the front PCB in the vacuum chamber work at the temperature higher than –50 degree C, according to their specifications.

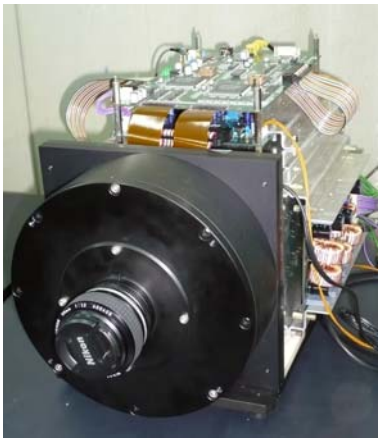

**Fig 1**. Evaluation camera

### *2.2. Experimental setup*

Fig. 2 shows the experimental set-up, which includes the evaluation camera, an LED strobe, the target, a sequencer for synchronization of the devices and a computer to control the whole system.

The LED strobe is controlled by a sequencer to synchronize the time of the illumination with that of image capturing. This means that the camera avoids unwanted light coming before and after image capturing. The LED strobe is set in frontside or backside of the target, depending on the experiment.

The main target is a laser-beam chopper rotating at 6,000 rpm at the maximum rotation speed, which makes recognizable movement of a reproduced image even taken at the maximum frame rate, 1 Mfps.

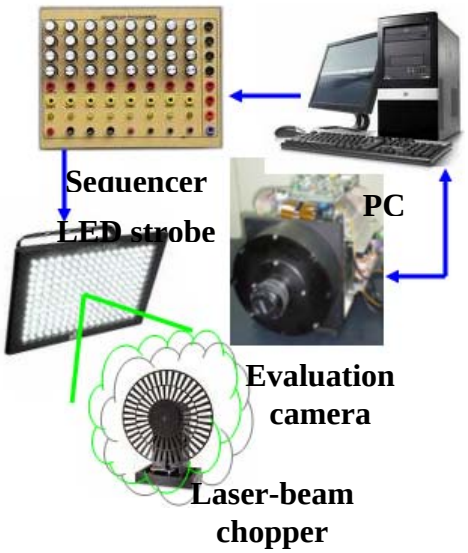


**Fig 2**. Block diagram of the experiment

## 3. Evaluation results

### *3.1. Sensitivity without CCM*

#### *3.1.1. Quantum efficiency*

One of the most important performance parameters of a video camera is QE, quantum efficiency. QE is defined as the number of collected electrons devided by the number of photons impinging on the device.

The experiments are performed with three kinds of lasers: red (650 nm), green (532 nm) and violet (405 nm). The camera is set up with very weak signal level by inserting many ND filters in

front of the lens. Then, the ND filters are removed one by one to find a proper signal level. Frame rate is kept at 8Kfps and temperature is -40$^0$C.

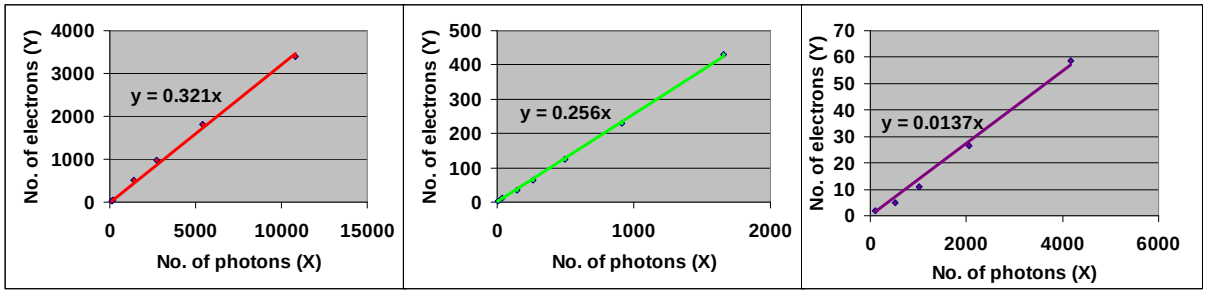


(a) Red: QE = 32.1% (b) Green: QE = 25.6% (c) Violet: QE = 1.37%

**Fig 3.** Quantum efficiency of the ISIS-V12 with different lasers

Fig. 3 shows QE of the ISIS-V12 for lasers with different wave length. QE of red and green lasers are respectively 32.1% and 25.6%. For the violet one, QE seriously drops to 1.37%.

QE for standard backside illuminated image sensors for visual light is between 70-90%, much higher than that of the ISIS-V12. To characterize basic performance, backside processes to increase the QE, except thinning, have not been applied to the currently available ISIS-V12 test sensors. This is the reason for the lower QE of the current test sensor. Thirty percent is sufficiently high for sensors without special backside processes. We will continue the experiments to evaluate contributions of each additional backside process. Then, it is expected that QE will increase to more than 80% after application of all these backside processes.

Very low QE for the violet laser is also due to lack of the additional backside processes.

### *3.1.2. Relative sensitivity compared with an existing ISIS*

Etoh et al have developed front-side-illuminated ISISes. Among them, the ISIS-V2 has been already mounted on a commercially-available ultra-high-speed video camera of 1 Mfps, developed and marketed by Shimadzu Corporation as SHIMADZU-HPV1. The sensitivity of the ISIS-V12 is compared with that of ISIS-V2 under the same temperature, illumination and optical conditions as follows:

Temperature: 25$^0$C, illumination intensity: 300 lx, lens: NIKKOR 50 mm, Iris F1.2 full (open). The CCM of the ISIS-V12 was inactivated.

Fig 4(a) and (b) respectively show the images taken by the evaluation camera of the ISIS-V12 at the frame rate of 8 kfps and by SHIMADZU-HPV-1 mounting the ISIS-V2 at much slower frame rate of 1 kfps. The image by ISIS-V2 camera is slightly darker than that of ISIS-V12. This proves that the ISIS-V12 has more than eight-time higher sensitivity than the ISIS-V2. As explained above, the QE of the current test sensor is about 30%. It is expected that, after proper additional backside processes, sensitivity of the ISIS-V12 will increase from twenty to thirty times higher than that of the ISIS-V2. When cooling and CCM are applied, relative sensitivity to noise level is much more increased.

## *3.2. CCM*

### *3.2.1. Role of CCM*

We are aiming at sub-ten-photon sensitivity in addition to the ultra-high frame rate. QE of common backside illuminated image sensors is about 80%. Therefore, incident light intensity with ten photons per pixel generates eight electrons. If the readout noise level is higher than eight electrons, signals of eight electrons is buried under the readout noise level. To solve this

problem, we introduced CCM to amplify the signal electrons to the level far beyond the readout noise level.

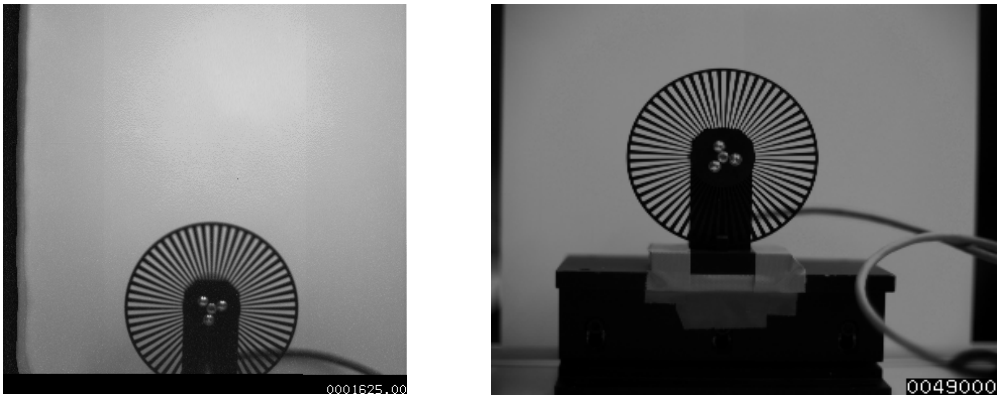

(a) ISIS-V12 8,000fps (200 kpixels)

(b) ISIS-V2 1,000fps (80 kpixels)

**Fig 4**. Comparison of sensitivity of ISIS-V12 (a) and ISIS-V2 (b)
Illumination: 300 lx, Lens: Nikkor 50 mm, F1.2, Temperature: 25 degree C, CCM of ISIS-V12 inactivated

CCM, charge carrier multiplication, is one of the most important part of the ISIS-V12 structure. It is effective to amplify a very weak signals. The CCM consists of multi-CCD steps with very high electric field. In the large electric field, signal electrons are accelerated to generate a very small number of secondary electrons. When this process is repeated N steps, the signal level and the additional noise associated with the impact ionization are increased, respectively, proportional to the number of steps N and to the square root of N. Therefore, the ratio of the signal level to the additional noise due to a CCM steps increases inversely proportional to the square root of N. After the multi-CCM steps, the number of signal electrons increase with relatively low additional noise.

CCM technology has three important features: 1) Amplification of signals with decreasing additional SNR, 2) CCM is placed before the readout amplifier, and 3) CCM is applicable only to CCD.

### *3.2.2. Amplification factor vs. CCM voltage*

Performance of CCM is tested by comparing that of a common amplifier installed in the evaluation camera. The sensor is cooled to -40 degree C and the frame rate was 8 kfps.

At first, CCM was inactinated, i.e., the voltage difference between two CCM voltages was set negative. The incident light was gradually decreased until the image became unrecognizable by our eyes, even if the amplification factor of the camera amplifier was maximized. Then, the camera amplification factor was set at 1.0 and voltage difference of CCM was gradually increased. Fortunately, the image of the chopper became detectable when the voltage difference surpassed 27.0 V.

The result is shown in Table 1. As shown in Table 1 (a), the original average signal level of the central area of the image frame was 12.6 $e^-$, which is sum of signal electrons and noises. For example, the CCM voltage difference is 27 V and 29 V, the average level is 286.4 $e^-$ and 3896.8 $e^-$, i.e., the amplification factor is about 23 and 314, respectively. On the other hand, the standard deviation increases with lower rate to 145.0 $e^-$ and 1711.0 $e^-$. Then, the signal-to-noise ratio, SNR, increases to 2.0 and 2.3 from orginal value 0.8, for which no image is recognizable. Further analysis showed the real signal level is about 4 $e^-$ and the total noise level is 8-9 $e^-$, which resulted in the average signal level about 12.6 $e^-$. The noise includes readout noise and dark current, which causes a part of

**Table 1**. Comparison of amplification of very weak signals by means of CCM and camera amplifier. (Frame rate: 8kfps, Iris: F16, 1/8 x 1/4 x 1/4 x 1/2 ND filtes applied)

(a)

| CCM voltage | Mean ($e^-$) | St. Dev. ($e^-$) | SNR |
|---|---|---|---|
| 0 ÷ 10 | 12.6 | 15.0 | 0.8 |
| 18.0 | 13.6 | 15.6 | 0.9 |
| 22.0 | 19.8 | 18.8 | 1.1 |
| 24.0 | 35.0 | 25.8 | 1.4 |
| 26.0 | 94.8 | 65.4 | 1.4 |
| 27.0 | 286.4 | 145.0 | **2.0** |
| 28.0 | 880.2 | 398.8 | **2.2** |
| 29.0 | 3896.8 | 1711.0 | **2.3** |

(b)

| Amplification factor | Mean ($e^-$) | St.Dev ($e^-$) | SNR |
|---|---|---|---|
| 5.0 | 58.4 | 63.6 | 0.9 |
| 10.0 | 119.4 | 128.8 | 0.9 |
| 20.0 | 228.2 | 253.2 | 0.9 |
| 30.0 | 348.8 | 378.8 | 0.9 |

fixed parttern noise. Therefore, if we subtract the fixed pattern noise by post-digital processing, the detection level of the CCM becomes less than 4 $e^-$.

When QE of the ISIS-V12 is improved to 80%, eight signal electrons >4 $e^-$, are generated from ten incident photons. Therefore, it is practically possible to develop a sub-ten-photon-sensitivity ultra-high-speed image sensor.

On the other hand, as shown in Table 1(b), if we use the camera amplifier, both the average and the standard deviation increase linearly, and the SNR stays at a constant value 0.9.

Fig. 4 compares images taken with the CCM and the camera amplifier under the very low illumination condition stated above in the Table 1. While, (a) for the CCM voltage difference 28 V and 29 V, the fun-shaped image of a quarter part of the chopper can be recognized, (b) the image taken with the camera amplifier of 30-time amplification provides only noises without the chopper image embeded under the noise.

CCM=24V CCM=26V CCM=27V CCM=28V CCM=29V

(a) CCM activated, camera amplifier inactivated

(b) Camera amplifier = 30 , CCM inactivated

**Fig 4**. Images taken with CCM and the camera amplifier

## 4. Conclusions

ISIS-V12, an image sensor with the maximum frame rate 1 Mfps with very high sensitivity was designed, fabricated and evaluated.

The quantum efficiency for red (650nm), green (532nm) and violet (405nm) lasers are respectively 32.1%, 25.6% and 1.37%. However, standard backside processes for increase the

QE have not been applied to the current test sensor. Therefore, it is expected that the QE of the ISIS-V12 with these processes will increase to the standard level of backside illuminated image sensors, 80%, which produces eight electrons for ten incident photons.

CCM, charge carrier multiplication, introduced to the ISIS-V12, together with backside illumination and cooling, achieved a very low image-detectable signal level, less than 4 e-.

Therefore, it was confirmed that it is practically possible to develop a sub-ten-photon-sensitivity ultra-high-speed image sensor.

We will continue experiments to evaluate contribution of each additional backside process to improve quantum efficiency, and improvements of the metal wiring to increase the frame rate up to 10 Mfps.

**References**

1. C.Vo Le *et al.,*"Toward 100 Mfps: an innovative ultra-high-speed video camera", *ITE Technical Report,* Vol.31, No. 3, pp. 1-4, 2007
2. T. G. Etoh *et al.,*"Evolution of ultra-high-speed CCD imagers", *Plasma and Fusion Res.,* vol.2, S1021, 2007.
3. T. G. Etoh *et al.,*"An image sensor which captures 100 consecutive frames at 1,000,000 frame/s", *IEEE Trans. Electron Devices,* Vol.50, No. 1, pp. 144-151, 2003.
4. T. G. Etoh *et al.,*"A CCD image sensor of 1Mframes/s for continuos image capturing of 103 frames", *Digest of Technical Papers, ISSCC'02,* Vol. 2, pp.46-46, 2002.
5. J. Hynecek *et al.,*"CCM-a new low-noise charge carrier multiplier suitable for detection of charge in small pixel CCD image sensors", *IEEE Trans. Electron Devices,* Vol.39, No.8, pp. 1972-1975,1992.
6. P. Karimov *et al.,*"Photo-triggering system for an ultra high speed video microscopy", *Review of scientific instrumennts 78,* pp. 113702- , 2007.

# ZERO GROUP VELOCITY BASED ON NEGATIVE REFRACTION IN PHOTONIC CRYSTALS

**Quang Minh Ngo, Sangin Kim, Hanjo Lim**

Department of Electrical and Computer Engineering, Ajou University
San 5, Woncheon-dong, Yeongtong-gu, Suwon 443-749, Korea
*Email: sangin@ajou.ac.kr*

**Abstract:** The fields of "slow" and "stopped" light have recently been topics of great interest, because of the possibilities of designing all-optical buffers and routers, quantum memories and improving interferometers. In this report, we numerically demonstrate the zero group velocity waveguide structure based on a negative refraction in photonic crystals. Previously, a positive index and negative index clad slab waveguide was proposed to implement the zero group velocity waveguide. However, all the current proposed negative index materials have Ohmic loss due to metal. In this work, we replaced the negative index material with a photonic crystal that shows negative refraction. In our waveguide design, the photonic crystal of negative refraction played a role of effective negative index material and the light trapping in the designed zero group velocity waveguide has been demonstrated numerically. The rich applications of the designed zero group velocity waveguide are discussed.

***Keywords:*** *Photonic crystals (PC), waveguides, trapping light.*

## 1. Introduction

A total reflected light rays can obtain a lateral shift from the position expected by geometrical trajectory, termed Goos-Hänchen (GH) shift [1]. Since its discovery in 1947, the research of GH shift has been extended to many areas, such as acoustics, quantum mechanics, surface physics and seismology. Recently, the exploration of left-handed materials brought on new interest in this research since it can lead to negative GH shift [2, 3].

Based on negative GH shift and waveguide theory [4], O. Hess and his colleagues [5] modelled how light would be affected if it travelled through a waveguide made from a material that had a core and two claddings with the different of refractive index signs. Acorrdingly, the cross points of the incident and reflected rays will sit inside the core and the effective thickness of the core is smaller than the physical one. By adiabatically reducing the physical thickness, the effective thickness of the core will eventually vanish. Therefore, the rays can be trapped. As can be seen, the negative GH shift at the interface plays a key role in this process. This technique may lead to applications in optical data processing, storage or quantum optical memories.

In this paper, we propose a photonic crystal (PC) waveguide structure that made from two materials: a core layer with a positive refractive index and two claddings made by two dimensional (2D)-PC that show negative refraction. The paper is organized as follow. In Sec. II the PC of negative refraction played a role of effective negative index material and the light trapping in the designed zero group velocity waveguide has been demonstrated numerically. Then, in Sec. III we will review potential future applications for our design structure, particularly in all-optical buffers and routers, quantum memories and improving interferometers. Although the field is still young, many promising applications have already been found. Simulations have been carried out by using finite-different time-domain (FDTD) and plane-wave expansion (PWE) methods.

## 2. Design and discussions of zero group velocity waveguide

Consider a waveguide structure as shown in Fig.1a, which has two claddings made by 2D-PC of triangular symmetry (with the lattice of a) of air holes (with the radius of r= 0.40a) in a dielectric ε= 12.25, and the waveguide core (refractive index of $n_w$, and thickness of d). The effective negative index ($\hat{n}$) of the two claddings can implement as similar to [6]. We restrict our analysis to TM modes whose electric field is polarized along the axis of the air holes, the PC claddings are similar to the isotropic medium with $\hat{n}$ = -1, when the operating frequency f= 0.306 (2πc/a). Thus, we will use this frequency as a critical value for all our calculations in the following.

As we know surface termination (C) plays a role in the distribution of the energy of the incident wave between the specularly reflected wave and the back-diffracted wave in a counter-propagating direction. Simply changing C, the wave can be completely back reflected or completely specularly reflected [7]. In our design, C= 0.5*r to be used can obtain a negative refraction optimization.

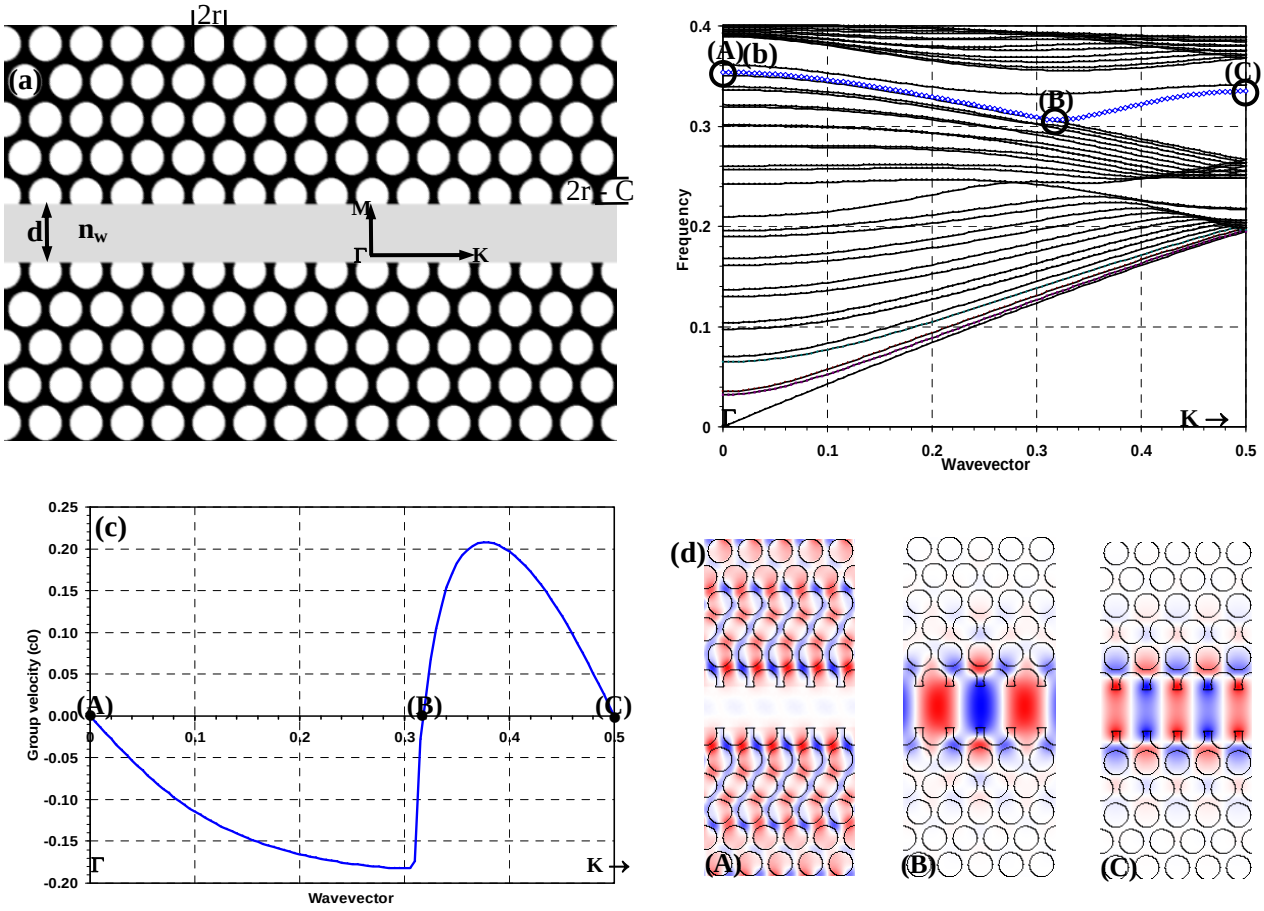


**Fig.1:** (a) A photonic crystal waveguide structure. (b) Typical waveguide dispersion of the TM modes for structure as in (a): core waveguide index ($n_w$) of 1.23 and its thickness (d) of $\left(\sqrt{3}\,a - 2.C\right)$; (c): Group velocity, $v_g$ in the waveguide in the unit of c., and (d): Field profiles of the modes at k=0 (**A**); k=0.318 (**B**), and k=0.5 (**C**).

Fig.1b shows the TM modes waveguide dispersion for a symmetric three-layer slab structure: the core dielectric has a refractive index of 1.23 and its thickness of $\left(\sqrt{3}\,a - 2.C\right)$; two cladding layers are made from 2D-PC mentioned above. We focus on the open-circle curve, this curve is seen to flatten for k~ 0; 0.5, and to be extremum for k~ 0.32, eventually, obtains a zero slope at k≅ 0; 0.5; and 0.318 (2π/a).

When n is refractive index of the medium in which light travels, the speed of light propagation in the medium will be c/n (c is the speed of light in the vacuum). Thus, n is the index indicating the deceleration of light. Note that the light is assumed here to be continuous wave (CW) of a single frequency. For pulse-like optical signals, the group refractive index $n_g$ is used in the place of n, and the velocity of optical pulses is usually expressed in terms of the group velocity, $v_g \equiv c/n_g$ ($n_g$ is the group index of the dispersion material). Here, $v_g$ is given by $(dk/d\omega)^{-1}$ for the angular frequency of light ω and its wave vector k. Fig. 1c illustrates the resulting $v_g$ of the waveguide mentioned in the fig. 1b. It should be noted that the gradient of the waveguide dispersion become zero at band edges (k= 0; and 0.5) and at middle (k= 0.318x2π/a), hence, addressed as the zero group velocity regime. For k< 0.318, the negative $v_g$ occurs in this structure, which means the light confines in the cladding layers. When k≥ 0.318, the light confines in the core waveguide, this effect can be cleared by positive $v_g$.

Fig.1d shows the mode profiles of several wave vector k points: (**A**) for k= 0, no field energy confines in the waveguide, which is not the waveguide mode. Entering other wave vector: k= 0.318 (**B**), and k= 0.5 (**C**), the modes do not penetrate into the claddings and, eventually, have their fields highly concentrated in the core waveguide. The zero group velocity at the pass band edges have proposed in the last many papers. In this work, we introduce the zero group velocity in the middle of pass band, which has the wave vector k= 0.318, corresponding to the frequency f= 0.306 (2πc/a). This frequency is below the light line, good confining light in the waveguide. In addition, this mode occurs at point where the $v_g$ changes sign, and therefore is conceptually to "left-handed" media, in which the $v_g$ is opposite to the phase velocity ($v_p$).

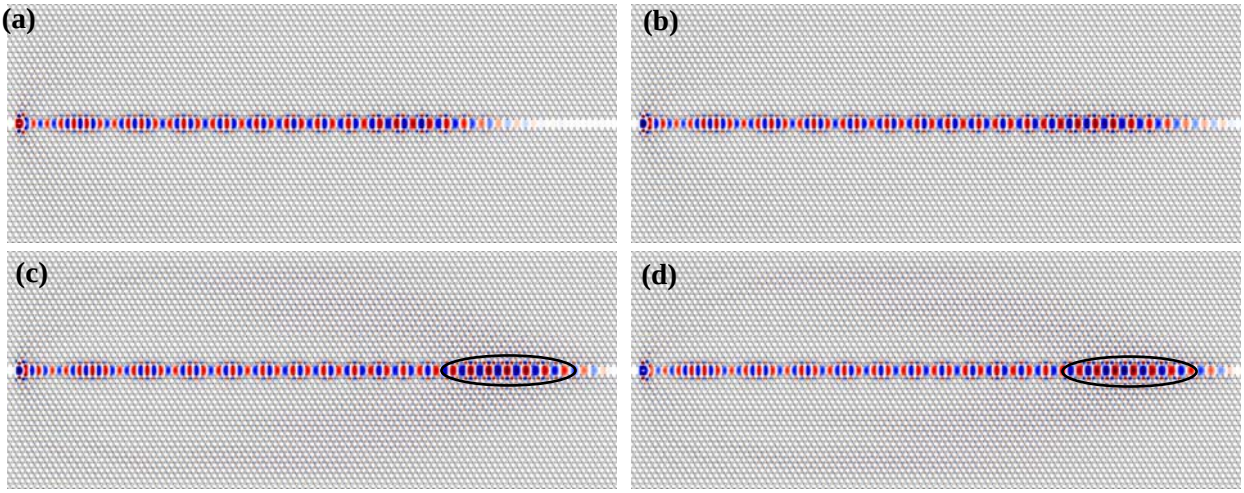


**Fig.2:** The snapshots of field distributions in the PC waveguide at: (a) t = 10000δt; (b) t = 13 600δt; (c) t = 16000δt; and (d) t = 80000δt (δt is a time step). Light trapping occurs at the re gion that has a critical index (n=1.23).

In order to investigate the light trapping in our PC waveguide, refractive index of core waveguide changes gradually from 1.65 to 1.10. The CW source with frequency f= 0.306 (2πc/a) is located at the input port of waveguide. The trapping of light is more intuitively recognized by tracing the trajectory of light ray inside the core for guide index nearly equal to the critical one mentioned above. Accordingly, a guided electromagnetic wave packet can be altogether trapped within a fixed area, spanning a continuous range of guide thickness in Fig. 2c, and Fig. 2d. Although, multimode should be occur in this frequency, but only zero group velocity mode will be existed in the waveguide, another modes are disappeared in the clad layers. These results show that the light trapping occurs in the PC waveguide structures based on negative refraction effect.

## 3. Potential applications

### *3.1. Slow light Mach-Zehnder interferometers*

Integrated Mach-Zehnder interferometer (MZI) devices are used extensively in optical modulators. Using slow light based on negative refraction instead of the coupled-cavity waveguide, this makes the distance, $L_\pi$, required to produce a $\pi$ shift in one arm of the MZI to be very short. Reducing the device length not only allows for space savings, but also decreases device power consumption. Additionally, the electrodes can be made smaller, thus reducing parasitics and further increasing operating bandwidth.

Because the index change is induced in only one arm of the interferometer, the result is that the pulses in the two arms of the MZI do not propagate at the same speed, and thus arrive at the output shifted slightly in time from one another (fig. 3a). We have termed this difference in arrival time deterministic optical jitter, $\Delta t$. The effect of this type of jitter on the output pulse depends on both the magnitude of the optical jitter in relation to the pulse width, as well as the bias of the MZI itself. When the optical jitter is comparable to or smaller than the pulse width, the result is pulse broadening in the case of constructive interference, or gross pulse distortion in the case of destructive interference. When the optical jitter is large in comparison to the pulse width, the pulses fail to interfere at all, resulting in two distinct output pulses regardless of the interferometer's bias.

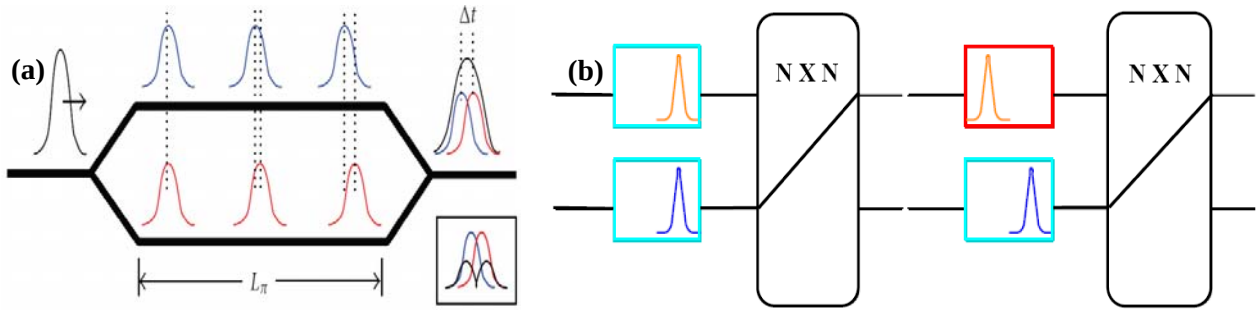


**Fig.3:** (a) When an index shift is induced in one arm of the interferometer, the group velocity in that arm changes. The pulses traveling in the two arms of the interferometer therefore arrive at the output separated in time by $\Delta t$, resulting in pulse distortion (broadening). In the worst case, where the pulses interfere destructively, the output pulse can even become double-humped (inset); (b): The ability to selectively slow down light in one input branch of an all-optical router could paradoxically speed up the flow of information, as collisions are prevented.

### *3.2. Optical buffering*

With an N x N all-optical switch (Fig. 3b-left), any of the input ports can be dynamically switched to any of the output ports. However, a serious problem can arise with this sort of architecture if two data packets arrive simultaneously at the switch, because the switch can only deal with one packet at a time. This problem is known as data packet contention.

By activating the slow light medium in one of the branches, one of the pulses is delayed, as shown in Fig. 3b-right. In this case, no contention occurs and the flow of information is sped up.

b. All-optical computing system

A very interesting potential application of stopped light is the possibility of storing information carried by light pulses, leading to a potential all-optical computing system. Current semi-conductor materials used in computing devices are reaching some of their limits, and an all-optical system would potentially enable us to go further in size reduction and calculation speeds.

## 4. Conclusion

To summarize, we have numerically demonstrated the zero group velocity waveguide based on a negative refraction in PCs. In our waveguide structure, the cladding layers are made by PC that shows negative refraction. Negative refraction effect plays a role of effective negative index material and the light trapping in the designed zero group velocity waveguide was demonstrated numerically. Unlike the zero group velocity waveguide of photonic band gap (PBG) type [8, 9], in our structure, PBG does not make sense, hence this structure is not useful to apply for the all-optical bistability based coupled waveguide-cavity PCs. It is certainly a very exciting field that will require careful study in years to come. After we submitted this paper for the conference [10], S. He *et. al*. reported a similar observation [11].

***Acknowledgments.*** *This work was supported by the BK 21 - Korea Research Foundation through MEMS/NANO photonics-based sensors and biomedical applications at Ajou University, Suwon, Korea*.

### References and links

1. F. Goos and H. Hanchen, Ann. Phys. (Leipzig) **1**, 333 (1947); ibid. **5**, 251 (1949).
2. P. R. Berman, “Goos-Hänchen shift in negatively refractive media,” Phys. Rev. E **66**, 067603 (2002).
3. I. Shadrivov, A. Zharov, and Y. S. Kivshar, “Giant Goos-Hanchen effect at the reflection from left-handed metamaterials,” Appl. Phys. Lett. **83**, 2713 (2003).
4. A. W. Snyder and J. D. Love, Optical waveguide theory (Chapman and hall, New York, 1983).
5. K. L. Tsakmakidis, A. D. Boardman, and O. Hess, “'Trapped rainbow' storage of light in metamaterials,”Nature **450**, 379 (2007).
6. M. Notomi, “Theory of light propagation in strongly modulated photonic crystals: Refractionlike behavior in the vicinity of the photonic band gap,” Phys. Rev. B **62**, 10696 (2000).
7. V. Mocella, P. Dardano, L. Moretti, and I. Rendina, “Influence of surface termination on negative reflection by photonic crystals,” Opt. Express **15**, 6605 (2007).
8. Y. A. Vlasov, M. O’Boyle, H. F. Hamann, and S. J. McNab, “Active control of slow light on a chip with photonic crystal waveguides,” Nature **438**, 65 (2005).
9. Sergei F. Mingaleev, Andrey E. Miroshnichenko, Yuri S. Kivshar, “Low-threshold bistability of slow light in photonic-crystal waveguides,”Opt. Express **15**, 12380 (2007).
10. http://www.iop.vast.ac.vn/activities/iwpa08/index.php?detail=prg
11. J. He, Y. Jin, Z. Hong, and S. He, “Slow light in a dielectric waveguide with negative refractive index photonic crystal cladding,”Opt. Express **16**, 11077 (2008).

# ULTRA-NARROW SPECTRA LASER IN MICRO-CAVITY: FABRICATION METHOD AND LASING EMISSION PROPERTIES

**Bùi Văn Thiện[a], Hà Xuân Vinh[b], Chử Thị Thu Hà[b], Trần Thị Châm[b], Phạm Văn Hội[b]**

[a)] Natural Science Faculty, College of Medicine in Thai nguyen
[b)] Institute of Materials Science, Vietnamese Academy of Science and Technology

**Abstract:** In this paper the fabrication method and lasing emission properties of spherical and/or toroidal micro-cavity lasers based on High-concentration Erbium-doped silica-alumina glasses are presented in detail. The lasing threshold of micro-cavity laser pumped by laser diodes is of hundred micro-watts and Q-factor of cavity has been achieved up-to $10^8$ in experiment. The emission power of WGM lasing from micro-cavity laser is of 0.05-0.5 mW that will be enough for applying in the quantum information and optical sensor techniques. The toroidal micro-cavity permits to decrease the polar-mode of WGMs, which help to obtain the single-mode emission from micro-cavity lasers.

***Keywords****: Rare-earth doped silica-alumina materials, Micro-cavity laser, WGM lasing.*

## 1. Introduction

Dielectric micro-cavities have attracted much attention due to their ability to entrap photons in the visible and NIR regions of the electromagnetic spectrum via total internal reflection [1]. Such photon confinement can be used for various purposes, ranging from fundamental studies on Quantum Electro-Dynamics (QED) [2] to more applied fields, such as the development of microscopic laser sources, tunable filters, and transducer mechanisms for optical sensing [3]. Due to the total internal reflection condition, photon entrapment works best for those cavity modes that propagate along the circumference of the cavity. Such modes are often referred to as Whispering-Gallery-Modes (WGMs) in analogy to an acoustic phenomenon discovered by Raleigh more than a hundred years ago [4]. As a glass spherical microcavity providing Q-factors in excess of $10^8$, silica toroidal microcavity resonators provide both long photon storage times and improved spatial confinement over microsphere resonators of comparable size [5]. Furthermore, with highly ideal, tapered-fiber coupling, efficient pumping and laser emission extraction are possible [6]. Among the solid-state microcavity lasers with ultrahigh-Q performance, Rare-earth doped glass microsphere lasers have been successfully demonstrated in last decade [7-10]. The optical modes of spherical dielectric cavity can be calculated by solving Helmholtz equations in spherical coordinates. A significant simplification occurs if the sphere consists of a homogeneous dielectric, and if the optical modes reflect with grazing incidence upon the dielectric-air boundary, such that the polarization can be assumed to be constant along the optical trajectories. Under this assumption the optical modes can be solved by the scalar wave equation approximation and solutions fall into TE n,m,l,p and TM n,m,l,p, where n is radial mode number, m is azimuthally mode number, l is polar mode number, and p is polarization state of mode [11]. In an ideal sphere cavity the optical modes possess (2l+1) degeneracy with respect to the azimuthally mode number m. The toroidal microcavity, which creates dense arrays of ultrahigh-Q microcavity structures in equatorial planes, can reduce modal spectra in comparison with microsphere cavity. In particular, single-mode operation was possible in these devices [12]. Recently, a toroidal microcavity has enabled access to Q-factors is excess of $10^8$, which was the highest value reported on a planar substrate. These toroidal microcavities were silica based and fabricated on silicon chips combining standard silicon technology with ultrahigh-Q fabrication techniques [13].

In this paper, we used surface-tension-induced structure of High erbium doped silica-alumina glass made by molten method to form spherical and/or modified toroidal microcavity laser and

study the lasing characteristics when these devices are coupled to a half tapered optical fiber. Our experiments are focused on high-Q microcavity (with ultra-narrow spectra of laser emission) and reduction of lasing-modes in the Er-doped silica-alumina glass modified toroidal lasers in comparison with microsphere lasers in previous studies [10, 14].

## 2. Experiments

### 2.1. Fabrication of Er-doped silica-alumina glass microcavity lasers

The microcavity lasers have been fabricated by multi-component Er-doped silica-alumina glasses (90 $SiO_2$ - $6Al_2O_3$: $4Y_2O_3$: $xEr_2O_3$, where x = 0.065-0.3 is a molar percent of $Er_2O_3$). We formed Er-doped silica-alumina glass microcavity in the form of sphere and/or modified toroid by following steps: first step is making Er-doped glass microsphere with diameters in the range of 30–100 m by molten method using electrical arc discharge or by $CO_2$-laser beam and second step is forming modified toroidal cavity by irradiation of $CO_2$- laser beam with pressure on microspheres via the silicon substrate. From high thermal conductive coefficient of silicon, the area of Si-substrate is important factor for making glass toroid. In our experiment, the area of Si-substrate was 1-2 $mm^2$.

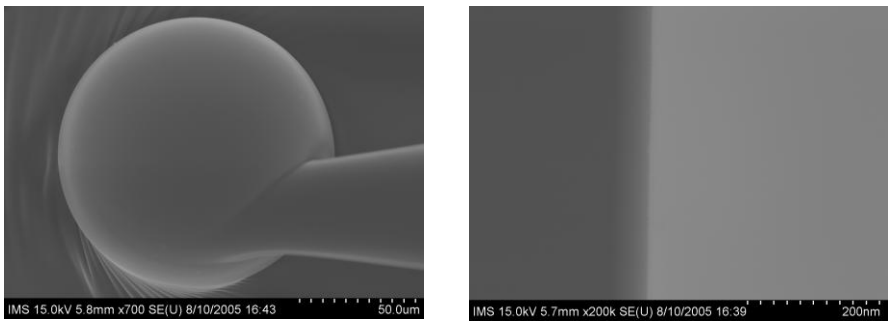


**Fig.1**. FE-SEM images of glass microsphere (left) and dielectric boundary of microsphere (right) made by thermal molten method

Using molten method, the solid glass toroids rely upon surface tension to create perfect smooth dielectric boundary, along which the WGMs are confined. Figure 1 shows the dielectric boundary with surface perfection up to nanometer scale. The diameters of sphere were of 40-200 m and the equatorial diameters and thickness of glass modified toroids was of 90-160 m and 20-30 m, respectively.

### 2.2. Excitation and extraction of WGMs in micro-cavity

The pump laser beam and the collected lasing WGMs are coupled to two different half tapered fibers. Efficient optical coupling to the glass micro-cavity both for pumping and for laser output extraction was performed with optical fiber tapers with waist diameter of 1 4 m, which made from the standard telecommunication single-mode fiber by chemical treatment in 15 mol% -HF solution. The diameters at the waist of fiber tapers were chosen to optimize phase matching and coupling to the fundamental WGM (*n =1, m = l*). We choose 976nm- laser diode adjusted the output power from 0 to 170 mW in single-mode emission (SDLO-2564-170) for excitation of Erbium ions. To couple light efficiently in and out of the micro-cavity laser, the half tapered optical fibers were aligned in the equatorial plane of micro-cavity. The micro-cavity laser was fixed and the half tapered fibers were attached to a micro-positioner with piezoelectric stage that allowed for their precise positioning with respect to the micro-cavity. The collected laser output fiber can be forward or backward with respect to the pumping direction. The non-absorbed pump beam and the luminescence or laser emission corresponding to the WGMs of the micro-cavity are separated with a de-multiplexing coupler 980nm / 1550nm. Thus we can analyze simultaneously the pump and the laser signals. The spectral characteristics of the emission

around 1550 nm were analyzed with a 0.01 nm resolution optical spectrum analyzer (OSA: Advantest Q8384) directly after the de-multiplexing coupler.

## 3. Results and discussions

The input threshold pump power can be obtained directly from experiment by setting the pump power from zero. In our Er-doped silica-alumina glass micro-cavity laser, we only obtained supper luminescent emission, when the pump power at wavelength of 976 nm was below 2.0 mW. The laser oscillation modes (WGMs) of the Er-doped glass micro-cavity are in the wavelength ranging from 1510 nm to 1610 nm (see fig. 2). Depending on the gain spectral region of the highly Er-doped silica-alumina glass, the lasing wavelength of the micro-cavity lasers varied within 1540-1610 nm range, which is in the both C- and L-bands.

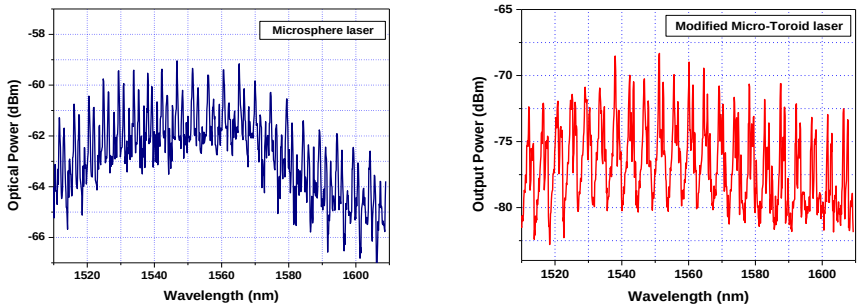


**Fig. 2**. Superluminescent spectra of micro-sphere (left) and micro-toroidal (right) lasers pumped by 976nm-laser beam with light power of 2mW (below threshold)

In addition, for any equatorial diameters of the sphere and/or toroid we obtained an enhancement of the laser intensity when increasing the Er-concentration from 1,250 to 3,000 ppm in the silica-alumina glass matrix. The lasing emission could be obtained by forward and backward coupling configuration.

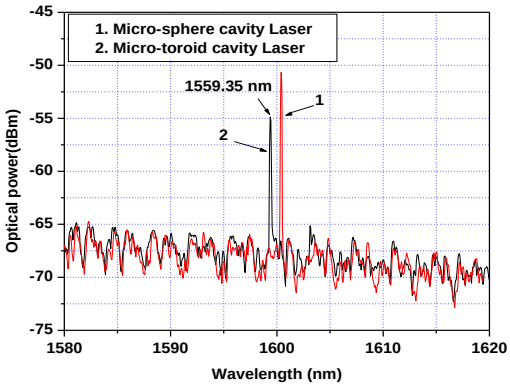


**Fig.3.** Single-mode WGM lasing from micro-sphere (1) and micro-toroid (2) lasers pumped at threshold by 976nm-laser beam with 2.2mW and 2.7mW, respectively.

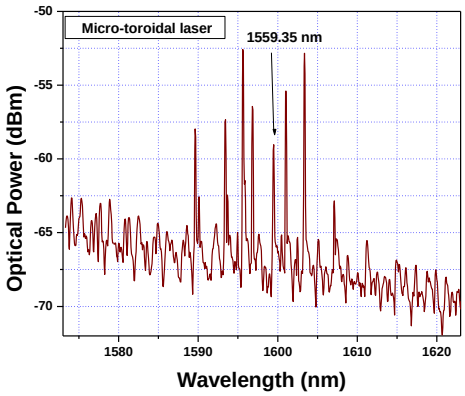


**Fig.4.** Multi-mode WGM lasing from micro-toroid cavity lasers pumped by 976nm-laser beam with 3mW.

Figure 3 shows the spectra of single-mode lasing at laser threshold obtained from 90 μm-diameter and from 110 μm – equatorial diameter of spherical and modified toroidal glass micro-cavity laser doped with 2,500 ppm of $Er^{3+}$ ions, respectively. The WGM lasing spectra rounding 1600 nm-wavelength gives good evidence for larger gain in L-band in highly Er-doped sol-gel silica-alumina glasses. By increasing the pump power the number of lasing modes was increased and the wavelength of lasing peak would be shifted to short range. Figure 4 presents multi-mode

lasing spectra from the same modified toroidal micro-cavity lasers, when pump optical power increased up to 3 mW. We can see, the lasing mode of toroidal micro-cavity laser at wavelength 1599.349 nm was the same at threshold, and all most of new lasing modes were shifted to the shorter band. The pump transmission was estimated about ~12 % in this measurement, so the actual coupled threshold pump power is estimated to be approximately 0.3 mW. As we known, the lasing threshold is a sensitive function of the cavity configuration and coupling gap width between toroidal surface and tapered fiber. In our experiment, we can remark, that threshold optical pump power in the case of toroidal micro-cavity is a same value in comparison with micro-spherical cavity. Experiment shows, that eventually lasing at 1600 nm can no longer supported with increasing pump power and/or gap width because they cannot be compensated by the relatively small gain at this wavelength range. When pump power was more than 10 mW the lasing spectra of micro-cavity lasers, in general, would be shifted to short-wavelength range. In our case, the WGMs of modified micro-toroidal laser had been distributed in the wavelength range 1550-1580 nm and the number of WGMs of this one was decreased in contradiction with large WGM spectra in range of 1540-1600 nm from micro-sphere laser at the same pumped condition (see fig. 5). Figure 6 demonstrates the highest WGM power lasing from micro-sphere laser with diameter of 110 □ m and the WGM amplified by EDFA. The maximum lasing output power of one WGM, we achieved, are of -3.2 dBm and of -5.5 dBm from the Er-doped silica-alumina glass spherical and/or toroidal micro-cavity lasers, respectively. The high output power of lasing WGMs in our micro-cavity lasers may be caused by good tapered-micro-cavity coupling at 976 nm – pump and a homogeneous distribution of Er-ions in the silica-alumina glasses.

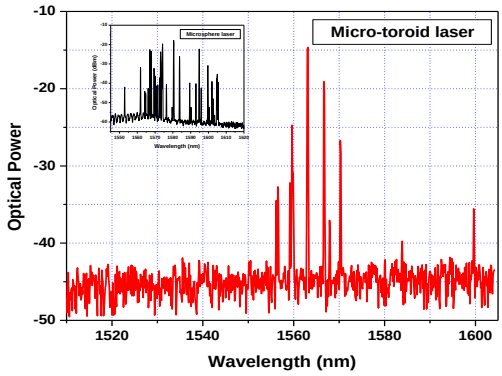


**Fig.5**. WGMs measured by the fiber taper coupling, when pump power is 90 mW (Lasing peak was at 1563.09 nm). Inset: WGM spectra from microsphere laser at same pump.

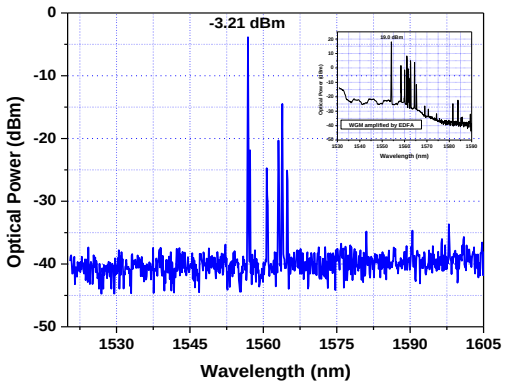


**Fig.6**. Highest power of -3.2 dBm of WGMs from micro-sphere cavity laser. Inset: WGM signal of 19 dBm amplified by EDFA.

Number of collected WGMs and laser output power depend upon many parameters such as loading conditions (i.e. waist diameter of half-taper fiber, gap width between taper fiber and cavity), diameter and eccentricity of sphere, Er-ion concentration. In the case of well satisfying phase condition, single-mode operation can be occurred. In our previous results [14], the single-mode lasing spectra was obtained when the gap width was changed in the range 0.2-1□ m. Figure 7 presents a series of WGM lasing wavelengths under varying gap width between taper fiber and surface of toroidal micro-cavity laser. The multi-mode (fig.7a) and single-mode lasing spectra (fig.7b) with output power of -19 dBm at the same wavelength of 1561.45 nm were obtained from modified toroidal micro-cavity laser, when the gap widths were changed from 1.5 to 0.5□ m, respectively.

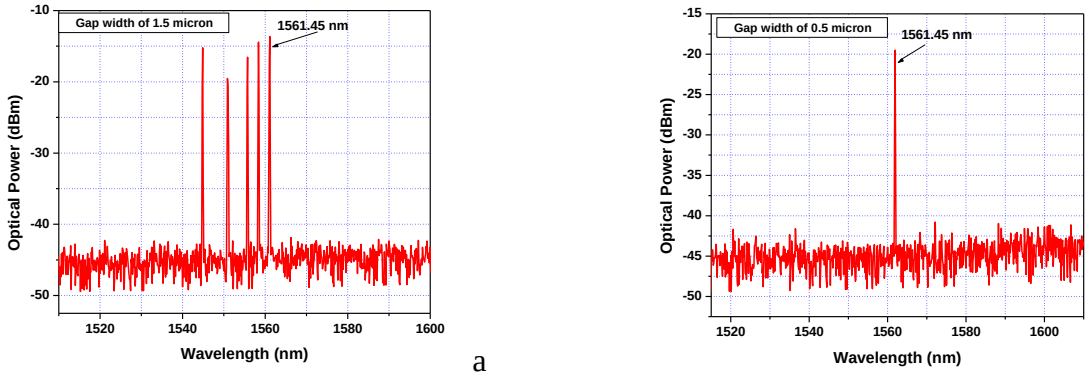


a

**Fig.7**. WGM lasing spectra obtained from toroid micro-cavity laser under varying gap width changed from 1.5 micron (a) to 0.5 micron (b). The WGM single-mode power was achieved up-to -19 dBm.

In practice, there are series of peaks in the single-mode obtained from OSA-Advantest Q8384 with resolution of 0.01 nm and these peaks should be analyzed by Fabry-Perot Etalon (FPE). Using formula $Q= \omega/\Delta\omega$ [13] for calculation of Q-factor, we obtained $Q= 5.10^7$-$10^8$ for our spherical and/or modified toroidal micro-cavities. This result was good agreement with the other one in the sources of [6-9].

## 4. Conclusions

In this paper we have been reviewed a method of fabrication and characterization of micro-cavity lasers based on Er-doped silica-alumina glasses, which has been lasing ultra-narrow spectra at 1550 nm-wavelength range. The lasing output powers of one whispering-gallery-mode were reached up to -3.2 and -5.5 dBm for spherical and modified toroid micro-cavity lasers, respectively. The Q-factor of glass micro-cavities was achieved up to $5.10^7$-$10^8$ and the reduction of lasing WGMs was obtained in the modified toroid micro-cavity laser in comparison with spherical micro-cavity under the same diameter and pumping conditions. We have been successfully controlled the number of lasing WGMs by changing the gap width between taper fiber and cavity and by waist diameter of taper. The single-mode spectra of Er-doped glass micro-cavity laser has output power and ultra-narrow line-width, to the best of authors' knowledge, suitable for applications in the field of quantum informatics and optical sensoring technique.

***Acknowledgment:*** *This work was financially supported National Natural Science Program in Physics of Vietnam 2006-2008 under Grant No. CB14. The authors would like to thank Prof. Acad. Nguyen Van Hieu for his fruitful advices and active support to this work. The authors express our appreciation to the State Key Lab. on Electronic Materials and Devices for testing equipments.*

## References

1. K. J. Vahala, *Optical microcavity*, Nature. **424**, (2003) 839
2. J. M. Gérard, B. Sermage, B. Gayral, B. Legrand, E. Costard, and V. Thierry-Mieg, *Enhanced Spontaneous Emission by Quantum Boxes in a monolithic optical microcavity*, Phys. Rev. Lett. **81**, (1998) 1110
3. F. Vollmer, D. Braun, A. Libchaber, M. Khoshsima, I. Teraoka, and S. Arnold, *Protein detection by optical shift of a resonant microcavity*, Appl. Phys. Lett. **80**, (2002) 4057
4. Weller, M. Himmelhuasa, *Radial cavity mode excitation in fluorescent core-shell microcavities*, Appl. Phys. Lett., **89**, (2006) 241105
5. D. K. Armani, T. K. Kippenberg, S. M. Spillane, and K. J. Vahala, *Ultra-high-Q toroid microcavity on a chip*, Nature, **421**,(2003) 925

6. M. Cai, O. Painter, and K. J. Vahala, *Observation of critical coupling in a fiber taper to a silica-microsphere Whispering-Gallery- Mode system*, Phys. Rev. Lett., **85**, (2000) 74
7. M.Cai, O.Painter, K.J.Vahala, *Fiber-coupler microsphere laser*, Opt.Lett., **25**, (2000) 260
8. L.Yang, K.J.Vahala, *Gain functionalization of silica microresonator,* Opt.Lett., **28**, (2003) 592
9. X.Peng, F. Song, S. Jiang, N.Peyghambarian, M. Kuwata-Gonokami, *Fiber-taper-coupler L-band $Er^{3+}$-doped tellurite glass microsphere laser*, Appl.Phys. Lett., **82**, (2003) 1497
10. V.H.Pham, T.T.H. Chu, Q.H.Hoang, *L-band emission of micro-sphere lasers based on Er-doped sol-gel silica-alumina glasses,* Appl. Phys. Lett., **87,** (2005) 161110
11. B.E.Little, J.P.Laine, H.A.Haus, *Analytic theory of coupling from tapered fibers and half-blocks into microsphere resonator*, J. Lightwave Technol., **17** (4), (1999) 704
12. L.Yang, D.K.Armani, K.J.Vahala, *Fiber-coupler Erbium microlasers on a chip*, Appl. Phys. Lett. **83**,(2003) 825
13. B.Min, T.J.Kippenberg, L.Yang, K.J.Vahala, *Erbium-implanted high-Q silica toroidal microcavity laser on a silicon chip*, Phys. Rev.A, **70**,(2004) 033803
14. Le Ngoc Chung, Chu Thi Thu Ha, Nguyen Thu Trang, Pham Thu Nga, Pham Van Hoi, Bui Van Thien, *High-power micro-cavity lasers based on highly Erbium-doped sol-gel aluminosilicate glasses,* J. Materials Sci & Engineer. B, **131**, (2006) 27

# ULTRAVIOLET LASER EMISSION FROM A MICRO-PULLING DOWN METHOD GROWN $CE^{3+}$:LICAALF$_6$

**Pham H. Minh[a,b,c], Cadatal Marilou [a,b], Nakazato Tomoharu[c], Estacio Elmer[c], Sarukura Nobuhiko[c], Suyama Toshihisa[d], Fukuda Kentaro [d,e], Kim Kyoung Jin[e], Yoshikawa Akira[e], Saito Fumiyoshi[e]**

[a)]Institute for Molecular Science, Myodaiji, Okazaki, Aichi 444-8585, Japan
[b)]The Graduate University for Advanced Studies, Hayama, Kanagawa 240-0193, Japan
[c)]Osaka University, 2-6 Yamadaoka, Suita, Osaka 565-0871, Japan
[d)]Tokuyama Corporation, Shibuya-ku, Tokyo 150-8383, Japan
[e)]Tohoku University, 2-1-1 Katahira, Aoboa-ku Sendai, 980-8577, Japan

**Abstract:** Recent improvements with the micro-pulling down method have made the quality of grown crystals comparable with those prepared by Czochralski, Bridgman, or other classical growth techniques. There is only one report on the successful lasing from a crystal grown by this technique. Lasing in the infrared region has been reported, in the case of oxide, with a YAG single-crystal fiber grown by this method. We have successfully grown laser quality Ce3+:LiCaAlF6 crystal using this method. Lasing at 290 nm with a maximum output energy of 1 mJ with absorbed pump energy of 6 mJ and a slope efficiency of 23 % is achieved.

## 1. Introduction

Micro-pulling down (μ-PD) method is a relatively new crystal growth technique mainly developed at Tohoku University, Japan [1,2]. Recent improvements of this method have made the quality of μ-PD method grown crystals comparable with those prepared by Czochralski (CZ), Bridgman, or other classical growth techniques. Owing to a fast growth speed, a high quality crystal can be grown using less than 1 g of raw material in 5 – 12 hours. This allows growth of large crystals at a shorter time and at a lower cost compared with other melt growth schemes [3,4]. Moreover, this method has the capability to control the shape of the grown crystal such as fiber, rod, tube, and so on. Presently, this method is suitable only for materials survey rather than the production of highly homogeneous, high-quality crystals. On the other hand, $Ce^{3+}$:LiCaAlF$_6$ (Ce:LiCAF) have found considerable attention because of their applications in various fields such as laser gain media, optical materials, and just recently, as scintillators [5,6]. There has been only one report on the successful lasing from a μ-PD method grown crystal, lasing in the infrared (IR) region has been reported in a Nd:YAG single-crystal fiber grown by this method [7]. This is the only report about lasing from a μ-PD method-grown crystal.

This paper presents the successful growth of a laser quality Ce:LiCAF crystal using the μ-PD method. We also report laser emission in the UV region at 290 nm. We have achieved a 23% slope efficiency from a Brewster-cut Ce:LiCAF. Our results not only reinforce the merits of this method as a useful tool for fluoride crystal growth but also provide a faster and more economical growth scheme for laser-grade crystals.

## 2. Lasing from Ce:LiCAF grown by Micro-Pulling down

The Ce:LiCAF crystal is grown by the μ-PD method modified for fluoride crystal growth as shown in Figure.1, High purity (>99.99%) CeF, $AlF_3$, $CaF_2$, and LiF (Stella Chamita) were used as starting materials. They were thoroughly mixed and placed inside a graphite crucible. The crucible was charged up to 100 vol% powder of starting materials or about 5-20 vol% regarding the melt. The chamber was then baked at 600 $^oC$ for 1 hour in order to remove oxygen traces from the moisture of raw materials and adsorbates on the chamber surface. Simultaneously, the chamber is further evacuated to $10^{-5}$ Torr. After baking, the recipient is filled with a mixture of

Ar and $CF_4$ until ambient pressure. Ar and $CF_4$ were used because they are not reactive with the graphite crucible. The crucible is then heated to a melting temperature of about 1450 $^oC$. The crystal is grown with complete solidification of the melt charged in the crucible and a pulling rate of 0.1 mm/min.

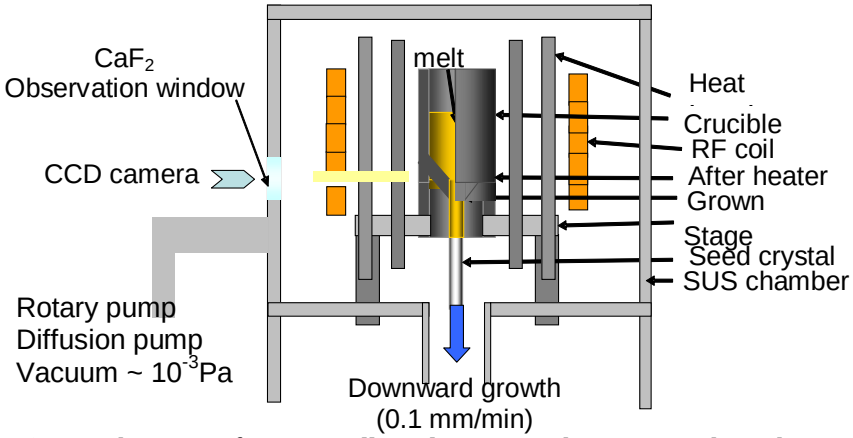


**Fig.1**. Schematic of Micro-pulling down growth system with RF heating.

It was grown using a radio frequency (RF) heated μ-PD apparatus with a graphite crucible Temperature is raised by induction heating of a conductor coil by electromagnetic induction. Currents are induced in the coil and these currents cause heating. The frequency used is varied to control the amount of current and consequently, the temperature. The 30-mm long, 2-mm wide crystal used in the experiment is shown in Fig 2. Both ends of the as-grown crystal did not have any coating; the c-axis is in the growth direction. Note that the sides of the crystal are not polished. The laser resonator is established by using a flat high reflector with > 99% reflection at 290 nm and a flat output coupler with a 60% transmission at 290 nm. The length of the laser cavity is 6 cm. The sample is simultaneously pumped by the fourth harmonics of two synchronized Nd:YAG lasers operating at 266 nm and 10 Hz repetition rate. Cylindrical lenses with a focal length of 300 mm are used to individually focus the pump beams onto opposite sides of the crystal. The distance of the lens to the sample is set at 260 mm to ensure that the beam excites the whole side with enough fluence without ablating the crystal. For reference, each side is consecutively pumped while maintaining the other parameters. The output energy is measured using an energy meter (Gentec ED100 joule meter). Fig. 3 shows the measured oscillator output energy as a function of the absorbed pump energy for one- and two-side pumping configurations.

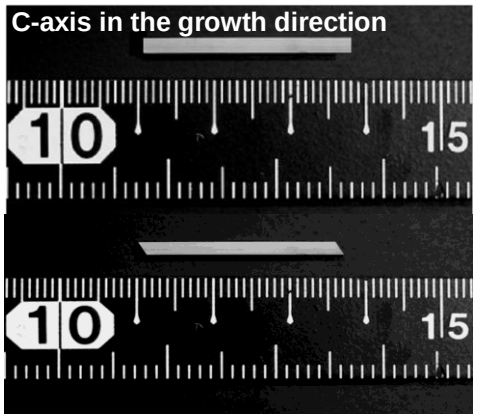


**Fig. 2.** Photograph of as-grown Ce:LiCAF crystal.

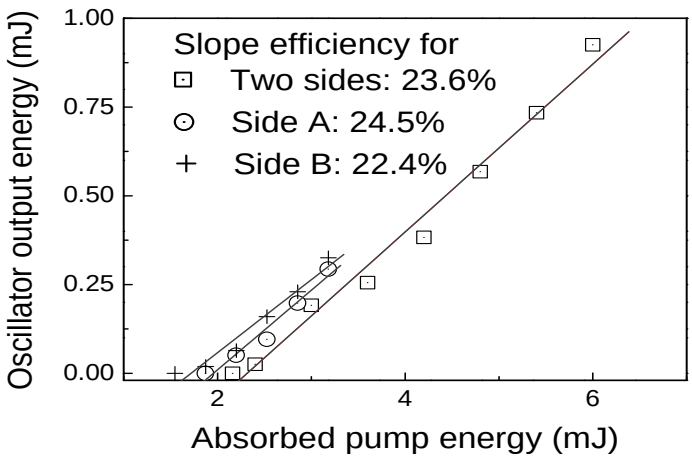


**Fig. 3.** Output energy as a function of absorbed pump energy for one-and two-side pumping configurations.

The absorbed pump energy takes into consideration the absorption coefficient of the Ce:LiCAF crystal. The sample is doped with 1 mol% $Ce^{3+}$ ions. Independent transmission measurements with the polished crystal reveal that roughly 10% of the pump energy is absorbed

The output energy remained linear with absorbed energy. We were able to achieve a slope efficiency of 23% for the one- and two-side pumping configurations. Slope efficiency and output energy for each side are comparable, indicating that the emission condition for individual sides is similar. For two-side pumping, slope efficiency and oscillator output energy is almost the same with that of one-side pumping configuration. Equally distributing the total pump energy to two sides yields the same output energy as pumping one side with the equivalent energy. This implies that two-side pumping is more advantageous than one-side-pumping by reducing damage to the crystal. Maximum output pulse energy of 1 mJ at 290 nm is achieved with absorbed pump energy of 6 mJ with a slope efficiency of 23%.

In summary, laser quality Ce:LiCAF crystal is successfully grown by the μ-PD method. Lasing at 290 nm is observed from a 30-mm long, 2-mm wide Brewster-cut crystal pumped on opposite sides with the fourth harmonics of two Q-switched, 10-Hz Nd:YAG lasers. Maximum output energy of 1 mJ and a slope efficiency of 23 % is demonstrated. This is the first demonstration of lasing in the UV region from a μ-PD method grown fluoride crystal. Flexibility and lower cost of this crystal growth scheme will drastically reduce the cost of crystal growth. This improvement will strongly enhance the application of Ce:LiCAF laser itself.

**References**

1. A. Yoshikawa, M. Nikl,G. Boulon, and T. Fukuda, Opt. Mater. 30,(2007), 6.
2. A. Yoshikawa, T. Satonaga, K. Kamada, H. Sato, M. Nikl, N. Solovieva, and T. Fukuda. J. Cryst. Growth 270, (2004), 427.
3. A.Novoselov, A. Yoshikawa and T. Fukuda,Current Topics in Cryst. Growth Res. 7, (2004), 87
4. A. Yoshikawa, T. Satonaga, K. Kamada, H. Sato, M. Nikl, N. Solovieva, and T. Fukuda. J. Cryst. Growth 270, (2004), 427.
5. M.A. Dubinskii, V.V. Semashko, A.K. Naumov, R.Y. Abdulsabirov, and S.L. Korableva. OSA Proc. Adv. Solid-State Lasers 15, (1993), 195.
6. M.A. Dubinskii, V.V. Semashko, A.K. Naumov, R.Y. Abdulsabirov, and S.L. Korableva. Laser Phys3, (1993), 216.
7. J. Didierjean, M. Castaing, F. Balembois, and P. Georges. Opt. Lett. 31, (2006), 3468

# CHARACTERISATION OF SEMICONDUCTOR OPTICAL AMPLIFIERS FOR ALL-OPTICAL REGENERATION

**M. N. Ngo [a], M. Gay [a], L. Bramerie [a], G. Girault [a] , Q. T. Le [a], J.-C. Simon [a], R. Brenot [b], G.-H. Duan [b] , D. Reid [c] , L. Barry [c]**

[a)] FOTON-CNRS, ENSSAT / Université de Rennes 1, 6 rue de Kerampont, 22305 Lannion, France, *ngo@enssat.fr*

[b)] Alcatel Thales III-V Lab, Route Départementale 128, 91767 Palaiseau, France, *guanghua.duan@3-5lab.fr*

[c)] RINCE, Dublin City University, Glasnevin, Dublin 9. Ireland, *liam.barry@dcu.ie*

**Abstract:** We report on the characterisations of different semiconductor optical amplifiers (SOA) which are designed and fabricated for All-Optical Regeneration. Dynamic measurements in pump-probe configuration show short time response of around 50 ps. Chirp measurements by FROG technique are also reported. The characterisations demonstrate the potential of these components to be associated with interferometer and optical filtering in order to achieve regeneration functions at bit rates of 40 Gbit/s and above.

***Key words**: Semiconductor optical amplifiers, all-optical regeneration*

## 1. Introduction

Until now, signal processing in long distance transmission systems is performed by optoelectronic repeaters. However the higher the bit rate, the more expensive and complex the optoelectronic repeaters. In this circumstance, all-optical devices become attractive solutions. Therefore, an all-optical solution should have criteria such as stability, compactness, simplicity of operation and low-power consumption. The two functionalities which are closest to implementation in real systems are wavelength conversion and regeneration.

Regenerators are principally fibre-based [1-3] or semiconductor-based devices [4-6]. These last ones offer many advantages: small size, simple electrical pumping, broad spectral range and opportunities for integration and mass production. Among these components, the semiconductor optical amplifier (SOA) with gain saturation, low optical and electrical power consumption and fast response is a good candidate. Moreover, novel generation of SOAs [7], quantum-dot SOA, and new SOA based technique [8] show performances at high bit rates, 40 Gbit/s for regeneration and up to 320 Gbit/s for wavelength conversion. Especially quantum dots SOAs are predicted to have a very fast response [9] and could induce lower additional chirp in the modulated signal than bulk ones, thereby allowing a longer transmission distance [10]. These results give strong motivations to exploit SOAs for all-optical regeneration. In this paper, we present characterisations of different SOA which are designed and fabricated for all-optical regeneration applications. All these SOAs emit in the C-band. Their gain recovery time responses are measured via pump-probe experiments. This parameter is primary to evaluating patterning effects and the bit rate at which these SOAs could be operated. At last, the study of chirp induction to evaluate linewidth enhancement factor (Henry factor) is also presented. The Henry factor is important in case of association with interferometers or shifted filtering techniques.

## 2. Characterized devices

Various SOAs from Alcatel-Thales III-V lab were characterized in the framework of the French project FUTUR. These SOAs, presented in table 1, are designed and fabricated in order to perform different functions of regeneration at 40 Gbit/s and 160 Gbit/s. As far as bulk

structure based SOAs, two chips were studied with the same length but with different confinement factor (20% and 80%). This last parameter affects significantly the time response which is important when the bit rate increases. These bulk structures were compared to a quantum dot SOA.

**Table 1**. Description of measured SOAs.

| SOA | Active structure | Optical confinement (%) | Chip length (mm) |
|---|---|---|---|
| 1 | Bulk | 20 | 1 |
| 2 | Bulk | 80 | 1 |
| 3 | Q. Dot | ~1 | 2 |

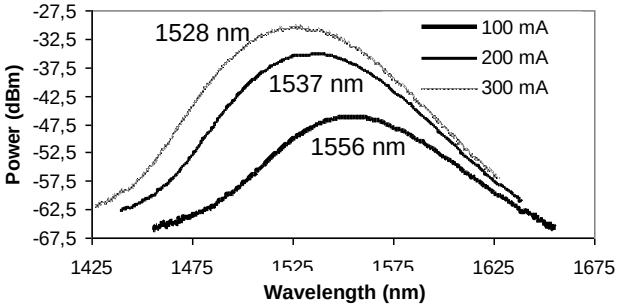


**Figure 1**. Amplified spontaneous emission of QD-SOA for different bias currents.

The two bulk SOAs had a gain peak around 1550 nm and an internal gain around 30 dB. For the QD-SOA, its spectral emission is displayed in figure 1 for different bias current. The emission peak is located in the C-band at bias current lower than 300 mA and covers almost the entire C-band for currents lower than 300 mA. In the literature, one of the first quantum dot structures emitting in the C-band was published in 2003 [11] and a little later some quantum dots structure have been exploited for all-optical regeneration [7, 12]. The internal gain of QD structure is 20 dB.

## 3. Gain dynamic measurement

SOA-based wavelength conversion and regeneration schemes exploit gain modulation, cross-phase modulation or four-wave mixing. When the gain modulation is used, attention must be paid to the gain recovery time of the SOA. More exactly, we consider this time response as the time that gain needs to recover from 10% to 90% of its steady-state value. We measure this time via a pump-probe configuration. The experimental measurement set-up is shown in the figure 2.

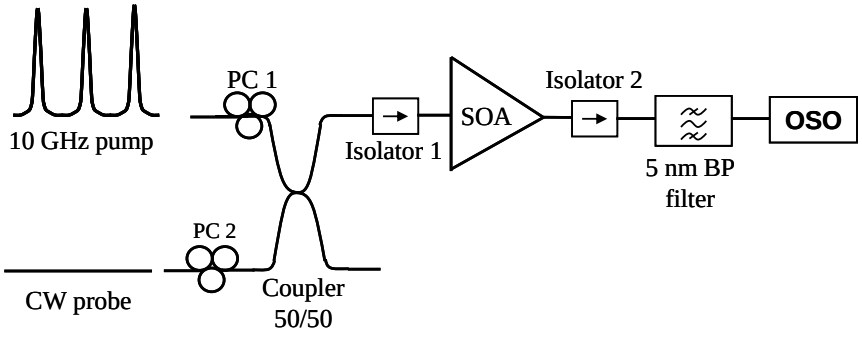


**Figure 2**. Scheme of gain dynamic measurement

A 10 GHz optical clock is injected into the SOA to modulate its gain. For each measured SOA, the pump wavelength is selected as the peak of the amplified spontaneous emission spectrum. The probe is provided by a CW tunable laser. A 5 nm optical Band Pass (BP) filter is used to reject the pump and select the probe to Optical Sampling Oscilloscope (OSO) with a time resolution of 1 ps. The gain recovery time is measured for different SOA and for different gain compressions. Results are shown in figure 3.

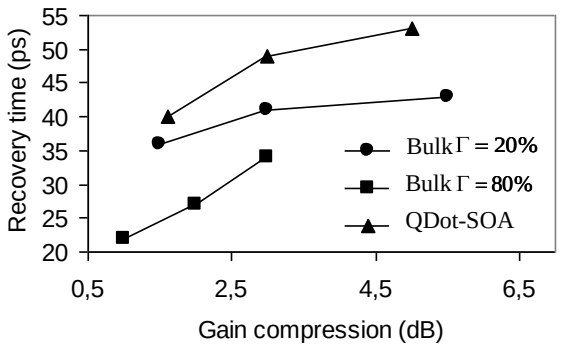


**Figure 3**. Gain recovery time as a function of gain compression.

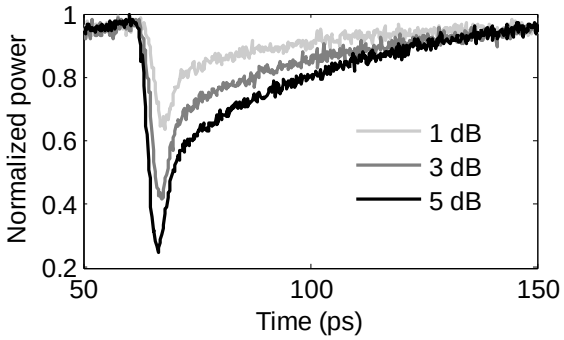


**Figure 4**. Waveforms of CW probe light at the QD-SOA output for various gain compressions, modulated by a 2.3 ps pulse pump.

In each case, the gain recovery times of the three SOAs increase with their gain compressions. This result could be explained by the fact that the greater the gain compression, the greater depletion of electrons in excited states by stimulated emission. The SOA#1 (See table 1) has a gain recovery time around 40 ps for 3 dB of gain compression and the second one has a smaller time around 27 ps for the same gain compression. The two SOA have the same length of waveguide. The gain recovery time of the 2$^{nd}$ structure is shorter because the gain recovery time is inversely proportional to the confinement factor [13]. At 40 Gbit/s, the bit slot is 25 ps long, therefore the slow time response of the SOA#1 may introduce patterning effects which could lead to signal degradations. On the contrary, the SOA#2 could be exploited at this bit rate with small gain compression (<3dB).

Sample 3 (QD-SOA) presents a gain recovery time of around 50 ps for 3 dB of gain compression. In the figure 4, we present the waveforms of the modulated probe at the QD-SOA output and for different gain compressions and a pump pulse width of 2.3 ps. Similar waveforms were also achieved with the SOA#1 and the SOA#2. These curves show the presence of ultrafast gain dynamic, which is dominated by intraband processes, and the presence of slower gain dynamic, which is linked to interband recombinations [14]. The two time constants were evaluated by combining two simple exponential functions, giving a time-constant of 2 ps for fast processes and a time-constant of 65 ps for slow processes. The measured time-constant of fast processes is limited by the input pump pulsewidth ; this time should be measured more exactly with shorter pulses and a higher time resolution device. Because of the slow processes, this SOA is not fast enough to operate at bit rate above 40 Gbit/s. However this time response was achieved with a SOA whose confinement factor was only 1%. If this parameter could be increased, we could significantly reduce the gain recovery time of the QD-SOA. Then we could expect a time response smaller than 10 ps with a confinement factor greater than 10% as it is shown thanks to simulations in the reference [9].

## 4. Induced chirp measurement

In some cases, it is useful to have SOAs which induce low chirp to avoid limited transmission distances. On the contrary, in the case of shifted filtering [8], or in interferometer configuration [15], the chirp induced plays an important role and it could be useful to evaluate Henry factor. By using the FROG (Frequency Resolved Optical Gating) technique, we have measured the induced chirp of a 10 GHz optical clock signal injected directly in the investigated SOA. The pulse-width is about 2 ps and initial pulses have a linear chirp. At the output of the SOA, the signal is analysed in phase and amplitude with a FROG to deduce

additional chirp. We investigated and compared the induced chirp by the two bulk SOAs, SOA#1 and SOA#2. Results are shown in the figure 5.

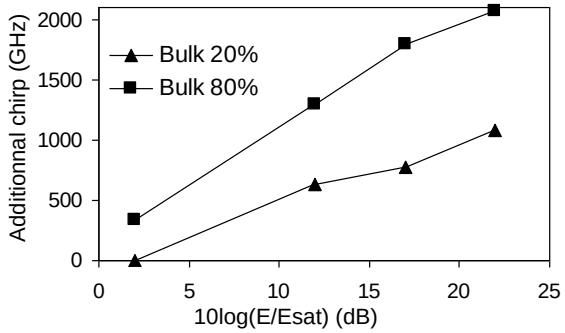


**Figure 5**. Induced chirp by SOA as a function of E/Esat.

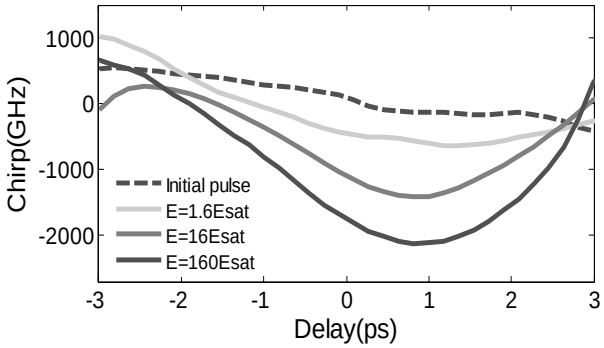


**Figure 6.** Chirp-form changes by SOA 80% confinement factor of a pulse for various E/Esat.

Because of the pump pulsewidth (2.3 ps) is much smaller than the gain recovery time of the two SOAs (superior to 20 ps), the SOAs are in saturation regime by energy. Then the additional chirp is measured for different values of ratio between the pulse and the SOAs saturation energies E/Esat. An additional chirp of 2000 GHz, which is measured at its maximum, is obtained with SOA#2 when the pulse energy was E=160Esat (or 10log(E/Esat)=22). With both bulk SOAs, the induced chirp increases rapidly when E/Esat increases. This result can be explained by the fact that the induced chirp is proportional to the rate of change of the gain compression and this increases with E/Esat. As expected, SOA#2 which possessed a high confinement factor (80%) induced twice as much chirp as SOA#1 with its lower confinement factor (20%). The higher frequency deviation is due to faster carrier dynamics of SOA#2. In figure 6, the chirp is plotted as a function of time indicating the chirp profiles of pulses before and after SOA#2. The initial pulse presents a linear chirp. At the output, the chirp is non-linear, typically with a pseudo-parabolic profile. This non-linear shape of the chirp could be difficult to compensate for, but the great induced chirp should be useful and exploitable in configurations in which phase modulation is used.

## 5. Conclusion

We characterized various SOAs in bulk and quantum-dot structures. The bulk SOA with the higher confinement factor has shown some potential to operate regeneration at 40 Gbit/s in weak gain compression (<3dB) regimes thanks to its fast gain dynamic (gain recovery time <25 ps). The QD-SOA has shown the presence of ultra-fast processes and slow processes and an effective 10%-90% gain recovery time of around 50 ps for 3 dB gain compression in spite of its small confinement factor (~1%). We also quantified the high level of chirp induced (2000 GHz) by bulk SOA, which could be exploited in configurations in which phase modulation is used.

***Acknowledgments***

*This work has been carried out in the framework of the French research program FUTUR and the European project ERA-SPOT1 (ORION 160). These programs are supported by "Région Bretagne", by FEDER and by "Ministère de la recherche". Results were achieved in the PERSYST platform and RINCE laboratory*.

**References**

1. P. Mamyshev, *Proc. ECOC1998*, pp. 475-476, 1998.
2. M. Asobe, T. Kanamori, K. I. Kubodera, *J. Quantum Electron*., vol. 29, no. 8, pp. 2325-2333, 1993.

3. N. J. Dohan, D. Wood, *Opt. Lett*., vol. 13, no. 1, pp. 56-58, 1998.
4. R. J. Manning, D. A. O. Devies, A. D. Ellis, D. M. Patrick, Proc. *Topical Meeting Opt. Amplifiers and their Applicat. (OAA'95)*, SaC1, Davos (Suisse), pp. 226-229, 1995.
5. K. Nishimura, R. Inohara, M. Tsurukawa, M. Usami, *Optical Fiber Communication Conference 2003*, paper TuP5, 2003.
6. O. Leclerc, G. Aubin, P. Brindal, J. Mangedey, H. Choumane, S. Barre, J. L. Oudar, *Electron. Lett*., vol. 36, no. 23, pp. 1944, 2000.
7. T. Akiyama, M. Ekawa, M. Sugawara , K. Kawaguchi, H. Sudo, H. Kuwatsuka, H. Ebe, A. Kuramata, and Y. Arakawa, *Optical Fiber Communication Conference 2005*, paper OWM2, 2005.
8. Y. Liu, E. Tangdiongga, Z. Li, H. de Waardt, A. M. J. Koonen, G. D. Khoe and H. J. S. Dorren, *Optical Fiber Communication Conference 2006*, paper PDP28, 2006.
9. M. Sugawara, T. Akiyama, N. Hatori, Y. Nakata, H. Ebe and H. Ishikawa, *Measurement Science and Technology*, vol. 13, pp. 1683-1691, 2002.
10. R. Brenot, M. D. Manzanedo, J.-G. Provost, O. Legouezigou, F. Pommereau, F. Poingt, L. Legouezigou, E. Derouin, O. Drisse, B. Rousseau, F. Martin, F. Lelarge, and G. H. Duan, *Proc.ECOC2007*, paper 08.6.6_1569044496, 2007.
11. C. Paranthoen, C. Platz, G. Moreau, N. Bertru, O. Dehaese, A. Le Corre, P. Miska, J. Even, H. Folliot, C. Labbe, et al., *J. Crystal Growth*, vol. 251, no. 1, pp. 230-235, 2003.
12. J. Renaudier, B. Lavigne, M. Jourdran, P. Gallion, F. Lelarge, B. Dagens, A. Accard, O. Legouezigou, and G. H. Duan, *Proc. ECOC 2005*, Th 4.3.4, 2005.
13. L. Zhang, I. Kang, A. Bhardwaj, N. Sauer, S. Cabot, J. Jaques, and D. T. Neilson, *Photon. Technol. Lett.*, vol. 18, no. 22, pp. 2323-2325, 2006.
14. M. van der Poel, E. Gehrig, O. Hess, D. Birkedal, and J. Hvam, "Ultrafast gain dynamics in quantum-dot amplifiers: Theoretical analysis and experimental investigations", *J. Quantum Electron.*, vol. 41, no. 9, pp. 1115-1123, 2005.
15. J. Leuthold, C.H. Joyner, B. Mikkelsen, G. Raybon, J.L. Pleumeekers, B.I. Miller, K. Dreyer and C.A. Burrus, *Electron. Lett*., vol. 36, no. 13, pp. 1129-1130, 2000.

# 1550 nm InGaAsP/InP SPOT SIZE CONVERTER SEMICONDUCTOR OPTICAL AMPLIFIER MODULES AND THEIR APPLICATION

**Vu Doan Mien, Vu Thi Nghiem, Dang Quoc Trung,**
**Pham Van Truong, Tong Quang Cong and Ngo Bich Cam**

Institute of Materials Science, Vietnamese Academy of Science and Technology,
18 Hoang Quoc Viet, Cau Giay, Hanoi, Vietnam,
*E-mail: mienvd@ims.vast.ac.vn*

**Abstract:** Semiconductor Optical Amplifier modules based on the new kind of 1550 nm InGaAsP/InP SOA chips with spot size converter have been prepared and characterized. The SOA chips have the angled-facet ($7^o$) or direct active regions with spot size converter in order to minimize the polarization dependence of gain and to have some other good optical properties. With the use of the new precision alignment equipment and UV curable adhesive for fixing processes we could prepare the SOA modules with the good characteristics such as small signal fiber-to-fiber gain (> 16 dB), high 3dB gain bandwidth (66 ÷ 77 nm), small ASE ripple (< 0.7 dBm), high saturation output signal power (3.7 ÷ 6.7 dBm) and low polarization sensitivity of gain (< 1.0 dB). The fiber ring lasers based on the SOA modules also have been prepared and characterized with the aim of using them as a light source for WDM in fiber optic communication systems. The fiber ring lasers based on SOAs and fiber Bragg gratings (FBGs) have the single longitudinal mode output with the high side mode suppression ratio (> 30 dB) or multimode operation depending on the number of FBGs in the ring.

***Key words**: Semiconductor Optical Amplifier, spot size converter, fiber ring laser, fiber Bragg grating.*

## 1. Introduction

Traveling wave (TW) semiconductor optical amplifiers (SOAs) will probably one of the key components in the next generations of optical networks where they could be used either as linear amplifier or in switching and wavelength conversion applications due to their strong nonlinearities. The advantages of SOAs are their compactness, potentially low cost, wide gain bandwidth and possibilities for monolithic integration with laser diodes or photodetectors.

In this report we developed the performance of SOA modules based on the 1550 nm InGaAsP/InP polarization- insensitive having a thin tensible-strained bulk active layer integrated with active width-tapered spot-size converters (SSCs). The SOA modules then were used as gain medium for producing the single mode or multimode fiber ring lasers together with the fiber Bragg gratings (FBGs). Such kinds of fiber ring lasers are intensively studied with the purpose of making new coherent light sources for wavelength division multiplexing (WDM) in modern fiber optic communication systems. With the single mode SOA fiber ring lasers one can make tunable laser source by changing the temperature or strain of the FBGs or by using optical tunable filter (OTF) [1]. The multimode SOA fiber ring lasers give the possibility of having several modes at the same time which are useful for WDM technique [2]. By using the modulation element inserted into the SOA fiber ring laser with the appropriate modulation frequency (MHz ÷ GHz) according to the fiber ring length one can have a mode-locked ring laser which can supply the train of very short and high magnitude pulses [3,4].

## 2. Experimental results and discussions

### *2.1. SOA module preparation and characterization*

Integration of SSCs with SOAs improves chip-fiber optical coupling and results in large fiber-to-fiber gain, high fiber-coupled saturation output power and a low fiber-coupled noise figure. However, the influence of SSCs on polarization sensitivity in gain must be reduced as much as possible. Passive-type of SSCs have the advantage that they have little influence on the polarization sensitivity [5]. The 1550 nm InGaAsP/InP SOA chips have been fabricated at Heinrich Hertz Institute (HHI) in Berlin. They have the angled-facet ($7^0$) or direct active regions integrated with spot size converters. At Institute of Materials Science (IMS) in Hanoi we performed fiber-to-fiber coupling for making SOA modules.

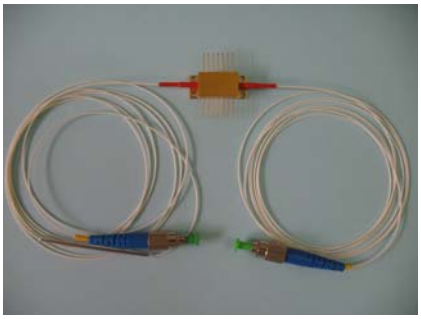

**Fig.1** Image of the prepared SOA module

For in-line amplification as well as for some functional applications of SOAs the output saturation power is an important parameter. The saturation output power of optical amplifiers is generally expressed as the following equation [5]:

$$P_s^f = CP_s^c = Ch\nu \frac{dw}{\Gamma} \frac{1}{g'} \frac{1}{\tau_n}$$

($P_s^f$: fiber-coupled saturation output power, $P_s^c$: chip-out saturation output power, $C$: chip-fiber coupling coefficient, $h$: Planck constant, $\nu$: optical frequency, $d$: laser active layer thickness, $w$: active layer width, $\Gamma$: optical confinement factor of active layer, $g'$: differential gain, $\tau_n$: carrier lifetime). As indicated in this equation, the chip-out saturation power depends on the chip design parameters as well as on the optical frequency of the operating light. However, for SOA module packaging, the most important parameter is the chip-fiber coupling coefficient $C$. As the more chip-fiber coupling coefficient achieved the more fiber-coupled saturation output power and more fiber - to - fiber gain can be realized.

The SOA chips have the length of 1250 μm and their active regions (width of about 2 μm) have the tapered regions with the end width of 0.8 μm. The SOA facets are coated with the AR $TiO_2/SiO_2$ layer in order to have very low reflection coefficient ($R < 10^{-5}$). The module preparation processes are about the same as in our previous work [6]. It means that at first we attached the SOA chip on the gilded copper heatsink with electrically and thermally epoxy Epo-tex H20E, then the gold wires of 25 μm in diameter were bonded with the metallic contacts on the chip for current supply. The small thermal sensor (10 KΩ at 25°C) also was attached to the heatsink with thermally conducting epoxy, and then the heatsink was attached to the peltier element. The SOA chip then was coupled with the single mode 9/125 tapered fibers which were made by electrical arc. The alignment system used here includes the Melles Griot six axis positioning system Nanomax-HS and high magnification stereomicroscope Carl Zeiss Stemi-2000. The coupling alignment was performed carefully to achieve the good chip-fiber coupling

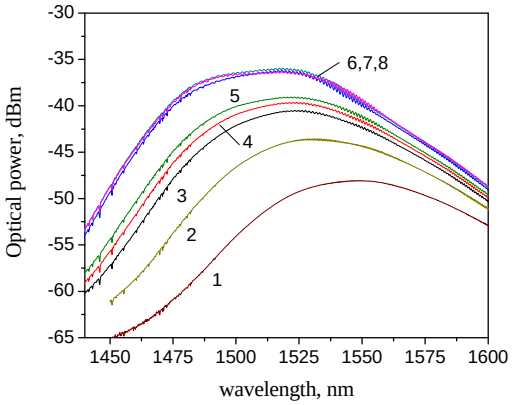


**Fig. 2**. ASE spectra of SOA module at the operating current of 50 mA (1), 70 mA (2), 90 mA (3), 100 mA (4), 110 mA (5), 120 mA (6), 130 mA (7), 140 mA (8) ($T = 25^0$C)

coefficient *C* for both chip facets. This depends strongly on the shape, symmetry and diameter of the tapered fiber ends, which was about 15 μm in our case, as well as on the level of fine adjustment possibility. After having good coupling alignment, the fibers were fixed on the heasink at first with small amount of UV adhesive NOA61, then with thermally curing epoxy Araldite 2014. These adhesives have small thermal expansion coefficient. The capping process finishes the SOA module packaging and then the modules are kept in the temperature case at $50^0$C during 8 hours for the characteristic stabilization. Fig. 1 shows the image of our prepared SOA module.

The amplified spontaneous emission (ASE) curves at the different SOA module operating dc currents $I_{SOA}$ of the prepared modules show that the ASE 3dB-bandwidths are much larger than those that we observed before for the ordinary SOAs (about 30 ÷ 35 nm) [6]. The optical spectra were measured with the optical spectrum analyzer (OSA) Advantest Q8384 (RBW = 0.01 nm). Here we can see the 3dB-bandwidths are in the range from 66 nm to 77 nm for the SOA dc operating currents changing from 50 mA to 140 mA as shown in Fig. 2. As the SOA operating current increases, the ASE peak wavelength shifts towards shorter wavelength (from 1547.1 nm to 1522.3 nm) due to the band-filling effect. We know that the gain curves are approximately the same as the ASE curves for SOAs and they have increasing peak power when the operating current increases. The lager ASE bandwidth or larger gain bandwidth shows the better performance of the spot size converter SOAs in comparison with the SOAs without SSCs because the larger bandwidth the more signals with different wavelengths can be amplified or processed in the communication networks. From the ASE curves we also can see the ripples of less than 0.2 dB for the SOA operating currents from 50 mA to 110 mA and less than 0.7 dB for the larger operating currents. The small ripples show the good quality of antireflection coating on the SOA facets. For the large operating currents (≥ 120 mA) the SOA chip gain has the saturation, so the ASE curves practically do not change.

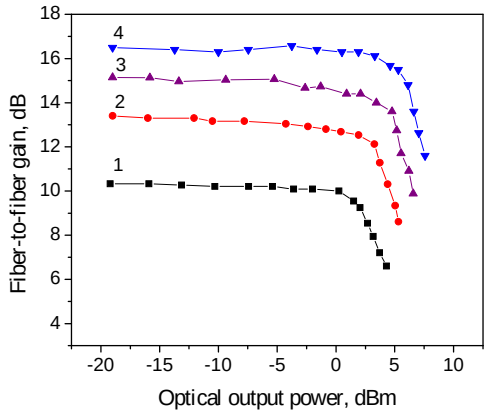


**Fig.3** Dependence of fiber-to-fiber gain on output power at the SOA operating current of 80 mA (1), 100 mA (2), 120 mA (3) and 140 mA (4) ($T$ = $25^0$C)

The SOA module gain curves in dependence on input and output optical powers also were measured with the input signal from cooled *λ/4* – shifted DFB laser module emitting the light of 1544.30 nm ($T$ = $25^o$C). The input signal power was changed with the variation optical attenuator (VOA) and input and output signal powers were measured with OSA. Fig.3 shows the fiber-to-fiber signal gains vs. signal output power at the different SOA operating currents. The small signal gain increases from 10 to 16 dB when the operating current increases from 80 mA to 120 mA. Comparing with the gain curves of the SOA chip (saturation gain ~ 22 dB at $I_{SOA}$ ~ 120 mA) we see that the optical coupling loss between the SOA chip and the fiber was estimated to be about 3 dB per chip facet and these values are quite the same for both facets in our case. The 3 dB saturation output power ranging from 3.7 dBm to 6.7 dBm when the operating current changes from 80 mA to 120 mA. These values are much higher than those of our ordinary SOA modules without SSCs [6]. The gain and saturation output power are approximately the same for the modules based on the SOA chips with the angled-facet ($7^o$) or direct active regions but the optical coupling was more difficult for the angled-facet chips. The measurements with the fiber polarization controller (PC) showed that the polarization sensitivity of SOA module's gain was

small (< 1.0 dB). These results were achieved due to the improvement of the chip design as well as the coupling and packaging processes.

### *2.2 SOA fiber ring laser*

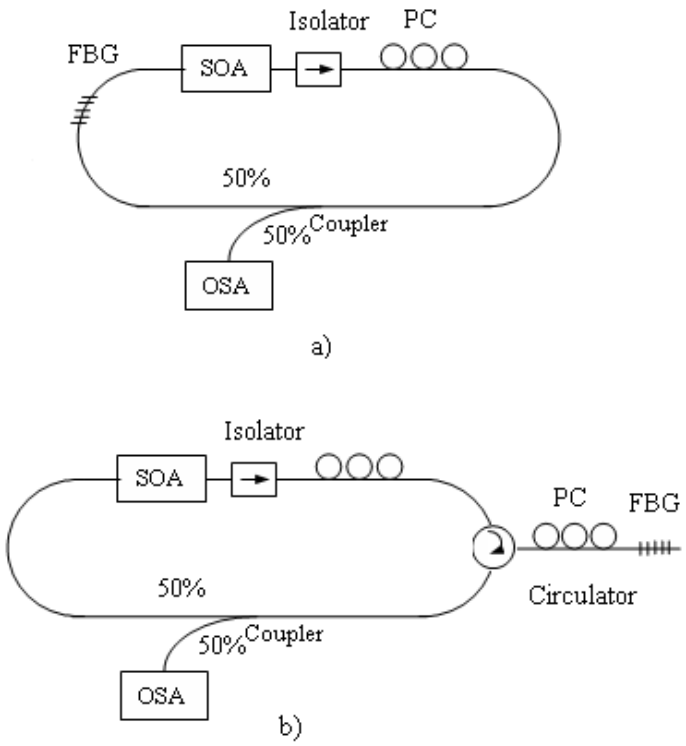


**Fig.4.** SOA fiber ring laser configuration without circulator (a) and with circulator (b)

As said above, one of the functional applications of the SOAs is a light source for WDM when it is used as gain cavity of the fiber ring laser. The prepared SOA modules were used as gain medium for the fiber ring lasers with the configurations shown in Fig. 4. The SOA modules in the ring operated with the dc current supply. The uniform single mode fiber Bragg gratings (FBGs) used for selective reflection at the Bragg wavelength: $\lambda_B = 2n\Lambda$ ($n$ is the effective index of the grating region and $\Lambda$ is the Bragg grating period) were fabricated at IMS in Hanoi. The ring laser optical spectra and output power were measured on OSA through the fiber power splitter 50:50. The isolator helped to stabilize the measurement results due to the limitation of the back reflection of light into SOA. The SOA fiber ring laser output power depends strongly on the polarization of light inside the ring, the measurements at different states of the fiber polarization controller (PC) showed that this polarization sensitivity of the fiber ring laser gain could be as much as 4 dB (while the polarization sensitivity of the SOA gain is less than 1 dB).

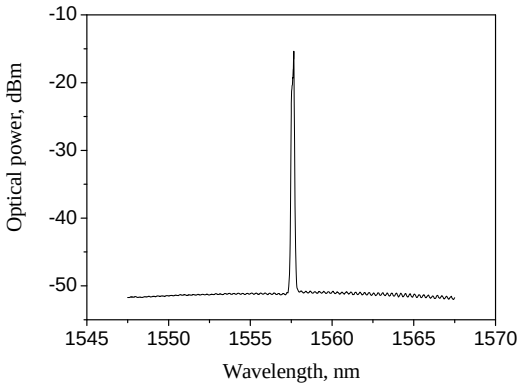


**Fig.5** Optical spectrum of SOA ring laser with circulator, $I_{SOA}$ = 60 mA

For both configurations of SOA fiber ring lasers without optical circulator (Fig. 4a) and with circulator (Fig. 4b) we obtained the single mode SOA fiber ring lasers which have the optical spectra as the spectrum indicated in Fig. 5 for the case of FBG with $\lambda_B$ = 1557.66 nm (reflection coefficient $R$ of 55%). The laser peak wavelength is also 1557.66 nm as the Bragg wavelength of FBG with 3 dB band width of about 0.07 nm (at $I_{SOA}$ = 60 mA). The side mode suppression ratio is more than 30 dB for any cases. Different FBGs with different Bragg grating periods were also tested for these ring laser configurations. Usually, the output power of the configuration without circulator is more than that of the configuration with circulator. This SOA ring laser has the threshold current of about 55 mA

(when the SOA gain is high enough) and its output power increases rapidly in the $I_{SOA}$ range from 60 mA to 120 mA, and then the saturation occurs at the output power of about 0.2 mW (Fig.6). At the same SOA (or ring laser) operating current, the output power of the configuration without circulator is much more due to the amplification of both reflection light ($R$ ~ 55%) and transmission light ($T$ ~ 45%) through FBG at 1557.66 nm while only the reflection light part is amplified by the SOA in the configuration with circulator. The laser threshold current for the last configuration also is more (~ 80 mA). Here the FBG together with the circulator plays the role of narrow bandwidth optical filter: the

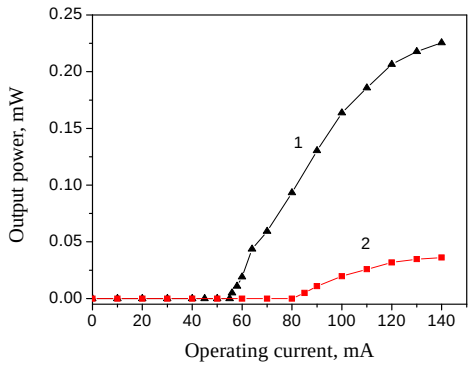


**Fig. 6** Light-current curves for SOA fiber ring lasers:
1- Configuration without circulator;
2- Configuration with circulator

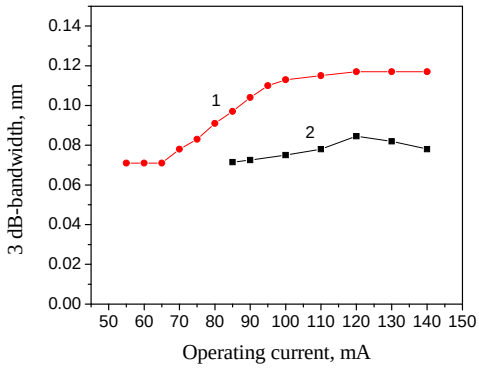


**Fig. 7**: Dependence of 3 dB-bandwidth of the laser line on SOA operating current:
1- Configuration without circulator;
2- Configuration with circulator

part of SOA's ASE power at the wavelength of 1557.66 nm amplified each time in the ring is reflected by the FBG through the circulator and therefore the laser optical spectrum bandwidth does not depend on the SOA operating current and nearly equals to the FBG 3 dB reflection bandwidth (~ 0.07 nm). While the optical spectrum bandwidth of the ring laser in the configuration without circulator depends on the grating bandwidth and also strongly depends on the SOA operating current, it increases with the increasing of $I_{SOA}$. This may be due to the multiple passages of the laser light through the SOA gain medium which leads to the increasing of optical power and enlarging of spectrum bandwidth at the same time (Fig. 7).

We also performed the experimental setup for the SOA ring laser as indicated in Fig. 4a but with two FBGs connected in serial. One FBG had the Bragg wavelength $\lambda_B$ = 1550.36 nm, another had $\lambda_B$ = 1547.12 nm. We obtained the multimode structure of the output spectra of this SOA fiber ring laser as indicated in Fig. 8. 3 dB bandwidth of each mode is about 0.2 nm. The multimode structure depends strongly on the polarization of light, the different spectra were obtained at the different states of the polarization controller. The separations between the neighbor modes are the same and equal to 1.6 nm which is haft of the detuning between the Bragg wavelengths of two FBGs (~ 3.2 nm). The nonlinear Four-Wave-Mixing (FWM) effect may occur in this case. Two reflected waves (1550.36 nm and 1547.12 nm) from the FBGs can cause the new conjugate wave with the high order FWM patterns when they are entering the SOA [6]. The multiple passages of the waves through the SOA can cause complicated FWM effect. The position of modes is shifted to the shorter wavelength region than both Bragg wavelengths. This can be explained that the higher SOA gain occurs at the shorter wavelength (peak of ASE curve is at 1518 nm when $I_{SOA}$ = 120 mA) so that the high order FWM patterns are amplified more than the lower order ones and they give the contribution to the observed laser modes. When we used two FBGs with the Bragg wavelengths far from each other (1547.12 nm and 1557.66 nm) no multimode structure was observed and it is may be due to the fact that FWM conversion efficiency decreases very fast with the increasing of the frequency detuning [6].

However, to understand better this multimode structure we should perform more experiments and the mode-locked SOA fiber ring lasers with the second SOA serving as the modulation element also should be studied.

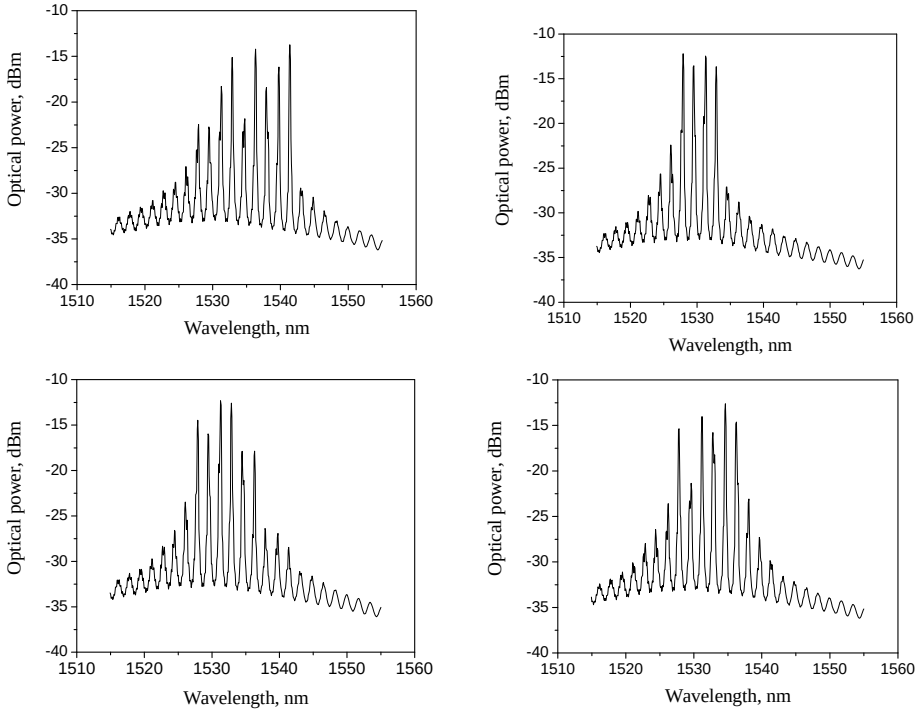


**Fig. 8**: Optical spectra of the SOA fiber ring laser with two FBGs at the different state of PC ($I_{SOA}$= 120 mA, $T$ = 25$^0$C)

## 3. Conclusions

In this report we present the packaging of SOA module based on the 1550 nm InGaAsP/InP SOA chips with spot size converter. The modules show the improved characteristics such as large gain bandwidth, high saturation output power and low polarization sensitivity of gain. The prepared modules were used for the first time at IMS as cavity gain medium in the fiber ring lasers. The SOA fiber ring lasers give single mode or multimode operations depending on the number of used FBGs in the rings. The SOA fiber ring lasers were characterized. However, these results are only the first ones and more experiments must be performed in order to understand the mechanism of the observed laser modes, especially the appearance of multimode in the SOA ring laser with two FBGs.

***Acknowledgement:*** *The authors express thanks to the National Council on Natural Sciences for its financial support.*

## References

1. Jun-ichi Kani,K. Iwatsuki. J. of Lightwave Tech., Vol. 23, No. 3, 2005, p. 1164 – 1169.
2. Chun – Liu Zhao, Zhaohui Li, M.S.Democan, Xiufeng Yang, Wei Jin. Optics Communications, Vol. 252, No.1-3, 2005, p. 52-57.
3. Wenyan Yang, Z. Wu, G. Xia. Optics Comms., Vol. 250, No.4-6, 2005, p. 384 - 388.
4. Ivan Evans, Colm O'Riodan, Michael J.Connelly, Liam P.Barry, Aisling M.Clarke, Prince M.Anandarajah. Optics Communications, Vol. 280, No.1, 2007, p. 142 – 146.
5. Ken Morito, Mitsuru Ekawa, Takayuki Watanabe, and Yuji Kotaki. J. Lightwave Technology, Vol.21, No.1, 2003, p.176 – 181.
6. Vu Doan Mien, Vu Thi Nghiem and Tong Quang Cong. ASEAN Journal of Science and Technology for Development. Vol.24, No. 1&2, 2007, p.21 - 28.

# A THREE-DIMENSIONAL NON-PARAXIAL BEAM PROPAGATION METHOD USING COMPLEX JACOBI ITERATION

**Khai Q. Le and Peter Bienstman [a], R. Godoy-Rubio [b], G. Ronald Hadley [c]**

[a)] Department of Information Technology, Ghent University-IMEC,
St-Pietersnieuwstraat 41, B-9000 Ghent, Belgium
[b)] Departamento de Ingeniería de Comunicaciones, University of Malaga, 29071, Spain
[c)] Sandia National Laboratories, Albuquerque, NM 87131 USA
*E-mail: khai.le@intec.ugent.be*

**Abstract:** A new complex Jacobi iterative technique adapted for the solution of three-dimensional (3D) non-paraxial beam propagation is presented. The effectiveness of our new approach is demonstrated in comparison with the traditional direct matrix inversion. Our method is targeted towards large waveguide structures with a long path length. The beam propagation equation for analysis of optical propagation in waveguide structures is based on a novel modified Pade(1,1) approximant operator, which gives evanescent waves the desired damping. The resulting approach allows more accurate approximations to the true Helmholtz equation than the standard Pade approximant operators.

## 1. Introduction

The non-paraxial or wide-angle (WA) beam propagation method (BPM) has become one of the most widely used techniques for the study of optical waveguide devices [1]. Different treatments of WA-BPM have been developed, including the rational approximants of the square root operator, the exponential of the square root operator, and the Pade approximant operator [2], for rectangular coordinates as well as an oblique coordinate system. The Pade-approximant-based WA-BPM is one of the most commonly used techniques for modeling optical waveguide structures. However, the method was originally limited to 2D structures due to the lack of efficient solvers. Recently, C. Ma *et al.* [3] presented a new 3D WA-BPM also based on Hoekstra's scheme. By using a technique for shifting the simulation window to reduce the dimension of the numerical equation and a threshold technique to further ensure its convergence, this approach shows accuracy and effectiveness. However, the resultant propagation scheme can be very slow if either the problem size is large or the structure or the boundary conditions are changing as the propagation proceeds, requiring frequent reinversions of the propagation matrix. Thus, it is imperative to find more efficient solution methods for 3D WA-BPM.

Recently, the complex Jacobi iterative method, a new iterative technique for solution of the indefinite Helmholtz equation, was introduced [4]. The method was shown to converge at a rate dependent only upon the grid size and effective absorption coefficient. For beam propagation of wave profiles within a 2D cross section, the beam propagation equation can be cast in terms of a Helmholtz equation with source term, but that equation needs to be solved efficiently since numerous propagation steps are routinely required during the course of a problem solution. For this purpose the complex Jacobi iterative (CJI) method is proposed and shown to be highly efficient due to the high effective absorption coefficient.

The beam propagation equation for analysis of optical propagation in waveguide structures is based on a modified Pade(1,1) approximant operator we propose here, which gives evanescent waves the desired damping. Our modified Pade approximant propagation operators allow more accurate approximation to the true Helmholtz equation and faster convergence when the CJI method is used for the modified Pade approximant-based WA-BPM than those of the standard Pade approximant approach [2]. Furthermore, since the utility of the CJI technique depends mostly upon its execution speed in comparison with the direct matrix inversion (DMI) method,

we also present several speed comparisons. Numerical implementations are carried out for 3D optical waveguide structures.

## 2. Modified pade approximant operators

On the past few years, Hadley proposed the WA-BPM algorithm based on the standard Pade approximation using the following recurrence relation with initial value of $\left.\frac{\partial}{\partial z}\right|_0 = 0$:

$$\left.\frac{\partial}{\partial z}\right|_{n+1} = i\frac{\frac{P}{2k}}{1-\frac{i}{2k}\left.\frac{\partial}{\partial z}\right|_n} \tag{1}$$

where $P = \nabla_\perp^2 + k_0^2(n^2 - n_{ref}^2) = \frac{\partial^2}{\partial x^2} + \frac{\partial^2}{\partial y^2} + k_0^2(n^2 - n_{ref}^2)$ with $k = k_0 n_{ref}$, $n_{ref}$ the reference refractive index, $k_0$ the vacuum wavevector.

For $\left.\frac{\partial}{\partial z}\right|_2$, this gives us the well-known Pade (1,1) approximant-based WA beam propagation formula as follows:

$$\frac{\partial H}{\partial z} \approx i\frac{\frac{P}{2k}}{1+\frac{P}{4k^2}}H \tag{2}$$

If Eq. (2) is compared with a formal solution of Eq. (1) in [2] written in the well-known form

$$\frac{\partial H}{\partial z} = i(\sqrt{P+k^2} - k)H = ik(\sqrt{1+X} - 1)H \tag{3}$$

where $X = \frac{P}{k^2}$, we obtain the approximation formula

$$\sqrt{1+X} - 1 \approx \frac{\frac{P}{2k^2}}{1+\frac{P}{4k^2}} = \frac{\frac{X}{2}}{1+\frac{X}{4}} \tag{4}$$

Since the operator X has a real spectrum, it is useful to consider the approximation of $\sqrt{1+X} - 1$ by the Pade approximant propagation operator. Figure 1 shows the absolute value of $\sqrt{1+X} - 1$ and its first-order Pade approximant called Hadley (1,1) as a function of X.

However, as the denominator of Hadley (1,1) gradually approaches zero, its absolute value

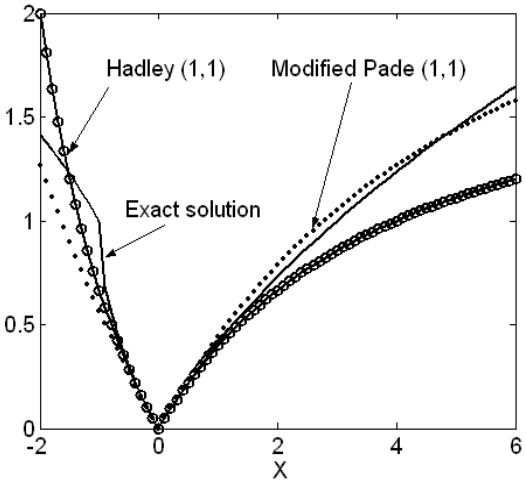


**Figure 1.** The absolute values of $\sqrt{1+X} - 1$ (solid line), its first-order standard Pade approximant (solid line with circles) and modified Pade approximant (dot line).

approaches ∞ as can clearly be seen in Figure 2. Physically this means that the standard Pade approximant incorrectly propagates the evanescent modes.

To circumvent this problem we propose a modified Pade approximant operator. First of all, following [5], by multiplying both sides of Eq. (1) with $-\frac{i}{k}$, we obtain

$$-\frac{i}{k}\frac{\partial}{\partial z}\bigg|_{n+1} = \frac{\frac{P}{k^2}}{2-\frac{i}{k}\frac{\partial}{\partial z}\bigg|_n} \tag{5}$$

We may rewrite Eq. (5) as follows

$$f_{n+1}(X) = \frac{X}{2+f_n(X)} \quad for\, n = 0,1,2... \tag{6}$$

where $f(X) = -\frac{i}{k}\frac{\partial}{\partial z}$.

Y. Y. Lu [5] has proved that Eq. (6) can provide a good approximation to $\sqrt{1+X}-1$ with the initial value of

$$f_0(X) = i\beta \quad where \;\; \beta > 0 \tag{7}$$

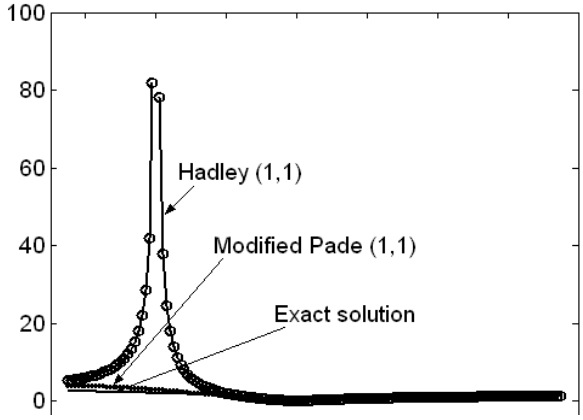


**Figure 2.** The absolute value of $\sqrt{1+X}-1$ (solid line), the first-order standard (solid line with circles) and modified (dot line) Pade approximant of $\sqrt{1+X}-1$ with respect to X (dot line).

Subsequently, we use this fact to go back to the original recurrence relation (1) and construct modified Pade approximant operators by using a different initial value of $\frac{\partial}{\partial z}\bigg|_0 = -k\beta$. For $\frac{\partial}{\partial z}\bigg|_2$ the first-order modified Pade(1,1) approximant operator is given as follows:

$$\frac{\partial H}{\partial z} \approx i\frac{\frac{P}{2k}}{1+\frac{P}{4k^2(1+\frac{i\beta}{2})}}H \tag{8}$$

The absolute value of the modified Pade(1,1) approximant of $\sqrt{1+X}-1$ is also depicted in Figure 1. It is seen that our modified Pade approximant operator (with $\beta = 2$) allows more accurate approximations to the true Helmholtz equation than the standard Pade approximant operator. Furthermore, the standard rational Pade approximant incorrectly propagates the evanescent mode as their denominator gradually approaches zero while the modified Pade approximant gives the evanescent mode the desired damping as clearly seen in Figure 2.

## 3. WA-beam propagation formulation

### *3.1.Basic equation*

By using the modified Pade(1,1) approximant, the 3D semivectorial WA beam propagation equation can be written as follows:

$$(1+\xi P)\phi^{n+1} = (1+\xi^* P)\phi^n \tag{9}$$

where $\xi = \frac{1}{4k^2(1+i\beta/2)} - \frac{i\Delta z}{4k}$, $\xi^*$ the complex conjugate of $\xi$ and $\Delta z$ the propagation step.

### *3.2. WA-BPM using CJI*

By dividing both sides of Eq.(9) by $\xi$, it may be written as an inhomogeneous Helmholtz equation

$$(\nabla_\perp^2 + k_0^2(n^2 - n_{ref}^2) + \frac{1}{\xi})\phi^{n+1} = (\frac{\xi^*}{\xi}P + \frac{1}{\xi})\phi^n \quad (10)$$

or

$$(\nabla_\perp^2 + k_0^2(n^2 - n_{ref}^2) + 4k_o^2 n_{ref}^2 \frac{1 + (1 + k^2\beta\Delta z/2)\beta/2 + ik\Delta z}{\left(1 + k^2\beta\Delta z/2\right)^2 + k^2\Delta z^2})\phi^{n+1} = source\ term \quad (11)$$

Thus the beam propagation can be cast as a 2D Helmholtz equation with source term in an effective medium with loss of $4k_0^2 n_{ref}^2 \frac{k\Delta z}{\left(1 + k_0^2 n_{ref}^2 \beta\Delta z/2\right)^2 + k^2\Delta z^2}$. This loss is high for a typical choice of $k\Delta z$. This is a condition that favors rapid convergence for the CJI method.

### *3.3. WA-BPM using DMI*

By discretizing Eq. (10), we find that

$$\begin{aligned} &A_{n+1}\phi_{i+1,j}^{n+1} + B_{n+1}\phi_{i-1,j}^{n+1} + C_{n+1}\phi_{i,j}^{n+1} + D_{n+1}\phi_{i,j-1}^{n+1} + E_{n+1}\phi_{i,j+1}^{n+1} \\ &= A_n\phi_{i+1,j}^{n} + B_n\phi_{i-1,j}^{n} + C_n\phi_{i,j}^{n} + D_n\phi_{i,j-1}^{n} + E_n\phi_{i,j+1}^{n} \end{aligned} \quad (12)$$

where

$$\begin{aligned} &A_{n+1} = B_{n+1} = \frac{1}{\Delta x^2}, \quad D_{n+1} = E_{n+1} = \frac{1}{\Delta y^2}, \\ &C_{n+1} = k_o^2(n^2 - n_{ref}^2) + \frac{1}{\xi} - 2(\frac{1}{\Delta x^2} + \frac{1}{\Delta y^2}), \\ &A_n = B_n = \frac{\xi^*}{\xi}\frac{1}{\Delta x^2}, \quad D_n = E_n = \frac{\xi^*}{\xi}\frac{1}{\Delta y^2}, \\ &C_n = \frac{\xi^*}{\xi}\left(k_0^2(n^2 - n_{ref}^2) + \frac{1}{\xi^*} - 2(\frac{1}{\Delta x^2} + \frac{1}{\Delta y^2})\right) \end{aligned} \quad (13)$$

Eq. (12) is an $M^2$ by $M^2$ matrix equation for an M by M mesh grid. However, each row of the coefficient matrix has no more than five non-zero values. As a result, this sparse matrix equation can be efficiently solved using various methods. In our calculations, the sparse matrix solver-UMFPACK package has been used.

## 4. Benchmark results

We now employ the WA-BPM using the new CJI and the traditional DMI methods to perform benchmark tests on 3D optical waveguide structures. We first consider the Gaussian

beam propagation in a straight rib waveguide and guided-mode propagation in a Y-branch rib waveguide. The width and height of the straight rib waveguide are $w = 2\,\mu m$ and $h = 1.1\,\mu m$. The guiding core has an index $n_f = 3.44$ and a thickness $t = 0.2\,\mu m$ while the refractive index of substrate and cover is $n_s = 3.4$ and $n_c = 1.0$, respectively. The Gaussian beam with a waist radius $w_0 = 0.3\,\mu m$ has been injected into the rib waveguide at wavelength $\lambda = 1.55\,\mu m$. Due to the large memory required for DMI, the small computational window of $2\,x\,2\,\mu m$ is discretized with a grid size of $\Delta x = \Delta y = 0.1\,\mu m$, and the short path length of $2\ \mu m$ is discretized with a propagation step size $\Delta z = 0.1\mu m$. The resulting runtime of DMI is 177.9 seconds while runtime for CJI is only 4.7 seconds.

**Table 1**: Quantitative comparison of runtimes of the direct matrix inversion and the complex Jacobi iteration for WA beam propagation in waveguide (WG) structures

| Structure | 3D | |
|---|---|---|
| Method | Straight rib WG | Y-branch rib WG |
| DMI | 177.9 s | 268.9 s |
| CJI | 4.7 s | 5.9 s |

For a Y-branch, the initial rib waveguide is split into two 5-degree tilted waveguides. The longitudinal dimension is $h_1 = 1\,\mu m$. The other structure parameters are same as the above straight rib waveguide. The fundamental mode of the ridge waveguide of width $w = 2\,\mu m$ for polarization TE mode at $1.55 - \mu m$ wavelength is used as the excited field at z=0. The propagation step size is $\Delta z = 0.1\mu m$. Due to the high effective loss in the propagation medium the complex Jacobi method performed propagation only in 5.9 seconds while DMI required an amount of 268.9 seconds. Table 1 shows the performance of the two methods for the optical waveguide structures chosen here. It is clearly seen that the runtime of the iterative method is substantially faster than that of the DMI method. For large problems requiring very large storage space and also for structures with a long path length with small propagation step size that require frequent matrix inversions, the DMI technique is numerically very intensive. In contrast, for typical choices of $k\Delta z$ the CJI technique offers rapid convergence and shorter runtimes.

## 5. Conclusion

A new complex Jacobi iterative method adapted for the solution of 3D WA beam propagation has been presented. We proposed the modified Pade approximant of the WA beam propagation operator that gives the evanescent waves the desired damping. The resulting approach allows accurate approximations to the true Helmholtz equation. Furthermore, a quantitative comparison of runtimes between the traditional direct matrix inversion and the new complex Jacobi iterative method for 3D WA beam propagation demonstrates convincingly that the complex Jacobi iterative method is very competitive for demanding problems.

## References

1 R. Scarmozzino, A. Gopinath, R. Pregla, and S. Helfert, "Numerical techniques for modeling guided-wave photonic devices," IEEE J. Sel. Top. Quantum Electron. **6**, 150-161 (2000).

2 C. Ma and E. V. Keuren, "A three-dimensional wide-angle beam propagation method for optical waveguide structures", Opt. Express 15, 402 (2007).

3 G. R. Hadley, "Wide-angle beam propagation using Padé approximant operators," Opt. Lett. **17**, 1426-1428 (1992).

4 G Ronald Hadley,"A complex Jacobi iterative method for the indefinite Helmholtz equation", J. Comp. Phys. 203, 358 (2005).

5 Y. Y. Lu, "A complex coefficient rational approximation of $\sqrt{1+x}$", *App. Numer. Math*. 27, 141 (1998).

# WDM COMPATIBLE 2R AND 3R REGENERATION BASED ON SATURABLE ABSORBER

**Q.T. Le[a], L. Bramerie[a], S. Lobo[a], M. Gay[a], V. Roncin[a], M. Joindot[a], J-C. Simon[a], A. Poudoulec[b], M. Van der Keur[b], C. Devemy[b], D. Massoubre[c], J-L. Oudar[c], G. Aubin[c], A. Shen[d], J. Decobert[d], G-H. Duan[d]**

[a)] FOTON-CNRS, ENSSAT/Université de Rennes 1, BP 80518, 22305 Lannion, France,
[b)] YENISTA OPTICS, BP 80429, 22304 Lannion, France
[c)] LPN-CNRS, Route de Nozay, F-91460 Marcoussis, France
[d)] Alcatel Thales III-V Lab, Route Départementale 128, 91767 Palaiseau, France
*E-mail: quang-trung.le@enssat.fr*

**Abstract:** A saturable absorber (SA) based on a vertical micro-cavity is of great interest for optical regeneration. In this paper, we report on the high potential of the SA for optical regeneration, both 2R and 3R regenerations are performed. A pigtailed chip SA with 8 independent fibres is assessed. We demonstrate experimentally the cascadability and WDM compatibility of this 2R module in a recirculation loop at 42.6 Gbit/s. In an all Erbium amplification system, the transmission distance is enhanced by a factor superior than 3 when the 2R regeneration is applied. This performance is obtained for 8 channels and over 13 nm for each channel. For the 3R regeneration set-up, a novel technique of all-optical synchronous modulation using cross saturation absorption in SA is also presented. The all-optical synchronous modulation is driven optically by the recovered clock from a self-pulsating laser device. Thanks to this technique, a transmission distance enhancement factor of 22.5 at 42.6 Gbit/s is experimentally obtained.

***Keywords:*** *all-optical regeneration, saturable absorber, synchronous modulation*

## 1. Introduction

An all optical regenerator could be one of the key devices for future optical networks as it allows reduction of transmission impairments and thus enhancement of transmission distance. In order to qualify itself as a viable alternative to the state-of-the-art optoelectronic regenerators, an all-optical regenerator must be easily scalable with the number of wavelength-division-multiplexing (WDM) channels.

Saturable absorber (SA), which is a vertical semiconductor based quantum-well micro-cavity, is of great interest for all-optical regeneration thanks to its noise reduction capacities and performances. Firstly, the SA provides an efficient and completely passive solution for noise reduction and extinction ratio enhancement at bit rates as high as 160 Gbit/s [1]; secondly, regeneration of a channel in a WDM multiplex has been shown with spatial demultiplexing [2]. Moreover, a WDM compatible solution has been proposed at 10 Gbit/s in order to fully reshape the signal [3].

In this paper, we present new results based on the first pigtailed SA device with 8 independent fibres [4]. Component homogeneity and spectral functionality are evaluated through switching contrast measurements. 2R and 3R regeneration functions, cascadability and wavelength tunability of the device are experimentally studied at 42.6 Gbit/s in a recirculating loop.

This paper is organized as follows. Section 2 presents the SA chip structure as well as SA module fabrication. Wide-band functional and homogeneity of the 8-channel SA module are demonstrated in section 3. Section 4 and 5 are devoted to the description and characterisation of 2R and 3R regenerator, respectively.

## 2. Module fabrication

The saturable absorber chip contains 7 MOCVD-grown InGaAs/InP quantum wells structure embedded in a micro-resonator. Quantum wells are located at the antinodes of intracavity intensity (figure 1.a). The bottom mirror is a broadband high-reflectivity metallic based mirror (Ag) and the top mirror is a multilayer dielectric mirror (2×[TiO2/SiO2]). A heavy-ion-irradiation shortens the absorption recovery time down to 5 ps [5, 6]. The device operates in a reflective mode, the reflectivity being small at low signal level, and high at high signal level.

A special fibre array has been developed by YENISTA OPTICS for efficiently interfacing the saturable absorber chip to 8 standard single mode fibres with 250 µm spacing. The fibre array is fixed to the mirror with an adhesive so that all the 8 out coming beams typically have a Mode Field Diameter (MFD) of 4.5 µm on the surface of the mirror. Focusing the beams on the mirror reduces the input power threshold required for the nonlinear effect of the mirror. This compact and low cost technique does not need any coupling optimisation [4].

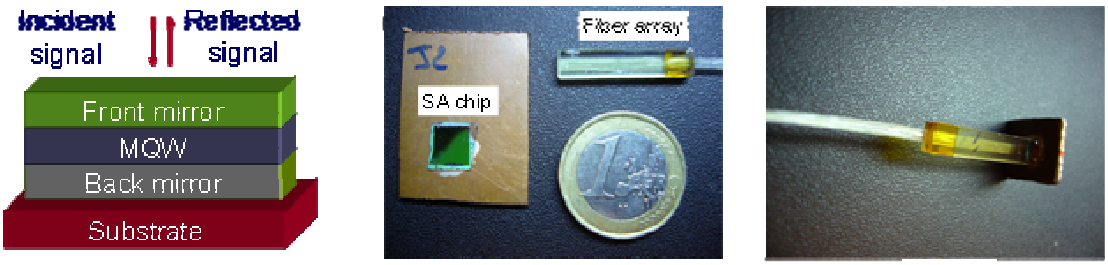


**Fig.1**: (a) SA structure; (b) Photograph of SA chip, fibre array (b) and SA module (c)

## 3. Module characterisation

Figure 2 presents the switching contrast of each channel as a function of average incident power and of probe wavelength obtained with an experimental setup using pump-probe measurement. The pump at 1532 nm is a RZ 33% signal modulated at 42.6 Gbit/s with sequence length of $2^{15}$-1 bit.

The first experiment, presented in the figure 2.a, depicts the measured switching contrast versus the average incident power for each channel. The probe signal is delivered by a CW laser source at 1546.6 nm corresponding to the minimum reflectivity of the SA module. With a high input pump signal power level, we obtain a cross modulation of SA absorption on probe signal. The switching contrast is obtained from the measurement of the mark-space extinction ratio of the probe signal. It corresponds to the extinction ratio enhancement in regeneration applications. For an input pump signal power of 12 dBm, the average switching contrast is 5.5 dB on all channels with a standard deviation of 0.9 dB which shows a really good homogeneity of the chip.

The second experiment, presented on figure 2.b, depicts the measured switching contrast versus the probe wavelength for each channel. The pump power is equal to 8 dBm. We observe a switching contrast higher than 3 dB from 1541 nm to 1559 nm for all the channels. This result demonstrates the compatibility of its contrast with WDM regeneration over a very wide-band signal spectrum.

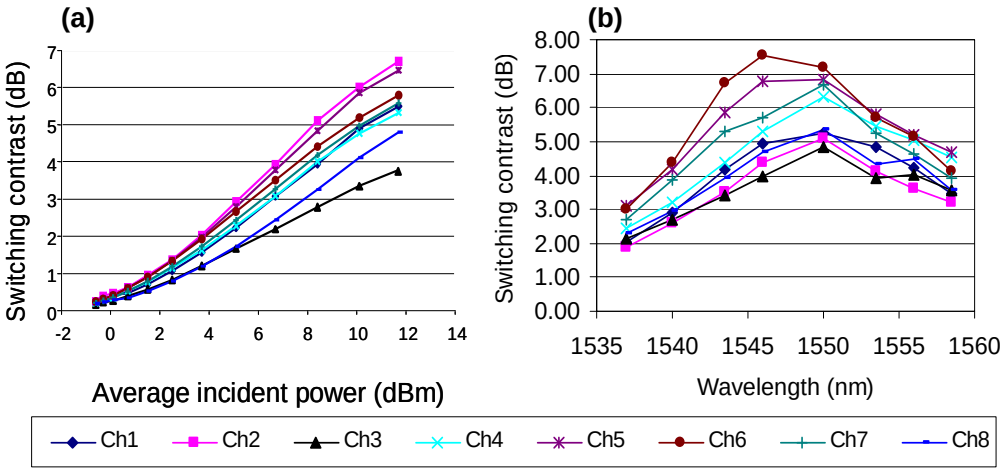


**Fig.2**: Experimental switching contrast of SA module versus mean input power (a) and versus probe wavelength (b)

## 4. 2R regeneration

The 42.6 Gbit/s transmission experiment is carried out with a 100 km recirculating loop (Fig. 2). Non-Zero Dispersion Shifted Fibre (NZ-DSF) is used and chromatic dispersion is partially compensated for by a Dispersion Compensating Fibre (DCF). Losses are compensated for essentially with Erbium amplification. The transmitter produces an RZ 33% signal modulated at 42.6 Gbit/s with a $2^{31}$-1 bit length sequence.

As complete 2R regeneration with reduction of 'mark' fluctuations is not ensured by the SA alone, the regeneration requires another appropriate nonlinear function [7]. In this paper, a fibre-based solution is used. The passive 2R regenerator is thus made of two stages: the first pulse compression stage comprising a nonlinear fibre (NLF) followed by an optical filter for equalisation of 'mark' levels [8], and the second stage made of the SA module for attenuation of the 'space' level. The nonlinear fibre in the pulse compression stage consists of a 1 km span of DSF (dispersion 0.1 $ps.nm^{-1}.km^{-1}$) and a 1 km span of standard NZ-DSF (dispersion 4.5 $ps.nm^{-1}.km^{-1}$). This stage requires an EDFA in order to ensure a high enough power (typically 18 dBm in our case) and to emulate significant nonlinear effects. An optical circulator allows injecting and recovering data signal in SA module.

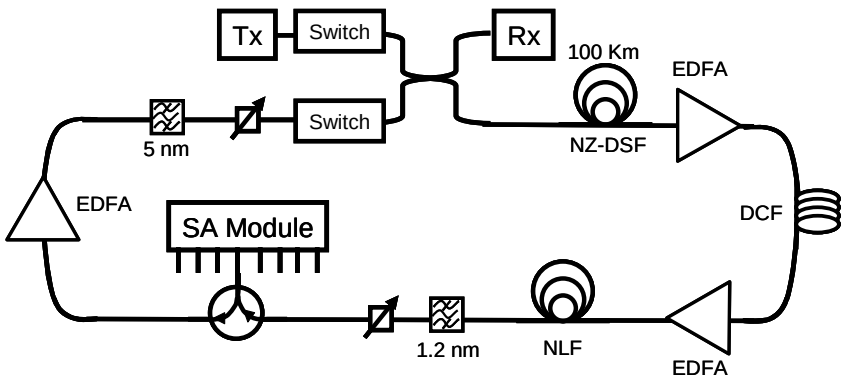


**Fig.3**: Experimental loop setup for characterization in 2R regeneration configuration

Firstly, the impact of the 2R regeneration was studied at a signal wavelength of 1546.6 nm. Figure 3.a presents the Bit Error Rate (BER) evolution as a function of the distance with and without regenerator (full triangles) for a launched power of 5 dBm corresponding to the optimal propagation length. After insertion of the 2R regenerator in the loop, we observe a significant

improvement of the transmission distance for each channel of the SA module. All the tested regenerative channels ensure a BER higher than $10^{-4}$ after a transmission distance of 4000 km.

We have also investigated the regeneration behaviour versus the signal wavelength for the channel C5 (Figure 3.b). We measured the Distance Improvement Ratio (DIR) corresponding to the ratio of the covered distances with and without regeneration for a given BER. Results show that the DIR is better than 3 over more than 13 nm (from 1541 to 1554 nm), demonstrating experimentally the wide-band behaviour of the device.

These results confirm the good homogeneity of the component and the wideband functionality ensuring WDM compatibility of the 8 channels with 100 GHz spacing integrated in a compact module. For the moment, the technique for 'mark' level equalisation (fibre followed by optical filter) is limiting for WDM application due to inter-channel nonlinearity. Moreover, a new design of the same type of nonlinear micro-cavity device should make it possible to reduce 'mark' level fluctuations on several channels simultaneously without the fibre compression stage [9, 10].

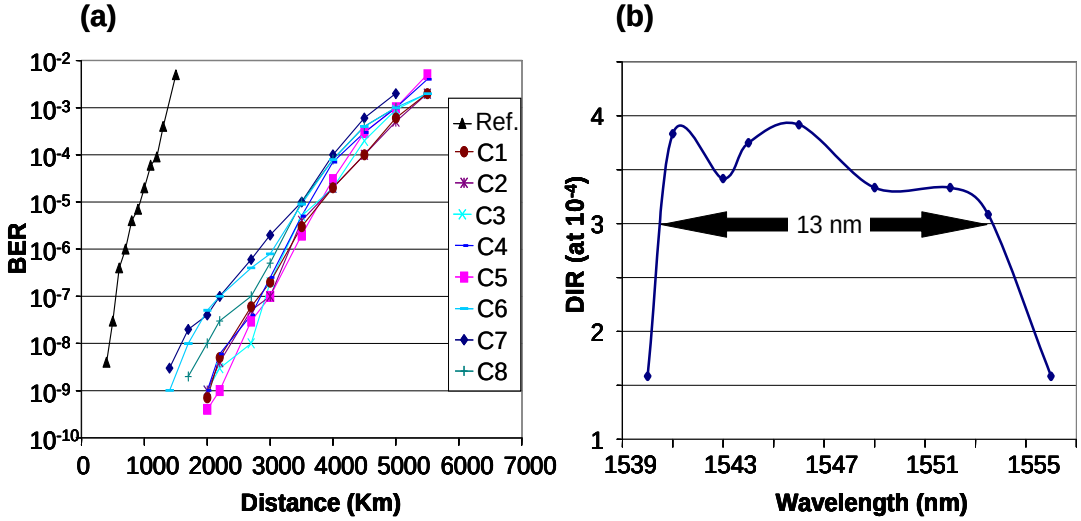


**Fig.4**: BER evolution versus distance without and with SA module (a) DIR evolution versus signal wavelength for channel 5 at BER = $10^{-4}$ (b)

## 5. 3R regeneration

Previously, the transmission quality enhancement using optical 2R regenerator and in-line synchronous modulation with optoelectronic clock recovery has been demonstrated [11, 12]. We report here the cascadability assessment of a 3R regeneration device based on a 2R regenerator and all optical synchronous modulation. The 2R regenerator is based on the combination of Self-Phase Modulation (SPM) in an optical fibre and Saturation Absorption (SA) in a quantum-well micro-cavity. All optical synchronous modulation is achieved by launching into the SA the optical clock obtained from an all optical clock recovery device using Self-Pulsating (SP) semiconductor lasers based on bulk and quantum-dot (QD) structures.

Figure 5.a presents the 2R regenerator architecture. The passive 2R regenerator has been described in the section above. The optical clock recovery (OCR) used in order to achieve the synchronous modulation (SM) consists of a double stage of Self Pulsating lasers from Alcatel Thales III-V lab (figure 5.b) [13]. The first stage is a bulk active layer Distributed Bragg Reflector (DBR) laser allowing a polarization insensitive clock recovery at 1548 nm. The second stage is a Self-Pulsating Quantum-Dot layer Fabry-Perot Laser (QD-SP) generating a high spectral purity optical clock at 1575 nm [14]. The association of these two lasers yields a polarisation insensitive OCR with performances in accordance with ITU recommendations.

The optical clock is then injected into the transmission line and launched into the SA. The relative delay between incoming data and recovered clock is controlled by an optical delay line

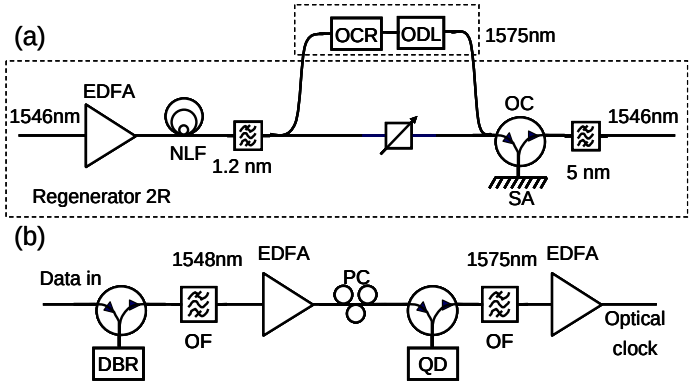


**Fig.5**: Schematic of regenerator architecture (a), and optical clock recovery part (b).

(ODL). The SM is obtained by cross absorption modulation in the SA. The optical clock is filtered out of the transmission line by the second OF.

Figure 6 presents the experimental setup. The transmission loop consists of 100 km NZ-DSF as described in the section above. In this experiment losses are compensated for using low noise Distributed Raman Amplification with on/off gain of approximately 10 dB per span.

Figure 7 shows the measured BER as a function of transmission distance with and without SM. Without SM, using only 2R regeneration, the BER grows rapidly due to timing jitter. However, a BER of $10^{-8}$ is reached after 8000 km corresponding to a factor 10 of transmission distance enhancement compared to the case without regeneration.

When the optical SM is applied, timing jitter is reduced on the data signal and the transmission distance is considerably enhanced (18000 km with a BER of $10^{-8}$ corresponding to a transmission distance enhancement factor of 22.5).

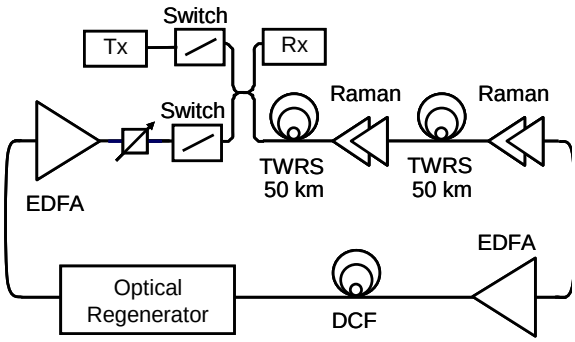


**Fig 6**: Schematic of the recirculation loop experiment.

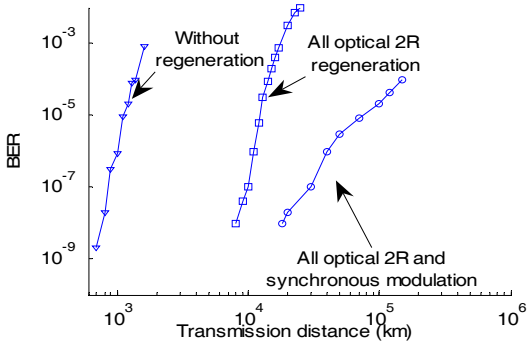


**Fig 7**: BER as function of transmission distance

## 6. Conclusions

In this review, we have reported the WDM compatibility of a simple, compact and completely passive 8-channel 2R regenerator module based on a saturable absorber. SA module average switching contrast is 5.5 dB on all channels and a switching contrast higher than 3 dB is attainable over 18 nm. We have also shown a distance improvement ratio (at BER of $10^{-4}$) of at least 3.3 in a 100 km regeneration span in recirculating loop. Finally, we have demonstrated a distance improvement ratio greater than 3 over 13 nm. This module is fully compatible with photonic integration, which could allow for a compact and low cost WDM 2R regeneration.

Thanks to an experimental cascadability assessment study, we demonstrated the efficiency of all optical synchronous modulation based 3R regenerator using cross absorption modulation in a SA micro-cavity, and a very compact clock recovery. We show a significant improvement in propagation distance of optical data at 42.6 Gbit/s. Future works will be focused on development of

new designs of SA micro-cavity for "mark" regeneration leading to compact and integrable fully 2R regenerator solutions.

***Acknowledgment:*** *This work has been carried out in the framework of the national projects Asterix and Rotor supported by French Government. We thank also the Region Bretagne and the European Union for financial support.*

## References

1. M. Gicquel-Guezo *et al.*, "290 fs switching time of Fe-doped quantum well saturable absorbers in a microcavity in 1.55 μm range", Applied Physics Letters, vol.85, no.24, pp. 5926-5929, 2004
2. A.Shen *et al.*, "4-channel saturable absorber module for high bit-rate regenerated WDM transmission", European Conference on Optical Communications, Tu 5.4.5, 2002
3. M. Gay *et al.*, "Cascadability and wavelength tunability assessment of a 2R regeneration device based on Saturable Absorber and semiconductor optical amplifier", Optical Fiber Communication Conference, OThB1, 2006
4. Bramerie *et al.*, "Cascadability and wavelength tunability assessment of a 2R regeneration device based on a 8 channel saturable absorber module," Optical Fiber Communication Conference, p. Postdeadline paper PDP1, 2007.
5. D. Massoubre *et al.*, "Scaling of the switching energy in microcavity saturable absorber devices", Applied Physics Letters, 88, 153513 (2006)
6. D. Massoubre *et al.*, "All-optical extinction ratio enhancement of a 160GHz pulse train using a saturable absorber vertical microcavity", Optics Lett., _31_, 537 (2006)
7. E. Burr *et al.*, "Signal Stability in Periodically Amplified Fiber Transmission Systems Using Multiple Quantum Well Saturable Absorbers for Regeneration," Journal of Lightwave Technology, vol. 24, no. 2, Feb 2006
8. D.Rouvillain *et al.*, "Optical 2R regenerator based on passive saturable absorber at 40 Gbit/s for WDM long haul transmissions," Electronics Letters, vol. 38, no. 19, pp. 1113-1114, 2002
9. H. Trung Nguyen *et al.*, "New passive all-optical semiconductor device for bit-1 level noise reduction," CLEO Europe IQEC2007, CI3-E-TUE.
10. M. Gay *et al.*, "Regeneration and Cascadability Assessment of a New Passive 2R Regenerator Based on a Dual-Stage Saturable Absorber gate," accepted for oral communication at European Conference on Optical Communications, September 2008
11. G. Raybon, "Optical 3R regeneration in 40 Gbit/s pseudo-linear transmission systems," Optical Fiber Communication Conference, pp. 191–193, 2003
12. D. Rouvillain *et al.*, "Novel polarization-insensitive synchronous modulator for 20 Gbit/s all-optical regeneration," Optical Fiber Communication Conference, pp. 83–84, 2002
13. B. Lavigne *et al.*, "First demonstration of a polarization insensitive low time jitter and optical noise tolerant all-optical clock recovery at 40 GHz using a self-pulsating laser tandem," Optical Fiber Communication Conference, p. Postdeadline paper PDP24, 2006
14. J. Renaudier *et al.*, "Active and passive mode-locking in buried ridge mode-locked quantum dots Fabry-Perot semiconductor lasers," European Conference on Optical Communications, vol. 3, 2005

# STUDY OF FIBEROPTIC ADD-DROP DEVICES USING FIBER-BRAGG-GRATING

**Phạm Thanh Bình[a], Phạm Văn Hội[a], Phạm Duy Long[a], Nguyễn Duy Trung[a], Ngô Ngọc Quang[b], Tạ Việt Hùng[b]**

[a] Institute of Materials Science, VAST, 18 Hoàng Quốc Việt Rd., Cầu giấy Dist, Hanoi
[b] Centre of High Tech Telecom, Dept. of Telecom & Informatics, 1 Láng Hạ str., Ba đình Dist., Hanoi

**Abstract:** In this paper we present the method of making Fiber-Bragg-Grating (FBG) using KrF-Excimer laser and Talbot interferometer and the use of FBG in the precise Add-Drop multiplexing for WDM bi-direction networks. Experiment shows that when the Bragg wavelength differs from signal wavelength, the intensity of dropped signal was decreased by Gaussian distribution law with their spacing. We proposed to use the Peltier cooler for adjusting the Bragg wavelength when the spacing between signal and/or Bragg wavelength is less than 0.25 nm. The Signal-Noise-Ratio (SNR) of dropped signal is more than 25 dB and the intensity of light is good enough for WDM bi-direction fiberoptic networks.

***Key words**: Making FBG, Fiberoptic Add-Drop Devices*

## 1. Introduction

Recent advances in fiber-optical communication technology, most notably in the area of high power Rare-earth doped fibers and fiber Bragg grating offer a host of new opportunities within future high speed communication systems. In order to fully exploit the Tbit/s-transmission capacity within DWDM networks, the use of all-optical processing technique such as optical regeneration, wavelength conversion, routing and add-drop multiplexing will ultimately be required [1]. Fiber Bragg Gratings (FBGs) have been rapidly developed for last decade because of their advantages such as small size, light weight, intrinsic insulating properties, and wavelength multiplexing, and distributed sensing possibilities [2-6]. More importantly, the FBG have a capacity of precisely wavelength detection and/or multiplexing capabilities; tens of gratings with different Bragg wavelengths arranged in several different fibers can be formed into structurally integrated quasi-distributed detection systems, which are much in demand for various engineering applications such as sensory and optical communications. In this paper we review development in add-drop multiplexing using FBG which has been designed and made in Vietnam. After short brief about principle of FBG formation by using phase mask writing and/or Talbot interferometer with a KrF excimer laser of 248 nm, we present the state-of-the-art in term of Add-drop devices using FBG and fiber-optic circulator for bi-direction WDM networks, and conclude by proposal of adjusting Bragg wavelength center to signal wavelength by Peltier cooler, when the wavelength spacing between them was less than 0.2 nm. We believe highlight the potential of combining the FBG and wavelength adjustment by temperature for stable optical processing applications.

## 2. Principle of fbg formation and add-drop devices

### *2.1. Principle*

The structure of the fiber Bragg grating is formed by photo-induced periodic refractive index modulation within the fiber core, which results in a series of grating planes formed along the fiber axis. If the Bragg condition is met, light signal that is coupled into the device and reflected at each of the grating planes will add constructively to form a back reflected signal with a centre

wavelength commonly known as the Bragg wavelength. It is known that the Bragg wavelength is given by the phase-matching condition:

$$\lambda_B = 2\, n_{eff}\, \Lambda \qquad (1)$$

Where $\lambda_B$ is the Bragg wavelength, $n_{eff}$ is the effective index of the fiber core and $\Lambda$ is the period of the fiber Bragg grating. When applying some physical perturbation (such as the strain, pressure or change of temperature) in the fiber, the effective index $n_{eff}$ of the core and the separation between two neighboring grating planes $\Lambda$ can be affected. In result, the Bragg wavelength $\lambda_B$ would be changed. By differentiating Eq. (1) with respect to the reflective Bragg wavelength $\lambda_B$, it can be expressed as:

$$\Delta\lambda_B/\lambda_B = \Delta n_{eff}/ n_{eff} + \Delta\Lambda/\Lambda \qquad (2)$$

Where $\Delta\lambda_B$ is the Bragg wavelength shift. $\Delta n_{eff}$ and $\Delta\Lambda$ are the changes in effective refractive index and the grating period, respectively. The relative magnitudes of the two changes depend on the type of perturbation to which the grating is subjected. A change in the temperature induces the shift of Bragg wavelength can be calculated as [7]:

$$\Delta\lambda_B/\lambda_B = [(1 - p_e)\, \alpha + \xi]\, \Delta T \qquad (3)$$

Where $\alpha$ is the linear thermal expansion coefficient, $p_e$ is the photo-elastic constant ($p_e \cong 0.22$ for germano-silicate fiber) and $\xi$ is the thermo-optic coefficient of fiber, respectively. For $GeO_2$:$SiO_2$ fibers, $\alpha$ is so small ($0.5 \times 10^{-6}$ /K) that the effect of thermal expansion is one order less than that of thermo-optic refractive index change ($\xi \cong 10^{-5}$/K). Therefore, the grating period variation ($\Delta\Lambda/\Lambda$) can be neglected. The shift of Bragg wavelength $\Delta\lambda_B/\lambda_B$ in Eq. (2) can be expressed simply as:

$$\lambda_B = 2\, \Delta n_{eff}\, \Lambda \qquad (4)$$

Eq. (4) can be used to predict the peak shift of an FBG under temperature change in the ambient rounding FBG. In our previous publication, we have reported that an average temperature sensitivity of our FBG measured from 301K to 358K corresponds to 11.3 pm / K and 164.4 pm / K for non-embedded and Teflon/Epoxy Nano-particle embedded FBG, respectively [8].

### *2.2. Formation of FBG and Add-Drop Devices*

We write FBG into a photosensitive germano-silicate single-mode fiber (Type J-fiber PSP) by using phase mask writing and/or Talbot interferometer with a KrF Excimer laser of 248 nm. The system of FGB writing by KrF Excimer laser is demonstrated in figure 1.

The laser pulse energy is 100 mJ with pulse duration and repetition of 10 ns and of 10-50 Hz, respectively. The length of FBG is 20 mm with 70-80% reflectivity and with a Bragg wavelength range of 1520-1570 nm. For making Add-drop Devices, the Bragg wavelength of FBG should be corresponded to Wavelength Grid Standard Recommended by ITU with spacing of 50 GHz and its spectral bandwidth is less than 0.2 nm for DWDM networks. Scheme of Add-drop devices using FBG and fiber-optic circulator for DWDM networks presents in figure 2. The circulator has insert loss and cross-talk less than 1.0 dB and -40 dB, respectively. The incoming-to-WDM signal is modulated at 2.5 Gbit/s and the channel is dropping directly within FBGs after circulator.

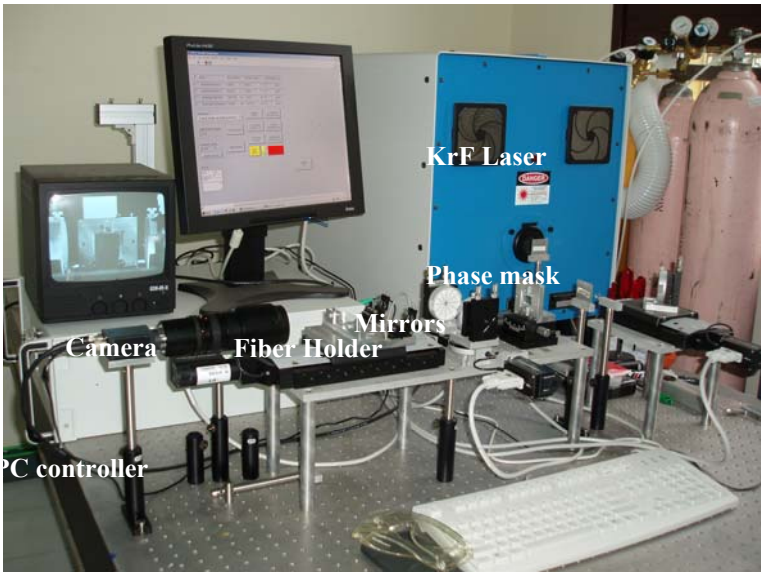


**Figure 1**. Schematic of UV-laser system for writing FBG in optical fibers

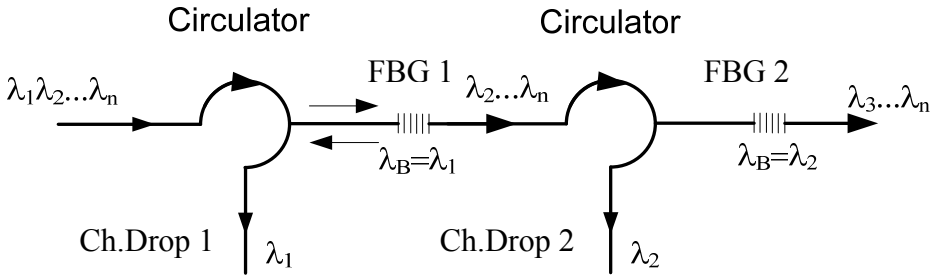


**Figure 2**. Schematic of Add-drop devices using FBG and circulator for DWDM networks

In practical work, it is very difficultly to make the Bragg wavelength center exactly equal to signal wavelength. In our experiment, the Bragg wavelength center of FBG differs from signal wavelength in the range of 0.02÷0.15 nm. These differences between Bragg's and signal wavelengths cause a decrease of reflected light power and of Signal-Noise-Ratio (SNR) at the detectors.

## 3. Results and discussions

The signal wavelengths were 1553.81 and 1557.06 nm with spectra bandwidth of 0.1 nm, which used in the Bi-direction WDM network. The Bragg wavelengths of FBGs used in the Add-drop device were 1553.84 and 1557.10 nm with spectra bandwidth of 0.2 nm and reflectivity of 89% and 70% for detection of signals, respectively. Figure 3 shows reflected spectra measured at channel drop ports number 1; 2 of Add-drop device. The value of suppression ratio between the dropped and through channels is typically less than 50 dB and it limited by the extinction ratio of the circulator and reflectivity of FBG.

The experimental results of Add-drop devices using FBG is shown in Table 1. Experiment shows that the FBG had a minimum side lobe extinction more than 35 dB in reflection. The channel suppression of 32-50 dB had been obtained in our particular Add-drop system.

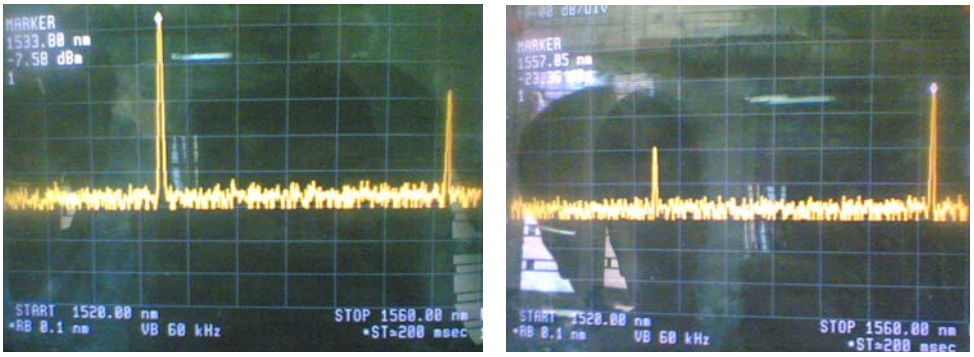


**Figure 3.** Reflection spectra of signal measured at dropped channel ports of Add-drop devices

**Table 1.** Experimental Results of FBG Add-drop device for two wavelengths of 1553 nm and 1557 nm

| Signal wavelength (nm) | FBG wavelength (nm) | Channel suppression (dB) | Dropped power at port 1 (dBm) | Dropped power at port 2 (dBm) |
|---|---|---|---|---|
| $\lambda_1$ = 1553. 81 | $\lambda_{B1}$= 1553.84 | 47.4 | -6.58 | - 51.0 |
| $\lambda_2$ = 1557.06 | $\lambda_{B2}$= 1557.10 | -54.0 | - 18.0 | 33.0 |

The Quasi-Gauss distribution [9] is an assumption that coincides best with the actual spectral intensity distribution of the laser beam and of FBG reflection. The intensity of reflected power from FBG is expressed by a modified Gauss function as:

$$I(\lambda_{B1}) = R_{FBG} I_0 \exp(-\Delta\lambda^2 / \Delta\lambda_0^2) \qquad (5)$$

Where, $R_{FBG}$ is reflectivity of FBG; $I_0$ is incoming signal spectral intensity; $\Delta\lambda_0$ is bandwidth of signal spectra and $\Delta\lambda$ is spacing between Bragg wavelength center and signal wavelength. Figure 4 shows the calculation results of the ratio of reflected signal to incoming signal intensities, when the bandwidth of signal and Bragg wavelength changed from 0.1 nm to 0.3 nm. Calculation shows that the intensity of reflected light from FBG strongly depends on spacing between FBG wavelength center and signal wavelength and on their bandwidths. The reflected intensity from FBG would be decreased on 50 percents of incoming signal intensity when the spacing between signal wavelength and Bragg wavelength center equal to FBG bandwidth. In practice, the ambient temperature rounding

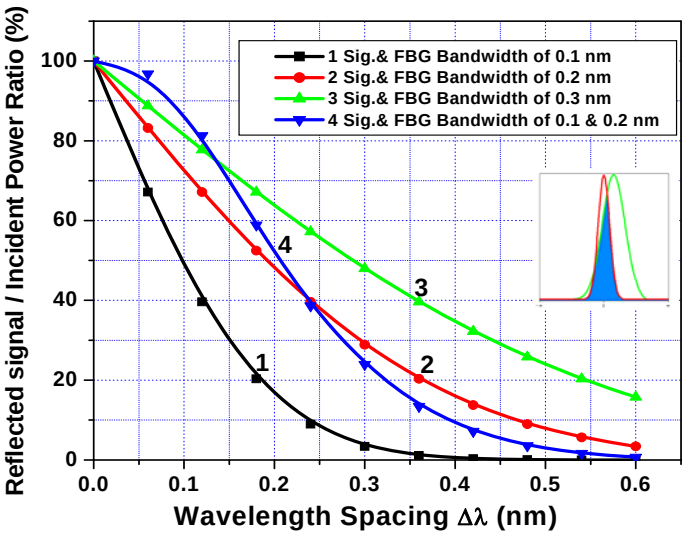


**Figure 4.** Calculation results of the Ratio of reflected signal to incident intensity depended on wavelength spacing between signal and FBG bandwidths ($R_{FBG}$ = 1). Inset: The cross-section of spectral intensity distribution of signal and FBG reflection according to modified Gauss function in equation (5)

FBG Add-drop multiplexing may be changed by time of day and/or year and then the dropped channel power would not be stable for long period of operation.

We propose the method for adjusting the Bragg wavelength center to signal wavelength using Peltier cooler. The FBG was glued in copper V-groove substrate, which attached on Peltier cooler with surface area of 1x3 $cm^2$. The Peltier cooler can be adjusted the temperature of substrate from $283^0$K to $323^0$K with accuracy of $0.2^0$K. From our previous publication [8], the temperature sensitivity of non-embedded FBG was of 11.3 pm / K, and then we can adjust the Bragg wavelength center in the range of 0.45 nm. The automatically process of stability of dropped channel power of FBG Add-drop multiplexing will be studied in next time.

## 4. Conclusions

In conclusion we have reviewed the method for writing FBG with various Bragg bandwidths in photosensitive germano-silicate fibers using KrF laser and Talbot interferometer. We have shown the design and testing results of FBG Add-drop multiplexing with the dropped channel suppression of 32-50 dB for bi-direction WDM networks. We consider our results of calculation ratio of Bragg reflected to signal intensities and the method for adjusting Bragg wavelength center to signal wavelength to highlight that these a most promising approach to controlling the efficiency and/or stability of dropped channel power of FBG Add-drop multiplexing in the practice.

***Acknowledgements:*** *This work is supported by National Science-Technology Council KC-01 of Ministry of Science and Technology of Vietnam under Contracts KC-01-13 /06-10 and by National Natural Science Program in Physics of Vietnam 2006-2008 under Grant No. CB14. The authors express our appreciation to the State Key Lab. on Electronic Materials and Devices for testing equipments.*

## References

1. D.J. Richardson, J.Y.Y. Leong, F. Parmigiani, P.J. Almeida, M. Ibsen, P. Petropoulos, *Recent developments in fibre technology and its application within high speed optical communications*, paper of IGNOIE – COE05, Sendai, Tokyo-Japan, 31 Jan-01 Feb., (2006) 6pp.
2. K.T.V.Grattan,T.Dr.Sun, *Fibre optic sensor technology: an overview,* Sens.Actuators A 82(2000)40-61.
3. K. O. Hill and G Meltz, *Fiber grating spectra*, J. Lightwave Technol. 15 (1997) 1263-1276.
4. A. D. Kersey, M.A. Davis, H. J. Patrick, M. LeBlance, K. P. Koo, C.G. Askins, M. A. Putnam, and E. J. Friebele, *Fiber grating sensors*, J. Lightwave Technol. 15 (1997) 1442-1463.
5. A. Othonos, *Fiber Bragg gratings*, Rev. Sci. Instrum. 68 (1997) 4309-4341.
6. K. O. Hill, Y.Fujii, D.C. Johnson, and B. S. Kawasaki, *Photosensitivity in optical fiber waveguides- Application to reflection filter fabrication*, Appl. Phys. Lett. 32 (1978) 647-649.
7. T. Mizunami, H. Tatehata, H. Kawashim, *High-sensitivity cryogenic fibre-Bragg-grating temperature sensors using Teflon substrates*, Mea.Sci.&Technol., 12 (2001) 914-917.
8. Pham Van Hoi, Pham Thanh Binh, Pham Tran Tuan Anh, Ha Xuan Vinh, Chu Thi Thu Ha, Nguyen Thu Trang, *Spectra profile expansion of Bragg wavelength on Nano-Particle Embedded Fiber-Bragg-Grating,* Sens.Actuators A 141(2008) 334-338.
9. J.A.B. Faria, *Modeling the Y-branched optical fiber bundle displacement sensor using a quasi-Gaussian beam approach*, Microwave Opt. Technol. Lett. 25 (2000) 138-141.

# RANDOM MICROLASER EXCITED BY THE THIRD HARMONIC OF Nd:YAG LASER

**Pham Van Thin, Nguyen Bich Hanh, Dinh Thi Yen, Nguyen The Binh, Ta Dinh Canh**

Department of Physics, Hanoi University of Science, VNU
334 Nguyen Trai, Thanh Xuan, Ha Noi
*E-mail: thebinh@vnu.edu.vn*

**Abstract**. Random microlaser emission from ZnO samples was observed and studied. We used the third harmonic (355nm) of a Nd:YAG laser (Quanta Ray Pro 230 Newport, USA) as pump source. The Nd:YAG laser was set to operate at Q-switching mode and the optical third harmonic generation with high conversion efficiency was produced by a KDP crystal to give laser pulses of 355nm wavelength, 5ns duration and repetition rate of 10Hz . Random microlaser emission was observed by a MS -257 spectrograph with CCD detection system (Oriel-Newport,USA). ZnO samples were synthesized using the chemical precipitation method under the effect of microwave. The results and discussions will be represented in this report.

## 1. Introduction

The possibility of lasing in disordered media was first predicted by Letokhov in 1967 [1], and random laser was first experimentally observed from the dielectric powders doped with neodymium in 1986 [2]. After that, random laser effect was investigated in many different media such as inorganic dielectrics, semiconductors, polymers, or liquids… In recent years, ZnO material has attracted great interest because of its potential to produce efficient blue and violet-light-emitting lasers for applications in photonics. ZnO material is a wide band-gap semiconductor (Eg ~ 3.3eV at room temperature). The excitonic emission may be realized for ZnO due to its large exciton binding energy (~60meV). The room temperature recombination of excitons in zinc oxide gives UV radiation in the range of 385 - 395nm with less than 200ps in intrinsic lifetime [5]. Until now, there have been many experimental investigations on observing random laser from ZnO by differential methods. In principle, it is suitable to excite lasing from zinc oxide by picosecond pulses because of its intrinsic lifetime 200ps so that during the pump pulse, spontaneous decay practically does not appear yet. In most of ZnO random laser studies, they used picosecond laser pulses as optical pumping source [3,8]. In case of laser pumping by nanosecond pulses, the lasing evolution becomes more complicated. They expect quasi-continuous lasing in ZnO material.[5,6]. The characteristic properties of lasing under nanosecond excitation are not yet interpreted fully. In the previous reports [4], we presented our results of observing stimulated emission and lasing from sol-gel and sputtering ZnO thin films under the Nitrogen pulse laser (337nm wavelength, 6ns pulse duration and peak power up to 500 kW). These lasing spectra was separated from spontaneous emission by a time-resolved spectrum measurement system using GDM1000 double grating monochromator coupling with a R-928 PMT (Hamamatsu, Japan) and a TDS - 2014 Tektronix oscilloscope.

In this paper, we report our studies on random lasing from ZnO powder excited by the third harmonic (355nm) of Nd:YAG laser with pulse duration of approximately 5ns. Spectra of random lasers were obtained by a MS-257 spectrograph (Oriel-Newport, USA) with a CCD detection . The lasing medium is the powder of zinc oxide which was made by a chemical - microwave method with particles size of approximately 50 - 150nm.

## 2. Experiments

### *2.1. Sample preparation*

ZnO powder was synthesized using the chemical precipitation method under the effect of microwave. Mixture of Zinc Nitrate and Sodium hydroxide (with 1:2 molar ratio) was stirred in the microwave oven for 10 minutes:

$Zn(NO_3)_2 + 2NaOH \rightarrow 2Zn(OH)_2 \rightarrow 2ZnO.$

The resulted solid was filtered and washed several times with distilled water and alcohol. Finally, it was dried and we got the solid material as ZnO powder. The average size and morphology of the ZnO particles were characterized by a JOEL-JSM5410LV Scanning Electron Microscopy (SEM).

Figure 1 shows SEM images of the ZnO powder. The average size of the particles is mainly distributed in the range of 50 to 150nm.

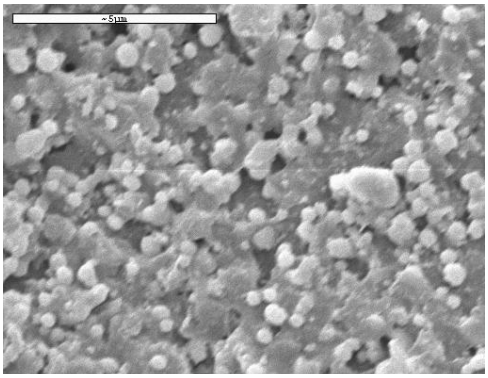

**Fig. 1**: The SEM image of the ZnO sample

### *2.2. Experimental setup*

Random laser spectra were measured by a MS-257 spectrograph (Oriel -Newport, USA).with an IntraSpec$^{TM}$ IV 1064x 256 pixel CCD detector. The probe limit is 3.8 femtoJun/cm$^2$, saturated exposure energy is 250 picoJun/cm$^2$, noise is low (< 13 electron) and working wavelength range is 180-1100nm. As a pump source, Nd:YAG laser (Quanta - Ray Pro 230 Newport, USA) was set to operate at Q - switching mode with laser pulse duration of 8ns, repetition rate of 10Hz and pulse energy up to 1200mJ at original wavelength (1064nm) and the second harmonic (532nm). We used KDP crystal (size 10x10x5mm) to generate the third harmonic (355nm) for exciting ZnO samples. The third harmonic generation was produced by Sum Frequency Generation (SFG) of the fundamental frequency and its second harmonic frequency in phase matching type I (o+o→e). The performance of conversion process is 25% and average density power can be up to 260mJ/cm$^2$ (The average power of laser beam was measured by MELLES GRIOT 13PEM001). Our experimental arrangement is shown in Fig.2.


**Fig. 2:** Experimental arrangement

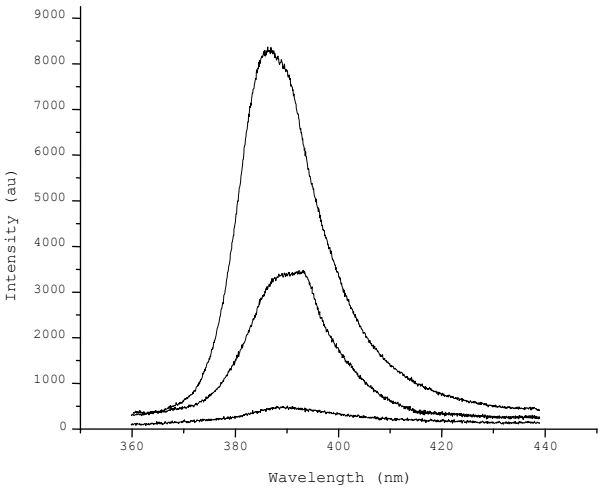


**Fig.3:** The emission spectra under multi -shot pumping (average energy of pumping pulses wasabout 5 mJ, 20mJ and 50mJ)

## 3. Results and discussion

After evaluating size and morphology of the ZnO particles in prepared samples, We measured emission spectra from the ZnO sample excited by 355nm laser pulses. Using MS-257

spectrograph with CCD detector we could register spectra of lasing during a given number of pumping pulses or during a single pumping pulse.

At a multi-shot pumping, with average energy raging from 5 to 50mJ we observed emission spectra from ZnO sample (Fig.3). The emission spectrum consists of a single broad band with peak at 390 - 391nm. With a rise of pumping energy the peak intensity increases quickly but there is not any shape individual lines as expected in picosecond pumping [8]. At a high pump power, the full width half maximum (FWHM) is about 15nm. Because the pump power is high enough in comparison with lasing threshold we think may be lasing occurred but laser emission spectra were superposed from shot to shot.

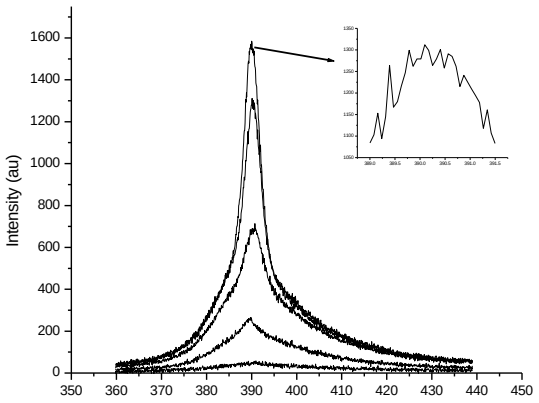


**Fig.4**: The emission spectra under single pumping pulse (average energy of pumping pulses was about 5 mJ, 20mJ , 30mJ, 40mJ and 50mJ)

In order to separate spectra we registered lasing spectra under a single pumping pulse. The results were shown in Fig.4. With higher pumping power, the emission band is narrower. When the pumping energy exceeded 30mJ, narrow emission bands with a FWHM smaller than 4nm appeared.. This narrow emission band width is an evidence of lasing from ZnO sample. The experimental results show that the laser emissions under single shot nanosecond pumping is different from that under picosecond pumping. There is not appearance of narrow lines in laser spectra from our ZnO sample even at high pumping power. At least, during initial part of a single pumping pulse shorter than intrinsic life time (~200ps) lasing appeared with some irregular narrow spikes. In our ZnO samples with the average particle size of 50 - 150nm, the scattering mean free path becomes less than the wavelength, photon may return to the scatter from which it was scattered before and it may results in a closed loop that serves as a resonator (Anderson localization). If the amplification along such a loop path exceeds the loss, laser action could occur with a characteristic narrow lines. During the duration 5ns of a single pumping pulse a quasi-continuous lasing occurred. The smoothed emission spectra may be due to the appearance of several lasing acts during a nanosecond pumping pulse.

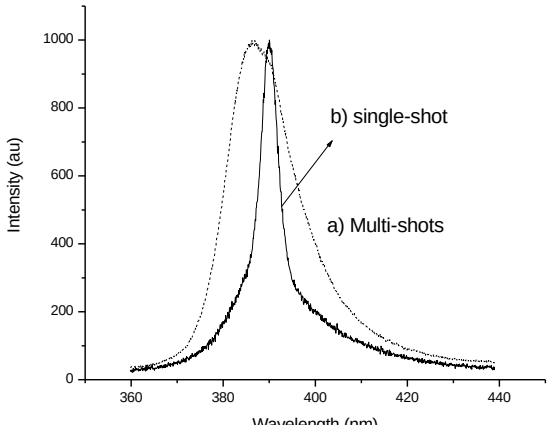


**Fig.5:** Comparison between emission spectra registered under single-shot and multi-shots

The laser spectrum obtained in this study is a wide range of wavelength from 388 to 392 nm. The comparison between laser spectra under single-pumping pulse and under multi pumping pulses was shown in Fig 5. During several nanosecond pumping pulses several irregular lasing spectra appeared and overlapped each other. The larger band width of laser spectra under multi-shot pulses showed that the laser spectrum is the result of a wavelength changing in lasing process. Due to pumping by nanosecond pulses much longer than intrinsic life time, lasing process composes several laser oscillations with different wavelengths. The lasing spectra changed from shot to shot and their superposition gives a larger band width. In addition, the lasing spectrum from ZnO powder also depends on morphology and

crystalline quality of the ZnO particles. It needs more studies to understand further lasing spectra of ZnO random laser pumped by nanosecond pulses.

It is interesting to find out what are the lasing characteristic properties under the nanosecond pumping. In particular, it may be expected to looking at a quasi-continuous lasing, an effect has not been investigated in the ZnO powders.

## 4. Conclusion

Our ZnO samples prepared by chemical - microwave method with particles size of approximately 50 - 150nm are suitable for random laser effect.. The UV laser spectrum obtained from the ZnO powder samples is in good agreement with theory. Origin of these emissions results from the exciton recombination and electron-hole plasma (EHP) recombination. The experimental results show that the laser emissions under single nanosecond pumping pulse is quite different from that under picosecond pumping pulses. Narrow lasing spectra from ZnO powder were observed but there was not the appearance of equidistant spikes in the spectra. During a single nanosecond pumping pulse, several laser modes are activated and superposed each other. In addition, the difference between the frequencies of these modes during different single shots gives a broad band in laser spectra registered under multi pumping pulses These results helped us to understand more clearly the dynamical process of ZnO random laser. However, it needs more studies to give a full interpretation for characteristic properties of random lasing from ZnO material.

***Acknowledgments***

*This work was supported by the National Basic Scientific Research Program (Project 4 061 06)*

## References

1. V.S. Letokhov, Zh. Eksp. Teor. Fiz. **53**, 1442 (1967) [Sov. Phys. JEPT **26**, 835 (1968)].
2. V. M. Markushev, V. F, Zolin, and Ch. M. Briskina, Zh. Prikl. Spectrosk. **45**, 847 (1986).
3. H. Cao, J.Y. Xu, Y. Ling, et al., IEER J. Sel. Top. Quantum Electron. **9**, 111 (2003).
4. Nguyen The Binh, Nguyen Van Hao, Nguyen Thi Hang, Duong Vu Truong, Pham Van Thin, Random laser in ZnO powder, Advances in Optics Photonics Spectroscopy and Applications, Vietnam Academic Press, 298-302 (2007).
5. V. M. Markushev, M. V. Ryzhkov, Ch. M. Briskina, H. Cao, L. A. Zadorozhnaya, E. I. Givargisov, H. Zhong, S.-W. Wang, and W. Lu, ZnO Random Laser Spectra under Nanosecond pumping, Laser Physics, 2007, Vol. 17, No. 9, pp. 1109–1118
6. V.M.Markushev, M.V. Ryzhkov, C.M. Briskina, Characteristic properties of ZnO random laser pumped by nanosecond pulses, Appl. Phys. B **84**, 333–337 (2006)
7. H. Cao, J.Y. Xu, D.Z. Zhang, S.-H. Chan, S.T. Ho, E.W. Seelig, X. Liu, and R.P.H. Chang, Spatial confinement of laser light in active random media, Phys. Rev.Lett., **84**: 5584–5587 (2000).
8. H. Cao and Y. G. Zhao, Random Laser Action in Semiconductor Powder, Phys.Rev.Lett, **82**, 2278 – 2281 (1999)
9. R.K. Thareja and A. Mitra, Random laser action in ZnO, Appl. Phys. B, **71**: 181–184 (2000).
10. Y. Ling, H. Cao, A.L. Burin, M.A. Ratner, X. Liu, and R.P.H. Chang, Investigation of random lasers with resonant feedback, Phys. Rev. A., **64**: 063808 (2001)

# INVESTIGATION OF SOLITON'S TRANSMISSION IN OPTICAL FIBERS USING DISPERSION MANAGEMENT TECHNIQUES

**Dinh Xuan Khoa, Bui Dinh Thuan and Tran Manh Hung**

Vinh University

**Abstract** In this paper, numerical methods are used to simulate the soliton's transmission in optical fibers using dispersion management techniques. The dependences of parameters such as the length $L_A$ between amplifiers, the ratio between the lengths of DCF and of normal optical fibers are defined so that in transmission process, soliton is in stable state.

## 1. Introduction

In optical fibers, soliton is formed by the balance between phase self modulation phenomenon and dispersion phenomenon caused by group velocity. The loss and the dispersion decrease soliton's transmission length and its stable. For long distance communication systems, the influence of dispersion caused by group velocity, phase self modulation and the change of power along fibers can be compensated by DCF and optical amplifiers. This techniques is called dispersion management techniques. It is used effectively because the system designer has a right to select optical fibers with different dispersion properties.

The transmission of pulses in optical fibers is described by nonlinear Schrodinger equation. This equation can be solved by back scattering method and pertubation techniques. But when the dispersion management techniques is used, the optical signal is transmitted along a fiber composed by different parts with different dispersion properties, analytical methods can not be applied. For this purpose, numerical methods are applied effectively. Different algorithms are proposed by many authors to solve nonlinear Schrodinger equation [1,3]. But in principle, these algorithms can be divided into 2 types[1]. The second method uses Fourier transformation to calculate private derivatives and transforms private derivative equations problem into normal differential equation problems.

## 2. Pulse transmission equation using dispersion management techniques

The transmission of ~ 5 ps optical pulses in optical fibers, when GVD, absorption and phase self modulation are considered, is described by the following equation [2,3,4,5]

$$\frac{\partial A}{\partial z} = -\frac{\alpha}{2}A - \frac{i}{2}\beta_2 \frac{\partial^2 A}{\partial t'^2} + i\gamma|A|^2 A \qquad (1)$$

where A=A(z,t) is the slow variance complex envelop function of optical field along optical fiber; $\alpha$ is the loss coefficient of optical fiber; $\beta_2$ is the second order dispersion coefficient; $\gamma$ is the nonlinear coefficient of optical fiber; and $t' = t - \frac{z}{v_g}$.

In general case, when the loss of optical fibers is small enough, $\beta_2$ <0 and the two characteristic lengths: $L_D = \frac{T_0^2}{|\beta_2|}$ of dispersion phenomenon, and $L_N = \frac{1}{\gamma P_0}$ of nonlinear phenomenon are approximately equal ($T_0$ is the width of input pulse, $P_0$ is the power of pulse peak)[2], the form of pulse is unchanged in transmission process, and it is soliton.

When the loss is considered, the presence of $\alpha$ leads to the change of power along the fibers. The influence of loss on phase modulation can be seen more clearly by putting:

$$A(z,t') = B(z,t')\exp\left(-\frac{\alpha z}{2}\right). \qquad (2)$$

Substituting (2) into (1), we obtain :

$$\frac{\partial B(z,t')}{\partial z} = \frac{i}{2}\beta_2 \frac{\partial^2 B(z,t')}{\partial t'^2} - i\bar{\gamma}|B(z,t')|^2 B(z,t') \qquad (3)$$

where $\bar{\gamma} = \gamma \exp(-\alpha.z)$. So the influence of loss is similar mathematically to un-loss case, except a nonlinear parameter, which depends on z.

For long distance communication systems, the influence of dispersion caused by group velocity and of the change of power along fibers can be compensated by dispersion management techniques. When this techniques is applied, the optical signal is transmitted along a fiber composed by different parts with positive and negative dispersion coefficients so that the influences of dispersion and nonlinear phenomena are reduced.

Using dispersion management techniques, the equation (3) can be re-written in the form:

$$\frac{\partial U}{\partial \xi} = \frac{i}{2} D(\xi) \frac{\partial^2 U}{\partial \tau^2} + iN^2 |U|^2 U \exp(\alpha\xi) \qquad (4)$$

where: $\tau = \frac{t'}{T_0} = \frac{(t - z/v_g)}{T_0}$, $\xi = \frac{z}{L_D}$ , $N^2 = \frac{L_D}{L_N}$, $U(\xi,\tau) = \frac{1}{P_0} B(\xi,\tau)$ and D is the dispersion coefficient, which depends on the transmission distance, and can be defined as [1,2]:

$$D(\xi) = \begin{cases} D_1 > 0, & 0 < \xi < \frac{L_1}{L_D} \\ D_2 < 0, & \frac{L_1}{L_D} < \xi < \frac{L_1}{L_D} + \frac{L_2}{L_D} \end{cases}$$

There are many different algorithms [1, 2, 8,7,] to solve numerically the equation (4). In this paper we use 4$^{th}$ order Runge - Kutta algorithm. The calculation of private time derivatives can be done using the Fourier transformation. Then the calculation of private space derivatives are calculated using the Runge Kutta algorithm . After using Fourier transformation to calculate private time derivatives, equation (4) becomes

$$\frac{d}{d\xi}(F[U]) = \left((-i\omega D)^2 \frac{i}{2}\right) F[U] + iN^2 F\left[|U|^2 U \exp(-\alpha\xi)\right] \qquad (5)$$

where F and $F^{-1}$ are Fourier transformations. Putting

$$V = \exp\left(\frac{i\omega^2}{2} D\xi\right) F[U], \qquad (6)$$

the equation (4) can be re-written as:

$$\frac{dV}{d\xi} = f(\xi, U), \qquad (7)$$

where:

$$f(\xi,U) = iN^2 \exp\left(\frac{i\omega^2}{2} D\xi\right)\left[ F\left[|U|^2 U \exp(-\alpha\xi)\right] \right] \qquad (8)$$

Using the 4$^{th}$ order Runge - Kutta algorithm for equation (7), the value of the function V at the position $\xi + \Delta\xi$ is calculated as

$$V(\xi+\Delta\xi)=V(\xi)+\frac{1}{6}[K_1+2(K_2+K_3)+K_4], \qquad (9)$$

where $K_i$ coefficients are as follows:

$$\begin{aligned} K_1 &= \Delta\xi.f(\xi,U(\xi,\tau)),\\ K_2 &= \Delta.f\left(\xi+\frac{\Delta\xi}{2},U(\xi,\tau)+\frac{1}{2}K_1\right),\\ K_3 &= \Delta\xi.f\left(\xi+\frac{\Delta\xi}{2},U(\xi,\tau)+\frac{1}{2}K_2\right),\\ K_4 &= \Delta\xi.f(\xi+\Delta\xi,U(\xi,\tau)+K_3). \end{aligned} \qquad (10)$$

From (9) and (8), the value of envelope function at the position $\xi+\Delta\xi$ is calculated as

$$U(\xi+\Delta\xi)=F^{-1}\left[V(\xi+\Delta\xi)\exp\left(\left(-\frac{i\omega^2}{2}D\right)(\xi+\Delta\xi)\right)\right]. \qquad (11)$$

The calculation error in (11) is of the order $(\Delta\xi)^5$.

## 3. Some results obtained

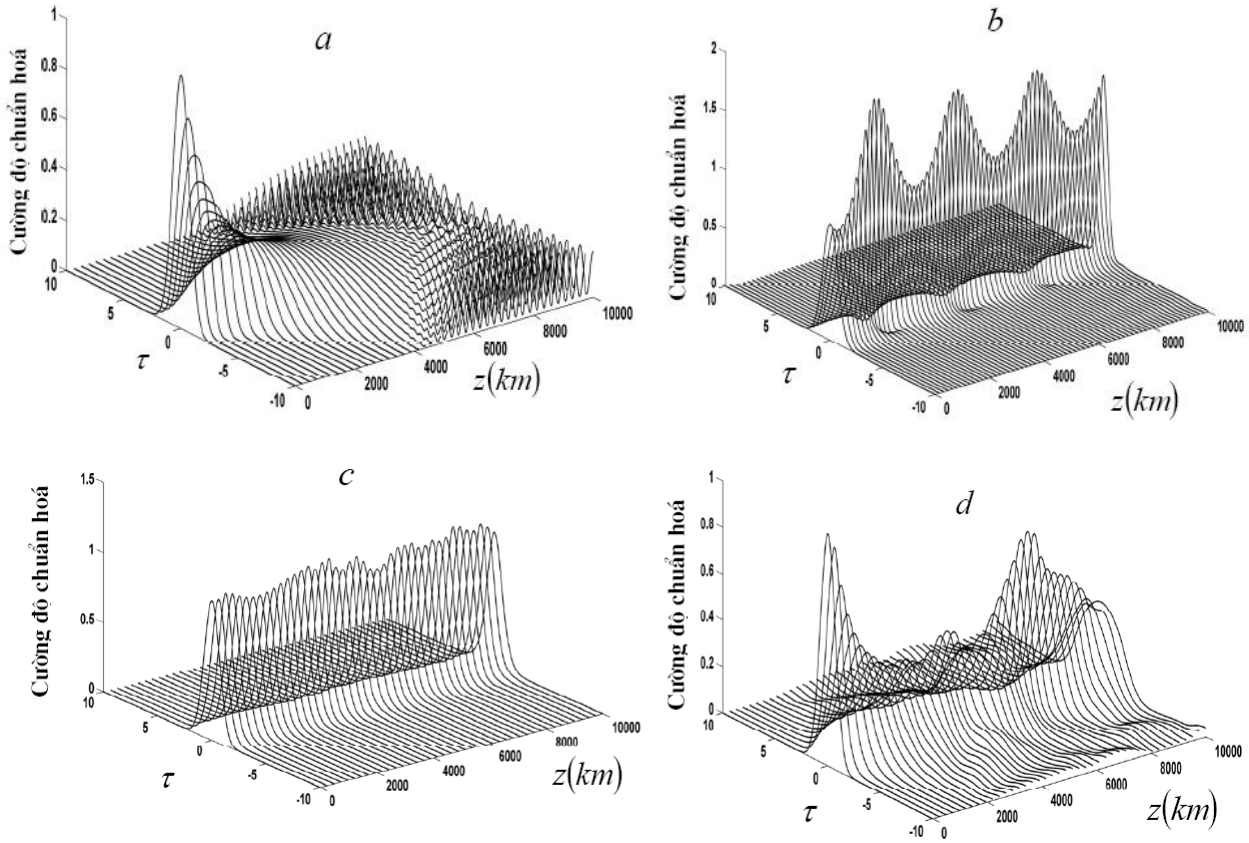


**Fig 1**. 3D graph describing soliton transmission process when dispersion management techniques is applied. a) $\frac{L_1}{L_2}=6$, b) $\frac{L_1}{L_2}=7$, c) $\frac{L_1}{L_2}=8$, d) $\frac{L_1}{L_2}=10$

The influence of absorption can be solve by optical amplifiers arranged periodically along the fiber. Its amplification factor is adjusted such us the consume between two amplifiers is compensated by the amplification factor of the amplifier. However, in each period, the pulse

intensity decreases. It influences the phase self modulation effect, destroying pulse form in transformation process. The maintenance of pulse form in transformation process depends on many design parameters, such as: power of input pulse, amplification distance, ratio between the lengths of DCF and normal optical fiber. In the numerical simulations performed below, we have used the algorithm presented in section II for solving equation (4). The values of the parameters are chosen as follow: the input pulse is Gaussian with peak power of -3dbm, the dispersion parameter of DCF $D_2$ = -100 ps/nm.km, the absorption factor $\alpha_2$ = 0.5 db/km, the nonlinear factor $\gamma_2$ =80(W.km)$^{-1}$, the dispersion parameter of normal fiber $D_1$ = 16 ps/nm.km, the absorption factor $\alpha_1$ = 0.2 db/km, the nonlinear factor $\gamma_1$ =20(W.km)$^{-1}$.

Fixing the amplification distance $L_A$ =80km and changing the lengths of DCF and of normal optical fiber in one period, we obtain the following Aresults (fig. 1)

In case of $L_1 = 7L_2$ (Fig. 1b), after a transmission distance of 800km, the pulse's width and form vibrate periodically. It is shown more detail in Fig 2.

In case of $L_1 = 8L_2$ (Fig. 1c), the influences of effects compensate for each other in each period, so that the vibration of pulse in transmission is negligible. In cases of $L_1 = 6L_2$ and $L_1 = 10L_2$ , the pulse is destroyed in transmission process. Changing the lengths of DCF and normal optical fiber in each period, it shows that with the above chosen parameters, the pulse form is maintained in transmission process when 1km of DCF compensates for 7-9 km of normal optical fiber .

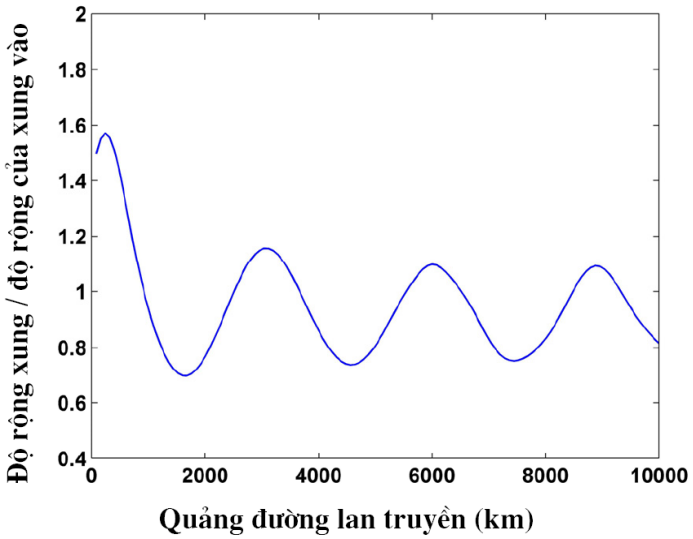


**Fig 2**. The change of pulse's width along transmission path

For communication system using amplifiers, the distance $L_A$ between amplifiers is an important design parameter. The larger $L_A$ is the better in order to reduce the cost. However, $L_A$ can not be chosen arbitrarily because it depends on other parameters, such as input pulse intensity, length of DCF in each period… In the case showed in Fig. 3, the parameters are chosen as in the case showed in Fig. 1, ratio between the lengths of DCF and normal optical fiber equal 10 in each period ($L_1$=10$L_2$) and the distance between amplifiers is changed.

When the distance $L_A$ =50km, the vibration of pulse is insignificant (Fig. 3a) and the soliton is in stable state. If the distance between amplifiers increases, the pulse is destroyed more quickly (Fig. 3b, 3c, 3d). So that the ratio between the lengths of normal optical fiber and of DCF in each period is inversely proportional to $L_A$.

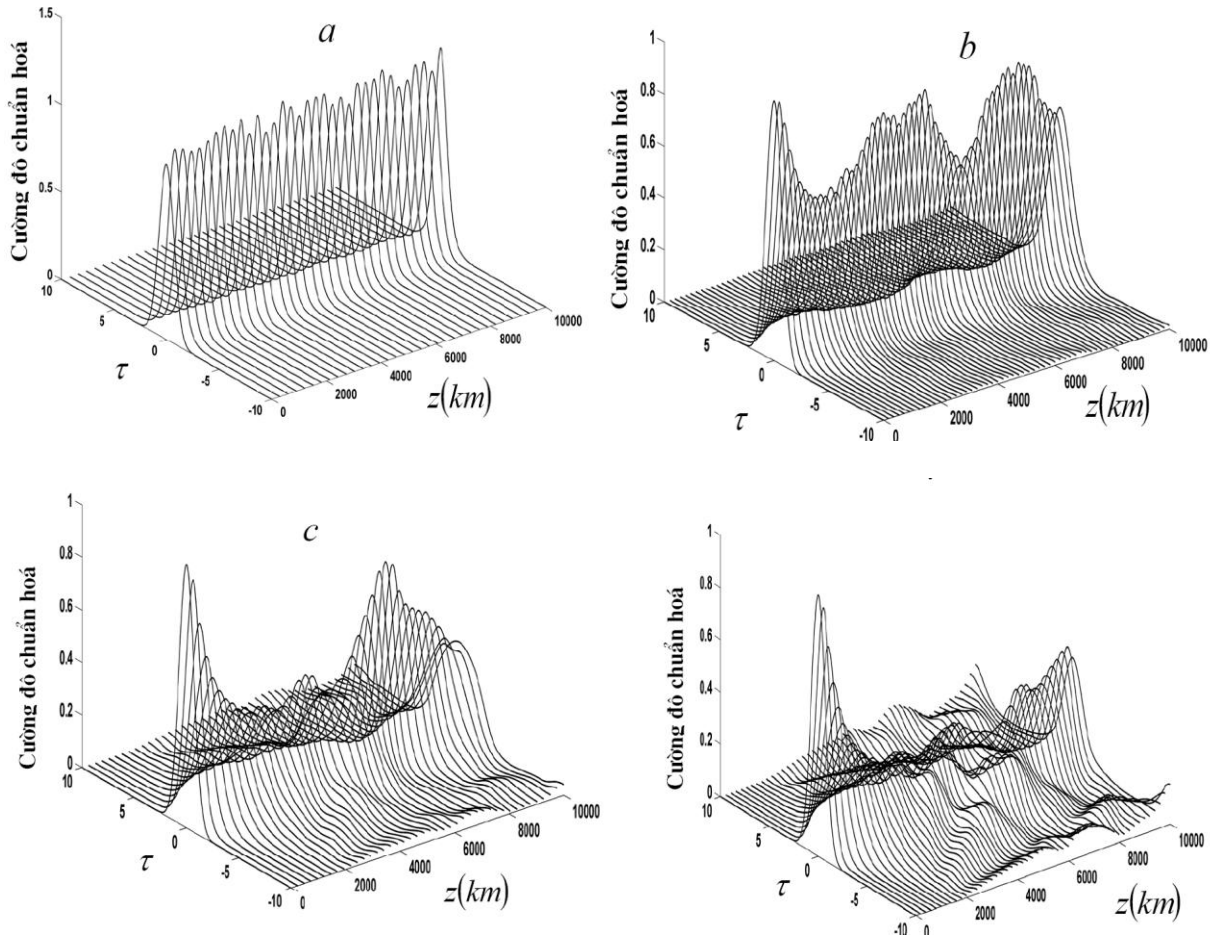


**Fig. 3**: 3D graph describing soliton transmission process when dispersion management techniques is applied for the case of $\frac{L_1}{L_2} = 10$ . a) $L_A = 50km$, b) $L_A = 60km$, c) $L_A = 80km$, d) $L_A = 100km$

## 4. Conclusion

In this paper, we use numerical methods to investigate the transmission of soliton using dispersion management techniques. The numerical simulations show that: the influences of dispersion and decreasing of power during the propagation of pulse in fiber can be managed by choosing appropriate characteristic distances ($L_A$ and the ratio of lengths of normal and dispersion compensating fibers). In particular case of $L_A$ = 80 km and $L_1=8L_A$ , we have observed stable propagation of pulse in fiber. Because of balance between two influences, the shape and width of pulse only oscillate periodically with small amplitudes.

The ratio between the lengths of normal optical fiber and of DCF in each period is inversely proportional to $L_A$.

## References

1. T. Schneider. Nonlinear Optics in Telecommunications, Springer, 2004.
2. G. P. Agrawal. *"Nonlinear Fiber Optics",* Academic, San Diego – 2001.
3. Cao long Van, Dinh Xuan Khoa, M.Trippenback, *Nhap mon quang hoc phi tuyen*, Vinh 2003.
4. Dinh Xuan Khoa and Bui Dinh Thuan *"Soliton study of Schrodinger equation by hirota method*", Vol 15, number 2, June 2005

5. Dinh Xuan Khoa and Bui Dinh Thuan *" Influence of Loss and High-order Dispersion on Soliton's Transmission in Optical Fibers"* Communications in physics Vol 17, March 2007, pp 17-22.
6. P.N. Butcher and D. Cotter, *The elements of nonlinear optics*, Cambridge University Press, New York, 1990.
7. A. Hasegawa and Y. Kodama, *Solitons in optical communication*, Oxford University Press, New York, 1995.
8. G.P.Agrawal and M.J.Potasek, *"Nonlinear pulse distortion in single mode optical fibers at the zero-dispersion wavelength"* Phys Rev. Vol 33, no 3. pp.1765 - 1776, 1986

# STABLE MANIPULATION DIELECTRIC SPHERE OF OPTICAL TRAPPING BY TWO COUNTER-PROPAGATING GAUSSIAN PULSED BEAMS

**Ho Quang Quy [a], Mai Van Luu [b]**

[a)] Institute of Applied Physics, NEWTECHPRO, Hanoi
[b)] Faculty of Physics, Vinh University, Vinh

**Abstract**: In this article the distribution of the radiation force acting on a Rayleigh dielectric sphere produced by optical trap from two counter-propagating Gaussian pulsed beams is presented. The analytical expressions for the scattering force and all components of the pondermotive force induced by two Gaussian pulsed beams, whose waists are placed with spatial interval ±d are derived. The simulating analysis shows that the radiation force can be greatly enhanced due to interval between two waists. Finally the stable manipulating region of the optical trap is discussed.

***Key words:*** *Optical trap, Gaussian pulsed beam, Radiation force.*

## 1. Introduction

In 1970, Ashkin [1] first demonstrated the optical trapping of particles using the radiation force produced by the focused continuous-wave (CW) Gaussian beam. Since that the optical trapping or tweezers has become a powerful tool for manipulating dielectric particles [2, 3].

Usually, optical traps or tweezers in many experiments are constructed by using the CW laser. It is well known that the CW laser with the power of a few milliwatt can only produce the radiation force with an order of a few pN to manipulate the micro-sized particles. Recently, Ambardekar et al. [4], Deng et al. [5] and Wang et al [6] used a pulsed laser to generate the large gradient force, up to 2500 pN within a short duration, about ps.

However, there is not any investigation about "how does the interval between two beam waist effects on the radiation force acting on Rayleigh particles if the optical trap consists from two focused counter-propagating pulsed Gaussian beams". In this paper, we have derived the analytical expressions for the longitudinal and transverse components of the radiation force under Rayleigh approximation. Based on the derived formula, we analyze the effect of the interval between two beam waists on the optical trapping and manipulating effect on the micro-sized particles. At last, we discuss the stable manipulating region of the trap.

## 2.Radiation force induced by two pulsed Gaussian beams

As shown in Fig.1, we consider the radiation force produced by two three-dimensional paraxial counter-propagating pulsed Gaussian beams acting on a Rayleigh dielectric sphere. The polarization direction of the electric field is assumed to be along the $x$ axis.

The expression for the electric field of the left Gaussian beam is defined by [6]

$$\vec{E}_l(\rho,z,t,d)=\hat{x}E_0\frac{ikw_0^2}{ikw_0^2+2(z+d/2)}\exp\left[-i\left(k\left(z+d/2\right)-\omega_0 t\right)\right]$$
$$\times\exp\left[-i\frac{2kz\rho^2}{\left(kw_0^2\right)+2(z+d/2)^2}\right] \qquad (1a)$$
$$\times\exp\left[-\frac{\left(kw_0^2\right)^2\rho^2}{\left(kw_0^2\right)^2+4(z+d/2)^2}\right]\exp\left[-\left(t-\left(z+d/2\right)c\right)^2/\tau^2\right],$$

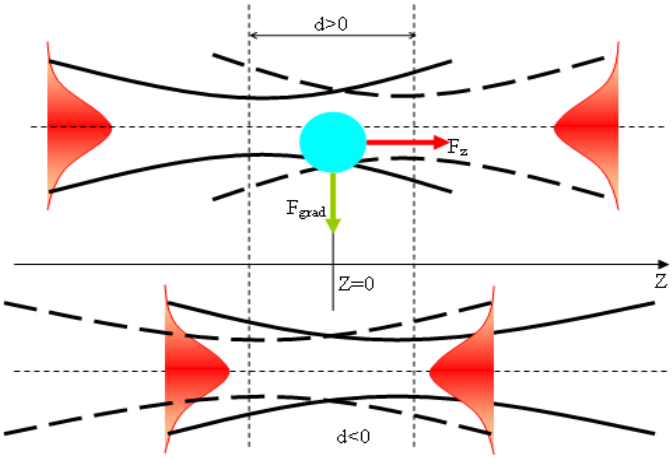


**Fig.1.** Schematics of a two counter-propagating laser beams radiating onto a particle

and analogically, we consider expression for the electric field of the right Gaussian beam as follow

$$\vec{E}_r(\rho,z,t,d)=\hat{x}E_0\frac{ikw_0^2}{ikw_0^2+2(z-d/2)}\exp\left[-i(k(z-d/2)-\omega_0 t)\right]$$
$$\times\exp\left[-i\frac{2k(z-d)\rho^2}{(kw_0^2)+2(z-d/2)^2}\right] \qquad (1b)$$
$$\times\exp\left[-\frac{(kw_0^2)^2\rho^2}{(kw_0^2)^2+4(z-d/2)^2}\right]\exp\left[-(t+(z-d/2)c)^2/\tau^2\right],$$

where $w_0$ is the spot radius of the beam waist at the plane $z=d/2$ for the right beam and $z=-d/2$ for the left one, $\rho$ is the radial co-ordinate, $\hat{x}$ is the unit vector of the polarization along the $x$ direction, $k=2\pi/\lambda$ is the wave number, $\omega_0$ is the carrier frequency, $\tau$ is the pulse duration and $d$ is the spatial interval between two beam waists. The sign of $d$ belongs to a placing correlation between two beam waists (see in fig.1). For the fixed input energy $U$ of a single pulsed beam, the constant $E_0$ is determined by $E_0^2=4\sqrt{2}U/\left[n_2\varepsilon_0 c w_0^2(\pi)^{3/2}\tau\right]$. Here $n_2$ is the refractive index of the surrounding medium. The corresponding magnetic field under paraxial approximation can be given by

$$\vec{H}(\rho,z,t,d)\cong\hat{y}n_2\varepsilon_0 c\vec{E}(\rho,z,t,d) \qquad (2)$$

where $c=1/(\varepsilon_0\mu_0)^{1/2}$ is the light speed in vacuum, and $\varepsilon_0$ and $\mu_0$ are the dielectric constant and permeability in the vacuum, respectively.

From the definition of the Poynting vector, we can readily obtain the intensity distribution:

$$I_l(\rho,z,t,d)=\left\langle\vec{S}(\rho,z,t,d)\right\rangle=\frac{P}{1+4(\tilde{z}+\tilde{d})^2}\exp\left[-\frac{2\tilde{\rho}^2}{1+4(\tilde{z}+\tilde{d})^2}\right]$$
$$\times\exp\left[-2\left(\tilde{t}-\frac{(\tilde{z}+\tilde{d})kw_0^2}{c\tau}\right)^2\right] \qquad (3a)$$

for left pulse, and

$$I_r(\rho,z,t,d)=\left\langle \vec{S}(\rho,z,t,d)\right\rangle = \frac{P}{1+4\left(\tilde{z}-\tilde{d}\right)^2}\exp\left[-\frac{2\tilde{\rho}^2}{1+4\left(\tilde{z}-\tilde{d}\right)^2}\right] \times\exp\left[-2\left(\tilde{t}+\frac{\left(\tilde{z}-\tilde{d}\right)kw_0^2}{c\tau}\right)^2\right] \tag{3b}$$

for right pulse, where $P=2\sqrt{2}U/\left[(\pi)^{3/2}w_0^2\tau\right]$. Here $\tilde{z}=z/kw_0^2$, $\tilde{d}=d/2kw_0^2$, $\tilde{\rho}=\rho/w_0$ and $\tilde{t}=t/\tau$.

For simplicity, we assume that the radius, $a$ of the particle is much smaller than the wavelength of the laser (i.e., $a<<\lambda$), in this case we can treat the dielectric particle as a point dipole. Assume that the refractive index of the particle is $n_1$ and $n_1>>n_2$.

As shown in Fig.1, there are two types of the radiation forces: the scattering force, $\vec{F}_{scat}$ and the gradient force, $\vec{F}_{grad}$, a part of the pondermotive force, $\vec{F}_p$.

By argument similar to that shown in work of Zhao [6] for one pulsed Gaussian beam, the scattering force and all components of the pondermotive force for two counter-propagating pulsed beams are given by

$$\vec{F}_{scat}(\rho,z,t,d)=\hat{z}n_2\alpha I_l(\rho,z,t,d)/c-\hat{z}n_2\alpha I_r(\rho,z,t,d)/c, \tag{4a}$$

$$\vec{F}_{grad,\rho}(\rho,z,t,d)=-\hat{\rho}2\beta I_l(\rho,z,t,d)\tilde{\rho}/\left[cn_2\varepsilon_0 w_0\left(1+4\left(\tilde{z}+\tilde{d}\right)^2\right)\right] -\hat{\rho}2\beta I_r(\rho,z,t,d)\tilde{\rho}/\left[cn_2\varepsilon_0 w_0\left(1+4\left(\tilde{z}-\tilde{d}\right)^2\right)\right], \tag{4b}$$

$$\vec{F}_{grad,z}=-\hat{z}\frac{2\beta I_l(\rho,z,t,d)}{n_2\varepsilon_0 ckw_0^2}\left[\frac{\left(\tilde{z}+\tilde{d}\right)k^2w_0^4}{c^2\tau^2}+\frac{k\tilde{t}w_0^2}{c\tau}+\frac{2\left(\tilde{z}+\tilde{d}\right)\left(1+4\left(\tilde{z}+\tilde{d}\right)^2-2\tilde{\rho}^2\right)}{\left(1+4\left(\tilde{z}+\tilde{d}\right)^2\right)^2}\right] +\hat{z}\frac{2\beta I_r(\rho,z,t,d)}{n_2\varepsilon_0 ckw_0^2}\left[\frac{\left(\tilde{z}-\tilde{d}\right)k^2w_0^4}{c^2\tau^2}+\frac{k\tilde{t}w_0^2}{c\tau}+\frac{2\left(\tilde{z}-\tilde{d}\right)\left(1+4\left(\tilde{z}-\tilde{d}\right)^2-2\tilde{\rho}^2\right)}{\left(1+4\left(\tilde{z}-\tilde{d}\right)^2\right)}\right], \tag{4c}$$

$$\vec{F}_t=-\hat{z}8\mu_0\beta I_l(\rho,z,t,d)\frac{\tilde{t}}{\tau}+\frac{\hat{z}8\left(\tilde{z}+\tilde{d}\right)\mu_0\beta I_l(\rho,z,t,d)kw_0^2}{c\tau^2} +\hat{z}8\mu_0\beta I_r(\rho,z,t,d)\frac{\tilde{t}}{\tau}-\frac{\hat{z}8\left(\tilde{z}-\tilde{d}\right)\mu_0\beta I_r(\rho,z,t,d)kw_0^2}{c\tau^2} \tag{4d}$$

where $\alpha=\left(128\pi^5a^6/3\lambda^4\right)\left[\left(m^2-1\right)/\left(m^2+2\right)\right]^2$ is the scattering cross section, $\beta=4\pi n_2^2\varepsilon_0a^3\left[\left(m^2-1\right)/\left(m^2+2\right)\right]$ is the polarizability, and $m=n_1/n_2$ [6, 7].

From Eqs.(4), it is found that the total scattering force can be neglected, $F_{scatt}=0$, because of counter-propagating of two beams. Thus the magnitude of the radiation force, especially longitudinal radiation force,

$$F_z=F_{grad,z}+F_t \tag{5}$$

and gradient force $F_{grad,\rho}$, are greatly affected by the spatial interval between two beam waists.

## 3. Numerical simulation and analysis

In following numerical simulation we choose the parameters as follows: $\lambda = 1.064\mu m$, $m = n_1 / n_2 = 1.592/1.332$ (the small glass sphere and water, for instance), $w_0 = 1\mu m$, $a = 5nm$, $\tau = 1ps$, and the input pulse is fixed to be $U = 0.1\mu J$ [7].

### *3.1. Distribution of $F_{grad,\rho}$ in the phase plane (ρ,t)*

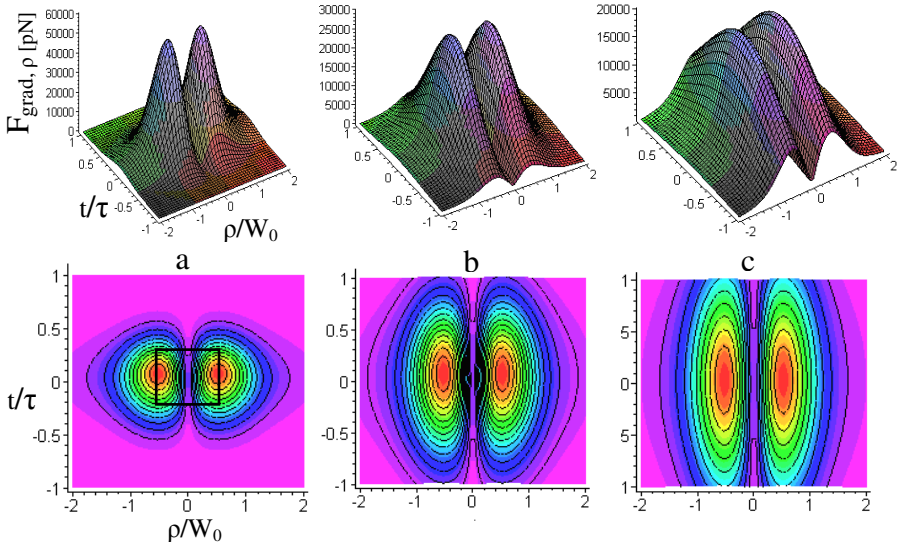


**Fig.2** The optical transverse forces, $F_{grad,\rho}$ in phase plane (ρ,t) for the pulses with different duration τ = 0.5ps (a); τ = 1ps (b); τ = 1.5ps (c);

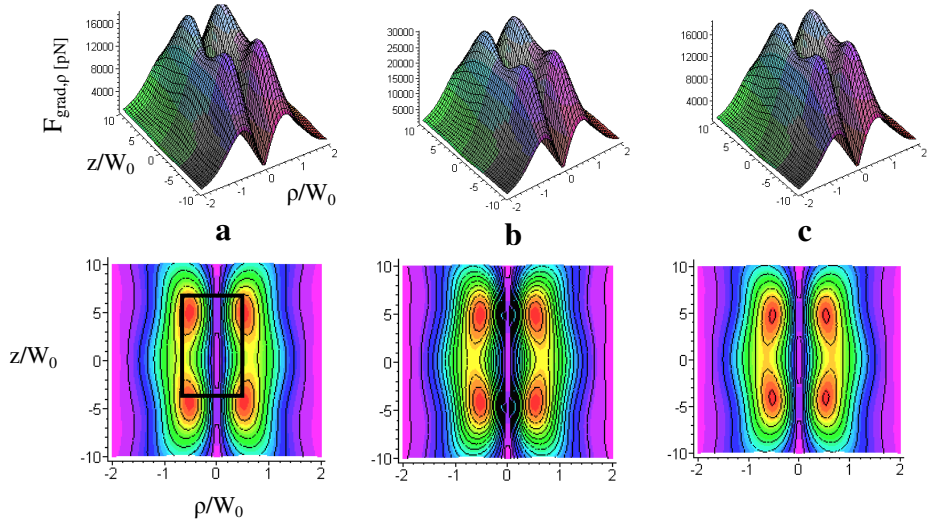


**Fig.3** The optical transverse force $F_{grad,\rho}$ in phase plane (z,ρ) for the pulses with duration τ=1ps at different times t= -0.5 τ (a); t= 0.0τ (b); t= 0.5 τ (c).

The optical gradient force $F_{grad,\rho}$ is calculated by expression (4b) with given parameters: $d = 10\mu m$, $w_0 = 1\mu m$, $t = (-1 \div 1)\tau$, $\rho = (-2 \div 2)w_0$ at $z = 5\mu m$ in the phase plane $(\rho, t)$ for some values of duration of pulses: $\tau = 0.5ps$ (a), $\tau = 1ps$ (b), and $\tau = 1.5ps$ (c) is illustrated in Fig.2.

One can see that the $F_{grad,\rho}^{\max}$ descreases with increasing of duration τ, but the optical trapping region in phase plane (ρ,t), noted by rectangle, is more and more wider. This means that the optical trap will be more stable, when use Gaussian pulse with the longer duration and that explains clearly why the optical trap is effectively made by CW laser.

### *3.2. Distribution of $F_{grad,\rho}$ in the phase plane (z,ρ)*

The distributions of transverse optical forces $F_{grad,\rho}$ for the pulse with duration $\tau = 1ps$ at different times are illustrated in Fig.3. The transverse force as so as $F_{grad,\rho}^{\max}$ change during the duration of optical pulse. The stable trap, the cylinder radius $w_0/2$ and length $d$, noted by rectangle, nearly is not changing.

The distributions of transverse optical forces $F_{grad,\rho}$ for the pulse with duration $\tau = 1ps$ at $t = 0$ for different intervals between two waist are illustrated in Fig.6. From this figure, it is clearly seen that for the pulses with larger $d$, the magnitude of the maximal force is reduced, meanwhile the optical transverse force has a larger stable trapping region, which is located at co-ordinate origin $z = 0$.

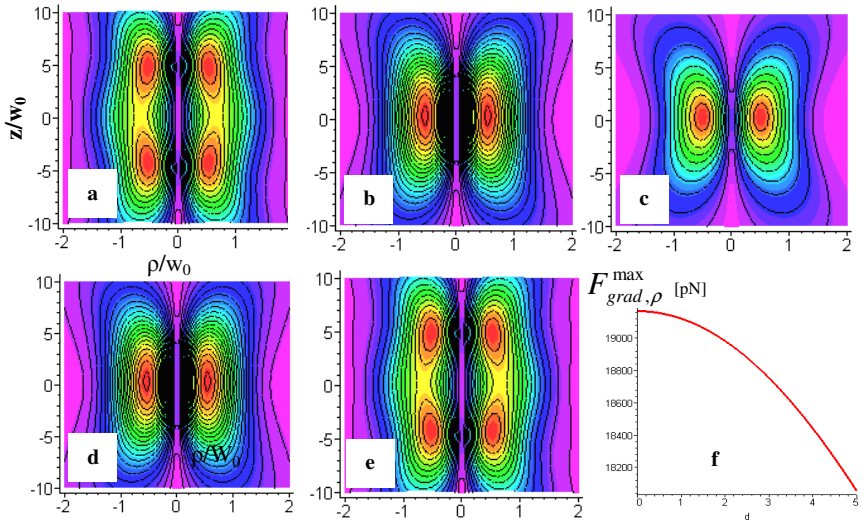


**Fig.4** The optical transverse force $F_{grad,\rho}$ in phase plane (z,ρ) for the pulses with duration τ=1ps, at t=0 for different interval between waists d=-10$w_0$ (a), d=-5$w_0$ (b), d=0 (c), d=5$w_0$ (d), d=10$w_0$ (e) and the dependence of the maximal

## 4. Condition for stable manipulation

In the above discussion, it is shown that there are regions used to manipulate the dielectric sphere. In order to know whether the particle could be effectively controlled in those regions, first we estimate the potential well induced by the radiation force, which must be deep enough to overcome the kinetic energy of the particle due to thermal fluctuation. The condition can be expressed by using the Boltzman factor [2], [8]:

$$R_{thermal} = \exp\left(\frac{-U_{\max}}{k_B T}\right) << 1, \tag{6}$$

where $U_{\max} = 2\pi\varepsilon_0 n_2 a^3 \left|\frac{(m^2-1)}{(m^2+2)}\right| \left|\vec{E}\right|^2_{\max}$ (7)

is the maximal value of the potential well, $k_B$ is the Boltzman constant, and $T$ is the absolute temperature of the ambient. In our above numerial examples, for the pulses with $\tau$=1ps, we

obtain $R_{thermal} \approx 1.36$. As $\tau$ decreases, $R_{thermal}$ becomes smaller and smaller. For example, $R_{thermal} \approx 0.95$ for $\tau$=0.8ps, $R_{thermal} \approx 0.04$ for $\tau$=0.1ps, and $R_{thermal} \approx 7.8\ 10^{-17}$ for $\tau$=0.01ps. From these numerical comparisons, it is clearly shown that Brownian motion could be overcome or ignored and the particles can be manipulated by the radiation force of the two counter-propagating pulsed beams with short duration.

Second, we consider the effect of the random diffusion of the small particle in the surrounding medium. As we know that during the repetition period of pulses, the radiation fore would vanish, and then the dielectric sphere would move under the gravity and the Brownian force. If the particle doesn't move out the trapping region in the repetition period, then the radiation force of the second irradiation can drag it back to the trapping region or manipulate the particle again. Assume the density of the small glass sphere to be $\rho_{glass}=2.410^3 kg/m^3$, then the gravity of the particle with a=10nm is about $F_{grav} \approx 6.25\ 10^{-8}$ pN, which much smaller than the radiation force (about $10^2$ pN in trapping region in Fig.2). Therefore, the effect of gravity can be ignored for the small "nano" particle.

When a particle moves freely inside a medium of viscosity $\eta$, it suffers the random Brownian motion. From the Stokes-Einstein relation, we can get the diffusion constant $D = k_B T / 6\pi\eta a$. For water with visosity $\eta = 7.977\ 10^{-4}$Pa.s at tempetrature T = 27°C, we obtain $D = 5.5\ 10^{-11} m^2/s$. If the trap repetition rate is larger than 10Hz, the particle diffuses into the region of $S = 0.55\ 10^{-11} m^2$ during the repetition period of trap. This diffusion region is maller than the range of radiation force induced by the pulsed beams (about $10^{-11} m^2$ in Fig.3 and Fig.4). Therefore the particle ould be effectively confined within the manipulating region of two counter-propagating pulsed beams.

## 5. Conclusion

In summary, we have theoretically investigated dynamic optical force produced by two counter-propagating Gaussian beams acting on the Rayleigh dielectric particle. We find that the radiation force produced by two counter-propagating pulsed beams depends on the pulse duration, beam waist, and interval between their focuses. The conditions for effectively trapping and manipulating the particles to avoid the thermal fluctuation, gravity and Brownian motion, are analyzed and discussed.

## References

1. A. Ashkin, "*Acceleration and Trapping of Particles by Radiation Pressure*," Phys. Rev. Lett. 24 (1970), pp. 156-159.
2. A. Ashkin, J. M. Dziedzic, J.E. Bjorkholm, S. Chu, "*Observation of a single-beam gradient force optical trap for dielectric particles*," Opt. Lett. 11 (1986), pp. 288-290.
3. A.Ashkin, " *Methods in cell biology*", M. P. Sheetz, ed. (Academic Press, San Diego, 1998), 55, pp. 1-27.
4. A. A. Ambardekar, Y. Q. Li, "*Optical levitation and manipulation of stuck particles with pulsed optical tweers*," Opt. Lett. 30 (2005), pp. 1797-1799.
5. J. L. Deng, Q. Wei, Y. Z. Wang, Y. Q. Li, „"*Numerical modeling of optical levitation and trapping of the stuck particles with a pulsed optical tweerz*," Opt. Express. 13 (2006), pp.3673-3680.
6. C. L. Zhao, L. G. Wang, X. H. Lu, "*Radiation forces on a dielectric sphere produced by highly focused hollow Gaussian beams*,"Phys. Lett. A (2006), pp. 502-506.
7. L.G. Wang et al, " *Effect of spatial coherence on radiation forces acting on a Rayleigh dielectic sphere*," Opt. Lett. 32 (2007), pp. 1393-1395.
8. A. Ashkin, "*Trapping of Atoms by Resonance Radiation Pressure*," Phys. Rev. Lett. 44 (1978), pp. 729-732.

# COLORLESS COMPONENTS FOR WDM-BASED OPTICAL ACCESS NETWORKS

**Q.-T. Nguyen[a], G. Girault[a], O. Vaudel[a], L. Bramerie[a], P. Besnard[a], A. Shen[b], G.H. Duan[b], C. Kazmierski[b],S. Lobo[a], M. Joindot[a], J.-C. Simon[a], N. Dupuis[b], A. Garreau[b], Z. Belfqih[c], P. Chanclou[c]**

[a)]FOTON-ENSSAT, CNRS UMR 6082. 6 rue de Kerampont, BP 80518, 22305 Lannion Cedex
[b)]Alcatel Thales III-V Lab. Route de Nozay, 91460 Marcoussis
[c)]France Telecom - Orange Labs, 2 avenue Pierre Marzin, 22307 Lannion
*E-mail: quocthai.nguyen@enssat.fr*

**Abstract.** This paper presents our work carried out in the colorless-component technologies for high bit-rate optical access networks, which are based on WDM-PON (wavelength division multiplexed passive optical networks). The colorless concept consists in using identical and wavelength independent components that will act as the generic transmitter in WDM-PON systems. The transmitted wavelength is imposed, for each colorless component, by an external optical signal. Our studies include two types of colorless components: The Injection-Locked Fabry-Perot laser (IL-FP) and the Reflective Electro-Absorption Modulator integrated with a Semiconductor Optical Amplifier (REAMSOA). For the IL-FP, the properties of the component strongly depend on the injected optical signal. We demonstrate the improvement by injection-locking of the laser's performances in terms of intensity noise, chirp and bandwidth. For the REAM-SOA, the static properties such as reflection gain and noise characteristic are examined. We demonstrate the feasibility of the REAM-SOA in a transmission experiment in a PON configuration at 10 Gbps with up to 25 km of SMF, using remote modulation technique.

***Keywords:*** *Injection-Locked Fabry-Perot Laser, Amplified Reflective Electro-Absorption Modulator, Remote Modulation, WDM-PON, Colorless Optical Access Networks.*

## 1. Introduction

With the increase of broadband services including high-speed Internet, data transfer, video-on-demand and other bandwidth-consuming services, the demand for high bit-rate access networks is rising rapidly. To respond to such a bandwidth demand, Fiber-To-The-Home (FTTH) technologies based on different passive optical network (PON) architectures have been developed. Among them, the wavelength division multiplexed PON (WDM-PON), in which each wavelength is dedicated to a
single subscriber, appears as the ultimate solution in terms of its very large capacity [1]. In order to enable flexibility and simplicity of such network, it is essential to develop wavelength-independent upstream transmitters, called colorless transmitters. For this purpose, colorless components are studied and developed for subscriber-side transmitter of WDM-based optical access networks.

To meet the "long-term" bandwidth requirement of access networks, 10 Gbps-capable colorless components are under focus. Some low-cost colorless solutions including spectrum-sliced of superluminescent-light-emitting diodes (SLEDs), amplified spontaneous emission (ASE) or supercontinuum source could be considered [2]. However, spectrum-slicing of SLEDs suffers from low power budget and spectrum slicing of ASE suffers from strong intensity noise, prohibitive at 10
Gbps. Wavelength-seeded reflective semiconductor optical amplifiers (RSOAs) could avoid the inconvenient of power budget and intensity noise, but it is limited by its low bandwidth [3]. By taking into account the bandwidth scalability, it seems interesting to develop two attractive solutions:

- A new generation of Fabry-Perot laser diode, which could be widely injection-locked, and directly modulated at 10 Gbps

- Anew 10 Gbps monolithically integrated Amplified Reflective Electro-Absorption Modulator (R-EAM-SOA), which separates the modulation and amplification function.

After a brief introduction in section 2 to WDM-PON system, we present in section 3 the IL-FP and their main characteristics. The static properties and performances in a 10 Gbps transmission system will be presented in section 4 for the REAM-SOA.

## 2. WDM-PON system architecture

In this paragraph, we present the basic principle of the WDM-PON system architecture, in which the colorless components are used as upstream transmitters. The network architecture is shown in figure 1.

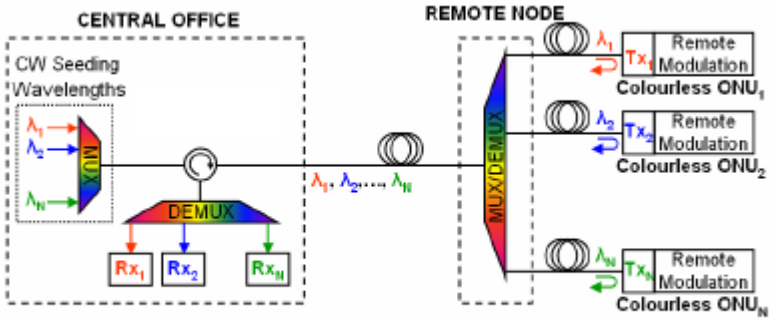


**Figure 1**: WDM-PON architecture for upstream transmission using colorless components

The WDM-PON is essentially based on a point-to-multipoint architecture. In order to distribute broadband services to the subscribers, the Central Office (CO) of the network operator is connected to the terminals located at subscriber's premises called Optical Network Units (ONU). The point-tomultipoint architecture is realized thanks to an intermediate point in the network called Remote Note (RN). It consists in a MUX/DEMUX, which separates and/or recombines each channel of different subscribers.

In the WDM-PON configuration, colorless components are identical and wavelength-independent at ONUs. They are used as the upstream transmitters as shown in Figure 1. The emitted wavelength of each component depends on the wavelength of the seeded signal coming from the CO. The upstream optical signals are modulated with the subscriber's data thanks to the modulation ability of the colorless components.

## 3. Injection-locked Fabry-Perot

Significant performance improvement by using injection-locking and laser processing simplicity are some advantages of IL-FP as colorless transmitter solution. The Fabry-Perot laser is a multi-mode laser, which can operate in a single-mode regime with wavelength-locking mechanism due to optical injection imposed.

The operation principle of IL-FP is sketched in figure 2a. An external continuous signal is injected into the Fabry-Perot cavity. The laser will then be "locked" at the injected wavelength. Thus, the ILFP re-emits at the same wavelength than the injected one. Thanks to the ability of the laser gain section to be directly modulated, the output optical signal is coded, carrying upstream data. An optimized antireflection coating is implemented on the front facet to enhance the input power sensitivity.

The figure 2b presents an example of IL-FP spectrum compared to free-running FP spectrum. The injected power level is around -10 dBm in this case. Strongly single-mode operation with a side-modesuppression-ratio (SMSR) around 40 dB can be achieved. The following paragraphs describe some performance enhancements of the IL-FP.

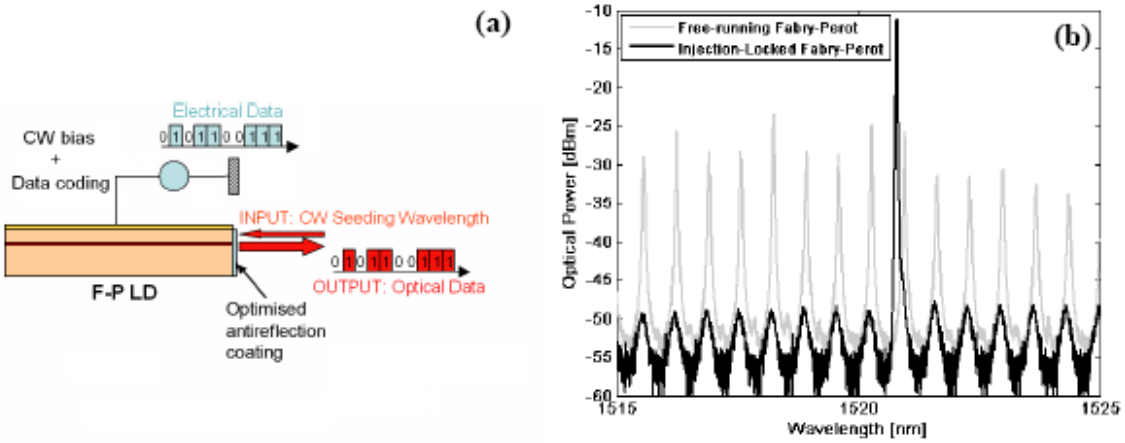


**Figure 2**: Injection-Locked Fabry Perot operation principle *(a)* and examples of laser spectrum *(b)*

### *Relative intensity noise and modulation properties*

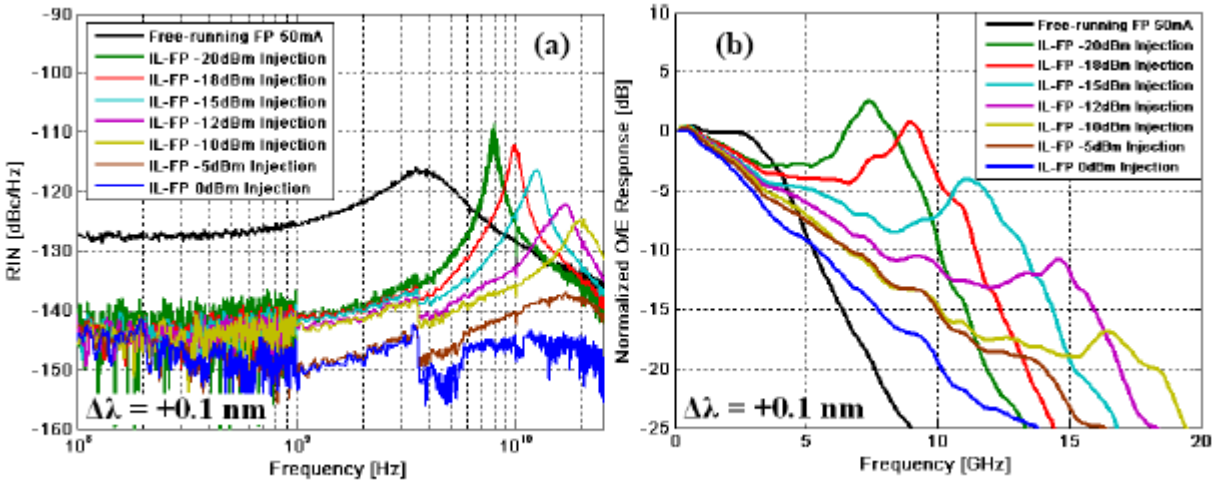


**Figure 3**: Intensity noise (RIN) characteristics *(a)* and normalized O/E frequency response *(b)*

The relative intensity noise (RIN) is an important parameter for semiconductor lasers in optical communications. The bulk Fabry-Perot laser usually presents a high intensity noise. In our experiment, the free-running Fabry-Perot laser has at 50 mA a RIN level higher than -130 dBc/Hz below 10 GHz. But with injection-locking by an external low-noise source, which has a RIN lower than -150 dBc/Hz, the RIN of the injected IL-FP is significantly reduced. It does not exceed -140 dBc/Hz, as shown in figure 3a, which corresponds to more than 10 dB of noise reduction. We also observe that the resonance frequency is strongly increased by the injection-locking. The higher the injected power is, the stronger noise-reduction is as well as the higher the resonance frequency is [10]. A resonance frequency higher than 20 GHz can be observed.

### *Linewidth enhancement factor*

The linewidth enhancement factor $\alpha$ H (also called alpha parameter or chirp parameter) characterizes the interdependence between amplitude modulation (AM) and frequency modulation (FM) under direct current modulation of semiconductor devices. It is mainly due to the asymmetry of the gain curve, which causes, through Kramers-Kronig relation, a non-zero dispersion at the frequency of maximum gain. It follows that an intensity modulation leads simultaneously to phase or frequency modulation. It is considered as one of the most limiting factors in performance of semiconductor laser in optical communication systems. To measure this factor, we use the method described in [10], which is based on the measurement of FM index over AM index ratio. In the free-running operation of the FP laser, the measurements cannot

have been performed because the linewidth of a mode is out of the range of our equipments (12.5 GHz-linewidth compared to 10 GHz-FSR of Fabry-Perot analyzer).

In case of injection-locking, we obtain relatively low values of αH. For-10 dBm of injected power, a linewidth enhancement factor around 1.9 could be achieved. When injected power increases, the locking mechanism is stronger but αH also increases. This fact is also experimentally observed in case of injection-locked DBR [6]. We obtain the linewidth enhancement factor around 2.8 and 4.2 for the injected power at -5 dBm and 0 dBm respectively. A low αH value allows a long transmission distance of the modulated signal, thus a long reach of optical access networks.

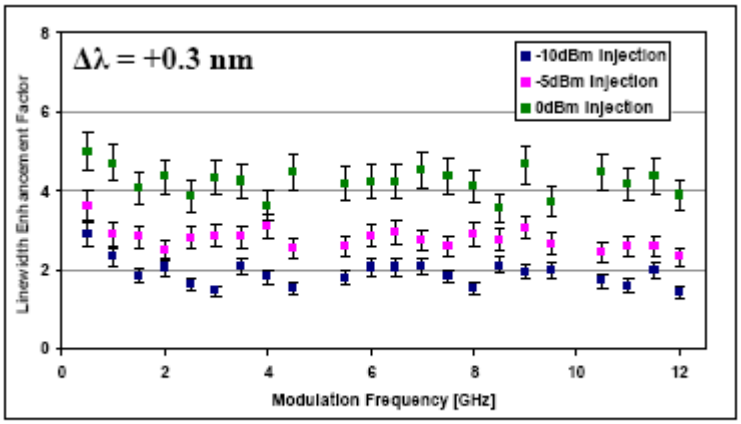


**Figure 4**: Linewidth enhancement factor vs modulation frequency

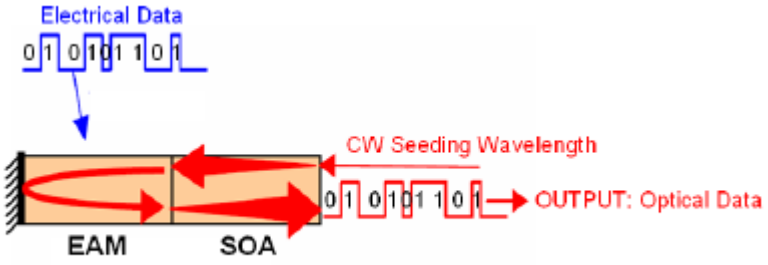


**Figure 5**: Schematic sketch of an REAM-SOA

## 4. Amplified reflective electro-absorption modulator

The Reflective Electro-Absorption Modulator is monolithically integrated with a Semiconductor Optical Amplifier (REAM-SOA). This component benefits from the large bandwidth of the EAM (10 Gbps and beyond) as well as from the power amplification function of the SOA. The operation principle of the colorless transmitter is given in figure 5.

Similar to the case of IL-FP in upstream transmission, a continuous signal coming from the CO is optically injected through the front facet of the component, pre-amplified in the SOA and finally modulated by the EAM. The modulated optical signal carrying upstream data is then reflected on the rear facet and boosted out by the SOA. While the input and output signals go through the same front
facet, the REAM-SOA is a one-port component, thus it requires simple and cost-effective packaging
technology.

### *4.1 Gain and noise characteristics*

In this paragraph, we present some static properties of the component. Since the system budget of access networks is always critical, the optical gain of the component is an important characteristic. Figure 6 presents the reflection gain of the REAM-SOA as a function of wavelength. We observe a positive reflection gain over a spectral range larger than 50 nm in L-band. This demonstrates the possibility of large spectral range loss-less operations of the colorless component. A spectral range larger than 40nm is obtained with an extinction ratio higher than 20 dB.

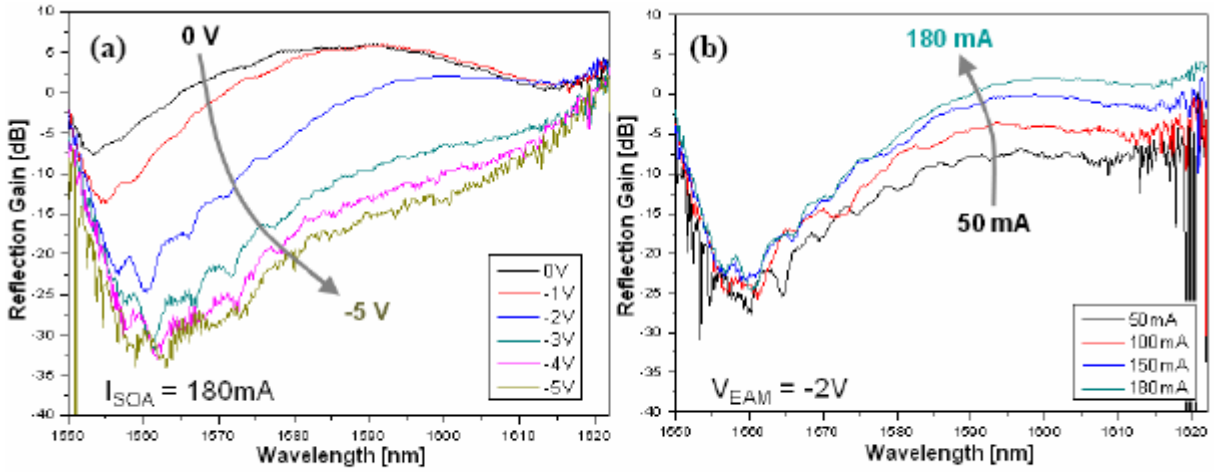


**Figure 6**: Reflection gain of REAM-SOA vs wavelength: For different EAM bias *(a)* and for different SOA currents *(b)*

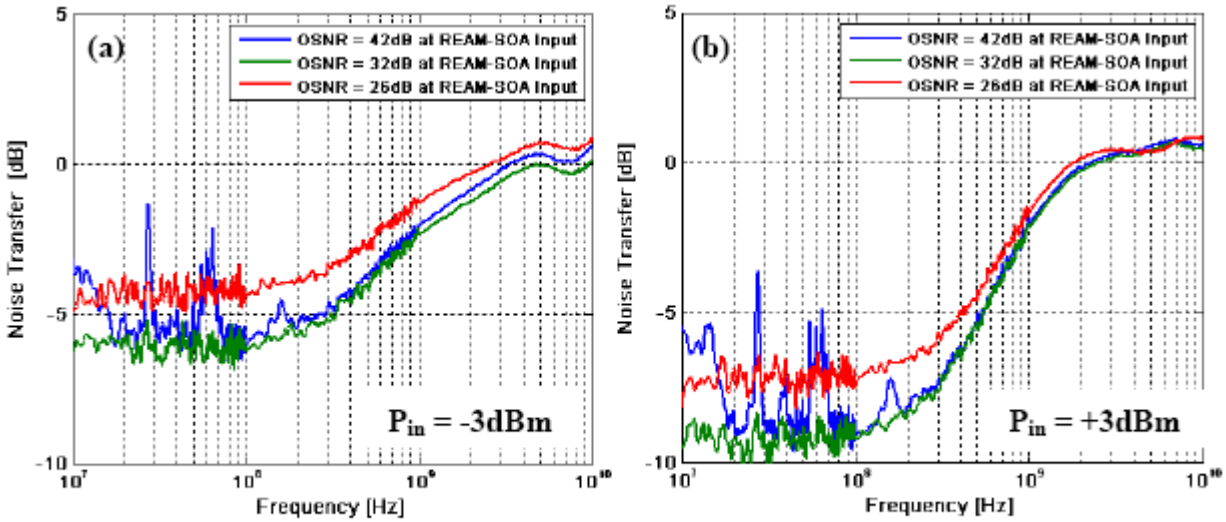


**Figure 7**: Intensity noise transfer function vs. frequency: For -3 dBm optical power input *(a)* and for +3 dBm optical power input *(b)*

Since the optical power injected into the component is relatively weak (signal coming from the Central Office), the noise level of this input signal is then considerable. Therefore, it is very interesting to examine the noise characteristics of the component. It is characterized by the noise transfer function shown in the figure 7 for different noise-level of the input signal. From measurements, a noise reduction of nearly 10 dB and respectively around 5 dB is obtained for an input power of +3 dBm and respectively -3 dBm.

### *4.2 Transmission experiment*

In order to demonstrate the feasibility of the REAM-SOA in a PON system at 10 Gbps, we evaluated the transmission quality of the system using REAM-SOA in a remote modulation configuration [7], i.e. the wavelength source coming from the CO is modulated at the ONU and then re-transmitted upward to the CO. The system configuration is presented in the figure 8a.

This is not really a PON-like system (based on point-to-multipoint architecture), but we could consider it as a wavelength channel in WDM-PON system. The result of bit-error-rate (BER) measurement ispresented in the figure 8b. An error-free 10 km transmission has been achieved. For 25 km transmission distance, an error floor at 5.10-11 is presented. This is due to the interferometric noise between the useful signal and the Rayleigh backscattering signal at the same wavelength presented in the system.

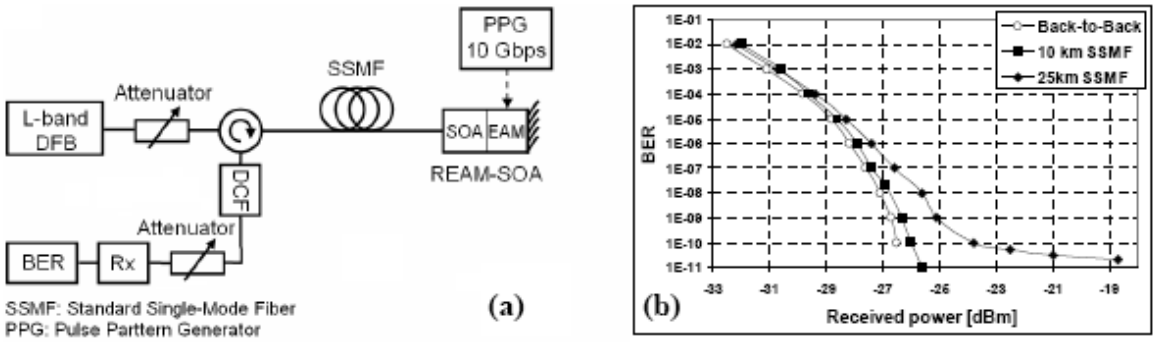


**Figure 8**: Transmission experiment in remote modulation configuration *(a)* and bit-error-rate measurement *(b)*

## 5. Conclusion

Colorless components based on Injection-Locked Fabry-Perot laser diode and Amplified Reflective Electro-Absorption Modulator have been studied and their main characteristics have been presented. The IL-FP presents low-noise, low-chirp and high-bandwidth capability thanks to injection-locking mechanism. The high-bandwidth, noise-reduction and lossless operation over a large spectral range have been obtained for the REAM-SOA. The feasibility of this component on a 10 Gbps system has also been demonstrated. All these results are very promising for using such simple devices as high speed, low-cost and simple packaging compatible colorless components for next generation optical access networks. Further works will be to improve the component performances such as fullycolorless C-band operation, polarization independence and high sensitivity vs injected power, in order to enable a real deployment in WDM-PON access systems.

***Acknowledgement***

*This work has been done in the framework of the French national project ANR ANTARES.*

**References**

1. Grobe, K. & Elbers, J., "PON Evolution from TDMA to WDM-PON", OFC NFOEC, Optical Society of America, 2008, NThD6
2. Lee, J. et al., "WDM-Based Passive Optical Network Upstream Transmission at 1.25 Gb/s Using Fabry-Perot Laser Diodes Injected With Spectrum-Sliced, Depolarized, Continuous-Wave Supercontinuum Source", Photonics Technology Letters, IEEE, 2006, 18, 2108-2110
3. Chanclou, P. et al., "Demonstration of RSOA-Based Remote Modulation at 2.5 and 5 Gbit/s for WDM PON", OFC NFOEC, Optical Society of America, 2007, OWD1
4. Kazmierski, C. et al., "Advanced component technologies for colourless access networks", SPIE APOC, 2007
5. Payoux, F. et al., "WDM-PON with Colorless ONUs", OFC NFOEC, Optical Society of America, 2007, OTuG5
6. Garreau, A. et al., "10Gbit/s Amplified Reflective Electro-absorption Modulator for Colorless Access Networks", IPRM, 2006, 168-170
7. G. Girault et al., "10 Gbit/s PON demonstration using a REAM-SOA in a bidirectional fiber configuration up to 25 km SMF", ECOC, 2008, P.6.08
8. Shen, A. et al., "Injection Locked DBR Laser Diode module for Access Applications", ECOC, 2007
9. Xu, Z. et al., "10 Gb/s WDM-PON Upstream Transmission Using Injection-Locked Fabry-Perot Laser Diodes", OFC NFOEC, Optical Society of America, 2006, JThB72
10. Wu, M. et al., "High-Speed Modulation of Optical Injection-Locked Semiconductor Lasers", OFC NFOEC, Optical Society of America, 2008, OThK3
11. C. Harder et al., "Measurement of the linewidth enhancement factor alpha of semiconductor lasers", Appl. Phys. Lett., Vol. 42, No. 4, 1983.

# A NOVEL SPLIT-STEP FOURIER METHOD TO SOLVE THE NONLINEAR SCHRÖDINGER EQUATION WITH A GIVEN ACCURACY

**T. N. Nguyen[a], T. Chartier[a] and T. H. Bui[b]**

[a)]Umr foton, enssat, 6, rue de Kerampont, 22300 Lannion, France; chartier@enssat.fr
[b)]Telecoms department, Posts and Telecoms Institute of Technology,
km 10, Nguyen Trai str., Hanoi, Vietnam

**Abstract** We report a novel split-step Fourier method based on the concept of local error to solve the nonlinear Schrödinger equation with a given accuracy.

## 1. Introduction

The nonlinear Schrödinger equation (NSE) governs nonlinear pulse evolution in optical fibres [1]. To model optical-fibre communications systems, the NSE is generally solved numerically. Several methods exist to solve the NSE, among them the split-step Fourier (SSF) methods are the most popular methods thank to their simplicity and efficiency [1,2]. The principle of the SSF methods is to divide the fibre length into small steps and to solve the effect of dispersion and nonlinearity separately in each step.
So far, there is no SSF method giving a criterion to choose the right step size corresponding to a given final accuracy. Generally, people perform simulations without knowing how accurate the results are if they do not carry out a very difficult and time-consuming procedure to find the accuracy of the final solution [2].
In this paper we present a method giving a criterion to choose the step size in order to reach any expected accuracy without calculating the reference solution.

## 2. Theory

In numerical simulations, a sampled signal $U$ is generally treated as a vector of dimension $k$: $U = [U_1, U_2, U_3, U_4,... U_k]$ where $U_i$ is a sample of signal. With the normalised time-resolution, the energy $E$ of the signal is related to the absolute value $\|U\|$ of $U$ by the following relation:

$$\|U\| = \sqrt{\sum_{i=1}^{k} U_i^2} = \sqrt{E} \cdot \qquad (1)$$

The SSF methods used in optical communications divide the transmission link into many small steps of size $h$ (segment). In each segment, the signal is treated by Fourier methods [1].
The final solution after $n$ segments is the numerical solution $U_n$. This solution has a certain error in comparison with the exact solution $U_a$. The higher the number of segments, the better the accuracy of the numerical solution. In most cases, $U_a$ cannot be found by analytical methods. $U_a$ can be approached by performing simulations with a very high number of steps and this procedure is often referred as the exact calculation.
Fig. 1 illustrates the evolution of both the numerical solution $U_n$ and the exact solution $U_a$ along the fibre in the space of dimension $k$. At the end of the fibre, the error between the numerical solution and the exact solution is calculated as follows [2-4]:

$$\delta_{final} = \frac{\|U_n - U_a\|}{\|U_a\|}, \qquad (2)$$

where $\|U\|$ is defined by equation (1).
Fig. 2 shows an example of evolution of a signal in the fibre after the three first segments. After each segment, we calculate the numerical solution (black point), the exact solution (white point,) and the local-exact solution (white point with a dash) which corresponds to the transformation of

the numerical solution using the exact calculation. A local error after segment *j* is defined as the error between the numerical solution $U_{n,j}$ and the local-exact solution $U_{a,j}^{local}$ :

$$\delta_{local,j} = \frac{\left\| U_{n,j} - U_{a,j}^{local} \right\|}{\left\| U_{a,j}^{local} \right\|} \qquad (3)$$

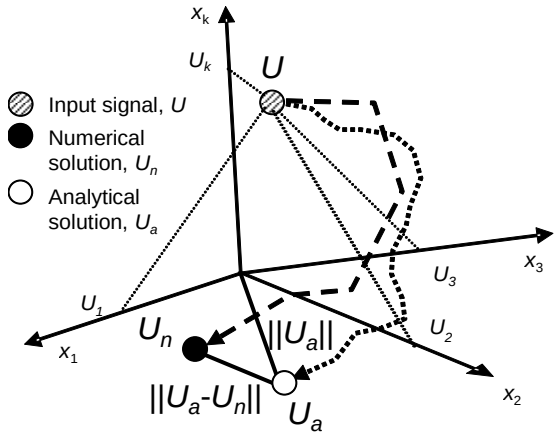


**Fig. 1***:* Evolution of both $U_n$ and $U_a$ along the fibre in the space of dimension k.

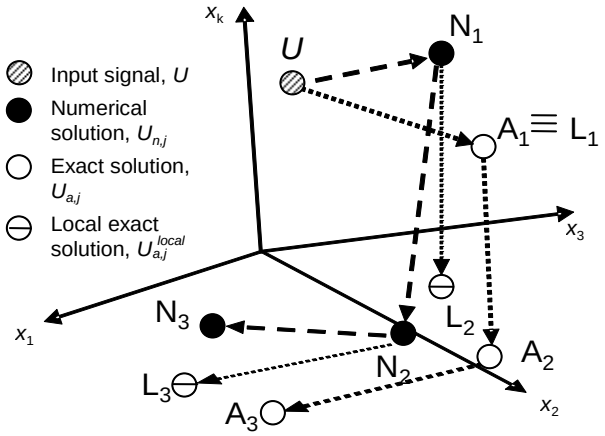


**Fig. 2***:* Evolution of the numerical, exact and local-exact solutions for the three first segments.

In the triangle $N_3L_3A_3$, it is obvious that:

$$N_3A_3 \leq N_3L_3+L_3A_3 \qquad (4)$$

Because the distance between N2 and A2 is very close, their exact solutions for the next segment keep the same distance: $L_3A_3 = N_2A_2$. Consequently, the inequality (4) becomes:

$$N_3A_3 \leq N_3L_3 + N_2A_2 \qquad (5)$$

With the same logic, in the triangle $N_2L_2A_2$:

$$N_2A_2 \leq N_2L_2 + L_2A_2. \qquad (6)$$

from (6), the inequality (5) becomes:

$$N_3A_3 \leq N_3L_3 + N_2L_2 + N_1L_1. \qquad (7)$$

If the fibre is lossless, relation (7) can be rewritten as:

$$\frac{N_3A_3}{\sqrt{E}} \leq \frac{N_3L_3}{\sqrt{E}} + \frac{N_2L_2}{\sqrt{E}} + \frac{N_1L_1}{\sqrt{E}} \qquad (8)$$

or $\delta_{final} \leq \delta_{local,3} + \delta_{local,2} + \delta_{local,1}$ (9)

If we now consider the fibre loss □, we write relation (7) as follows:

$$\frac{N_3A_3}{\sqrt{E_3}} \leq \frac{N_3L_3}{\sqrt{E_3}} + \frac{N_2L_2}{\sqrt{E_3}} + \frac{N_1L_1}{\sqrt{E_3}} \qquad (10)$$

or $$\frac{N_3 A_3}{\sqrt{E_3}} \le \frac{\xi_3 N_3 L_3}{\sqrt{E_3}} + \frac{\xi_2 N_2 L_2}{\sqrt{E_2}} + \frac{\xi_1 N_1 L_1}{\sqrt{E_1}} \quad (11)$$

or $$\delta_{final} \le \xi_3 \delta_{local,3} + \xi_2 \delta_{local,2} + \xi_1 \delta_{local,1} \quad (12)$$

where $\xi_i = \sqrt{\frac{E_i}{E_3}} = e^{\frac{\alpha(L-L_i)}{2}}$, $L_i$ is the distance from the input end of the fibre to the end of segment $j$ and $L$ the fibre length,. Quantity $\delta_i \delta_{local,i}$ is the effective local error named $\delta_{local\text{-}eff,i}$.
Relation (12) illustrates the fact that the final error is always less or equal than the sum of all the effective local errors. Consequently, if we can control the effective local error in such a way that the sum of all the effective local errors is equal to a given value, we ensure that the final error is under this value. To control the sum of all the effective local errors, the procedure, applied to the symmetrized-SSF method (S-SSFM) [1], is the following:

1) Carry out the simulation using the S-SSFM for $U(z, T)$ with a step of size $h$ to find the solution at $z + h$, called the coarse solution $U_c$.
2) Carry out the calculation using the S-SSFM for $U(z, T)$ with 2 steps of size $h/2$ to find the solution at $z + h$, called the local-exact solution $U_a^{local}$. Since the error using the S-SSFM is of third order in the step size, the accuracy of $U_a^{local}$ is about $2^3$ times better than the accuracy of $U_c$ [1].
3) Estimate of the local error $\delta_{local}$ according to (3).
4) Calculate the factor $F$ defined as the ratio between the presumed error $\delta_{pre}$ and the bound error $\delta_{bound}$

$$F = \frac{\delta_{pre}}{\delta_{bound}} \quad (13)$$

The presumed error $\delta_{pre}$ is calculated by assuming that the rest of the transmission is solved using steps of size $h$ and that the error on each step is the same as $\delta_{local}$ :

$$\delta_{pre} = \sum_{i=1}^{\frac{L-z}{h}} \delta_{local} e^{i\frac{\alpha h}{2}} = \delta_{local} e^{\frac{\alpha h}{2}} \left( \frac{e^{\alpha \frac{L-z}{2}} - 1}{e^{\frac{\alpha h}{2}} - 1} \right) \quad (14)$$

The bound error $\delta_{bound}$ is defined as the difference between the target error $\delta_G$ and the accumulation of the effective local errors:

$$\delta_{bound} = \delta_G - \int_0^z \delta_{local-eff} dz = \int_0^z \delta_{local} e^{\alpha(L-z)/2} dz \quad (15)$$

5) Find the next step-size:
   - If $F > 2$, then discard the solution in Step 1 and recalculate with a new step-size.
   - If $F \le 2$ then take $U_c$ as the solution at $z + h$ and take a new step-size for the next step.

   The new step-size is calculated by dividing the present step size $h$ by a factor $F^{1/3}$. The division by the factor $F^{1/3}$ ensures to minimize the difference between the presumed error and the bound error for the next segment.

The algorithm presented above is repeated for each segment to the end of the fibre. The initial step-size of this algorithm is $L$.

## 3. Results and discussion

We have simulated the transmission of a single pulse over 50 km in a SMF fibre (dispersion: 17 ps/nm/km; nonlinearity: 1.3 $W^{-1}km^{-1}$; fibre loss: 0.2 dB/km). Three cases have been considered: (a) the nonlinearity of the fibre is dominant: $N^2 = 10$, where $N$ is soliton order [1]; (b) the dispersion of the fibre is dominant: $N^2 = 1/10$ and (c) both phenomena are comparable: $N = 1$. The pulse duration is 10 ps according a sech shape. The signal is described in a window of 320

ps with 2048 samples. The reference solution was found by using the S-SSFM with steps of 5 cm of length.
Table 1 summaries the results for target accuracies of $10^{-2}$, $10^{-3}$ and $10^{-4}$. As expected, the final errors are well bounded by the target values in all cases and are close to the expected values.

**Table 1***:* Calculated errors when applying our method to simulate signal transmission over 50 km of SMF.

| $\square_G$ | $10^{-2}$ | $10^{-3}$ | $10^{-4}$ |
|---|---|---|---|
| $N^2 = 10$ | $0.75 \times 10^{-2}$ | $0.70 \times 10^{-3}$ | $0.69 \times 10^{-4}$ |
| $N^2 = 1/10$ | $0.24 \times 10^{-2}$ | $0.34 \times 10^{-3}$ | $0.30 \times 10^{-4}$ |
| $N^2 = 1$ | $0.20 \times 10^{-2}$ | $0.24 \times 10^{-3}$ | $0.24 \times 10^{-4}$ |

## 4. Conclusions

We have presented a novel method to solve the nonlinear Schrödinger equation based on the split-step Fourier method. By giving a simple criterion to choose the step size, our *controlled-local-error method* allows to reach a given accuracy for the final solution. This simple method allows avoiding difficult time-consuming procedures to determine the step size corresponding to a given accuracy as in the classical method. The results of the simulations show the efficiency of the method.

***Acknowledgements:*** *This work is supported by the Conseil Régional de Bretagne.*

## References

1. G. P. Agrawal, Nonlinear Fiber Optics, 2nd Ed., Academic Press, Inc. (1995).
2. C. J. Rasmussen, OFC 2001, Anaheim, USA, WDD29-1 (2001).
3. O. V. Sinkin *et al.*, IEEE JLT **21**, p. 61 (2003).
4. T. N. Nguyen *et al.*, IWPA 2006, Cantho, Vietnam, p. 254 (2006).

# TWO-STOKES GENERATION IN RAMAN MICROCHIP- AND MINI- LASERS: SEMI-CLASSICAL MODEL AND EXPERIMENT.

**S.V. Voitikov[a], A.S. Grabtchikov[a], A.A. Demidovich[b], M.B. Danailov[b], and V.A. Orlovich[a]**

[a)]Stepanov Institute of Physics, National Academy of Sciences of Belarus
68 Nezalezhnasti Ave., 220072 Minsk, Belarus. *E-mail: s.voitikov@dragon.bas-net.by*
[b)]Laser Lab Sincrotrone-*Trieste, SS14, km.163.5 34012 Trieste, Italy*

The semi-classical theory of microchip- lasers with transient intracavity stimulated Raman scattering (SRS) frequency conversion waves has been developed. The model is based on a treatment of intracavity multiwave SRS in which Raman-medium dephasing and multiwave mixing are taken into account. Intracavity transient SRS-conversion and generation of fundamental and two Stokes pulses, absorber saturation and recovering, and depletion of the inversion in the laser active medium are analyzed. The set of laser equations consists of equations for fundamental and two Stokes waves and equations for two collective amplitudes of Raman-medium vibrations. Two-Stokes generation in microchip- laser has been investigated experimentally. At 0.9W pump power the average 1st and 2nd Stokes powers and fundamental power reached the values of 20–25 and 50 mW correspondingly. Pulse energy changes from 0.9 to 0.8 μJ for the 1st Stokes and from 0.1 to 0.4 μJ for the 2nd Stokes waves with pump power increase from 0.4 to 0.9 mW. The calculated 1st and 2nd Stokes and fundamental pulse shapes agree well the experimental ones. The effect of multiwave mixing is considered in detail and it is shown, that it shortens the 2nd Stokes pulse and increases its energy.

***Key words****: microchip- and mini- laser; intracavity stimulated Raman scattering; semi-classical theory; multiwave mixing*

## 1. Introduction

Recently for the purposes of irradiation frequency shifting of Q-switched microchip- and mini-lasers with longitudinal diode-laser pump it was proposed to use intracavity stimulated Raman scattering (SRS) conversion [1,2] which is one of the most effective ways of frequency shifting. It was demonstrated that microchip lasers based on neodymium-doped media can generate under passive Q-switch nano- and sub-nanosecond pulses with a peak power up to tens of kilowatts [1-3]. This allows to get an effective nonlinear conversion of fundamental frequency and to create a new generation of ultra- compact lasers radiating from visible to UV spectral ranges. Stokes-shifted pulses with duration of 18-20 ns down to sub-100 ps and energies in the 10 microJ range have been obtained. Such pulse durations are close to a dephasing time of Raman-medium collective vibrations. The process of intracavity SRS conversion becomes therefore transient, and the dynamics of Stokes-pulse formation is strongly influenced by the temporal dynamics of the Raman-medium induced polarization and excitation. The peak power rise up to several tens or hundred kW in microchip- and mini-lasers could enable both Raman-medium excitation and intracavity generation of high order Stokes pulses. In this case the intracavity transient mixing of fundamental and Stokes waves could contribute significantly in the process of SRS conversion.

At present there are several works where, on the basis of phenomenological models of passive/active Q-switched microchip lasers with intracavity generation of the 1st Stokes wave, the pulse dynamics was described and some parameters of the Stokes pulses were calculated or estimated (see Ref.[2] and references therein). These works are based on a quasi-stationary approximation for the SRS process which is valid only in case where generated pulses are much longer than the Raman medium dephasing time. In the phenomenological models multiwave mixing is not taken into account. Several semi-classical models of Raman lasers have also been

proposed, where quasi-stationary SRS and quasi-stationary multiwave mixing processes were described [5-8], but these models could be applied to quasi-stationary SRS conversion only.

In this work the model of two Stokes microchip- and mini-lasers based on the semi-classical theory of intracavity SRS conversion is developed. The model describes fundamental (laser) and Stokes pulses generation and conversion, inversion replenishment and depletion in an active medium, and the absorber saturation and recovery. It takes into account dephasing of collective vibrations and excitation of Raman-medium, effect of activator-atom thermalization within the laser multiplets in an active medium, and ground- and excited-state absorption of a saturable absorber.

## 2. Model of microchip- and mini-laser with intracavity SRS conversion

Here we consider microchip-lasers with 4- multiplet activator-atom doped crystals (e.g. $Nd^{3+}$-doped crystals) as active medium, and 4-level atom doped crystals (e.g. $Cr^{4+}$-doped crystals) as saturable absorber. Correspondingly, we use the 4-multiplet model that takes into account the effect of activator-atom thermalization [2] to describe inversion replenishment and depletion in an active medium, and the 4-level model of an absorber that takes into account ground and excited state absorption [9]

Because in microchip- and mini-lasers output beam divergence is small then the transversal Gaussian distributions of laser, 1st and 2nd Stokes beams in an active medium, saturable absorber and Raman medium will be characterized by an efficient for every given laser element radius $r_{L(S1,S2)}^{(m)}$ ($m=am$ for an active medium, $m=sa$ for a saturable absorber, and $m=Rm$ for a Raman medium, respectively). Using the semi-classical approach proposed in Ref.[10] for transient SRS-conversion and description of amplification/absorption in *Nd*-doped crystals as active medium from Ref.[2], and description of absorption in $Cr^{4+}$-doped crystals as absorber from Ref.[9] it can be shown that the rate equations for the fundamental (laser), 1st and 2nd Stokes waves, $A_{L(S1,S2)}(t)$, in a laser with intracavity SRS conversion into Stokes waves read

$$\frac{dA_L(t)}{dt}=\frac{1}{2}c\sigma_{am}\int_0^{\infty}dr2\pi r\frac{2}{\pi\ r_L^{(am)\ 2}}\exp\ -2r^2/\pi\ r_L^{(am)\ 2}\quad n_u(r,t)-n_l(r,t)\ \frac{A_L(t)}{L_L}-\frac{1}{2}c\sigma_{24}n_{a0}\frac{A_L(t)}{L_L}$$

$$-\frac{1}{2}c(\sigma_{13,L}-\sigma_{24,L})\int_0^{\infty}dr2\pi r\frac{2}{\pi\ r_L^{(sa)\ 2}}\exp\ -2r^2/\pi\ r_L^{(sa)\ 2}\ \frac{A_L(t)}{L_L}-\frac{1}{2}c\alpha_{L,tot}\frac{A_L(t)}{L_L}+ \qquad (1)$$

$$i\pi L^{(Rm)}N\left(\frac{\partial\alpha}{\partial q}\right)\sqrt{\frac{\omega_L\omega_{S1}}{\mu_L\mu_{S1}L_LL_{S1}}}A_{S1}(t)Q_{L,S1}(t)+\frac{1}{2}\beta_{sp}\int_0^{\infty}dr2\pi r\frac{2}{\pi\left(r_L^{(am)}\right)^2}\exp\left(-2r^2/\pi\left(r_L^{(am)}\right)^2\right)\frac{n_u(r,t)}{\tau_{ul}},$$

$$\frac{dA_{S1}(t)}{dt}=-\frac{1}{2}c(\sigma_{13,S1}-\sigma_{24,S1})\int_0^{\infty}dr2\pi r\frac{2}{\pi\ r_{S1}^{(sa)\ 2}}\exp\left(-\frac{2r^2}{\pi\ r_{S1}^{(sa)\ 2}}\right)n_a(r,t)\frac{A_{S1}(t)}{L_{S1}}-\frac{1}{2}c\sigma_{24,S1}n_{a0}\frac{A_{S1}(t)}{L_{S1}}-$$

$$\frac{1}{2}c\alpha_{S1,tot}\frac{A_{S1}(t)}{L_{S1}}+i\pi L_{Rm}N\left(\frac{\partial\alpha}{\partial q}\right)\left[\sqrt{\frac{\omega_L\omega_{S1}}{\mu_L\mu_{S1}L_LL_{S1}}}A_L(t)Q_{L,S1}^*(t)+\sqrt{\frac{\omega_{S1}\omega_{S2}}{\mu_{S1}\mu_{S2}L_{S1}L_{S2}}}A_{S2}(t)Q_{S1,S2}(t)\right], \qquad (2)$$

$$\frac{dA_{S2}(t)}{dt}=-\frac{1}{2}c(\sigma_{13,S2}-\sigma_{24,S2})\int_0^{\infty}dr2\pi r\frac{2}{\pi\ r_{S2}^{(sa)\ 2}}\exp\ -2r^2/\pi\ r_{S2}^{(sa)\ 2}\ n_a(r,t)\frac{A_{S2}(t)}{L_{S2}}$$

$$-\frac{1}{2}c\sigma_{24,S2}n_{a0}\frac{A_{S2}(t)}{L_{S2}}+i\pi L_{Rm}N\left(\frac{\partial\alpha}{\partial q}\right)\sqrt{\frac{\omega_{S1}\omega_{S2}}{\mu_{S1}\mu_{S2}L_{S1}L_{S2}}}A_{S1}(t)Q_{S1,S2}^*(t)-\frac{1}{2}c\alpha_{S2,tot}\frac{A_{S2}(t)}{L_{S2}}, \qquad (3)$$

where $\sigma_{am}$ is the spectroscopic stimulated emission cross-section of activator atoms in an active medium, $n_u(r,t)$ and $n_l(r\ t)$ are the 2D-densities of activator atoms in the upper and lower laser levels within the upper and lower laser multiplets, respectively, $\tau_{ul}$ is the lifetime of activator

atoms in the upper laser level, $\alpha_{L(S1,S2)}$ is the fundamental (1st and 2nd Stokes) wave internal loss, $R_{L(S1,S2)in}$ and $R_{L(S1,S2)out}$ are the reflection coefficients at the fundamental (1st and 2nd Stokes) wavelength of a rear and output mirrors, respectively, $\beta_{sp}$ is the fraction of laser photons spontaneous emitted into laser mode, $\sigma_{13,L(S1,S2)}$ and $\sigma_{24,L(S1,S2)}$ are the ground and excited state cross-sections of fundamental (1st and 2nd Stokes) wave absorption in a saturable absorber, $n_a(r,t)$ is the 2D-density of absorbing atoms in the ground state in an absorber, $n_{a0} = N_a L_{sa}$, $N_a$ is the 3D- density of absorbing atoms in an absorber, $L_{sa}$ is the saturable absorber length, $N$ is the Raman-active atom density, $\partial\alpha/\partial q$ is the derivative of Raman-medium polarizibility with respect to space coordinate, $L_{Rm}$ is the Raman-medium length, $\omega_{L(S1,S2)}$ is the cycling frequency of a fundamental (1st and 2nd Stokes) wave, $\mu_{L(S1,S2)}$ is the Raman-medium refractive index at the fundamental (1st and 2nd Stokes) wavelength, $L_{L(S1,S2)}$ is the cavity optical length at the fundamental (1st and 2nd Stokes) wavelength, and $Q_{L,S1}(t)$ and $Q_{S1,S2}(t)$ are the amplitudes of the Raman-medium collective vibrations generated in the processes of fundamental-to-1st Stokes wave conversion and 1st-to-2nd Stokes wave conversion, respectively. The first term in the right-hand side of Eq.(1) describes stimulated emission in an active medium. The second and the third terms in the right-hand side of Eq.(1) describe the absorption, the fourth term describes intracavity SRS conversion of a fundamental wave into a 1st Stokes wave. The third term in the right-hand side of Eq.(2) describes the fundamental-to-1st Stokes wave SRS conversion and the 1st Stokes-to-2nd Stokes wave SRS conversion. The third term in the right-hand side of Eq.(3) describes the 1st Stokes-to-2nd Stokes wave SRS conversion.

For the amplitudes of the collective vibrations the rate equations are

$$\frac{\partial Q_{L,S1}(t)}{\partial t} = \frac{i}{2m\omega_0\pi}\left(\frac{\partial\alpha}{\partial q}\right)\left[\frac{1}{r_L^{(Rm)\,2} + r_{S1}^{(Rm)\,2}}\sqrt{\frac{\omega_L\omega_{S1}}{\mu_L\mu_{S1}L_L L_{S1}}}A_L(t)A_{S1}^*(t)\;1-2N_{L,S1,L,S1}(t)\right. \qquad (4)$$

$$\left. + \frac{\delta_{L,S1;S1,S2}}{r_L^{(Rm)}r_{S2}^{(Rm)} + r_{S1}^{(Rm)\,2}\left(\frac{r_L^{(Rm)}}{2r_{S2}^{(Rm)}} + \frac{r_{S2}^{(Rm)}}{2r_L^{(Rm)}}\right)}\sqrt{\frac{\omega_{S1}\omega_{S2}}{\mu_{S1}\mu_{S2}L_{S1}L_{S2}}}A_{S1}(t)A_{S2}^*(t)\left(-2N_{L,S1,S1,S2}(t)\right)\right] - \frac{Q_{L,S1}(t)}{T_2},$$

$$\frac{\partial Q_{S1,S2}(r,t)}{\partial t} = \frac{i}{2m\omega_0\pi}\left(\frac{\partial\alpha}{\partial q}\right)\left[\frac{1}{r_{S1}^{(Rm)\,2} + r_{S2}^{(Rm)\,2}}\sqrt{\frac{\omega_{S1}\omega_{S2}}{\mu_{S1}\mu_{S2}L_{S1}L_{S2}}}A_{S1}(t)A_{S2}^*(t)\;1-2N_{S1,S2;S1,S2}(t)\;+\right.$$

$$\left. \frac{\delta_{L,S1;S1,S2}}{r_L^{(Rm)}r_{S2}^{(Rm)} + r_{S1}^{(Rm)\,2}\left(\frac{r_L^{(Rm)}}{2r_{S2}^{(Rm)}} + \frac{r_{S2}^{(Rm)}}{2r_L^{(Rm)}}\right)}\sqrt{\frac{\omega_L\omega_{S1}}{\mu_L\mu_{S1}L_L L_{S1}}}A_L(t)A_{S1}^*(t)\left(-2N_{L,S1;S1,S2}(t)\right)\right] - \frac{Q_{S1,S2}(r,t)}{T_2}, \qquad (5)$$

where $T_2$ is the Raman-medium dephasing time, $\delta_{L,S;S1;S2}$ is the coupling factor of multiwave mixing, $N_{L,S1;L,S1}(t)$, $N_{L,S;\,S1;S2}(t)$, and $N_{S1,S2;S1;S2}(t)$ are the densities of Raman active atoms in the excited state averaged over the products of spatial modes.

If the pulses duration is sufficiently exceeds the Raman-medium dephasing time ($T_2$) then instead of equations (1-5) we have only the first three ones for the wave amplitudes in which the quasistationary solutions of Eqs.(4,5) for the collective vibration amplitudes are substituted. Thus, as a special case we obtain the known semi-classical quasistationary model of a laser with intracavity SRS conversion developed in Ref. [5-8]. If the phase relations are not valuable and only 1st Stokes wave is generated we obtain the known phenomenological description of

intracavity SRS conversion widely applied for modeling and/or estimation of microchip- and mini-lasers.

## 3. Experiment and discussion

Pulse dynamics of a microchip-laser with intracavity SRS conversion has been investigated experimentally. In the laser *Nd(10%):LSB* crystal with thickness of 1.24 mm was chosen as an active medium. The coating on the rear side of the crystal having high reflectivity ($R_{Lin}$=99.8%) in the 1050-1250nm wavelength range and high transmission (95%) at 808nm served as a rear mirror. The other side of the crystal was AR coated ($R \leq 0.2\%$). The crystal was mounted on a copper heat sink with a thermo-conductive compound. The Raman media was a 2 mm thick $BaWO_4$ crystal plate. $Cr^{4+}$:*YAG* plate with thickness of 0.75mm and initial transmittance of 84% was used as a saturable absorber. The absorber and the Raman plates were AR/AR coated ($R \leq 0.2\%$) at 1050-1250 nm. The output coupler had reflection coefficients of 99% at 1063 nm, 97% at 1180nm, and 77% at 1320 nm.

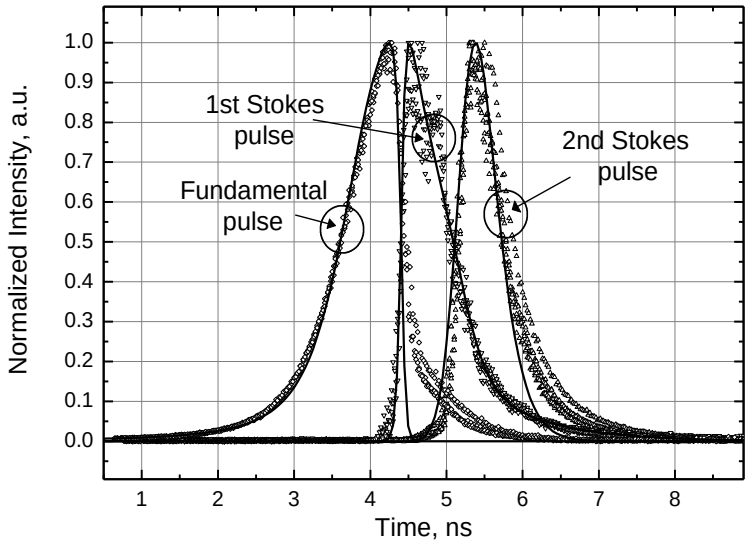


**Fig.1**. Experimentally measured (dots) and numerically calculated (lines) fundamental, 1st and 2nd Stokes pulse shapes

The dependences of the average output power of fundamental and two Stokes waves, the pulse repetition rate and the output pulses energy on the pump power in the range of 490 to 940 mW have been measured experimentally. The average power of Stokes waves reaches the value of ≈ 15 – 25 mW while the average output power of fundamental wave reaches the value of ≈ 50 mW. The total average output power of all waves is about 90 mW at the pump power about 940 mW. The pulse repetition rate is in kHz range with the maximum value of 37 kHz. With the increase in pump power the 1st Stokes pulse energy slowly decreases from ≈ 0.95 down to ≈ 0.65 μJ while the 2nd Stokes pulse energy slowly increases from ≈ 0.1 to ≈ 0.5 μJ.

In Fig.1 the several repetitions of the experimentally measured at the pump power of 810 mW fundamental, 1st and 2nd Stokes pulse shapes (dots) are presented. As it is seen the pulses are repeated stably and their durations are about ≈ 0.85, 0.66, and 0.62 ns for the fundamental, 1st and 2nd Stokes waves, respectively. Also in Fig.1 we show the numerically calculated on the basis of Eqs.(1-6) the pulse shapes which are very close to the experimental ones. Moreover, in addition to the experimental and theoretical pulses coincidence the calculations show good agreement of the time delay between the fundamental, 1st and 2nd Stokes pulses with experimentally determined ones. It is obtained in numerical modeling that the larger/smaller the coupling factor the shorter/longer the time delay of the 2nd Stokes pulse appearance. According to numerical modeling the fundamental pulse duration is practically independent on multiwave mixing in a two Stokes microchip-laser while the 1st and 2nd Stokes pulse duration should decrease with the coupling factor increase.

## 4. Conclusion

The semi-classical theory of microchip- and mini- laser with intracavity transient or quasistationary SRS conversion of laser (fundamental) wave into two frequency shifted waves has been developed. The rate equations for fundamental and two Stokes waves and the rate equations for collective vibration amplitudes of Raman-medium induced polarization have been obtained. The developed theory takes into account dephasing of Raman-medium induced polarization and intracavity transient multiwave mixing. It is shown that known at the moment phenomenological and semi-classical models of microchip- and mini- laser with intracavity SRS conversion are the spatial cases of the proposed theory. Two Stokes generation of *Nd:LSB* (active medium) - *Cr:YAG* (saturable absorber) - $BaWO_4$ (Raman medium) microchip-laser has been experimentally investigated. The dependences of the average output power of fundamental and two Stokes waves, the pulse repetition rate and the output pulses energy on the pump power as well as pulses shapes have been measured experimentally, and good agreement of numerical modeling with experimental result has been obtained.

## References

1. A.A. Demidovich, P.A.Apanasevich, L.E. Batay, A.S. Grabtchikov, A.N. Kuzmin, V.A. Lisinetskii, V.A. Orlovich, O.V. Kuzmin, V.L.Hait, W.Kiefer, M.B. Danailov, Appl. Phys. B **76**, 509 (2003).
2. A.A. Demidovich, S.V. Voitikov, L.E. Batay, A.S. Grabtchikov, M.B. Danailov, V.A. Lisinetskii, A.N.Kuzmin, V.A. Orlovich., Opt. Commun, **263**, 52 (2006).
3. J.J. Zayhowski, J.Harrison, Miniature Solid-State Lasers, in *Handbook of Photonics*, part 8, pp. 326-393. Ed.-in-Chif Mool G. Gupta, CRC Press LLC, 1997.
4. S.V. Voitikov, A.A. Demidovich, L.E. Batay, M.B. Danailov, A.N. Kuzmin, Opt. Commun. **251,** 154 (2005).
5. J.K. Brasseur, K.S. Repasky, and J.L Carlsten. Opt. Lett., **23**, 367 (1998)
6. K. S. Repasky, J. K. Brasseur, L. Meng, J. L. Carlsten. JOSA B, **15**, 1667 (1998)
7. J. K. Brasseur, P. A. Roos, K. S. Repasky, J. L. Carlsten. JOSA B, **16**, 1305 (1999)
8. Lei S. Meng. Continuous-wave Raman Laser in $H_2$: Semiclassical Theory and Diode-pumping Experiments. PhD thesis, Department of Physics, Montana State University, Bozeman, MT 59717 August 2002
9. Xiao and M. Bass, IEEE J. Quantum Electron., **33**, 41 (1997).
10. S. V. Voitikov, A. A. Demidovich, A. S. Grabtchikov, V. N. Burakevich, V. A. Lisinetskii, M. B. Danailov, V.A. Orlovich., Proc. of SPIE, **6731**-93 (2007)

# OPTIMIZATION OF PUMPING PARAMETERS FOR THULIUM-DOPED FIBER AMPLIFIERS

**M.A.Khodasevich, S.A.Koval and G.V.Sinitsyn**

B.I.Stepanov Institute of Physics, National Academy of Sciences of Belarus
68 Nezalezhnasti ave., 220072 Minsk, Belarus
e-mail: m.khodasevich@ifanbel.bas-net.by
Received: date / Revised version: date

**Abstract**. A completely spectrally and spatially resolved theoretical model of a silica-host thulium-doped fiber amplifier is presented. In contrast to the models reported so far, multimodal structure of emission is taken into account. Several promising pumping schemes are considered. Genetic algorithm is implemented for pumping scheme optimization to attain the maximum gain or minimum gain ripple. The results obtained allow to select the best parameters for each considered scheme.
***Key words**: thulium-doped fiber amplifier, genetic algorithm.*
**PACS**. 42.81.-i Fiber optics - 42.55.Wd Fiber lasers -42.81.Wg Other fiber-optical devices

## 1. Introduction

Continuously increasing demand for capacity in the telecommunication systems stimulates investigations on the optical bandwidth expansion. Current long-haul transmission systems utilize erbium doped fiber amplifiers (ED-FAs), that operate in the C- and L-bands (1530 -1565 nm and 1565-1625nm, respectively) and multi-pumped fiber Raman amplifiers with bandwidth up to 100 nm. The C- and L-bands represent only a small portion of the low-loss spectral region available in standard single-mode fibers (1440 - 1650 nm) or fibers with low OH absorption. The next spectral expansion following the C- and L-bands is the S-band (1460 - 1530 nm). Among the most promising candidates for optical amplification in this spectral region are the thulium-doped fiber amplifiers (TDFAs).

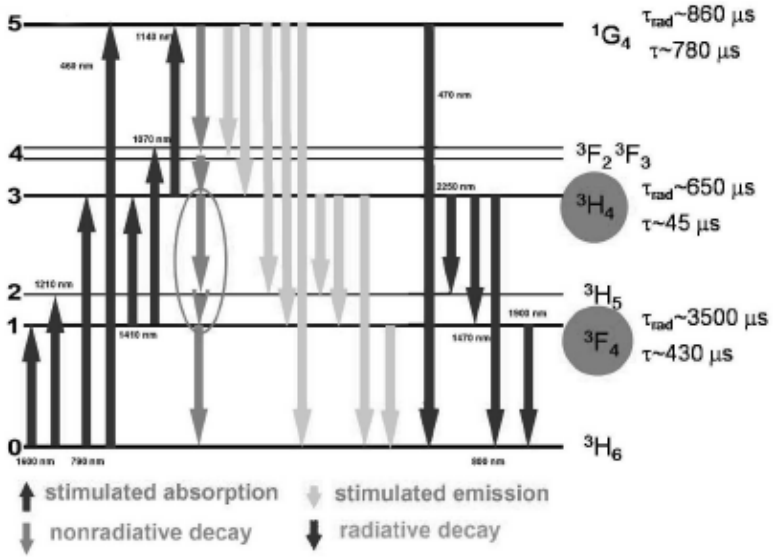


**Fig. 1.** $Tm^{3+}$ level diagram with the transitions involved in the model.

Stimulated emission in *Tm*3+ ions at wavelengths around 1470 nm occurs between 3*H*4 and 3*F*4 energy lev-els. Two main problems complicate the use of this transition.

Firstly, *Tm*3+ behaves as a four-level laser system, where the lifetime of the upper level is shorter than that of the lower level. This problem can be solved by using different up-conversion schemes of pumping.

The second problems is possible non-radiative decay of 3*H*4 level via intermediate 3*H*5 level, which has large probability, especially in the conventional silica fiber host. Therefore most of TDFAs are based on low phonon energy fiber materials, for example fluoride composites.

However, the usage of non-silica materials results in problems with fabrication, exploitation and splicing to the standard telecommunication fiber.

Complicated energy level diagram and the impossibility of obtaining analytical results under any reasonable assumptions are the reasons why only few TDFA models are reported up to this date in contrast to the comprehensively studied EDFAs. Among them one can emphasizethe model by Peterka *et al.* [2]. However, all the existing models have the disadvantage of disregarding the mode structure of emission in wide wavelength range that is characteristic for TDFA. Actually, amplified spontaneous emission (ASE) is generated in TDFA in 400-2200 nm spectral range, shorter wavelength limit of which corresponds to 3 -9 modes under general step-index fiber parameters.

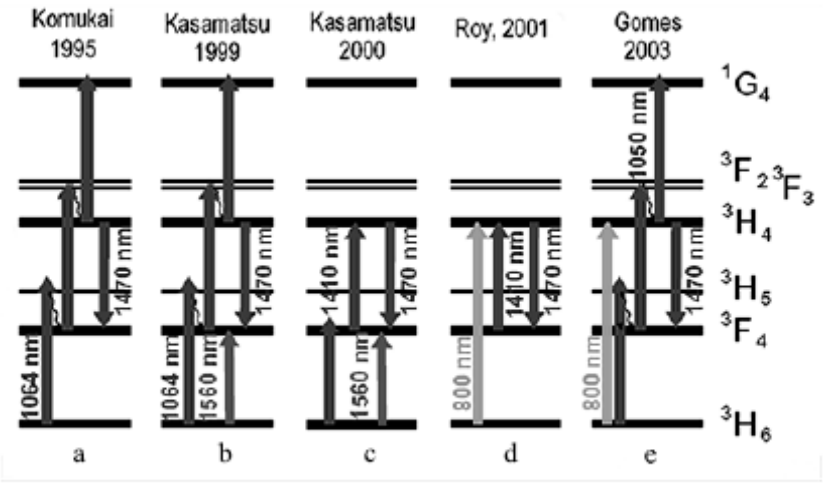


**Fig. 2.** Several TDFA pumping schemes.

## 2. Theoretical model

We consider here an S-band thulium-doped silica fiber amplifier. Following assumptions are implemented:

- Cooperative effects are neglected (*Tm*3+ concentration is supposed to be low { 1.5£10¡19 *cm¡*3)
- Homogeneously broadened thulium spectra
- Step-index fiber
- Monochromatic multi-wavelength pumping
- Wavelength-division multiplexed (WDM) signals
- Wide-band ASE.

Our model is based on the ordinary rate and propagation equations, which are presented for four levels as the non-radiative decay rates from 3*F*2, 3*F*3 and 3*H*5 levels to the respective underlying levels are high (*À* 105*s¡*1), so corresponding populations can be neglected.

Usually rate equations are written for average level populations at certain longitudinal coordinate, whichimplies the coincidence of transverse profiles of *Tm*3+ concentration and each level population density. We do not use this assumption, thus all items in the rate equations are considered to be local (i.e. correspond to certain (*r; Á; z*) point of the fiber):

$$\begin{aligned}\frac{dN_1}{dt} = {} & N_0(W_{01}+W_{02})- \\ & -N_1(W_{10}+W_{13}+W_{14}+A_1^{nr}+A_{10}^{r})+ \\ & +N_3\,(W_{31}+W_{32}+A_3^{nr}+A_{32}^{r}+A_{31}^{r})+ \\ & +N_5(A_{51}^{r}+A_{52}^{r}) \quad (1)\end{aligned}$$

$$\frac{dN_3}{dt} = N_0 W_{03} + N_1(W_{13} + W_{14}) - \\ - N_3\left(W_{35} + W_{32} + W_{31} + W_{30} + A_3^{nr} + \sum_{j=0}^{2} A_{3j}^{r}\right) + \\ + N_5(A_5^{nr} + A_{54}^{r} + A_{53}^{r}) \quad (2)$$

$$\frac{dN_5}{dt} = N_0 W_{05} + N_3 W_{35} - \\ - N_5\left(W_{50} + A_5^{nr} + \sum_{j=0}^{4} A_{5j}^{r}\right) \quad (3)$$

$$N_t = N_0 + N_1 + N_3 + N_5 \quad (4)$$

where *Ni* = *Ni*(*r; Á; z*) is the *i*-th level population density, *Nt* { *Tm*3+ ions concentration, *Wij* = *Wij*(*r; Á; z*) -
stimulated emission/absorption rates, *Arij* and *Anri* - radiative and nonradiative spontaneous relaxation rates respectively. *Wij* expression that takes into account mode structure of emission has the following form:

$$W_{ij}(r,\phi,z) = \int_{\lambda=0}^{\infty} \frac{\sigma_{ij}(\lambda)}{hc} \sum_m (P_m^+(z,\lambda) + \\ + P_m^-(z,\lambda))\,\overline{\psi_m(r,\phi,\lambda)} d\lambda \quad (5)$$

Where $\sigma_{ij}(\lambda)$ is the respective transition cross-section, $P_m^+(z,\lambda)$ and $P_m^-(z,\lambda)$ - emission powers, propagating in forward (signal codirectional) and backward directions respectively, *m* is the index of emission modes $\overline{\psi_m(r,\phi,\lambda)}$ - normalized mode envelope $(\int \overline{\psi_m(r,\phi,\lambda)} r\ dr\ d\phi = 1)$. .

Obtained from 1-5 explicit expressions for *Ni* under stationary conditions are omitted here because of their excessive size.

System of propagation equations includes expressions for forward/backward pumps, forward/backward ASE and WDM signals. Their full set is rather extensive, so only one equation of each type is listed (each equation refers to a single mode *m*).
Signal:

$$\frac{dP_{sm}(\lambda,z)}{dz} = P_{sm}(\lambda,z) \int_0^b \int_0^{2\pi} (\sigma_{31} N_3(r,\phi,z) - \\ - \sigma_{13} N_1(r,\phi,z) - \sigma_{01} N_0(r,\phi,z))\,\overline{\psi_{sm}(r,\phi,\lambda)}\ r\ dr d\phi \quad (6)$$

1064 nm pump power:

$$\frac{dP_{pm}^+(\lambda,z)}{dz} = -P_{pm}^+(\lambda,z) \int_0^b \int_0^{2\pi} (\sigma_{02} N_0(r,\phi,z) + \\ + \sigma_{14} N_1(r,\phi,z) + \sigma_{35} N_3(r,\phi,z))\,\overline{\psi_{pm}(r,\phi,\lambda)}\ r\ dr d\phi \quad (7)$$

ASE in 800 nm region:

$$\frac{dP_{ASEm}^+(\lambda,z)}{dz} = P_{ASEm}^+(\lambda,z) \int_0^b \int_0^{2\pi} (\sigma_{30} N_3(r,\phi,z) - \\ - \sigma_{03} N_0(r,\phi,z))\,\overline{\psi_{ASEm}(r,\phi,\lambda)}\ r\ dr d\phi + \\ + 2\frac{hc^2}{\lambda^3}\sigma_{30} \int_0^b \int_0^{2\pi} N_3(r,\phi,z)\,\overline{\psi_{ASEm}(r,\phi,\lambda)}\ r\ dr d\phi \quad (8)$$

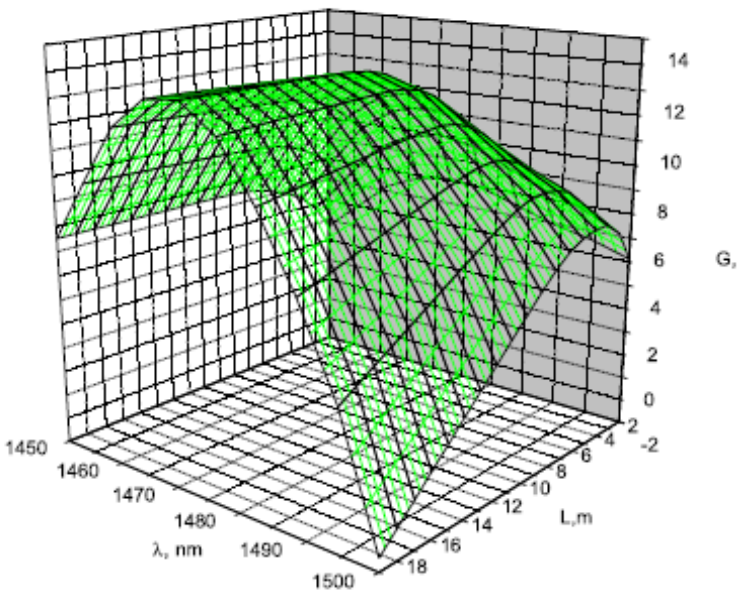


**Fig. 3.** The dependence of TDFA gain spectrum G over amplifier length L. Combined two-directional pumping is used, forward pump of 1 W at 1410 nm, backward one of 0.1 W at 1560 nm.

Propagation equations system is solved numerically using iterative double-direction integration chain. As all the equations are local, two integrations must be performed: transverse one to obtain total power increment at certain ¯ber section and longitudinal one to derive emission propagation dynamics.

Following fiber parameters were chosen for numerical modelling: step-index fiber with 2.6 ¹m core diameter, numerical aperture of 0.3, core refraction index of 1.5. An example of the results obtained is shown in fig.3.

## 3. Ga application for tdfa pumping scheme optimization

The goal of the work is the pumping scheme optimization intended to obtain the maximum gain or the minimum gain ripple of TDFA. We use here the genetic algorithm method that has proven its effectiveness in wide range of problems where direct analytical methods are not applicable. GA can be briefly characterised as a heuristic search algorithm, utilized for the solution of optimisation and modelling problems by consistent selection, combination and variation of the sought parameters with the use of mechanisms, similar to the biological evolution. GA is stochastic by its nature and is dependent neither on initial conditions nor on the search space properties. Generally GA as an optimization method is more effective than Monte-Carlo methods or direct search space screening.

The following algorithm features have been chosen:

- Fixed population size of 50 persons
- 8 bit parameter coding
- Multipoint crossover operator with the number of break points equal to the parameter quantity
- Crossover probability of 60%
- Uniform mutation operator with 95% probability of at least one bit inversion
- 3 ranked tournament as the selection method
- Removal of duplicated persons with the double probability mutation operator
- Elitism { 2 individuals with the maximal fitness are preserved for the next generation.

There is no consistent and strict mathematical GA theory these days, so these features were mainly determined as the result of numerical experiments.

Pumping scheme optimisation was carried for the schemes in fig. 2 under the following assumptions:

- Maximal gain or minimal gain ripple as the sought parameters.
- Pump wavelengths and forward/backward pump powers ratio as the variable parameters (both possible pumping directions are taken into account).

- Pump wavelengths are varied across the respective transition absorption band.
- Total pump power of 1 W, signal power of 1£10¡5 W.
- Spectrum flattening is carried in 1450 { 1500 nm range around the gain maximum (1470 nm).
- The ratio of the average gain to the gain unevenness over the considered spectral region as the gain ripple criterion.

GA demonstrates high convergence speed (see fig. 4). In 50 £ 20 = 1000 goal function calculations GA gives same result precision as Monte-Carlo method does in 105 calculations.

The results of pump powers and wavelengths optimization are shown in fig. 5 - 6. Corresponding optimal pumping parameters are listed in tables 1 - 2. Pumping schemes are labeled according to fig. 2. One can see that for both optimization criteria pumping schemes utilizing 1410 nm pump (namely, *c* and *d*) demonstrate the best results. Another interesting conclusion is the redundancy of 1560 nm pump in scheme *b* - both maximal gain and minimal gain ripple are achieved by using single forward pump at 1026 nm.

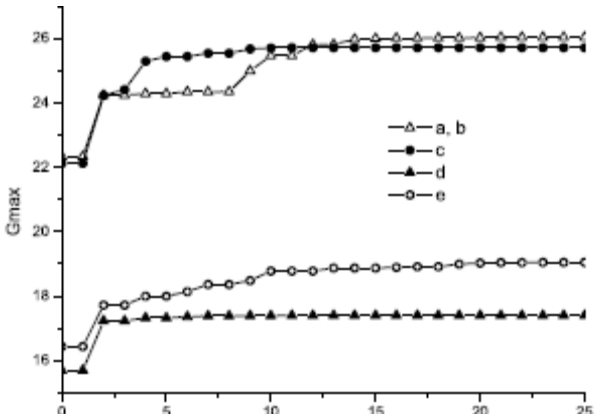


**Fig**. **4**. Maximum gain *Gmax* over the generation number *n* for the considered TDFA pumping schemes labeled according to fig.2.

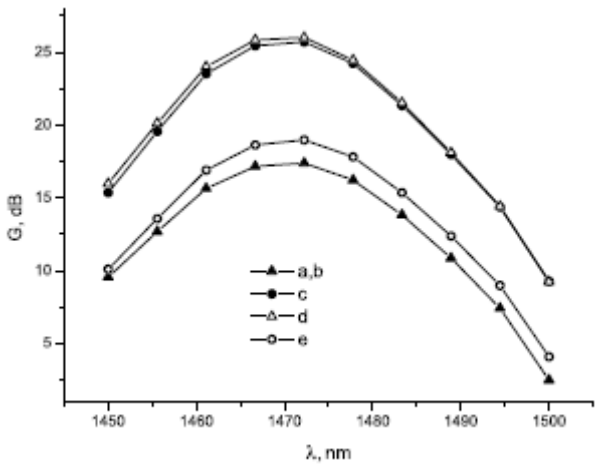


**Fig. 5**. Maximum gain spectra for the considered TDFA pumping schemes.

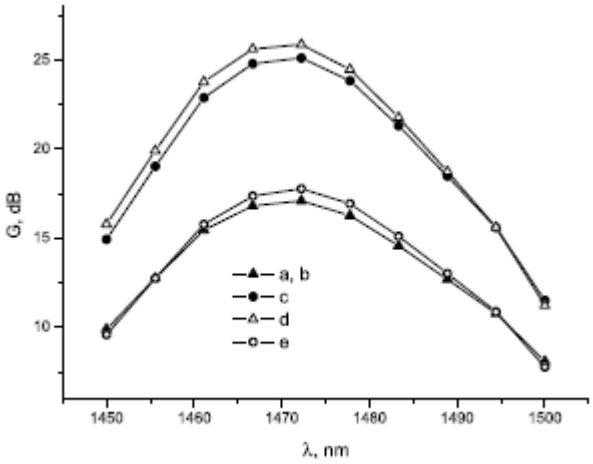


**Fig. 6**. Minimum gain ripple spectra for the considered TDFA pumping schemes.

**Table 1.** Optimal TDFA parameters (maximum gain).

| Pumping scheme | forward pump wavelength, nm | backward pump wavelength, nm | forward pump ratio |
|---|---|---|---|
| a,b | 1026 | — | 1.000 |
| c | 1630 | 1399 | 0.262 |
| d | 785 | 1399 | 0.385 |
| e | 830 | 1026 | 0.094 |

**Table 2.** Optimal TDFA parameters (minimum gain ripple).

| Pumping scheme | forward pump wavelength, nm | backward pump wavelength, nm | forward pump ratio |
|---|---|---|---|
| a,b | 1026 | — | 1.000 |
| c | 1645 | 1399 | 0.283 |
| d | 792 | 1399 | 0.432 |
| e | 833 | 1026 | 0.112 |

## 4. Conclusion

Completely spectrally and spatially resolved TDFA model is presented and used for optimizing wavelengths and powers of bidirectional pumping for several upconversion pumping

schemes. The distinguishing feature of our model is taking into account the mode structure of emission in spectral range 400-2200 nm characteristic for TDFA. Genetic algorithm method is used to find the pumping parameters for attaining the maximum gain or minimum gain ripple of TDFA in 1450-1500 nm spectral
band.

The obtained results allow to select two best suited pumping schemes for achieving the maximum gain: forward pumping at 785 or 1630 nm and backward pumping at 1399 nm with 0.39 or 0.26 forward/total pumping power ratio. For achieving the minimum gain ripple the optimized parameters are the following: forward pumping at 792 or 1645 nm and backward pumping at 1399 nm with 0.43 or 0.28 forward/total pumping power ratio.

The following goal of our investigation will be an analysis of stability of pumping schemes against temporal deviation of pumping powers and wavelengths.

**References**

1. Mitchell M., *An Introduction to Genetic Algorithms*. Cambridge, MA:MIT Press, 1998.
2. Peterka P., B. Faure, W. Blanc, M. Karasek and B. Dussardier, Optical and Quatum Electronics, 36, (2004) 201.
3. Komukai T., T. Yamamoto, T. Sugawa, Y. Miyajima, IEEE J.Quantum Electronics, 31, (1995) 1880.
4. Kasamatsu T., Y. Yano, T. Ono, El. Lett., 36, (2000) 1607.
5. Gomes, A.S.L., M.T. Carvalho, M.L. Sundheimer, C.J.A.Bastos-Filho, J.F. Martins-Filho, J.P.V der Weid and W.Margulis. Opt. Lett., 28, (2003) 334.
6. Roy F. *et al.*, OFC'2000, OSA Technical Digest Series, paper WA6-1, 2000.
7. Lee, W.J., B. Min, J. Park and N. Park, OFC-2001 Technical Digest Anaheim, 2, (2001) pp. TuQ 5-1-4.

# SOLID-STATE SOURCES OF HIGH ENERGY AND HIGH AVERAGE POWER RADIATION BASED ON RAMAN CONVERSION OF ND:YAG LASERS RADIATION

**V.A. Orlovich[(a)], H.J. Eichler[(b)], V.A. Lisinetskii[(a)]**

[(a)]B. I. Stepanov Institute of Physics, National Academy of Sciences of Belarus,
68, Nesalezhnasti Ave. 220072 Minsk, Belarus
E-mail: v.orlovich@dragon.bas-net.by
[(b)]TU Berlin — Institut fuer Optik und Atomare Physik,
Str.d.17.Juni 135, D-10623 Berlin, Germany

Stimulated Raman scattering (SRS) is a one of widely used methods of laser radiation frequency conversion. It allows generating efficiently laser radiation at wavelengths difficult for usual laser generation. The sources based on solid-state Raman media are of the special interest due to their compactness, low threshold and high efficiency. Solid-state Raman converters of femotsecond [1], picosecond [2], nanosecond [3,4], and continuous-wave [5] radiation were created.

However there are some problems related with a Raman conversion of high power radiation in solid-state media. These are parasitic generation of high-order Stokes components [3], heating of Raman medium and thermal lens formation [4] and high divergence of converted radiation at high pulse energy [3]. Therefore the energy and power of output radiation in solid-state Raman converters was small (several tens of millijoules and several watts) and $M^2$ factor was high (order of 20). However for many applications the radiation sources with high average power or high pulse energy or with low divergence are required. The present work is devoted to the development of such sources based of Raman conversion in barium nitrate crystal of fundamental and second harmonic of Nd:YAG lasers.

The first sources are barium nitrate Raman lasers generating first (wavelength - 1197 nm), second (wavelength - 1369 nm) and third (wavelength - 1599 nm) Stokes pulses with repetition rate of 10 Hz and with energies higher than 100 mJ for each component. The main difficulty in Raman conversion of high energy pulses to a certain order Stokes component is a parasitic generation of a Stokes component of the next order. This generation decreases efficiency of required generation. The suppression of this parasitic generation is possible in Raman laser (when Raman medium is placed in cavity). It is possible to increase the threshold and to avoid the next-order Stokes generation using the cavity mirrors with optimal reflectivity for required Stokes component and low reflectivity for next-order Stokes component. Practically mirrors have a finite reflection (several percents) at next-order Stokes wavelengths and the next-order Stokes generation occurs decreasing the required Stokes efficiency.

We developed and realized the method of suppression of parasitic next-order Stokes generation. This method involves the use of folded cavities with a selective, low reflective at next-order Stokes wavelength mirrors. Barium nitrate Raman lasers with such three- or four-mirrors folded cavity were created and investigated. The setup of Raman laser for first Stokes generation with a three-mirrors folded cavity is shown in the figure 1a. The created Raman lasers were pumped with a 30 ns pulses at 1064 nm wavelength and provide first Stokes pulses with energy of 156 mJ (quantum efficiency – 66%) and second Stokes pulses with energy of 104 mJ (quantum efficiency – 44%). The Raman laser generating third Stokes pulses with energy of 116 mJ (quantum efficiency – 63%) was also realized. In this laser the parasitic fourth Stokes generation was suppressed not with a folded cavity but due to absorption in barium nitrate crystal. The dependencies of pulse energies of first, second and third Stokes radiations generated in created Raman lasers on pump energies are presented in figure 1b. $M^2$ factor of all Stokes beams was about 20.

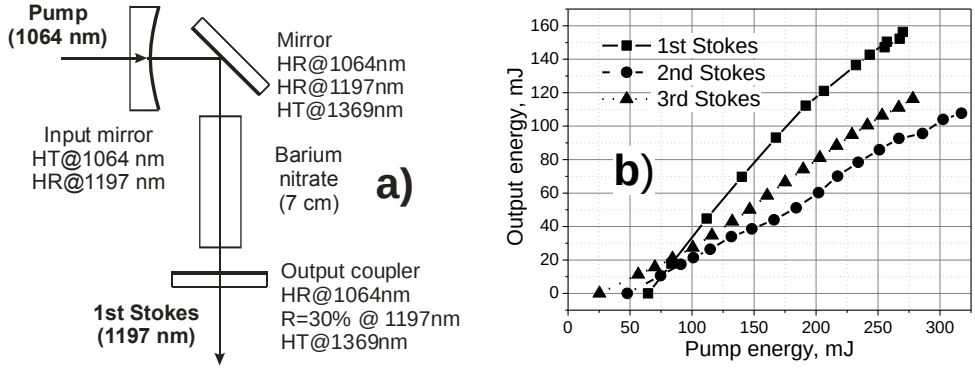


**Fig.1**. Raman laser for first Stokes generation (a) and dependencies of first, second and third Stokes pulse energies on pump energy (b).

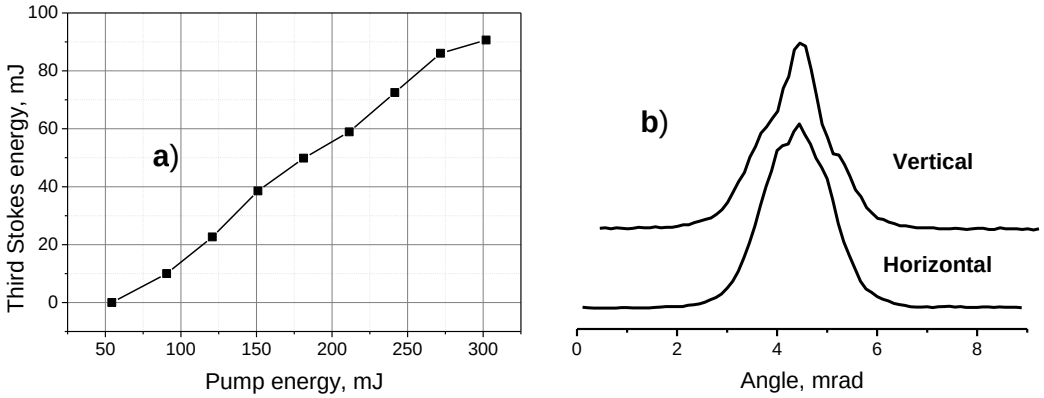


**Fig.2**. Energy of the third Stokes pulses vs. pump pulse energy (a) and horizontal and vertical profiles of third Stokes radiation (b).

The third Stokes generation in barium nitrate is of great practical interest. This radiation is in eye-safe spectral region and can find various applications (for instance, can be used in lidar for $CO_2$ sensing in atmosphere). The Raman laser pumped with a 10 ns pulses and generating third Stokes radiation with a high peak and average power was the second laser source developed. As we stated above, to generate efficiently third Stokes radiation at 30 ns pulse pumping it is enough to use usual two mirrors stable cavity. However when 10 pulses are used as a pump the fourth Stokes generation occurs in spite of absorption of this radiation in barium nitrate, because of smaller third Stokes pulses duration and higher peak power. Nevertheless the energy of third Stokes pulses of 93 mJ was reached (see figure 2a) at pump pulse energy of 300 mJ. This corresponds to the quantum efficiency of 47 %. Peak power of third Stokes was 10 MW, pulse repetition rate – 20 Hz, average power – 1.8 W. The heating of barium nitrate crystal and negative thermal lens formation was observed but was quite small. $M^2$ factor of third Stokes beam was about 15. Spatial profiles of this beam are presented in the figure 2b.

The third laser source is a Raman laser generating high average output power. The heating of Raman medium and thermal lens formation are the main problems related with Raman conversion of high average power radiation. In barium nitrate crystal thermal lens is negative. If this lens is strong, the Raman laser cavity gets unstable and the losses of Stokes components of different order increases. The negative effect of thermal lens on generation in barium nitrate Raman laser with plane-parallel was observed at output power of only 0.22 Вт [4]. This lens led to the 76 % output power decrease. The use of stable cavity allows, as it was stated above, obtaining third Stokes radiation with average power of 1.8 W. The influence of thermal lens was small in this case. However this influence will be significantly stronger even for stable cavity at pump power of several tens of watts.

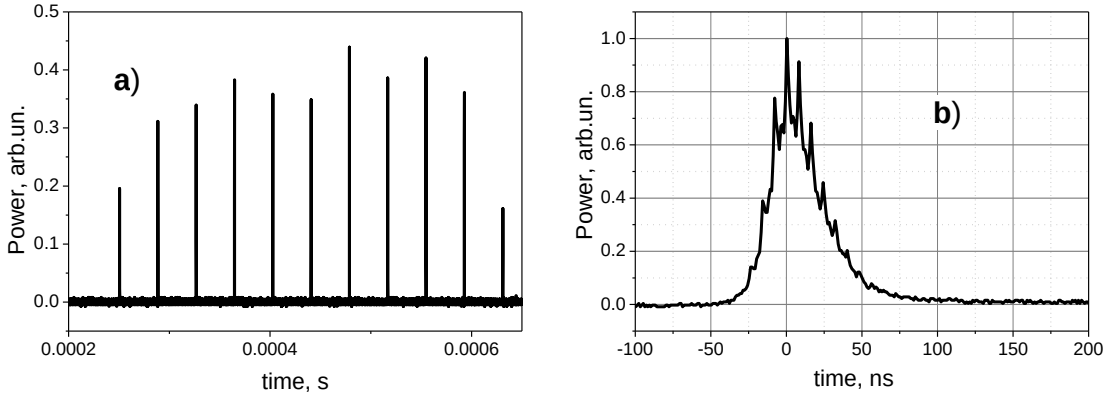


**Fig.3**. Oscilloscope traces of pump burst (a) and of a single pump pulse (b).

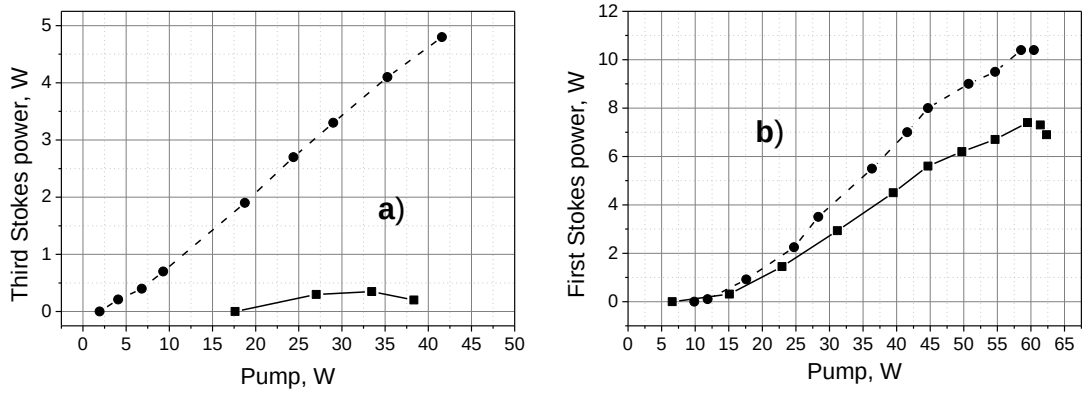


**Fig.4**. The dependencies of third Stokes (a) and of first Stokes (b) average powers on pump average power. Solid line – thermal lens is not compensated, dashed line – thermal lens is compensated.

In developed Raman laser pump power was up to 60 W. A single-mode Nd:YAG laser system was used as a pump source. It was flash lamp pumped with repetition rate of 100 Hz. System produced a burst of 11 pulses per one short (see figure 3a). The duration of each pulse was about 50 ns (see figure 3b), the distance between pulses – 40 μs. Spectral width of pump radiation was 0.02-0.03 $cm^{-1}$. Raman laser consisted of 7 cm long barium nitrate crystal placed in the cavity formed with a spherical input mirror (curvature radius of 1500 mm) and flat output coupler. We used two different output couplers for the first and the third Stokes generation. For all output couplers cavity length of Raman laser was 18 cm

It was found that both at first and third Stokes radiation the thermal lens made the Raman laser cavity unstable. This led to the average power of output third Stokes radiation of only 0.35 W at pump power of 33 W. The divergence of the third Stokes beam was about 4 mrad. The effect of thermal lens to first Stokes average power was significantly less. The quantum defect for the first Stokes generation is three times lower than for the third Stokes generation and the thermal lens is weaker. More over the first Stokes generation is not so sensitive to the cavity stability as the third Stokes generation. As a result the third Stokes output power of more than 7 W was obtained at pump power of 60 W. However the divergence of the first Stokes was very high (about 200 mrad).

The positive lenses were inserted in Raman laser cavity to compensate thermal lens. Figure 4 shows the dependencies of first and third Stokes output average powers on pump powers both for cavities with thermal lens compensation and without it. At first Stokes generation the lens with focal length of 500 mm was used. This lens allows one to increase average output power up to 10 W (quantum efficiency – 20%). The divergence was decreased down to 0.2 mrad. At third Stokes generation lenses with focal lengths of 1000 mm, 250 mm, 200 mm and 125 mm were used. The thermal lens was compensated totally only with use of 125 mm lens. In this case the third Stokes output power was 5 W at pump power of 40 W (quantum efficiency – 17 %). The divergence was also 0.2 mrad.

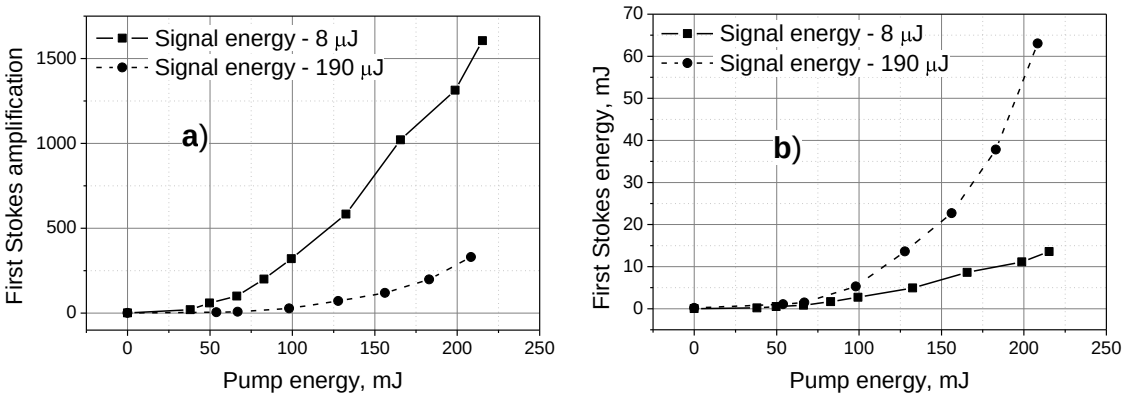


**Fig.5**. The dependencies of the first Stokes amplification (a) and of amplified Stokes energy (b) on pump pulse energy.

The main disadvantage of high energy radiation sources based on solid-state Raman lasers is a high value of $M^2$ factor of output radiation. This complicates the application of this radiation in lidars and rangefinders, and makes it difficult the further its nonlinear conversion. Raman amplification is an alternative approach that allows obtaining high energy pulses. In spite of Raman generation when only a pump beam irradiates the Raman medium while Stokes radiation arises from noise, in Raman amplification pump and Stokes radiation are both incident on the Raman medium. Raman amplification was well studied before in gases [6]. It was shown, that when a low divergent Stokes signal radiation is used the amplified Stokes radiation also has a low divergence. Thereby the fourth laser source is a radiation source based on Raman laser and Raman amplifier.

The Stokes seed was generated in barium nitrate Raman laser. The pump radiation was focused strongly in this laser providing the first Stokes generation with a $M^2$ factor of only 1.5. We investigated two regimes for the Raman generator. In the first one the energy of the Stokes seed pulses incident on the Raman amplifier was 8 μJ, while in the second one this energy was 190 μJ.

Figure 5a shows the dependencies of the first Stokes energy amplifications (ratio of amplified Stokes energy to Stokes signal energy) on pump energy both for Stokes seed pulses with energies of 8 μJ and 190 μJ. The amplification of Stokes pulses with energy of 8 μJ was up to 1600 at pump pulse energy of 215 mJ, while the amplification of Stokes pulses with energy of 190 μJ was 330 at pump pulse energy of 208 mJ. The lower value of amplification for Stokes signal pulses with energy of 190 μJ as compared with 8 μJ Stokes signal pulses is related with saturation of Raman amplification due to pump depletion. Indeed, the energy of amplified pulses for Stokes signal pulses with energy of 190 μJ is five times higher than for Stokes signal pulses with energy of 8 μJ. The dependencies of amplified Stokes energies on pump energy are seen in the figure 5b. It is evident, that for 190 μJ Stokes signal pulses the amplified Stokes energy was 63 mJ at pump energy of 210 mJ, what corresponds to the conversion efficiency of 30 % (quantum conversion efficiency is 34 %). For 8 μJ Stokes signal pulses the amplified Stokes energy was about 14 mJ, what corresponds to the conversion efficiency of 6 % (quantum efficiency – 7 %). Our estimations show that the use of one more stage of Raman amplification allows obtaining pulses with energy of 350 mJ at pump pulse energy of 500 mJ.

The $M^2$ factor of amplified Stokes beam was also small - 2.2. This is significantly smaller than $M^2$ factor of output radiation of Raman lasers and even smaller than $M^2$ factor of pump radiation (3).

The fifth laser source developed in this work is a source of UV radiation (wavelength – 282 nm) for sounding of ozone in the troposphere [7]. The source consist of barium nitrate Raman laser pumped with second harmonic of Nd:YAG laser (532 nm) generating the first Stokes

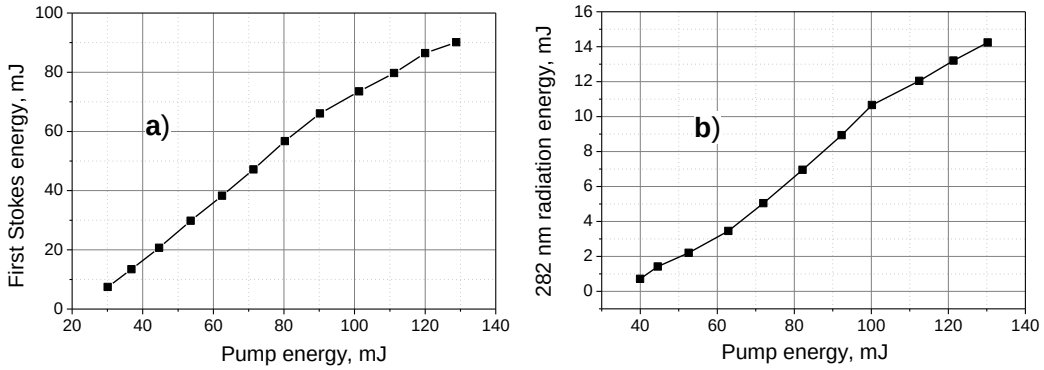


**Fig.6**. The dependencies of the first Stokes energy and of the second harmonic of the first Stokes energy on pump pulse energy.

radiation (wavelength – 563.4 nm) and second harmonic generator based on DKDP crystal. To obtain first Stokes pulses with high energy and efficiency it was necessary to suppress second Stokes generation (wavelength 599 nm). This was realized with the use of four mirrors folded cavity with a selective mirrors. As a result the generation of first Stokes pulses with energy of 90 mJ was achieved. Quantum efficiency was up to 70 %. The first Stokes radiation was frequency doubled. The pulses of second harmonic of the first Stokes radiation had energy up to 14 mJ. The efficiency of conversion of pump radiation to the radiation with a wavelength of 282 nm was about 11%.

So in this work we almost solved the problems related with parasitic next-order Stokes generation, with Raman medium heating and negative thermal lens formation. We showed the possibility of generation in solid-state Raman media of radiation with a high energy and small divergence. Five different laser sources based on Raman conversion in barium nitrate crystal were created. These sources can find various applications, for example for sounding of ozone, $CO_2$ gas, aerosols, for laser surgery, for art-works cleaning.

## References

1 A. S. Grabtchikov, R. V. Chulkov, V. A. Orlovich, M. Schmitt, R. Maksimenko, and W. Kiefer, Optics Letters **28** (11), 926 (2003).
2 P. Cerny and H. Jelynkova, Optics Letters **27**, 360 (2002).
3 C. He and T. H. Chyba, Optics Communications **135** (4), 273 (1997).
4 N. Takei, S. Suzuki, and F. Kannari, Applied Physics B **74** (6), 521 (2002).
5 A. S. Grabtchikov, V. A. Lisinetskii, V. A. Orlovich, M. Schmitt, R. Maksimenka, and W. Kiefer, Optics Letters **29** (21), 2524 (2004).
6 A. Mandl, R. Holmes, A. Flusberg, S. Fulghum, and D. Angeley, Journal of Applied Physics **66**, 4625 (1989).
7 V. V. Ermolenkov, V. A. Lisinetskii, Y. I. Mishkel, A. S. Grabchikov, A. P. Chaikovskii, and V. A. Orlovich, Journal of Optical Technology **72** (1), 32 (2005).

# OXYFLUORIDE GLASS-CERAMICS AS HOST MATERIAL FOR ERBIUM-DOPED FIBER AMPLIFIERS: ULTIMATE INFORMATION CHARACTERISTICS

**M.A.Khodasevich and Y.A.Varaksa**

B.I.Stepanov Institute of Physics, National Academy of Sciences of Belarus
68 Nezalezhnasti ave., 220072 Minsk, Belarus
*E-mail: m.khodasevich@ifanbel.bas-net.by*

**Abstract**. Novel figures of merit are proposed to compare host materials for EDFA, namely, the ultimate spectral efficiency of information transmission (information rate density) and total capacity in a certain spectral band. Using such figures the characteristics of the optical fiber amplifiers implemented on the basis of oxyfluoride glass-ceramics are investigated. Information rate density and information capacity in the range of 1520-1570 nm are calculated. A potential for improving fiber-optic amplifier characteristics by use of glass-ceramics is confirmed.

***Key words****: erbium-doped fiber amplifier, oxyfluoride glass-ceramics, ultimate spectral efficiency of infor-mation transmission.*
*PACS. 42.25. Bs - 42.79. -e -42.79. Gn - 42.81. -i*

## 1. Introduction

It is well known that for erbium-doped fiber amplifiers (EDFAs) the fluoride host material is preferred over the oxide one to avoid non-radiative transitions of erbium ions. However, the synthesis of °uoride crystals is complicated, their stability and fiberizability are problematic. One of the possible solutions is transparent erbium-doped oxyfluoride glass-ceramics. It is two-phase system containing fluoride crystallites that are controllably grown within oxide glass by appropriate heat treatment. Such materials combine excellent luminescent properties of erbium ions in fluoride crystallites with the good fiberizability of oxide glass.

To compare host glasses for EDFA several figures of merit can be used. All of them are spectroscopic characteristics of the glass e.g. peak emission cross section of erbium ions and they do not characterize the entire device (optical amplifier). With regard to utilizing host material for EDFA which is designed to amplify multiplexed optical signals in communication lines, a more straightforward way is to select information characteristics of EDFA for comparing applicability of various host materials.

Our objective is to use novel informational figures of merit for evaluation of glass-ceramics host materials for EDFAs.

## 2. Novel informational figures of merit

The promising host materials for EDFA should meet a number of requirements. They must not contain a significant amount of impurities absorbing in the wavelength band used. A high solubility of dopant in host material is required. A host material should be chemically and physically stable. Non-radiative losses should not be significant at dopant concentrations sufficient for achieving high gain. Finally, a promising host material should ensure superior noise characteristics and pump power conversion efficiency as compared with existing EDFAs.

A number of host glasses are proposed for using in EDFAs, e.g. silicate, phosphate, bismuth, tellurite glasses etc. The figures of merit for comparing them are peak emission cross section of erbium ions, the full width of the emission band at half maximum, a lifetime of erbium ions in the excited state, a product of the peak emission cross section and the full width at half maximum. Such characteristics do not specify the EDFA operation as a component of communication system. To evaluate a fiber quality in respect of information transmission a novel figure of merit is proposed [1] - ultimate spectral efficiency of information transmission. It is

defined as an amplifier capacity (maximum amount of information rate, bit/s) per unit frequency band. Other term used for designation of ultimate spectral efficiency of information transmission is information rate density *ID*.

In the previous work [1] a number of host glasses (silicate, tellurite, phosphate and borate glasses) for EDFA have been compared using information rate density in an unsaturated gain regime of EDFA operation. It should be noted that information density is dependent on the signal wavelength, so the result of evaluation depends on the wavelength selected. In [1] the signal wavelength was se-lected on the gain plateaus of EDFAs concerned. However such a choice is voluntary to some extent. This figure of merit is not taking into account the gain bandwidth of an amplifier. Thus an idea of using EDFA capacity arises to compare various host materials [2].

The capacity *C* of EDFA in the frequency band $\Delta\nu$ is defined as:

$$C = \int_{\Delta\nu} ID(\nu)\, d\nu \qquad (1)$$

To calculate information rate density *ID* and capacity of EDFA we use the number-state model for narrow-band linear boson communication channel [3]. The model assumes that information is transmitted by a number of quanta in longitudinal modes of electromagnetic field. The near IR bandwidth of EDFA is still much lower than the signal
frequency. Assuming no fiber nonlinearity, we can use the following equation for information rate density [4]:

$$ID = \log_2\left(1 + \frac{SNR(0)}{F_0^{min}}\right) + \\ + \frac{SNR(0)}{F_0^{min}} \log_2\left(1 + \frac{F_0^{min}}{SNR(0)}\right) \qquad (2)$$

where *SNR*(0) is optical signal-to-noise ratio at the EDFA input, $F_0^{min}$ is minimum EDFA optical noise figure. So an ultimate spectral efficiency of information transmission is determined by input noise and the only amplifier parameter $F_0^{min}$.

### 3. EDFA operation in unsaturated gain regime

We consider the unsaturated gain regime of EDFA operation. This regime is typical for present amplifiers in fiber-optic communication lines. A consideration of such a regime is advantageous in view of rather simple theoretical description allowing analytical solution. At quasi-two-level pumping in the unsaturated gain regime and at pump power much greater than aggregate signal and amplified spontaneous emission (ASE) power the following analytical equations for $F_0^{min}(\nu)$ and gain *G* are valid [5]:

$$F_0^{min}(\lambda) = 2\frac{\alpha}{\alpha_p}\frac{\eta}{1+\eta_p}\int_{q_L}^{q_0} \frac{\exp\left(\frac{\alpha}{\alpha_p}\frac{\eta-\eta_p}{1+\eta_p}x\right)}{x^{\frac{\alpha}{\alpha_p}}}\, dx \times \\ \times \exp\left[\frac{\alpha}{\alpha_p}\left(\ln(q_0) - \frac{\eta-\eta_p}{1+\eta_p}q_0\right)\right] + \frac{1}{G(\lambda)}\,, \qquad (3)$$

$$G(\lambda) = \exp\left[\frac{\alpha}{\alpha_p}\left(\frac{\eta-\eta_p}{1+\eta_p}(q_0 - q_L) - \ln\frac{q_0}{q_L}\right)\right]\,. \qquad (4)$$

Here $\alpha$ and $\alpha_p$ are absorption coefficients of amplifier fiber at signal and pump wavelengths, respectively, $\eta = \sigma_e(\lambda)/\sigma_a(\lambda)$ , $\eta_p = \sigma_e(\lambda_p)/\sigma_a(\lambda_p)$, $\sigma_e(\lambda_p)$ designates emission cross section at pump wavelength $\lambda_p, \sigma_a(\lambda)$ is absorption cross-section at signal wavelength. The quantities *q*0 and *qL* are input and output pump power normalized on the saturation power.

The equations are valid if the following conditions are met: the background absorption is negligible compared to erbium ions absorption, the erbium doping is uniform over the fiber core

cross section, the fundamental mode cross section for pump, signal and ASE is of the same Gaussian shape, and the EDFA gain band is homogeneously broadened.

The host materials under consideration are samples of glass-ceramics described in [6]. They differ in the temperature of heat treatment of virgin glass. The following designations are used further: G - virgin erbium-doped host glass, GC600, GC630, GC650 { glass-ceramics resulting from heat treatment of virgin glass at a temperature of 600, 630, 650 degrees centigrade, respectively. The modeling of EDFA operation for host materials indicated have been performed on the basis of the above equations. Then the proposed figures of merit have been calculated and used for evaluation of host materials.

## 4. Results

On the Fig. 1 the calculated gain spectra are shown for all materials considered, for about 20 dB specified gain value at 1535 nm. It can be seen that all glass-ceramics are characterized by better performance in terms of gain value in the range 1500-1600 nm than the virgin glass.

Fig. 2 shows the dependence of information rate density at one specific wavelength (1550 nm - the plateau of gain spectrum) on the pump power. Rapid growth of *ID* value as pump power grows slows down at approximately 3 mW. At higher pump values all materials considered show nearly equal performance, but at lower pump values GC600 demonstrates superior performance.

Fig. 3 shows the results of performance evaluation for EDFAs implemented on the basis of oxyfluoride glass or glass-ceramics using an integral figure of merit, namely capacity in the spectral band from 1520 to 1570 nm. It is

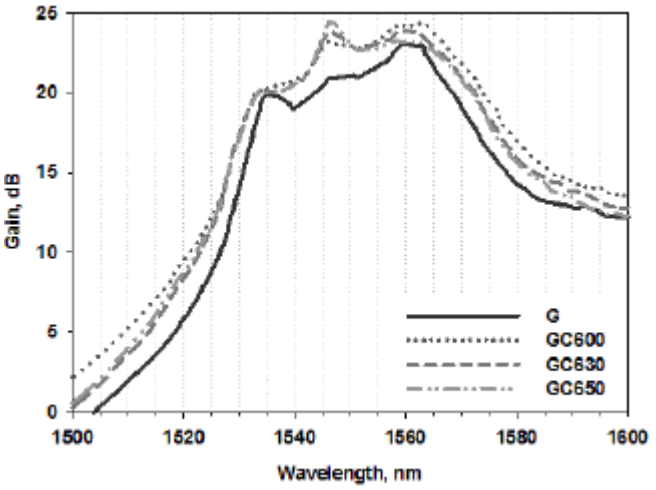


**Fig. 1**. Gain spectra of EDFAs for given value *G '* 20 dB at 1535 nm.

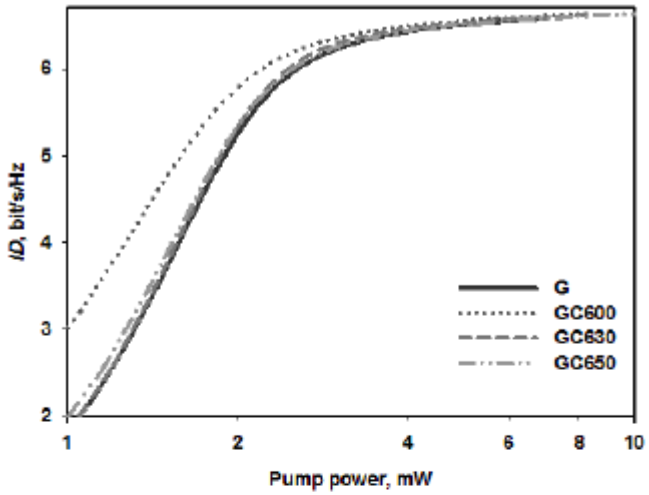


**Fig. 2.** Information rate density at 1550 nm vs pump power.

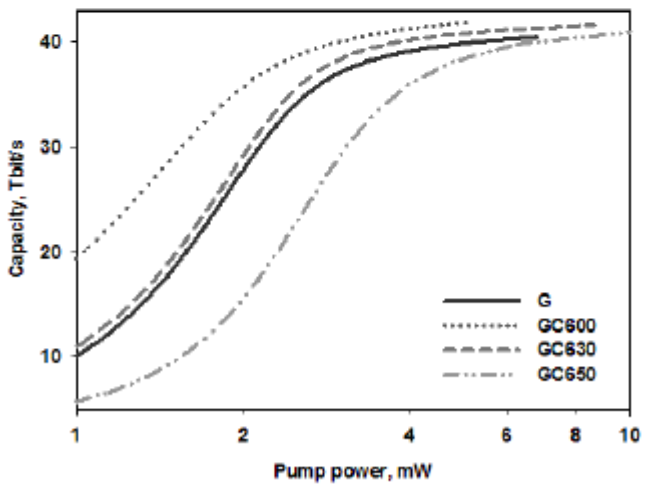


**Fig. 3.** Capacity in the spectral range 1520-1570 nm vs pump power.

clarified that the influence of thermal treatment depends on the temperature substantially. The capacity dependence on pump power is almost identical for virgin oxyfluoride glass and glass-ceramics treated at $630^{\circ}C$. Thermal treatment at $650^{\circ}C$ leads to significant drop in total capacity. The best result obtained is for glass-ceramics treated at $600^{\circ}C$. It should be noted, that the capacity dependence on pump power demonstrates saturation at high pump power values (higher than 4 mW). The total estimated capacity for the best material revealed - glass ceramics treated at $600^{\circ}C$ - exceeds 41 Tbit/s at 5 mW pump power.

The Table 1 which is based on the data from [6] shows the values of one of the traditional figures of merit, namely the product of the peak emission cross section value and the emission spectrum full width at half maximum. One can see that this figure of merit is nearly equal for all host materials considered, so it proves to be useless in this particular situation, while the proposed figure of merit allows to rank host materials according their communicational performance.

| Host material | FWHM[nm]* $\sigma_e(\lambda_{peak})[cm^2] * 10^{20}$ |
|---|---|
| G | 37.96 |
| GC600 | 38.25 |
| GC630 | 38.40 |
| GC650 | 38.07 |

**Table 1**. The product of the peak emission cross section value and the emission spectrum full width at half maximum.

## 5. Conclusion

Novel figures of merit (information rate density and capacity in the unsaturated gain regime) are proposed for comparing the applicability of oxy°uoride glass-ceramics for erbium-doped fiber amplifiers, considered as an element of an optical communication system. We show that the mentioned characteristics are more informative than other figures of merit (peak emission cross section of erbium ions, the full width of the emission band at half maximum, lifetime of erbium ions in the excited state, product of the peak emission cross section and the full width at half maximum, etc.).

The results obtained show the distinct dependence of information rate density at the plateau of gain spectrum and amplifier capacity in the spectral range 1520-1570 nm on the glass-ceramics heat treatment temperature. An increase of heating temperature over $600^{\circ}C$ results in the decrease of capacity in spite of further enhancement of the product of the peak emission cross section and the full width at half maximum.

***Acknowledgement:*** *This work is implemented under support of BRFFI (grant 08R-169).*

## References

1. Khodasevich M.A., G.V. Sinitsyn, Y.A.Varaksa, Optics and Spectroscopy 101, (2006) 757-761.
2. Varaksa Y.A., M.A. Khodasevich, G.V. Sinitsyn, Optics and Spectroscopy 104, (2008) 130-134.
3. Lebedev D.S., L.B. Levitin, Inf. Control 9, (1966) 1-22.
6. 4 M.A.Khodasevich, Y.A.Varaksa: Oxy°uoride glass-ceramics as host material for EDFAs
7. Sinitsyn G.V., M.A.Khodasevich, Optics and Spectroscopy 97, (2004) 464{467
8. Desurvire E. *Erbium-Doped Fiber Amplifiers, Principles and Application*. New York: Wiley-Interscience, 1994, 770.
9. Chen D., Y.Wang , Y.Yu, E.Ma, Journal of Solid State Chemistry 179, (2006) 1445-1452

# POSSIBLE APLICATIONS OF Tm:KYW LASER IN MICROSURGERY

**L.E. Batay[a], A.A. Demidovich[a], A.I. Vodchits[a], V.A. Orlovich[a]**
**N.B. Gorbunova[b], T.V. Kuznetsova[b] and V.S. Ulastchik[b].**

[a)] B.I. Stepanov Institute of Physics of NASB, Nezaleznosti ave. 68, 220072 Minsk, Belarus, E-
*E-mail: l.batay @ dragon.bas-net.by*
[b)]Institute of Physiology of NASB, Akademicheskaya Str. 28, 220072 Minsk, Belarus

**Abstract:** Thulium lasers generating in a spectral region of ~2 μm coincident with absorption maximum of water are perspective for laser surgery. In this report we present experimental results on application of continuous-wave thulium laser for radiation treatment of blood-vessels *in vivo.* At laser radiation power of 250-300 mW at the output of fiber (power density of 95-115 W/cm$^2$) the local coagulation of peritoneum vessels of live rat was reached in ~3-5 seconds. The results of laser experiments are supplemented with histological analysis of alteration in the walls of bloodstream.

Lasers generating in the middle infrared region (MIR) are of interest recently as potentially applicable for medicine, in particular in surgery. Precision effective coagulation and ablation of tissues are possible due to strong absorption of optical energy by them. The main absorbent component (chromophore) for radiation with wavelengths more than 1.4 μm is water, at that absorption of water in the MIR spectral region increases reaching its maximum value at ~3 μm. Another two intensive absorption maxima correspond to spectral regions of ~1.5 μm and ~2 μm. Absorption coefficients at these wavelengths are about 100 cm$^{-1}$. Absorption of laser radiation energy manifests itself in temperature rise of tissues and thermally induced biological effects. Denaturation of proteins occurs at 60-70 0C, vaporization of water at ~100 0C, and at higher temperatures tissue carbonization begins. Lasers generating in the spectral region of 1.9 μm coincident with absorption region of $OH^-$ group belonging to water molecule are very promising for those areas of surgery for which precision local tissue removal is required, namely in neurosurgery, tumor resection, cardiology, ophthalmology etc.

At present main medical lasers generating in the wavelength region of ~2 μm are pulse powerful holmium lasers with lamp pumping, in particular lasers on the basis of Ho:YAG active medium [see, for example, 1]. In scientific literature the variants of using for surgical purposes of continuous-wave fiber thulium lasers with laser diode pumping are also considered [2]. Such lasers are based on silica optical fiber doped by $Tm^{3+}$ ion as active medium and pumped in the spectral region of ~790 nm. Diode-pumped lasers are compact, effective, don't need high electrical voltage application, their design is based only on all-solid state components. However as the absorption region of $Tm^{3+}$ ions in glass matrix lies near 790 nm it is difficult to use for their pump commercial high power AlGaAs laser diodes radiating at the wavelengths of 800-810 nm and used for neodymium active media pumping.

The choice of a laser generation regime (continuous wave ore pulse) is, in essence, the choice between thermal and mechanical mode of tissue destruction. Use of laser pulses with pulse width less than thermal relaxation time of irradiated tissues restricts thermal effects to minimum [3], but may form stress waves destroying tissues [4]. It is obvious that penetration of these stress waves into surrounding healthy tissues leads to their undesirable damaging.

Absence of mechanical ruptures of tissues occurring often at using of high intensive pulse laser radiation is one of the advantages of continuous-wave (CW) laser applications. Laser destruction of tissues (ablation) under influence of lasers generating in CW regime at wavelengths of visible and near infrared (NIR) spectral ranges was considered in [5-7]. As it was proposed in [6] tissue ablation can be considered as three-phase process. First, tissue heating and increase of pressure under the tissue surface occur, then the process of explosive vaporization

begins, and at higher temperatures tissue carbonization and evaporation take place. Using of radiations with the wavelengths lying in MIR spectral range where absorption coefficients of tissues are very high due to water absorption brings to the following fact: the process of carbonization is not obligatory for tissue evaporation [2]. Therefore the laser influence on a tissue is not accompanied by tissue necrosis at boundaries of an irradiation zone. It is very important in those situations when irradiated tissue must regenerate. The process of coagulation of biological tissue begins at the initial stages of its heating, at reaching of the temperatures about 65-70 0C, and is converted into the process of ablation only at rather high power density of the incident laser radiation.

Thus all the above stated allows one to suppose that applications of lasers generating in CW regime in spectral region of ~2 μm may be very promising for microsurgical manipulations, in particular, in ophthalmology and neurosurgery. The practical interest is connected with laser systems which distinguishing features are compactness, effectiveness, easy control of output characteristics. Such systems can be created on a basis of diode pumped all-solid-state lasers meeting all the necessary requirements.

In this work in the experiments modeling laser coagulation of blood vessels on animals we demonstrated the possibility of application of compact diode-pumped thulium laser on the basis of potassium yttrium tungstate, doped by thulium ions $Tm^{3+}$ ($Tm^{3+}$:$KY(WO_4)_2$, or Tm:KYW) for the purposes of microsurgery.

The main advantage of $Tm^{3+}$:KYW crystal is a broad and intensive absorption band in 770 – 815 nm range with a maximum of absorption at 802 nm. It allows one to use as pump radiation sources the commercially available laser diodes generating the radiation in 805-808 nm spectral range. At $Tm^{3+}$ concentration of $C_{Tm}$ = 6 at. %, the maximum absorption coefficient of $Tm^{3+}$:KYW is equal to $\alpha = 21$ см$^{-1}$ (E⊥c), and generation efficiency of the crystal reaches ~40 % [8, 9]. Additional doping of $Tm^{3+}$:KYW with $Yb^{3+}$ ions permits one to create a pump channel near ~ 980 nm where commercial powerful laser diodes based on InGaAs emit the radiation. However, generation efficiency of $Yb^{3+}$,$Tm^{3+}$:KYW pumped near 980 nm (absorption maximum $\lambda_{max}$ = 981 nm) is 2.5 times less than at excitation of thulium ions at 805 nm [9]. As the atomic radii of $Y^{3+}$ and $Tm^{3+}$ ions are close each other, $KY(WO_4)_2$ crystal can be doped with $Tm^{3+}$ up to high levels (over 12 at. %). Growing technology for this crystal is sufficiently simple, so the crystal is a relatively cheap. Therefore, this crystal is of great interest for creating the sources of radiation at 2 μm.

For active element pumping, a fiber coupled laser module (ATC-SD, St.–Petersburg, Russia) with output power up to 3.8 W (continuous-wave regime) was used. The laser module wavelength was 806 nm at 25 °C, using temperature tuning one could change the pump wavelength to lower values close to absorption maximum of the active medium. Using SMA-connector, output of optical fiber of laser module was adapted with an optical module for collimating pump laser beam and focusing it into active element. The cavity of thulium laser had a configuration close to semi-spherical one. It as formed by flat input mirror $M_1$ deposited on the input face of the active element $Tm^{3+}$:KYW and spherical output mirror $M_2$. As the curvature radius of $M_2$ was equal to 30 mm, the common geometrical length of resonator was about 29.5 mm. Output face of active element was anti-reflection coated for the range of 1800-2000 nm.

The optical scheme of Tm:KYW laser used in the experiments is shown in Fig. 1.

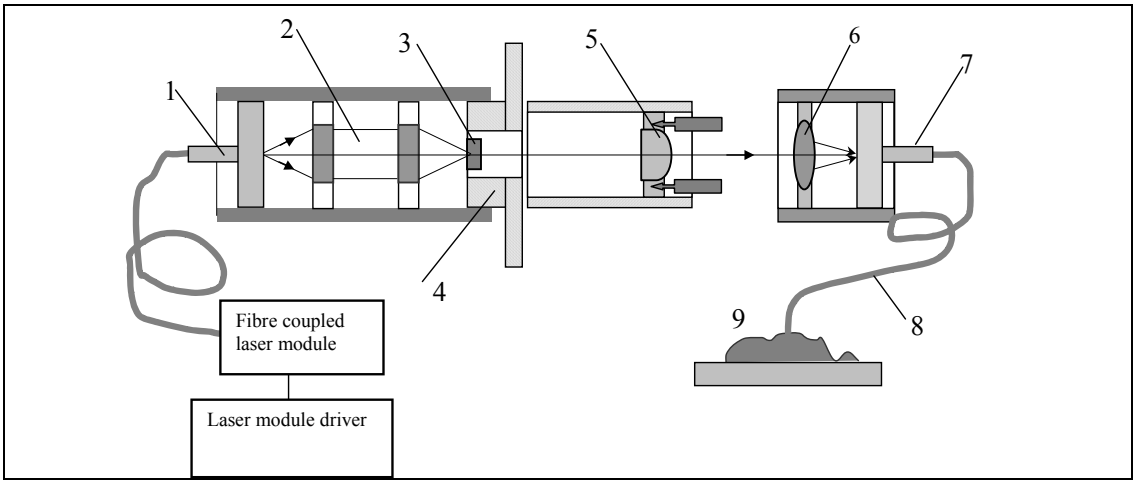


**Fig. 1**. The scheme of diode pumped Tm:KYW laser with fiber output of the radiation. 1 – output of the laser module fiber; 2 – collimating and focusing optical module; 3 – Tm:KYW crystal with deposited mirror $M_1$; 4 – copper heatsink; 5 – output mirror M2; 6 – focusing lens; 7 – input of the optical fiber; 8 – optical fiber with the diameter 600 μm; 9 – experimental animal.

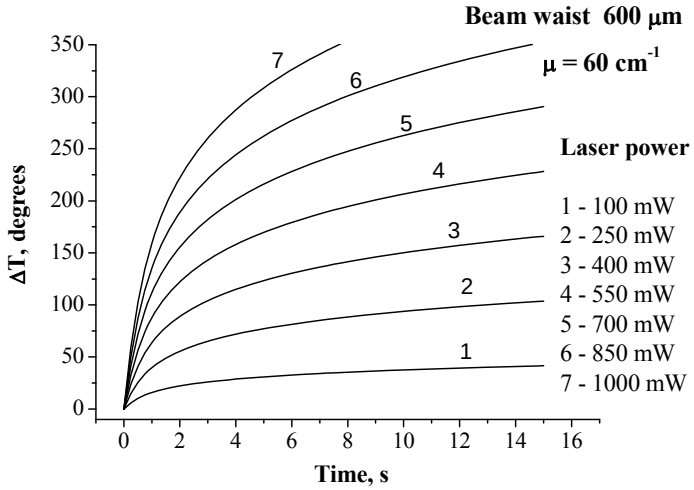


**Fig. 2**. Modeling of the temperature rise in a centre of an incident laser beam having Gaussian distribution.

Beam waist is 600 μm, tissue absorption coefficient is 60 $cm^{-1}$ (tissue absorption at the wavelength of 2 μm).

Active element was mounted inside the copper heat remover. Heat generated due to pump of the crystal was removed only in a passive way. No other special efforts for active element cooling were undertaken.

At pump power of 3.75 W, the output power of thulium laser amounted more than 300 mW (threshold pump power was ~ 500 mW). According to preliminary modeling of the temperature rise in a biological tissue [10] the given thulium laser power was sufficient for laser coagulation. Therefore, we didn't make further optimization of output parameters of thulium laser.

In Fig.2 the results of modeling of the temperature rise in a centre of an incident laser beam having Gaussian distribution are shown for beam waist of 600 μm and tissue absorption coefficient equal to 60 cm-1 (tissue absorption at the wavelength of 2 μm). It is evident that temperature rise of ΔT~50 degrees can be reached in a few seconds.

A spectral width of the radiation of $Tm^{3+}$:KYW (6 at. %) laser was equal to ~ 10 nm, spectrum maximum was in 1970-1980 nm spectral range and changed depending on resonator

tuning. This effect is connected with a broad spectral width of $Tm^{3+}$:KYW radiation and redistribution of selective intracavity losses.

For irradiation of biological tissues, thulium laser was equipped with fiber output of the radiation. Multimode silica fiber with spectral range of transmission of 0.2 – 2.2 μm was used (Q/Q600/660 WF, «Polironic», Russia). The diameter of optical fiber was 600 μm. The length of fiber was equal to 2 m. Radiation of thulium laser was focused into fiber with a lens with a focal length of ~ 10 cm. Output power reached of ~ 85 % of input one at the output of fiber.

The experiments were performed on adult rats. After lancing of peritoneum of narcotized experimental animal the access to blood-vessels located in an abdominal wall was opened. During all time of the experiment animal was alive, blood circulation in vessels was not interrupted. Laser coagulation of vessels was conducted at contact between optical fiber and vessel's wall, as this regime allowed estimating the laser power density in the coagulation area. At laser radiation power of 250-300 mW at the output of fiber (power density of 95-115 W/cm$^2$) the local coagulation of peritoneum vessels of live rat was reached in ~3-5 seconds.

Photos shown in Fig. 3 demonstrate the results of the experiment on photocoagulation of blood vessels with the radiation of continuous-wave thulium laser based on Tm:KYW. The coagulation zones are indicated with arrows. Tissues placed near the areas of coagulation are visually non-destructed.

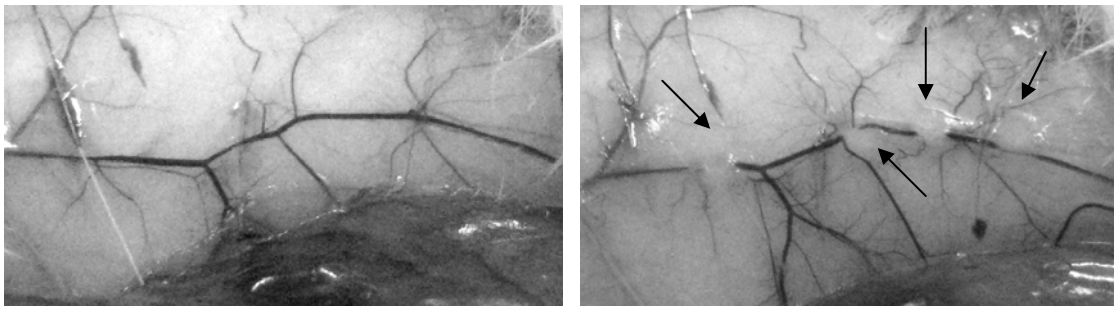

a b

**Fig. 3**. Coagulation of blood-vessels located in an abdominal wall of adult rat. a – before coagulation; b – after coagulation (coagulation fields are indicated with arrows).

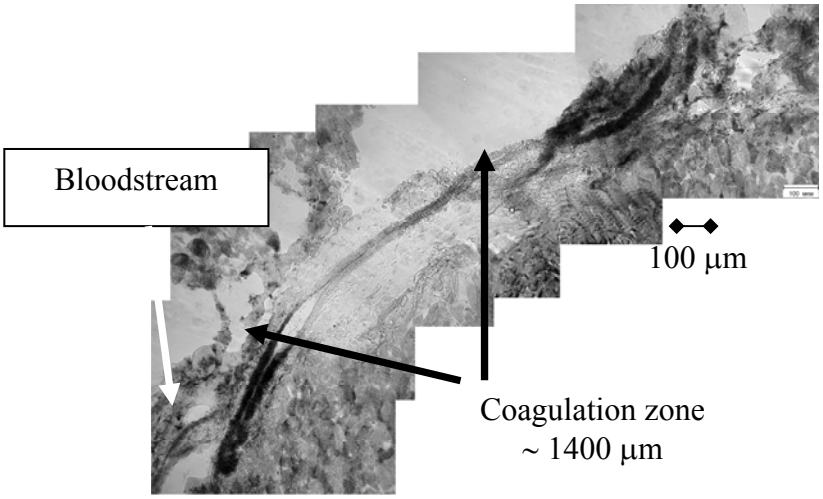


The results of the experiments on laser coagulation were supplemented with histological analysis of alteration in the walls of bloodstream. Histological studies were fulfilled for blood

vessels taken for analysis both immediately after coagulation and in 1 hour after coagulation, at that during this 1 hour narcotized rat was alive.

In Fig.4 one can see photo of the longitudinal section of blood-vessels located in an abdominal wall in a 1 hour after coagulation stained with hematoxylin – eosin. It is seen that bloodstream is completely blocked in the coagulation area of ~1400 μm.

The results obtained justifies that compact, effective, and low power photocoagulator for precise medical manipulations may be developed on a basis of diode-pumped Tm:KYW laser. Such coagulator is very promising for microsurgery, in particular for ophthalmology, neurology, facial surgery. Further optimization of the output parameters of Tm:KYW laser will bring to widening its possible applications.

**References**

1. M. Goggin, F. Lavery, Br. J. Ophthalmol. 81541 (1997)
2. M.C. Pierce, S.D. Jackson, M.R. Dickinson, Lasers Surg. Med. **25**, 407 (1999)
3. J.T. Walsh, T.J. Flotte, T.F. Deutsch, Lasers Surg. Med. **9**, 314 (1989)
4. J.P. Cummings, J.T. Walsh. Appl. Opt. **32**, 494 (1993)
5. G.L. LeCarpentier et al. IEEE Trans. Biomed. Eng. **40**, 188 (1993)
6. R.M. Verdaasdonk, C. Borst, M.J.C. van Gemert. Phys. Med. Biol. **35**, 1129 (1990)
7. P.D. Youell, M.R. Dickinson, T.A. King. Proc. SPIE. **2077**, 109 (1993)
8. L.E. Batay, A.N. Kuzmin, A.S. Grabtchikov et al. Appl. Phys. Lett. **81**, 2926 (2002)
9. L.E. Batay, A.A. Demidovich, A.N. Kuzmin, et al. Appl. Phys. B. **75**, 457 (2002)
10. L.E. Batay, D.N. Busko, A.I. Vodchits et al. Proc. SPIE, **6734** (2007)

# QUANTUM-MECHANICAL THEORY AND EXPERIMENT ON INTRACAVITY TRANSIENT RAMAN CONVERSION AND MULTIWAVE MIXING IN Q-SWITCHED MICROCHIP LASERS.

**S.V. Voitikov[a], A.S. Grabtchikov[a], A.A. Demidovich[b], M.B. Danailov[b], and V.A. Orlovich[a]**

[a)]Stepanov Institute of Physics, National Academy of Sciences of Belarus 68 Nezalezhnasti Ave., 220072 Minsk, Belarus. *E-mail: s.voitikov@dragon.bas-net.by*
[b)]Laser Lab Sincrotrone-Trieste, SS14, km.163.5 34012 Trieste, Italy

**Abstract:** Quantum theory of diode-pumped passively Q-switched microchip lasers with intracavity transient and quasi-stationary stimulated Raman scattering (SRS) conversion has been developed, where dynamics of Raman medium excitation, collective vibration dephasing, and intracavity multiwave mixing of the laser, Stokes and anti-Stokes waves are taken into account. By means of canonical transformation we construct the Hamiltonian describing the intracavity electromagnetic field, the Raman medium and their interaction. A branching set of coupled Heisenberg-Langevin dynamic equations has been obtained for the amplitudes of the generated laser, Stokes and anti-Stokes waves, the collective vibration amplitudes and the population of the excited states of the Raman medium. It is shown that the ordinary phenomenological and quasi-stationary semi-classical models for this class of lasers are the special cases of the developed here quantum description. Output characteristics of a microchip laser with coupled cavities have been investigated experimentally. Numerical modeling agrees well with experimental results on generation of 1st and 2nd Stokes pulses with duration less than 100 ps. Effect of intracavity multiwave mixing on high order Stokes pulse parameters and efficiency of SRS conversion has been discussed.

***Keywords:*** *quantum theory of Raman laser; intracavity stimulated Raman scattering; Heisenberg-Langevin dynamic equations; multiwave mixing; two Stokes generation*

## 1. Introduction

Passively Q-switched diode-pumped microchip lasers are compact, simple and cheap laser sources delivering pulses with typical duration from sub-nano to few nano-seconds with peak powers that can exceed 10 kW at repetition rates above 10 KHz, and have therefore attracted substantial interest in the last decade. Further step in making these sources very interesting was the introduction of intracavity Raman generation [1] that is known to be highly effective for frequency shifting. As a result, Stokes-shifted pulses with duration of 18-20 ns down to sub-100 ps and energies in the 10 microJ range have been obtained. In such lasers the short Stokes pulse generation occurs in conditions where the development and decay of the SRS process has duration comparable to the dephasing time of the Raman medium. The process of intracavity SRS conversion becomes therefore transient, and the dynamics of Stokes-pulse formation is strongly influenced by the temporal dynamics of the Raman-medium induced polarization and excitation. In addition to transient character of intracavity SRS conversion in microchip-lasers could become possible generation of 2nd Stokes and anti-Stokes waves assisted by intracavity multiwave mixing. Due to the short Raman medium lengths used in microchip-lasers the processes of multiwave mixing could have large coupling coefficients that gives in a Raman medium an additional contribution to the rate of increase in the induced polarization irradiating at the second Stokes wave frequency and therefore decreases the threshold for its generation. As a result it is the mutual effect of transient intracavity SRS and multiwave mixing that will determine the efficiency of fundamental wave conversion into different frequency shifted components.

Microchip lasers with intracavity Raman conversion are hence quite a unique laser system that differs radically from ordinary microchip lasers (without frequency conversion), because its dynamics and output parameters are determined not only by the absorption, gain and relaxation in the laser medium and saturable absorber, but also by the excitation and relaxation of the Raman medium and mixing of generated waves.

The presently available theoretical description and models of lasers with intracavity Raman generation have limited applicability to the above described complicated regime of operation. There are several works (see Ref.[1,2] and references therein) where on the basis of phenomenological models of Q-switched microchip lasers with intracavity generation of the first Stokes wave, the dynamics of pulse formation has been described and some parameters of the Stokes pulses have been calculated or estimated. These works use a quasi-stationary approximation for the Raman generation which is valid only in case where the Stokes pulses are much longer than the Raman medium dephasing time. In addition, in the above mentioned works the waves are described in terms of intensity (or, equally, by photon number or photon density), which does not allow to take into account multiwave mixing. Semi-classical models of Raman lasers have also been proposed, where field description of the waves has been used (see Ref.[3,4] and references therein) and quasi-stationary SRS and multi-wave mixing processes are described. However, in [3,4] excitation and dephasing dynamics of the Raman medium as well as the inverse influence of the Stokes components on the laser wave generation were not taken into account that limits the applicability of these models for full description of the considered here microchip SRS lasers. Recently we proposed the quantum-mechanical description of intracavity transient Raman conversion based on canonical transformation of the Hamiltonian of the electromagnetic field and Raman medium [5]. This approach allows to obtain Heisenberg-Langevin dynamic equations for the amplitudes of the intracavity of laser (fundamental), Stokes and anti-Stokes fields, induced polarization, and excitation of the Raman medium which we apply in this work to two Stokes intracavity Raman generation in a microchip-laser.

## 2. Theory and experiment on intracavity transient Raman conversion

Using the approach of Ref.[5] one can obtain in slowly varying amplitude and rotating wave approximations for the two Stokes microchip-laser with intracavity SRS conversion the following Heisenberg-Langevin dynamic equations for field amplitudes, $A^{\pm}_{L(S_1,S_2)}$, and dynamic equations for the material operators:

$$\frac{dA_L^-(t)}{dt} = \left.\frac{dA_L^-(t)}{dt}\right|_{am} + \left.\frac{dA_L^-(t)}{dt}\right|_{sa} + i\ \ \omega_L - \omega_{LR}\ \ A_L^-(t) - \frac{i}{2}K_{LL}\ \ \Sigma_{LL}^0 - \Sigma_{LL}^2(t)\ \ e_L e_L A_L^-(t) + K_{LS_1}\Sigma_{LS_1}^-(t) e_L e_{S_1} A_{S_1}^-(t) - \frac{1}{2}\gamma_L A_L^-(t) + \exp(-i\omega_L t)F_L^-(t), \quad (1)$$

$$\frac{dA_{S_1}^-(t)}{dt} = \left.\frac{dA_{S_1}^-(t)}{dt}\right|_{am} + \left.\frac{dA_{S_1}^-(t)}{dt}\right|_{sa} + i\ \ \omega_{S_1} - \omega_{S_1 R}\ \ A_{S_1}^-(t) - \frac{i}{2}K_{S_1S_1}\ \ \Sigma_{S_1S_1}^0 - \Sigma_{S_1S_1}^2(t)\ \ e_{S_1}e_{S_1}A_{S_1}^-(t) + K_{S_1S_2}\Sigma_{S_1S_2}^-(t) e_{S_1}e_{S_2}A_{S_2}^-(t) - K_{LS_1}^*\Sigma_{LS_1}^+(t)e_L e_{S_1}A_L^-(t) - \frac{1}{2}\gamma_{S_1}A_{S_1}^-(t) + \exp(-i\omega_{S_1}t)F_{S_1}^-(t), \quad (2)$$

$$\frac{dA_{S_2}^-(t)}{dt} = \left.\frac{dA_{S_2}^-(t)}{dt}\right|_{am} + \left.\frac{dA_{S_2}^-(t)}{dt}\right|_{sa} +$$

$$i\ \omega_{S_2} - \omega_{S_2R}\ \ A_{S_2}^-(t) - \frac{i}{2}K_{S_2S_2}\ \ \Sigma_{S_2S_2}^0 - \Sigma_{S_2S_2}^2(t)\ \ e_{S_2}e_{S_2}A_{S_2}^-(t) - \qquad (3)$$

$$K_{S_1S_2}^*\Sigma_{S_1S_2}^+(t)e_{S_1}e_{S_2}A_{S_1}^-(t) - \frac{1}{2}\gamma_{S_2}A_{S_2}^-(t) + \exp(-i\omega_{S_2}t)F_{S_2}^-(t),$$

where $L$, $S_1$, and $S_2$ stands for the laser, 1st Stokes, and 2nd Stokes waves, respectively, $\omega_{L(S_1,S_2)}$ and $\omega_{L(S_1,S_2)R}$ are the cycling frequencies of corresponding waves and resonator modes, the coefficients $K_{\lambda\mu}$ and $K_{\lambda\mu}^z$ determine the rate of Raman scattering, $\gamma_{L(S_1,S_2)}$ are the reciprocal relaxation rates of corresponding waves in a laser resonator, $F_{L(S_1,S_2)}^{\pm}(t)$ is Langevin field noise, $e_{L(S_1,S_2)}$ are the parameters of spatial mode overlapping, and the coefficients $\Sigma_{LL(S_1S_1,S_2S_2)}^0$ and $\Sigma_{LL(S_1S_1,S_2S_2)}^2$ determine Stark shifts for the corresponding waves.

In Eqs.(1-3) we have introduced the slowly varying amplitudes of Raman-medium collective vibrations, $\Sigma_{MN}^{\pm}(t), MN = LS_1, S_1S_2,$ that describes the dynamics of increase and relaxation of Raman-medium induced polarization,

$$\frac{d\Sigma_{MN}^-(t)}{dt} = i((\omega_M - \omega_N) - \omega)\Sigma_{MN}^-(t) + i\sum_{PP=LL,S_1S_1,S_2S_2,A_1A_1} K_{PP}\Sigma_{MN,PP}^-(t)e_Pe_PA_P^+(t)A_P^-(t) -$$
$$\sum_{PQ=LS_1,S_1S_2} K_{PQ}\ \ \Sigma_{MN,PQ}^0 - \Sigma_{MN,PQ}^2(t)\ e_Pe_QA_P^-(t)A_Q^+(t) - \gamma^-\Sigma_{MN}^-(t) + G_{MN}^-(t), MN = LS_1, S_1S_2. \qquad (4)$$

where $\gamma^-$ is the Raman-medium reciprocal dephasing (induced polarization relaxation) time and $G_{MN}^-(t)$ is the noise. It should be noted that the third term (summing with respect to $PQ$) in the right-hand side of Eq.(4) describes two-photon SRS when $MN=PQ$ and intracavity multiwave mixing when $MN\neq PQ$ while the fourth one is responsible for the transient character of intracavity SRS-conversion and Raman-medium dephasing. The coefficient $\Sigma_{MN,PQ}^0$ determines how large or small could be the rate of two-photon SRS and/or multiwave mixing and depends in its turn on the overlapping of the involved spatial modes. As is known from experiments the transverse intensity profile of the fundamental, Stokes and anti-Stokes beams in microchip- and mini-lasers is well described by Gaussian distribution corresponding to $TEM_{00}$ cavity modes. In this case the field modes should be the standing waves formed by forward- and backward-running Gaussian beams and the coefficients $\Sigma_{LS_1(S_1S_2),LS(S_1S_2)}^0$ for two-photon (cascade) SRS read

$$\Sigma_{LS_1(S_1S_2),LS(S_1S_2)}^0 \approx D\frac{L^{Rm}}{4}\frac{2}{\pi\ \ r_{L(S_1)}^{\ 2} + r_{S_1(S_2)}^{\ 2}}, \qquad (5)$$

while for multiwave mixing the corresponding coefficients are

$$\Sigma_{LS_1,S_1S_2}^0 \approx D\frac{L^{Rm}}{4}\delta_{L,S1;S1,S2}\frac{2}{\pi r_Lr_{S2} + \pi\ \ r_{S1}^{\ 2}\left(\frac{r_L}{2r_{S2}} + \frac{r_{S2}}{2r_L}\right)}, \qquad (6)$$

where $D$ is the Raman-active atom density, $L^{Rm}$ is the Raman-medium length, $\delta_{L,S1;S1,S2}$ is the multiwave-mixing coupling factor, and $r_{L(S_1,S_2)}$ is the mode waist radius.

For the excited-state population of Raman-active atoms, $\Sigma_{MM}^2(t)$, we obtain the equation

$$\frac{d\Sigma^2_{MN,PQ}(t)}{dt} = -\sum_{RT=LS_1,S_1S_2} 2K_{RT}\Sigma^-_{MN,PQ,RT}(t)e_R e_T A^+_R(t)A^-_T(t) + H.a. \; -\gamma^z\Sigma^2_{MN,PQ}(t) + G^2_{MN,PQ}(t), \quad (7)$$

$\gamma^z$ is the reciprocal time of the Raman-medium inversion relaxation and $G^2_{MM}(t)$ is the corresponding noise. The equations for the collective amplitudes $\Sigma^-_{MN,PQ,RT}(t)$, (where $MN(PQ,RT) = LS_1, S_1S_2$) can be developed in the same way as it has been above done for $\Sigma^-_{LS_1(S_1S_2)}(t)$ in Eqs.(4,7). It should be noted that in the case of negligible Raman-medium excitation $\Sigma^2_{MN,PQ}(t)$ and $\Sigma^2_{MM}(t)$ could be omitted in the right-hand sides of Eqs.(1-4) that cuts the equation branching and sufficiently simplifies further analysis.

It can be shown that that the proposed quantum description of microchip-lasers with intracavity SRS conversion derived here includes as special cases the phenomenological and quasi-stationary theories of Raman microchip lasers used in the literature [1-4]

Thus, the branching set of coupled Heisenberg-Langevin equations describing the dynamics of the laser, Stokes and anti-Stokes waves, as well as the dynamics of the atomic (molecular) operators that determine the Raman medium induced polarization, and the population of the Raman medium excited states has been obtained.

## 3. Experiment and discussion

One case of particular practical importance and interest is the coupled cavity Raman microchip-laser generating 1st and 2nd Stokes pulses with duration in the 100 ps (and even sub-100 ps) range. In this case the transient character of SRS-conversion and multiwave mixing in the Raman medium will strongly affect the laser dynamics and output pulse parameters. To check the validity of the proposed here quantum theory we have carried out experimental investigation of such lasers generating two Stokes pulses with duration less than 100 ps. Pulse dynamics of coupled cavity Q-switched *Nd,Cr:YAG/Ba(NO$_3$)$_2$* microchip-laser has been investigated and two Stokes pulses with duration of 92 and 86 ps, respectively, have been obtained. On the basis of the proposed here quantum theory we have modeled pulse dynamics. The results are presented in Fig.1. As it is seen, the numerical data show satisfactory agreement with experiment. Numerical analysis allows concluding that Raman-medium dephasing makes pulses longer while the multiwave mixing effect is in pulses shortening and in increase in SRS conversion efficiency.

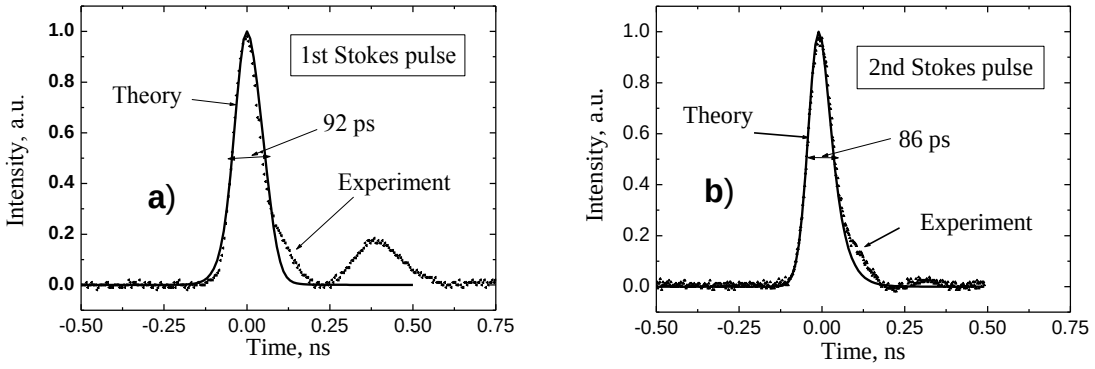


**Fig.1.** Pulse shapes of (a) 1st and (b) 2nd Stokes waves

## 4. Conclusion

Quantum theory of diode-pumped microchip lasers with passive Q-switching and transient (as well as quasi-stationary) intracavity Raman conversion has been developed. The developed theory takes into account the dynamics of the Raman medium dephasing and excitation, and mixing of different intracavity waves, including anti-Stokes and high order Stokes components. The branching set of coupled Heisenberg-Langevin equations describes the dynamics of the laser, Stokes and anti-Stokes waves, as well as the dynamics of the Raman medium induced polarization, and the population of the Raman medium excited states. It is shown that the ordinary phenomenological and quasi-stationary semi-classical models for this class of lasers are the special cases of the developed here quantum description. Numerical modeling agrees well with experimental results on generation of $1^{st}$ and $2^{nd}$ Stokes pulses with duration less than 100 ps.

## References

1. A.A. Demidovich, S.V. Voitikov, L.E. Batay, A.S. Grabtchikov, M.B. Danailov, V.A. Lisinetskii, A.N.Kuzmin, V.A. Orlovich, Opt. Commun. **263**, 52 (2006)
2. S. Pearce, C.L.M. Ireland, P.E. Dyer, Opt. Commun. **260**, 680 (2006)
3. J.C. Bienfang, W. Rudolph, P.A. Roos, L.S. Meng, and J.L. Carlsten, J. Opt. Soc. Am. B **19**, 1318 (1998)
4. P.A. Roos, L.S.Meng, S.K. Murphy, J.L. Carlsten, J. Opt. Soc. Am. B. **21**. 357 (2004)
5. S.V. Voitikov, A.S. Grabtchikov, A.A. Demidovich, M.B. Danailov, and V.A. Orlovich, Opt. Commun. **281**, 5202 (2008)

# ON THE EFFICIENCY OF TERAHERTZ EMISSION CAUSED BY THE OPTICAL RECTIFICATION OF FEMTOSECOND LASER PULSES IN ELECTROOPTIC SEMICONDUCTOR CRYSTALS

**A.M. Goncharenko, V.L. Malevich, G.V. Sinitsyn**

B.I.Stepanov Institute of Physics, Nezalezhnasti ave. 68, Minsk, Belarus 220072
*E-mail: g.sinitsyn@ifanbel.bas-net.by*

In recent years an effective technique for generation and detection of free-space terahertz (THz) electromagnetic pulses has been worked out. [1]. THz spectral region (0.1-10 THz) is of great interest for biology, medicine, physics of condensed matter and others. It was shown that THz beams can be used for detection and visualization of explosives and drugs of abuse. Due to the capacity of THz radiation to penetrate through closes, paper and some of plastics it can be used for visualization of hidden objects. The main reason confining the spread of the THz time-domain spectroscopy is the high cost of THz setup which is determined primarily by the expensive exciting femtosecond lasers. A serious effort oriented on optimization of THz spectroscopy setups and on the search for price reduction resources has been made.

In this article various methods of THz pulses emission and detection are analyzed and compared for two types of femtosecond lasers generating at the wavelengths of 800 nm and 1040 nm.

Photoconductive antennas excited by femtosecond laser radiation are widely used both for generation and detection of THz pulses [1]. The main problem in the manufacture of this antennae is to form a semiconductor layer that should be photosensitive at the laser wavelength and have subpicosecond carrier lifetimes and high resistivity. To make the photoconductive structures with very short subpicosecond carrier lifetimes the very complex and expensive technologies such as molecular beam epitaxy and ion implantation should be used. The next problem is that the efficiency of the photoconductive THz emitters decreases at high excitation level because of a saturation effect.

In the most of THz time-domain spectroscopy setups low-temperature grown GaAs layers are used in THz antennas which are activated by Ti:sapphire laser generating femtosecond pulses at the wavelength of about 800 nm. However, recently compact ytterbium-based active media lasers generating femtosecond radiation at the wavelength of about 1040 nm were designed. At this wavelength the efficiency of GaAs photoconductive antenna essentially decreases since the photon energy is lower than the band edge of GaAs.

Bare semiconductor surface illuminated by femtosecond laser pulses can also effectively generate THz pulses [2]. Recently it was found that the most effective THz emission is achieved in (111) *p*-InAs excited at the wavelength of about 800 nm [3]. When 1040 nm laser pulses are used for the excitation of InAs surface, the efficiency of THz emission slightly diminishes although it remains high enough [4]. The electric field amplitude of THz pulses emitted from InAs surface is approximately one order of magnitude lower than that emitted from GaAs photoconductive antenna activated by 800 nm radiation. However, InAs THz emitter is easier in manufacture than photoconductive antenna and, that is more important, it can be used at the longer wavelength of 1040 nm. It was established earlier [5] that THz emission from InAs surface is caused, to a large extent, by the electric field induced optical rectification. At low excitation level, a surface built-in electrical field due to the band bending is mainly responsible for this effect, whereas at high excitation the electrical field caused by the spatial separation of electrons and holes excited near the surface is important. Fig. 1 shows the results of numerical Monte Carlo simulation of the spatio-temporal evolution of electrical potential at the InAs surface excited by 150-fs Ti:sapphire laser pulses [5].

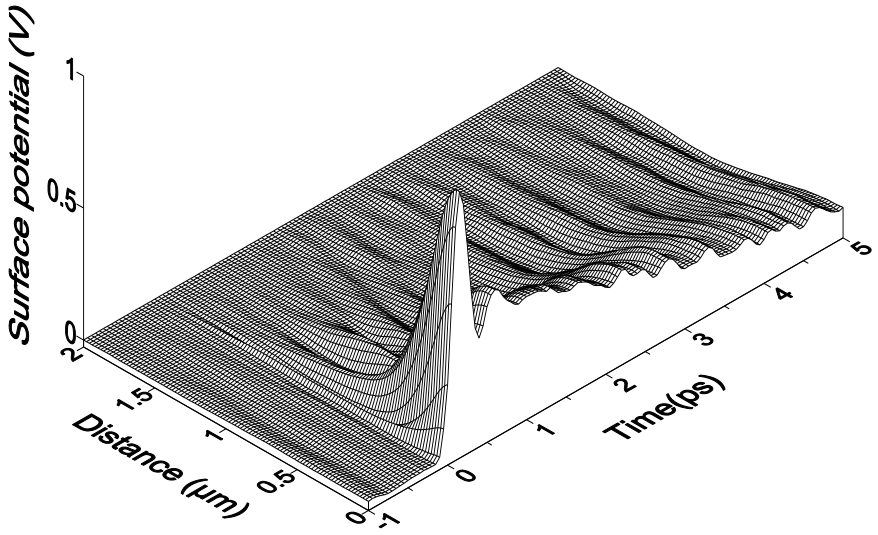


**Fig. 1**. Spatio-temporal dynamics of the surface electrical potential in InAs excited by 150-fs laser pulse with the wavelength 800 nm

One can see that the electrical field as large as $2 \cdot 10^5$ V/cm is developing during the laser illumination over distances reaching ~0.5 μm. This field is comparable with built-in surface electrical field in InAs and due to the third-order nonlinear susceptibility they can induce nonlinear optical polarization following the optical pulse envelope.

The optical rectification of femtosecond laser pulses in electro-optical crystals is used often for generating THz radiation. In this case to provide a large yield of THz emission the phase matching condition should be fulfilled, that is the optical group velocity and THz phase velocity should be close enough so that the interaction length of the optical and THz pulses is greater than the thickness of the electro-optic crystal. Besides, the crystal should be transparent at the wavelength of the exciting radiation and weakly absorb in THz spectral region. An important point is that the electro-optical crystals can be also used for the coherent detection of THz pulses [6]. In this approach THz electric field induces a refractive index change in electro-optical crystal and then this change is detected by measuring an ellipticity degree of ultrashort laser pulse propagating through the crystal. It is apparent that the frequency bandwidth of this detector is also defined by the phase-matching condition so that this detector can detect solely those spectral components of THz pulse for which the phase velocity is close to the group velocity of the probing optical pulse.

Under Ti:sapphire laser excitation in THz setups cubic ZnTe crystals having $\bar{4}3m$ symmetry are most commonly used for THz emission and detection. For these crystals the group velocity at the wavelength of about 800 nm is very close to the phase velocity at the frequency of 1 THz. The bandwidth of electro-optical ZnTe detectors can be much larger than the bandwidth of detectors based on the photoconductive antennae. However, when 1040 nm laser pulses are used, the phase matching condition is not satisfied so good as at the wavelength of 800 nm and the coherence length ranging up to a few millimeters in the previous case decreases to several hundreds of micrometers. In addition, ZnTe as electro-optic detector has a disadvantage that the presence of far-infrared absorption near the transverse optical phonon frequency at 5.3 THz essentially limits its frequency response. Thus, to extend the frequency range of THz emitters and detectors based on electro-optic effect other crystals such as GaAs, GaP, GaSe can be more suitable. For instance, with the use of (110) GaP crystal one can detect THz radiation up to a frequency of about 7 THz [7]. This crystal is particularly attractive for generation and detection of THz pulses when femtosecond laser generating at the wavelength of about 1040 nm is used. As follows from experimental data on the optical and THz dispersion in GaP, with the use of the ytterbium lasers (1040 nm) the coherence length can be estimated as

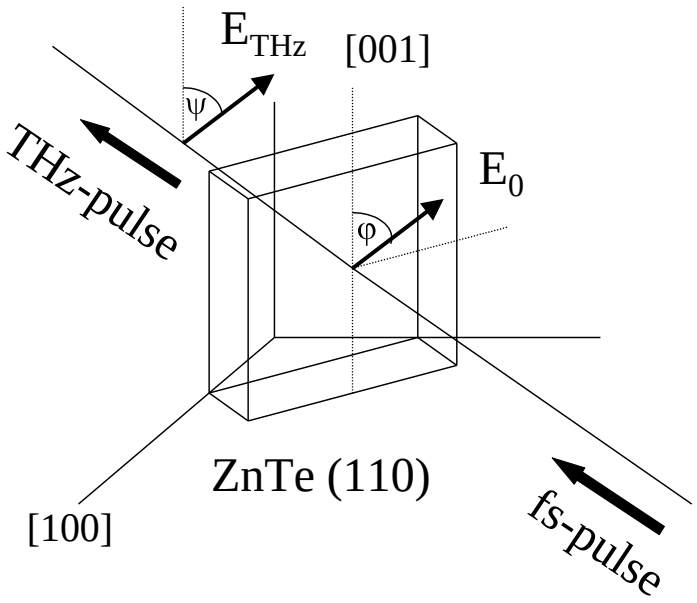


**Fig. 2.** Optical and THz beams orientation with respect to the crystal axes at THz emission caused by optical rectification

$l_c = \pi c / \omega_T \left| n - \lambda\, dn/d\lambda - n_T \right|$ ($c$ is the velocity of light in vacuum; $n_T$ and $n$ are the refractive indexes at THz frequency $\omega_T$ and at the wavelength $\lambda$ of femtosecond laser used accordingly). The coherence length $l_c$ achieves several millimeters for THz radiation in the frequency range of 0.1-5 THz.

Let us consider orientation and polarization dependencies of THz emission caused by the optical rectification of femtosecond optical pulses in cubic electro-optical crystals. Figure 2 shows the directions of polarization of the optical and THz beams falling perpendicular onto the surface of the (110)-oriented crystal ($\varphi$ is the angle between the electrical field of the optical beam and [001] direction).

The optical rectification in ZnTe and GaP crystals of $\bar{4}3m$ symmetry is determined by the second-order nonlinear susceptibility tensor $\chi_{i,jk}$ that has six non-zero components equal to each other: $\chi_{i,jk} = d_{14}$, $i \neq j \neq k$. Calculating nonlinear polarization vector in the crystallographic coordinate system and transforming it from this system to the laboratory system with *z*–axis oriented along [001] direction and *x*–axis directed perpendicular to (110) surface of the crystal we find the expression for the nonlinear polarization vector $\vec{P} = -d_{14} E_0^2 \sin\varphi \{\cos\varphi, \sin\varphi/2\}$ ($E_0$ is the electrical field amplitude of the optical beam). Hence, it follows that the absolute value of the polarization vector is proportional to $\sin\varphi\sqrt{1 - 3/4\sin^2\varphi}$ and it attains maximum value $d_{14} E_0^2 / \sqrt{3}$ under the condition $\sin\varphi = \sqrt{2/3}$. The electrical field of generated THz radiation is directed at the angle $\psi = \arccos\left( \sin\varphi / \sqrt{4 - 3\sin^2\varphi} \right)$ to *z*-axis. By this means THz emission has a maximum when the electrical field of the optical beam is oriented at an angle $\varphi \approx 55°$ to the [001] crystal axis.

The polarization and orientation dependencies of the efficiency of THz detection in ZnTe was analyzed in the article [8]. It has been established that the most optimum alternative is to use (110) crystal. THz field should be directed along [001] crystal axis and perpendicular to the electrical field of the optical beam. It is evident that the same geometry is optimal for detectors based on GaP. It should be pointed out here that (110)-oriented ZnTe and GaP plates

can be prepared with a relative ease because (110) planes in these crystals are the cleavage planes.

In conclusion, our analysis shows that InAs can be used as an effective THz emitter under excitation at the wavelengths both 800 nm and 1040 nm. Electro-optical crystal ZnTe of (110) cut is an effective THz emitter and detector when using femtosecond radiation of Ti:sapphire laser. When laser on ytterbium-based active media is used for excitation one should preferably use GaP for THz pulses emission and detection.

**References**

1. K. Reimann. Rep. Progr. Phys. 70, 1597(2007).
2. X.-C. Zhang, B.B. Hu, J.T. Darrow, D.H. Auston. Appl. Phys. Lett. 56,1011(1990).
3. R. Adomavičius., A. Urbanowicz, G. Molis, A. Krotkus, E. Šatkovskis. Appl. Phys. Lett.85,2463(2004).
4. R. Adomavičius, G. Molis, A. Krotkus, V. Širutkaitis. Appl. Phys.Lett.87, 261101(2005).
5. A. Krotkus, R. Adomavicius, G. Molis. V.L. Malevich. J. Nanoelectr. Optoelectr. 2,108(2007).
6. D. H. Auston and M. C. Nuss, IEEE J. Quantum. Electron. 24**,** 184(1988).
7. Q. Wu, X.-C. Zhang. Appl.Phys. Lett. 70, 784(1997).
8. P.C.M Planken, H.-K Nienhuys, H.J Bakker, T. Wenckenbach. J. Opt. Soc. Amer. B. 18, 313(2001).

# OPTICAL DATA PROCESSING DUE TO CONTROLLED SWITCHING WAVES IN NONLINEAR INTERFEROMETERS WITH A SPECIFIED PATTERN OF OPTICAL THICKNESS

**A.M.Goncharenko, G.V.Sinitsyn, A.V.Lyakhnovich, S.P.Apanasevich**

B.I.Stepanov Institute of Physics, National Academy of Sciences of Belarus
Nezalezhnasti ave. 68, Minsk, Belarus 220072
*E-mail: g.sinitsyn@ifanbel.bas-net.by*

**Abstract.** A model for analysis of transverse effects in optical bistability of thin nonlinear Fabry-Perot interferometers with a predetermined pattern of intermediate layer optical thickness is developed. A switching wave front behavior is studied as wave crosses the boundary between areas of different thickness, conditions of its tunneling through a barrier of a variable height are investigated. Control of speed and limits of switching wave propagation is demonstrated.

This contribution is devoted to studying dynamics of interaction of spatially confined light fields with thin optically nonlinear and bistable media with transverse diffusion of nonlinearity parameter which are placed between mirrors of Fabry-Perot interferometer (FPI) and characterized by the given modulation of their optical thickness. Due to such a modulation unidirectional controllable switching waves and soliton-like dissipative structures can be initiated in the above bistable layers and this may appear promising for optical information processing and transfer by means of controlled transverse shift. Interest to investigations of this kind is caused by the well-expressed tendency to ever higher integration of photonics devices with electronic integrated circuits. It is worth noting here that the technology of microelectronic devices production is based on a layer-by-layer growth of semiconductor structures and every of layers is characterized by 2D distribution of parameters, i.e. by 2D topology. Accordingly, the use of a similar topological patterning may appear to be very promising for designing and creation of photonics devices to be conjugated with electronic components. At the same time the influence of patterning is not considered explicitly even by the leading researchers in the field of nonlinear dynamics of bistable systems with 2D transverse distribution. Thus, in the present report an attempt is made to expand the functional potentialities of nonlinear system in which optical data transformation is performed by applying to it a given 2D pattern.

Switching waves in optical bistability are known for decades and studied both theoretically and experimentally. In Fig. 1 the experimental evidence of switching wave propagation over an area of uniform input intensity profile is shown. They can propagate in both or just in one direction depending on initial and border conditions. Here the transmitted intensity distributions are registered in the successive moment of time (following each other in 40 ms) by means of CCD camera. The resonators with thermal nonlinearity of intermediate layers were used in this experiment as bistable Fabry-Perot interferometers.

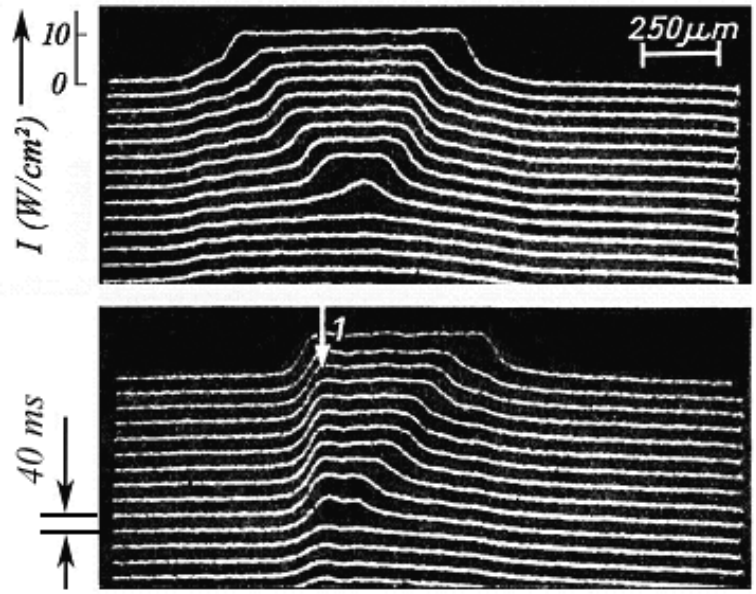


**Fig. 1**. Switching waves in bistable Fabry-Perot interferometer

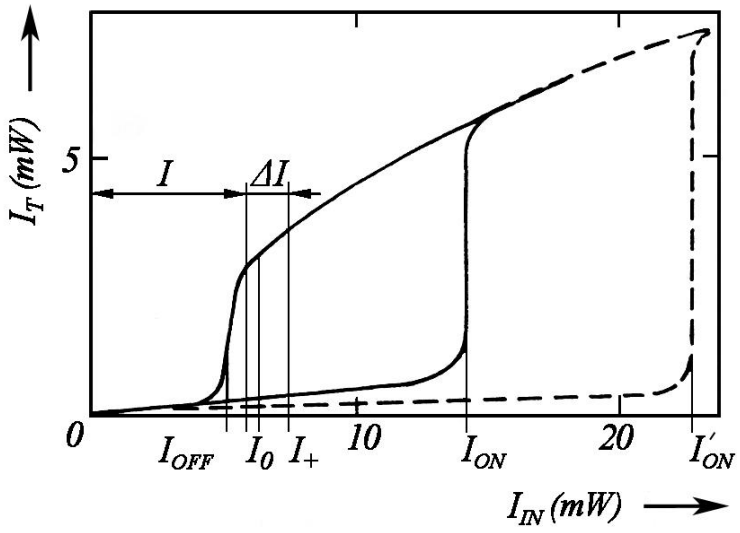


**Fig. 2**. Inversion of the switching wave propagation direction

The next Fig. 2 demonstrates some characteristic values of input intensity in the context of bistable switching of a wide aperture nonlinear interferometer. Switching intensities are labeled as $I_{OFF}$ and $I_{ON}$ (or $I'_{ON}$ for a higher initial detuning). There exists a value of input holding intensity $I_0$ which corresponds to the stopped state of switching wave (its speed equals zero at this intensity) [1]. At higher intensities switching wave spreads over the whole uniform illuminated area (positive speed) and at lower intensities the area of switched-on state shrinks and finally causes the bistable interferometer to switch off to the low transmission state. Thus, at $I_0$ inversion of switching waves propagation direction can be observed.

A theoretical model for analysis of specific transverse effects in optical bistability and description of autowave processes in thin nonlinear Fabry-Perot interferometers with a predetermined pattern of intermediate layer optical thickness is developed. The specific feature of the model in comparison with earlier numerical simulations is the account of the predefined transverse nonuniformity of interferometer intermediate layer optical thickness.

It is supposed, that during the process of interferometer fabrication some zones of the certain geometry are formed artificially in a plane of its intermediate layer by introducing the desired modulation of nonlinear medium refractive index or geometrical spacing between interferometer

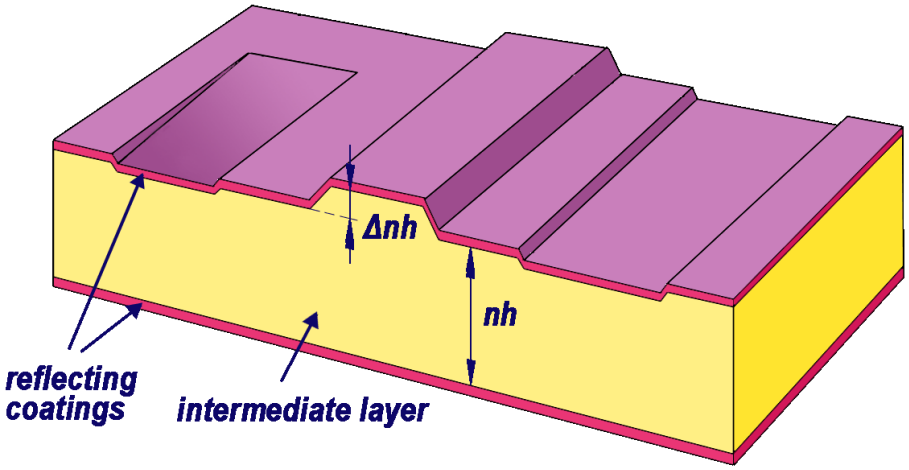


**Fig. 3**. Modulation of the optical thickness of Fabry-Perot interferometer

mirrors (see Fig. 3). These zones are some kind of channels inside which optical thickness differs from the thickness of the neighbor areas. The purpose of creating such specified pattern of channels is to provide acceleration, inhibition, stopping and steady propagation in a desired direction of switching waves which play the role of information signal carrier in planar optical information processing systems. to direct and limit the propagation of autowave processes can be formed.

Physical parameters of the nonlinear medium are chosen corresponding to vacuum deposited thin-film Fabry-Perot interferometers on the basis of ZnS, ZnSe compounds. As promising materials for intermediate layer one can also mention some other semiconductor, polymer and liquid crystal media, opal-like photon crystals.

Here, as well as in earlier models of an optical bistability, diffraction of light on transverse nonuniformities of nonlinear medium is neglected and left out of account due to small thickness of intermediate layer, and time of light field build-up in an interferometer is considered to be small in comparison with characteristic transient time of the system. These restrictions do not break a generality of developed model since they can become apparent only at submicrometer scale of nonuniformity or at light intensity changing in a femtosecond range.

The only basic requirement to a material of intermediate layer in the framework of the given model is the presence of nonlinearity parameter diffusion from the illuminated area into a shadow zone.

The fundamental mathematical model is based on solving the nonlinear partial differential equation of the second order of parabolic type for the parameter *u* of medium nonlinearity with the account of multibeam interference in a thin intermediate layer of a Fabry-Perot interferometer.

Its quasi two-dimensional modification can be written as:

$$\rho c\frac{\partial u}{\partial t} = k\nabla^2 u + Q\left[I_{IN}(t)F(r),u\right] - \rho c\frac{u}{\tau}, \qquad \text{where}$$

$$F(r) = \frac{(1-R)(1+R\cdot e^{-\alpha h})}{(1-R\cdot e^{-\alpha h})^2 + 4R\cdot e^{-\alpha h}\sin^2\left\{\pi\left[\varepsilon(r) + \frac{m+\varepsilon(r)}{n_0(r)}\delta n(r)\right]\right\}} \cdot \frac{(1-e^{-\alpha h})}{\alpha h}$$

All the values involved correspond to those used in our earlier simulations [2]. Nonlinear parameter of the medium can be temperature, density of the photoexcited carriers, elastic tensions, etc. Spatial modulation of optical thickness is given by the chosen dependences of distance $h(r)$ between resonator mirrors, of detuning parameter $\varepsilon(r)$ and/or a initial value of refraction index $n_0(r)$ on transverse coordinate.

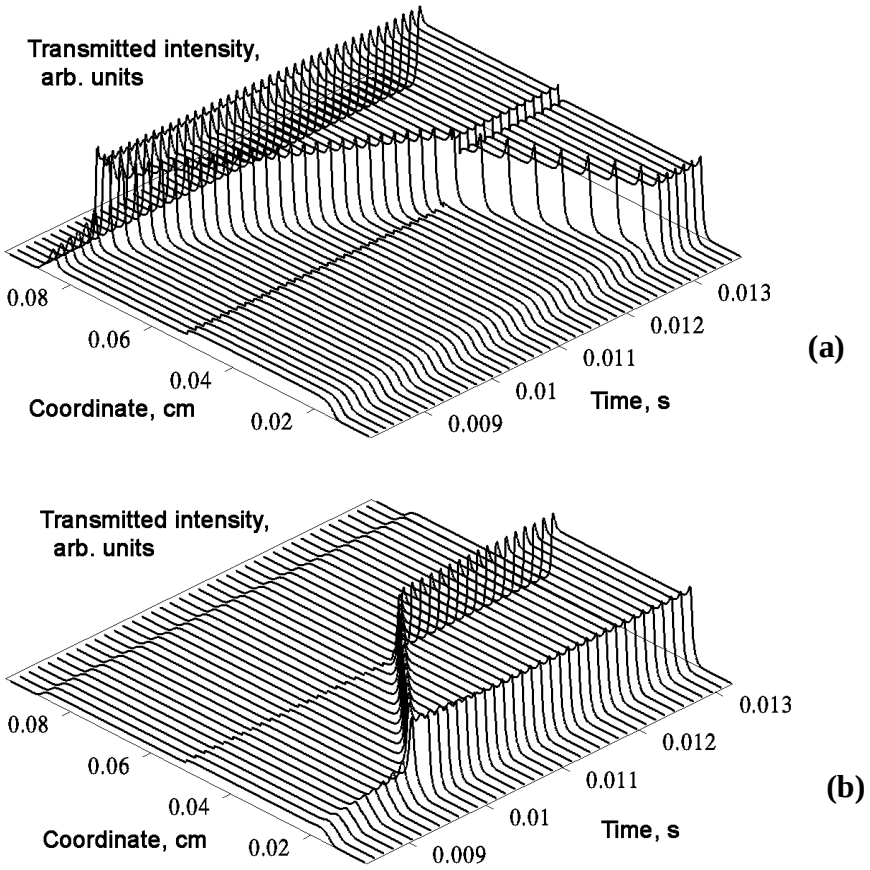


**Fig. 4.** Switching wave crosses the boundary between two areas with the initial detuning parameters of –1,5 (r ranges from 0 to 0,05 cm) и –1,7 (0,05–0,1 cm): (a) penetration — the input intensity is 1,8 kW/cm$^2$ and switching wave approaches the boundary from the side of a higher initial detuning; (b) blocking — the input intensity is 1,6 kW/cm$^2$ and switching wave approaches the boundary from the side of a lower initial detuning.

Basically, these dependences can be chosen of any type with a typical optical thickness modulation amplitude of up to one half of radiation wavelength. However, linearly increasing or decreasing dependences are of the greatest interest from the practical point of view for smooth stopping/accelerating the movement of switching waves fronts, or stepwise dependences for blocking this movement. In particular, step dependence can be approximated by function $h(r) = h_0 + \Delta h / (1 + e^{-A_j (r - r_j)})$, where $\Delta h$, $A_j$, $r_j$ are the parameters which determine amplitude, steepness and spatial position of the step in the input holding intensity profile.

In the framework of the model developed a behavior and transformation of switching wave front is investigated in detail as the wave crosses the step boundary between areas of different optical thickness. Parameters of optical thickness difference and gradient of thickness change at the boundary have been varied for different intensities of holding light beam with a “flat” uniform intensity distribution. The possibility is shown to control the speed of switching wave propagation to the extent that area of switching wave existence is strictly confined in 2D plane with the formation of the channel for propagation of the switched-on state of bistable interferometer by means of creating the specific pattern of optical thickness of the nonlinear intermediate layer. The simulation results in Fig. 4(a) give the evidence that switching wave, when crossing the boundary between areas, certainly permeates into the area with a lower initial detuning, and speed of its further propagation increases.

Passage of the wave in the backward direction can be blocked, as shown in Fig. 4(b), if the condition is met that intensity $I_{IN}$ of input holding beam is less than intensity $I_{v0}$ corresponding to

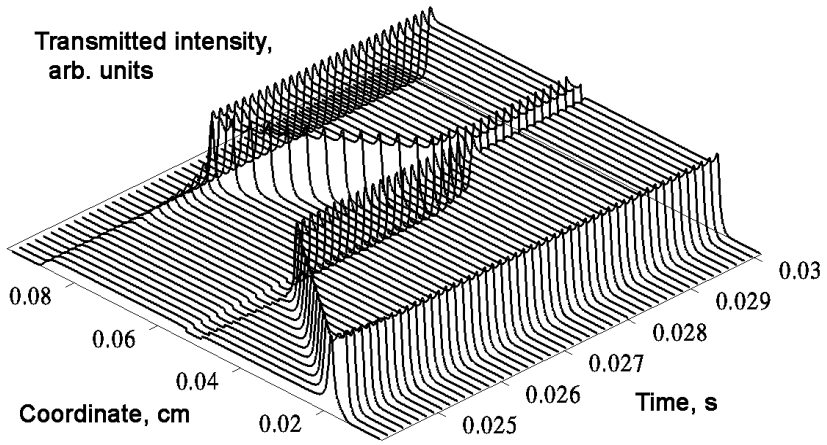


**Fig. 5.** Switching on the barrier area to the state of high transmission die to combined influence of two wave fronts coming from the both sides at the barrier width of 35 μm. Barrier height is determined by the initial detuning values of –1,7 (within the barrier area) and –1,5 (both side areas), input intensity equals 1,6 kW/cm$^2$.

zero speed of wave front at all other given parameters for area with a greater initial detuning (an optical nonreciprocal element).

The conditions of switching wave tunneling through a barrier of a variable width (coordinate) and height (optical thickness) are also investigated. The height of the barrier is found to have a weak influence on the process of switching wave tunneling, i.e. the wave either gets through the barrier or not in the same way as it did before regardless of the barrier height being varied in rather wide range. More crucial factor is the width of the barrier. As numerical simulation shows, the barrier of a width that is essentially smaller than the diffusion length of nonlinear parameter don't bring any noticeable features in the dynamics of the system. The barrier of a width much greater than diffusion length of medium nonlinearity parameter is obviously impenetrable for wave propagation and appears to be a "solid" barrier. However, when a width of the barrier is comparable with the diffusion length the possibility remains to switch on the barrier area of the nonlinear layer the state of high transmission. Such a possibility is realized at a combined influence on a barrier area of two wave fronts coming from both sides, as shown in Fig. 5.

System behavior presented here realizes logical two-operand function "AND", transmission state of barrier area or corresponding light signal transmitted through this area being considered as the result of operation. At the same time the interface between planar circuits which are intended for inter-chip data transport and free space or optical fiber connections is realized.

Thus, the simulation results demonstrate the potential of "patterned" planar bistable interferometers with transverse non-uniformity of optical thickness for expansion of functionality of optical data transmission systems and shift routing. In particular, optical thickness "patterning" can be useful in the devices, operation algorithms of which utilize different signal delay times depending on the section of information circuit which is active at the moment and transmits the signal (circuits with a variable signals delay).

In conclusion, a method to control autowave processes in the plane of thin bistable interferometers by means of profiling their optical thickness according to a specified pattern is developed. Nonreciprocal propagation of switching waves in such interferometers is discovered. It allows to design and form planar waveguide channels, areas designed to store soliton-like structures, regions to delay and to accelerate their motion, as well as nodes where propagating wave fronts and domain walls can be split or merged. This has a potential for development of novel methods of optical information processing and data transfer based on controlled transverse data shift and switching.

Partial support of BRFFR, contract Ф07К–73, is gratefully acknowledged.

**References**

1. Rozanov N.N. Spatial Hysteresis and Optical Patterns. Berlin: Springer, 2002. 308 p.
2. Apanasevich S.P., Lyakhnovich A.V., Sinitsyn G.V. 2D all-optical shift registers: numerical simulation // Institute of Physics Conference Series, Optical Computing International Conference. – 1995. – No. 139. – Part 1, – P. 109–112.

# LONGITUDINAL DISTRIBUTION OF EXCITED ACTIVE CENTERS IN LASER ROD SIDE-PUMPED BY LASER DIODES

**Ho Quang Quy[a], Mai Van Luu[b], Vu Ngoc Sau[b], Nguyen Canh Loi[b]**

[a]Journal of Sciences Techniques and Technology for Military-NEWTECHPRO
[b]University of Vinh

**Abstract** The expression for longitudinal distribution of excited active centers in laser rod side-pumped by laser diode array is introduced by using statistical approximation, Einstein postulates and Gaussian beam theory. Some results are simulated by using Maple software. From that we can discuss about the influence of parameters as azimuthal angle, place of diode array and sparseness of laser diodes on longitudinal distribution of excited centers in solid-state laser rod to avoid the thermal effect and Bragg effect.

***Key words:*** *Solid-state laser, laser diode side-pumped, coherent pump, thermal effect, Bragg effect.*

## 1. Instruction

The solid-state laser side-pumped by laser diodes (LD) is one of advantage lasers and has been interesting in by theoreticians and technicians [1], [2]. High efficiency can be obtained because there is a good special match between the emission spectrum of pump beam and the absorption spectrum of solid-state laser (because of the "coherent" pump). The optimum relation between the size of the pump beam and the mode volume was obtained by theoretical analysis and experiment, which includes thermally induced diffraction loss [3]. A good spatial match between the pump beam and the laser mode volume can be obtained by using the end-pumping scheme, but the pump energy decreases exponentially along the axial direction. Side-pumping geometry can be used to achieve high output powers [2]. For an oscillator, one might use a near-Gaussian distribution centered around the rod axis to help achieve $TEM_{00}$ output; for amplifier, one might use illumination to achieve the best radial uniformity [4]. In the Xie's work, the relationship between the size of pump beam and the mode volume by using space-dependent rate equations, which include the thermally induced diffraction loss is analyzed. In our previous work [5], the distribution of excited active centers (EAC) in cross-section of laser rod is analyzed to correct mistakes in Xie's work, i, e. neglecting the role of interval between LD and laser rod and the "lens" role of laser rod in space-dependent rate equations. Up to now, there is not any attention paid on the longitudinal distribution of EAC (or pumping energy deposition in vertical-section of laser rod), which is neglected by assumption that distribution of LD arrays around the laser rod produces an azimuthal uniform illumination. Here we analyze the relationship between the longitudinal distribution of EAC in laser rod and the azimuthal angle, the place of LD array and sparseness of them by using statistical approximation, Einstein's postulate and Gaussian beam theory.

## 2. Expression of longitudinal distribution of excited active centers

The far field of LD, i.e. the spatial radiation distribution measured at a large distance from output mirror can be expressed by near-Gaussian function [6]. If the half-power width (azimuthal angle describing a dimension of emitting area) of LD is $\Omega$ ($^o$), the emitting beam is considered as a space Gaussian distribution with amplitude

$$U(x,y) = A_0\left[\frac{W_0}{W(y)}\right]\exp\left[-\frac{x^2}{W^2(y)}\right] \quad (1)$$

where the coordinate X-axis is chosen as rod axis, the coordinate Y-axis is chosen as propagating direction, the beam waist can be expressed by [7]

$$W_0 = \lambda / \Omega , \tag{2}$$

$$W(y) = W_0 \left[ 1 + \left( \frac{y}{b} \right)^2 \right]^{1/2} \tag{3}$$

is the radius at point y in propagating direction, and

$$b = W_0^2 \pi / \lambda \tag{4}$$

is the confocal parameter.

The optical intensity $I(x,y) = |U(r)|^2$ is the function of axial and radial distance x and y

$$I(x,y) = I_0 \left[ \frac{W_0}{W(y)} \right]^2 \exp\left[ -\frac{2x^2}{W^2(y)} \right] \tag{5}$$

where $I_0 = |A_0(0,0)|^2$.

We consider a two-side-pumping geometry, in which two n-LD arrays (*n*-number of LDs), are placed symmetrically at $y = -d$ and $y = d$, the ends of laser rod and of two arrays are placed at Y-axis and parallel with X-axis. The sparseness of laser diodes in array is characterized by sparseness parameter (distance between two neighbor LDs) *a*.

As Einstein postulate, the density of EAC is proportional to the absorption coefficient (*B)*, density of active particle in laser rod ($\rho$) and intensity of exciting field, so we can express the density of EAC at point (x, y) as follow by one (left) i$^{th}$ beam

$$Q_{left,i}(x,y) \propto B\rho I(x,y) = B\rho I_0 \left[ \frac{W_0}{W(d+y)} \right]^2 \exp\left[ -\frac{2|x-(i-1)a|^2}{W^2(d+y)} \right]; i = 1..n \tag{6}$$

and by right i$^{th}$ beam

$$Q_{right,i}(x,y) \propto B\rho I(x,y) = B\rho I_0 \left[ \frac{W_0}{W(d-y)} \right]^2 \exp\left[ -\frac{2|x-(i-1)a|^2}{W^2(d-y)} \right]; i = 1..n \tag{7}$$

We consider that the optical field of every LD excite active center independently, i.e. it obeys statistical approximation. From exps. (6) and (7) we have expression for total density of EAC at point (x,y) in vertical-section (X,Y) by all of LD as follow

$$Q(y,y) \propto \sum_{i=1}^{n+1} Q_{right,i}(x,y) + \sum_{i=1}^{n+1} Q_{left,i}(x,y) = B\rho I_0 \sum_{i=1}^{n+1} \left[ \frac{W_0}{W(d-y)} \right]^2 \exp\left[ -\frac{2|x-(i-1)a|^2}{W^2(d-y)} \right] + \left[ \frac{W_0}{W(d+y)} \right]^2 \exp\left[ -\frac{2|x-(i-1)a|^2}{W^2(d+y)} \right] \tag{8}$$

It is acceptable that density of EAC as shown in Eq.(8) describes the energy storage of pump beam in laser rod. Thus the pump energy distribution in plane (X,Y) can be defined as the longitudinal distribution of EAC, and it is described by following expression.

$$S(x,y)=\frac{Q(y,y)}{B\rho I_0}=\sum_{i=1}^{n+1}\left[\frac{W_0}{W(d-y)}\right]^2\exp\left[-\frac{2|x-(i-1)a|^2}{W^2(d-y)}\right]+\left[\frac{W_0}{W(d+y)}\right]^2\exp\left[-\frac{2|x-(i-1)a|^2}{W^2(d+y)}\right] \quad (9)$$

## 3. Simulation and discussion

In Fig.2 there are intensity distributions in plane (X,Y) simulated by Maple software for optical field of two placed at distance $d$=40mm LD arrays, which consisted from 13 LDs with wavelength $\lambda$=0.86μm, azimuthal angle $\Omega$=15$^o$ and sparseness parameter $a$=10mm (Fi.g1).

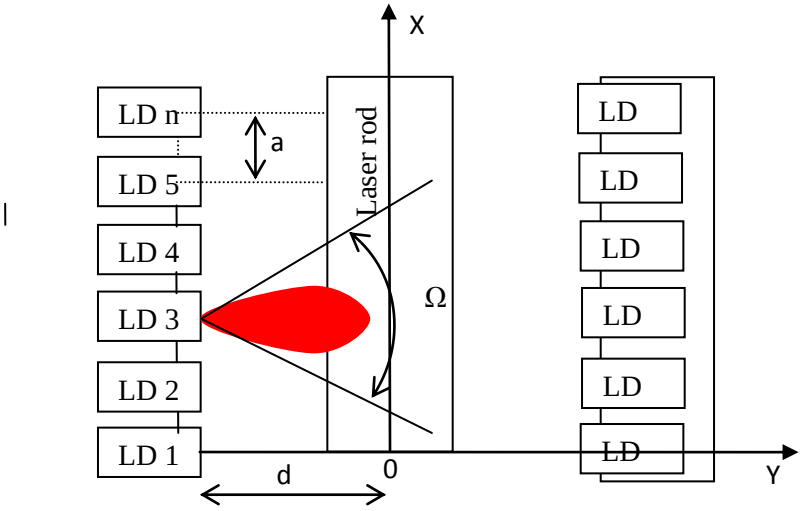


**Fig.1** Two side-pumping geometry

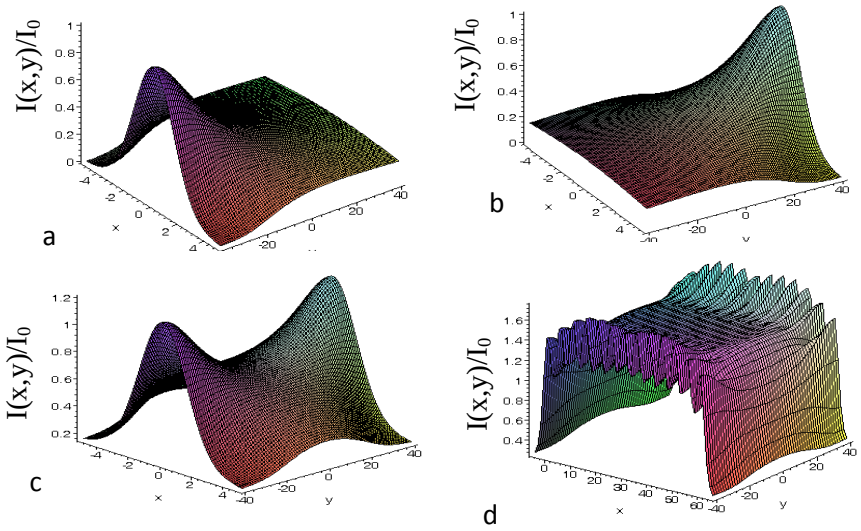


**Fig2.** Distribution of Intensity of LD in (x, y)
with Ω=15$^o$, λ=0.86μm, d=40mm, a=10mm for the left beam (a),
the right(b),the sum (c)and for two side pump with 13 LD (d).

From Fig.3, we can see that EACs distribute nearly regularly in Y-axis, but periodically in X-axis, i.e. the Gaussian power is not the same at any cross-section of laser rod. As shown in the work [8], the distribution of pump energy assigns the temperature distribution, finally assigns

distribution of refractive index in laser rod. The periodicity of pump intensity distribution in Fig.1d causes periodicity of distribution of EACs, consequence causes periodicity of refractive index along laser rod axis. With periodicity of refractive index laser rod becomes a thermal Bragg grating. The appearance of Bragg grating in laser rod will influence properties of laser generation. This unwished phenomenon is caused by diffraction of Gaussian beams and overlapping of them. To avoid it, we investigate here influence of azimuthal angle, sparseness of LD array and placing distance of arrays from laser rod axis on longitudinal distribution of EACs in vertical-section. In Fig.3, we present distribution of EACs in laser rod with some values of distances from LDs array to laser rod for the case of $\Omega$=25$^o$, $a$=5mm.

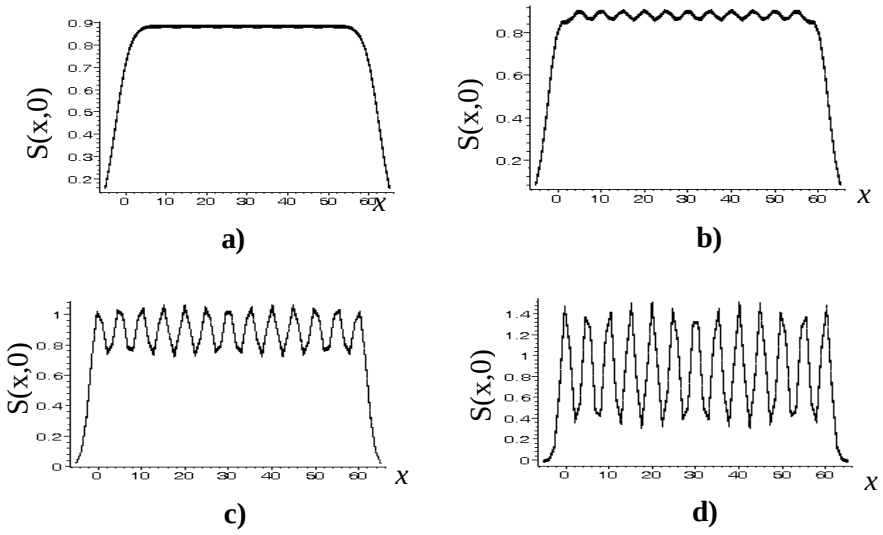


**Fig.3** Distribution of EAC in axis of laser rod with Ω=25$^o$, λ=0,86μm, a=5mm for some values of d: 20mm (a); 15mm(b), 10mm(c) and 5 mm(d)

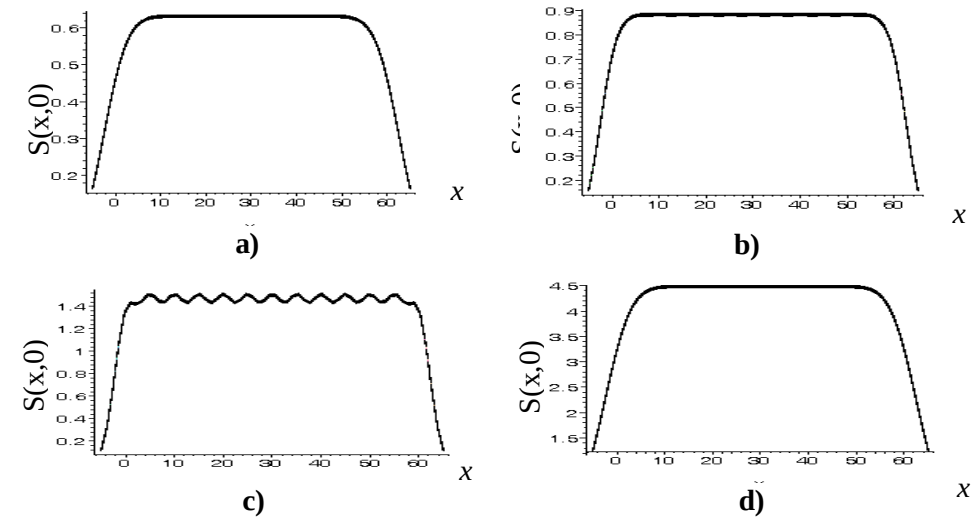


**Fig.4** Distribution of EAC in axis of laser rod with λ=0,86μm, a=5mm, d=20 mm for some values of half-width angle of LD: Ω=35$^o$(a); 25$^o$(b), 15$^o$ (c) and 5$^o$(d)

We can see that, for $d$=20mm, density of EACs is the same at every point in laser rod axis. For other cases the periodicity appears. Using fixed distance $d$=20mm, in Fig.4 there are distribution of EACs with same values of azimuthal angle. We can see that distribution is absolutely regular for cases of $\Omega$=35$^o$ and $\Omega$=5$^o$. For other cases the periodicity appears with different levels.

The dependence of distribution of EACs on sparseness parameter of LD array with $d$=20 and $\Omega$=5$^o$ is simulated and illustrated in Fig.5. One can see that the magnitude of periodicity

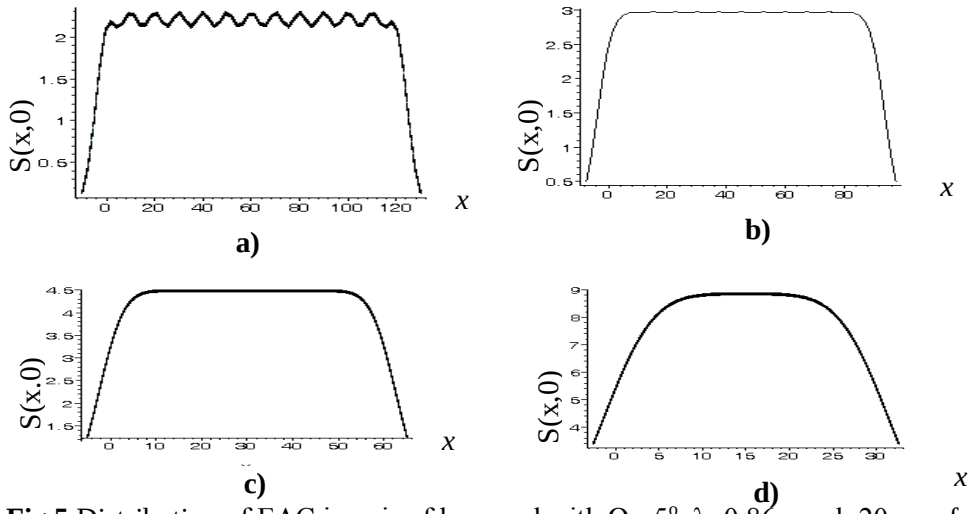


**Fig.5** Distribution of EAC in axis of laser rod with Ω =5°, λ=0,86μm, d=20 mm for some values of placed period of LD in array: a=10(a); 7.5(b), 5(c) and 2.5mm(d)

decreases with decreasing of sparseness parameter, i.e. increasing quantity of LDs. Moreover, in all cases, the magnitude of EACs distribution (maximum density) depends on chosen collection of parameters. The maximum of EAC density is reached if $d$=5mm (in Fig.3), $\Omega$=5° (in Fig.4) and $a$=2.5mm (in Fig.5).

## 4. Conclusion

The side pumping by LD arrays is used to increase pump power in laser rod, but it may decreases qualities of laser generation. The periodical distribution of EACs causes the periodically changing of refractive index, which leads to appear thermal effect and Bragg grating in laser rod. To avoid this unwished effect, the optimal collection of parameters LDs array as sparseness (a), location (d) and azimuthal angle (Ω) must be chosen so that the distribution of EACs is equal along the laser rod.

## References

1. W. Xie et al, "*Fluorescence feedback control of an active Q-switched diode-pumped Nd:YVO$_4$ laser*, " Appl. Opt., Vo. 39 (2000), pp. 978-981.
2. R. J. St. Piere et al, "*Diode array pumping kilowatt laser*," IEEE J. Sel. Top. Quantum Electron., Vol.3 (1997), pp.53-58.
3. Y. F. Chen et al, "*Optimization in scaling fiber-coupled laser-diode and-pumped lasers to higher power: influence of thermal effect*," IEEE J. Quantum Electron. Vol.33 (1997), pp. 1424-1429.
4. S. B. Sutton et al, "*Simple analytical method to calculate the radial energy deposition profile in an isotropi diode-pumped solid-state laser rod*," Appl. Opt., Vol.35 (1996), pp. 5937-5948.
5. H.Q. Quy et al, "*Pump energy deposition inside four-sides pumped solid-state laser rod*," J. Commun. in Phys., vol., (2008), accepted to publish.
6. M. G. Amann et al, "*High-power light sources for optical communication, Active and Passive components,* " Telecom. Reports 6 (1983), special issue "Optical Communications", pp. 79-90.
7. Iu. V. Baiborodin, L. Z. Kpiksynov and O.N. Litvinenko, "*Cpravocznik po laserpnoi technike*," "Technika", Kiev (1978), p.99 (in Russian).
8. W. Xie et al, "*Influence of the thermal effect on TEM$_{00}$ mode output power of a laser-diode side-pumped solid-state laser*," Appl. Opt., Vol.39, No.30 (2000), pp.5482-5487.

# IMPROVEMENT OF THE PREPARATION OF THE OPTICAL SILICA PLANAR WAVEGUIDE SPLITTER MODULES AND THEIR CHARACTERIZATIONS

**Vu Doan Mien, Le Quoc Minh, Nguyen Thanh Binh,**
**Vu Thi Nghiem, Pham Van Truong and Tong Quang Cong**

Institute of Materials Science, Vietnamese Academy of Science and Technology
18 Hoang Quoc Viet, Cau Giay, Hanoi, Vietnam.
*E-mail: mienvd@ims.vast.ac.vn*

**Abstract:** The optical splitter module preparation based on the 1x4 or 1x8 planar silica splitter chips and single mode v-groove fiber arrays has been studied. The improvement of packaging method was implemented, so the preparation speed increased remarkably and the splitter characteristics were improved. The special UV curable adhesive NOA 61 has been used for fixing module's components for the long time operation of the modules under the hard conditions such as high temperature and high humidity. At the same time, the UV curable adhesive serves as an index-matching material which helps to increase the coupling efficiency between the splitter chips and v-groove fiber arrays from 5% to 8%. The prepared optical splitter modules have good average insertion loss (10.5 dB and 7.4 dB for 1x8 and 1x4 splitters, respectively), good uniformity (< 0.40 dB), small polarization dependence PLD (< 0.10 dB) and low crosstalk. The modules can operate in the wavelength range from 1.26 μm to 1.6 μm, so they can be used as an optical power splitter or a combiner for the cable TV (CATV) and fiber optic data transmission systems.

***Key words:*** *optical splitter module, planar silica splitter chips, v-groove fiber arrays, UV curable adhesive, insertion loss, uniformity, PLD*

## 1. Introduction

Broadband WDM communication systems highly demand the passive optical networks for distributive communication services which need broadband optical power splitter/combiners for splitting/combining the optical power of the signals. 1xN splitter is one of the key components in the subscriber optical networks to divide and optical signal into two or more branches. Furthermore, the hybrid fiber/coaxial cable (HFCC) television systems and fiber-to-the-home (FTTH) systems also need the optical power splitters in a large amount. The optical planar waveguide 1xN power splitters have several advantages over the fiber splitters such as compactness, polarization independence, and an equal power splitting is easily achieved for large amount of N branches (16, 32,…). Among the technologies using different materials for fabrication of PLC power splitters (polymers, ion exchange glass, silica,…) the technology, which has silica ($SiO_2$) core waveguides having the same reflective index as optical fibers, is paid much of attention. However, the researches mainly focus on the methods of preparation of the low loss planar splitter chips [1-3] while the works on packaging of the planar splitter modules are much less publicized. The packaging of the photonic device usually may contribute main part in device's cost. Recently, Sui Guo-rong et al reported about the automatic optic waveguide chip packaging system which reduces packaging time and as well as packaging loss [4] but there is no works on manual packaging of the splitter chips.

In this work we report about the improvement of the silica planar waveguide splitter module preparation towards reducing packaging time and waveguide loss by manual optic waveguide chip packaging system. We have achieved the big progress in splitter module preparation in comparison with our previous work [5].

## 2. Experimental results and discussions

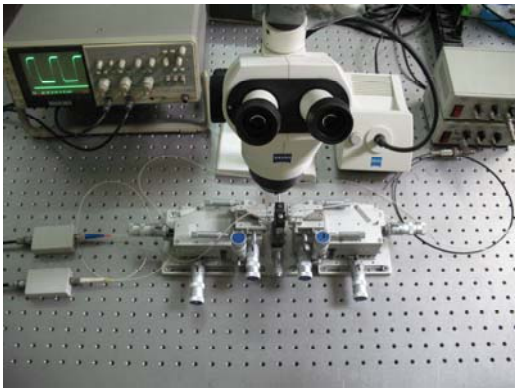

**Fig.1** Manual planar waveguide splitter module packaging system

The silica optical planar waveguide (PLC) 1x4 and 1x8 splitter chips (SOI) and v- groove fiber arrays from Wooriro company were used for making planar optical splitters. The single mode fiber arrays are finished with the FC/PC connectors. The splitter chips and fiber arrays have the sandwich structure where the waveguides and 9/125 single mode fibers are placed between two quartz substrates. Splitter chips and fiber arrays have the angled-facet polishing sides with the angle of $8^o$ for decreasing the reflections from the interface of silica and air. The splitter chips with the Y-junction structure (or Y-branch tree) have the dimensions of 2.5 x 2.5 x 10 mm and the spacing between

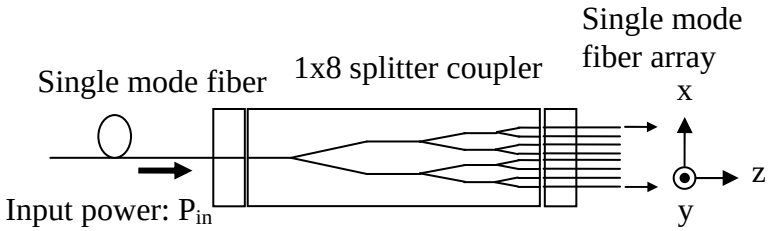


**Fig. 2** Alignment coupling of 1x8 splitter and v-groove fiber arrays

waveguides is 250 μm. The waveguide channels have the cross-section dimensions of 5x5 $\mu m^2$. To make optical coupling we use the specialized for waveguide coupling six-axis Konzu Fine Pitch Positioner FPP03-13 with sub-micron positioning accuracy and high magnification (33 ÷ 250 times) stereomicroscope Carl Zeiss Stemi 2000C. The single mode InGaAsP/InP FP and DFB laser modules (λ = 1310 nm and 1550 nm) prepared by us were used as the optical signal sources for alignment and characterization of the prepared splitter modules. The output light signals were monitored with PIN InGaAs photodiode modules which were prepared also by us.

Figure 1 shows the manual planar waveguide splitter module packaging system at Institute of Materials (IMS) in Hanoi.

The process of coupling was difficult because we needed to have the exact alignment at the same time for both input port (1 channel) and output ports (4 or 8 channels) of the splitter chips with the fiber arrays (Fig. 2). Normally, the commercial high-precision product, 250 nm in the spacing of core, may have a maximum core positional derivation of 0.5 μm, which can be controlled to within 0.1 μm. Multi-channel array coupling principle is an extension of the single core case. Errors of fabrication or photomask addressing lead to errors in the spacing between the channels and waveguide chips. As a result, it is impossible to reach maximum coupling efficiency simultaneously in all channels. Although, these errors are born with the chip, users still hope for as low as possible the loss and difference of each channel. Therefore, homogenization of coupling efficiency of each channel is an important parameter to be considered in alignment. Then, two indexes are practically employed here: the sum of the insertion loss of all channels (to be minimized), and the difference between the maximum and minimum insertion loss of all channels (to be minimized). The latter is defined as homogeneity. Since the loss of device (the origin of the losses occurring in the Y-branch splitter is in the

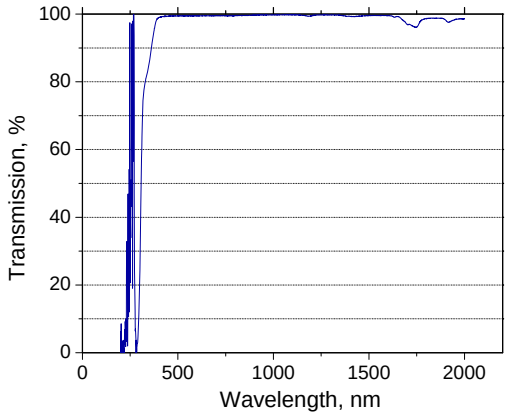


**Fig.3** Transmission spectrum of cured adhesive NOA 61

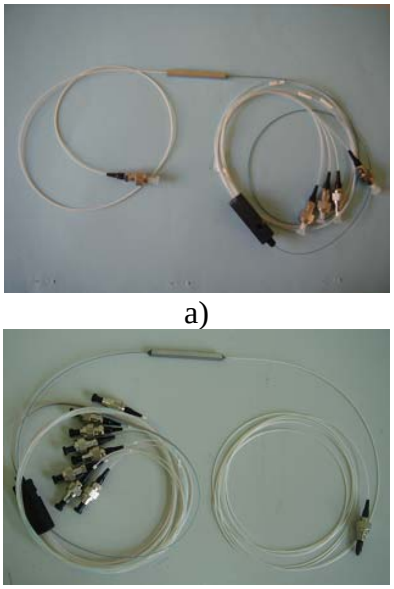

a)

b)

**Fig. 4** Image of the prepared 1x4 (a) and 1x8 PLC (b) splitter modules

branching point) is fixed, the main factor affecting insertion loss is the end-coupling loss (dB). Besides, refractive index matching material inserted between the ends of the fiber and the waveguide also effectively suppresses end reflection.

Initial manual adjustment was performed by using the multimode fiber (as a receiving signal fiber) to align the 1-channel single mode fiber array (as input signal fiber) with the waveguide chip. Then the multimode fiber was replaced by the 4-(or 8-) channel single mode fiber array and the further adjustment is needed. Usually, sampling channels 1 and 4 (or 1 and 8) were monitored first at an operating wavelength of 1550 nm, after achieving their good and equal coupling efficiencies during the alignment, the other channels were monitored. The alignment is completed when the channel insertion loss was less than 8 dB and 11 dB on all channels for 1x4 and 1x8 splitters, respectively, and the homogeneity index of all channels was less than 0.4 dB. It is difficult to define the end-coupling loss separately from the total loss for the channels. But according to Sui Guo-rong et al [4] their average end-coupling loss for 1542.4 nm wavelength operation of 1x8 quartz optical waveguide splitter was 0.1 dB. In our case, the best results were achieved when the distance between splitter chip and fiber array is about 1 μm. We have to note that the Y-junction structure on the waveguide chip is difficult to see due to its transparency so we used the prepared by us white light LED modules to enhance the visibility of the waveguide structure during the optical alignment.

After having good alignment we use UV curable NOA 61 epoxy for attaching the waveguide chip and v-groove fiber arrays: the liquid epoxy was dripped directly into the slits between the splitter chip and fiber arrays (Fig. 2). Norland Optical Adhesive 61 (NOA 61) is a clear, colourless, liquid photopolymer that is cured by ultraviolet light with maximum absorption within the range of 350-380 nm. The recommended energy required for full cure is 3 Joules/sq. cm in these wavelengths and for that we use UV light curing system Thorlabs CS410 with the maximum UV light power of 90 mW/cm$^2$. The UV irradiation power and time was studied for the best epoxy curing. Our optimum curing time is remarkably fast: 10 seconds for pre-curing and 5 minutes for final curing. Cured NOA 61 layer (~20 μm) on the quartz substrate by the same way was measured for reflective index and transparency. Reflective index *n* was measured by prism coupler method on Metricon Model 2010 Prism Coupler and *n* is 1.5530 and 1.5383 at the wavelength of 632.8 nm and 1551 nm, respectively. The cured NOA 61 also has excellent clarity: transmission is 98 ÷ 99% in the wavelength range from 0.4 μm to 2.0 μm as result

**Table 1**. Main characteristics of some prepared 1x4 and 1x8 splitter modules

| Prepared 1x4,1x8 optical splitter module | Total splitter efficiency η, % | | Average insertion loss, dB | | Uniformity, dB | | PLD,dB |
|---|---|---|---|---|---|---|---|
| | 1310 nm | 1550 nm | 1310 nm | 1550 nm | 1310 nm | 1550 nm | 1550 nm |
| Module N3 (1x4) | 76 | 78 | 7.2 | 7.1 | 0.3 | 0.3 | 0.09 |
| Module N7(1x4) | 77 | 80 | 7.1 | 6.8 | 0.3 | 0.3 | 0.09 |
| Module N8(1x4) | 80 | 81 | 7.0 | 6.9 | 0.2 | 0.2 | 0.09 |
| Module N6 (1x8) | 79 | 77 | 10.1 | 10.2 | 0.2 | 0.2 | 0.09 |
| Module N7 (1x8) | 80 | 84 | 10.0 | 9.8 | 0.3 | 0.3 | 0.09 |
| Module N8 (1x8) | 81 | 81 | 9.9 | 9.9 | 0.3 | 0.3 | 0.09 |
| Module (1x8) (therm. epoxy) | 65 | 68 | 10.9 | 10.7 | 0.6 | 0.5 | 0.08 |
| Commercial module (1x8) | 76 | 75 | 10.2 | 10.2 | 0.4 | 0.4 | 0.08 |

measured on UV-VIS-NIR Spectrophotometer Cary 5000 (Fig. 3). Therefore, transparent cured NOA 61 epoxy with the reflective index of about 1.54 at 1550 nm, low shrinkage and a slight flexibility is quite suitable for using as a index matching and fixing material for the silica waveguide chips and fiber arrays which have the operating wavelength from 1.26 to 1.6 nm. By this way we could reduce very much packaging time as well as insertion loss on all channels in comparison with our previous splitter module preparation without using UV NOA 61 adhesive [5].

After all we put the well connected waveguide chip and fiber arrays into the metallic housing which was then hermetically sealed with the thermal curable epoxy. The complete hardening of the epoxies was performed at the temperature of $60^oC$ during 8 ÷ 10 hours in the temperature case. This thermal treatment also improves the adhesion of the NOA 61 with quartz and completes the splitter module preparation. Figure 4 shows the image of the prepared 1x4 and 1x8 PLC splitter modules.

The experimental setup for measurement of the main characteristics of the splitter modules the same as in our previous work [5]. The optical power meter Noeys OPM 5 with the sensitivity of ± 5 nW was used for power measurement. The 1310 nm and 1550 nm LD modules served as input signal source were placed on the peltier elements for stabilizing their output power. The prepared splitter modules were measured for the total coupling efficiency $\eta$ ($\eta = \Sigma P_{out,i} / P_{in}$, where $P_{out,i}$ is the output power of the *i* output channel, $P_{in}$ is the input power) which is equal the sum of end- coupling efficiency and splitter chip waveguide efficiency. The insertion loss ($-10log(P_{out,i}/P_{in})$) was measured for each output channel with the accuracy of ± 0.10 dB. The uniformity of the output channel power distribution and the polarization dependence loss (PDL) were also measured.

Table 1 presents the measurement results of the main characteristics of some of the prepared 1x4 and 1x8 splitter modules. Our prepared modules have the total coupling efficiency η = 76 ÷ 81 % and 78 ÷ 84 % at the wavelength of 1310 nm and 1550 nm, respectively. The average insertion loss of all the prepared 1x4 splitter modules is about 7.8 dB and 7.4 dB for 1310 nm

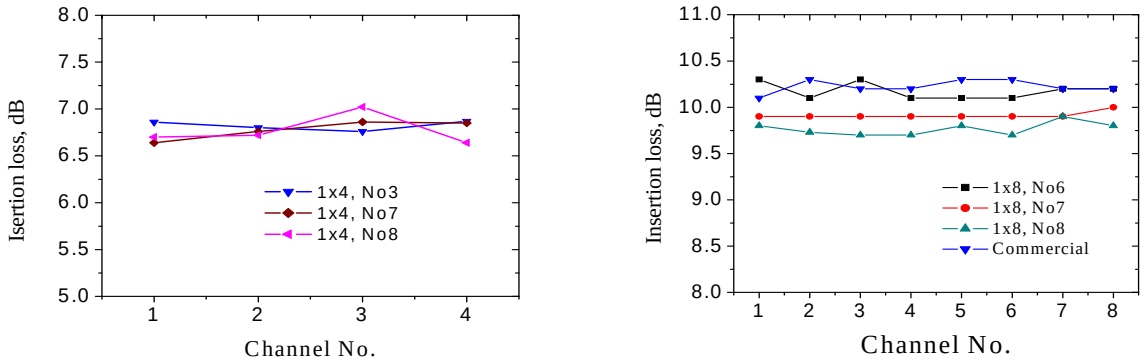


a) b)

**Fig.5** Insertion loss of the different channels for 1x4 (a) and 1x8 (b) PLC splitter modules

and 1550 nm, respectively. These values are 10.9 dB and 10.5 dB for 1310 nm and 1550 nm, respectively, for all the 1x8 splitter modules. The uniformity (< 0.40 dB) and PLD (< 0.10 dB) of our prepared 1x4 and 1x8 modules also are good. These values of the main splitter characteristics are comparable with the characteristics of the commercial modules (TeemPhotonics Co.) and much better than the corresponding values of the 1x8 modules prepared in our previous research [5] which are also indicated in the table. The fixing adhesive NOA 61 serves at the same time as an index matching material, so the total splitter efficiency increased by 12 to 15% (output splitter channel insertion loss decreased by 0.7÷ 0.9 dB) in comparison with the modules where we used thermal curable epoxy for fixing (when small misalignment during hardening also is possible) [5].

**Fig.6** Image of the splitter box with SC/APC connectors using in CATV systems

Figure 5 shows the insertion loss curves for the output channels of the prepared 1x4 and 1x8 optical splitter modules at 1550 nm (for comparison the insertion loss curve of commercial 1x8 splitter module is also shown). Comparing the coupling efficiency after alignment and after applying the UV epoxy it is very important to note that with the use of the epoxy NOA 61 as the adhesive and index matching material we could improve the coupling efficiency from 5 % to 8% due to the decreasing the reflection of light from four quartz-air boundaries with the angle of $8^o$. Because quartz has the reflective index of 1.48 (leading to the reflection at one quartz-air boundary of 4% if the facets with the angle of $0^o$) so here we have good index matching because the reflective index of the NOA 61 epoxy is about 1.54. We also have to mention, that cured NOA 61 has the transparency of more than 98%. In addition, by using UV curing epoxy we can decrease very much the splitter module preparation time, which now mainly depends only on the time needed for optical alignment.

When the splitter modules work as a combiner to combine the different light signal powers (such as in fiber-to-the-home networks and for Internet applications in CATV networks) it is very important that the signal from one channel does not influence the signal from another one. For our prepared splitter modules this kind of crosstalk is very low. The measurement shows that the crosstalks at 1550 nm is around -30 dB and - 40 dB for the 1x4 and 1x8 splitters, respectively. (It reduces about 20 dB when we used FC/APC connectors instead of FC/PC connectors for the fiber arrays because the reflection from the FC/APC connector ends is reduced very much).

We performed also the treatment for the prepared optical planar splitter modules in the conditions of high and low temperatures by putting them in the temperature case with the temperature range changing from $10^0$C to $60^0$C and the different humidity values (50% to 98%).

The insertion loss practically does not change and also no considerable change in the other main splitter characteristics of all the prepared modules was observed. Some of the 1x4 and 1x8 prepared splitter modules are using in the CATV systems for power splitting of the television signals. Figure 6 shows the image of the splitter boxes with SC/APC connectors using in CATV systems where the prepared 1x4 splitter modules are applied.

## 3. Conclusions

We have succeeded in packaging the 1x4 and 1x8 optical planar splitter modules based on the silica planar splitter chips and v-groove fiber arrays with good characteristics such as insertion loss, uniformity and PDL. The technology of precise coupling multi-channel waveguide with v-groove single mode fiber arrays has been developed. The UV curable adhesive NOA 61 with the transparency of more than 98 % in the wide wavelength range and the refractive index of about 1.54 was used for connecting the splitter chips and v-groove fiber arrays and at the same time increased the coupling efficiency from 5% to 8% due to index matching effect. By using UV curable adhesive the prepared modules have much better characteristics than the modules prepared with the thermal curable epoxy. By this way we can reduce very much packaging time as well as the insertion loss on all channels. The improved characteristics of the prepared modules are comparable with commercial splitter's ones. The prepared splitters were tested in aging conditions and can be used in the data communications systems and cable television systems for power splitting/combining the optical signals.

***Acknowledgement****: The authors express sincere thanks to the Vietnamese Academy of Science and Technology for its financial support for this work.*

## References

1. By Hong Ma, Alex K.Y.Jen and Larry R. Dalton. No19, Vol.14, October 2002, pp 1339-1365.
2. Zigang Zhou, Xumei Duan. Optics Communications. Vol. 266, No.1, 2006, p.129 - 131.
3. K.K. Chung, H.P. Chan, P.L. Chu. Optics Communications. Vol. 267, No.2, 2006, p.367 - 372.
4. Sui Guo-rong, Chen Bao-xue, Zhou Jian-zhong, Fu Chang-song, Iso Mamoru. Optics Communications. Vol. 281, No.6, 2008, p.1515 – 1521.
5. Vu Doan Mien, Vu Thi Nghiem and Pham Van Truong. ASEAN Journal of Science and Technology for Development. Vol.24, No.1&2, 2007, p.67 - 72.

# GENERATION OF UV-VIS TRANSFORM LIMITED PICOSECOND PULSE PUMPED BY PICOSECOND Nd:YAG LASER

**Do Quang Hoa[a], Nguyen Trong Nghia[a], Trinh Dinh Huy[a], Totaro Imasaka[b]**

[a)] Laboratory of Molecular Photonics, Institute of Physics
[b)] Department of Applied Chemistry, Kyushu University (Japan)

**Abstract:** A distributed feedback dye laser based on the first order Bragg scattering is reported. The DFB laser using mixed dye RhB and DCM in different solvents: methanol, ethanol, propylene carbonate pumped by second harmonic generation of a picosecond Nd:YAG laser provides a wide tuning range on laser wavelength. A high efficient extraction of the picosecond pumping power from an amplification medium is studied. The energy transfer from RhB to DCM is not only extended wavelength tuning range but also lengthened the working time of DCM dye. Using a BBO crystal for second harmonic generation of fundamental wavelength, a transform limited pulse laser of c.a. 6 pm FWHM, 10 ps in UV region is recorded.
***Keywords**: Picosecond laser, short pulse, dye laser*

## 1. Introduction

The short pulse laser sources are used in the many fields such as spectroscopic temporal resolving analysis [1, 2], basic studies on the depopulation of atoms and molecules in excited state [3], definition of the cross-section using two-photons absorption process [4]. The distributed feedback (DFB) laser is widely employed for organic dye lasers due to their simple and low cost fabrication and their easily observed laser characteristics. An important aspect of DFB structures is that the grating period ($\Lambda$) of the periodic index or gain pattern sets the laser emission wavelength following the relation $\lambda = 2\Lambda n_{eff}/m$, where $n_{eff}$ is the effective refractive index of the guided mode responsible for lasing and $m$ is the order of diffraction responsible for the feedback. Thus, the laser emission wavelength may be tuned within the gain spectrum of the medium (typically ~40 nm) by altering either $\Lambda$ or $n_{eff}$, while the gain spectrum can be displaced throughout the near UV to near infrared with the use of different laser dyes. In other hand, a single picosecond laser pulse could be extracted from the series of picosecond laser pulse of DFB by a quenching cavity attached to the DFB oscillator [5]. Up to now, by our knowledge, the approaches on characteristics of the distributed feedback dye laser (DFDL) pumped by a picosecond pulse sources has not reported.
In this work, a quenching DFB dye laser oscillator pumped by second harmonic Nd:YAG of 120 ps pulsewidth is employed for generation a single UV-VIS picosecond transform limited laser pulse of 10 ps. An amplifier stage in quasi-longitudinal configuration is used to attain a high power efficiency of DFB laser.

## 2. Experimental arrangement

The diagram for experiment is shown in Fig.1. A picosecond SHG of Nd:YAG laser (Continuum, Leopard, 120 ps, 10 Hz) is employed as a pump source of the dye laser. The oscillator of DFB is a cell of 3×3 mm contained circulation mixed dye solution (RhB/DCM) in PC (propylene carbonate) or methanol solvent with concentration of $3\times10^{-3}$M/L for DCM and $1\times10^{-4}$M/L for RhB. An aluminum mirror is directly adhered to one face of the cell formed a quenching cavity shared common active medium of the DFB oscillator. This cavity is suitable for quenching cavity using a pumping source with pulsewidth of 120 ps, due to round trip of photon inside cavity is comparable to leading edge time of the pumping laser. The pulse energy of 180μJ of second harmonic generation of Nd:YAG laser divided to two beams by a couple mirror with top angle of $15^o$ is focused onto dye cell formed a well known DFB oscillator [5].

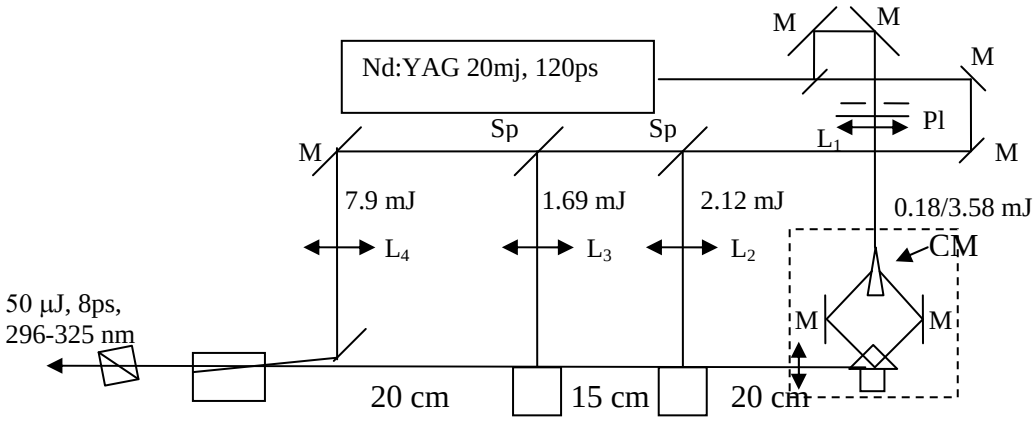


**Figure 1**. Laser dye: DCM of concentration of $3\times10^{-3}$ M/L (osc), $1\times10^{-4}$ ($1^{st}$ amp) and $3\times10^{-4}$ (final amp) in polypropylene carbonate; CM: Beam divider by couple mirror; $L_1$: cylindrical lens (f=300 mm); $L_2$, $L_3$: cylindrical lens (f=100 mm); $L_4$: convex lens (f=500 mm)

The output pulse is amplified in three amplifier stages, in which two stages of side pumping and another one of quasi longitudinal pumping. Two pre-amplifiers contained $1\times10^{-4}$ M/L circulation DCM dye solution used in this laser arrangement can be explained as follow: for efficient power extraction from an amplification medium, the seed pulse needs to have certain intensity, close to the saturation fluence. The seed pulse before amplification is only hundreds nJ, and can only extract energy if it is focused to a relatively small diameter. In order to get enough gain in the first stage it is actually used "over-pumped" process, meaning that significant amounts of amplified spontaneous emission (ASE) are generated, comparable to the energy of the amplified pulse. Using two pre-amplifiers, the amplified pulse is now sufficiently intense to compete with ASE in the final stages. Thus, ASE emission is decreased in the laser beam. Corresponding to pulsewidth of pumping source (120 ps), the efficient gain of amplified medium is reached shorter than 100 ps meaning that it is equilibrium to passed light distance of 3 cm. Therefore, a low amplified effect is observed in side-pump structure. In our experimental arrangement, a quasi-longitudinal configuration of final amplifier is selected to increase amplified effect. The gain is varied of amplification medium along pumping direction in the same beam line of DFB laser, so this allows the maximum energy extraction contained in the post amplifier. The other advantage of typical post amplifier (a cell of 10×20 mm) in picosecond pumping configuration is shown by a reducing of ASE contribution (c.a. 5%) in laser output. The UV beam is approached by second harmonic generation of fundamental beam using a BBO crystal 6×6×5 mm (VLOC Co.). The characters of DFB laser is monitored by a wavemeter (WA 5500, Burleigh), an autocorrelator, and microjoule meter (molectron, M3-J5).

## 3. Characterization of laser system

### *3.1. Wavelength tunability*

The influence of mixed dye RhB/DCM on laser properties is investigated. The mixed dye is prepared in various solvents as methanol, ethanol and propylene carbonate (PC). The observed approaches of the tunable range and the laser spectral shift for difference solution are studied. The solvent of PC is used because of suitable laser generation. The laser wavelength is tuned from 592 nm to 664 nm with central wavelength 628 nm. As shown in Fig.2, the tuning bandwidth of RhB/DCM laser is large than single dye DCM. Two purposes of RhB doped in DCM are (i) expansion of laser emission range of laser DCM to shift blue, and (ii) an extension

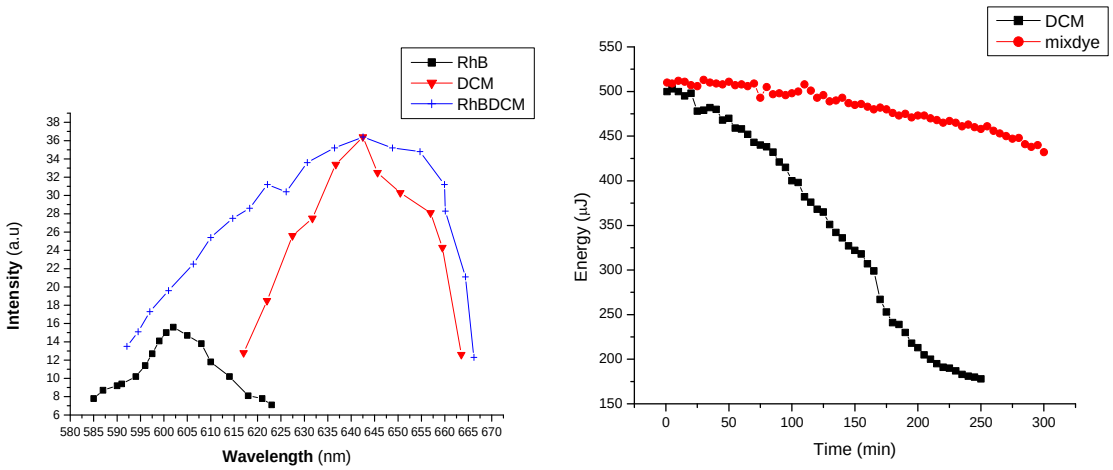


**Figure 2.** (a) Tuning range of DFB laser using single dye and mixture dye; (b) the degradation of laser output for two cases of single DCM and mixture dye

of lifetime DCM solution, especially in the amplifier's stages. Normally, single DCM solution in methanol is quickly degraded under illuminated high fluence. DCM is in the merocyanine class dye. Therefore, DCM molecules are easily damaged under high fluence [6]. Rhodamine B-doped in the mixed dye solution played a donor role, which has a high absorbance at pumping wavelength of 532 nm, should be shared the exciting energy and then transferring to acceptor DCM molecules. Therefore, mixed dye solution of RhB/DCM not only broadens laser tuning range but also improves the lifetime of working solution.

### *3.2. Spectral properties*

The shape of the spectral band of DFB laser is strongly dependent on the pump level. Normally, the line width of DFB is slightly broadened when the pumping energy closed to the threshold. In this experiment, a pumping level of 2 times above threshold is used. The line width of this laser as shown in Fig.3 is about (0.5±0.1) $cm^{-1}$ at the both fundamental and SGH

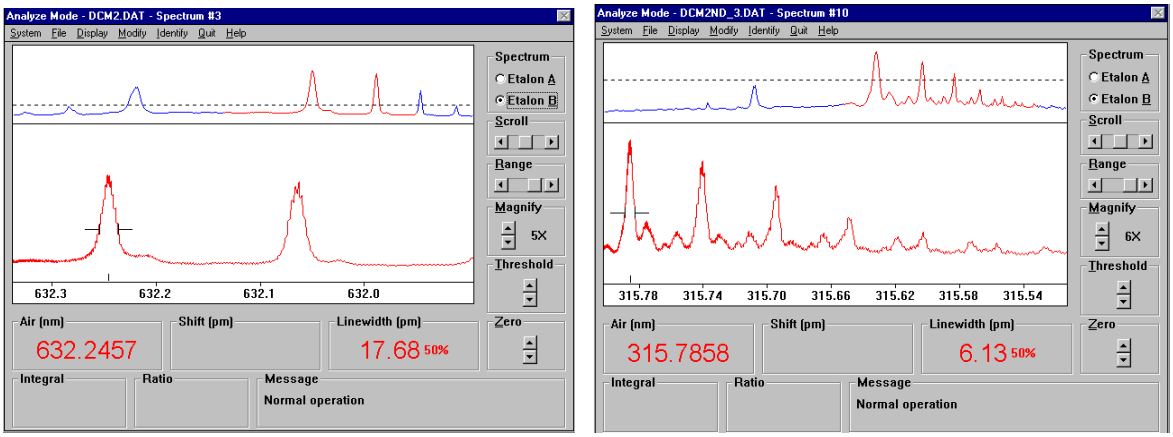


**Figure 3.** The linewidth of DFB laser at fundamental wavelength and SGH in UV region.

wavelength. The spectral line width is unchanged during tuning range of DFB laser. We recognized that the line width is almost remained with variation in about 2÷3 mm of the medium active length. This could be explained by the short pulse generation of DFB laser combined to quenching cavity. It leads to a bandwidth of output laser is attained to transform-limited value.

### *3.3. Temporal property*

An autocorrelator is employed to measure the pulsewidth of DFB laser at fundamental wavelength. The temporal distortion of SGH pulse due to propagation through non-linear crystal is neglected in our experiment. A typical profile measured by the autocorrelator is shown in Fig.4. The pulse width of 8.2±0.2 ps is obtained at the wavelengths in tuning range, which is over 10 times shorter than the pumping pulse. Normally, depending on the pump level the pulse profile is sometimes modified to show some structures on the envelope. In our experiment, at pump power closed to 2 times above threshold this structure is inexplicitly displayed. The quenching effect almost removes sub-pulses in profile of DFB laser. The pulse shape can be predicted easily as a Fourier-transform of an entire spectrum. The product of pulsewidth and linewidth of DFB laser pulse attained 0.441 for Gaussian shape is obtained.

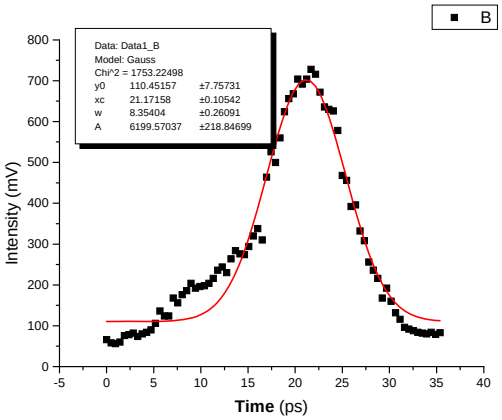


**Figure 4**. The pulse width of quenched DFDL at 632.245 nm using the autocorrelator

## 4. Conclusion

In this report, we have demonstrated picosecond laser pulse generation from the oscillator distributed feedback dye laser and amplifier system using mixed dye solution of RhB/DCM. A wide tuning range over 70 nm of picosecond pulse with Fourier transform limitation in visible and UV region is approached. A compression of pulse effect over 10 times is recorded using the pump source pulse of 120 ps. The DFDL pulse is suitable for the applications in Ionization Mass Spectroscopy method or the determination of lifetime on excited state of the molecules in gas phase.

### *Acknowledgement*

*The paper is supported by the National Basic Research Program on Natural Science and the collaboration of Center for Quantum Electronics, Institute of Physics (VAST) and Department of Applied Chemistry, Kyushu University (Japan).*

### Reference

1. G.J. Blanchard. **Applied Spectroscopy**, vol.3, No.3 (2001)
2. J. Aschenbrücker, U. Steegmüller, N.P. Ernsting, M. Buback1, J. Schroeder, J. Jasny. **Appl. Phys. B** 65, 441–444 (1997)
3. D.Q. Hoa, T. Uchimura, T. Imasaka, N.D. Hung. **Sci. & Techno. Adv. Mat.** vol.7, No. 7, 714-717 (2006).
4. Martin Kauert, Patrick C. Stoller, Martin Frenz and Jaro Ricka. **Optics Express**, vol. 14, No. 18, 8434-8447 (2006)
5. D.Q. Hoa, N.Takeyasu, T. Imasaka, N.D. Hung. **Rev. Sci. Instrum. 74**, 28-31, (2003).
6. P.R. Hammond. **Opt. Comm.**, vol 29 (3), 331-333 (1979)

# OUTPUT INTENSITIES OF NONLINEAR COUPLER

**Ho Quang Quy [a], Vu Ngoc Ssau [b], Nguyen Thi Thanh Tam [c]**

[a] Academy of Military Science and Technology
[b] Faculty of Technology, Vinh University
[c] Faculty of Physics, QuangNam University
*E-mail: hoquy1253@yahoo.com*

**Abstract:** The equations for two waves propagating in nonlinear coupler are derived. Solving those equations, the expressions describing relationship between output intensities from both output gates of coupler on input intensity are introduced. The influence of the input intensity, length of coupler on output intensities are simulated and discussed.

***Key words:*** *Optical fiber, Optical Coupler, Kerr effect, Wave Coupling.*

## 1. Introduction

When two waveguides are sufficiently close, light can be coupled from one waveguide to the other [1,2,3,4]. A nonlinear direction coupler works based on this principle. The refractive indices and the dimensions of the waveguides may be selected so that when the input optical power is low, it is channeled into the other waveguide; when it is high the refractive indices are altered in the nonlinear material and the power remains in the same waveguide. The detuning induced by Kerr nonlinearity effectively switches the input signal from one waveguide to the other. Normally the cores of both two fibers are nonlinear (Fig.1a). In this article we consider the core of one of fibers is linear Kerr medium, the other one is linear (Fig.1b). By propagating equation of coupling waves [1, 6], we introduce the expressions describing the relationship of output intensities at two output ports and input intensity of light. By Maple software the influence of input intensity and of the coupler length on this relationship is simulated and discussed.

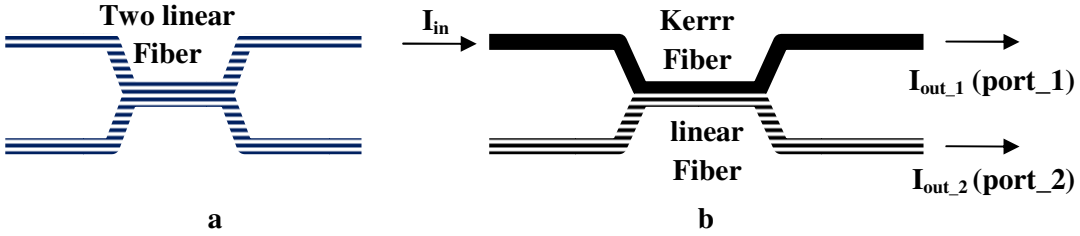


**Fig.1** Coupler with two linear fibers (a) and with one linear fiber and one nonlinear fiber (b)

## 2. Wave equations in nonlinear coupler

Consider a wave with intensity

$$E(x,y,z,t) = \sum A_i(z)\phi_i(x,y)\exp[i(\omega t - \beta_i z)] \quad (1)$$

where $\phi_i(x,y)$ is transverse space mode of i-field; $\beta_i$ is the propagating coefficient; $A_i(z)$ is the amplitude, propagates in the nonlinear coupler with refractive indexes given by:

$$n_1^2(x,y) = n_s^2(x,y) + \delta n_1 = n_s^2(x,y) + \Delta n_1^2(x,y) + n_{nl}^2\left|E(x,y)\right|^4 \quad (2)_1$$

$$n_2^2(x,y) = n_s^2(x,y) + \delta n_2 = n_s^2(x,y) + \Delta n_2^2(x,y) \quad (2)_2$$

where $n_s$ is the refractive index of clad; $\Delta n_1$ is the linear refractive of core of Kerr fiber; $n_{nl}$ is the nonlinear refractive coefficient of Kerr fiber; $\Delta n_2$ is the refractive index of core of linear fiber.

Two waves in coupler satisfy following equation [1, 3, 6]

$$\left(\Delta_T + \omega^2\mu\varepsilon(x,y) - \beta_i^2\right)E_i(x,y) = -\mu\delta\varepsilon(x,y)E_i(x,y) \tag{3}$$

Substituting (1), (2) into (3), using slowly varying approximation and after some arrangement we have

$$\frac{dA_1(z)}{dz} = -iC_{11}A_1(z) - iC_{nl}A_1(z) - iC_{12}A_2(z)\exp\left[i(\beta_1 - \beta_2)z\right] \tag{4}_1$$

$$\frac{dA_2(z)}{dz} = -iC_{22}A_2(z) - iC_{21}A_1(z)\exp\left[-i(\beta_1 - \beta_2)z\right] \tag{4}_2$$

where

$$C_{ij} = \frac{\omega\varepsilon_0}{4}\iint \phi_i^*(x,y)\Delta n_i^2\phi_j(x,y)dxdy$$

which describes the coupling of two waves in fiber number $i$;

$$C_{ii} = \frac{\omega\varepsilon_0}{4}\iint \phi_i^*(x,y)\Delta n_j^2\phi_i(x,y)dxdy$$

which describes the noise from neighbor fiber;

$$C_{nl} = \frac{\omega\varepsilon_0}{4}\iint \phi_i^*(x,y)n_{nl}^2\left|E(x,y)\right|^4\phi_i(x,y)dxdy$$

which describes influence of Kerr effect in nonlinear fiber.

In the nonlinear coupler, it is real that magnitude of $n_{nl}$ greatly smaller one of $\Delta n_1$ and $\Delta n_2$, ($\Delta n_1 \approx \Delta n_2 \approx 0.015$ [4] meanwhile $n_{nl} = (10^{-16} \div 10^{-14})\text{cm}^2/\text{W}$[5]) so $C_{nl}$ slowly varies with changing of amplitude $A_1$ . From that we can consider

$$C_{nl} \approx \frac{\omega\varepsilon_0 n_{nl}^2 I_{in}^2}{4} \approx const \tag{5}$$

From (4) we can see that coefficients $C_{11}$, $C_{22}$, $C_{nl}$ make the changing of propagating coefficient $\beta_i$ .

If $A_1(z)\exp(-i\beta_1 z)$ and $A_2(z)\exp(-i\beta_2 z)$ are roots of noiseless equation for the every fiber, we have

$$\left(\frac{dA_i(z)}{dz} - \beta_i^2\right)E = 0$$

Then from (4) we can rewrite

$$\begin{aligned} A_1(z) &= A_1'(z)\phi_1(x,y)\exp\left[-i(C_{11} + C_{nl})z\right] \\ A_2(z) &= A_2'(z)\phi_2(x,y)\exp\left[-i(C_{22})z\right] \end{aligned} \tag{6}$$

and

$$\begin{aligned} \frac{dA_1'(z)}{dz} &= iC_{12}A_2'(z)\exp\left[i(2\Delta\beta)z\right] \\ \frac{dA_2'(z)}{dz} &= -iC_{21}A_1'(z)\exp\left[-i(2\Delta\beta)z\right] \end{aligned} \tag{7}$$

with

$$2\Delta\beta = (\beta_1 + C_{11} + C_{nl}) - (\beta_2 + C_{22}) = (\beta_1 - \beta_2 + C_{11} - C_{22}) + C_{nl}\,.$$

### 3. Power transferring of nonlinear coupler

Solving (7) with considering $A_1(0) = A_0$ (input amplitude of wave in Kerr fiber) $A_2(0) = 0$ (input amplitude of wave in linear fiber) and we have

$$A_1^{'}(z) = A_0 \exp(i\Delta\beta z)\cos\left(z\sqrt{(\Delta\beta)^2 + C_{12}C_{21}}\right) - i\frac{(\Delta\beta)\sin\left(z\sqrt{(\Delta\beta)^2 + C_{12}C_{21}}\right)}{\sqrt{(\Delta\beta)^2 + C_{12}C_{21}}}$$
$$A_2^{'}(z) = iA_0 \exp(i\Delta\beta z)C_{21}\frac{(\Delta\beta)\sin\left(z\sqrt{(\Delta\beta)^2 + C_{12}C_{21}}\right)}{\sqrt{(\Delta\beta)^2 + C_{12}C_{21}}} \quad (8)$$

Consider two fiber in coupler have same linearity, i.e. $C_{11}=C_{22}$ , $C_{12}=C_{21}=C$ and there is a linear resonant coupling, i.e., $\beta_1 = \beta_2$ (two waves propagate with same propagating coefficient in linear fiber), then we have $\Delta\beta = \frac{C_{nl}}{2}$

and

$$A_1^{'}(z) = A_0 \exp(izC_{nl}/2)\cos\left(z\sqrt{(C_{nl}/2)^2 + C^2}\right) - i\frac{(C_{nl}/2)\sin\left(z\sqrt{(C_{nl}/2)^2 + C^2}\right)}{\sqrt{(C_{nl}/2)^2 + C^2}}$$
$$A_2^{'}(z) = iA_0 \exp(izC_{nl}/2)C_{21}\frac{(C_{nl}/2)\sin\left(z\sqrt{(C_{nl}/2)^2 + C^2}\right)}{\sqrt{(C_{nl}/2)^2 + C^2}} \quad (9)$$

The optical power of wave in fiber is given by

$$P(z) \cong \left|A'(z)\right|^2 \quad (10)$$

Using (10) and substituting (5) into (9) we have expressions for output intensity from port-1 and from port_2 as follow

$$I_{out1} = I_{in}\left[1 - \frac{C^2}{\frac{\omega^2\varepsilon_0^2 n_{nl}^4 I_{in}^4}{16} + C^2}\sin^2\left(z\sqrt{\frac{\omega^2\varepsilon_0^2 n_{nl}^4 I_{in}^4}{16} + C^2}\right)\right]$$
$$I_{out2} = I_{in}\left[\frac{C^2}{\frac{\omega^2\varepsilon_0^2 n_{nl}^4 I_{in}^4}{16} + C^2}\sin^2\left(z\sqrt{\frac{\omega^2\varepsilon_0^2 n_{nl}^4 I_{in}^4}{16} + C^2}\right)\right] \quad (11)$$

*If $n_{nl}$=0, i.e. for linear coupler, the expressions (11) coincides with that shown in work of Jonathan [1] and Agraval [6].* From (11) can see a portion of intensity periodically transfers from one fiber into other (see Fig.2). For the linear coupler ($n_{nl}$=0), the length $L_{coh}=\pi/2C$ is defined as coherent length, for which intensity in one fiber transfer completely into second one.

The most useful of linear coupler is the "3dB" coupler, for which a half of power in one fiber transfers into second one when its length is a half of coherent length, i.e., $L_{3dB}=L_{coh}/2$.

But, for nonlinear coupler the coherent length can be introduced from (11):

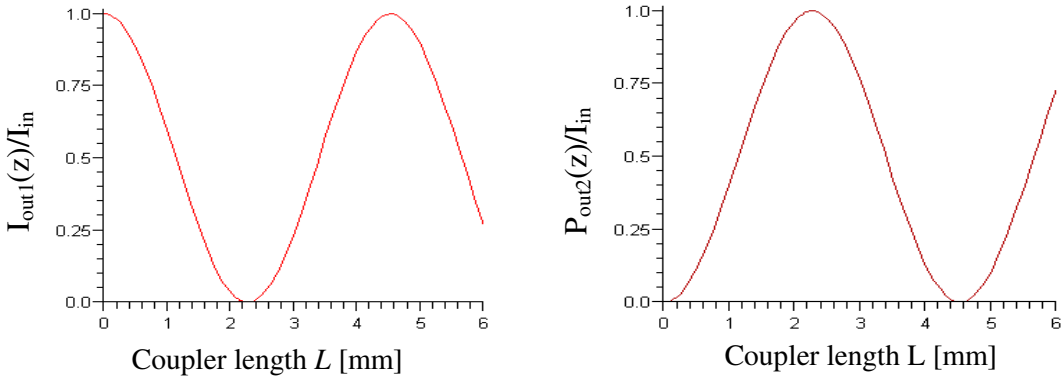


**Fig.2** Periodical transfer of Intensity from one fiber to other of linear coupler: λ=1.33μm, C=0.694/mm [1], $n_{nl}$=0, Δβ=0.

$$L_{cohnon} = \frac{arcsin\left(\sqrt{\frac{\frac{\omega^2\varepsilon_0^2 n_{nl}^4 I_{in}^4}{16}+C^2}{C^2}}\right)}{\sqrt{\frac{\omega^2\varepsilon_0^2 n_{nl}^4 I_{in}^4}{16}+C^2}} \tag{12}$$

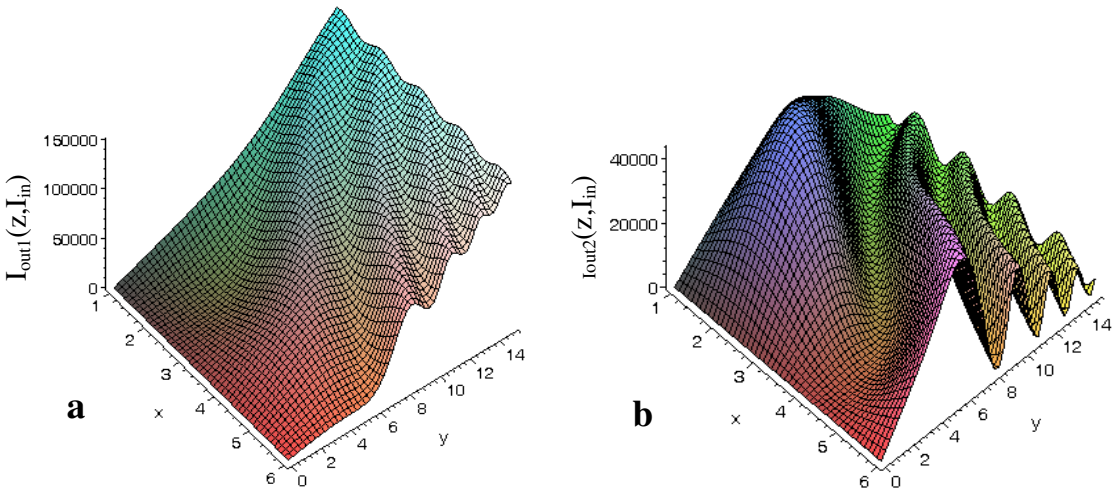


x: coupler length [mm] y: input intensity [ $.10^5$ W/mm$^2$]

**Fig.3** Output intensity from port 1(a) and port 2(b) vs input intensity λ=1.33μm, C=0.694/mm [1], $n_{nl}$=5.010$^{-8}$mm$^2$/W, Δβ=0,

Using Eqs. (11) we simulate the dependence of output intensities from port_1, $I_{out1}$ and port_2, $I_{out2}$ on input intensity, $I_{in}$ by Maple software for the nonlinear coupler of $\lambda$=1.33μm, C=0.694/mm [1], $n_{nl}$=5.010$^{-8}$mm$^2$/W, Δβ=0. From Fig.3 we can see that when input intensity is low ($y$<6, i.e. $I_{in}$<6.10$^4$W/mm$^2$), most input intensity in nonlinear waveguide is channeled into linear waveguide; when it is high the intensity remains in the nonlinear waveguide. Moreover, when input intensity is high ($y$>6) and the coupler length is long ($x$>3mm) intensities in two waveguides change periodically.

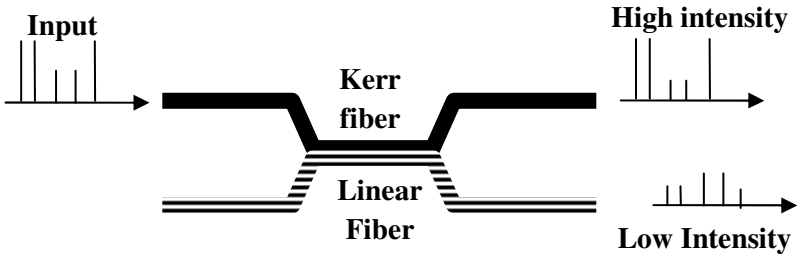


**Fig.4** A nonlinear directional coupler (sorting a sequence of weak and strong pulses)

The oscillating amplitude of intensities decreases with increasing of input intensity. Therefore, we can conclude that the nonlinear coupler can be used not only as switching and performing logic operations, this device can be also used to sort a sequence of weak and strong pulses, separating them into the two output ports of it, as illustrated in Figure 4.

## 4. Conclusion

The expressions for intensity transferring between fibers of nonlinear Kerr coupler are derived by wave equations with proposing Kerr effect as a small noise. From those expressions the coherent length and "3dB" length of nonlinear coupler are found out. They depend on input intensity of wave and nonlinear coefficient of refractive index. The output intensities from two ports of coupler are simulated for example case. Fact that magnitude and oscillation of output intensity depends on input intensity and coupler length. Its behaviour an be used for sorting a sequence of weak and strong pulses, consequently for redistribution of laser beam. Those problems together with the all-nonlinear coupler will be investigated in the next article.

## References

1. J. M. Jonathan, "*Introduction for optical waveguides and fibers*", "Summer School", Doson (2004), p.245.
2. T. Tanable, Opt. Switching, OPN (2005), p. 35.
3. Winnie Ning Ye, "*All-optical signal processing using nonlinear periodic structures: A study of temporal response*," MA. Thesis, University of Toronto, 2002, pp. 7-9.
4. Schneider, H., Zeidler G., "*Manufacturing processes and designs of optical waveguides*", Telcom Report, Special Issure "Optical communication", V.6, 1983, p.31.
5. H.Q.Quy, "*Applied Nonlinear Optics*", HNU. Pub., 2007, p.219.
6. G. P. Agraval, "*Application of nonlinear fiber optics*," San diego San Francisco New York Boston London Sydney Tokyo, Academic Press, (2001), pp. 76-90.

# MONOCHROMATIC LIGHT SOURCES IN TESTING IMAGE INTENSIFIER TUBES

**Krzysztof Chrzanowski**

[1)] Military University of Technology, 2 Kaliski str., 00-908 Warsaw, Poland
[2)] Inframet, Graniczna 24, Kwirynow, 05-082 Stare Babice, Poland

**Abstract**. Military standards and literature sources recommend use of polychromatic light source of 2856K color temperature in testing image intensifier tubes. Tungsten halogen bulbs are standard sources of radiation used in commercially available test stations. However, there are two main disadvantages of tungsten bulbs: short life time and temporal changes of both light power and light spectrum. Application of monochromatic semiconductor sources in testing of image intensifiers as possible alternative of halogen bulbs is analyzed in this paper. It is shown that, if calibrated properly, monochromatic semiconductor sources can be used in stations for testing image intensifier tubes.

## 1. Introduction

Military standards require use of polychromatic light sources of 2856K color temperature in testing image intensifier tubes[1-6]. Tungsten halogen bulbs have been standard sources of radiation used in commercially available test stations for last few decades in testing image intensifier tubes [7,8]. However, tungsten halogen bulbs have several significant limitations. First, they are not stable and emitted flux varies significantly in time. Second, they are characterized by short life time. Third, due to significant temporal inertia it is necessary to use mechanical shutters to enable tests of temporal characteristics of the II tubes.

Here we will analyze possible application of monochromatic semiconductor sources (LED diodes) in testing of image intensifier tubes. These monochromatic sources are much more stable, are characterized by negligible temporal inertia and do not cause polychromatic aberration. Such sources are used sometimes in commercially available stations for testing II tubes [7,8]. However, so far their applications have been limited to use in measurements of imaging parameters (resolution, MTF, image quality etc) of II tubes when, according to MIL standards, requirements on accuracy of illumination level are low. Here we are to investigate if it is possible to use semiconductor light sources in testing photometric parameters of II tubes (luminous sensitivity, luminance gain, etc) when requirements on accuracy of illumination level are high.

## 2. General theory

Sensitivity of image intensifier tubes depends significantly on wavelength. Therefore, illumination of the photocathode with 2856K color temperature light is not equivalent to illumination with monochromatic light of the same radiation power. However, let us analyze if properly calibrated monochromatic sources can replace 2856K color temperature halogen bulbs in test equipment to be used for testing image intensifier tubes and if accurate measurement of photometric parameters of II tubes is still possible.

Quantitative relationships between input illuminance and output luminance is measured during the photometric tests of II tubes. The MIL standards state very precisely the necessary illuminance levels of 2856K color radiation to be used during measurement of photometric parameters of II tubes. The conversion coefficient between the illuminance level of 2856K light and the equivalent illuminance level of monochromatic light depends on spectral sensitivity curve of the tested tube that can vary with different tubes. Therefore we should use different

conversion coefficients in order to calibrate properly the monochromatic source used during tests of tubes of different spectral sensitivity.

This feature is a significant drawback of semiconductor light sources but still in case of testing large number of II tubes of the same spectral sensitivity such monochromatic sources should be an interesting alternative of typical halogen bulbs.

## 3. Correction coefficient

In order to calibrate properly monochromatic source to be used instead of standard polychromatic light sources we will need an instrument that is sensitive to both polychromatic and monochromatic light. Let us make an assumption that we will use typical illuminance meters of spectral characteristics identical as spectral characteristics of humans eye as the sensing instrument of both polychromatic and monochromatic illumination at tube photocathode plane. The illuminace meters of sensitivity over 1 mlx are relatively low cost meters available at photometric laboratories.

**Fig.1**. Photos of exemplary image intensifier tubes

Next, let as assume that we will use a monochromatic source emitting light in the spectral range where both the tested II tubes and the illuminance meters are sensitive: from about 0.5 μm to 0.65μm.

Now, let us analyse a situation when the photocathode of the image intensifier tube was illuminated using polychromatic 2856 K light and the illuminance meter recorded illuminance level $E_{p,}$ and when the photocathode of the image intensifier tube was illuminated using monochromatic light the illuminance meter recorded illuminance level $E_m$. Let us find what is the relationship between $E_p$ and $E_m$ necessary to achieve situation when both light sources generate the same luminance level at the screen of the illuminated II tube.

The light coming to the photocathode represent a certain stimulus that is measured by the illuminance meter in photometric units perfectly suitable for humans eye. Here however, let us analyse a case when the receptor of this stimulus is not human eye but image intensifier tube of significantly different spectral curve. If we use a light meter of spectral curve identical as tube curve then the corrected indication of the illuminace meter illuminated using polychromatic light $E_p(cor)$ would be:

$$E_p(cor) = E_p \cdot \frac{\int ii(\lambda) \cdot M(\lambda,2850) d\lambda}{\int vi(\lambda) \cdot M(\lambda,2850) d\lambda} \qquad (1)$$

where

ii(λ) is the spectral curve of the tested image intensifier tube, vi(λ) is the spectral curve of human eye, $M$(λ, 2856K) is spectral exitance of polychromatic light source of 2856 K color temperature.

In case of a monochromatic light source the corrected indication $E_m(cor)$ of the sensing instrument of spectral curve identical as spectral curve of the II tube is equal to

$$E_m(cor) = E_m \cdot \frac{ii(\lambda_m)}{vi(\lambda_m)}. \qquad (2)$$

The monochromatic light source is equivalent to polychromatic light source when

$$E_p(cor) = E_m(cor) \qquad (3)$$

This means that this equality is fulfilled when:

$$E_m \cdot \frac{ii(\lambda_m)}{vi(\lambda_m)} = E_p \cdot \frac{\int ii(\lambda) \cdot M(\lambda,2850) d\lambda}{\int vi(\lambda) \cdot M(\lambda,2850) d\lambda} \quad (4)$$

Finally we get

$$E_m = E_p / \cdot CF \quad (5)$$

where *CF* is the conversion factor that equals:

$$CF = \frac{\int vi(\lambda) \cdot M(\lambda,2850) d\lambda}{\int ii(\lambda) \cdot M(\lambda,2850) d\lambda} \cdot \frac{ii(\lambda_m)}{vi(\lambda_m)} \quad (6)$$

The meaning of the formula (5) is that if the required by the MIL standards illuminance level of polychromatic light is $E_p$ then we should use a monochromatic source that generate output signal at the illuminance meter equal to $E_p/CF$.

As we see in Eq.6 the conversion factor *CF* depends mostly on two parameters. First it depends on spectral curve of the tested tube *ii*(λ). This means that different conversion coefficients should be used when testing tubes of different spectral curves. Second, it depends on wavelength of the monochromatic source. As we see in (Fig.3) the value of conversion factor *CF* can vary rapidly over the wavelength 0.6 μm and therefore the wavelength of the light source should be determined accurately if we want to use the formula (6).

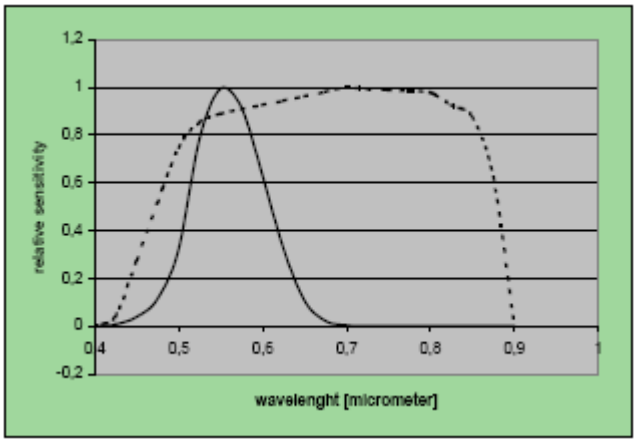


**Fig.2**. Relative sensitivity function
a)continuous line: illuminance meter,
b)III gen tube

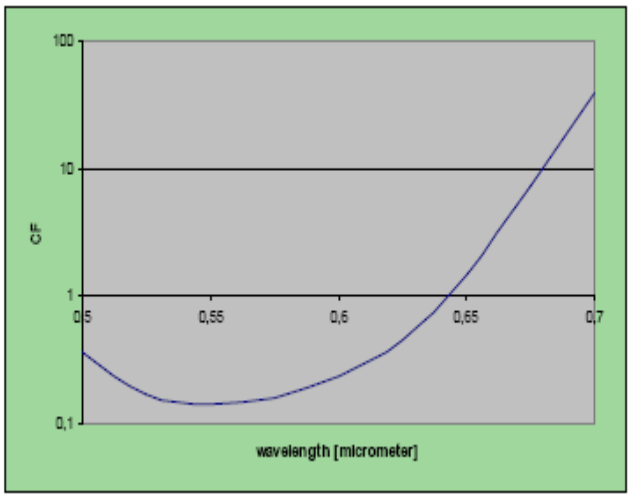


**Fig.3**. Dependence of CF conversion coefficient on wavelength of the semiconductor light source when III get tube of relative sensitivity shown in Fig. 1 is to be tested

## 4. Experimental verification

In order to verify the formula (6) there was carried our an experiment to measure luminance gain of three III generation II tubes using two versions of ITS-P stations from Inframet:
a)ITS-P/F test station equipped with typical halogen bulb as a light source
b) ITS-P/F2 test station equipped with 0.6 μm LED light source.

ITS-P/F2 station was recalibrated using the formula (6) using known spectral sensitivity curve of the tested II tubes and spectral sensitivity curve of the illuminance meter (both shown in Fig.2) and average wavelength of the monochromatic light source. The test results are shown in Tab.1.

Tab.1. Measurement results of luminance gain using two different stations

| Tube number | Luminance gain [cd lx/m^2] (at 0.00002 lx) | | Relative error [%] |
|---|---|---|---|
| | ITS-P/F | ITS-P/F2 | |
| 1 | 12400 | 12900 | 4.0 |
| 2 | 9800 | 10700 | 9.1 |
| 3 | 15200 | 14800 | 3.9 |

As we see in Tab. 1 two test stations that use different light sources generated different measurement results of luminance gain of tested II tubes. The differences are not negligible as they can be as high as almost 10%. However, if we consider that typical errors during measurement of photometric parameters of modern II tubes are often as high as 30% or more then we can consider the error level presented in Tab.1 as reasonably acceptable. We should keep in mind that MIL standards accepts light sources of relative accuracy below the level 25%.

## 5. Conclusions

Short life time and temporal variability of halogen bulbs used as calibrated light sources in commercially available stations for testing image intensifier tubes reduce significantly reliability and accuracy of such test stations. It was shown in this paper that it is possible to replace halogen bulbs by LED light sources and still keep the accuracy of a typical test station using calibrated halogen bulbs. In this way it was verified a possibility to design a new generation of test stations equipped with semiconductor light sources of significantly extended reliability.

## References

1. MIL-PRF-49052G "Image intensifier assemby, 18 millimiter microchannel wafer, MX-9916/UV, 1999
2. MIL-STD-1858, Image intensifier assemblies, performance parameters of; 1981
3. Mark A. Sartor; John W. Pecina; Carl Paul; Bill Helms; Dennis L. Alsman , System for the automatic inspection of image intensifier tubes, Visual Information Processing V, pp.110-121, 1996.
4. Leon A. Bosch, Image intensifier tube performance is what matters, Image Intensifiers and Applications II, pp.65-78, 2000.
5. Sergio Ortiz; Deitze Otaduy; Carlos Dorronsoro , Optimum parameters in image intensifier MTF measurements, Electro-Optical and Infrared Systems: Technology and Applications, pp.382-391, 2004.
6. Dennis L. Alsman; Carl Paul; Mark A. Sartor, Machine vision image analysis capability for image intensifier tubes and systems, Low-Light-Level and Real-Time Imaging Systems, Components, and Applications Conference, pp.90-99, 2003.
7. http://www.hoffmanengineering.com
8. http://www.inframet.com

# MÁY PHÁT THÔNG SỐ QUANG HỌC CỘNG HƯỞNG ĐƠN (SRO) DÙNG TINH THỂ PHI TUYẾN $LiN_bO_3$ QUÉT BƯỚC SÓNG PHÁT BẰNG QUAY GÓC HỢP PHA

**Trần Bá Chữ, Nguyễn Trọng Tuấn, Nguyễn Mạnh Thắng, Hoàng Anh Đức**

Viện Điện Tử-Viễn Thông. 17, phố Hoàng Sâm, Cầu Giấy, Hà Nội

**Tóm tắt:** Máy phát thông số quang học cộng hưởng đơn (SRO), hoạt động với tinh thể phi tuyến $LiN_bO_3$ phát trong dải hồng ngoại gần, bơm bằng laser YAG-Nd tần số 10Hz, quét bước sóng trong vùng hồng ngoài gần bằng cách quay tinh thể đã được nghiên cứu chế tạo. Với tinh thể $LiN_bO_3$ dài 40mm, cắt ở góc hợp pha $47^o$ so với quang trục của tinh thể, máy SRO cộng hưởng sóng Idler trong vùng 3,33μm, phát bước sóng Signal 1,54μm đạt hiệu suất trên 10% với mật độ công suất ngưỡng bơm 18MW/cm$^2$. Với sóng Signal 1,54μm sẽ được ứng dụng để chế tạo máy đo xa laser an toàn cho mắt và sóng Idler 3,33μm của máy SRO sẽ sử dụng cho hệ LIDAR phát hiện khí Methane trong khí quyển.

## 1. Mở đầu

Máy phát thông số quang học (OPO) được nghiên cứu nhiều về lý thuyết cũng như thực nghiệm [1], [2], [3], đặc biệt để tạo nguồn sáng kết hợp có thể thay đổi bước sóng để ứng dụng cho quang phổ, cho Lidar nghiên cứu ô nhiễm môi trường khí quyển. Năng lượng phát và phẩm chất phổ phụ thuộc vào cấu trúc của buồng cộng hưởng (BCH) của OPO. Ở máy phát thông số cộng hưởng kép (DRO) công suất ngưỡng bơm tương đối thấp, do cả hai sóng Signal và Idler đều cộng hưởng trong một BCH, nên hiện tượng cạnh tranh mode và sự kích thích nhiều nhóm dao động riêng (được gọi là cluster) làm cho độ phẩm chất phổ của sóng phát không phải là lý tưởng nên không dùng được cho quang phổ.

Để loại bỏ những nhược điểm trên, người ta sử dụng máy phát thông số quang học cộng hưởng đơn (SRO) [1], [4], ở đó chỉ một sóng phát sinh cộng hưởng trong BCH, trong khi sóng bơm và sóng phát sinh thứ hai truyền không cộng hưởng qua BCH của OPO. Phẩm chất phổ chùm tia phát của SRO được hoàn thiện, tuy nhiên công suất bơm ngưỡng sẽ cao hơn so với DRO, nhất là tinh thể phi tuyến có tính lưỡng chiết (do ba chùm tương tác không trùng nhau).

Trong công trình này chúng tôi nghiên cứu máy phát SRO hoạt động với tinh thể phi tuyến $LiN_bO_3$ cắt ở góc hợp pha $47^o$ bơm bằng laser YAG-Nd tần số lặp 10Hz. Chúng tôi thiết lập đường cong bước sóng phát theo góc hợp pha của tinh thể và tính toán công suất bơm ngưỡng của SRO, đồng thời so với số liệu thực nghiệm đo đạc được.

## 2. Đường cong quét của bước sóng phát theo góc hợp pha

Cho chùm tia laser có tần số $\omega_p$ được gọi là sóng bơm có phân bố Gauss vào tinh thể có hệ số phi tuyến bậc II khác 0 đặt trong một BCH. Hình 1.

Quá trình tương tác thông số phi tuyến sẽ sinh ra trong tinh thể hai sóng Signalvà Idler có tần số $\omega_s$, $\omega_i$ thoả mãn hệ thức năng lượng sau:

$$\omega_p = \omega_i + \omega_s \qquad (1)$$

$$\vec{k}_p = \vec{k}_i + \vec{k}_s \qquad (2)$$

trong đó: véctơ $\vec{k}_m$ (m=i, s, p) là vectơ sóng với $k_m = \frac{2\pi n_m}{\lambda_m}$, $n_m$ là chiết suất của tinh thể phi tuyến ứng với bước sóng $\lambda_m$.

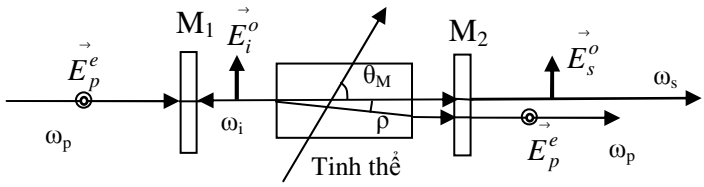


**Hình 1**: Mô hình tương tác 3 sóng trong tinh thể phi tuyến đặt trong BCH của SRO

Nếu sóng bơm có tần số $\omega_p$ cố định, thì hai sóng phát sinh có thể điều chỉnh bước sóng nhờ thay đổi điều kiện hợp pha (2) và sóng phát sinh có thể quét trong vùng rộng. Thay đổi điều kiện hợp pha chính là thay đổi góc hợp pha $\theta_M$, góc tạo bởi quang trục của tinh thể với trục của chùm tia tới. Ta tính góc hợp pha của tinh thể đối với bước sóng phát của SRO dùng tinh thể $LiN_bO_3$ .

Tinh thể $LiN_bO_3$ là tinh thể đơn trục âm, có hệ số phi tuyến hiệu dụng cho OPO bơm ở bước sóng 1,064μm [5] là $d_{eff}=5{,}3.10^{-12}$ m/V. Tinh thể được sử dụng với tương tác loại I ($e_p$-$o_i o_s$), nghĩa là sóng bơm là bất thường, sóng Signal và Idler là sóng thường. Để tính chiết suất tia thường và bất thường ta sử dụng phương trình Sellmeier [5]:

$$n_o^2 = 4.9048 + \frac{0.11768}{\left(\lambda^2 - 0.0475\right)} - 0.027169\lambda^2$$
$$n_e^2 = 4.5820 + \frac{0.099169}{\left(\lambda^2 - 0.04443\right)} - 0.02195\lambda^2 \qquad (3)$$

bước sóng λ tính bằng μm.

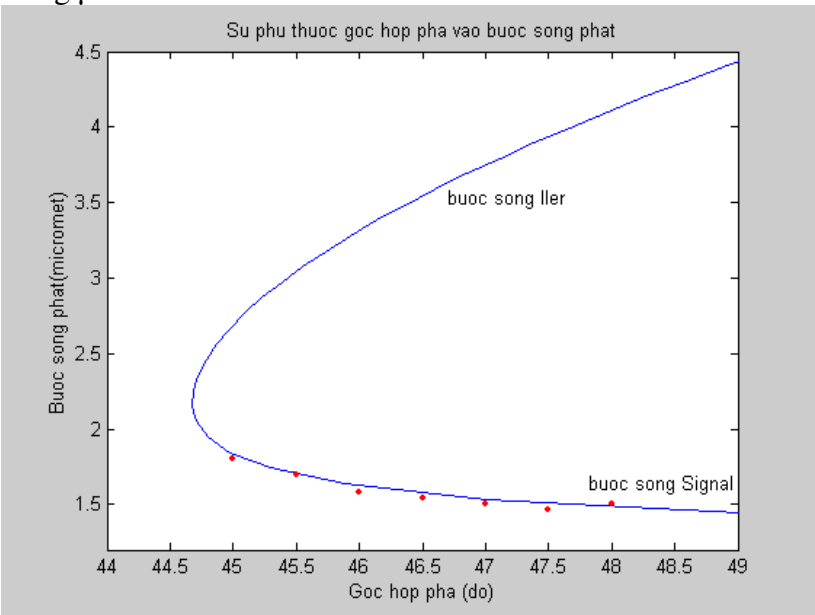


**Hình 2**. Sự phụ thuộc của bước sóng phát vào góc hợp pha trong SRO-$LiNbO_3$ bơm bằng laser YAG-Nd bước sóng 1,064μm
(Đường liên tục là đường lý thuyết; Đường chấm là đường thực nghiệm)

Trong SRO hoạt động với tinh thể được cắt với góc hợp pha theo công thức sau:

$$Sin^2\theta_M = \frac{n_{ep}^2}{n_{ep}^2(\theta)} \cdot \frac{n_{op}^2 - n_{ep}^2(\theta)}{n_{op}^2 - n_{ep}^2} \qquad (4)$$
$$n_{ep}(\theta) = \left(\frac{n_{os}}{\lambda_s} + \frac{n_{oi}}{\lambda_i}\right)\lambda_p$$

$$\frac{1}{\lambda_p} = \frac{1}{\lambda_i} + \frac{1}{\lambda_s}$$

trong đó, trị số $n_{ep}(\theta)$ và bước sóng được tính từ các công thức (1) và (2).

Thay các trị số của chiết suất vào (4), sử dụng máy tính ta vẽ được đường cong biểu diễn sự phụ thuộc cuả bước sóng phát theo góc hợp pha $\theta_M$ của SRO-$LiN_bO_3$ bơm bằng laser YAG-Nd bước sóng 1,064μm. Hình 2 là đường cong bước sóng phát quét theo góc hợp pha loại I.

## 2. Thực nghiệm

Chúng tôi tiến hành thực nghiệm theo sơ đồ hình 3:

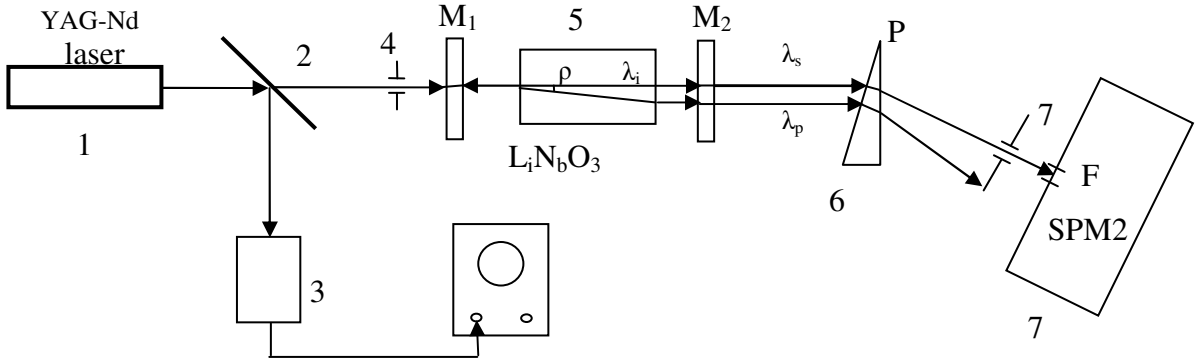


**Hình 3.** Sơ đồ thiết bị thí nghiệm
1. Laser YAG-Nd; 2. Bản mặt song song phản xạ 8% đối với bước sóng 1,064μm;
3. Máy đo công suất laser; 4. Diaphram; 5. SRO; 6. Lăng kính KRS5;
7. Máy đơn sắc;

Máy Laser YAG-Nd (của hãng Quantel) phát xung có độ rộng từ 7-10ns, tần số lặp 5-10Hz ở bước sóng 1,064μm với chùm tia có đường kính 0,5cm, bơm cho máy phát thông số SRO hoạt động với tinh thể $LiN_bO_3$ (của hãng AOTK, Inc.) dài 4cm, có góc lưỡng chiết ρ=0,018 rad, cắt ở góc hợp pha 47$^o$, có độ hấp thụ ở các bước sóng làm việc α = 0,01. Tinh thể $LiN_bO_3$ được đặt trên giá tinh chỉnh có thể quay theo trục thẳng đứng để thay đổi góc hợp pha $\theta_M$ và đặt trong BCH dài 6cm, cấu tạo bởi hai gương phẳng song song (của Hãng Laser Component GmbH), gương trong suốt ở vùng bước sóng Signal phát 1,54μm và sóng bơm 1,064μm, phản xạ 100% ở vùng sóng Idler 3,33μm (cộng hưởng sóng 3,33μm).

Sử dụng lăng kính KBS5 để tách sóng phát khỏi sóng bơm còn dư. Bước sóng của chùm tia phát của SRO được xác định bằng máy đơn sắc SPM-2. Công suất phát của SRO được đo bằng máy đo công suất laser: Power/Energy Meter của Hãng Melles Griot.

Vì tinh thể được cắt một góc hợp pha 47$^o$ so với quang trục, nên chùm tia sóng bơm $\lambda_p$ = 1,064μm thẳng góc với mặt trước của tinh thể, trùng với trục của BCH của SRO thì điều kiện hợp pha cũng được thỏa mãn đối với sóng Signal $\lambda_s$ = 1,54μm và Idler $\lambda_i$ = 3,33μm.

- Khi cho công suất của chùm tia laser YAG-Nd bơm tăng đến 3,54MW, SRO bắt đầu phát. Vậy công suất bơm ngưỡng là $P_{th}$ =3,54MW tương ứng với mật độ công suất $I_{th}$=18MW/cm$^2$ (Với diện tích của tiết diện chùm tia bơm là $\pi\frac{w_p^2}{4} = 0{,}196cm^2$).
- Khi quay tinh thể để thay đổi góc hợp pha $\theta_M$, bước sóng phát của SRO tương ứng với góc hợp pha được thể hiện các điểm trên hình 2.
- Ở bước sóng phát 1,54μm ứng với góc $\theta_M$ = 47$^o$, khi tăng công suất bơm đến 4,7MW, công suất của sóng sóng phát của SRO đo được cỡ 0,45MW tương ứng với hiệu suất

biến đổi 10%. Khi tiếp tục tăng công suất bơm ta có đường biểu diễn hiệu suất biến đổi η của SRO theo $I_p/I_{th}$ (Hình 4) (đường chấm).

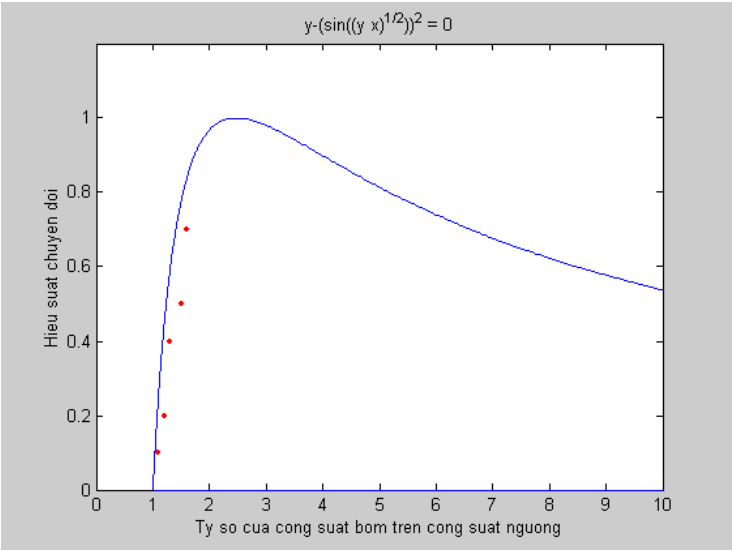


**Hình 4.** Hiệu suất biến đổi η theo hệ số bơm trên ngưỡng $P_p/P_{th}$ ở bước sóng phát 1,54μm (Đường liên tục là đường tính toán lý thuyết; Đường chấm là đường thực nghiệm)

## 4. Biện luận

Mật độ công suất của sóng bơm cần thiết để đạt được đến ngưỡng được tính theo công thức [6].

$$I_{th} = \frac{1{,}12}{K g_s l_{eff}^2}\left(\frac{L}{t_p C} Ln\frac{P_s}{P_n} + 2\alpha l + Ln\frac{1}{\sqrt{R}} + Ln2\right)^{1/2} \qquad (5)$$

Với

$$K = \frac{8\pi^2 d_{eff}^2}{\lambda_s \lambda_i n_s n_i n_p \varepsilon_0 C} \qquad (6)$$

(C là tốc độ ánh sáng, $\varepsilon_o$ là hằng số điện môi)

V□i

$$g_s = \frac{1}{1+(w_s/w_p)^2} \qquad (7)$$

($w_s$ là đường kính của chùm tia signal)

$$l_{eff} = \frac{\sqrt{\pi} w_p}{2\rho} \qquad (8)$$

(ρ là góc lưỡng chiết của tinh thể)

Trong công thức (5) thành phần $LnP_s/P_n$ biểu diễn sự mất mát từ sóng bơm để tạo nên sóng phát sinh cho đến khi đạt ngưỡng phát, nó có giá trị vào khoảng 33 [6], α là hệ số hấp thụ của tinh thể, $l$ là chiều dài của tinh thể, L là chiều dài BCH, $t_p$ độ dài của xung bơm, R là độ phản xạ của gương BCH đối với sóng cộng hưởng.

Với các số liệu thực nghiệm ở trên áp dụng cho máy SRO - $LiN_bO_3$ (R = 1) bơm với xung dài 8ns, phát sóng signal có bước sóng 1,54μm đường kính chùm tia $w_s$ = 0,4cm, thay vào công thức (8), (7), (6) và (5) ta tính được giá trị mật độ công suất ngưỡng của sóng bơm $I_{th}$ = 17,5MW/cm$^2$. So sánh với số liệu đo thực nghiệm và tính toán từ công thức là phù hợp.

Hiệu suất biến đổi η theo hệ số bơm trên ngưỡng $P_p/P_{th}$ được tính theo công thức [9].

$$\eta = Sin^2\left[(\eta I_p / I_{th})^{1/2}\right] \qquad (9)$$

Đường cong lý thuyết của η theo (9) được thể hiện bằng đường liên tục trên hình 4. So sánh đường cong lý thuyết và đường cong thực nghiệm (các điểm hình tròn) thấy có sự phù hợp tương đối giữa lý thuyết và thực nghiệm.

Sau đây là các hình ảnh trong phòng thí nghiệm

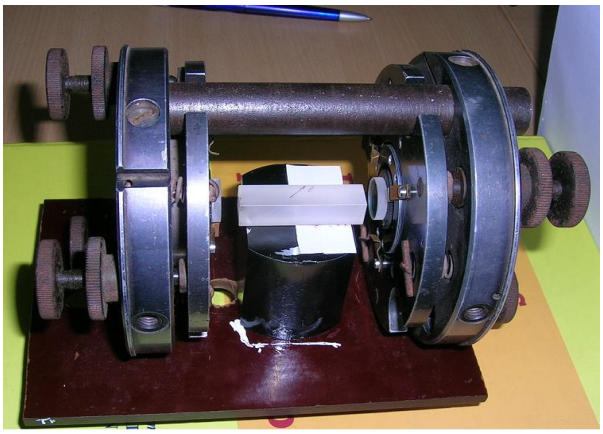

**Hình 5a**. Buồng cộng hưởng của SRO tạo bởi 2 gương phẳng với tinh thể $LiNbO_3$


**Hình 5b**. Hệ thống thiết bị nghiên cứu SRO

## 5. Kết luận

Chúng tôi đã nghiên cứu tạo được máy phát thông số quang học cộng hưởng đơn phát trong vùng hồng ngoại gần (quét từ 1,3μm đến 1,7μm) hoạt động với tinh thể $LiNbO_3$ quay góc hợp pha, bơm bằng laser YAG-Nd có bước sóng 1,064μm, tần số lặp 10Hz. Các giá trị thực nghiệm đo được của công suất bơm ngưỡng và hiệu suất biến đổi của máy SRO phù hợp với giá trị tính toán lý thuyết.

Trong thời gian tới có thể cho phát sóng Idler ở bước sóng trong vùng 3,33μm bằng cách thay gương của BCH-SRO chúng tôi có thể nghiên cứu quang phổ hấp thụ của khí Methane phục vụ cho nghiên cứu Lidar để phát hiện Methane trong không khí [7].

***Lời cảm ơn:*** *Công trình này được tài trợ của "Chương trình nghiên cứu cơ bản cấp Nhà nước thuộc lĩnh vực Khoa học Tự nhiên"*

### Tài liệu tham khảo

1. Tran Ba Chu and M.Broyer *J. Physisque N$^o$ 45 (1984) 1599 - 1606*
2. R.Fischer, P.V Nickles, Tran Ba Chu and L.W.Wieczorek *Annalen der Phys. 39. N$^o$ (1982) 287-294.*
3. K.L.Vodopynov, F.Ganikhanov, J.P.Maffetone, I.Zwieback, and W.Rudeeman *Optics Letters. 25 N$^o$ 11 (2000) 841-843.*
4. T.H.My, F.Bretenaker, C.Drag and J.M,Mellkonian, *Proc. Of Inter, Work on Photonic and Appl. Can Tho, VN, 8/15-19, 2006, p93.*
5. AOTK, Inc. Catalog.
6. W.Koechner – "Solid state laser engineering" 5$^{th}$ Edition, Springer, p.624-626.
7. A.I.Karapuzikov, T.V.Ptashnile and G.G Matvienko, *IR. Phys and Tech 41 (2000) 87-89.*

# NGUỒN PHÁT XUNG LASER PICÔ-GIÂY TỬ NGOẠI CÓ TẦN SỐ LẶP LẠI CAO, TOÀN RẮN VÀ KÍCH THƯỚC NHỎ

**Đỗ Quốc Khánh, Nguyễn Trọng Nghĩa, Nguyễn Đình Hoàng, Nguyễn Xuân Tuấn và Nguyễn Đại Hưng**

Trung tâm Điện tử học lượng tử, Viện Vật lý,
Viện Khoa học và Công nghệ Việt Nam
10 Đào Tấn, Ba Đình, Hà Nội

**Tóm tắt:** Chúng tôi trình bày việc phát triển một nguồn laser toàn rắn phát xung laser picô-giây tử ngoại có tần số lặp lại 8,8 MHz, bắt đầu từ việc nghiên cứu và phát triển một nguồn laser rắn Nd:$YVO_4$ mode-locking tần số xung thấp và một bộ khuếch đại laser rắn. Bộ khuếch đại sử dụng tinh thể Nd:$YVO_4$ được bơm liên tục bằng một laser bán dẫn đã khuếch đại đoàn xung picô-giây có tần số lặp lại 8,8 MHz ở bước sóng 1064 nm tới công suất trung bình 850 mW. Chùm laser picô-giây này đã được biến đổi bước sóng tới 532 nm (130 mW), 355 nm và 266 nm nhờ sử dụng các tinh thể phi tuyến trong cấu hình quang học gọn và đơn giản. Ứng dụng của hệ laser tử ngoại này trong nghiên cứu quang tử cũng được trình bày.

## 1. Mở đầu

Các nguồn laser phát xung ngắn ở vùng tử ngoại UV cần trong nhiều ứng dụng và nghiên cứu quang phổ. Để tạo các xung laser UV như vậy, người ta có thể sử dụng các hiệu ứng quang phi tuyến (nhân tần hoặc/và trộn tần số) của các laser xung cực ngắn mode-locking, tuy nhiên năng lượng xung của laser xung mode-locking thường khá nhỏ cỡ nanô-june [1-6]. Để biến đổi hiệu quả tần số laser, công suất đỉnh của xung laser đòi hỏi có được giá trị cao nhất có thể. Trong báo cáo này, chúng tôi trình bày việc phát triển một nguồn laser toàn rắn, mode-locking thụ động, phát xung laser picô-giây tử ngoại có tần số lặp lại cao, bắt đầu từ việc nghiên cứu và phát triển một hệ laser rắn Nd:$YVO_4$ được mode-locking thụ động bằng gương bán dẫn hấp thụ bão hoà (SESAM) phát xung cực ngắn ở tần số thấp [7]. Sau đó, một bộ khuếch đại toàn rắn Nd:$YVO_4$ được bơm liên tục bằng một laser bán dẫn, đã được phát triển để khuếch đại những xung picô-giây ở bước sóng hồng ngoại 1064 nm tới công suất trung bình 850 mW. Nhờ giảm tần số phát xung và khuếch đại, công suất đỉnh của xung laser chùm laser picô-giây có thể tăng lên hàng chục lần (20) và chúng có thể được biến đổi hiệu quả bước sóng đến 532 nm (130 mW) và vùng UV như 355 nm và 266 nm nhờ các tinh thể phi tuyến trong cấu hình quang học đơn giản. Một số ứng dụng của hệ laser tử ngoại này trong nghiên cứu quang tử đã được trình bày.

## 2. Thực nghiệm

Hệ phát xung laser tử ngoại UV được bắt đầu từ hệ laser rắn Nd:$YVO_4$ xung cực ngắn được mode-locking thụ động bằng gương bán dẫn hấp thụ bão hoà (SESAM). Việc phát triển hệ laser này và các thông số của laser đã được chúng tôi báo cáo trong tài liệu [7], trong đó tần số phát xung laser mode-locking khoảng 80 MHz. Để định hướng sử dụng các bức xạ laser vào các nghiên cứu quang phổ của các đối tượng quang tử và sinh học, hệ laser rắn Nd:$YVO_4$ xung cực ngắn được mode-locking thụ động này đã được thiết kế để cho phép laser hoạt động ở tần số phát xung laser thấp <10 MHz, nhờ sử dụng buồng cộng hưởng dài [8]. Laser phát chuỗi xung mode-locking có độ dài 10 ps (FWHM), tần số lặp lại 8.8 MHz ở bước sóng 1064 nm có công suất trung bình khoảng 300 mW. Để đạt được hiệu suất chuyển đổi tần số cao, một hệ khuếch đại rắn đã được sử dụng để thực hiện việc khuếch đại năng lượng xung laser. Cấu hình quang học để phát các xung laser picô-giây trong vùng nhìn thấy và tử ngoại được trình bày trên Hình 1.

Các yếu tố chính của hệ: (1) - Nguồn bơm laser bán dẫn, công suất liên tục cực đại 2 W, tại bước sóng 808 nm. (2) - Thấu kính bơm, tiêu cự f = 2.5 cm. (3), (7) - gương cầu tiêu cự f = 7.5 cm. (4) - tinh thể Nd:$YVO_4$ (Casix) có một mặt tinh thể mạ gương phản xạ cao ở bước sóng laser 1064 nm và phủ chống phản xạ ở 808 nm, mặt kia phủ chống phản xạ ở bước sóng 1064 nm. (5) – gương cầu tiêu cự f = 15 cm. (6) – gương phẳng, (8) – gương cầu tiêu cự f = 5 cm, (9) – tinh thể KTP, (10) – gương lưỡng chiết, phản xạ cao ở 532 nm. (11), (12), (14) – gương phẳng.(13) - tấm nửa sóng. (15) - thấu kính hội tụ. (16) – tinh thể BBO. Toàn bộ nguồn xung laser tử ngoại hoàn toàn sử dụng các yếu tố rắn và được đặt trên bàn quang học kích thước nhỏ (40 x 60 cm).

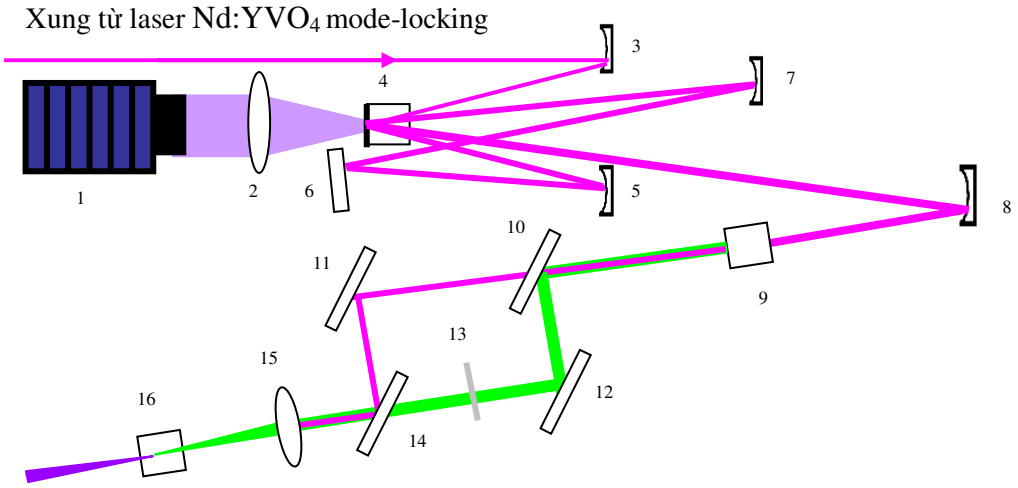


**Hình 1:** Hệ thống phát xung laser picô-giây tử ngoại tần số lặp lại cao.

### *Hoạt động của hệ thống*

Chuỗi xung từ laser mode-locking [8] được đưa vào tinh thể Nd:$YVO_4$ nhờ gương cầu (3), sự chồng chập thể tích tốt nhất giữa vết bơm và chùm laser là điều kiện để đạt được hiệu suất khuếch đại cao nhất. Chùm laser sau khi khuếch đại tới gương cầu (5) và gương dẫn (6), tới gương cầu (7), và lại được hội tụ một lần nữa vào tinh thể Nd:$YVO_4$. Công suất laser sau hai lần khuếch đại lớn nhất thu được là 850 mW, ứng với hệ số khuếch đại của hệ cỡ gần 3 lần. Đặc trưng công suất sau một lần và hai lần khuếch đại được biểu diễn trên hình 2. Những cố gắng để khuếch đại chùm laser nhiều lần đã được thực hiện, tuy nhiên cấu hình khuếch đại nhiều lần truyền không cải thiện được hệ số khuếch đại của hệ (<3) và đòi hỏi thêm nhiều linh kiện quang học laser khác.

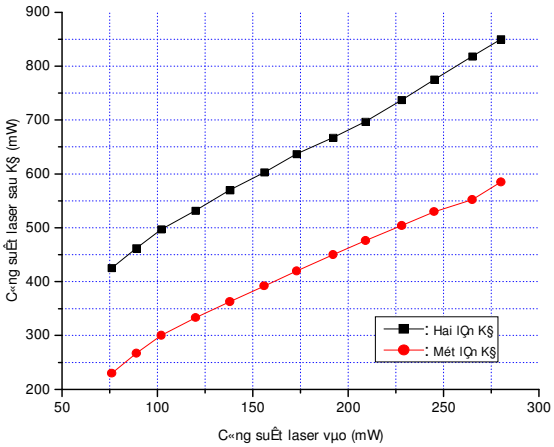


**Hình 2:** Đặc trưng công suất của chùm laser sau bộ khuếch đại 2-lần .

Sau hai lần khuếch đại chùm laser rắn có năng lượng lớn được hội tụ lên tinh thể quang phi tuyến KTP (CASIX) dài 5 mm nhờ gương cầu (8) có tiêu cự f = 10 cm nhằm thực hiện việc chuyển đổi bước sóng từ 1064 nm đến bước sóng 532 nm do hiệu ứng phát hoạ ba bậc hai. Trong trường hợp của chúng tôi, công suất trung bình cực đại thu được ở bước sóng 532 nm là 130 mW, tương ứng với hiệu suất chuyển đổi năng lượng cực đại cỡ 15 %. Đặc trưng công suất của quá trình chuyển đổi bước sóng được biểu diễn trên hình 3. Tuy nhiên, tinh thể KTP được sử dụng nhân tần số ở đây là sẵn có của phòng thí nghiệm - chưa được lựa chọn tối ưu. Những hiệu suất biến đổi hoạ ba bậc hai lớn hơn là rõ ràng có thể đạt được[9].

Phát xạ laser picô-giây ở 355 nm được tạo ra bằng cách sử dụng gương phẳng lưỡng chiết (10) để tách thành hai chùm laser ở 1064 nm và 532 nm. Kết hợp với các gương phẳng (11), (12), (14) theo cấu hình giao thoa kế Michelson, hai chùm laser này được hội tụ lên tinh thể BBO nhờ thấu kính (15) (Hình 1). Điều chỉnh tinh thể BBO sao cho đạt được góc phù hợp pha và điều chỉnh độ dài của nhánh giao thoa kế sao cho để hai chùm laser gặp nhau ở cùng một điểm hội tụ trong tinh thể. Mặc dù chưa có các linh kiện quang học laser thích hợp (tinh thể phi tuyến, gương laser và các tấm Lamda/2 ở các bước sóng laser...) để tối ưu thí nghiệm, công suất trung bình thu được ở bước sóng 355 nm là 5 mW. Trong các thí nghiệm tương tự, các tác giả khác đã đạt được công suất trung bình hàng chục lần lớn hơn [9].

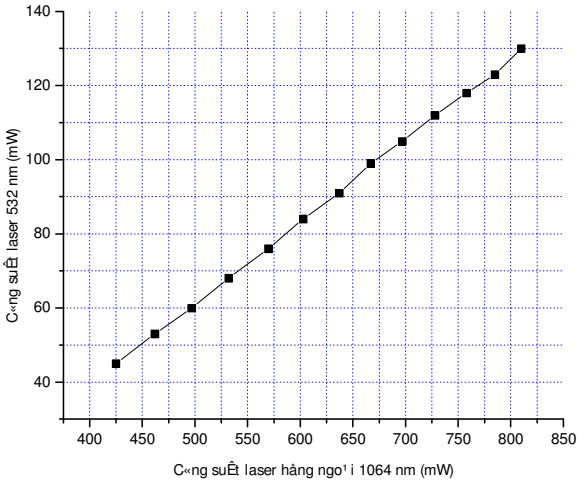


**Hình 3:** Công suất trung bình của chùm 532 nm do hiệu ứng phát hoạ ba bậc hai

Bức xạ laser picô-giây tử ngoại ở 266 nm đã thu được bằng cách sử dụng trực tiếp hiệu ứng phát hoạ ba bậc hai cho chùm laser picô-giây 532 nm với tinh thể quang phi tuyến BBO. Tương tự, trong điều kiện cho phép của phòng thí nghiệm, công suất trung bình cực đại của laser ở bước sóng 266 nm cỡ 5 mW (chưa tối ưu phân cực và tinh thể).

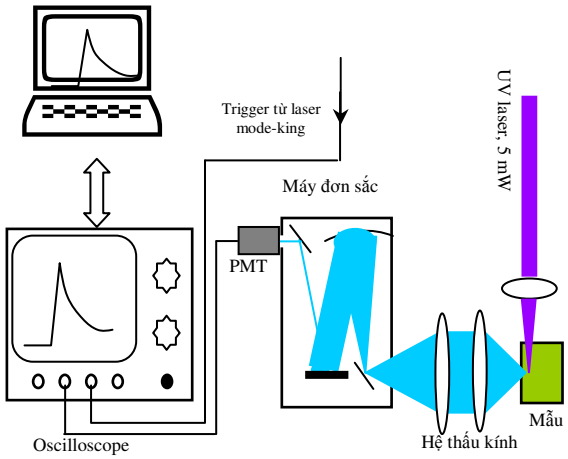


**Hình 4:** Hệ đo phân giải thời gian kích thích bằng laser tử ngoại.

Có thể nói đây là những bức xạ laser picô-giây đầu tiên trong vùng nhìn thấy và tử ngoại được phát ở phòng thí nghiệm Việt Nam. Các bức xạ laser này đã được sử dụng trong những thí nghiệm đầu tiên là để đo phổ huỳnh quang phân giải theo thời gian của một số phân tử, hệ thí nghiệm này được trình bày trên hình 4.

Hệ đo sử dụng máy đơn sắc Oriel Cornerstone$^{TM}$ 260 (USA, 1200 l/mm) với khả năng phân giải 0,10 nm, dải bước sóng hoạt động 200 - 1200 nm. Trong trường hợp đo phổ huỳnh quang, hệ sử dụng đầu thu tín hiệu quang học là PMT (Hamamatzu) và khả năng phân giải thời gian của hệ đo là 1 ns (thời gian đáp ứng của PMT là 1 ns, dao động kí số LeCroy 500 MHz). Trong trường hợp đo thời gian tắt huỳnh quang của các phân tử chất màu, hệ sử dụng đầu thu tín hiệu quang học là một photodiode nhanh (Hamamatzu) và khả năng phân giải thời gian của hệ đo là 0.2 ns (thời gian đáp ứng của photodiode là 0.2 ns, dao động kí số Textronik 1 500 MHz - 20 GS/s). Như vậy, khi sử dụng hệ đo này và các laser picô-giây tử ngoại là nguồn kích thích quang học, một số nghiên cứu quang tử có yêu cầu phân giải theo thời gian đã được thực hiện.

### *Đo thời gian tắt quang của phân tử*

Chúng tôi đã tiến hành đo thời gian tắt huỳnh quang của các phân tử chất màu Coumarin được pha trong dung môi ethanol với nồng độ $10^{-3}$ M/l. Chúng có phổ hấp thụ trong vùng 320 nm - 440 nm nên các mẫu huỳnh quang đã được kích thích bởi các xung picô-giây ở bước sóng 355 nm. Kết quả đo được biểu diễn trên Bảng 1 và trùng hợp tốt với các kết quả đã công bố [10].

**Bảng 1:** Thời gian sống của một số phân tử chất màu họ Coumarin.

| STT | Phân tử màu/ ethanol | Huỳnh quang max | Thời gian sống (ns) |
|---|---|---|---|
| 1 | Coumarin 30 | 483 nm | 3.1 |
| 2 | Coumarin 47 | 450 nm | 2.7 |
| 3 | Coumarin 120 | 550 nm | 3.6 |
| 4 | Coumarin 152a | 504 nm | 2.8 |
| 5 | Coumarin 450 | 470 nm | 3.0 |

### *Đo phổ huỳnh quang phân giải theo thời gian của phân tử*

Trên hệ đo này chúng tôi đã thực hiện đo phổ huỳnh quang phân giải theo thời gian của một số phân tử chất màu Coumarin. Đây là các phân tử có phổ hấp thụ trong vùng tử ngoại, kết quả đo phổ huỳnh quang phân giải theo thời gian của một số phân tử chất màu Coumarin 30/ethanol được trình bày trên hình 5.

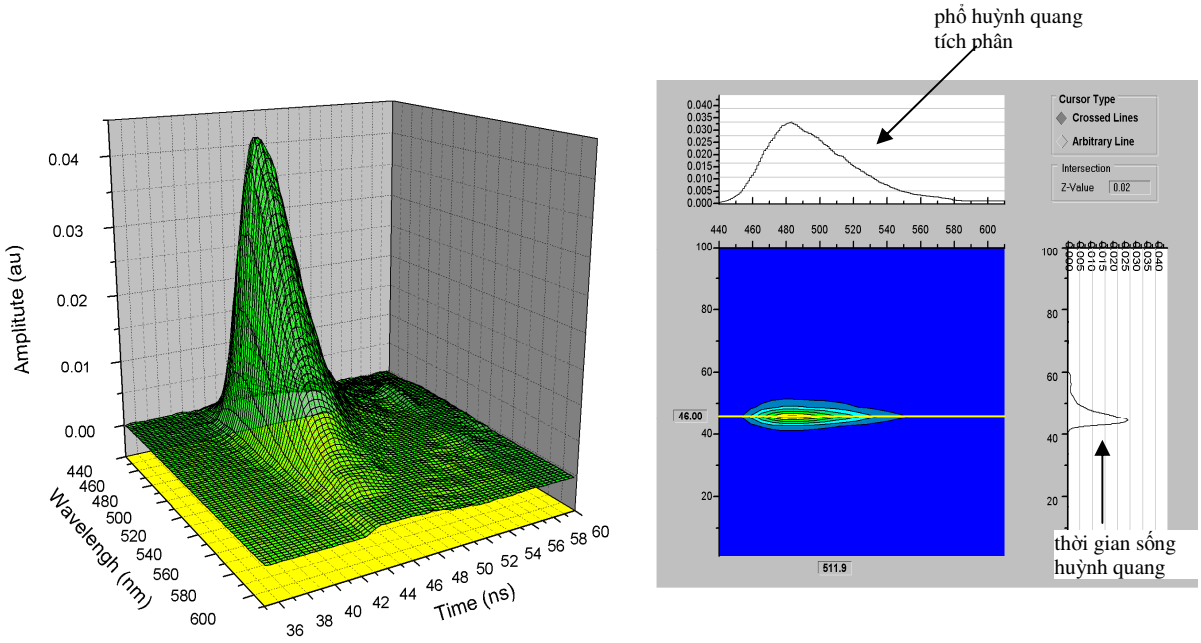


**Hình 5:** Phổ phân giải theo thời gian của Coumarin 30 /ethanol.

Phổ huỳnh quang phân giải theo thời gian cho ta thông tin cả về phổ huỳnh quang tích phân và thời gian sống của phân tử. Ngoài ra, phổ huỳnh quang phân giải theo thời gian của một số chất màu đánh dấu huỳnh quang trong sinh học cũng đã được nghiên cứu và báo cáo [11].

## 3. Kết luận

Một nguồn laser toàn rắn, xung picô-giây, tần số lặp lại cao, được bơm liên tục bằng laser bán dẫn, có thể phát ở các bước sóng 532 nm, 355 nm hoặc 266 nm đã được phát triển thành công tại Phòng Quang tử - Viện Vật lý, Viện KH&CN VN. Hệ laser và bộ khuếch đại laser có cấu hình quang học đơn giản và có kích thước nhỏ, được đặt trên một bàn quang học. Trên cơ sở thiết bị laser UV này, một số nghiên cứu quang tử có khả năng phân giải cao (0.2 ns) đã được thực hiện.

***Lời cảm ơn***

*Các tác giả trân trọng cám ơn sự tài trợ kinh phí từ Chương trình NCCB cấp Nhà nước cho Đề tài $N^0$ 403306 và Chương trình Laser của Viện KH & CN VN.*

**Tài liệu tham khảo**

1. D. Meshulach, Y. Barad, and Y. Silberberg. *Measurement of ultra-short optical pulses by third-harmonic generation*. J. Opt. Soc. Am. B/Vol. 14, No. 8/August 1997
2. Richard S. Tasgal, Marek Trippenbach, M. Matuszewski, and Y. B. Band. *Highly nonlinear dynamics of third-harmonic generation by focused beam.* Phys. Rev. A 69, p.13809 (2004)
3. Guo-Ding Xu, Tie-Wei Ren, Yue-Hua Wang, Yong-Yuan Zhu, Shi-Ning Zhu, and Nai-Ben Ming. *Third-harmonic generation by use of focused Gaussian beams in an optical superlattice* J. Opt. Soc. Am. B/Vol. 20, No. 2/February 2003
4. H.H. Hoa, Do Q. Hoa, J. Matsumoto, T. Imasaka, N. Dai Hung. *Procceding of 3rd IWOMS-99*, p.625-628 (1999)
5. F. Druon, F. Balembois, P. George and A. Brun. *Advances in Photonics and Applications*, (Eds. E. Gacobino, P. Brechignac et al., Vietnam National University Press, 2001) p.349
6. Vladimir V. Konotop. *Simultaneous second- and third-harmonic generation in one-dimensional photonic crystals*. J. Opt. Soc. Am. B/Vol. 16, No. 9/September 1999.
7. Do Quoc Khanh, N. Trong Nghia et al. *Advances in Photonics and Applications*, (Eds. N. Van Hieu et al., Vietnam Academic Press, 2007) p.303-308.
8. Do Quoc Khanh, N. Trong Nghia et al. *V th National Conference on Optics and Spectroscopy*, 10-14 Sep. 2008 Nha Trang (P1-19).
9. Handbook of Nonlinear Optical Crystals (Eds. V.G. Dmitriev, G.G. Guadyan and D.N. Nikogosyan, Springer Verlag,1995)
10. Ulrich Brackmann. *Laser dyes*. Lambda Physik (2000)
11. N. Thanh Binh, N. Dinh Hoang, N. Trọng Nghia, Do Q. Khanh et al. *V th National Conference on Optics and Spectroscopy*, 10-14 September. 2008 Nha Trang, Vietnam (C-04).

# PHƯƠNG PHÁP QUANG HỌC ĐÁNH GIÁ KÍCH THƯỚC CỦA ĐẦU DÒ NANO DÙNG CHO THIẾT BỊ HIỂN VI QUANG HỌC CẬN TRƯỜNG

**Dương Chí Dũng[a], Lê Duy Tuấn[a], Lê Hoàng Hải[a],**
**Yakovlev E. B.[b], Veiko V. P.[b], Kirillovski V. K.[b]**

[a)] Đại học kỹ thuật Lê Quý Đôn, 100 Hoàng quốc Việt, Hà Nội
[b)] Saint-Petersburg State University of Information Technologies, Mechanics and Optics

**Tóm tắt:** Đầu dò nano dùng trong các thiết bị hiển vi quang học cận trường (Scanning near-field optical microscope), thường được chế tạo từ sợi quang bằng cách vuốt nhọn đầu sợi quang đến kích thước nano nhờ phương pháp đốt nóng bằng tia laser hay phương pháp khắc axit. Sau đó phần vuốt nhọn được mạ phản xạ, ngoại trừ phần đầu dò để cho ánh sáng đi qua. Kích thước nano của đầu dò có vai trò quyết định đến độ phân giải của thiết bị hiển vi quang học cận trường. Chính vì vậy, đánh giá kích thước của đầu dò quang học sau khi chế tạo cũng là một bài toán có tính cấp thiết. Trong bài báo này, các tác giả sẽ trình bày phương pháp chế tạo đầu dò quang học bằng phương pháp sử dụng tia laser và phương pháp quang học đánh giá kích thước của đầu dò thông qua phân bố cường độ ánh sáng sau khi truyền qua đầu dò.

## 1. Mở đầu

Thiết bị hiển vi quang học cận trường (SNOM) là một trong những dạng thiết bị hiển vi quét đầu dò. Nguyên lý làm việc của nó dựa trên việc dùng một nguồn sáng có kích thước nhỏ hơn nhiều lần bước sóng ánh sáng quét trên bề mặt của vật cần nghiên cứu. Khoảng cách từ đầu dò đến bề mặt của vật trong quá trình quét được giữ cố định bởi phương pháp lực phân tử, và khoảng cách này nằm trong khoảng 10nm. Ánh sáng từ nguồn sáng có kích thước nhỏ này sau khi phản xạ hoặc khúc xạ qua bề mặt vật sẽ được ghi lại, và từ đó hình ảnh của bề mặt vật sẽ được tái tạo lại với độ phân giải tương đương với kích thước của nguồn sáng. Để tạo được nguồn sáng có kích thước nhỏ, người ta thường sử dụng sợi quang có một đầu được vuốt nhọn đến kích thước nano. Toàn bộ phần vuốt nhọn được mạ phản xạ, chỉ chừa lại phần đỉnh của đầu dò không được mạ. Khi ánh sáng laser được đưa vào sợi quang, do có lớp mạ phản xạ mà ánh sáng không đi ra ngoài mà lan truyền đến tận đầu dò và qua đầu dò đi ra ngoài.

Để đánh giá kích thước của đầu dò quang học sau khi chế tạo, có nhiều phương pháp khác nhau. Phổ biến nhất hiện nay là dùng kính hiển vi điện tử để quan sát và đánh giá kích thước đầu dò. Ngoài ra, có thể xác định kích thước đầu dò bằng cách lắp trực tiếp đầu dò vào thiết bị hiển vi quang học cận trường và tiến hành quét bề mặt vật mẫu. Căn cứ vào hình ảnh thu được của bề mặt vật mẫu mà đánh giá hình dạng và kích thước đầu dò.

Tuy nhiên các phương pháp kể trên đòi hỏi thiết bị hiện đại và khó thực hiện để kiểm tra một số lượng lớn đầu dò sau khi chế tạo. Chính vì vậy chúng ta cần một phương pháp đơn giản hơn để đánh giá kích thước của đầu dò quang học.

Như chúng ta đã biết, sóng ánh sáng khi đi qua đầu dò quang học có kích thước nhỏ hơn bước sóng sẽ bao gồm 2 thành phần là evanescent wave và radiating wave. Thành phần evanescent wave suy giảm rất nhanh và khoảng cách mà nó lan truyền thường rất nhỏ, khoảng vài chục nanomet. Còn thành phần radiating wave có thể lan truyền xa. Nếu ghi lại phân bố cường độ sáng của thành phần này trên một mặt phẳng xác định vuông góc với đầu dò, chúng ta có thể xây dựng lại phân bố của chúng trên mặt phẳng chứa đầu dò, và qua đó đánh giá được kích thước của đầu dò [1-4].

Vấn đề quan trọng nhất là làm sao ghi lại được phân bố của ánh sáng trên toàn bộ mặt phẳng vuông góc với đầu dò và cách đầu dò một khoảng cách xác định. Điều này hiển nhiên là không thể thực hiện được. Tuy nhiên cường độ ánh sáng với góc nghiêng lớn là rất nhỏ và có thể bỏ qua. Trong bài báo này, chúng tôi cũng sẽ trình bày phương pháp sử dụng CCD và phần mềm tự

viết để đo phân bố cường độ sáng với việc mở giải động ghi tín hiệu của CCD lên tới $10^4$. Điều đó giúp cho chúng ta thu nhận được nhiều thông tin hơn về phân bố cường độ sáng trong mặt phẳng far-field, cũng có nghĩa là việc đánh giá kích thước đầu dò được chính xác hơn.

## 2. Chế tạo đầu dò quang học từ quang sợi bằng đốt nóng bởi laser.

Sơ đồ thí nghiệm kéo đầu dò quang học từ sợi quang được biểu diễn trên hình 1. Chùm tia laser $CO_2$ phát liên tục sau khi qua gương phản xạ được truyền tới phần tử hình nón. Phần tử hình nón có tác dụng mở rộng chùm tia laser và hướng chùm tia tới gương phản xạ mặt xuyến. Gương mặt xuyến sẽ hội tụ chùm tia laser lên bề mặt của sợi quang được đặt nằm dọc theo trục của gương. Góc của phần tử hình nón và bề mặt gương xuyến được thiết kế để sao cho chùm tia laser hội tụ vuông góc lên bề mặt của sợi quang. Nhờ vậy mà hiệu suất chế tạo đầu dò được tăng lên [5].

Khi tia laser hội tụ lên bề mặt của sợi quang, vùng sợi quang này sẽ hấp thụ tia laser và bị đốt nóng đến nhiệt độ nóng chảy. Nhờ lực kéo tác động lên 2 đầu của sợi quang mà vùng sợi quang bị nóng chảy sẽ được kéo nhọn đến khi đứt. Lực kéo có thể dùng lò xo, quả nặng hay nam châm điện. Các tham số ảnh hưởng đến quá trình kéo là diện tích vùng bị đốt nóng, công suất của laser, và lực kéo. Các kết quả nghiên cứu sự ảnh hưởng này được trình bày cụ thể trong công trình [6].

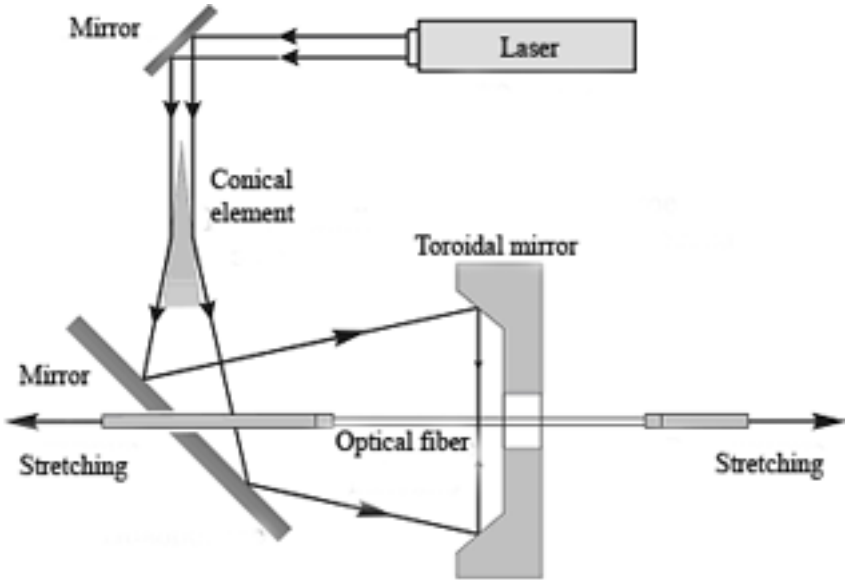


**Hình 1**. Sơ đồ thí nghiệm kéo đầu dò quang học từ sợi quang, sử dụng phương pháp đốt nóng bằng laser $CO_2$.

Đầu dò quang học sau khi kéo được mạ phản xạ bằng phương pháp bốc bay nhiệt. Trong quá trình mạ, đầu dò được đặt nghiêng 1 góc khoảng $20^0$ so với hướng bay hơi của kim loại, nhờ vậy mà phần đầu dò không bị kim loại che kín. Ảnh chụp một đầu dò trước và sau khi mạ được trình bày trong hình 2.

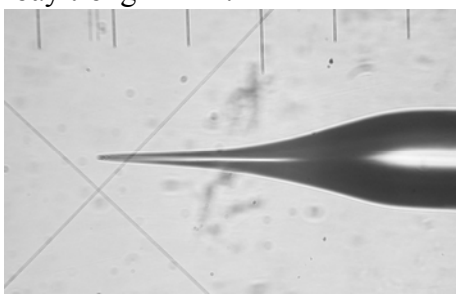
a)

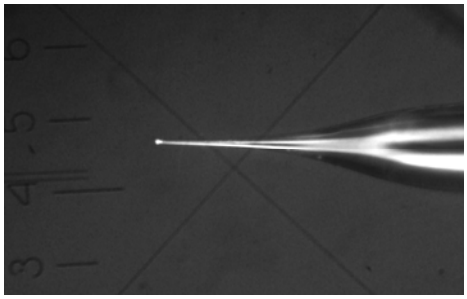
b)

**Hình 2.** Ảnh chụp đầu dò quang học. a) chưa có lớp mạ; b) lớp mạ bằng nhôm và ánh sáng laser đỏ truyền qua đầu dò.

### 3. Ghi phân bố cường độ sáng của ánh sáng khi đi qua đầu dò.

Sơ đồ thực nghiệm đo phân bố cường độ ánh sáng sau khi đi qua đầu dò quang học được trình bày trên hình 3. Tia laser ánh sáng đỏ ( $\lambda = 680nm$ ) được hội tụ bởi thấu kính và được đưa vào đầu dò. Khi đi qua phần vuốt nhọn của đầu dò, nhờ có lớp mạ phản xạ mà ánh sáng không đi ra ngoài mà truyền qua đầu dò, mặc dù đã bị suy giảm cường độ. Đầu dò được đặt vuông góc và rất gần ma trận CCD (khoảng cách từ đầu dò đến CCD, $h = 3 \div 4$ *mm*). Toàn bộ đầu dò và CCD được đặt trong 1 hộp tối để giảm nhiễu.

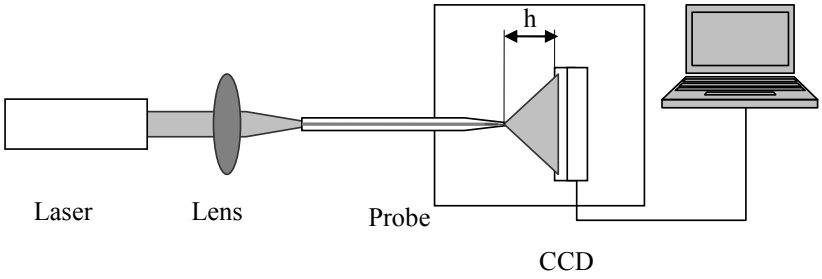


**Hình 3**. Sơ đồ thí nghiệm ghi phân bố cường độ ánh sáng sau khi đi qua đầu dò quang học.

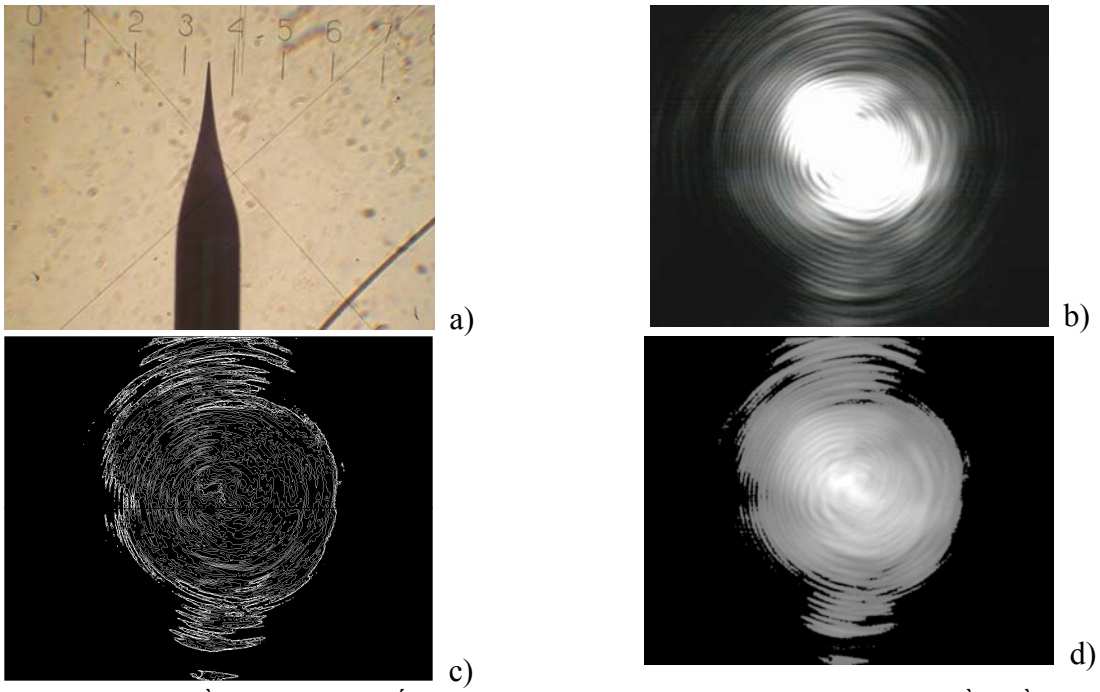


**Hình 4**. a) ảnh chụp đầu dò; b) phân bố cường độ sáng ghi bởi CCD không sử dụng phần mềm, khoảng cách từ đầu dò đến CCD là 3 mm; c) tập hợp các đường isophoto; d) phân bố cường độ sáng thu được khi sử dụng phần mềm.

Một chương trình phần mềm được viết cho CCD nhằm nâng cao khả năng ghi nhận tín hiệu của CCD. Thông thường, để CCD có thể ghi được những tín hiệu yếu, cần phải tăng độ nhạy và thời gian phơi sáng của CCD. Tuy nhiên khi đó những tín hiệu có cường độ lớn sẽ bị bão hòa trên hình ảnh ghi được, và chúng ta sẽ mất thông tin về phân bố cường độ sáng ở vùng tín hiệu có cường độ mạnh. Để giải quyết vấn đề này, chúng tôi đã ứng dụng phương pháp isophotometry, theo đó phần mềm sẽ tự động điều khiển CCD-camera để ghi lại một loạt các hình ảnh với thời gian phơi sáng khác nhau, từ nhỏ đến lớn. Với mỗi thời gian phơi sáng nhất định, ta thu được một đường isophoto. Từ tập hợp các đường isophoto phân bố cường độ sáng sẽ được xây dựng lại [7].

Theo phương pháp isophotometry thì dải cường độ sáng có thể ghi lại được chỉ phụ thuộc vào khả năng thay đổi thời gian phơi sáng của CCD. Trong các thí nghiệm của mình, chúng tôi sử

dụng CCD đen trắng VAC-135 có dải thời gian phơi sáng tương đối từ 1÷2047, và do đó phân bố cường độ sáng cực đại và cực tiểu ghi được có tỷ lệ $I_{\max}/I_{\min} \approx 10^3 - 10^4$, trong khi đó, nếu không sử dụng phần mềm thì tỷ lệ này chỉ là $10^2$.

Kết quả đo và sử phân bố cường độ sáng sử dụng phương pháp isophtometry được trình bày trên hình 4.

## 4. Một số kết quả ghi phân bố cường độ sáng

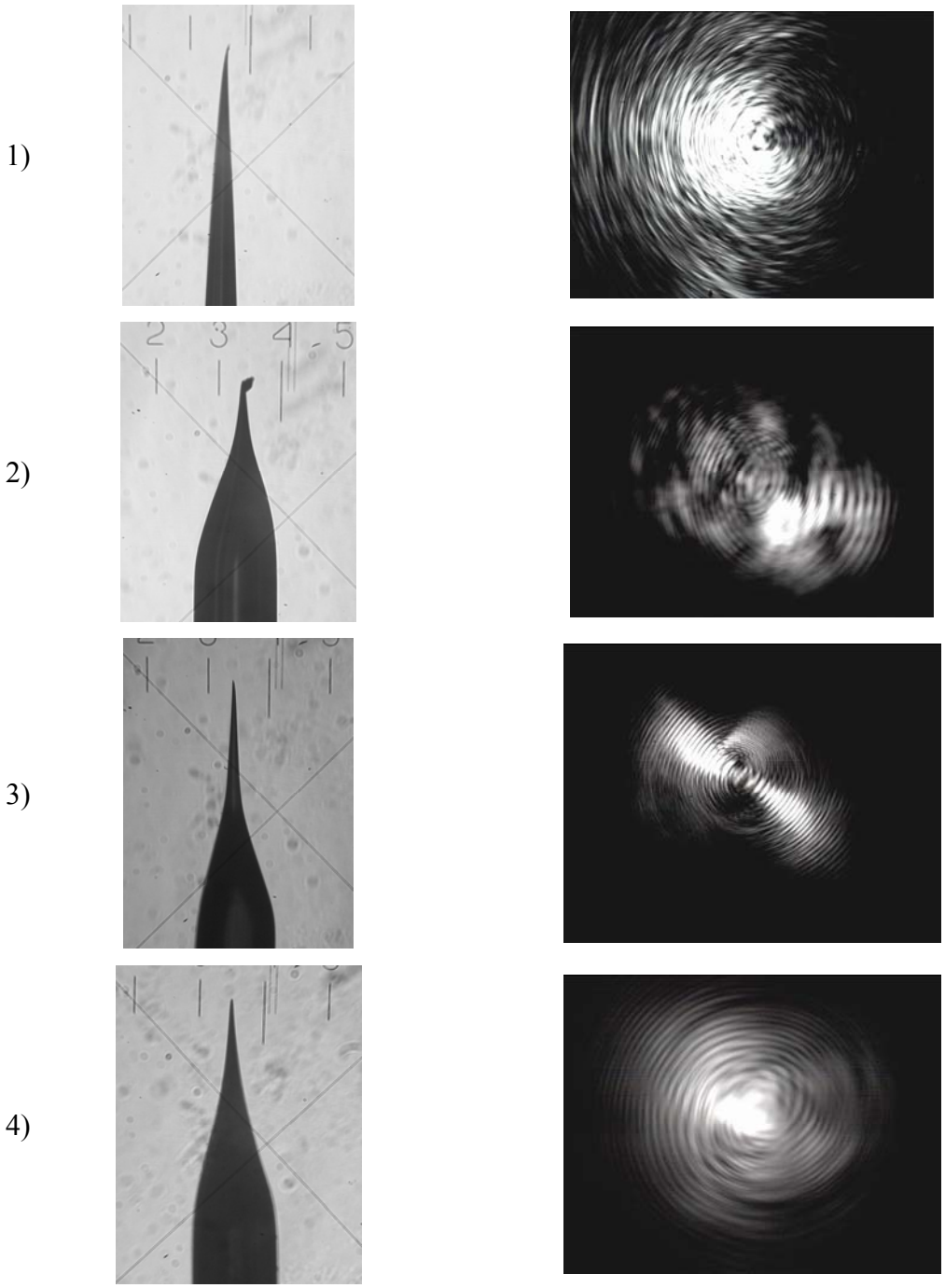


Hình 5. Đầu dò quang học và phân bố cường độ sáng tương ứng. Khoảng cách từ đầu dò đến CCD là 4 mm.

Một số hình ảnh của đầu dò và hình ảnh phân bố cường độ sáng tương ứng được trình bày trong hình 5. Căn cứ vào ảnh chụp đầu dò qua kính hiển vi quang học và phân bố cường độ sáng tương ứng, chúng ta có thể rút ra một số kết luận như sau:

- Đầu dò bị cong (đầu dò 1) cho phân bố nửa sáng nửa tối.
- Hạt kim loại dính trên đầu dò (tạo ra trong quá trình mạ) gây ra điểm sáng chói trên phân bố cường độ sáng (đầu dò 2).
- Đầu dò 3 có dạng elip, và do đó trong phân bố cường độ sáng có 2 cánh sáng chói. Hai cánh này song song với đường kính lớn của elip.
- Một đầu dò chất lượng tốt sẽ cho phân bố cường độ sáng tròn đều và đối xứng
- Trên các hình ảnh phân bố cường độ sáng đều có cấu trúc dạng vân, đó là kết quả của giao thoa ánh sáng giữa các điểm sáng có cường độ mạnh là tâm và cạnh của đầu dò [8, 9].

## 5. Phương pháp quang học đánh giá kích thước đầu dò qua phân bố cường độ sáng.

Như đã nói ở trên, việc đánh giá kích thước của đầu dò có ý nghĩa quan trọng, vì đầu dò quy định khả năng phân giải của thiết bị hiển vi. Riêng đối với đầu dò quang học thì kích thước ở đây được hiểu là kích thước của nguồn sáng, nó cũng gần với kích thước của đầu dò.

Trên cơ sở phân bố cường độ sáng ghi được tại mặt phẳng vuông góc với đầu dò, có thể tái tạo lại phân bố cường độ sáng tại mặt phẳng chứa đầu dò bằng phương pháp biến đổi Fourier ngược. Tuy nhiên, để thực hiện biến đổi Fourier ngược, chúng ta cần biết phân bố biên độ phức, tức là ngoài phân bố về biên độ cần phải biến cả phân bố về pha. Trong trường hợp này, do kích thước của đầu dò nhỏ hơn bước sóng, nên sóng truyền tới đầu dò được coi là sóng phẳng, còn sóng khi đi qua đầu dò sẽ có mặt sóng hình cầu. Nhờ đó, biết khoảng cách từ đầu dò đến CCD, ta có thể tính được phân bố về pha của ánh sáng trên mặt phẳng của ma trận CCD. Khi biết phân bố ánh sáng trên cả về biên độ và pha, ta có thể tái tạo lại phân bố ánh trên trên mặt phẳng vuông góc chứa đầu dò. Kết quả được biểu diễn trên hình 6.

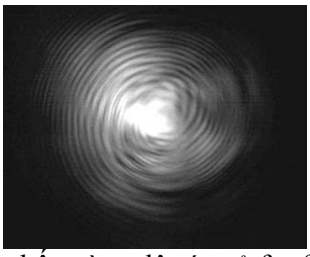

Phân bố cường độ sáng ở far-field

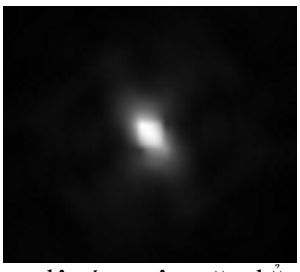

Phân bố cường độ sáng trên mặt phẳng vuông góc chứa đầu dò

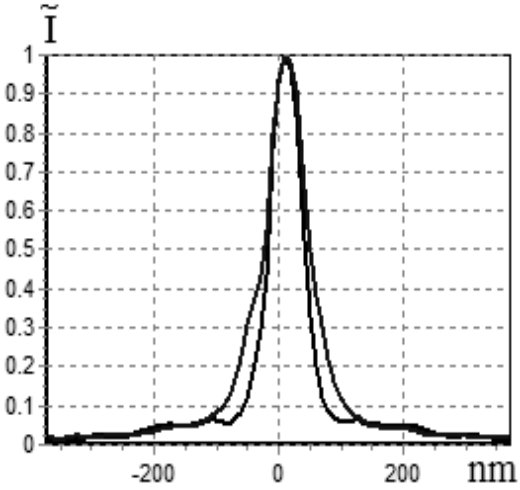


Đường cong cường độ sáng tại tâm của đầu dò (theo phương thẳng đứng và nằm ngang)

**Hình 6.** Phân bố ánh sáng trên mặt phẳng vuông góc chứa đầu dò

Để so sánh, chúng tôi cũng sử dụng những phương pháp khác để đánh giá kích thước của cùng một đầu dò. Trên hình 7a là ảnh chụp của đầu dò nhờ kính hiển vi điện tử. Hình 7b biểu diễn hình ảnh của đầu dò kiểm tra bằng thiết bị hiển vi quét đầu dò sử dụng lực phân tử, và hình 7c biểu diễn kết quả của phương pháp đánh giá thong qua phân bố cường độ sáng ở far-field. Cả 3 phương pháp trên đều cho kết quả giống nhau ($d \approx 320$ nm).

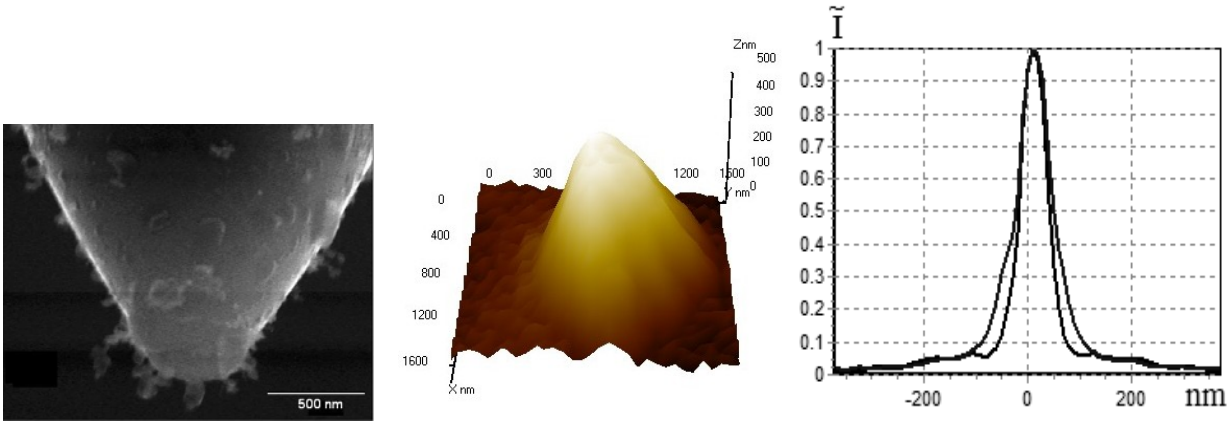


a) b) c)

Hình. 7. Đánh giá kích thước đầu dò bằng các phương pháp khác nhau.

## 6. Kết luận

Thông qua phân bố cường độ sáng ở far-field có thể tái tạo lại phân bố cường độ sáng tại chính đầu dò, qua đó có thể đánh giá được kích thước của đầu dò quang học. Để phục vụ cho bài toán này chúng tôi đã xây dựng thành công phần mềm cho phép mở rộng dải đo của CCD theo nguyên lý isophotometry, nhờ đó mà nhận được nhiều thông tin hơn về phân bố cường độ sáng, đồng thời phần mềm cũng cho phép phục hồi lại phân bố cường độ sáng trên đầu dò, qua đó có thể đánh giá được kích thước cũng như chất lượng của nó. Kết quả đo theo phương pháp đã đề xuất hoàn toàn phù hợp với các phương pháp tin cậy khác như sử dụng kính hiển vi điện tử hay sử dụng thiết bị hiển vi quét đầu dò.

### Tài liệu tham khảo

1. Heinzmann, D. W. Pohl. Scanning Near-field optical microscopy, App. Phys. A,Vol.59, 1994, 89-101.
2. C. Obermuller, K. Karrai. Far field characterization if diffracting circular apertures, Appl. Phys. Lett., **67** (23), 1995, 3408-3410.
3. Вейко В.П., Вознесенский Н.Б., Гусев А.Е., Иванова Т.В., Родионов С.А. Возможность определения параметров вторичных источников света, меньших длины волны, по характеристикам дальнего поля, Оптический журнал. Т. 65. № 10, 1998, 49-53.
4. D. Van Labeke, D. Barchiesi, F. Baida. Optical characterization of nanosources used in scanning near-field optical microscopy, J. Opt. Soc. Am. A, Vol. 12(4), 1995, 695-703.
5. K. A. Atlasov, V. P. Veiko, A. I. Kalachev. Technology Optimization of the Laser – Assisted SNOM – Tips Stretching, Proceedings of SPIE, V. 5399, 2003, 63-68.
6. Dương Chí Dũng, "Nghiên cứu chế tạo đầu dò nano tích hợp dùng cho thiết bị hiển vị quét đầu dò", luận án tiến sỹ 2007, Thư viện quốc gia.
7. В.К. Кирилловский, Ле Зуй Туан. Фундаментальные проблемы широкодипазонного исследования электромагнитного излучения и новый подход к разработке методов и аппаратуры, Международный оптический конгресс "Оптика - XXI век". Санкт-Петербург, 16 - 20 Октября 2006г.
8. Н. Б. Вознесенский. Математическое моделирование процессов распространения и дифракции света в наноструктурах, Сборник материалов всероссийского совещания "Зондовая микроскопия-2000". Нижний Новгород. 28 февраля-2 марта 2000 г. С.142-146.
9. D. J. Shin, A. Chavez-Pirson, S. H. Kim, S. T. Jung, and Y. H. Lee. Diffraction by a subwavelength-sized aperture in a metal plane. J. Opt. Sco. Am. A, Vol. 18, No 7.2001

# ẢNH HƯỞNG CỦA THAM SỐ CHIRP TỚI XUNG SÁNG TRONG HỆ THÔNG TIN QUANG

**Mai Thị Huệ, Trịnh Đình Chiến**

ĐHKH Tự nhiên, Đại học Quốc gia Hà nội

**Tóm tắt:** Bằng việc sử dụng phương trình truyền cơ bản, chúng tôi đã khảo xung lối vào dạng Gauss có chirp tuyến tính khi truyền qua sợi quang đơn mode sẽ bị mở rộng hoặc bị nén trên đường truyền. Sự mở rộng xung hay nén xung còn phụ thuộc vào tham số chirp và khoảng cách truyền. Sự ảnh hưởng của độ rộng phổ của nguồn quang học lên tốc độ bit cũng được khảo sát.

## 1. Mở đầu

Khi sử dụng hệ thông tin quang gặp phải một số vấn đề như: hao phí, tán sắc trên đường truyền … Sử dụng bộ khuếch đại quang sẽ giải quyết tốt được hao phí trên đường nhưng vấn đề tán sắc vẫn còn nhiều khó khăn. Để giảm ảnh hưởng của tán sắc vận tốc nhóm, có thể dùng nguồn laser có độ rộng dải hẹp và hoạt động gần với bước sóng tán sắc bằng không $\lambda_{ZD}$ của sợi quang [1 - 4]. Tuy nhiên trong thực tế để làm được điều này rất khó.

Do vậy bằng phương trình truyền xung cơ bản, khảo sát xung dạng Gauss có chirp tuyến tính sẽ bị mở rộng hoặc bị nén do tán sắc gây ra trên đường truyền. Đồng thời đã đánh giá được sự ảnh hưởng của độ rộng phổ của nguồn quang học và khoảng cách truyền lên tốc độ bít trong hệ thông tin quang dùng sợi quang đơn mode.

## 2. Phương trình cơ bản

Phương trình truyền xung cơ bản trong sợi quang đơn mode [1]:

$$\frac{\partial A}{\partial z}+\beta_1\frac{\partial A}{\partial t}+\frac{i}{2}\beta_2\frac{\partial^2 A}{\partial^2 t}-\frac{1}{6}\beta_3\frac{\partial^3 A}{\partial^3 t}=0 \qquad (1)$$

Trong đó: β là hằng số truyền. Với $\Delta\omega << \omega_0$, khai triển $\beta(\omega)$ theo chuỗi Taylor xung quanh tần số $\omega_0$ và lấy đến thừa số khai triển bậc 3:

$$\beta(\omega)=\bar{n}(\omega)\frac{\omega}{c}\approx\beta_0+\beta_1(\Delta\omega)+\frac{1}{2}\beta_2(\Delta\omega)^2+\frac{1}{6}\beta_2(\Delta\omega)^3 \qquad (2)$$

$A(z,t)$ biên độ biến đổi chậm:

$$A(z,t)=\frac{1}{2\pi}\int_{-\infty}^{\infty}d(\Delta\omega)\tilde{A}(0,\Delta\omega)\times\exp\left[i\beta_1 z\Delta\omega+\frac{i}{2}\beta_2 z(\Delta\omega)^2+\frac{i}{6}\beta_3 z(\Delta\omega)^3-i\Delta\omega t\right]$$

## 3. Ảnh hưởng của xung laser có chirp truyền qua sợi quang đơn mode

Giả sử xung laser dạng Gauss truyền qua sợi quang có biên độ lối vào:

$$A(0,t)=A_0\exp\left[-\frac{1+iC}{2}\left(\frac{t}{T_0}\right)^2\right] \qquad (4)$$

C là tham số chirp tần số tuyến tính: $\delta\omega(t)=-\frac{\partial\Phi}{\partial t}=\frac{C}{T_0^2}t$. Nghiệm có dạng :

$$A(z,t)=\frac{1}{2\pi}\int_{-\infty}^{\infty}\tilde{A}(0,\Delta\omega)\exp\left(\frac{i}{2}\beta_2 z\omega^2+\frac{i}{6}\beta_3 z\omega^3-i\omega t\right)d\omega \qquad (5)$$

Với $\tilde{A}(0,\omega) = A_0\left(\frac{2\pi T_0^2}{1+iC}\right)^{1/2} \exp\left[-\frac{\omega^2 T_0^2}{2(1+iC)}\right]$ là hàm biến đổi Fourier của A(0,t).

Nếu bước sóng mang khá xa bước sóng tán sắc bằng zero ($\beta_3 \approx 0$) thì:

$$A(z,t) = \left(\frac{A_0 T_0}{\left[T_0^2 - i\beta_2 z(1+iC)\right]^{1/2}}\right)\exp\left(-\frac{(1+iC)t^2}{2\left[T_0^2 - i\beta_2 z(1+iC)\right]}\right) \qquad (6)$$

Phương trình (6) chỉ ra xung Gauss vẫn giữ nguyên dạng Gauss trên đường truyền và độ rộng xung thay đổi theo khoảng cách truyền z:

$$\frac{T_1}{T_0} = \left[\left(1+\frac{C\beta_2 z}{T_0^2}\right)^2 + \left(\frac{\beta_2 z}{T_0^2}\right)^2\right]^{1/2} \qquad (7)$$

Hệ số mở rộng $T_1/T_0$ là hàm của khoảng cách truyền $z/L_D$, $L_D = T_0^2/|\beta_2|$ là độ dài tán sắc được dùng như một phép đo chuẩn hoá thích hợp đối với khoảng cách z để đánh giá ảnh hưởng của tán sắc.

$$\frac{T_1}{T_0} = \left[\left(1+C\frac{z}{L_D}\right)^2 + \left(\frac{z}{L_D}\right)^2\right]^{1/2} \qquad (8)$$

$$z_{\min} = \left[|C|/\left(1+C^2\right)\right]L_D; \quad T_1^{\min}/T_0 = 1/\left(1+C^2\right)^{1/2} \qquad (9)$$

Việc tạo ra xung có chirp bị nén một cách thích hợp rất thuận lợi trong việc thiết kế các hệ thông tin quang. Với $C\beta_2 < 0$ xung bị nén trên đường truyền sau đó mở rộng đồng nhất.

Tuỳ thuộc vào các tham số chirp khác nhau của xung truyền qua sợi quang đơn mode và hệ số tán sắc sợi quang ($\beta_2 > 0$) sẽ mở rộng đồng nhất hoặc bị nén xung và đạt giá trị nén xung tối ưu sau đó mở rộng đồng nhất ở khoảng cách truyền nhất định (hình 1). Khi C = 0, xung mở rộng trên đường truyền với hệ số $\left[1+\left(z/L_D\right)^2\right]^{1/2}$. Khi C > 0, xung mở rộng đồng nhất trên đường truyền. Khi C < 0, ban đầu xung bị nén tới khoảng cách truyền tối ưu sau đó lại bị dãn trên đường truyền ; $C_1$ = -0,5 thì $T_1^{\min} = 0,89T_0$, $z_{\min} = 0,4L_D$, $C_2$ = -2: $T_1^{\min} = 0,42T_0$, $z_{\min} = 0,4L_D$, $C_3$ = -3: $T_1^{\min} = 0,32T_0$, $z_{\min} = 0,3L_D$.

Như vậy thực nghiệm sẽ tuỳ chọn xung có thông số C truyền qua sợi quang với độ dài xác định để xung bị nén tối ưu và mở rộng đồng nhất sử dụng nén xung sáng ngoài buồng cộng hưởng thu được xung cực ngắn. Trong truyền dẫn xung dạng soliton lựa chọn thông số phù hợp để bù trừ tự biến điệu pha để dạng xung không thay đổi.

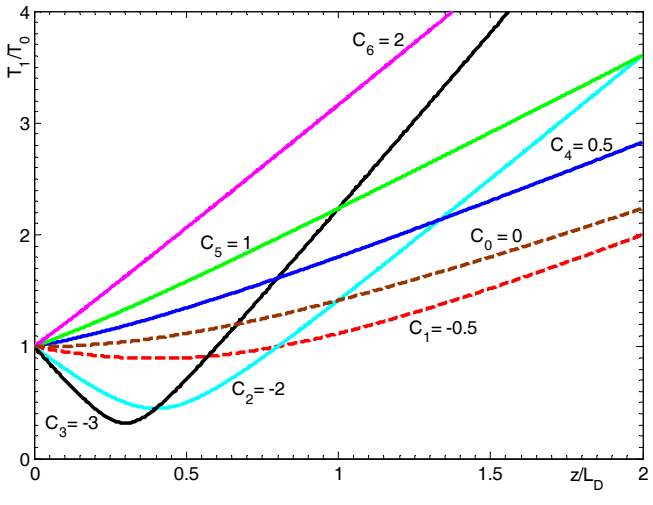


**Hình 1**: Hệ số mở rộng xung phụ thuộc vào khoảng cách truyền $\beta_2 > 0$

## 4. Giới hạn tốc độ bit khi xung laser truyền trong thông tin quang

Khi xét tới tán sắc bậc cao ( $\beta_3 \neq 0$ ), nguồn quang có độ rộng phổ lớn, với nguồn dạng Gauss có độ rộng phổ RMS $\sigma_\omega$ thì hệ số mở rộng [1]:

$$\frac{\sigma}{\sigma_0} = \left[ \left( 1 + \frac{C\beta_2 L}{2\sigma_0^2} \right)^2 + \left( 1 + V_\omega^2 \right) \left( \frac{\beta_2 L}{2\sigma_0^2} \right)^2 + \left( 1 + C^2 + V_\omega^2 \right) \frac{1}{2} \left( \frac{\beta_3 L}{4\sigma_0^3} \right)^2 \right]^{1/2} \quad (10)$$

$V_\omega = 2\sigma_\omega \sigma_0$; $\sigma_0$ là độ rộng RMS của xung vào dạng Gauss ( $\sigma_0 = T_0 / \sqrt{2}$ ):

Giới hạn tốc độ bit của hệ thông tin quang dùng sợi quang đơn mode do tán sắc sợi quang sẽ khác nhau và phụ thuộc vào độ rộng phổ nguồn.

### *4.1. Các nguồn quang học có độ rộng phổ lớn ( $V_\omega >> 1$ )*

Bỏ qua ảnh hưởng của chirp tần số (C = 0), chỉ khảo sát ảnh hưởng của tán sắc sợi quang vào tốc độ truyền thông tin trong sợi quang.

- *Hệ thông tin hoạt động ở xa vùng bước sóng tán sắc zero ( $\beta_3 \approx 0$ )*

Do C = 0 và $V_\omega >> 1$, (13) trở thành:

$$\frac{\sigma}{\sigma_0} = \left[ 1 + \left( \frac{\beta_2 L \sigma_\omega}{\sigma_0} \right)^2 \right]^{1/2} = \left[ 1 + \left( \frac{DL\sigma_\lambda}{\sigma_0} \right)^2 \right]^{1/2} \quad (11)$$

$\sigma_\lambda$ là độ rộng phổ nguồn RMS, độ rộng xung lối ra: $\sigma = \left( \sigma_0^2 + \sigma_D^2 \right)^{1/2}$

$\sigma_D = |D| L \sigma_\lambda$ là độ mở rộng phổ do tán sắc.

Khoảng thời gian của rãnh bít $T_B = 1/B$, thông thường $\sigma \leq T_B / 4$ thì khoảng 95% năng lượng xung vẫn duy trì trong rãnh bít. Trong giới hạn $\sigma_D >> \sigma_0, \sigma \approx \sigma_D = |D| L \sigma_\lambda$

$$BL|D|\sigma_\lambda \leq 1/4 \quad (12)$$

Xét laser màu có $\sigma_\lambda$ = 5 nm, D = 17 ps/( km - nm), $L_{max}$ = 18 km ta được sự phụ thuộc của tốc độ bit vào khoảng cách truyền trong sợi quang (hình 2).

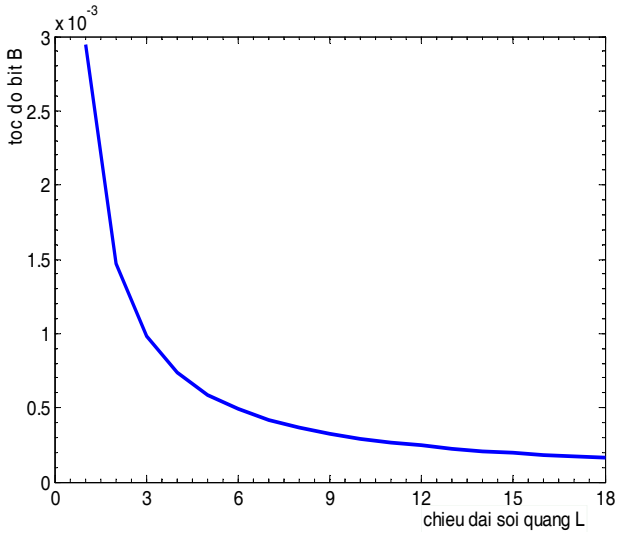


**Hình 2**: B(L) khi $\beta_3 \approx 0$

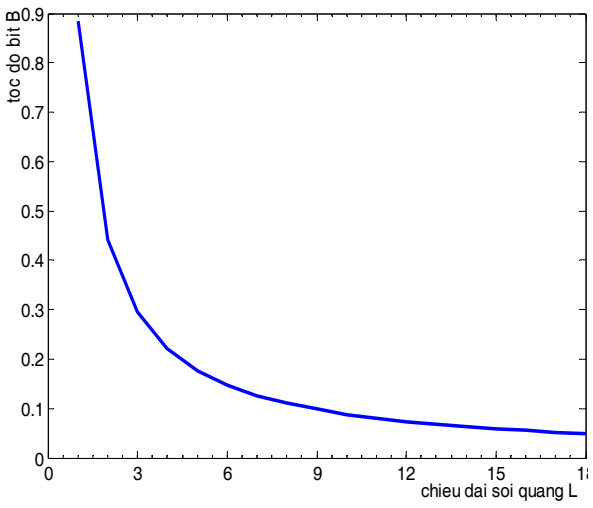


**Hình 3**: B(L) khi $\beta_2 \approx 0$

- *Hệ thông tin hoạt động tại bước sóng tán sắc* zero *( $\beta_2 = 0$ )*

Do C = 0 và $V_\omega >> 1$, (10) có dạng:

$$\frac{\sigma}{\sigma_0}=\left[1+\frac{1}{2}\left(\frac{\beta_3 L\sigma^2{}_\omega}{\sigma_0}\right)^2\right]^{1/2}=\left[1+\frac{1}{2}\left(\frac{SL\sigma^2{}_\lambda}{\sigma_0}\right)^2\right]^{1/2} \qquad (13)$$

$\beta_3$ thay cho độ dốc tán sắc S, độ rộng xung lối ra:

$$\sigma=\left[\sigma_0^2+\left(SL\sigma_\lambda^2\right)^2/2\right]^{1/2}=\left(\sigma_0^2+\sigma_D^2\right)^{1/2} \qquad (14)$$

$\sigma_D=|S|L\sigma_\lambda^2/2$. Khi $\sigma_D >> \sigma_0$, có giới hạn vào tốc độ bit:

$$BL|S|\sigma_\lambda^2 \le 1/\sqrt{8} \qquad (15)$$

Xét laser màu có $\sigma_\lambda$ = 5 nm, D = 17 ps/( km - nm) tại λ =1,55 μm, L = 18 km, S = 0.08 ps(km – nm$^2$) ta được sự phụ thuộc của tốc độ bit vào khoảng cách truyền trong sợi quang (hình 3).

### *4.2. Nguồn quang học với độ rộng phổ nhỏ ($V_\omega << 1$)*

- *Hệ thông tin hoạt động ở xa vùng bước sóng tán sắc zero ($\beta_3 \approx 0$)*

  Từ (10) có:

$$\frac{\sigma}{\sigma_0}=\left[\left(1+\frac{C\beta_2 L}{2\sigma_0^2}\right)^2+\left(\frac{\beta_2 L}{2\sigma_0^2}\right)\right]^{1/2} \qquad (16)$$

Với trường hợp độ rộng phổ hẹp, sự mở rộng do tán sắc phụ thuộc vào độ rộng phổ ban đầu. Thực tế $\sigma$ có thể là nhỏ nhất bằng cách chọn giá trị tối ưu của $\sigma_0$. $\sigma_{\min}=\left(|\beta_2|L\right)^{1/2}$ khi $\sigma_0=\sigma_D=\left(|\beta_2|L/2\right)^{1/2}$.Với $4B\sigma \le 1$, tốc độ bit giới hạn:

$$B \le \frac{1}{2\beta_2 L\left(\left(1+C^2\right)+1\right)^{1/2}} \qquad (17)$$

### *Khảo sát sự phụ thuộc của tốc độ bit vào tham số chirp C*

Do ảnh hưởng của buồng cộng hưởng laser với L = 100 km, $\beta_2=20\,ps^2/km$ từ (17) ta được hình vẽ 4- hình 5

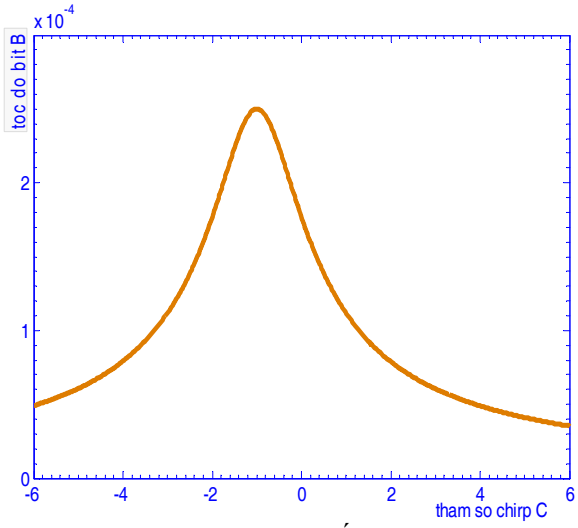


**Hình 4**: Sự phụ thuộc của tốc độ bit vào tham số chirp (λ xa $\lambda_{ZD}$)

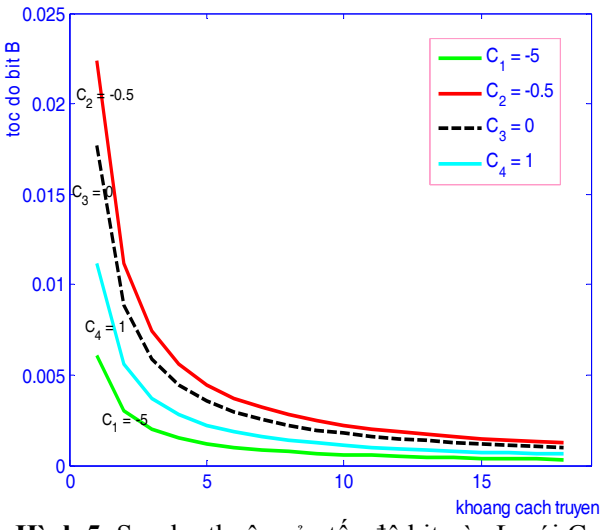


**Hình 5**: Sự phụ thuộc của tốc độ bit vào L với C khác nhau (λ xa $\lambda_{ZD}$)

- *Hệ thông tin hoạt động ở gần vùng bước sóng tán sắc zero ( $\beta_2 \approx 0$)*

  $V_\omega << 1$ và $\beta_2 \approx 0$, có độ rộng xung:

$$\frac{\sigma}{\sigma_0} = \left[1 + \left(1 + C^2\right)\frac{1}{2}\left(\frac{\beta_3 L}{4\sigma_0^3}\right)^2\right]^{1/2} \qquad (18)$$

  Khi giá trị tối ưu $\sigma_0 = \left(|\beta_3| L/4\right)^{1/3}$ thì:

$$\sigma_{\min} = \left(\frac{3 + C^2}{2}\right)^{1/2} \left(|\beta_3| L/4\right)^{1/3} \qquad (19)$$

  Với $4B\sigma \le 1$ thì giới hạn tốc độ bit :

$$B\left(|\beta_3| L\right)^{1/3} \le \frac{1}{2\sqrt{3 + C^2}} \qquad (20)$$

***Khảo sát sự phụ thuộc của tốc độ bit vào tham số chirp C***

Do ảnh hưởng của buồng cộng hưởng laser màu được đồng bộ mode bị động với L = 100 km, $\beta_3 = 0.1\, ps^3/km$ từ ta được hình vẽ 6 - hình 7.

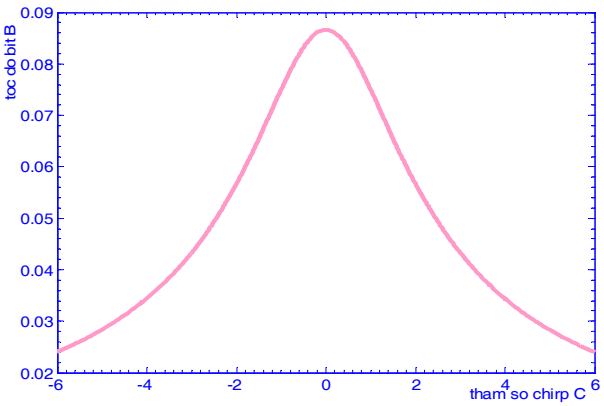


**Hình 6**: Sự phụ thuộc của tốc độ bit vào tham số chirp hoạt động gần $\lambda_{ZD}$

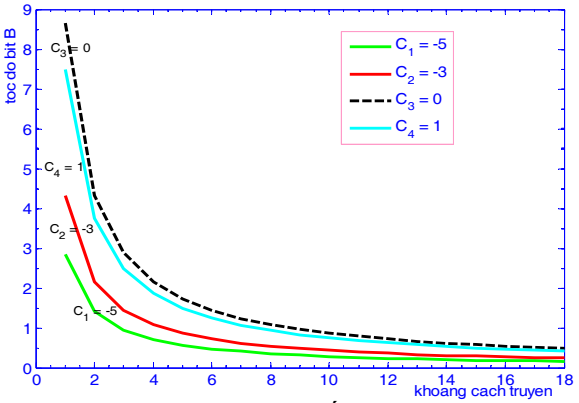


**Hình 7**: Sự phụ thuộc của tốc độ bit vào L với C khác nhau (λ gần $\lambda_{ZD}$)

Nhận xét:

Tuỳ thuộc vào nguồn quang học có độ rộng phổ lớn hay hẹp thì tốc độ bit truyền trong sợi quang phụ thuộc vào L và C là khác nhau.

Nguồn quang rộng (C = 0) (VD laser bán dẫn…) nếu bước sóng laser hoạt động xa $\lambda_{ZD}$ thì B sẽ lớn hơn so với trường hợp $\lambda_{Laser}$ hoạt động gần $\lambda_{ZD}$ trên cùng đường truyền.

Nguồn phổ hẹp (VD laser DFB) (chỉ khảo sát C = const): $\lambda_{Laser}$ gần $\lambda_{ZD}$ thì B luôn lớn hơn $\lambda_{Laser}$ xa $\lambda_{ZD}$ và đạt giá trị cực đại ở giá trị C xác định. (h4 và h5).

$V_\omega << 1$ thì ở những quãng đường truyền khác nhau với từng giá trị C thì B là khác nhau và có dạng hình6, hình 7.

Như vậy khảo sát sự phụ thuộc của B vào khoảng cách truyền, độ rộng nguồn laser chiếu vào sợi quang, dạng xung có chirp hoạt động ở dải bước sóng xác định thì thực nghiệm sẽ điều chỉnh được tốc độ truyền tin tối ưu và không bị hao phí trên đường truyền.

## 5. Kết luận.

- Khảo sát ảnh hưởng của tham số chirp của xung dạng Gauss truyền vào sợi quang đơn mode sẽ dãn xung hoặc bị nén xung trên đường truyền, nên thực nghiệm sẽ dễ dàng xác định xung qua sợi quang để sử dụng nén xung sáng ngoài BCH tạo xung cực ngắn.

- Nghiên cứu nguồn Laser phổ rộng và phổ hẹp ảnh hưởng tới tốc độ truyền tin và đánh giá được tốc độ bit tăng hay giảm trên đường truyền , phụ thuộc cả vào giá trị tham số chirp xác định của xung Laser.

**Tài liệu tham khảo**

1. Govind, P.Agranal , *Fiber – optical communication Systems*, Volume 1, John Wiley & Sons, Inc, 1997.
2. 2. Govind, P.Agranal, *Fiber – optical communication Systems*, Volume 2, John Wiley & Sons, Inc, 1997.
3. Pierr Halley, Fiber optic Systems; John Wiley & Sons, 1987.
4. G. Cerullo, S. Longhi, M. Nisoli, S. Stagira, and O. Svelto, *Problems in Laser Physics*, Klwer Academix Plenum Publishers, 2002.

# ẢNH HƯỞNG CỦA CHIRP TẦN SỐ VỚI CÁC XUNG SÁNG CÓ BƯỚC SÓNG KHÁC NHAU TRONG BUỒNG CỘNG HƯỞNG CỦA LASER MÀU ĐỒNG BỘ MODE

**Mai Thị Huệ, Trịnh Đình Chiến, Giang Mạnh Khôi**

ĐHKH Tự nhiên, Đại học Quốc gia Hà nội

**Tóm tắt**: Khảo sát ảnh hưởng của Chirp tần số gây ra bởi chất màu hoạt chất Laser Rh6G và chất hấp thụ bão hoà DODCI trên cơ sở xây dựng đường cong tán sắc của các chất màu đó. Trên cơ sở đó đánh giá ảnh hưởng của chirp tần số với các bước sóng hoạt động khác nhau của cộng hưởng Laser.

## 1. Mở đầu

Trong Laser màu dạng vòng được động bộ mode bằng phương pháp bị động, có nhiều yếu tố ảnh hưởng đến quá trình hình thành xung và những thông số của xung như: môi trường hoạt chất Laser, chất hấp thụ bão hoà dùng để đồng bộ mode bị động, sự phản xạ ở các gương …

Những ảnh hưởng này là rất quan trọng và một số vấn đề đã được khảo sát [1 - 4]. Tuy nhiên ở đây ta chỉ khảo sát ảnh hưởng của chirp tần số gây ra bởi chất màu hoạt chất Laser Rh6G và chất hấp thụ bão hoà DODCI trên cơ sở xây dựng đường cong tán sắc của các chất màu đó. Trên cơ sở đó đánh giá ảnh hưởng của chirp tần số đối với các bước sóng hoạt động khác nhau của buồng cộng hưởng Laser.

## 2. Phương trình cơ bản

Dựa trên lý thuyết điện tử cổ điển Lorentz đã giải thích thành công hiện tượng tán sắc [2]. Xuất phát từ phương trình chuyển động của điện tử khi có mặt của ánh sáng bên ngoài.

$$m\ddot{r} = -m\omega_1^2 r - gr + eE \qquad (1)$$

Trong đó: $f_1 = eE$ là lực cưỡng bức của trường sáng bên ngoài.

$f_2 = - kr = - m\omega^2_1 r$ là lực chuẩn đàn hồi.

$f_3 = - gr$ là lực hãm hay lực ma sát, $\frac{g}{m} = \gamma$: hệ số tắt dần.

Ánh sáng tức là sóng sáng đơn sắc tần số ω: $E = E_0 e^{ico.t}$

r: Ly độ dao động của điện tử quanh vị trí cân bằng.

m: Khối lượng của điện tử, e điện tích của điện tử.

Chiết suất n và hệ số hấp thụ k được xác định theo biểu thức:

$$\left[ n^2(\omega) = 1 + \frac{N_0 e^2}{\varepsilon_0 m}\left( \frac{\omega_1^2 - \omega^2}{\left[\left(\omega_1^2 - \omega^2\right)^2\right] + \omega^2\gamma^2} \right) \right]$$

$$n^2(\lambda) = 1 + \frac{N_0 e^2}{\varepsilon_0 m} \frac{\left(\lambda^2 - \lambda_1^2\right)\lambda_1^2\lambda^2}{\left[\left(\lambda^2 - \lambda_1^2\right)^2 2\pi c + \lambda_1^4\lambda^2\gamma^2\right]} \qquad (2)$$

Và

$$\left[ k(\omega) = \frac{\frac{N_0 e^2}{\varepsilon_0 m}\omega\gamma}{c\left[\left(\omega_1^2 - \omega^2\right)^2 + \omega^2\gamma^2\right]} \right]$$

$$k(\lambda) = \frac{N_0 e^2 \gamma \lambda_1^4 \lambda^3}{\varepsilon_0 mc\left[(2\pi c)^3\left(\lambda^2 - \lambda_1^2\right)^2 + (2\pi c)\gamma^2 \lambda_1^4 \lambda^2\right]} \quad (3)$$

Các biểu thức (2) và (3) cho ta đường cong tán sắc và đường cong hấp thụ.

## 3. Đường cong tán sắc và phổ hấp thụ đối với chất hấp thụ bão hoà DODCI và của hoạt chất màu Rh6G

### *3.1. Đường cong tán sắc và phổ hấp thụ đối với chất hấp thụ bão hoà DODCI.*

$C_{23}H_{23}N_2N$ là chất hấp thụ bão hoà thường dùng trong buồng cộng hưởng của laser màu. Từ phương trình (2) về mặt lý thuyết có thể giả sử phương trình chiết suất phụ thuộc vào bước sóng laser chiếu tới:

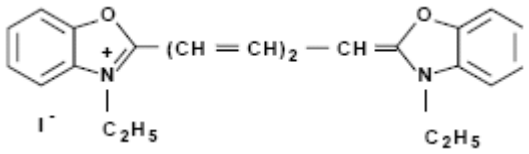


$$n^2(\lambda) = 1 + \frac{0{,}97864876.10^{-6}\left(\lambda^2 - 528^2\right)\lambda^2.528^2}{\left(\lambda^2 - 528^2\right)^2 + 528^4.9{,}6.10^{-9}} \quad (4)$$

Với hệ số tắt dần của môi trường $\gamma = 9{,}6.10^{-9}$, bước sóng dao động riêng của các điện tử trong phân tử DODCI là 528 nm.

Hệ số hấp thụ của DODCI phụ thuộc vào bước sóng laser màu:

$$k(\lambda) = \frac{131.10^{16}\lambda^2}{\left(\lambda^2 - 528^2\right)^2 + 94{,}86558.10^{-7}\lambda^2} \quad (5)$$

Dùng phần mềm Matlab ta được đường cong tán sắc và phổ hấp thụ của DODCI phụ thuộc vào bước sóng của laser màu chiếu tới trong $\lambda$ (300 ÷ 1000 nm).

Nhận xét:

Đường cong tán sắc của DODCI có tồn tại vùng tán sắc thường (chiết suất giảm khi bước sóng tăng) khi bước sóng ánh sáng tới $\lambda < 495$ nm ,$\lambda > 585$ nm và tán sắc dị thường (chiết suất tăng khi bước sóng tăng) khi bước sóng ánh sáng tới 495 ÷ 595 nm.

Phổ hấp thụ của DODCI đạt cực đại hấp thụ khi bước sóng đơn sắc chiếu tới $\lambda = 528$ nm.

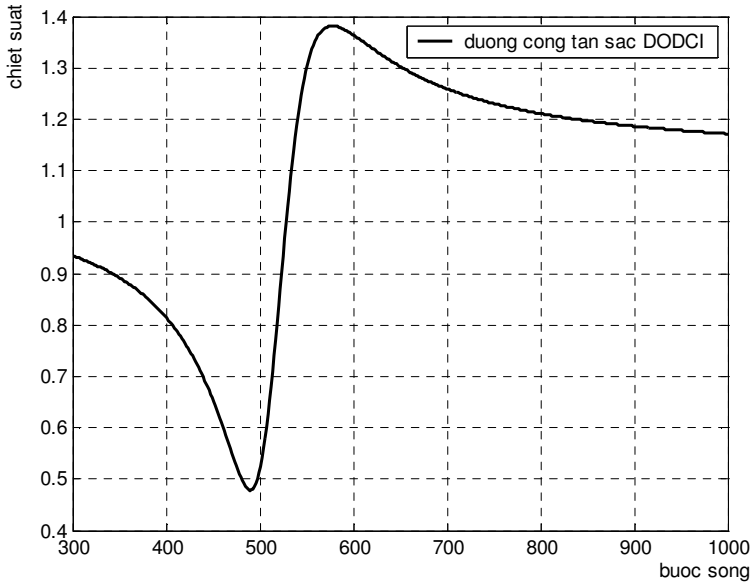


**Hình 1**: Đường cong tán sắc của DODCI

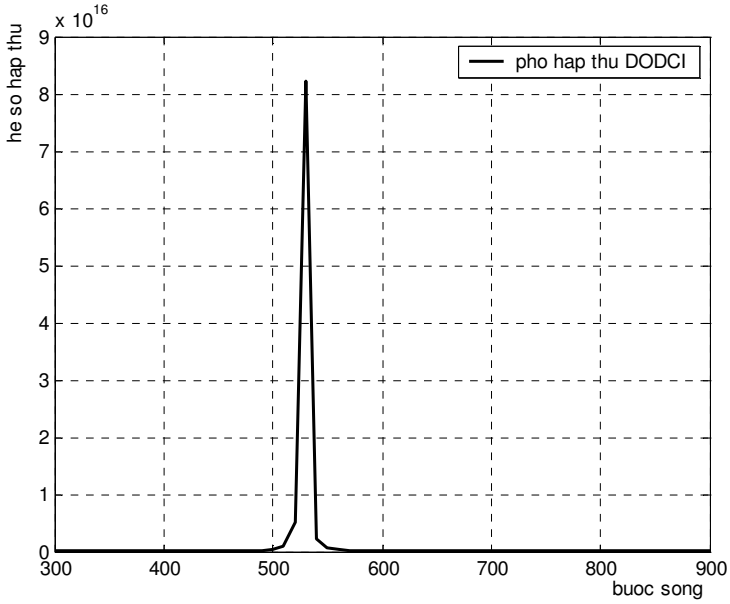


**Hình 2**: Phổ hấp thụ của DODCI

### *3.2. Đường cong tán sắc của hoạt chất màu Rhodamine 6G*

$C_{28}H_{31}N_2O_3Cl$ là một chất màu đã được thương mại hoá, hàng năm trên toàn thế giới đã bán được khoảng 150 tấn dùng làm hoạt chất trong buồng cộng hưởng laser màu. Cũng từ (2) giả sử phương trình chiết suất phụ thuộc vào bước sóng laser chiếu tới có dạng:

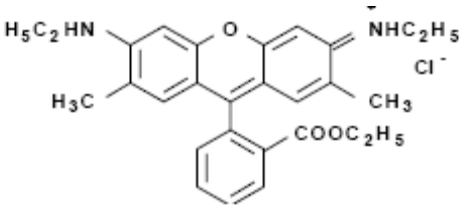

$$n^2(\lambda) = 1 - \frac{1{,}00014688.10^{-6}\left(\lambda^2 - 568^2\right)\lambda^2.568^2}{\left(\lambda^2 - 568^2\right)^2 + 568^4.2{,}99.10^{-9}} \qquad (6)$$

Có được đường cong tán sắc của Rhodamine 6 G như hình vẽ (3.3) khi bước sóng laser đồng bộ mode bị động chiếu tới trong vùng $(300 \div 1000)$ nm.

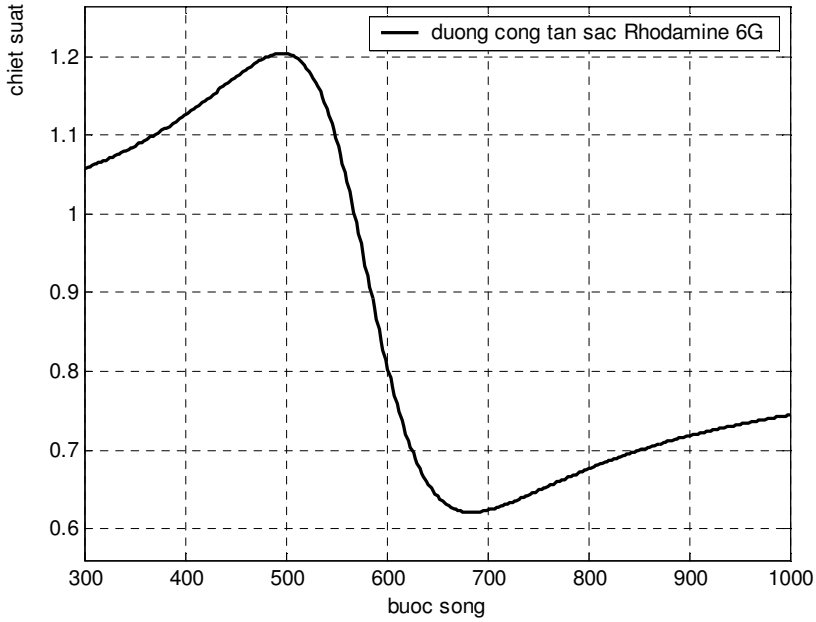


**Hình 3**: Đường cong tán sắc của Rhodamine 6G

Nhận xét:

Đường cong tán sắc của Rhodamine 6G tồn tại vùng tán sắc thường và tán sắc dị thường.

Khi bước sóng ánh sáng tới cỡ $\lambda < 500$ nm và $\lambda > 650$ nm thì có hiện tượng tán sắc thường. Khi bước sóng ánh sáng tới cỡ 500 ÷ 650 nm thì có hiện tượng tán sắc dị thường.

Đường cong tán sắc của Rhodamine 6G phù hợp với dạng đường thực nghiệm đã khảo sát trong trường hợp tạo xung cực ngắn đối với laser màu.

## 4. Ảnh hưởng của chirp do hoạt chất và do hấp thụ bão hoà

Dựa vào đường cong tán sắc ta có thể xác định được $\frac{dn}{d\lambda}$ và $\frac{d^2n}{d\lambda^2}$ của Rh6G và của DODCI.

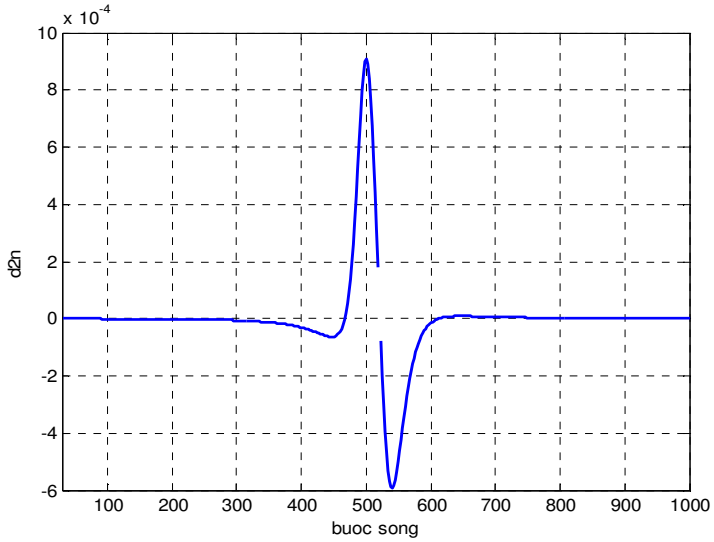


**Hình 4**: Đạo hàm bậc hai của chiết suất theo bước sóng của DODCI

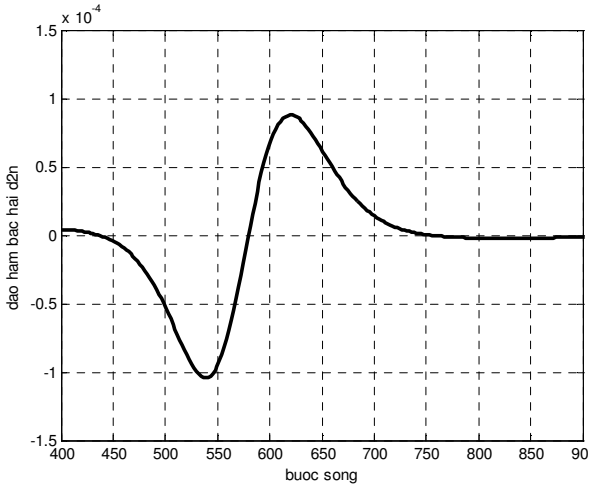


**Hình 5**. Đạo hàm bậc nhất của chiết suất theo bước sóng của Rh 6G

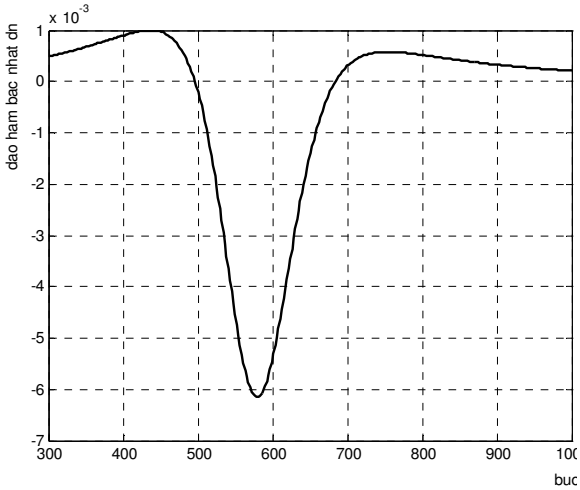


**Hình 6**. Đạo hàm bậc hai của chiết suất theo bước sóng của Rh 6G

*Nhận xét:*

Khi bước sóng laser biến thiên từ 450 ÷700 nm hoạt chất màu Rhodamine 6G tạo ra xung có upchirp hoặc downchirp.

Khi chiếu laser Ar $\lambda$ = 514,5 nm với Rhodamine 6G có $d^2n/d\lambda^2$=3,7868.$10^{-4}$; DODCI có $d^2n/d\lambda^2$=-7.7684.$10^{-5}$, phù hợp với thực nghiệm khi xung truyền qua chất khuếch đại thì sẽ tạo ra biến điệu tần số tăng (upchirp), khi qua môi trường hấp thụ bão hoà thì tần biến điệu tần số giảm (downchirp) dẫn đến việc bù trừ chirp và tạo ra xung cực ngắn.

Khi chiếu laser Ar $\lambda$ = 585 nm với Rhodamine 6G có $d^2n/d\lambda^2$=2,1536.$10^{-5}$; DODCI có $d^2n/d\lambda^2$=-6,6407.$10^{-5}$, phù hợp với thực nghiệm khi xung truyền qua chất khuếch đại thì sẽ tạo ra biến điệu tần số tăng (upchirp), khi qua môi trường hấp thụ bão hoà thì tạo biến điệu tần số giảm (downchirp) dẫn đến việc bù trừ chirp và tạo ra xung cực ngắn. Vì vậy thấy được tạo chirp trong buồng cộng hưởng laser màu đồng bộ mode bị động tạo ra xung cực ngắn cỡ fs.

Khảo sát sự ảnh hưởng của buồng cộng hưởng laser màu đối với một số bước sóng laser khi truyền qua môi trường khuếch đại Rhodamine 6G và chất hấp thụ bão hoà DODCI, ta có các bảng số liệu sau:

**Bảng 1**: Bảng số liệu thông số của DODCI theo bước sóng

| $\lambda$ (nm) | n($\lambda$) | dn/d$\lambda$ | $d^2n/d\lambda^2$ |
|---|---|---|---|
| 515 | 0,7391 | 0,0192 | 3,7868.$10^{-4}$ |
| 560 | 1,3560 | 0,0035 | -3,2214.$10^{-4}$ |
| 585 | 1,3786 | -6,6407.$10^{-4}$ | -6,4463.$10^{-5}$ |
| 605 | 1,3574 | -0,0013 | -0,83919.$10^{-5}$ |
| 630 | 1,3252 | -6,3524.$10^{-5}$ | 7,3466.$10^{-6}$ |

**Bảng 2**: Bảng số liệu thông số của Rhodamine 6G theo bước sóng

| $\lambda$ (nm) | n($\lambda$) | dn/d$\lambda$ | $d^2n/d\lambda^2$ |
|---|---|---|---|
| 515 | 1,1945 | -0,0011 | -7,7684.$10^{-5}$ |
| 560 | 1,0454 | -0,0054 | -7,2270.$10^{-5}$ |
| 585 | 0,8966 | 0,0061 | 2,1536.$10^{-5}$ |
| 605 | 0,7835 | -0,005 | 7,6499.$10^{-5}$ |
| 630 | 0,6839 | -0,0029 | 8,3928.$10^{-5}$ |

## 5. Kết luận

Khảo sát ảnh hưởng của chirp tần số với các xung sáng có bước sóng khác nhau trong buồng cộng hưởng của laser màu đồng bộ mode đã cho thấy nguyên nhân gây ra chirp là do sự tán sắc của hoạt chất màu laser và tán sắc của chất hấp thụ bão hoà. Ảnh hưởng của chirp tần số với các bước sóng khác nhau là khác nhau đối với hoạt chất và chất hấp thụ. Điều này cũng phù hợp với các thực nghiệm. Do vậy, tuỳ điều kiện cụ thể của bố trí thực nghiệm mà người ta tìm thấy các bù trừ chirp để đạt được xung cực ngắn phát từ laser một cách thích hợp.

***Lời cảm ơn**: Công trình được hoàn thành dưới sự hỗ trợ kinh phí của đề tài QT – 07 - 12.*

### Tài liệu tham khảo

1. C. Ruliliere, Femtosecond laser pulses, Springer - Verlag Berlin, 1998
2. J. Herrmann, B. Wilhelmi, Laser for Ultrashort Light pulses, Verlag - Berlin, 1986.
3. T.D.Chien and al, Investigating the pulse interactions in the saturable absorber, communication in Physics, Vol.12, No 3, 2002.
4. T.M.Hung, T.D.Chien, D.X.Khoa, communication in Physics, Vol.15, No2, 101 - 107 (2005)

# PHÁT TRIỂN MỘT HỆ THỐNG LASER Nd: $YVO_4$ MODE-LOCKING THỤ ĐỘNG PHÁT XUNG PICÔ-GIÂY CÓ TẦN SỐ XUNG THẤP

**Đỗ Quốc Khánh [a], Nguyễn Trọng Nghĩa [a], Nguyễn Đình Hoàng [a], Nguyễn Văn Hảo [b] và Nguyễn Đại Hưng [a]**

[a)] Trung tâm Điện tử học lượng tử, Viện Vật lý
Viện Khoa học và Công nghệ Việt Nam
[b)] Khoa KHTN&XH - Đại học Thái Nguyên

**Tóm tắt:** Những kết quả nghiên cứu và phát triển một hệ thống laser rắn Nd:$YVO_4$ được bơm liên tục bằng laser bán dẫn**,** phát xung picô-giây mode-locking tại 1064 nm với tần số xung thấp tới 8.8 MHz đã được trình bày. Sự hoạt động laser mode-locking thụ động thu được nhờ sử dụng một gương bán dẫn hấp thụ bão hoà (SESAM) trong một buồng cộng hưởng dài (15 m). Buồng cộng hưởng được thiết kế theo cấu hình phản xạ nhiều lần giữa hai gương cầu bán kính 2 m và được gập đôi bởi hai gương phẳng, nhờ vây hệ laser có thể bố trí trên bàn quang học (120 x 40 cm) mà không sử dụng một yếu tố quang học đặc biệt. Khi sử dụng công suất bơm 2000 mW ở 808 nm từ laser bán dẫn, hệ laser phát đoàn xung 10 ps với tần số xung 8.8 MHz có công suất trung bình 450 mW, tương ứng với công suất xung 5,5 kW. Một số ứng dụng của hệ laser này trong nghiên cứu quang tử cũng được trình bày.

## 1. Mở đầu

Các laser phát xung cực ngắn đang đóng vai trò quan trọng và không thể thiếu được ở các nghiên cứu quá trình động học xảy ra nhanh trong các lĩnh vực vật lý, sinh học, hoá học…, do vậy việc phát triển các nguồn laser rắn, mode-locking, phát xung cực ngắn đang rất được quan tâm [1-7]. Tuy nhiên, tần số xung lặp lại của các nguồn laser rắn, mode-locking bình thường là cao và nằm trong khoảng 60-80 MHz, điều này hạn chế rất nhiều ứng dụng của laser (do đối tượng đo và/hoặc hệ đo). Thực tế, các laser mode-locking có tần số xung lặp lại < 10 MHz là thích hợp cho các phép đo phân giải thời gian với các đối tượng có thời gian đáp ứng trong khoảng từ hàng trăm picô-giây đến vài trục nanô-giây (các đối tượng y-sinh học, hoá học). Vì mục đích này, các van điện-quang nhanh thường được sử dụng để giảm tần số xung lặp lại của các laser mode-locking, tuy nhiên một thiết bị van điện-quang như vậy là khá đắt (20 000 U$D), do vậy, một số giải pháp quang học khác đã được đề nghị [8-10]. Trong báo cáo này, chúng tôi trình bày những kết quả nghiên cứu và phát triển một hệ thống laser rắn Nd:$YVO_4$ được bơm liên tục bằng laser bán dẫn**,** phát xung picô-giây mode-locking tại 1064 nm với tần số xung <10 MHz. Sự hoạt động laser mode-locking thụ động thu được nhờ sử dụng một gương bán dẫn hấp thụ bão hoà (SESAM) trong một buồng cộng hưởng dài có cấu hình phản xạ nhiều lần giữa hai gương cầu (2 m) và được gập đôi bởi hai gương phẳng phản xạ toàn phần. Hệ laser được bố trí trên bàn quang học (120 x 40 cm) và không sử dụng các yếu tố quang học đặc biệt. Khi sử dụng công suất bơm 2000 mW ở 808 nm của một laser bán dẫn, hệ laser phát một đoàn xung 10 ps với công suất trung bình 450 mW, tương ứng với công suất xung 5,5 kW. Ứng dụng của hệ laser này trong nghiên cứu quang tử cũng được trình bày.

## 2. Tính toán mô phỏng quá trình truyền chùm laser trong BCH

Trên cơ sở nghiên cứu, tính toán và thiết kế để có được một buồng cộng hưởng laser mode-locking đủ dài (tần số xung lặp lại < 10 MHz), hoạt động laser mode-locking ổn định, hiệu suất laser cao và có cấu trúc thu gọn nhất có thể, chúng tôi đã phát triển cấu hình buồng cộng hưởng có sử dụng nhiều lần phản xạ giữa hai cặp gương cầu bán kính R = 2m và được gập đôi bằng hai gương phẳng (Hình 1), tương tự cấu hình [11]. Giả thiết chùm laser có phân bố Gauss, sử dụng lý thuyết hàm Gauss và ma trận truyền ABCD, quá trình truyền của chùm laser trong buồng cộng

hưởng đã được mô phỏng cũng như tính toán, lựa chọn tối ưu về vị trí các yếu tố quang học trong buồng cộng hưởng. Với cấu hình buồng cộng hưởng này (Hình 1), một số yếu tố quang học quan trọng có ảnh hưởng mạnh tới hoạt động của laser như vị trí của gương cầu $M_2$, $M_5$ và gương ra $M_{12}$ đã được nghiên cứu như được trình bày dưới đây.

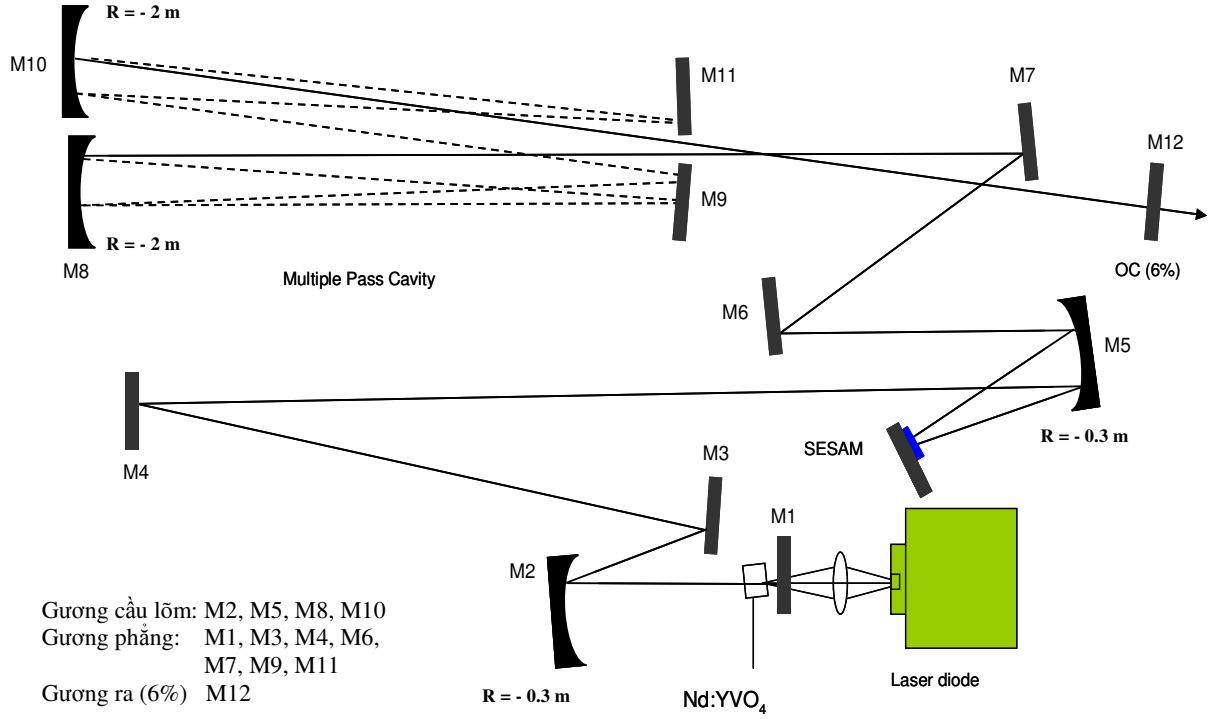


**Hình 1**. Cấu hình của BCH laser Nd:$YVO_4$ mode-locking thụ động bằng SESAM sử dụng cấu hình hai cặp gương phẳng – gương cầu để tạo nhiều lần phản xạ.

**2.** :nập

tốt nhất giữa vùng bơm và chùm laser, vì vậy ảnh hưởng trực tiếp đến hiệu suất của laser. Kết quả tính toán cho thấy khoảng dịch chuyển cho phép (so với vị trí gương cuối $M_1$) trong khoảng 154 ÷ 160 mm, vị trí tối ưu cỡ 158 mm.

### 2.2. Ảnh hưởng của vị trí gương cầu $M_5$

Gương cầu $M_5$ có chức năng hội tụ năng lượng laser trong BCH lên SESAM, làm bão hoà SESAM và đảm bảo cho laser hoạt động ở chế độ mode-locking. Khoảng dịch chuyển cho phép (so với vị trí SESAM) trong khoảng 152 ÷ 160 mm. Kết quả tính toán xác định được vị trí tối ưu cho gương cầu $M_5$ cỡ 154 mm.

### 2.3. Ảnh hưởng của vị trí gương ra $M_{12}$

Vị trí tương đối của gương ra $M_{12}$ với gương cầu $M_{10}$ có ảnh hưởng rất nhiều tới hiệu suất laser cũng như chế độ hoạt động mode-locking. Kết quả mô phỏng xác định được khoảng dịch chuyển cho phép trong khoảng 1 m ÷ 2.5 m và vị trí tối ưu cho gương ra $M_{12}$ cỡ 1 m.

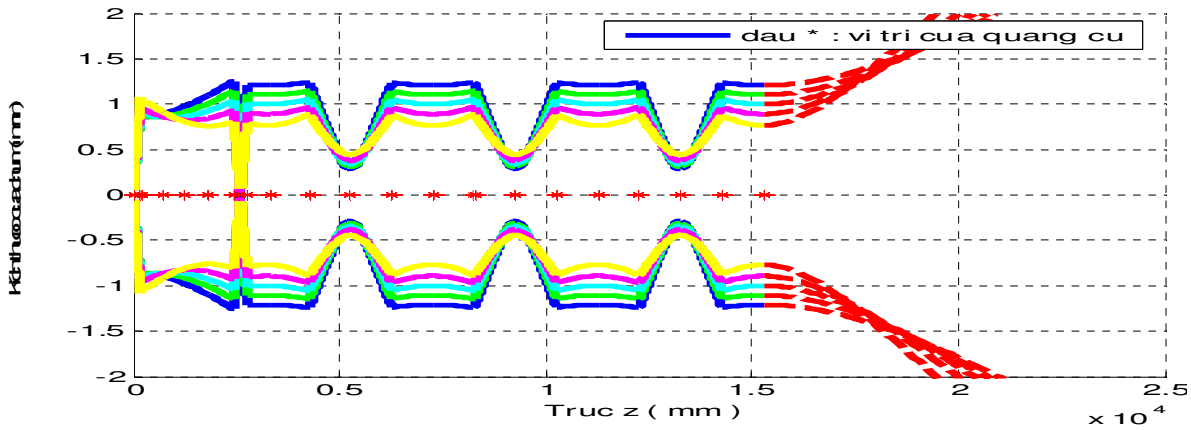


**Hình 2:** Ảnh hưởng của vị trí gương cầu $M_2$ đến chùm laser trong BCH.

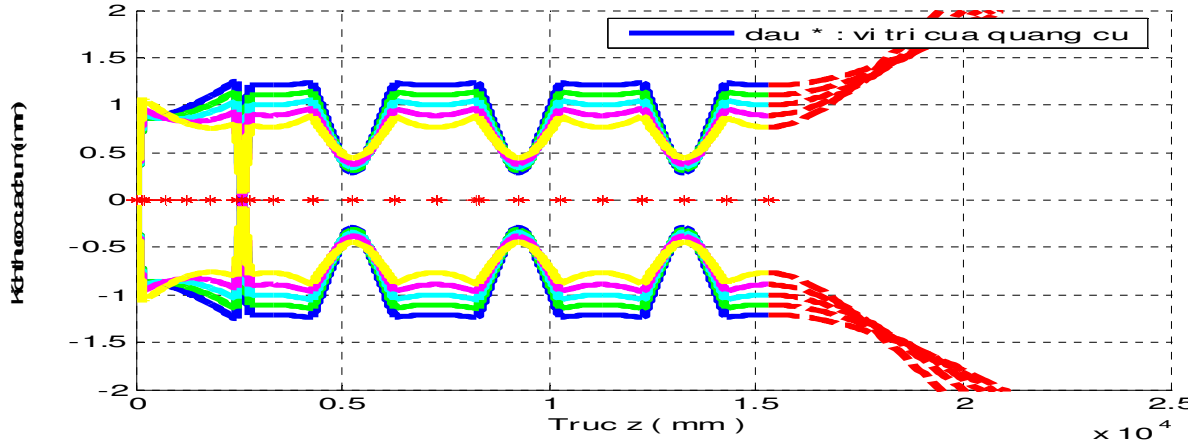


**Hình 3:** Ảnh hưởng của vị trí gương cầu $M_5$ đến chùm laser trong BCH.

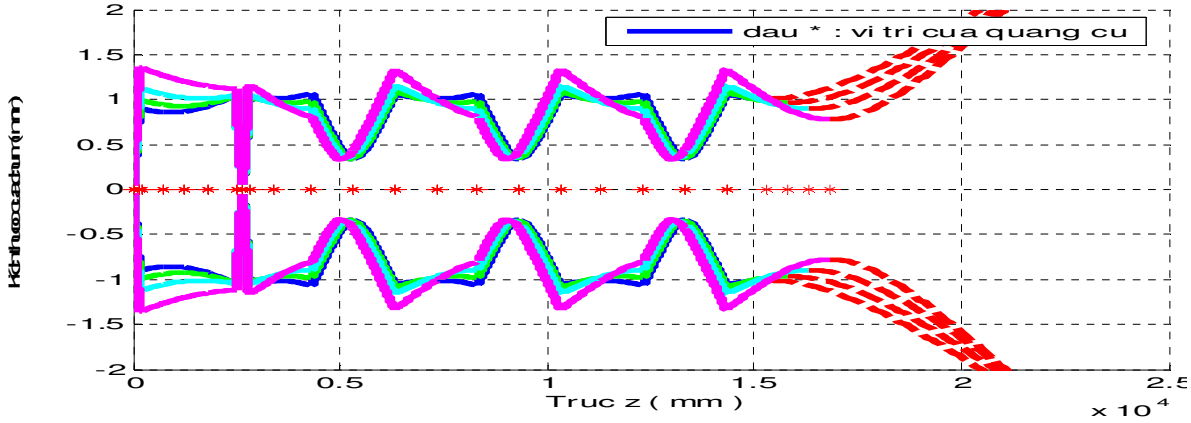


**Hình** ởng của vị trí gương ra đến chùm laser trong BCH.

## 3. Kết quả thực nghiệm

Dựa trên kết quả tính toán và mô phỏng quá trình laser trong BCH, kết hợp điều kiện thí nghiệm thực tế, chúng tôi đã lựa chọn được các thông số tối ưu cho các yếu tố quang học trong BCH laser như sau: khoảng cách từ gương cầu $M_2$ tới gương cuối $M_1$ là 158 mm, vị trí gương cầu $M_5$ cách SESAM 154 mm, gương ra cách gương $M_{10}$ 1,5 m. Với các thông số đã chọn, các đặc trưng của laser đã được nghiên cứu và trình bày trên Hình 5.

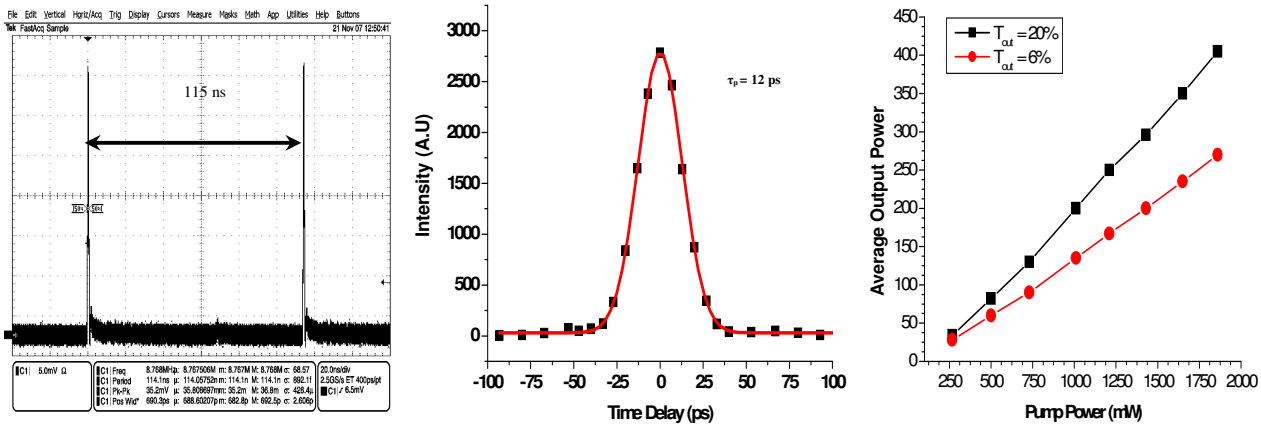


**Hình 5:** Đặc trưng của laser mode-locking.
a. Chuỗi xung mode-locking, b. Vết tự tương quan cường độ, c. Đặc trưng công suất của laser.

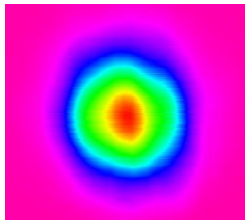

**Hình 6:** Phân bố năng lượng của chùm laser

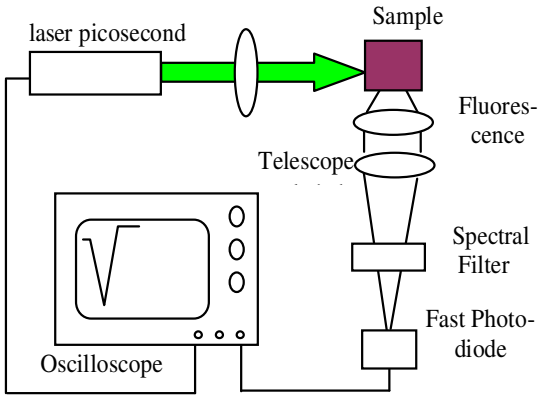


**Hình 7:** Hệ đo thời gian sống của phân tử.

Độ rộng xung thu được bằng phép đo tự tương quan cường độ là cỡ 10 ps, chu kì xung 115 ns (tương ứng với tần số lặp lại 8,8 MHz và chiều dài BCH khoảng 15,2 m). Qua việc nghiên cứu khảo sát phân bố cường độ của chùm laser ta thấy rằng: phân bố chùm laser có dạng phân bố Gauss, laser phát mode cơ bản $TEM_{00}$ (Hình 6). Đặc trưng năng lượng của laser cũng được khảo sát bằng việc sử dụng hai gương ra với hệ số truyền qua tương ứng là 20 % và 4 %, năng lượng trung bình cực đại 450 mW thu được với gương ra truyền qua 20 % tương ứng với công suất xung tới 5,5 kW.

## 4. Ứng dụng của hệ laser

Với hệ laser này chúng ta đã có thể tiến hành nghiên cứu các đối tượng có yêu cầu phân giải về thời gian rất nhanh (từ vài trăm picô-giây đến vài chục nano-giây). Trên cơ sở đó, chúng tôi đã xây dựng một hệ đo phân giải thời gian (Hình 7).

*Các thông số chính của hệ đo:*

- Laser mode-locking độ rộng xung 10 ps, tần số lặp lại 8,8 MHz, bước sóng 1064 nm hoặc 532 nm.
- Dao động ký số Tektronic 1,5 GHz, tốc độ lấy mẫu 20 GS/s.
- Photodiot nhanh thời gian đáp ứng 200 ps.

Hệ đo này có khả năng phân giải thời gian là 200 ps, như vậy nó cho phép tiến hành một số nghiên cứu về ảnh hưởng của dung môi hay nồng độ phân tử màu hữu cơ lên thời gian sống của phân tử hoặc quá trình truyền năng lượng giữa các phân tử chất màu hữu cơ với nhau [13] và phổ huỳnh quang kích thích 2-photon phân giải theo thời gian [14].

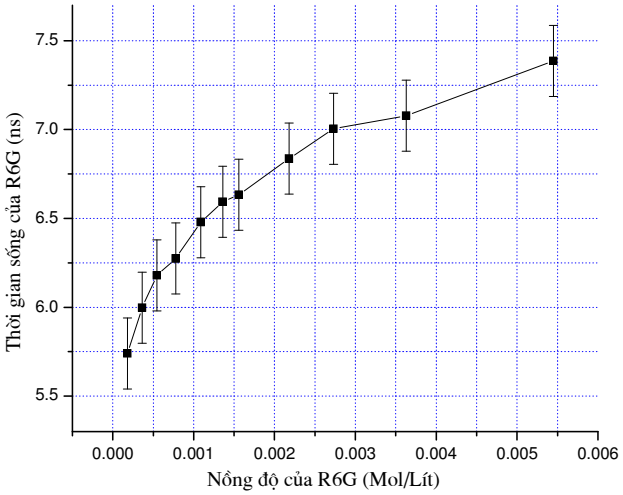


**Hình 8:** Thời gian sống phân tử R6G theo nồng độ.

Sự ảnh hưởng của nồng độ phân tử màu hữu cơ Rhodamine 6G (Lambda Physik – CHLB Đức) được pha trong dung môi ethanol lên thời gian tắt huỳnh quang đã được nghiên cứu. Với các nồng độ thay đổi từ (2 x $10^{-4}$ đến 5,5 x$10^{-3}$ M/l), thời gian sống của phân tử màu hữu cơ Rhodamine 6G - được đo bằng thời gian tắt huỳnh quang trung bình – có sự thay đổi đáng kể, như trình bày trên Hình 8, với sai số phép đo 0,2 ns. Thời gian tắt huỳnh quang trung bình của phân tử Rhodamine 6G/ ethanol bị kéo dài từ 5,75 ns (5 x $10^{-4}$ M/l) đến 7,30 ns khi tăng nồng độ đến 5 x $10^{-3}$ M/l). Điều này cũng đã được phát hiện bởi các công trình khác và được giải thích do hiện tượng tái hấp thụ [12].

## 5. Kết luận

Một hệ thống laser rắn Nd:$YVO_4$ được bơm liên tục bằng laser bán dẫn**,** phát xung picô-giây mode-locking tại 1064 nm với tần số xung thấp tới 8,8 MHz đã được thiết kế và chế tạo thành công. Các tính toán lý thuyết và mô phỏng quá trình laser trong buồng cộng hưởng và các đặc trưng của laser đã được nghiên cứu tường minh. Đặc biệt, nhờ kết quả này, chúng tôi đã xây dựng thành công một hệ đo phân giải thời gian với khả năng phân giải hiện có tới 0,2 ns. Do vậy, một số ứng dụng của laser này trong lĩnh vực quang tử, y sinh đã được thực hiện như các phép đo thời gian sống của phân tử chất màu hữu cơ, thời gian sống của phân tử donor và acceptor trong quá trình truyền năng lượng giữa hỗn hợp chất màu Rhodamine (donor)– Perylene Red (acceptor) và phổ huỳnh quang kích thích 2-photon phân giải theo thời gian.

***Lời cảm ơn***

*Các tác giả trân trọng cám ơn sự tài trợ kinh phí từ Chương trình NCCB cấp Nhà nước (Đề tài $N^0$ 403 306) và Chương trình Laser của Viện KH & CN VN.*

**Tài liệu tham khảo**

1. Ursula Keller, *Nature*, Vol. 424 (2003), p. 831- 837.
2. R. Paschotta, U. Keller, *Appl. Phys. B*, Vol. 73 (2001), p. 653 - 662.
3. A. K Komarov, K.P Komarov, *Opt. Comm*, Vol. 183 (2000), p. 265 - 270.
4. E. Sorokin, I.T Sorokina, E. Wintner, *Appl. Phys. B*, Vol. 73 (2001), p. 3 - 14.
5. F. Salin and U. Keller. *Appl. Phys. B* (Special Issue on Ultrafast Optics) V.70 (2000)
6. Do Quoc Khanh, N. Trong Nghia et al. *Advances in Optics, Spectroscopy, Photonics and Applications* (Eds. N. Van Hieu et al. Vietnam Academic Press, 2007) p.303-308.
7. Do Quoc Khanh, N. Trong Nghia et al. *ASEAN Journal on Science & Technology for Development, V. 24, 1-2, p.59-66 (2007)*
8. S. Lévêque – Fort, S. Forget, D. Papadopulos et al. *Amplification of a low repetition rate passively mode-locked diode-pumped Nd: YVO4 laser to fluorescence imaging.* Advances in

Photonics and Applications (Eds. B. Anita, G. Denardo et al. Vietnam National University Press) p.343 (2004).
9. V. Z. Kolev, M. J. Lederer, B. Luther Davies and A.V. Rode. *Opt. Lett.* 28, p. 1275 (2003)
10. S. H. Cho, F. X. Kartner, U. Morgner, E. P. Ippen, and J. G. Fujimoto, J. E. Cunningham and W. H. Knox, *Opt. Lett.* 26, p 560 (2001).
11. H. Welling and B. Wellegehausen, *Applied Optics, High resolution Michelson Interferometer for Spectral Investigations of Laser. Appl. Opt.* p.1986 (1972)
12. W. Becker, A. Bergmann, G. Biscotti, Becker & Hickl GmbH, Berlin, *Two-Photon Fluorescence Excitation by Picosecond Diode Lasers*
13. V.T.T. Duong, D. Q. Khanh, N.T. Nghia , T.D. Huy, N.D. Hoang, N.T. Binh, N. Dai Hung. *Proceeding of 5$^{th}$ National Conference on Solid State Physics*, p.1047 (2007).
14. N. Thanh Binh, N. Dinh Hoang, N. Trong Nghia, D. Quoc Khanh, N. Dai Hung. *V th-National Conference on Optics and Spectroscopy. 10-14 Sept. 2008, NhaTrang, Vietnam (C-04).*

# MÔ PHỎNG HỆ KHUẾCH ĐẠI QUANG SỢI PHA TẠP ERBIUM (EDFA)

**Hà Xuân Vinh[a,b], Phạm Văn Hội[b)], Phạm Thanh Bình[(b)], Chử Thị Thu Hà[(b)]**
**Trần Thị Châm[(b)], Đỗ Khánh Vân[(b)].**

[a)] Viện Nghiên Cứu và Ứng dụng Công Nghệ Nha Trang
[b)] Viện Khoa Học Vật Liệu.

**Tóm tắt:** Trong bài báo này, chúng tôi xây dựng chương trình mô phỏng khuếch đại quang trong sợi thuỷ tinh pha tạp Erbium. Đây là bài toán khá phức tạp, do có nhiều hiện tượng vật lý xảy ra trong quá trình hoạt động và số lượng phương trình vi phân khá nhiều. Chúng tôi đã chia vùng bước sóng thông tin từ 1475nm đến 1625nm thành nhiều kênh thông tin cách nhau 1nm. Như vậy chúng ta có hệ phương trình với hơn 300 phương trình vi phân cho các kênh ASE thuận nghịch, kênh tín hiệu và phân bố công suất của laser bơm cho sợi. Chương trình mô phỏng đã tính toán được các thông số tối ưu cho hệ khuếch đại như: Chiều dài sợi pha tạp Erbium, hệ số khuếch đại, công suất quang bão hòa ở lối ra, hệ số nhiễu của mạch EDFA. Các kết quả tính toán khá phù hợp với các kết quả thực nghiệm. Với chương trình mô phỏng, chúng tôi đã khảo sát các phân bố công suất của tín hiệu và công suất bơm dọc theo chiều dài sợi quang pha tạp Erbium. Đồng thời chương trình này cũng có thể tạo một số biến số mới có liên quan đến các hiện tương vật lý như sự tụ đám và chuyển đổi ngược trong hệ EDFA.

## 1. Giới thiệu

Các hiện tượng vật lý xãy ra trong quá trình hoạt động của hệ thống khuếch đại quang sợi pha tạp Erbium (EDFA) là rất phức tạp, trong đó quan trọng nhất là hiện tượng khuếch đại tín hiệu phát xạ ngẫu nhiên (ASE). Với hiện tượng ASE ta phải khảo sát theo cả 2 hướng thuận và nghịch so với hướng truyền tín hiệu bởi vì phát xạ ngẫu nhiên xãy ra theo cả 2 hướng.

Quá trình mô phỏng hệ còn có khó khăn là số lượng kênh tín hiệu trong vùng thông tin rất nhiều.

Vùng tín hiệu dùng trong thông tin nằm trong khoảng 1475nm đến 1625nm với độ rộng của các kênh tín hiệu và ASE là 1nm. Như vậy chúng ta phải giải bài toán với hơn 300 kênh ASE thuận nghịch, kênh tín hiệu và laser bơm cho sợi.

Theo mô hình đơn giản của hệ 2 mức, sự thay đổi mật độ trạng thái ở 2 mức theo 2 phương trình sau:

$$\frac{dN_2}{dt} = -\frac{1}{\tau}N_2 - (N_2\sigma_s^e - N_1\sigma_s^a)\Phi_s - (N_2\sigma_p^e - N_1\sigma_p^a)\Phi_p$$

$$\frac{dN_1}{dt} = \frac{1}{\tau}N_2 + (N_2\sigma_s^e - N_1\sigma_s^a)\Phi_s + (N_2\sigma_p^e - N_1\sigma_p^a)\Phi_p$$

Với $N = N_1 + N_2$ ; $\Phi_s = I_s / h\nu_s$ ; $\Phi_p = I_p / h\nu_p$ .

Hệ phương trình này cho phép biểu diễn mật độ trạng thái $N_2$ qua công suất của tín hiệu và công suất bơm:

$$N_2(z) = \left( \frac{\tau\sigma_s^a\Gamma_s P_s(z)/Ah\upsilon_s + \tau\sigma_p^a\Gamma_p P_p(z)/Ah\upsilon_p}{\tau(\sigma_s^a+\sigma_s^e)\Gamma_s P_s(z)/Ah\upsilon_s + \tau(\sigma_p^a+\sigma_p^e)\Gamma_p P_p(z)/Ah\upsilon_p + 1} \right) N$$

Khi tích phân theo tất cả các kênh trong vùng thông tin với độ rộng băng tần ASE là $\Delta\lambda$ = 1nm và độ dài sóng của các kênh là $\lambda_i$ ta có:

$$N_2(z) = \left( \frac{\sigma_s^a\lambda_s\Gamma_s P_s(z) + \sigma_p^a\lambda_p\Gamma_p P_p(z) + \sum_j \sigma_j^a\lambda_j\Gamma_j P_j^{ASE}(z)}{(\sigma_s^a+\sigma_s^e)\lambda_s\Gamma_s P_s(z) + (\sigma_p^a+\sigma_p^e)\lambda_p\Gamma_p P_p(z) + \sum_j (\sigma_j^a+\sigma_j^e)\lambda_j\Gamma_j P_j^{ASE}(z) + Ahc/\tau} \right) N$$

Trong đó $P_j^{ASE}(z) = P_j^{ASE+}(z) + P_j^{ASE-}(z)$ tương ứng với ASE theo chiều thuận và chiều nghịch.

Phương trình biểu diễn phân bố công suất tín hiệu dọc theo chiều dài sợi pha tạp Erbium như sau:

$$dP_p / dz = (-N_2\sigma^{'} - N_1\sigma_p^a)\Gamma_p P_p - \alpha_p P_p \quad \text{(P 1)}$$

$$dP_s / dz = (N_2\sigma_s^e - N_1\sigma_s^a)\Gamma_s P_s - \alpha_s P_s \quad \text{(P 2)}$$

$$dP_j^{ASE+} / dz = (N_2\sigma_j^e - N_1\sigma_j^a)\Gamma_j P_j^{ASE+} + N_2\sigma_j^e\Gamma_j hc\Delta\nu_j / \lambda_j - \alpha_j P_j^{ASE+} \quad \text{(P 3)}$$

$$dP_j^{ASE-} / dz = -(N_2\sigma_j^e - N_1\sigma_j^a)\Gamma_j P_j^{ASE-} - N_2\sigma_j^e\Gamma_j hc\Delta\nu_j / \lambda_j + \alpha_j P_j^{ASE-} \quad \text{(P 4)}$$

Với j chạy từ 1 đến 150.

Như vậy khi phân chia vùng thông tin 1475nm đến 1625nm thành 150 kênh cách đều nhau 1nm chúng ta có hệ hơn 300 phương trình vi phân liên kết nhau qua mật độ trạng thái kích thích $N_1$ và $N_2$.

## 2. Thuật toán giải chương trình

Hệ phương trình vi phân (P 1-4) được chúng tôi lập trình và giải trên máy tính nhờ phần mềm Matlab.

Việc giải mô hình trên bằng phương pháp số khá phức tạp. Trong đó điều kiện biên của các kênh ASE tại 2 đầu z=0 và z=L chưa được xác định.

Để thực hiện giải hệ phương trình trên chúng tôi đã thực hiện tích phân theo 2 chiều thuận và nghịch nhiều lần để xác định được các điều kiện biên.

Thuật toán giải hệ phương trình P1-4 được tiến hành như sau:

- Tính tích phân theo chiều thuận từ z=0 đến z=L với các điều kiện ban đầu tại z=0 đã biết là $P_p(0)$, $P_s(0)$ và $P_j^{ASE+} = 0$; còn điều kiện biên $P_j^{ASE-}$ tại z=0 chưa biết nhưng được giả định là bằng 0. Kết quả tích phân cho ta giá trị của $P_j^{ASE+}(L)$, dùng giá trị này để tính tích phân theo chiều ngược lại từ z=L đến z=0.
- Tiến hành lấy tích phân theo chiều nghịch từ z=L đến z=0 với các điều kiện ban đầu tại z=L đã biết là $P_p(L)$, $P_s(L)$, $P_j^{ASE-} = 0$; và $P_j^{ASE+}$ lấy từ tích phân lần trước. Kết quả tích phân sẽ cho ta giá trị của $P_j^{ASE-}(0)$, như vậy chúng ta đã có các giá trị ban đầu tại z=0 là $P_p(0)$, $P_s(0)$, $P_j^{ASE+}(0) = 0$; và $P_j^{ASE-}(0)$.
- Thực hiện một lần nữa việc lấy tích phân từ z=0 đến z=L ta sẽ có được kết quả các giá trị phân bố công suất quang của các tín hiệu dọc theo chiều dài sợi từ z=0 đến z=L.
- Quá trình được thực hiện lặp cho đến khi các giá trị biên hội tụ.

Các thông số được dùng [3] để thực hiện tính toán trong mô phỏng

| | | |
|---|---|---|
| Nồng độ $Er^{3+}$ | $4.27 \times 10^{-25}$ $m^{-3}$ | (1040 mol ppm, 5800 wt ppm). |
| Diện tích lõi pha tạp | $15.21 \times 10^{-12}$ $m^2$. | |
| Diện tích mốt tín hiệu | $22.69 \times 10^{-12}$ $m^2$. | |
| Diện tích mốt bơm | $17.23 \times 10^{-12}$ $m^2$. | |
| Thời gian sống mức 2 | $11 \times 10^{-3}$ sec | |
| Tiết diện hấp thụ ở bước sóng bơm 980 nm | $2.22 \times 10^{-25}$ $m^2$. | |

## 3. Thảo luận các kết quả mô phỏng

Các kết qủa thu được từ chương trình mô phỏng như sau:

- Phổ tín hiệu và ASE.

Trên hình 1a, đồ thị tương ứng với tín hiệu vào P_in bằng 0 chính là tín hiệu ASE khi không có tín hiệu vào. Khi có tín hiệu thông tin, phổ ASE tự động giảm mạnh do năng lượng đã dồn cho phần công suất tín hiệu, công suất tín hiệu vào càng lớn nền nhiễu ASE càng giảm thấp. Điều này đã được chúng tôi khảo sát từ thực nghiệm.

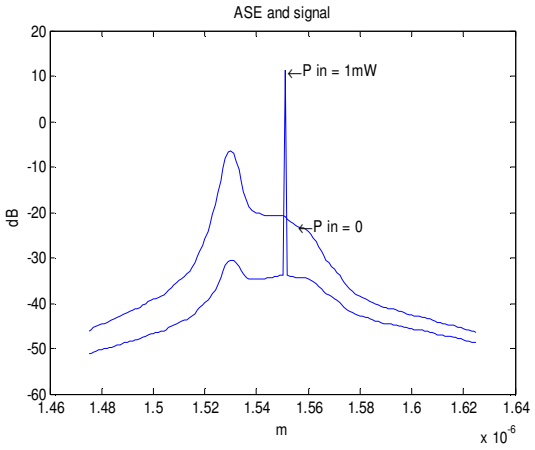


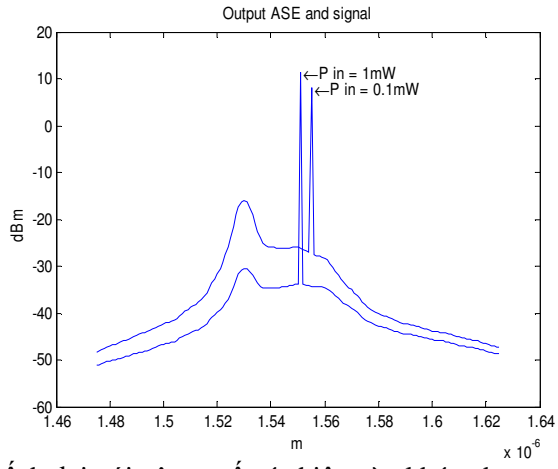


**Hình 1a,b**: Phổ tín hiệu ở lối ra của mạch khuếch đại với công suất tín hiệu vào khác nhau.

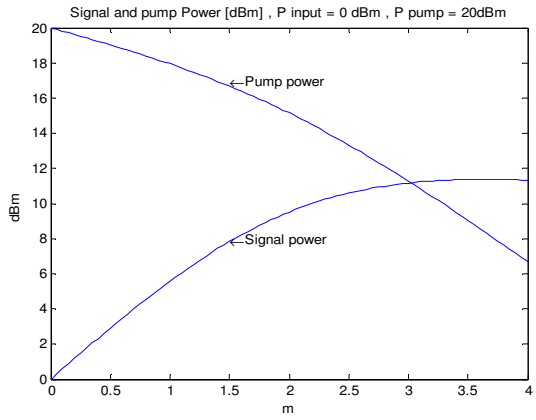


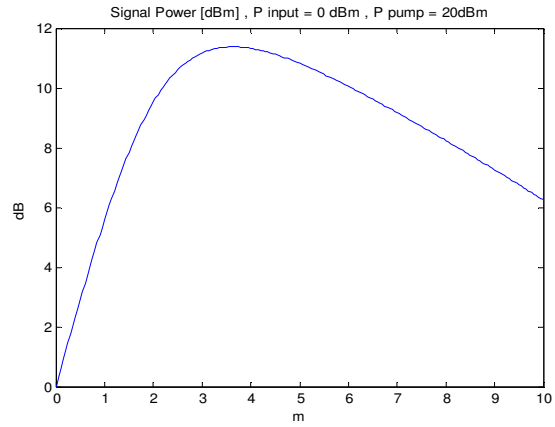


**Hình 2 a,b**: Phân bố công suất của tín hiệu và của laser bơm theo chiều dài sợi.

m mạnh do năng lượng đã dồn cho phần công suất tín hiệu, công suất tín hiệu vào càng lớn nền nhiễu ASE càng giảm thấp. Điều này đã được chúng tôi khảo sát từ thực nghiệm.

- Kết quả mô phỏng phân bố công suất theo chiều dài sợi:

Các kết quả tính toán rất phù hợp với lý thuyết thực nghiệm. Từ đồ thị 2b chúng ta thấy với công suất bơm 20dBm, công suất tín hiệu cực đại tại vị trí 4m tính từ đầu sợi, sau đó bị suy giảm dần do sự hấp thụ trong sợi. Ta có chiều dài tối ưu của loại sợi này là 4m.

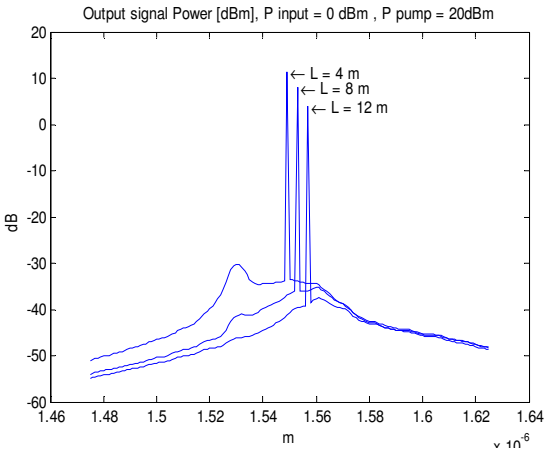


**Hình 3:** Sự thay đổi công suất và dạng phổ tín hiệu lối ra theo chiều dài của sợi pha tạp

Với cùng tín hiệu lối vào P_input = 0dBm (1mW) và công suất bơm P_pump =20 dBm (100mW) chiều dài sợi pha tạp càng dài sẽ làm suy hao tín hiệu càng nhiều do sự hấp thụ ở phần sau của sợi.

- Sự phụ thuộc của hệ khuếch đại vào công suất bơm và công suất tín hiệu.

Dạng phổ vùng bước sóng 1530 nm cho chúng ta thấy tình trạng công suất bơm. Nếu bơm yếu (13dBm) dạng phổ vùng này sẽ không nhô cao. Khi bơm đủ công suất (hơn 20 dBm) phổ vùng 1530 nm sẽ có đỉnh nhô lên.

Với tín hiệu vào bé chúng ta tính được hệ số khuếch đại càng lớn. Hệ số khuếch đại (G=P_out/P_in) theo kết quả mô phỏng trên sẽ giảm dần khi tín hiệu vào tăng lên.

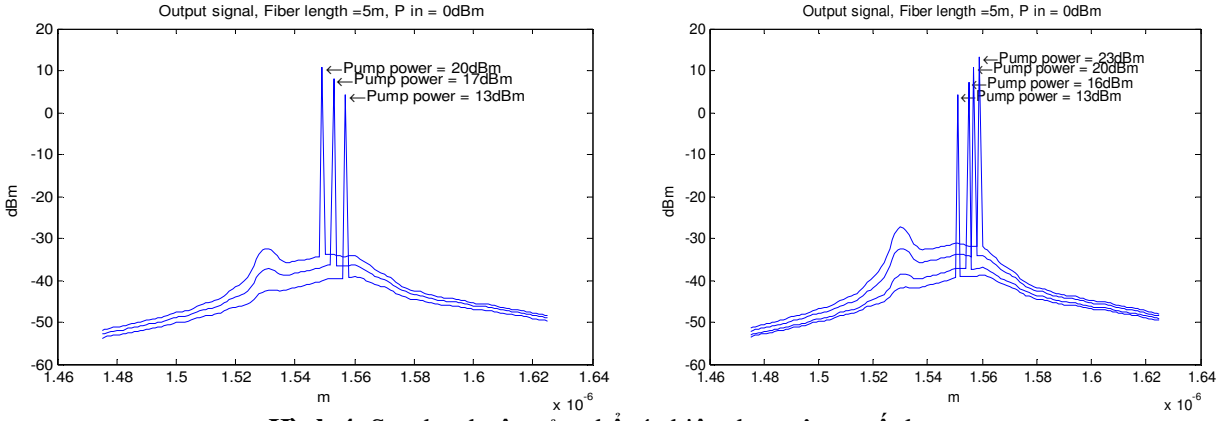


**Hình 4**: Sự phụ thuộc của phổ tín hiệu theo công suất bơm.

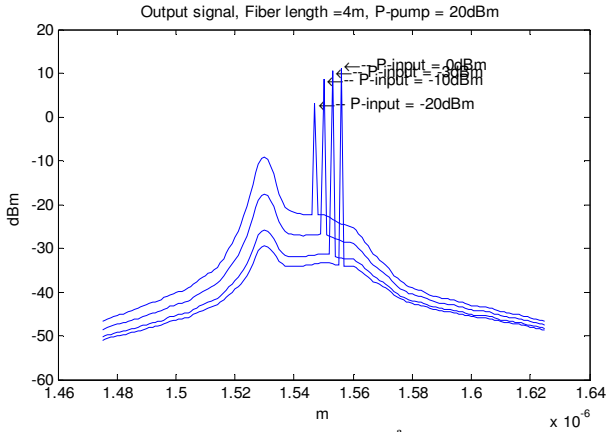


**Hình 5**: Sự phụ thuộc của phổ tín hiệu theo tín hiệu vào.

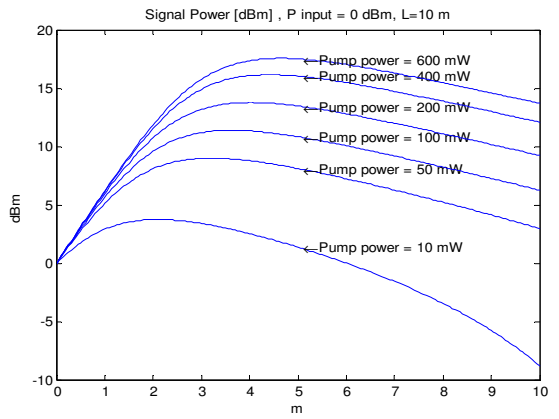


**Hình 6**: Sự phụ thuộc công suất tín hiệu vào chiều dài khi công suất bơm thay đổi.

Kết quả mô phỏng cho thấy dù tăng công suất bơm rất lớn, gấp 300 lần từ 10 mW đến 300 mW nhưng công suất tín hiệu và chiều dài tối ưu của sợi vẫn không tăng nhiều. Điều này cho thấy hệ đã đạt đến bão hoà do cấu trúc của sợi và nồng độ Erbium pha tạp.

## 4. Kết luận

Chương trình mô phỏng trên là công cụ khảo sát hệ khuếch đại quang sợi pha tạp Erbium (EDFA). Các kết quả thu được khá phù hợp với thực nghiệm và lý thuyết.

Chương trình là một công cụ để khảo sát hệ EDFA trong điều kiện thực nghiệm khó khăn. Do việc hàn nối các sợi pha tạp Erbium khó thực hiện hơn loại cáp quang thường. Hơn nữa chúng ta cũng không có nhiều loại sợi để khảo sát.

Với các kết quả đạt được từ mô hình này, chúng ta có thể thay đổi tùy ý các thông số của hệ khuếch đại để có được các kết quả khác nhau, từ đó chúng ta có thể định hướng và giải thích các kết quả thực nghiệm.

Ngoài ra chương trình còn phối hợp với các số liệu thực nghiệm tìm ra thông số tối ưu trong từng yêu cầu của mạch khuếch đại quang sợi cụ thể, tính toán được các thông số của EDFA như hệ số khuếch đại bão hoà, tạp âm của hệ.

### Tài liệu tham khảo

1. Michel J.F.Dogonnet, “Rare Earth Doped Fiber lasers and Amplifiers”, Marcel Dekker, New York, 1993.
2. John M.Senior, “Optical Fiber communications”, John Wiley & sons, New York, 1997
3. Wysocki, “Broadbank Operation of Doped Fiber Sources” John Wiley & sons, New York, 1997.

# ĐỘNG HỌC CỦA LASER RẮN $Nd^{3+}$:$YVO_4$ ĐƯỢC BIẾN ĐIỆU THỤ ĐỘNG BẰNG SESAM VÀ BƠM LIÊN TỤC BẰNG LASER BÁN DẪN

**Nguyễn Trọng Nghĩa [a], Nguyễn Đình Hoàng [b], Đỗ Quốc Khánh [a], Hoàng Hữu Hoà [b] và Nguyễn Đại Hưng [a]**

[a)] Trung tâm Điện tử học Lượng tử, Viện Vật lý,
Viện Khoa học và Công nghệ Việt Nam,10 Đào Tấn, Ba Đình, Hà Nội
[b)] Đại học Huế

**Tóm tắt:** Các kết quả nghiên cứu lý thuyết và thực nghiệm về động học của hệ laser rắn $Nd^{3+}$:$YVO_4$ được biến điệu độ phẩm chất (Q-switching) thụ động bằng gương bán dẫn hấp thụ bão hòa (SESAM) đã được trình bày. Các kết quả nghiên cứu lý thuyết đã được so sánh và cho thấy phù hợp tốt các kết quả thực nghiệm. Laser này có thể phát xung ngắn tới 22 ns (nanô-giây) tại bước sóng 1064 nm và có tần số xung lặp lại tới 2,2 MHz khi được bơm liên tục bằng một laser bán dẫn tại bước sóng 808 nm.

## 1. Mở đầu

Các laser rắn Q-switching phát xung ngắn có rất nhiều ứng dụng trong nghiên cứu cũng như trong các ứng dụng thực tế. Trong những năm gần đây, các laser $Nd^{3+}$:$YVO_4$ biến điệu độ phẩm chất (Q-switching) bằng các chất hấp thụ bão hòa rắn được nhiều nhà nghiên cứu trên thế giới quan tâm. Một trong những chất hấp thụ bão hòa rắn đang được sử dụng phổ biến để biến điệu thụ động các laser $Nd^{3+}$:$YVO_4$ là tinh thể Cr:YAG. Ưu điểm của các hệ thống laser này là cấu trúc đơn giản, hoạt động ổn định và có kích thước nhỏ, phát các xung nanô-giây với tần số xung lặp lại <100 kHz [1-5]. Từ đầu những năm 1990, gương bán dẫn hấp thụ bão hoà (SESAM) bắt đầu được sử dụng trong các laser mode-locking với vai trò vừa là gương của buồng cộng hưởng (BCH) vừa là chất hấp thụ bão hòa [6-9]. Sau đó linh kiện quang học SESAM được sử dụng để Q-switching thụ động trong các laser micro-chip [8]. Gần đây, một số chất hấp thụ bão hoà bằng bán dẫn đã được sử trong các laser rắn thông thường có buồng cộng hưởng (BCH) cỡ vài xăng-ti-mét (cm) để phát các xung Q-switching nanô giây [9]. Trong bài báo này, chúng tôi trình bày các kết quả nghiên cứu động học của các hệ laser rắn sử dụng hoạt chất $Nd^{3+}$:$YVO_4$ được bơm liên tục bằng laser bán dẫn và được biến điệu độ phẩm chất (Q-switching) thụ động bằng SESAM. Động học của laser này và các đặc trưng của xung laser đã được nghiên cứu lý thuyết và so sánh với các kết quả thực nghiệm. Laser này có thể phát xung ngắn tới 22 ns giây tại bước sóng 1064 nm và có tần số xung 2,2 MHz. Theo hiểu biết của chúng tôi, đây là tần số xung lặp lại cao nhất thu được trong các hệ laser rắn $Nd^{3+}$ biến điệu thụ động bằng SESAM.

## 2. Nghiên cứu với phương trình tốc độ

Chúng tôi nghiên cứu hệ phương trình tốc độ của laser 4 mức [10] áp dụng cho laser $Nd^{3+}$:$YVO_4$ Q-switching thụ động bằng SESAM:

$$\frac{dN}{dt} = w_P(n_0 - N) - \frac{N}{\tau} - w_L N \qquad (1)$$

$$\frac{dN_a}{dt} = w_a N_a - \frac{N_a + n_{0a}}{\tau_a} \qquad (2)$$

$$\frac{dS}{dt} = \langle v \rangle \left[ \langle \sigma \rangle N S + \langle \sigma_a \rangle N_a S - \left( \langle \eta_1 \rangle + \langle \eta_2 \rangle \right) S \right] + \gamma \hbar \omega N / \tau \qquad (3)$$

trong đó, N, $n_0$, $\tau$ là nghịch đảo độ tích lũy, mật độ ion $Nd^{3+}$ và thời gian sống huỳnh quang của môi trường hoạt chất. $N_a$, $n_{0a}$, $\tau_a$ là nghịch đảo độ tích lũy, mật độ hạt hấp thụ và thời gian hồi phục của môi trường hấp thụ bão hòa. $w_p$, $w_L$ là xác suất chuyển mức do bơm và xác suất bức xạ cưỡng bức của môi trường hoạt chất. $w_a$ là xác suất chuyển mức do hấp thụ bức xạ laser của môi trường SA. $\langle\eta_1\rangle, \langle\eta_2\rangle$ là trung bình của mất mát vô ích và có ích của BCH laser và được tính theo công thức:

$$\langle\eta_1\rangle = \frac{1}{L}\left(l\eta_{1m} + l_a\eta_{1a}\right) + \ln\left(\frac{1}{R_1}\right)\Big/(2L) \tag{4}$$

$$\langle\eta_2\rangle = \frac{1}{2L}\ln\frac{1}{R_{out}} \tag{5}$$

trong đó, L là chiều dài hình học của BCH, $R_{out}$ là hệ số phản xạ của gương ra, (1- $R_1$) đặc trưng cho mất mát trên các gương còn lại của BCH. l, $\eta_{1m}$ là chiều dài và hệ số hấp thụ bức xạ laser của môi trường hoạt chất, $l_a$, $\eta_{1a}$ là chiều dài và hệ số hấp thụ tuyến tính của SA tại bước sóng laser 1064 nm. $\langle\sigma\rangle = \frac{l_p}{L}\sigma$ là tiết diện bức xạ cưỡng bức trung bình của môi trường hoạt chất và $\langle\sigma_a\rangle = \frac{l_a}{L}\sigma_a$ là tiết diện hấp thụ trung bình của chất hấp thụ ở trong BCH có chiều dài hình học L. $\gamma$ là hệ số thể hiện sự đóng góp của huỳnh quang vào bức xạ laser. $\langle v\rangle$ là vận tốc trung bình của ánh sáng laser trong BCH:

$$\langle v\rangle = \frac{cL}{nl + l_a n_a + L - (l + l_a)} \tag{6}$$

Sử dụng hệ phương trình (1 – 3), chúng tôi đã giải bằng phương pháp số để tiến hành khảo sát các đặc trưng: độ rộng xung và tần số xung của laser Nd Q-switching bằng SESAM. Hệ phương trình này được giải số bằng phương pháp Ơle. Các kết quả lý thuyết được so sánh với kết quả thực nghiệm cho thấy sự phù hợp khá tốt của mô hình lý thuyết.

## 3. Thực nghiệm, kết quả và bàn luận

Hình 1 thể hiện sơ đồ của laser Nd:$YVO_4$ Q-switching bằng SESAM. Laser Nd:$YVO_4$ được bơm liên tục bằng laser bán dẫn ATC - C2000 có công suất cực đại ở chế độ liên tục là 2 W tại bước sóng 808 nm. BCH laser có chiều dài hình học là 17 mm, gồm một gương cầu có bán kính - 25 mm, SESAM và một gương chia chùm. Như vậy, SESAM ngoài chức năng của một SA còn được sử dụng như một gương phản xạ cao của BCH. Tấm chia chùm trong BCH là một tấm quang học có độ dày mỏng (0.2 mm) và hệ số phản xạ thấp (<2 %) tại bước sóng 1064 nm. Do phản xạ trên hai mặt của tấm chia chùm laser đi ra ngoài, BCH laser có hai lối ra với cường độ xấp xỉ nhau. Một BCH laser như vậy có chất lượng (Q) rất cao – như được sử dụng trong kỹ thuật phát xung ngắn dumping-cavity. Laser Nd:$YVO_4$ Q-switching thụ động có ngưỡng phát cỡ 40 mW.

Công suất ra của laser Nd:$YVO_4$ được đo bằng đầu đo năng lượng 13 PME001 (Melles Griot, USA). Xung laser được thu bằng photodiode Hamamatsu nhanh (200 ps) và hiển thị trên dao động kí số Tektronic 1,5 GHz -20 GCh/s. Kết quả đo đặc trưng công suất (trên lối ra 2) cho thấy cường độ laser ra tại bước sóng 1064 nm tăng tuyến tính với cường độ bơm của laser bán dẫn (Hình 2).

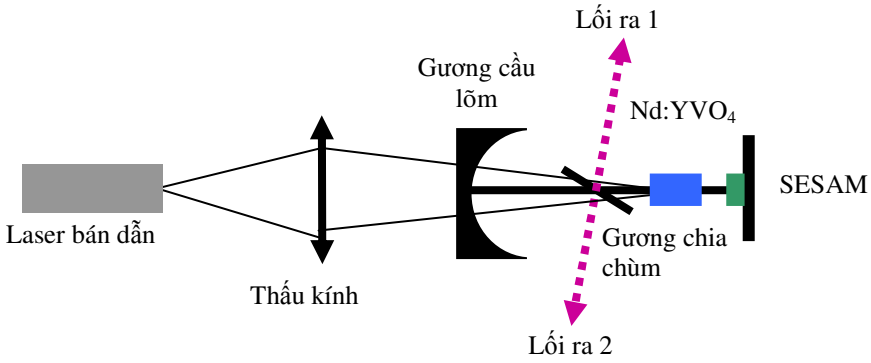


**Hình 1:** Cấu hình laser xung Nd:$YVO_4$ Q-switching bằng SESAM

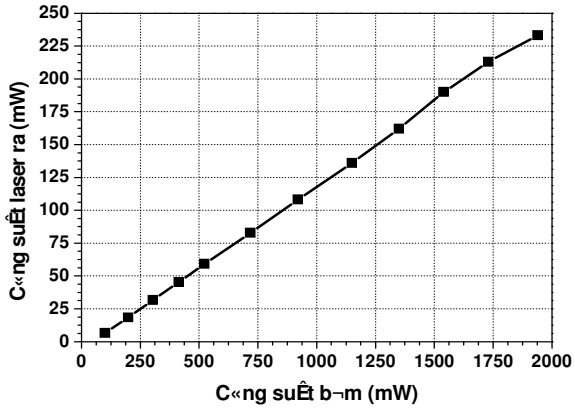


**Hình 2:** Đặc trưng công suất của laser Nd:$YVO_4$ Q-switching bằng SESAM

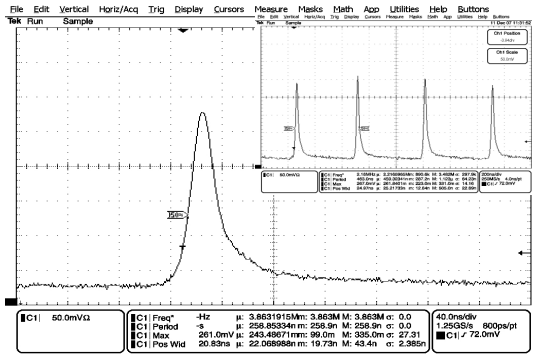

**Hình 3:** Xung và chuỗi xung laser Nd:$YVO_4$ Q-switching bằng SESAM

Hình 3 trình bày dạng xung và chuỗi xung laser Nd:$YVO_4$ Q-switching khi cường độ laser bơm là 1950 mW. Tại cường độ bơm này, laser Nd:$YVO_4$ Q-switching bằng SESAM có công suất phát tại lối ra 2 là 230 mW (tương ứng với khoảng 460 mW trên cả hai lối ra) với độ rộng xung laser là 22 ns, tần số xung là 2,2 MHz.

Các khảo sát sự phụ thuộc của độ rộng và tần số xung laser Nd:$YVO_4$ theo cường độ bơm đã được thực hiện bằng thực nghiệm cũng như trên mô hình lý thuyết bằng cách giải hệ phương trình tốc độ (1 – 3) với các mức bơm (công suất bơm/ngưỡng bơm) khác nhau.

Các tham số quang học của môi trường hoạt chất, SESAM và BCH sử dụng để giải hệ phương trình tốc độ (1 – 3) được cho trong Bảng 1. Hệ số phản xạ trên gương ra của BCH được xác định bằng cách lấy 1 trừ đi tổng hệ số phản xạ trên hai hướng của gương chia chùm.

Sự thay đổi của độ rộng xung và tần số lặp lại xung khi thay đổi mức bơm từ 2 tới 48 lần trên ngưỡng đã được khảo sát. Kết quả cho thấy, trong phạm vi mức bơm trên, độ rộng xung laser giảm phi tuyến khi tăng mức bơm (Hình 4), khi mức bơm càng cao độ rộng xung giảm càng chậm. Trong khi đó, tần số xung laser tăng phi tuyến theo mức bơm. Khi bơm càng cao trên ngưỡng tần số lặp lại có xu hướng tăng chậm dần (Hình 5). Chúng đều thể hiện sự phù hợp tốt giữa các kết quả lý thuyết và thực nghiệm đã thu được.

| **Bảng 1** | |
|---|---|
| l - Chiều dài môi trường hoạt chất [m] | $3 \times 10^{-3}$ |
| n - Chiết suất môi trường hoạt chất tại bước sóng 1064nm | 1,9573 |
| $\eta_{lm}$ - Hệ số hấp thụ tại 1064nm của môi trường hoạt chất [$m^{-1}$]. | 17 |
| $\sigma_p$ - Tiết diện hấp thụ do bơm của môi trường hoạt chất tại bước sóng bơm 808 nm [$m^2$] | $2,5 \times 10^{-23}$ |
| $\sigma$ - Tiết diện bức xạ cộng hưởng của mức laser trên [$m^2$] | $2,5 \times 10^{-22}$ |
| $\tau$ - Thời gian sống của mức laser trên [s] | $98 \times 10^{-6}$ |
| $n_0$ - Mật độ ion Nd trong môi trường hoạt chất [$m^{-3}$] (pha tạp 1,1% mol) | $1,26 \times 10^{26}$ |
| $T_{0a}$ - Hệ số truyền qua ban đầu của SA (khi cường độ ánh sáng tới yếu) | 0,96 |
| $T_{max}$ - Hệ số truyền qua khi SA bị bão hòa | 0,972 |
| $\sigma_a$ - Tiết diện hấp thụ của SA [m2] | $3.7 \times 10^{-21}$ |
| $\tau_a$ - Thời gian hồi phục của mức SA [ps] | 10 |
| $l_a$ - Chiều dày của SA [μm] | 100 |
| $n_a$ - Chiết suất chất hấp thụ bão hoà tại bước sóng laser. | 1,82 |
| $R_{out}$ - Hệ số phản xạ của gương ra | 0,94 |
| L - Chiều dài hình học của BCH [mm] | 17 |
| $(1- R_1)$ [%] | 12 |
| $\gamma$ | $10^{-3}$ |

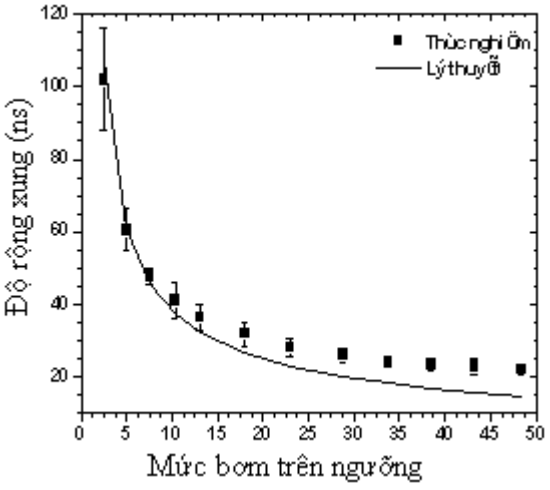


**Hình 4.** Sự phụ thuộc của độ rộng xung vào mức bơm trên ngưỡng của laser Q-switching

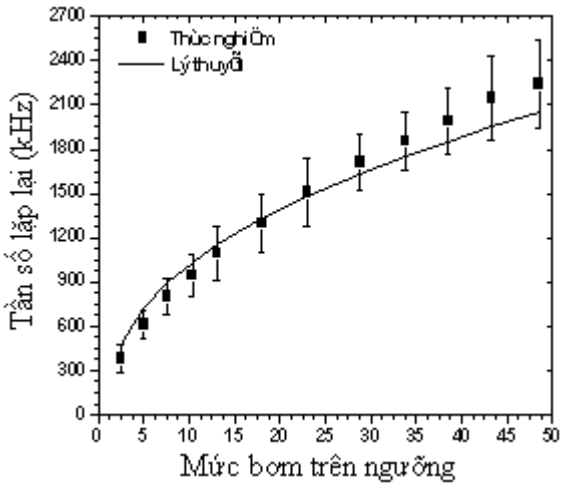


**Hình 5.** Sự phụ thuộc của tần số xung vào mức bơm trên ngưỡng của laser Q-switching

## 4. Kết luận

Chúng tôi trình bày các kết quả nghiên cứu về động học của hệ laser rắn Nd:$YVO_4$ được Q-switching thụ động bằng SESAM. Laser Nd:$YVO_4$ có công suất phát trung bình lớn nhất là 460 mW (trên cả hai lối ra) với độ rộng xung ngắn nhất 22 ns và tần số lặp lại xung 2,2 MHz. Các kết

quả nghiên cứu lý thuyết về sự phụ thuộc của độ rộng và tần số xung vào mức bơm của laser bán dẫn phù hợp tốt với các kết quả thực nghiệm. Đây là hệ laser rắn Nd:$YVO_4$ được Q-switching thụ động bằng một gương bán dẫn hấp thụ bão hòa (SESAM) có tần số lặp lại xung cao nhất hiện nay.

***Lời cảm ơn:*** *Các tác giả trân trọng cám ơn sự tài trợ kinh phí từ Chương trình NCCB cấp Nhà nước cho Đề tài* $N^0$ *403306 và Chương trình Laser của Viện KH&CN VN.*

**Tài liệu tham khảo**

1. C. Li, J. Song, D. Shen et al, ***Appl. Phys. B70*** (2000), p.471
2. N. D. Laia, M. Brunel, F. Bretenaker et al., ***Eur. Phys. J***. D 19 (2002) p.403
3. G. Xiao, M. Bass; ***IEEE J. Quant. Electron***, 33 (1997) p.41.
4. H. Chen, E. Wu, H. Zeng; ***Opt. Comm.*** 230 (2004) p.175.
5. J. Liu, J. M.Yang, J.L. He; ***Opt. Comm.*** 219 (2003) p.317.
6. C. Honninger, G. Zhang, U. Keller, and A. Giesen, ***Opt. Lett.,*** vol. 20, pp. 2402 (1995).
7. U. Keller, D. A. B. Miller, G. D. Boyd et al. ***Opt. Lett.,*** vol. 17 (1992) p. 505.
8. G. J. Spühler, R. Paschotta, R. Fluck, B. Braun, M. Moser, G. Zhang, E. Gini, and U. Keller, ***J. Opt. Soc. Am. B.,*** Vol. 16 (1999) p. 376 .
9. Yong-Gang Wang, Xiao-Yu Ma, Ji-Ying Peng, Hui-Ming Tan, and Long-Sheng Qian, ***Appl. Opt.*** 45 (2006) p.16 .
10. L.V. Tarasov, *"Laser Physics*", MIR publishers, p. 283-291 (1983).

# NGHIÊN CỨU ẢNH HƯỞNG CỦA CÁC HIỆU ỨNG PHI TUYẾN LÊN HOẠT ĐỘNG CỦA FIBER COUPLER

**Vũ Ngọc Sáu[a] ,Phạm Thiết Trường[b]**

[a)] Khoa Công nghệ trường Đại học Vinh
[b)] Khoa Vật lý, Đại học Đồng Tháp

## 1. Mở đầu

Trong thời đại ngày nay, vai trò của việc truyền tải và xử lý thông tin mà đặc biệt là thông tin quang đóng góp một không nhỏ. Mạng thông tin quang được sử dụng rộng rãi nhờ có các tính năng rất ưu việt như: băng tần hoạt động hầu như không có giới hạn, hao tổn năng lượng thấp, dễ khuếch đại tín hiệu trong quá trình truyền dẫn, cho phép nâng cấp dung lượng và định tuyến linh hoạt. Fiber coupler là một thành phần của sợi quang nó giúp phân phối lại tín hiệu quang một cách có định hướng. Nó có thể được dùng để tổng hợp hai hay nhiều tín hiệu từ các sợi quang khác nhau thành một, hoặc cũng có thể tách tín hiệu từ một cổng quang thành hai hay nhiều tín hiệu khác nhau tùy vào mục đích cần sử dụng.

Trong khuôn khổ bài báo này, chúng tôi chỉ trình bày những ảnh hưởng của các hiệu ứng phi tuyến tác động lên fiber coupler có hai cổng vào và hai cổng ra. Phần cuối là những nhận xét về kết quả.

## 2. Phương trình truyền xung trong fiber coupler

### *2.1. Những đặc trưng của coupler*

Về nguyên tắc, để tạo được một coupler với hai cổng vào và hai cổng ra thì hai sợi quang phải được đặt gần nhau về mặt không gian, sao cho tín hiệu lan truyền trên sợi quang này có thể chuyển sang truyền sang sợi quang kia và tạo nên hiện tượng ghép mode giữa hai sợi quang. Người ta sử dụng phương pháp ghép mode giữa các sợi quang để tạo nên chuyển mạch ánh sáng hay điều biến tùy thuộc vào các yêu cầu cụ thể mà có các ứng dụng khác nhau. Thông thường để tạo nên được một coupler thì các sợi quang này chỉ có một không gian nhất định mà tại đó chúng rất "sát nhau", được gọi là chiều dài liên kết (coupling length) của một coupler định hướng (directional coupler). Chiều dài này phụ thuộc vào các yếu tố như: khoảng cách giữa các sợi quang, chiết suất sợi quang, dạng hình học của sợi quang. Trong hình vẽ 1.1, cho ta một sơ đồ của một fiber coupler, trong đó các lõi của các sợi quang đơn mode có kết cấu giống nhau trong vùng giới hạn trung tâm sao cho khoảng cách giữa các lõi cỡ đường kính của nó. Hình 1.1 mô tả một xung quang học được tách ra và truyền trên hai sợi quang khác nhau phụ thuộc vào công suất đỉnh (peak power) của nó.


**Hình 1.** Minh họa sơ lược về sự chuyển mạch phi tuyến trong một sợi quang liên kết. Sự khác nhau giữa các xung ở cổng vào và cổng ra phụ thuộc vào các công suất đỉnh

### *2.2. Phương trình mode liên kết*

Xét một tín hiệu với tần số thành phần là $\omega$, giải phương trình Helmholtz:

$$\nabla^2 \tilde{E} + \tilde{n}^2(x,y)k_0^2 \tilde{E} = 0 \qquad (2.1)$$

Trong đó: $\tilde{E}(r,\omega)$ là kí hiệu phép biến đổi Fourier của trường điện từ *E(r,t)* đối với thời gian.

$k_0 = \dfrac{\omega}{c} = \dfrac{2\pi}{\lambda_0}$ với $\lambda_0$ là bước sóng chân không của ánh sáng.

$\tilde{n}(x,y) = n_0$ là hệ số khúc xạ trong mặt phẳng $(x,y)$ ngoại trừ vùng bị chiếm bởi lõi hai sợi quang (tại đây chiết suất bằng chiết suất của lõi sợi quang.

Trong lý thuyết mode liên kết, ta sử dụng phương pháp gần đúng để giải nên ta có thể viết lại phương trình (2.1) về dạng:

$$\tilde{E}(r,\omega) \approx \hat{e}\left[\tilde{A}_1(z,\omega)F_1(x,y) + \tilde{A}_2(z,\omega)F_2(x,y)\right]e^{i\beta z} \qquad (2.2)$$

Với $\beta$ là hệ số lan truyền chưa xác định.

$\hat{e}$ là độ phân cực định hướng của trường quang học, độ phân cực này được giữ nguyên trong quá trình lan truyền tín hiệu.

$F_m(x,y)$ với *m = 1,2* là hàm phân bố không gian ứng với mode cơ bản thứ *m* mà không phải xét tới sự tồn tại của lõi khác.

Phương trình (2.2) mô tả hàm trường trong sợi quang gồm hai thành phần: thành phần phụ thuộc không gian và thành phần phụ thuộc thời gian, vì viết trong không gian Fourier nên phần phụ thuộc vào thời gian là không tường minh.

Giải phương trình (2.1) ta tìm được hàm $F_m(x,y)$ thỏa mãn phương trình:

$$\frac{\partial^2 F_m}{\partial x^2} + \frac{\partial^2 F_m}{\partial y^2} + \left[n_m^2(x,y)k_0^2 - \overline{\beta}_m^2\right]F_m = 0 \qquad (2.3)$$

$\overline{\beta}_m$ là hằng số lan truyền mode.

$n_m(x,y) = n_0$ mọi điểm trong mặt phẳng *x,y* ngoại trừ phần bị chiếm chỗ bởi lõi thứ *m*

Bằng cách thế phương trinh (2.2) vào phương trình (2.1), nhân kết quả với số hạng $F_1^*$ hoặc $F_2^*$, sử dụng phương trình (1.4.3), và lấy tích phân trong toàn bộ mặt phẳng (x,y). Sau đó sử dụng phép khai triển $\overline{\beta}_m(\omega)$ theo chuỗi Taylo với tần số $\omega_0$, thay $\omega - \omega_0$ bằng đạo hàm theo thời gian trong nghịch đảo phép biến đổi Fourier ta viết được phương trình mode liên kết theo thời gian về dạng:

$$\frac{\partial A_1}{\partial z} + \frac{1}{v_g}\frac{\partial A_1}{\partial t} + \frac{i\beta_2}{2}\frac{\partial^2 A_1}{\partial t^2} = i\kappa A_2 + i\gamma(|A_1|^2 + \delta|A_2|^2)A_1 \qquad (2.4)$$

$$\frac{\partial A_2}{\partial z} + \frac{1}{v_g}\frac{\partial A_2}{\partial t} + \frac{i\beta_2}{2}\frac{\partial^2 A_2}{\partial t^2} = i\kappa A_1 + i\gamma(|A_2|^2 + \delta|A_1|^2)A_2 \qquad (2.5)$$

Trong đó: $\upsilon_{gm} = 1/\beta_{1m}$ là vận tốc nhóm

$\beta_{2m}$: vận tốc nhóm tán sắc của lõi thứ m.

$\gamma = n_2 k_0 / A_{eff}$ được gọi là tham số phi tuyến

$A_1$, $A_2$ là biên độ xung

Chỉ số dưới dùng để nhận biết 1 lõi riêng đã suy giảm từ các tham số $v_g, \beta_2, \gamma$ từ đó ta có những giá trị giống nhau cho cả hai lõi

Phương trình (2.4) và (2.5) được gọi là phương trình truyền xung của trong coupler.

## 3. Các hiệu ứng phi tuyến trong coupler

### *3.1. Hiệu ứng tự biến điệu pha (self – phase modulation): SPM*

Sự phụ thuộc cường độ của hệ số khúc xạ dẫn tới SPM gây ra sự biến đổi pha phi tuyến, kết quả là dẫn tới sự dịch tần và mở rộng phổ của xung quang học. Khi SPM bao gồm cả sự lan truyền của một dòng thông tin quang (an optical bit stream) trong các sợi quang bị chi phối bởi phương trình Schrodinger phi tuyến:

$$i\frac{\partial A}{\partial z}-\frac{\beta_2}{2}\frac{\partial^2 A}{\partial T^2}+\gamma|A|^2A=\frac{i\alpha}{2}A \qquad (3.1)$$

ở đây hệ số mất mát sợi do hệ số $\alpha$ gây ra, còn hệ số $\beta_2$ và γ là ảnh hưởng của các hiệu ứng tán sắc vận tốc nhóm (GVD) và XPM tương ứng.

Khi ta khử số hạng cuối cùng trong phương trình (3.1) với phép biến đổi:

$$A(z,T)=\sqrt{P_0}\exp\left[-\frac{\alpha z}{2}\right]U(z,T) \qquad (3.2)$$

Với $P_0$ là công suất đỉnh của các xung đầu vào, ta đưa phương trình (3.1) về dạng sau:

$$i\frac{\partial U}{\partial z}-\frac{\beta_2(z)}{2}\frac{\partial^2 U}{\partial T^2}+\gamma P_0 p(z)|U|^2U=0 \qquad (3.3)$$

Ở đây sự biến thiên công suất theo một đường truyền sợi điều khiển độ mất mát làm ảnh hưởng tới hệ số tuần hoàn *p(z),* được định nghĩa như sau: $p(z)=e^{-\alpha z}$ giữa hai bộ khuếch đại nhưng trở thành một vị trí xác định tập trung trên mỗi bộ khuếch đại.

Dễ dàng giải được phương trình (3.3) theo phương pháp giải tích. Trong một trường hợp đặc biệt $p = 1$ và $\beta_2$ là một hằng số không xác định, phương trình được rút gọn đến phương trình Schrodinger phi tuyến chuẩn và các nghiệm có dạng của các soliton. Trong một trường hợp đặc biệt khác, đó là sự lan truyền xung dạng vuông trong một sợi quang với hằng số $\beta_2$. Sử dụng phép biến đổi sau:

$$U(z,T)=\sqrt{p(z,T)}\exp\left[i\int_0^T v(z,T)dT\right] \qquad (3.4)$$

Trong phương trình (3.3), vấn đề lan truyền xung đưa về dạng phương trình động học chất lưu, trong những biến này thì $\rho$ và $v$ tương ứng với vai trò của mật độ cư trú và vận tốc của một chất lưu. Trong trường hợp quang học thì những biến trên đại diện cho cường độ và độ dịch tần của xung (chirp of the pulse). Với một xung dạng vuông thì vấn đề lan truyền xung trở nên đồng nhất với "breaking a dam" và được áp dụng theo phép giải tích trong giới hạn của sự tán sắc nhỏ (cỡ khoảng WKB). Phương pháp này hữu ích cho những hệ thống sóng ánh sáng (lightwave) ở dạng NRZ và cung cấp ý nghĩa vật lý đáng kể.

Từ một quan điểm thực tế, hiệu ứng của SPM sẽ gây nên sự dịch tần của xung và sự mở rộng phổ của nó. Trong trường hợp không có tán sắc ($\beta_2=0$) thì phương trình (3.3) có thể giải bằng phương pháp giải tích trong phạm vi của tần số chirp và sự mở phổ của nó. Soliton có dạng $U(z,T)=U(0,T)\exp[i\phi_{NL}]$, ở đây SPM gây ra sự dịch chuyển pha bởi hệ số:

$$\phi_{NL}=\gamma P_0 L_{eff}|U(0,T)|^2 \qquad (3.5)$$

Sự thay đổi pha cực đại: $\phi_{\max}=\gamma P_0 L_{eff}$ có ý nghĩa là xác định số lượng tần số chirp. Như một bản phác thảo về đường dẫn sóng, những hiệu ứng SPM là không đáng kể khi $\phi_{\max}\langle 1$ hoặc $P_0<\alpha/\gamma$, ở đây ta sử dụng $L_{eff} = 1/\alpha$ . Với những giá trị tiêu biểu của α và γ, SPM sẽ trở nên quan trọng tại các mức công suất đỉnh đạt giá trị trên 25mW. Từ đó, với những mức năng lượng giới hạn SBS thấp hơn 10mW, SPM ít ảnh hưởng tới giới hạn mất mát những hệ thống sóng ánh sáng. Khi sự mất mát trong sợi quang được bù đắp bởi việc sử dụng những bộ khuếch đại quang sẽ làm thay đổi những trạng thái trên. Những hiệu ứng SPM có thể tích lũy trên khắp đường

truyền. Nếu những máy khuếch đại được sử dụng là $N_A$ thì sự dịch chuyển pha cực đại trở thành $\phi_{\max} = \gamma P_0 N_A L_{eff}$. Với kết quả này thì công suất đỉnh giới hạn với $P_0 < \alpha/\gamma N_A$ hoặc thấp hơn 3mW cho những đường truyền chỉ sử dụng 10 bộ khuếch đại. Rõ rang là, SPM có thể là yếu tố chủ yếu cho những hệ thống sóng ánh sáng kéo dài.

Một phương pháp biến đổi được sử dụng để xác định SPM gây ra sự dịch tần, đó là phương pháp tách bước, trong đó những hiệu ứng SPM và GVD được xét một cách riêng rẽ và nó cũng qui ước sự mở rộng xung một cách hợp lý. Trong một sự mở rộng của phương pháp này, SPM gây ra sự dịch tần được xem như có tác động đến tham số dịch tần tại cuối đầu ra. Sử dụng một gần đúng nhiễu loạn, trong đó số hạng phi tuyến trong phương trình (3.3) là tương đối nhỏ, là khá hợp lý. Chúng ta tập trung vào việc sử dụng phép gần đúng này cho những hệ có sự mất mát và quản lý tán sắc.

Giá trị căn quân phương của độ rộng xung có thể được tính toán bằng cách sử dụng:

$$\sigma = \left[\left\langle T^2 \right\rangle - \left\langle T \right\rangle^2\right]^{1/2}$$

Với:
$$\left\langle T^m \right\rangle = \frac{\int_{-\infty}^{+\infty} T^m |U(z,T)|^2 dT}{\int_{-\infty}^{+\infty} |U(z,T)|^2 dT} \tag{3.6}$$

Đối với xung đối xứng: $<T> = 0$ và $\sigma^2$ được cho xấp xỉ bởi:

$$\sigma^2(z) = \sigma_L^2(z) + \gamma P_0 f_S \int_0^z \beta_2(z_1)\left[\int_0^{z_1} p(z_2)dz_2\right]dz_1 \tag{3.7}$$

Trong đó: $\sigma^2$: độ rộng RMS được chờ đợi trong trường hợp tuyến tính ( $\gamma = 0$). $f_S$: tham số ảnh hưởng tới hình dạng của xung ở đầu vào và được định nghĩa như sau:

$$f_S = \frac{\int_{-\infty}^{+\infty} |U(z,T)|^4 dT}{\int_{-\infty}^{+\infty} |U(z,T)|^2 dT} \tag{3.8}$$

Đối với một xung Gauss có $U(0,T) = \exp\left[-\frac{1}{2}\left(T/T_0\right)^2\right]$ thì $f_S = 1/\sqrt{2} \approx 0{,}7$

Đối với xung có dạng vuông thì $f_S = 1$

### *3.2. Hiệu ứng điều biến pha chéo (cross – phase modulation):XPM*

Xét trường hợp hệ WDM (wavelength – division multiplexing) *M* kênh. Trường quang tổng hợp có thể được viết như sau:

$$A(z,T) = \sum_{m=1}^{M} A_m(z,T)\exp[i(\omega_m - \omega_0)T] \tag{3.9}$$

Trong đó: $\omega_m$ : tần số mang của kênh thứ *m*

$\omega_0$ : tần số được chọn để trùng hợp với một số kênh trong thực tế.

Sử dụng phương trình của quá trình khuếch đại được điều khiển ta thu được tập hợp các phương trình Schrodinger phi tuyến liên kết của *M* :

$$i\frac{\partial A_j}{\partial z} + \frac{i}{v_{gj}}\frac{\partial A_j}{\partial z} - \frac{\beta_{2j}}{2}\frac{\partial^2 A_j}{\partial T^2} + \gamma\left(|A_j|^2 + 2\sum_{m\neq j}^{M}|A_m|^2\right)A_j = \frac{i\alpha}{2}A_j \tag{3.10}$$

Trong đó: $j = 1,\ldots,M$

$v_{jg}$ : là vận tốc nhóm.

$\beta_{2j}$ : tham số tán sắc (GVD parameter)

Hệ số mất mát α và tham số phi tuyến γ được sử dụng giống nhau cho tất cả các kênh.

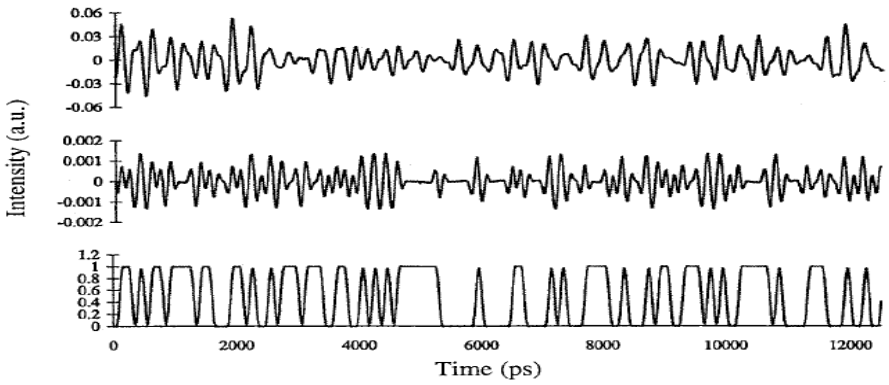


**Hình 2.** XPM gây ra sự biến đổi công suất trong một đầu dò CW cho một đường truyền 130km (ở giữa) và một đường truyền 320km (ở trên đỉnh) với sự quản lý tán sắc. Một dòng bit NRZ trong kênh bơm được biểu diễn bởi sơ đồ ở cuối

Trong phương trình trên thì hiệu ứng trộn bốn sóng (FWM) được bỏ qua, việc giả thiết hiệu ứng GVD quá lớn so với hiệu ứng FWM trở nên phù hợp với pha.

Nói chung, tập hợp các phương trình của *M* được giải bằng phương pháp giải số. Nó có thể được giải bằng phương pháp giải tích trong trường hợp sóng liên tục (CW) với kết quả $A_j(L) = \sqrt{P_j}\exp[i\phi_j]$, trong đó $P_j$ là công suất đầu vào và kết quả dịch chuyển pha phi tuyến từ sự phối hợp của XPM và SPM mang lại bởi:

$$\phi_j = \gamma L_{eff}\left(P_j + 2\sum_{m\neq j} P_m\right) \tag{3.11}$$

Giải pháp CW có thể áp dụng gần đúng cho NRZ (nonreturn to zero) – những hệ thống hoạt động với tốc độ bit tương đối thấp. Pha $\Phi_j$ của một kênh đặc biệt sẽ thay đổi từ bit này tới bit khác phụ thuộc vào những dạng bit của các kênh lân cận. Trong trường hợp xấu nhất mà tất cả các kênh có 1 bit trong cùng một thời gian thì XPM gây ra dịch chuyển pha lớn nhất. Nếu công suất đầu vào được giả thiết như nhau trong mỗi kênh, giá trị lớn nhất được xác định bởi:

$$\phi_{\max} = \left(\frac{\gamma}{\alpha}\right)(2M-1)P_{ch} \tag{3.12}$$

Trong đó: $L_{eff}$ được thay thế bởi tỉ số (1/α), giả sử $\alpha L >> 1$. XPM gây ra sự gia tăng dịch chuyển pha tuyến tính với *M* và có thể trở nên khá lớn. Năm 1984, người ta đo được độ gia tăng này cho trường hợp hai kênh. Ánh sáng từ hai laser bán dẫn hoạt động với bước sóng gần 1,3 *μm* và 1,5 *μm* được đưa vào sợi quang dài 15km. Dịch chuyển pha tại 1,5 *μm* gây ra bởi sóng 1,3 *μm* cùng truyền được đo bằng cách sử dụng một giao thoa kế. Một giá trị của $\Phi_{max} = 0{,}024$ được tìm thấy cho $P_{ch} = 1$mW. Giá trị này thỏa mãn với giá trị tiên đoán 0,022 từ phương trình (3.12).

Nói một cách chính xác, XPM gây nên dịch chuyển pha không ảnh hưởng tới quá trình thực hiện của hệ nếu những hiệu ứng GVD là không đáng kể. Tuy nhiên, bất kỳ sự tán sắc nào trong những sợi quang biến đổi phụ thuộc vào dịch chuyển pha tới sự dao động của công suất, biến đổi SNR tại máy thu. Sự biến đổi này có thể được hiểu là không phải sự biến đổi pha phụ thuộc thời gian dẫn tới sự dịch tần mà ảnh hưởng tới tán sắc – gây ra sự mở rộng của tín hiệu. Hình 1.2 chỉ ra rằng XPM gây ra những biến đổi của một đầu dò CW với một kênh bơm 10 Gb/s điều biến sử dụng dạng NRZ. Công suất đầu dò dao động gần như hơn 6% sau khi 320km của sợi quang phân tán. Giá trị RMS của những dao động phụ thuộc vào công suất của kênh và có thể giảm bớt bởi thấp hơn nó. Như một sự tiên đoán nếu ta sử dụng điều kiện $\Phi_{max} < 1$ ở phương trình (2.1.13) thì công suất kênh được giới hạn tới:

$$P_{ch} < \frac{\alpha}{\gamma(2M-1)} \tag{3.13}$$

Những giá trị tiêu biểu của α và γ, $P_{ch}$ phải thấp hơn 10mW thậm chí được 5 kênh và giảm tới khoảng 1mW cho hơn 50 kênh.

## 4. Kết luận

Những kết quả trên cho ta thấy, tín hiệu lan truyền trong coupler bị ảnh hưởng bởi các hiệu ứng phi tuyến. Hiệu ứng tự biến điệu pha SPM trong quá trình lan truyền tín hiệu có thể gây nên hiện tượng dịch chuyển tần và sự mở rộng phổ của xung. Hiệu ứng biến điệu pha chéo XPM giữa các tín hiệu quang có thể gây ra các hiện tượng như nén xung và vỡ sóng, sự mất ổn định điều biến trong giới hạn tán sắc thường và sự dịch chuyển tần số của soliton.

### Tài liệu tham khảo

1. Govind P. Agrawa, *Applications of nonliear fiber optic*, Academic press, 2001.
2. Myron W. Evans, *Mordern nonliear optics*, part I, 2001.
3. Robert W. Boyd, *Nonliear optics*, Academic Press. Inc, 1992.

# ẢNH HƯỞNG CỦA CHIRP TUYẾN TÍNH LÊN CÁC ĐẶC TRƯNG CỦA XUNG GAUSS TRONG MÔI TRƯỜNG TÁN SẮC LÀ SỢI QUANG ĐƠN MODE

**Trịnh Đình Chiến[a], Bùi Xuân Kiên[b], Bùi Văn Hải [c]**

[a)] Đại học KHTN - Đại học Quốc Gia Hà Nội
[b)]Đại học Điện Lực
[c)]Đại học kỹ thuật Lê Quý Đôn

**Tóm tắt:** Trong quá trình lan truyền xung trong sợi quang, yếu tố tác sắc của môi trường ảnh hưởng tới các đặc trưng của xung luôn tồn tại. Trong đó phải kể tới đặc trưng cường độ đỉnh xung và độ rộng xung, tuy nhiên sẽ là khác nhau đối với các xung vào có sự biến điệu tần số. Việc khảo sát ảnh hưởng của chirp tần số tới đặc trưng cường độ đỉnh xung cực ngắn lan truyền (fs) có giá trị ứng dụng cao.

## 1. Mở đầu

Trong công nghệ truyền thông thông tin quang, vấn đề được quan tâm đến đó là quá trình truyền tín hiệu. Tín hiệu được truyền đi trong sợi quang sẽ chịu ảnh hưởng của các hiện tượng phi tuyến làm cho các xung lan truyền bị giãn ra, đặc trưng là các chirp tần số. Trong sợi quang thì có nhiều yếu tố gây chirp. Đơn giản như sự tán sắc gây ra chirp tuyến tính (linear chirp), ngoài ra còn có SPM (self-phase modulation), XPM (Cross-phase modulation),...

## 2. Phương trình lan truyền xung

Để thu được phương trình lan truyền xung, chúng ta xuất phát từ hệ phương trình maxwell và thực hiện một số phép biến đổi nhỏ ta có:

$$\Delta E(z,t) = \frac{\partial^2}{\partial z^2} E(z,t) = \mu_0 \frac{\partial^2}{\partial t^2} D(z,t) \qquad (1)$$

Biến đổi Fourier cả hai vế phương trình (1) ta thu được:

$$\frac{\partial^2}{\partial z^2} E(z,\omega) + \omega^2 \mu_0 D(z,\omega) = 0 \qquad (2)$$

Hay:
$$\frac{\partial^2}{\partial z^2} E(z,\omega) + \beta^2(\omega,E).E(z,\omega) = 0 \qquad (3)$$

Ở đây $\beta^2(\omega,E) = \omega^2 \mu_0 \varepsilon_0 \varepsilon(\omega,E) = k_0^2.n^2(\omega,E)$, $k_0$ là véc tơ sóng trong môi trường chân không, n là chiết suất của môi trường

Biểu thức cường độ trường có dạng:

$$E(z,t) = \mathrm{Re}[A(z,t)e^{i(\omega_0 t - \beta_0 z)}] = \frac{1}{2}[A(z,t).e^{i(\omega_0 t - \beta_0 z)} + c.c] \qquad (4)$$

Với $\omega_0$ tần số trung tâm, $\beta_0 = \frac{\omega_0}{c} n(\omega_0) = k_0 n(\omega_0)$

Vì hàm bao A(z,t) biến thiên chậm theo z và t, cho nên biến đổi Fourier biểu thức của trường ta có:

$$E(z,\omega) = \int_{-\infty}^{\infty} A(z,t)e^{-i\omega t}dt = \frac{1}{2}e^{-i\beta_0 z}\int_{-\infty}^{\infty} A(z,t)e^{-i(\omega-\omega_0)t}dt + \frac{1}{2}e^{i\beta_0 z}\left(\int_{-\infty}^{\infty} A(z,t)e^{-i(\omega-\omega_0)t}dt\right)^* \qquad (5)$$
$$= \frac{1}{2}e^{-i\beta_0 z}A(z,\omega-\omega_0) + \frac{1}{2}e^{i\beta_0 z}A^*(z,-\omega-\omega_0)$$

Thay (5) vào (3) và đồng thời sử dụng gần đúng hàm bao biến thiên chậm $\left|\frac{\partial^2 A}{\partial z^2}\right| << \beta_0 \left|\frac{\partial A}{\partial z}\right|$ ta thu được:

$$-2i\beta_0 \frac{\partial A(z,\omega-\omega_0)}{\partial z} + (\beta^2 - \beta_0^2)A(z,\omega-\omega_0) = 0 \qquad (6)$$

Mặt khác ta luôn có thể viết: $\beta^2 - \beta_0^2 = (\beta+\beta_0)(\beta-\beta_0) \approx 2\beta_0(\beta-\beta_0)$

Khí đó phương trình (6) được viết lại:

$$\frac{\partial A(z,\omega-\omega_0)}{\partial z} + i(\beta-\beta_0)A(z,\omega-\omega_0) = 0 \qquad (7)$$

Trong đó β(ω) có thể được khai triển thành chuỗi Taylor quanh tần số trung tâm $\omega_0$ như sau:

$$\beta(\omega) = \beta(\omega_0) + \beta'(\omega_0)(\omega-\omega_0) + \frac{1}{2!}\beta''(\omega_0)(\omega-\omega_0)^2 + ..$$

Ở đây $\begin{cases} \beta(\omega_0) = \beta_0 \\ \beta'(\omega_0) = \beta'_0 \\ \beta''(\omega_0) = \beta''_0 \end{cases}$

Phương trình (7) viết lại:

$$\frac{\partial A(z,\omega-\omega_0)}{\partial z} + i\left[\beta'(\omega-\omega_0) + \frac{\beta_0''}{2}(\omega-\omega_0)^2\right]A(z,\omega-\omega_0) = 0 \qquad (8)$$

Biến đổi Fourier ngược phương trình (8) ta thu được:

$$i\frac{\partial}{\partial z}A(z,t) + i\beta'_0\frac{\partial}{\partial t}A(z,t) + \frac{\beta''_0}{2}\frac{\partial^2}{\partial t^2}A(z,t) = 0 \qquad (9)$$

Phương trình (9) có lời giải giải tích trong trường hợp hàm bao của xung ở điểm đầu lan truyền có dạng Gauss. Để loại bỏ đạo hàm bậc nhất ta đưa vào biến số mới z' = z; t' = t - $\beta'_0$.z, đồng thời biến đổi Fourier cả hai vế thu được:

$$\frac{\partial A(z,\omega)}{\partial z'} = \beta''_0\,\omega^2 A(z',\omega) \qquad (10)$$

Phương trình (10) có nghiệm:

$$A(z,\omega) = A(0,\omega).\exp\left(\frac{i}{2}\beta''_0\,\omega^2 z\right) \qquad (11)$$

## 3. Khảo sát các đặc trưng của xung sáng lan truyền trong sợi quang trong trường hợp xung vào dạng Gauss có chirp

Xung sáng dạng Gauss lan truyền trong các sợi quang với biên độ xung đi vào có dạng như sau:

$$A(0,t) = A_0 \exp\left[-\frac{1+iC}{2}\left(\frac{t}{T_0}\right)^2\right] \qquad (12)$$

Ở đó $A_0$ là biên độ đỉnh xung. Tham số $T_0$ là nửa độ rộng tại điểm có cường độ bằng 1/e cường độ đỉnh xung, tham số C thể hiện chirp tần số tuyến tính của xung

Biến đổi Fourier từ biểu thức (12):

$$A(0,\omega) = A_0\left(\frac{2\pi T_0^2}{1+iC}\right)^{\frac{1}{2}} \exp\left[-\frac{\omega^2 T_0^2}{2(1+iC)}\right] \qquad (13)$$

Thay (13) vào (11), khi đó (11) chuyển thành:

$$A(z,\omega) = A_0\left(\frac{2\pi T_0^2}{1+iC}\right)^{\frac{1}{2}} \exp\left[\frac{i}{2}\beta''_0\,\omega^2 z - \frac{\omega^2 T_0^2}{2(1+iC)}\right] \qquad (14)$$

Biến đổi Fourier ngược hàm A(z,ω) ta thu được nghiệm của phương trình (9) như sau:

$$A(z,t) = \left(\frac{A_0 T_0}{\left[T_0^2 - i\beta''_0\, z(1+iC)\right]^{1/2}}\right)\exp\left[-\frac{(1+iC)t^2}{2\left[T_0^2 - i\beta''_0\, z(1+iC)\right]}\right] \qquad (15)$$

Phương trình này chỉ cho chúng ta thấy xung ra vẫn giữ nguyên dạng Gauss trong quá trình lan truyền. Và độ rộng của xung lan truyền thay đổi phụ thuộc vào quãng đường lan truyền như sau:

$$\frac{T_1}{T_0} = \left[\left(1+\frac{C\beta''_0\, z}{T_0^2}\right)^2 + \left(\frac{\beta''_0\, z}{T_0^2}\right)^2\right]^{1/2} \qquad (16)$$

Ở đó $T_1$ là nửa độ rộng xung đi ra và tỉ số thời gian nửa độ rộng xung ra/vào phụ thuộc vào tỉ số quãng đường trên chiều dài tán sắc $z/L_D$, với $L_D = T_0^2/|\beta''_0|$ được gọi là chiều dài tán sắc. Đối với một xung không có chirp (C = 0) sự mở rộng là $\left[1+\left(z/L_D\right)^2\right]^{1/2}$ và độ rộng xung tăng tới $\sqrt{2}$ khi mà $z = L_D$.

Dùng phần mềm Matlab chúng tôi khảo sát độ rộng xung, cường độ đỉnh phụ thuộc và tham số chirp và thu được kết quả như sau:

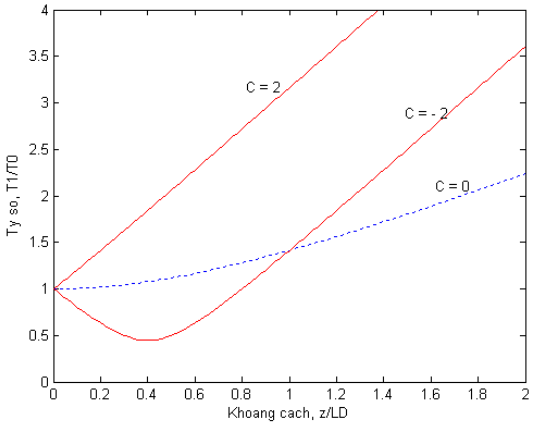


**Hình 1.** Sự phụ thuộc $T_1/T_0$ theo $Z/L_D$ với các giá trị C khác nhau

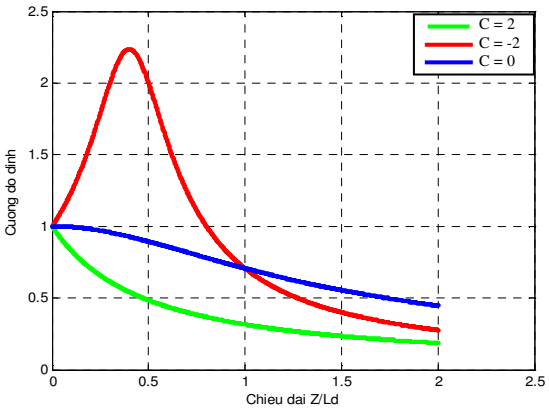


**Hình 2**. Sự phụ thuộc cường độ đỉnh xung theo $Z/L_D$ với các giá trị C khác nhau

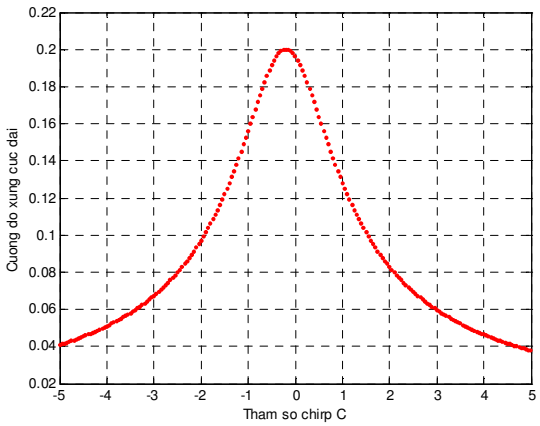


**Hình 3**. Cường độ cực đại phụ thuộc vào tham số chirp C

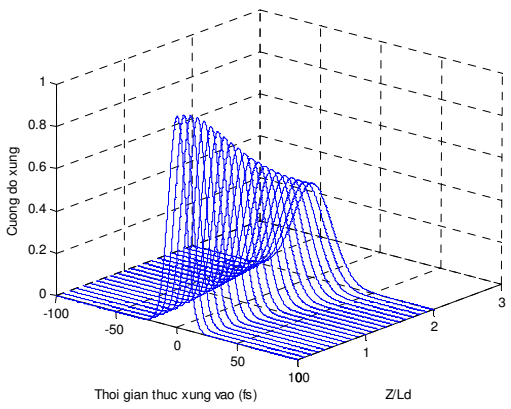


**Hình 4.** Dạng xung lan truyền theo $Z/L_D$ với giá trị C= 0

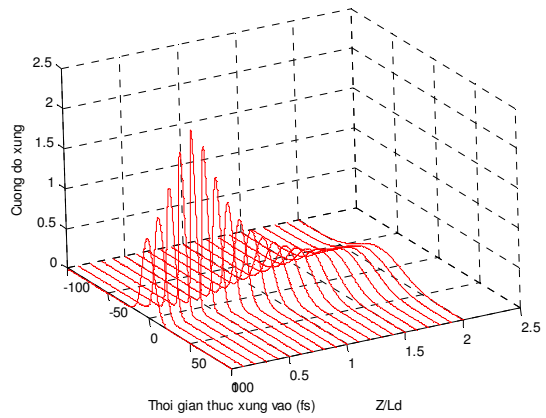


**Hình 5.** Dạng xung lan truyền theo $Z/L_D$ với giá trị C= -2

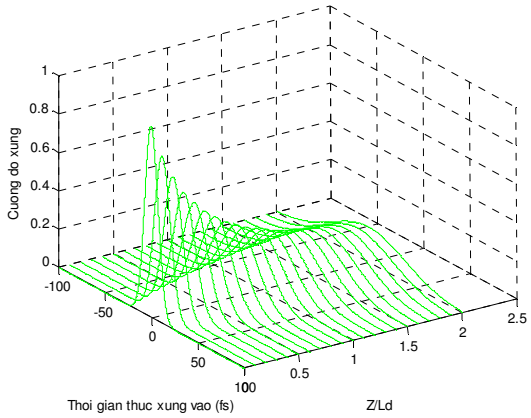


**Hình 6**. Dạng xung lan truyền theo $Z/L_D$ với giá trị C= 2

Từ hình vẽ ta nhận thấy với giá trị C > 0 có sự mở rộng đồng nhất và sự mở rông này lớn hơn với trường hợp xung không cho chirp (C = 0). Với C < 0 xung sáng nén lại sau đó mới có sự mở rộng. Tương ứng ta thu được cường độ đỉnh xung như hình 2

Hình 3 cho ta thấy cường độ đỉnh xung phụ thuộc vào tham số chirp C. Nếu giá trị C tăng lên thi cường độ đỉnh giảm rất nhanh, xung mở rộng nhanh.

## 4. Kết luận

Bài báo trình bày sự ảnh hưởng cụ thể của chirp tần số lên sự mở rộng và hình dạng của xung lan truyền trong sợi quang, xác định được mức độ ảnh hưởng của tham số chirp C:

- Với giá trị C > 0 xung bị mở rộng đồng nhất và tăng nhanh theo $Z/L_D$ do đó cường độ của xung nhanh chóng giảm. Và C càng lớn thì cường độ xung giảm cành nhanh
- Với giá trị C < 0 xung bị nén lại (tại vị trí có $Z/L_D = 0,4$) sau đó mới có sự mở rộng (so với trường hợp C = 0). Giá trị C càng lớn thì xung càng bị nén nhưng sau đó sự mở rộng tăng rất nhanh

Từ việc khảo sát này chúng ta sẽ tìm được tham số chirp C phù hợp cho quá trình lan truyền để sao cho sự mở rộng xung là bé nhất

### Tài liệu tham khảo

1. Bernd Wilhelmi (1989), *" Light pulse compression "* Harwood Academic.
2. Claude Rulliere (1998), " *Femtosecond laser pulses*", Springer.
3. Chih – Chiarng Chen (February 2000), " *Colliding – pulse mode – locked semiconductor laser with a multimode – interference waveguide amplifier* ", Elsevier Science Ltd.
4. Ding Yongkui (August 2003), "*Pulse amplitude equalization in a harmonically modelocked fiber laser using a dispersion imbalanced non-linear loop mirror* ", Elsevier Science Ltd.
5. Elsevier Science Ltd, *Diode – pumped 593.5 nm cw yellow laser by type – I CPM LBO intracavity sum – frequency – mixing*.
6. E.P. Ippen (1973), "*Dye laser* " Springer – Verlag Berlin.
7. F.I. Khatri (November 1994), " *Models for self – limited additive pulse mode – locking* ", Elsevier Science Ltd.
8. Iwao Kitazima (December 1996), " *Joint operation of double CPM and FCM in a Nd:YAG laser* ", Elsevier Science Ltd.
9. J. Chesnoy and L. Fini (October 1986), " *Stabilization of a femtosecond Dye laser synchronously pumped by a frequency – doubled mode – locked YAG laser* ".
10. P.W.Smith, M.A. Duguay and E.P. Ippen (1994) " *Mode – locking of laser* " Pergamon, Oxford, NewYork.

# NGHIÊN CỨU SỰ TRUYỀN NĂNG LƯỢNG CỘNG HƯỞNG GIỮA HAI PHÂN TỬ LASER MÀU HỮU CƠ

**Nguyễn Đình Hoàng, Đào Duy Thắng, Phùng Việt Tiệp, Đỗ Quốc Khánh, Nguyễn Xuân Tuấn và Nguyễn Đại Hưng**

Trung tâm Điện tử học lượng tử, Viện Vật lý, Viện KH&CN Việt Nam
10 Đào Tấn, Ba Đình, Hà Nội
*E-mail: ndhoang@iop.vast.ac.vn*

**Tóm tắt:** Quá trình truyền năng lượng giữa phân tử hữu cơ Rhodamine 6G (donor) và Malachite Green (acceptor) trong dung dịch đã được nghiên cứu nhờ đo trực tiếp thời gian sống trên trạng thái kích thích (hay thời gian tắt dần huỳnh quang) của phân tử donor khi nó được kích thích quang học bằng một laser Nd:$YVO_4$ mode-locking (xung laser 12 picô-giây ở 532 nm tần số xung 9 MHz). Với độ phân giải thời gian của hệ thống đo là < 0,25 ns, thời gian sống của phân tử donor đã được đo khi có các nồng độ acceptor khác nhau đã cho phép xác định loại cơ chế truyền năng lượng cộng hưởng chiếm ưu thế và cung cấp các thông tin quan trọng khác của quá trình truyền năng lượng này.

## 1. Mở đầu

Thời gian sống của các phân tử trên trạng thái kích thích là một thông số động học quan trọng, đặc trưng cho phân tử trong một môi trường và cung cấp những thông tin như về: khả năng hấp thụ, phát xạ và laser; sự biến đổi cấu trúc phân tử và đặc biệt trong sự truyền năng lượng giữa hai phân tử khác nhau và các thông số cơ bản của quá trình này... Nghiên cứu sự truyền năng lượng giữa hai phân tử hữu cơ khác nhau là một vấn đề quan trọng và lý thú đã được quan tâm rất sớm trong các nghiên cứu khoa học về sự sống với các quá trình lý–hoá –sinh phong phú và phức tạp [1]. Ngay trong lĩnh vực vật lý quang tử, người ta đã sử dụng hỗn hợp các loại phân tử màu khác nhau và quá trình truyền năng lượng giữa chúng để tăng hiệu suất phát laser, mở rộng vùng phổ hoạt động laser hay tăng cường hiệu suất bơm... [2-8]. Có hai cơ chế truyền năng lượng chính đã được nghiên cứu trong các quá trình truyền năng lượng: cơ chế truyền năng lượng bức xạ và cơ chế truyền năng lượng cộng hưởng (không bức xạ) lưỡng cực – lưỡng cực. Trong cơ chế truyền năng lượng bức xạ, có hai bước xảy ra: trước tiên, phân tử donor kích thích phát xạ photon, sau đó acceptor hấp thụ phát xạ của donor và phát xạ photon của acceptor. Như vậy, cường độ phát xạ của donor bị ảnh hưởng do sự hấp thụ của acceptor, tuy nhiên, quá trình phát xạ của donor là độc lập, thời gian sống của donor trên trạng thái kích thích là không thay đổi. Trong cơ chế truyền năng lượng cộng hưởng lưỡng cực – lưỡng cực, sự tương tác giữa phân tử donor và phân tử acceptor xảy ra trong thời gian mà phân tử donor nằm trên trạng thái kích thích (trước khi donor phát xạ photon). Thời gian sống trên trạng thái kích thích của phân tử donor sẽ bị ảnh hưởng bởi tương tác với phân tử acceptor. Như vậy, việc xác định thời gian sống trên trạng thái kích thích của các phân tử cho phép người ta thu được các thông tin về quá trình truyền năng lượng giữa chúng.

Trong báo cáo này, chúng tôi trình bày việc nghiên cứu sự truyền năng lượng giữa phân tử màu hữu cơ donor Rhodamine 6G và acceptor Malachite Green trong dung dịch, nhờ xác định thời gian sống của phân tử màu hữu cơ trên trạng thái kích thích trong quá trình truyền năng lượng. Các kết quả thu được cho phép xác định loại cơ chế truyền năng lượng cộng hưởng chiếm ưu thế và cung cấp các thông tin khác trong quá trình truyền năng lượng: khoảng cách truyền năng lượng tới hạn hay là khoảng cách Foster ($R_0$), tốc độ truyền năng lượng (k*), hiệu suất truyền năng lượng giữa các phân tử... Theo hiểu biết của chúng tôi, đây là nghiên cứu được thực hiện lần đầu ở Việt nam dựa trên việc đo thời gian sống của phân tử với độ phân giải tới 0,25 ns và với kích thích quang học bằng laser mode-locking picô-giây.

## 2. Thực nghiệm

### *2.1. Phân tử Rh6G và Malachite Green*

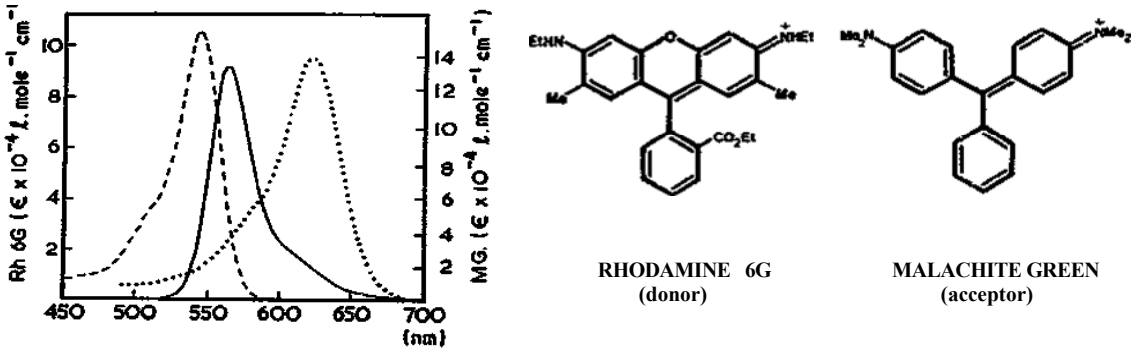


**Hình 1**: a) Phổ hấp thụ, phổ huỳnh quang và b) Cấu trúc phân tử của Rh 6G và MG [12].

Phân tử màu hữu cơ bao gồm nhiều nguyên tử, có cấu trúc năng lượng phức tạp với nhiều mức dao động và mức quay. Trong nhiệt độ phòng, hầu hết các phân tử ở trạng thái cơ bản $S_0$ theo phân bố Boltzmann. Khi hấp thụ ánh sáng kích thích, phân tử chất chuyển từ trạng thái điện tử cơ bản $S_0$ lên trạng thái điện tử kích thích $S_l$, $S_2$... Quá trình này tương ứng với phổ hấp thụ băng rộng của phân tử. Trên trạng thái kích thích, các phân tử hồi phục rất nhanh không phát xạ xuống mức dao động thấp nhất của $S_1$. Sau thời gian sống τ, các phân tử dịch chuyển phát xạ xuống mức $S_0$ (trong thời gian cỡ $10^{-9}$ giây) tương ứng với phổ huỳnh quang băng rộng của phân tử. Thời gian sống trung bình của phân tử màu τ trên trạng thái kích thích được biểu diễn bằng:

$$1/\tau = K_{bx} + K_{kbx}$$

Ở đây, $K_{bx}$ và $K_{kbx}$ là các hằng số đại diện cho các quá trình dịch chuyển phát xạ và không phát xạ của phân tử. Các phân tử mầu hữu cơ dùng cho laser có huỳnh quang rất mạnh, hiệu suất huỳnh quang lượng tử là xấp xỉ bằng một, các quá trình không phát xạ là nhỏ. Do vậy, sự tắt dần cường độ huỳnh quang $I_F(t)$ của phân tử được biểu diễn bằng:

$$I_F(t) = I_F(0)\exp(-t/\tau_D) \quad (1)$$

Thời gian sống trung bình của phân tử màu τ trên trạng thái kích thích (hay là thời gian tắt dần huỳnh quang) của các phân tử màu hữu cơ phụ thuộc mạnh vào dung môi, nồng độ chất màu, nhiệt độ và tạp chất...

Phân tử Rhodamine 6G là một trong những phân tử màu hữu cơ tiêu biểu phát xạ mạnh ở vùng 556-590 nm, có độ bền quang cao và phát xạ rất tốt cả trong dung dịch và khi được pha tạp vào nền rắn với hiệu suất huỳnh quang lượng tử xấp xỉ đơn vị [9]. Phân tử Malachite Green (MG) là phân tử màu hữu cơ có hấp thụ mạnh ở vùng 550 - 650 nm. Đặc biệt, MG có hiệu suất huỳnh quang lượng tử rất thấp ($10^{-4}$) và thời gian sống trên trạng thái kích thích rất ngắn 2 ps, đây là phân tử màu hay được sử dụng làm chất hấp thụ bão hoà trong buồng cộng hưởng laser [10]. Hình 1 trình bày các phổ huỳnh quang và phổ hấp thụ đã được chuẩn hoá trong dung môi ethanol và cấu trúc của Rhodamine B và Malachite Green [11]. Sự chồng chập giữa phổ huỳnh quang của Rhodamine 6G và phổ hấp thụ của Malachite Green là điều kiện cần cho một sự truyền năng lượng giữa phân tử donor Rhodamine 6G và phân tử acceptor Malachite Green (MG).

$$D^* + A \rightarrow D + A^*$$

D: donor (rhodamine 6G), A: acceptor (Malachite Green). $D^*$ : donor ở trạng thái kích thích, $A^*$ là acceptor ở trạng thái kích thích. Chúng ta nghiên cứu sự truyền năng lượng giữa phân tử màu donor Rhodamine 6G và phân tử màu acceptor Malachite Green (MG) bằng việc đo thời gian sống của các phân tử donor khi có mặt của những nồng độ acceptor riêng phần khác nhau.

### *2.2. Hệ đo thời gian sống của các phân tử*

Hình 2 trình bày hệ thiết bị đo thời gian sống của phân tử trên trạng thái kích thích bằng phương pháp huỳnh quang. Mẫu đo là các dung dịch Rhodamine 6G /ethanol ($10^{-3}$ M/l) không có và có MG với các nồng độ khác nhau (Bảng 1). Các dung dịch này được kích thích bởi xung laser 12 ps ở bước sóng 532 nm với tần số xung lặp lại 9 MHz phát từ một laser Nd:$YVO_4$ được hoạt động ở chế độ mode-locking và nhân đôi tần số - hệ laser này được thiết kế và phát triển tại Viện Vật lý, Viện KH&CN VN [12]. Cường độ laser kích thích được hạn chế để tránh bức xạ cưỡng bức có thể xảy ra từ phân tử màu Rh6G. Do hấp thụ và đặc biệt là phát xạ trực tiếp từ MG là rất nhỏ và sử dụng photodiode để thu, việc sử dụng kính lọc phổ để tách phát xạ của MG là không bắt buộc. Khác với thí nghiệm trước đây [13] với bức xạ bơm ở 532 nm, hai phân tử donor Rhodamine B và acceptor PR đều có thể được kích thích trực tiếp. Sự phát xạ của acceptor có thể gây ra do ba quá trình kích thích: kích thích trực tiếp, truyền năng lượng bức xạ và truyền năng lượng không bức xạ từ donor RhB sang acceptor PR. Như vậy, trong trường hợp này, việc đo thời gian sống của phân tử chưa đủ thông tin để nghiên cứu sự truyền năng lượng. Việc nghiên cứu sự truyền năng lượng giữa Rh6G và MG ở đây có nhiều thuận lợi: phổ huỳnh quang của phân tử donor chồng chập với phổ hấp thụ của phân tử acceptor và ánh sáng bơm chủ yếu kích thích phân tử donor. Sự phát xạ do hấp thụ trực tiếp ánh sáng bơm của phân tử acceptor là có thể bỏ qua, do đó chỉ có sự truyền năng lượng giữa donor và acceptor.

Ánh sáng laser picô-giây được hội tụ trên mẫu nhờ một thấu kính. Ánh sáng huỳng quang của mẫu được hệ 02 thấu kính hội tụ vào PIN photodiode (S 9053 Hamamatsu; 1,5 GHz) sau khi đi qua các kính lọc phổ thích hợp để chuyển thành xung điện và đưa vào một máy hiện sóng số (Textronik TDS-7154B; 1,5 GHz và tốc độ lấy mẫu 20 GS/s). Một photodiode khác (Hamamatsu, Japan) thu xung laser kích thích để tạo tín hiệu đồng bộ (trigger) cho máy hiện sóng. Dạng xung huỳnh quang tắt dần thu nhận được có thể được quan sát trên màn hình, được xử lý bằng phần mềm tương thích phân tích quy luật huỳnh quang tắt dần và thời gian sống của phân tử. Với việc thu nhận trực tiếp xung laser 12 ps ở 532 nm, hằng số thời gian của toàn bộ hệ thống đo $\tau_h$ đã được xác định là 0,25 ns. Như vậy, thời gian tắt dần huỳnh quang $\tau_D$ được xác định từ giá trị thời gian đo được trên tín hiệu $\tau_D$ ' và hằng số thời gian của hệ đo: $\tau_D = [(\tau_D')^2 - (\tau_h)^2]^{1/2}$

## 3. Kết quả và bàn luận

### *3.1 Thời gian sống của phân tử donor*

Cường độ huỳnh quang tắt dần theo thời gian của phân tử donor $I_Q(t)$ khi không có mặt phân tử acceptor được biểu diễn qua (1).

Cường độ huỳnh quang tắt dần của phân tử donor $I_Q(t)$ khi có mặt phân tử acceptor là [1]:

$$I_Q(t) = I_Q(0)\exp\{-[t/\tau_D + 2\gamma(t/\tau_{DA})^{1/2}]\} \quad (2)$$

với $\gamma = C_A / C_0$ và $C_A$ là nồng độ acceptor và $C_0 = 3000/2\pi^{3/2}NR_0^3$ (3)

$R_0$ (cm) là khoảng cách truyền năng lượng Foster. Thời gian sống của phân tử màu donor, $\tau_D$, trên trạng thái kích thích của phân tử donor khi không có mặt phân tử acceptor. $\tau_{DA}$ là thời gian sống của phân tử donor khi có acceptor.

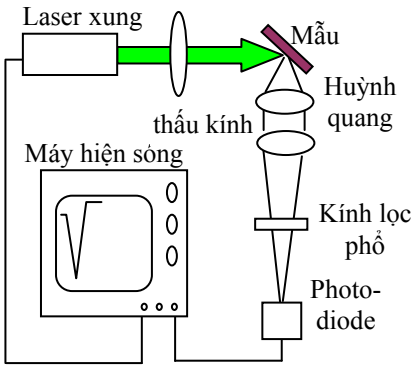


**Hình 2**: Hệ đo thời gian sống của phân tử bằng phương pháp huỳnh quang

**Bảng 1:** Thời gian sống của phân tử Rh6G

| TT | $C_D$ ($10^{-3}$ M/l) | $C_A$ ($10^{-3}$ M/l) | $\tau_{DA}$ (ns) |
|---|---|---|---|
| 1 | 1 | 0 | 4,5 |
| 2 | 1 | 0,3 | 3,7 |
| 3 | 1 | 0,6 | 3,1 |
| 4 | 1 | 1,2 | 2,8 |
| 5 | 1 | 3 | 1,7 |

Bảng 1 trình bày thời gian sống của phân tử màu donor, $\tau_D$, trên trạng thái kích thích khi không có mặt phân tử acceptor và khi có mặt phân tử acceptor với những nồng độ khác nhau.

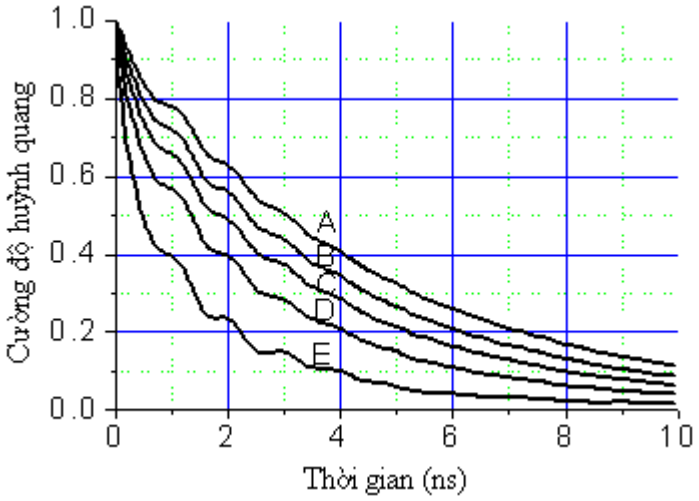


**Hình 3:** Sự tắt dần cường độ huỳnh quang của Rh 6G ($1\times10^{-3}$) khi không có (A) và có MG (B) $0,3\times10^{-3}$ M/l; (C) $0,6\times10^{-3}$ M/l; (D) $1,2\times10^{-3}$M/l; (E) $3\times10^{-3}$M/l.

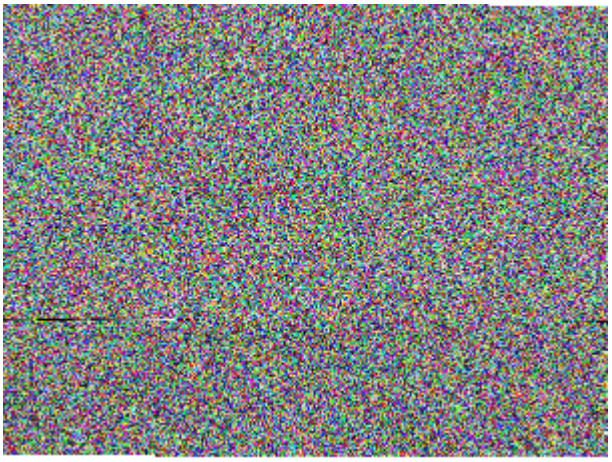

**Hình 4: a)** Cường độ huỳnh quang theo thời gian của dung dịch R6G ($1\times10^{-3}$ M/l) và MG ($0,6\times10^{-3}$ M/l ) trong ethanol.

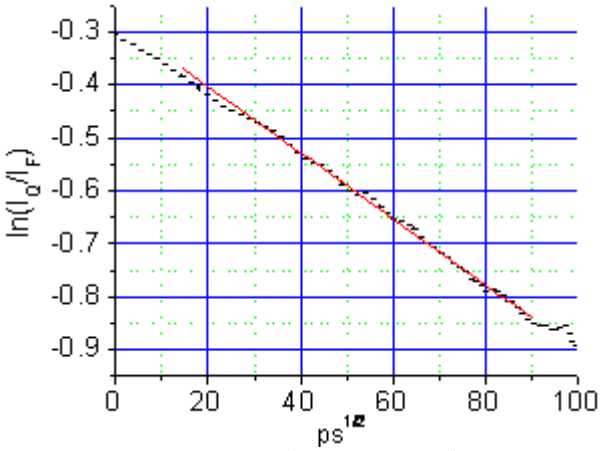


**b)** $\ln(I_Q(t)/I_F(t))$ biểu diễn theo $t^{1/2}$. $I_Q(t)$: Rh 6G $1\times10^{-3}$ M/l, MG $0,6\times10^{-3}$ M/l, $I_F(t)$: Rh 6G $10^{-3}$ M/l.

Thời gian sống của phân tử donor Rh 6G khi có mặt acceptor luôn ngắn hơn thời gian sống của nó khi không có mặt acceptor (mẫu A) và nó càng giảm đi rõ rệt khi nồng độ acceptor tăng

(Bảng 1). Rõ ràng, sự truyền năng lượng giữa R6G-MG là cơ chế truyền năng lượng cộng hưởng và nó có vai trò lớn khi nồng độ acceptor tăng.

Dưới đây, chúng ta xác định các thông số của quá trình truyền năng lượng cộng hưởng giữa phân tử Rhodamine 6G và Malachite Green trên cơ sở các giá trị thời gian sống của phân tử donor đã thu được qua thực nghiệm.

Nếu gọi $I_Q(t)$ là hàm tắt dần huỳnh quang donor theo thời gian khi có mặt acceptor, ta có [1]:

$$I_Q(t) = I_Q(0)\exp\{-[t/\tau_D + 2\gamma(t/\tau_{DA})^{1/2}]\} \tag{4}$$

Tỷ số giữa cường độ huỳnh quang của donor khi có mặt và không có mặt phân tử acceptor là:

$$\frac{I_Q(t)}{I_F(t)} = \frac{I_Q(0)}{I_F(0)}\exp[-2\gamma(t/\tau_{DA})^{1/2}] \tag{5}$$

Việc biểu diễn đồ thị $\ln[I_Q(t)/I_F(t)]$, hàm của tham số $t^{1/2}$, là đường tuyến tính có hệ số góc tỷ lệ với - $2\gamma\,\tau_{DA}^{-1/2}$. Hình 4b trình bày một đồ thị như vậy với nồng độ của acceptor là 0,6 x $10^{-3}$ M/l. Nếu $k_{D^*\to A}$ là tốc độ truyền năng lượng và được xác định bởi [1]:

$$k_T(R) = \frac{1}{\tau_D}\left(\frac{R_0}{R}\right)^6 \tag{6}$$

R là khoảng cách tương tác giữa các phân tử.

$$R = R_0\left(\frac{\tau_{DA}}{\tau_D - \tau_{DA}}\right)^{1/6} \tag{7}$$

E là hiệu suất truyền năng lượng của donor sang acceptor.

$$E = 1 - \frac{\tau_{DA}}{\tau_D} \tag{8}$$

Dựa trên các công thức (2)–(8) và sử dụng kết quả thực nghiệm thu được, các thông số của quá trình truyền năng lượng cộng hưởng giữa donor Rh6G và acceptor Malachite Green đã được tính (Bảng 2). Chúng ta đặc biệt chú ý đến thông số quan trọng nhất ở đây là khoảng cách Foster, $R_0$, trong độ chính xác của thực nghiệm hiện có những giá trị của khoảng cách Foster là hội tụ tại 53 $A^o$. Giá trị này phù hợp tốt với các kết quả của các tác giả khác đã công bố ngay cả khi sử dụng những phương pháp khác nhau [11,14,15].

**Bảng 2:** Các thông số thu được của quá trình truyền năng lượng cộng hưởng giữa donor Rhodamine 6G và acceptor Malachite Green

| Nồng độ acceptor, $C_A$ ($\times 10^{-3}$M/l) | $R$ ($A^0$) | γ | $C_0$ ($\times 10^{-3}$M/l) | $R_0$ ($A^0$) | $k_{D^*\to A}$ ( $\times 10^8$ ) | E |
|---|---|---|---|---|---|---|
| 0,3 | 68,4 ± 1 | 0,1 ± 0,05 | 3 ± 0,1 | 53.0 ± 3,0 | 0,48 | 0,18 |
| 0,6 | 61,4 ± 1 | 0,21 ± 0,1 | 2,9 ± 0,1 | 53,5 ± 4,5 | 1,02 | 0,32 |
| 1,2 | 56,8 ± 1 | 0,38 ± 0,2 | 3,1 ± 0,1 | 52,1 ± 5,2 | 1,32 | 0,38 |
| 3 | 47,9 ± 1 | 0,95 ± 0,5 | 3,1 ± 0,1 | 52,1 ± 7,5 | 3,66 | 0,62 |

## 4. Kết luận

Quá trình truyền năng lượng giữa các phân tử màu hữu cơ Rhodamine 6G (donor) và Malachite Green (acceptor) trong dung dịch đã được nghiên cứu nhờ đo trực tiếp thời gian sống

của các phân tử donor khi chúng được kích thích quang học bằng một laser mode-locking (xung laser 12 picô-giây ở 532 nm tần số xung 9 MHz). Việc xác định được thời gian sống của phân tử donor khi có mặt các nồng độ acceptor khác nhau đã cho phép khẳng định loại cơ chế truyền năng lượng cộng hưởng chiếm ưu thế và đã cung cấp các thông tin quan trọng khác của quá trình truyền năng lượng cộng hưởng giữa hai phân tử.

***Lời cảm ơn:*** *Các tác giả trân trọng cám ơn sự tài trợ kinh phí từ Chương trình NCCB cấp Nhà nước cho Đề tài* $N^0$ *403306 và Chương trình Laser của Viện KH&CN VN.*

**Tài liệu tham khảo**

1. Jóeph R. Lakowicz. *Principle of Fluorescence Spectroscopy*, p. 443-468, Springer (2006)
2. M. Fukuda, K. Komada and K. Mito, *Jap. Appl. Phys. Lett.* Part II. 40, L440 (2001)
3. M. Canva, P. Geoges, J. P. Perelgritz, A. Brun et al. *Appl. Opt*. 34, p. 428 (1995)
4. M. Dubois, M. Canva, A. Brun, F, Chaput and J.P. Boilot, *Appl. Opt*. 35, p. 3193 (1996).
5. P. Y. Lu, Z. X. Yu, R. R. Alfano and J. I. Gersten, *Phys. Rev***,** p. 2100 (1983).
6. H.H. Hoa, Do Q. Hoa, J. Matsumoto, T. Imasaka *Procceding of* $3^{rd}$ *IWOMS-99*, p. 625-628 (1999)
7. T. Hong Nhung, M. Canva, F. Chaput, H. Goudket et al. *Opt. Commun.* 232, p. 343-351 (2004)**.**
8. N. Tat Thanh, Pham Hong Minh et al. *Advances in Photonics and Applications* (Vietnam National University Press, 2005) p. 334-338.
9. Ulrich Brackmann, *Lambda Physik*, Lambdachrome®, Laser Dyes. (2002)
10. E.P. Ippen, C.V. Shank and A. Bergman, *Chem. Phys. Lett*. 38, p. 611 (1976)
11. G. Porter and C. J. Tredwell, *Chem. Phys. Lett.* 56, p. 278 (1978).
12. Do Quoc Khanh, N. Trong Nghia et al. *Advances in Optics, Spectroscopy, Photonics and Applications* (Vietnam Academic Press, 2007) p. 303-308.
13. [13] Vu T.T Duong, Do Quoc Khanh, N. Trong Nghia et al. *Proc. Vth-National Conference on Solid state Physics,* p.1047- 1050 (2007)
14. D. Rehm and K. B. Eisenthal, *Chem. Phys. Lett*. 9, p. 387 (1971).
15. K. B. Eisenthal, *Accounts Chem, Res*. 8, p.118 (1975).

# SỰ PHÁT HÒA BA BẬC HAI TỪ BỀ MẶT TINH THỂ THẠCH ANH

**Nguyễn Thế Bình, Phạm Văn Thường, Nguyễn Thị Linh**.

Khoa Vật Lý - Trường Đại học Khoa học Tự nhiên - Đại học Quốc gia Hà Nội
334 Nguyễn Trãi Hà nội. *E-mail: thebinh@vnu.edu.vn*

**Tóm tắt:** Một hệ đo tín hiệu hoà ba bậc hai quang học (SH) từ bề mặt tinh thể đã được nghiên cứu hoàn thiện tại phòng thí nghiệm. Để có thể khảo sát được thuộc tinh bề mặt vật liệu cần phải đo được sự phụ thuộc vào góc phương vị của hai thành phần tín hiệu SH phân cực thẳng song song và vuông góc với mặt phẳng tới. Chúng tôi đã lựa chọn sơ đồ chiếu sáng và thu theo phương vuông góc với bề mặt tinh thể. Các thí nghiệm đã được tiến hành nhằm giải quyết vấn đề đo các tín hiệu SH bề mặt rất yếu này. Nguồn sáng kích thích bề mặt được sử dụng là laser Nd:YAG (Quanta- Ray Pro 230) bước sóng 1064nm hoạt động ở chế độ Q-switching cho xung 8ns năng lượng có thể tới 1200mJ với tần số lặp lại 10Hz. Nguồn thu tín hiệu SH là máy quang phổ đa kênh MS -257 CCD (Newport). Hệ đo được kiểm định bằng phép đo tín hiệu SH bề mặt của đơn tinh thể ZnSe (001) với cấu trúc phổ SH bề mặt đã biết. Một bản thạch anh (bản λ/2) tuỳ ý được sử dụng như một mẫu thử để đo. Các kết quả đo đạc thực nghiệm phù hợp tốt với lý thuyết mở ra khả năng ứng dụng hệ đo SH trong nghiên cứu các bề mặt vật liệu quang tử, vật liệu sinh học và đặc biệt là các vật liệu cấu trúc nano.

***Từ khoá:*** *Hòa ba bậc hai quang học* (SHG)

## 1. Cơ sở lý thuyết khảo sát bề mặt bằng SHG

Để khảo sát SHG bề mặt người ta thường sử dụng sơ đồ ba lớp có độ phân cực phi tuyến kẹp ở giữa hằng số điện môi ε' trên giao diện (z=0) (hình 1).

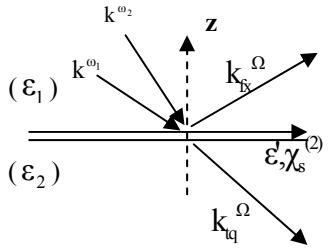


**Hình 1:** Mô hình 3 lớp

Khi một bề mặt hoặc giao diện giữa hai môi trường điện môi hằng số $\varepsilon_1$ và $\varepsilon_2$ được chiếu sáng bởi hai sóng ánh sáng tần số $\omega_1$ và $\omega_2$, độ phân cực phi tuyến bậc hai dẫn đến hiệu ứng phát tần số tổng trên bề mặt có thể viết là:

$$P^{\Omega=\omega_1+\omega_2} = \chi^{(2)}(\Omega).E^{\omega_1}E^{\omega_2} \qquad (1)$$

Trong đó: $\chi^{(2)}$ là tenxơ độ cảm phi tuyến bậc 2

$E^{\omega_1}$ là cường độ điện trường ánh sáng tần số $\omega_1$

$E^{\omega_2}$ là cường độ điện trường ánh sáng tần số $\omega_2$

Sự phát hoà ba bậc hai (SHG) là trường hợp riêng khi $\omega_1 = \omega_2 = \omega$, $\Omega = 2\omega$.

Trong gần đúng lưỡng cực điện, độ phân cực phi tuyến bậc hai chỉ khác không trong môi trường không có đối xứng tâm nghịch đảo. Đối với các môi trường có đối xứng tâm, sự phát hoà ba bậc hai bị cấm bên trong khối tinh thể nhưng cho phép trên bề mặt hoặc giao diện nơi đối xứng nghịch đảo bị phá vỡ. Vì vậy tín hiệu SH bề mặt cho thông tin đặc trưng của bề mặt. Độ dày lớp giao diện này phụ thuộc vào bản chất vật liệu, thông thường vào cỡ một vài lớp đơn phân tử ~10Å, rất nhỏ so với bước sóng khảo sát. Để đặc trưng cho SHG bề mặt người ta đưa ra đại

lượng độ cảm phi tuyến bề mặt $\chi_S^{(2)}$ liên quan đến độ phân cực phi tuyến bề mặt $\mathbf{P}_S$ trên một đơn vị diện tích tạo bởi điện trường trên bề mặt khảo sát.

Trong toạ độ Đề - các có thể viết các thành phần của vectơ $\mathbf{P}_S$ như sau :

$$P_{S,i}^{\Omega}=\chi_{S,ijk}^{(2)}(\Omega).E_j^{\omega_1}\ E_k^{\omega_2} \qquad (2)$$

Trong đó tổng được lấy theo chỉ số lặp lại.

Bức xạ phát ra bởi quá trình phi tuyến này sẽ truyền vào cả môi trường 1 và 2. Hướng của bức xạ phụ thuộc vào hai hệ thức. Thứ nhất đó là hệ thức bảo toàn momen đối với thành phần song song của vectơ sóng trên bề mặt.

$$k_{\parallel}^{\Omega}=k_{\parallel}^{\omega_1}+k_{\parallel}^{\omega_2} \qquad (3)$$

Thứ hai là hệ thức tán sắc đối với bức xạ phi tuyến truyền vào trong các môi trường 1 và 2:

$$k^{\Omega}.k^{\Omega}=\varepsilon(\Omega).(\Omega/c)^2 \qquad (4)$$

$\varepsilon=\varepsilon_1$ hoặc $\varepsilon_2$ tương ứng với khi truyền trong môi trường 1 và 2. Biểu thức cường độ tín hiệu tần số tổng $\Omega$ có thể nhận được bằng cách giải phương trình Maxwell đối với thành phần phân cực phi tuyến (2). Kết quả cường độ tín hiệu tần số tổng ở tần số $\Omega$ là:

$$I^{\Omega}=\frac{8\pi^3\Omega^2\sin^2\theta^{\Omega}}{c^3\sqrt{\varepsilon_1(\Omega)\varepsilon_1(\omega_1)}\varepsilon_1(\omega_2)}|e^{\Omega}\chi_S^{(2)}e^{\omega_1}e^{\omega_2}|^2I^{\omega_1}I^{\omega_2} \qquad (5)$$

$e^{\Omega}.e^{\omega_1}.e^{\omega_2}$ là các vectơ phân cực đã bị chuyển đổi trên giao diện xác định từ các vectơ đơn vị và phép biến đổi Fressnel đối với sóng tới [1,2]. Đối với các vật liệu có đối xứng tâm sự phát tần số tổng của khối là bị cấm trong gần đúng lưỡng cực điện nên có thể bỏ qua.

Xét trường hợp SHG với $\omega_1=\omega_2=\omega, \Omega=2\omega$. biểu thức (2) được viết lại như sau:

$$P_{S,i}^{2\omega}=\chi_{S,ijk}^{(2)}(2\omega).E_j^{\omega}E_k^{\omega} \qquad (6)$$

Trong đó $E_j E_k = E_k E_j$ và các thành phần SHG tuân theo hệ thức $\chi^{(2)}_{S,ijk}=\chi^{(2)}_{S,ikj}$

Để đơn giản ta xét trường hợp ánh sáng tới vuông góc với bề mặt của tinh thể. Trong tọa độ Đề-các chọn trục z là trục ánh sáng chiếu tới, x-y là mặt phẳng biểu diễn bằng bề mặt của mẫu, φ là góc giữa vectơ E của ánh sáng tới và trục x (góc phương vị).

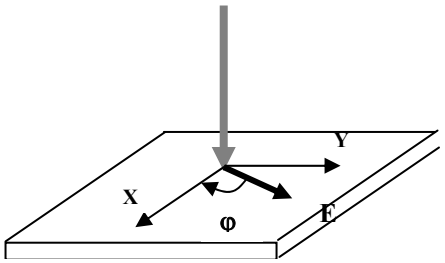


**Hình 2:** Cấu hình chiếu sáng vuông góc

Khi đó (6) đơn giản chỉ còn:

$$\begin{cases}P_{S,x}^{2\omega}=\chi_{S,111}^{(2)}E_x^2+\chi_{S,122}^{(2)}E_y^2+2\chi_{S,112}^{(2)}E_xE_y\\ P_{S,y}^{2\omega}=\chi_{S,211}^{(2)}E_x^2+\chi_{S,222}^{(2)}E_y^2+2\chi_{S,212}^{(2)}E_xE_y\end{cases} \qquad (7)$$

Trong đó $E_x = E\cos\varphi$ và $E_y = E\sin\varphi$

Cường độ SHG theo trục x và y như sau:

$$I_x=A.\left|\chi_{s,111}^{(2)}\cos^2\varphi+\chi_{s,122}^{(2)}\sin^2\varphi+\chi_{s,121}^{(2)}\sin2\varphi\right|^2 \qquad (8)$$

$$I_y=A.\left|\chi_{s,211}^{(2)}\cos^2\varphi+\chi_{s,222}^{(2)}\sin^2\varphi+\chi_{s,212}^{(2)}\sin2\varphi\right|^2 \qquad (9)$$

A là hệ số phụ thuộc vào tần số, cường độ ánh sáng tới và hệ số điện môi của môi trường.

Từ biểu thức (8) và (9) ta thấy cường độ SHG phụ thuộc vào góc phương vị φ và cấu trúc đối xứng bề mặt. Đối với từng đối xứng bề mặt khác nhau thì các yếu tố tenxơ cảm phi tuyến không giống nhau dẫn đến cường độ SHG đối với từng đối xứng là khác nhau. Ở đây chúng tôi chỉ tính toán với đối xứng thường gặp là đối xứng 3m và đối xứng m. Đối với đối xứng 3m, chỉ có thành phần $\chi_{S,111}^{(2)} = -\chi_{S,122}^{(2)} = -\chi_{S,212}^{(2)}$ là không triệt tiêu [1,2] suy ra :

$$\rightarrow \begin{cases} I_x = A\left|\chi^{(2)}_{S,111}\right|^2 \cos^2 2j \\ I_y = A\left|\chi^{(2)}_{S,111}\right|^2 \sin^2 2j \end{cases} \qquad (10)$$

Đối với đối xứng m, chỉ có thành phần $\chi^{(2)}_{S,111}, \chi^{(2)}_{S,122}, \chi^{(2)}_{S,212}$ là không triệt tiêu [1] dẫn đến :

$$\rightarrow \begin{cases} I_x = A\left|\chi^{(2)}_{S,111}\cos^2 j + \chi^{(2)}_{S,122}\sin^2 j\right|^2 \\ I_y = A\left|\chi^{(2)}_{S,212}\sin 2j\right|^2 \end{cases} \qquad (11)$$

Sử dụng ngôn ngữ lập trình matlab chúng tôi đã vẽ đồ thị lý thuyết của các phương trình (10) và (11) ứng với giá trị cụ thể của A và $\chi^{(2)}_S$:

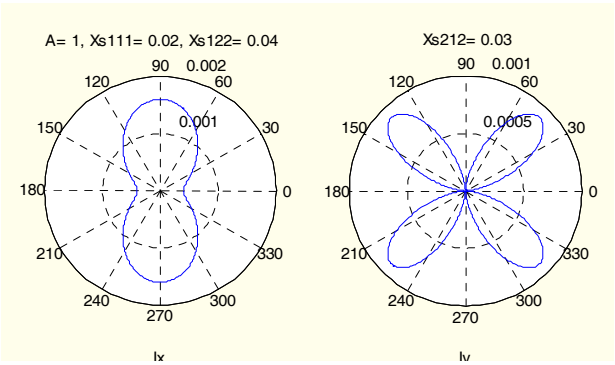


**Hình 3:** Phân bố cường độ SH bề mặt đối xứng 3m đối với hai thành phần phân cực vuông góc $I_x$ và $I_y$ , với A=1, $\chi^{(2)}_{S,111}$=0.04

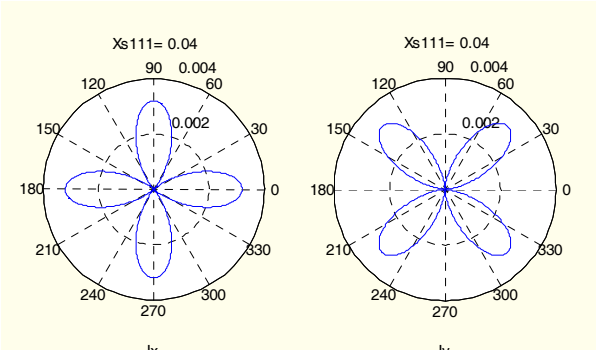


**Hình 4:** Phân bố cường độ SH bề mặt đối xứng m đối với hai thành phần phân cực vuông góc $I_x$ và $I_y$ , với A=1, $\chi^{(2)}_{S,111}$=0.02,$\chi^{(2)}_{S,122}$= 0.04,$\chi^{(2)}_{S,212}$=0.03

Qua đó ta thấy cường độ tín hiệu SH đối với hai thành phần phân cực thẳng vuông góc $I_x$ và $I_y$ đạt cực đại tại các góc phương vị khác nhau. Như vậy thông qua đo đạc cường độ SHG bề mặt trong thực nghiệm và so sánh với lý thuyết có thể xác định cấu trúc đối xứng bề mặt và tìm hiểu những thuộc tính bề mặt của tinh thể .

## 2. Kết quả thực nghiệm và thảo luận

Với những thiết bị hiện có tại phòng thí nghiệm chúng tôi đã bố trí cấu hình chiếu sáng vuông với góc với bề mặt tinh thể. Sơ đồ bố trí như trên hình 5**.** Trong đó $L_1$, $L_2$ là các thấu kính; $P_1$, $P_2$ là các kính phân cực; $F_2$ là kính lọc tần số ω; $M_1$ là gương lưỡng hướng sắc phản xạ 2ω và cho truyền qua ω.

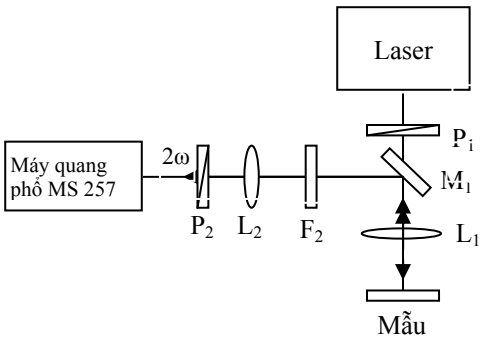


**Hình 5:** Sơ đồ thu SHG bề mặt

Tinh thể được đặt trên một giá đỡ có thể tinh chỉnh được 3 chiều và góc phương vị được điều khiển bằng motor bước ghép nối với máy tính, bước quay nhỏ nhất của motor bước là $1,8^0$ (Hình 6). Với giá đỡ tinh thể do chúng tôi tự chế tạo này góc phương vị có thể điều khiển hoàn toàn tự động theo mong muốn với những góc quay nhỏ và tinh thể luôn quay xung quanh một truc cố định.

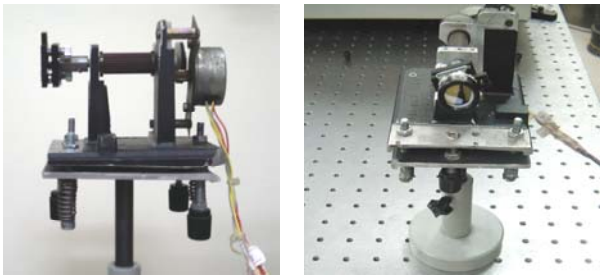

**Hình 6**. Giá đỡ tinh thể điều khiển bằng motor bước

Tín hiệu SHG bề mặt được thu bằng máy quang phổ MS-257 (Oriel-Newport, USA). Máy quang phổ này dùng hệ thu CCD (charge couple device) IntraSpec$^{TM}$ IV 1064x 256 pixel với độ nhạy 100 lần cao hơn mạng điôt PDA. Giới hạn dò là 3,8 femto Jun/cm$^2$, năng lượng phơi sáng bão hoà 250 pico Jun/cm$^2$, ồn đọc thấp (<13 electron) và vùng phổ làm việc là 180-1100nm. Tín hiệu SHG bề mặt thu qua máy quang phổ dùng cách tử phân giải cao nên lọc được hoàn toàn các bước sóng không mong muốn. Nguồn bơm chúng tôi sử dụng trong thí nghiệm này là Laser Quanta Ray Pro 230 Nd:YAG có bước sóng cơ bản 1064nm, hoạt động ở chế độ Q-switch, độ rộng xung 8ns, tần số lặp lại 10Hz, năng lượng xung tối đa 1200mJ

**Hình 7a**

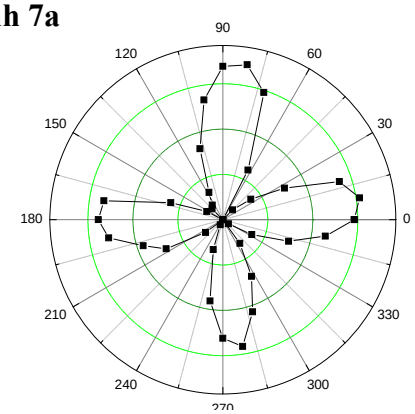


**Hình 7b**

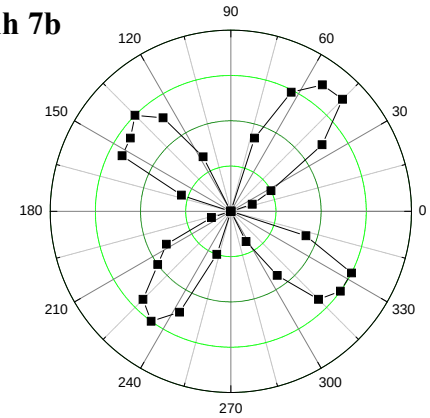


**Hình 7a :** Sự phụ thuộc vào góc phương vị của $I_x$ -cường độ SH từ bề mặt tinh thể ZnSe (001)
**Hình 7.b :** Sự phụ thuộc vào góc phương vị của $I_y$ -cường độ SH từ bề mặt tinh thể ZnSe (001)

Tinh thể ZnSe (001) thuộc nhóm điểm $4\bar{3}m$ đã được khảo sát lý thuyết từ trước [8], có cấu trúc phổ SHG đã biết, được sử dụng làm mẫu chuẩn để xác định chế độ hoạt động của hệ thiết bị . Sau khi xử lý và biểu diễn trên tọa độ cực, kết quả đo tín hiệu SH bề mặt được biểu diễn trên hình 7 .

Kết quả thực nghiệm thu được phù hợp khá tốt với những tính toán lý thuyết đối với tinh thể ZnSe. Điều này đã khẳng định hệ đo tín hiệu SHG bề mặt mà chúng tôi đã xây dựng thực hiện đã có chất lượng tốt, đủ khả năng phân biệt các thành phần tín hiệu bề mặt rất yếu với các tổ hợp phân cực khác nhau của chúng. Từ đây có thể sử dụng sơ đồ này để nghiên cứu tính chất, thuộc tính của các bề mặt vật liệu khác.

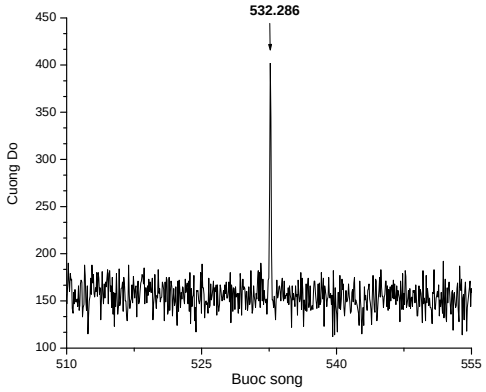


**Hình 8:** Bước sóng SHG thu được từ bề mặt thạch anh

Để thử nghiệm, chúng tôi đã đo SHG bề mặt của một bản λ/2 bằng Thạch anh. Do sử dụng sơ đồ chiếu sáng vuông góc, không cần phải chú ý đến trạng thái phân cực thẳng của chùm bơm. Tín hiệu SH rất yếu yếu từ bề mặt Thạch anh thu trên máy quang phổ MS-257 có phổ rất sắc nét, tỷ lệ tín hiệu trên ồn cao (hình 8). Các thành phần phân cực $I_x$ và $I_y$ của tín hiệu SH được lọc lựa nhờ kính phân cực $P_2$ và được đo với các vị trí góc phương vị khác nhau. Kết quả được biểu diễn theo tọa độ cực như trên hình 9.

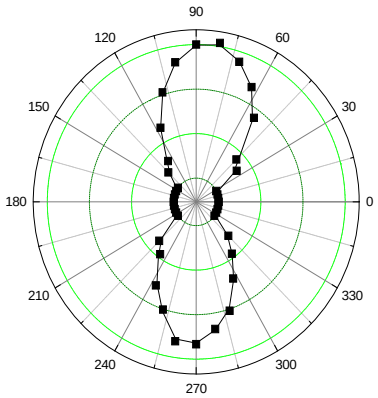


**Hình 9a:** Sự phụ thuộc vào góc phương vị của thành phần cường độ SH $I_x$ từ bề mặt tinh thể thạch anh

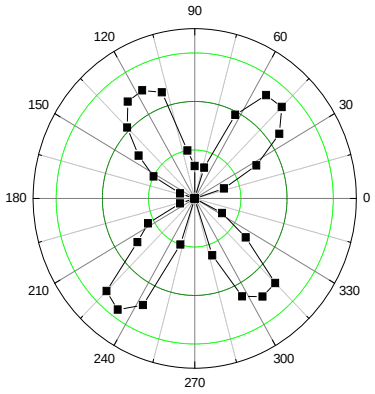


**Hình 9b:** Sự phụ thuộc vào góc phương vị của thành phần cường độ SH $I_x$ từ bề mặt tinh thể thạch anh

Ta thấy cường độ SHG từ bề mặt của bản λ/2 bằng thạch anh có phân bố đối xứng quay hoàn toàn giống phân bố trên hình 4, phù hợp với đối xứng bề mặt loại m ( $\alpha$-$SiO_2$)

## 3. Kết luận

Những phép đo ở trên đã được lặp lại nhiều lần đều cho thấy cùng kết quả chứng tỏ hệ đo SHG của chúng tôi đã xây dựng có độ tin cậy cao. Việc thu được đối xứng quay của các thành phần phân cực SH bề mặt rất yếu này là một thành công mới trong quá trình nghiên cứu xây dựng một hệ đo quang phổ hoà ba bậc hai bề mặt của chúng tôi. Kết quả đã thu được mở ra khả năng ứng dụng của hệ đo này nhằm khảo sát các bề mặt vật liệu khác nhau đặc biệt là các bề mặt vật liệu cấu trúc nano rất nhạy với SHG bề mặt ví dụ các hạt nano bạc, nano vàng v.v…và tiến tới khảo sát các vật liệu sinh học. Đây đang là vấn đề đang thu hút được nhiều quan tâm trên thế giới.

***Lời cảm ơn :*** *Chúng tôi xin trân trọng cám ơn sự hỗ trợ tài chính của đề tài NCCB mã số 4 061-60 trong Chương trình nghiên cứu khoa học Cơ bản Nhà nước để thực hiện nghiên cứu này*

**Tài liệu tham khảo**


1. Y.R.Shen Surface contribution versus bulk contribution in surface nonlinear optical spectroscopy.Appl.Phys.B 68,295-300 (1999)
2. T.F.Heinz ,H.Ponath and G.Stegeman Nonlinear optical effects at surface and interface electromagnetic phenomena Elsevier, Amsterdam,1991
3. Chikashi Yamada and Takahiro Kimura 193 Phys.Rev.Lett.**70**, 2344(1993)
4. N.Butcher and D.Cotter The elements of nonlinear optics. Cambridge University England 1990.
5. P.Guyott-Sionnest,W.Chen and Y.R Chen, Phys.Rev.B 33,8254 (1986)
6. H.Sano, G. Mizutani Phys.Rev. B70,1(2004)
7. Nguyen The Binh, *"Surface probe by second harmonic generation"* Advances in Photonics and Applications, pp . 75-81 (2004).
8. Nguyen The Binh, *"The polarization dependences of surface second harmonic generation".* Proceeding of the 9th APPC, Hanoi Vietnam 2004.p. 525-529
9. Nguyen The Binh, Do Thi Thu Hanh *"Crystalline Surface Probe by Optical Second Harmonic Generation"* Osaka-Asia Pacific- Hanoi Forum 2005, Osaka University Press p.299-300 (2005)